Spectroscopic and Chemometric Investigations into the Modes of Action of Anti-Diabetic and Anti-Cancer Drugs

THE UNIVERSITY OF SYDNEY

By

Brad Swarbrick

A thesis submitted in fulfilment of the requirements for the degree of Doctor of Philosophy (Science)

The University of Sydney

2021

Certificate of authorship and originality

I certify that the work in this thesis has not been previously submitted for a degree, nor has it been submitted as part of the requirements for a degree except as fully acknowledged within the text.

I also certify that the thesis has been prepared and written by me. Any help that I have received in the course of my research and the preparation of this thesis has been acknowledged. In addition, I certify that all the information sources and literature referenced have been recorded in the thesis.

NAME:

DATE:

Acknowledgements

It is not possible to complete such a venture without a group of dedicated support personnel with specific areas of expertise behind you. In this respect, my research has been greatly enhanced by the support of various members and groups within the University of Sydney.

First and foremost, I am truly grateful to my supervisors, Prof. Peter Lay and Dr. Elizabeth Carter for their expertise and support during my project, your understanding and flexibility have allowed me to get to this stage. To Dr. Aviva Levina, you are the rock behind the Lay research group and without your constant support and expertise, I don't think this thesis would have been possible. Thank you for your wonderful insights and instruction in cell biology and related testing protocols.

I would like to make special mention to the following people who have helped me along the way in the various areas of biological, spectroscopic and chemometrics analysis. To Prof. David James, Dr James Krycer and Dr Jacki Stockli of the Charles Perkins Centre, thank your assistance and especially to Dr Krycer for your insights into adipocyte biology and cell culturing techniques, this was one of the most challenging cell lines to culture and your help will always be remembered.

Research was undertaken on the Infrared Microspectroscopy (IRM) beamline at the Australian Synchrotron, part of ANSTO. To Drs. Mark Tobin, Jittaporn (Pimm) Vongsvivut and Keith Bambery at the Australian Synchrotron, many thanks for your expertise in infrared spectroscopy and data interpretation. Acknowledgment of travel funding to the Australian Synchrotron is also given to ANSTO. I also acknowledge travel funding provided by the international synchrotron access program (ISAP), managed by the Australian Synchrotron, and funded by the Australian Government for travel to the Advanced Light Source (APS) in Chicago for research performed using their synchrotron facilities, however, this work was not published in this thesis.

Having worked in industry for nearly 20 years before starting this Ph.D., I had the privilege of working with a number of world recognised experts in chemometrics and pharmaceutical production. I would not be the chemometrician I am today without the guidance and mentoring of Dr Frank Westad of Ideltechs Norway, you are a colleague and friend for life. To Prof. Kim Esbensen, thank you for instilling the discipline required for completing a research project. Coming from industry, I am used to solving problems quickly and moving onto the next task, but in a research environment, the world is a lot

different. Thank you for guiding me through the path from sampling to analysis. It was truly an honour to co-author a textbook with you and write so many critical reviews with you regarding the (mis)use of chemometrics.

This research was facilitated by access to Sydney Analytical, a core research facility at the University of Sydney. To my colleagues at Sydney Analytical, Drs. Joonsup Lee and Michelle Wood, thank you for your support and for putting up with my antics, especially Joonsup, who had to share an office with me for a number of years. There was always laughter and fun times when we were together. I would also like to extend a warm thanks to Ms Therese Harrison at Sydney Analytical for our interesting conversations and the work we did in conservation using vibrational spectroscopy and chemometrics. To Dr. Nick Proschogo, although we planned many times to incorporate our work together, it never eventuated, however, I am truly thankful to you for being there when I needed someone to talk to when thinks got tough.

Vibrational spectroscopic projects cannot proceed without instrument vendors and their support. In this regard, I would like to thank Mr. David Marston, Dr. Koman Tam and Mr. Roger Wagner from Bruker who helped me with instrument and software issues, Mr Andrew Bales from Agilent Technologies, thanks you for being a friend for over 20 years. In respect to the new quantum cascade laser technology, I would like to thank Dr. Adrian Cernescu of NeaSpec instruments for helping me to obtain some amazing images of microvesicles.

I would like to thank my colleagues in the Lay research group for interesting discussion and support. In particular, I would like to thank Mr. Thomas Stewart for helping me survive the trip to the Advanced Light Source in Chicago, getting through those 20 hr days was a challenge, but we seemed to have found a way to laugh through the delirium. To Ms. Kartika Wardhani, thanks you for helping me with the flow cytometry studies, we got some really good results out of that work. To my friend Anthony Chetcuti, thank you for your wisdom and making the world a better place to be in when you were around.

For financial support during my Ph.D. I am grateful to the School of Chemistry for the Florence Mabel and Henry Bertie Gritton research scholarship and also for being awarded the Joan R. Clark research scholarship where I spent seven weeks at the Advanced Light Source (APS). Thanks to Drs. Stefan Vogt and Barry Lai for assisting me in my research and acknowledgement of travel support for my research is given to the APS by the Argonne National Laboratory. Thanks also goes to the Australian Institute for Nanoscale

Science and Technology (AINST) at the university of Sydney for the inaugural AINST postgraduate top-up scholarship. I am also thankful for financial support from Discover and LIEF grants provided by Professor Lay.

Most importantly, you are nothing without the support of family and friends. To my wife Sarah, your unconditional love and support have made this possible. Your constant prodding to get the thesis out of the way has got it to this stage. To our children, James and Amy, I hope the work performed in this thesis and my examples in life serve as an inspiration to you and that you see there is benefit in hard work and passion.

List of Publications

M.J. Tobin, J. Vongsvivut, D.E. Martin, K.H. Sizeland, M.J. Hackett, R. Takechi, N. Fimorgnari, V. Lam, J.C. Mamo, E.A. Carter, B. Swarbrick, P.A. Lay, D.A. Christensen, D. Perez-Guaita, E. Lowery, P. Heraud, B.R. Wood, L. Puskar, K.R. Bambery, Focal plane array IR imaging at the Australian Synchrotron, Infrared Physics & Technology, Volume 94, 2018, Pages 85-90,

Table of Contents

Chapter 1 Spectroscopic and Chemometric Investigations into the Modes of Action of Vanadium Prodrugs for Better Understanding of the Metabolic Syndrome 1

1.1 Introduction: The Sugar Epidemic 2

1.2 Fructose Metabolism 5

1.3 Metabolic Syndrome; its Causes, Complications and Effects 8

1.4 Insulin and Insulin Resistance 11

1.4.1 Insulin 11

1.4.2 Insulin Resistance 13

1.4.3 Fructose Induced Insulin Resistance 16

1.4.4 Endothelin Induced Insulin Resistance 17

1.5 Insulin Mimetics and Insulin Enhancers 19

1.5.1 Vanadium as an Insulin Mimetic 21

1.5.2 Vanadium as an Anti-Cancer Therapeutic. 25

1.5.3 Oxidative Stress and Reactive Oxygen, Nitrogen and Chlorine Species 28

1.6 Vibrational Spectroscopy 32

1.6.1 Fourier Transform Infrared Microspectroscopy 32

1.6.2 Synchrotron Based FTIR Microspectroscopy 36

1.7 Design of Experiments (DoE) and Multivariate Data Analysis (MVDA) 38

1.7.1 Rational Design of Experiments (DoE) 38

1.7.1.1 Design Types 39

1.7.1.2 Design Construction and Terminology 40

1.7.1.3 Regression Model for DoE 42

1.7.1.4 The Box-Behnken Design 43

1.7.2 Multivariate Data Analysis (MVDA) 44

1.7.2.1 Principal Component Analysis (PCA) 45

1.7.2.2 Partial Least Squares Regression (PLSR) 49

1.7.2.3 Partial Least Squares Discriminant Analysis (PLS-DA) 51

1.7.2.4 MVDA Terminology 53
1.8 Hyperspectral Image Analysis (HSI) 55
1.9 Aims and Thesis Outline 57
Chapter 2 Experimental 60
2.1 Chapter Overview 61
2.2 Materials 61
2.3 Cell Culture Protocols 63
2.3.1 Culture of 3T3-L1 Adipocytes 63
2.3.2 Culture of HepG2 Cells 64
2.4 Cell Counting 64
2.5 General Cell Seeding and Fixation Protocol onto Calcium Fluoride Substrate 64
2.5.1 3T3-L1 pre-adipocyte seeding protocol 64
2.5.2 HepG2 seeding protocol 65
2.5.3 Cell Fixation Protocol 65
2.6 Cell Treatment Protocols 65
2.6.1 Preparation of Glucose, Fructose and Vanadate Stock Solutions 66
2.6.2 General Sugar-Vanadate Treatment Protocols 66
2.6.3 Inducement of Insulin Resistance in 3T3-L1 cells 67
2.6.4 Cisplatin Treatments of HepG2 Cells 67
2.6.5 Doxorubicin Treatments of HepG2 Cells 67
2.7 Cell Viability Assay 67
2.8 Spectroscopic and Hyperspectral Imaging Methodology 68
2.8.1 Laboratory Based FTIR Measurements 68
2.8.2 Synchrotron Based FTIR Measurements 69
2.8.2.1 Point- and Raster-Scanning 69
2.8.2.2 Four Beam Synchrotron FPA Imaging 69
2.8.3 Spectral Data Acquisition and Processing 70
2.9 ^{51}V NMR Spectroscopy 70

2.10 Data Analysis Methodology 70

Chapter 3 Optimisation of Fourier Transform Infrared (FTIR) Microspectroscopic Point Scanning and Focal Plane Array (FPA) Imaging 72

3.1 Introduction 73

3.2 Parameters, Protocols and Spatial Resolution 73

3.3 Substrates 77

3.4 Optimisation of Point and Raster Scanning Data Acquisition Parameters of the Bruker Hyperion 3000 Microscope at The Australian Synchrotron. 78

3.4.1 Sample Selection and General Instrument Setup 78

3.4.2 Optimisation of Spectral Coadditions 80

3.4.3 Optimisation of Spectral Processing of SR-FTIR Data 85

3.4.3.1 Multiplicative Scatter Correction (MSC) 86

3.4.3.2 Normalisation and Derivatives 86

3.4.3.3 Standard Normal Variate (SNV) 87

3.4.3.4 Spectral Analysis: 3000-1000 cm^{-1} Region 87

3.4.3.5 Spectral Analysis: 1800-1000 cm^{-1} Region 90

3.4.3.6 Reduced Wavenumber Region Comparison of Small and Large Pinholes 92

3.4.4 Justification of Coadditions Used to Acquire Spectral Data 94

3.5 Infrared Chemical Mapping at the Australian Synchrotron 97

3.5.1 Large Pinhole Assessment 98

3.5.1.1 Effect of Step Size 101

3.5.1.2 Effect of Condenser Focus 101

3.5.2 Small Pinhole Assessment 104

3.6 Depth Profiling Study 107

3.7 Optimisation of Raster Scanning Data Acquisition Parameters for the Bruker Hyperion 3000 Microscope at Sydney Analytical. 110

3.7.1 Optimisation of Aperture Size and Spectral Coadditions. 110

3.7.2 Assessment of Spectral Variability. 115

3.8 Focal Plane Array IR Imaging 116
3.8.1 Laboratory based FPA Imaging 116
3.8.2 Four Beam Synchrotron Radiation FPA Imaging 118
3.9 A Note on Spectral Variability 124
3.10 Chapter Summary 125
Chapter 4 Vibrational Spectroscopic Investigations of Adipocytes as Models of Diabetes and Metabolic Syndrome. 127
4.1 Introduction 128
4.2 Experimental Design and Objectives 130
4.3 Results 131
4.3.1 Vanadate Cytotoxicity 131
4.3.2 FTIR Chemometric Assessments of Insulin Sensitive Single Cells 133
4.3.3 FTIR Chemometric Assessments of Insulin Resistant Single Cells 140
4.3.4 Comparison of Insulin Sensitive and Insulin Resistant Cells 146
4.3.5 Effects of Sugars and Vanadate on Insulin Sensitive and Resistant 3T3-L1 Adipocytes Using Single Cell Point Spectra FTIR Microspectroscopy. 149
4.3.5.1 Analysis of Sugar Treatments, Insulin Sensitive 3T3-L1 Adipocytes (Block 1) 150
4.3.5.2 Analysis of Vanadate Sugar Treatments, Insulin Sensitive 3T3-L1 Cells (Block 2) 152
4.3.5.3 Analysis of Sugar Treatments, Insulin Resistant 3T3-L1 Adipocytes (Block 3) 156
4.3.5.4 Analysis of Vanadate-Sugar Treatments, Insulin Resistant 3T3-L1 Adipocytes (Block 4) 159
4.3.5.5 Comparison of Block Treatments 162
4.3.5.6 Analysis of Centre Points 162
4.4 Discussion 165
4.4.1 Vanadate as an Insulin Mimetic and Cytotoxic Agent 165
4.4.1.1 Vanadate as an Insulin-Mimetic/Enhancer 166

4.4.1.2 Vanadate as a Cytotoxic Agent 169
4.4.2 Fructose Metabolism and Induced Oxidative Stress 172
4.4.2.1 Fructose Metabolism in Insulin-Sensitive Adipocytes 172
4.4.2.2 Fructose Metabolism in Insulin-Resistant Adipocytes 175
Chapter 5 Spectroscopic and Chemometric Investigations of the Effects of Vanadate, Cisplatin and Doxorubicin Towards the HepG2 Cell Line 180
5.1 Introduction – The HepG2 Cell Line as a Model of Insulin Resistance, Metabolic Disorders and Anti-Cancer Therapies 181
5.2 Experimental Design and Objectives 182
5.3 Results 184
5.3.1 Cytotoxicity of Vanadate, Cisplatin and Doxorubicin towards HepG2 Cells Using MTT Assay 184
5.3.2 Investigation of the Cytotoxicity of Vanadate, Cisplatin and Doxorubicin Towards HepG2 Cells Using FTIR Microspectroscopy. 184
5.3.2.1 Chemometric Assessment of Vanadate Treated HepG2 Cells Cytotoxicity Study 188
5.3.2.2 Chemometric Assessment of Cisplatin Treated HepG2 Cells 192
5.3.2.3 Chemometric Assessment of Doxorubicin Treated HepG2 Cells 195
5.3.2.4 Comparison of Vanadate, Cisplatin and Doxorubicin Treatments of HepG2 198
5.3.3 Investigation of Vanadate Action on HepG2 Cells Using Full Factorial Design: Sugar and Vanadate Treatments. 202
5.3.4 Analysis of Designed Experiment Using Single Point Spectra. 206
5.3.4.1 Analysis of Sugar Treatments (Block 1) 207
5.3.4.2 Analysis of Sugar-Vanadate Treatments (Block 2) 210
5.3.4.3 Overall Factorial Design Analysis 213
5.3.4.4 Assessment of Centre Points 215
5.4 Discussion 217
5.4.1 Modes of Action of Metallodrugs 217

5.4.2 Vanadate Mode of Action 217
5.4.3 Vanadate Cytotoxicity Towards HepG2 219
5.4.3.1 Growth Phase Model 220
5.4.3.2 Apoptosis and Cell Death Phase 222
5.4.3.3 Protein Aggregation/Phenotype Change Phase 225
5.4.4 Comparison of Vanadate to Cisplatin and Doxorubicin Modes of Action 227
5.4.5 Fructose Induced Metabolic Changes in HepG2 230
5.4.5.1 Designed Cytotoxicity Assay Experiment 230
5.4.5.2 Sugar Metabolism by HepG2 Cells 231
5.4.5.3 Sugar-Vanadate Metabolism by HepG2 Cells 233
5.4.5.4 Effect of Sugars and Vanadate at Non-Cytotoxic Concentrations 235
Chapter 6 FPA Imaging of Adipocytes 237
6.1 Introduction 238
6.1.1 Laboratory Based FPA Imaging 238
6.1.2 Synchrotron Focal Plane Array (FPA) Measurements 239
6.1.3 The Diffraction Limit Applied to FPA Imaging 240
6.2 Experimental Design and Objectives 240
6.3 Results 241
6.3.1 Effects of Sugar and Vanadate on Insulin Sensitive and Resistant 3T3-L1 Cells using Laboratory-Based Focal Plane Array (FPA) FTIR Spectroscopy 241
6.3.1.1 HIA Assessment of Block 1 Treatments 245
6.3.1.2 HIA Assessment of Block 2 Treatments 251
6.3.1.3 HIA Assessment of Block 3 Treatments 256
6.3.1.4 HIA Assessment of Block 4 Treatments 260
6.3.2 Effects of Sugar Treatments of 3T3-L1 Adipocytes Using Synchrotron FPA Microspectroscopy 268
6.3.2.1 FPA Analysis of Glucose Treated Adipocytes on 0.2 mm CaF_2 Substrates 268

6.3.2.2 FPA Analysis of Glucose Treated Adipocytes on 0.5 mm CaF_2 Substrates 270

6.3.2.3 FPA Analysis of Glucose Treated Adipocytes on 1.0 mm CaF_2 Substrates 273

6.4 Discussion 275

Chapter 7 Conclusions and Further Work 278

7.1 Conclusions 279

7.1.1 FTIR Microspectroscopy as a Tool for Investigating Pro-drug Induced Biochemical Changes 279

7.1.2 Optimisation of Spectral Data Acquisition Parameters and Processing Methods 279

7.1.3 FTIR Microspectroscopic Assessment of 3T3-L1 Adipocytes 283

7.1.4 FTIR Microspectroscopic Assessment of HepG2 Cells 285

7.1.5 FPA Hyperspectral Image Analysis of 3T3-L1 Adipocytes 289

7.2 Future Work 290

References 295

Appendices 338

Appendix 1 339

Appendix 2 341

List of Figures

Figure 1.1: The structure of the disaccharide sucrose, glucose and fructose (only the predominant chemical structures are given). 2

Figure 1.2: Sugar metabolism in the liver. Sucrose is cleaved in the small intestine into glucose and fructose. Glucose metabolism is regulated by the insulin pathway, whereas fructose metabolism is unregulated. In this figure, the following definitions are: HK, hexokinase; FK, fructokinase; ADP, adenosine diphosphate; ATP, adenosine triphosphate; PHI, phosphohexose isomerase; F-1-P, fructose-1-phosphate; G-6-P, glucose-6-phosphate; F-6-P, fructose-6-phosphate; F-1,6-P, fructose 1,6-biphosphate; PFK-1, phosphofructokinase; GA, glyceraldehyde; G-3-P, glycerol-3-phosphate; DAHP, dihydroxyacetone phosphate; GA-3-P, glyceraldehyde-3-phosphate; PK, pyruvate kinase; Acetyl-CoA, acetyl coenzyme A; NADHP, nicotinamide adenine dinucleotide phosphate; and TCA, tricarboxylic acid cycle (citric acid or Kreb's cycle). Each enzyme plays its role in converting glucose and fructose into energy stores for utilisation by the various tissues in the body. Adapted from Port, *et al*. Curr Opin Endocrinol Diabetes Obesity, 2012, 19:367-374, with permission Wolters Kluwer Health, Inc.[20] 4

Figure 1.3: Conceptualisation of the ghrelin, insulin and leptin cascade. Preprandial signalling through ghrelin results in the feeling of hunger. After food ingestion and breakdown, nutrients, including sugars such as glucose and fructose are metabolised, primarily in the liver until a feeling of satiety has been reached. Adipose tissue then releases leptin which crosses the blood brain barrier and signals the hypothalamus to limit the intake of more food.[17] 6

Figure 1.4: Diagrammatic and optical micrograph of a single 3T3-L1 mouse adipocyte cell collected during this work. 7

Figure 1.5: Circulatory insulin binds to the α-subunit of the insulin receptor (tyrosine kinase), which then autophosphorylates at the trans-membrane β-subunit to activate its catalytic activity. This triggers a complex sequence of cascades, including activation of PI3K and PIP_3 to TC10 activation and translocation of GLUT4 to the cell membrane, to facilitate glucose entry into the cell for metabolism. Glucose is converted into glycogen for storage and excess glucose can also be converted into TAGs and free fatty acids (FFA).[60,63] Adapted by permission from Springer Nature, Saltiel and Kahn, Insulin signalling and the regulation of glucose and lipid metabolism, copyright, 2001.[60] Created with BioRender.com. 12

Figure 1.6: GLUT2 transports glucose into the liver for metabolism, energy storage (glycogen) and its subsequent release through the process of gluconeogenesis. It can also use glucose for gene expression, or mitochondrial processing of pyruvate via the Kreb's cycle into Acyl-CoA for further conversion into fatty acids. For acronyms see **Figure 1.2** in addition to: F-1,6-Pase, fructose 1,6-biphosphate kinase; PEPCK, phosphoenolpyruvate carboxykinase; SREBP, sterol regulatory element binding protein; HNF, hepatic nuclear factor; FoxA, forkhead protein; PGC1, PPARγ-co-activator 1; ACC, acetyl-CoA carboxylase; and FAS, fatty-acid synthase. Adapted by permission from Springer Nature, Saltiel and Kahn,[60] Insulin signalling and the regulation of glucose and lipid metabolism, copyright, 2001. Created with BioRender.com. 13

Figure 1.7: Model of insulin resistance in endothelial cells. Elevated levels of Ang II, FFAs, glucose, and proinflammatory cytokines induced by insulin resistance and diabetes result in the stimulation of PKC isoforms to phosphorylate IRS1/2 and PI3K and inhibition of the IRS/PI3K/Akt pathway. The stimulation of the SOS/Grb2/MAPK pathway by insulin is unaffected or even enhanced. The selective loss of insulin activity via the IRS/PI3K/Akt pathway causes the reduction of its antiatherosclerotic action and contributes to acceleration of atherosclerosis and other cardiovascular pathologies in diabetes. PTEN, phosphatase and tensin homolog. Adapted from the American Diabetes Association, King, *et al.* Selective Insulin Resistance and the Development of Cardiovascular Diseases in Diabetes: The 2015 Edwin Bierman Award Lecture, 2016, copyright, all rights reserved.[86] Created with BioRender.com. 16

Figure 1.8: Fructose induces insulin resistance through the overproduction of TAG/VLDL and through the uric acid pathway. GLUT5 fructose transport leads to phosphorylation by F1K in an unregulated manner to result in rapid depletion of ATP. This activates the uric acid pathway leading to a reduction in insulin-dependent NO-mediated vascular dilation and other cellular effects in adipocytes. *De novo* lipogenesis (DNL) produces intracellular triglycerides that can induce insulin resistance. Adapted from Johnson, *et al.*[39] Hypothesis: Could Excessive Fructose Intake and Uric Acid Cause Type 2 Diabetes? *Endocrine Reviews*, 2009, 30(1):96-116, by permission of Oxford University Press. 18

Figure 1.9: Chemical structure of Endothelin-1 (ET-1) a potent vasoconstrictor with pro-atherosclerotic activity. 19

Figure 1.10: The chemical structures of the phosphate and vanadate groups are similar. The V-O bond lengths in vanadate are not much longer than those of the P-O bond lengths (1.7 vs 1.54 Å).[133-134].....22

Figure 1.11: PTP inhibition by vanadate. Bis(maltolato)oxovanadium(IV) (BMOV) is used as an example. BMOV is orally ingested and is postulated to remain intact until it reaches its target site of action. Physiological conditions promote the oxidation of the V(IV) complex to V(V) as the vanadate ion. Adapted by permission from Springer Nature, Rehder.[136], Vanadium in Health Issues, copyright, 2001. Created with BioRender.com.....23

Figure 1.12: Modes of cellular uptake of anti-diabetic/anti-cancer vanadium compounds. Reproduced by permission from John Wiley and Sons, Levina, A. and Lay, P. A.,[111] Stabilities and Biological Activities of Vanadium Drugs: What is the Nature of the Active Species? Chemistry - An Asian Journal, copyright, 2017. 24

Figure 1.13: The complex pathways of action of vanadium compounds as anticancer therapeutics. Cytotoxic effects are induced via DNA cleavage pathways or via cell membrane degradation through lipoperoxidation. Chemoprevention is induced via pathways that minimise the production or inactivate carcinogen derived metabolites (possibly extracellular vesicles come into this category). The most common pathway, as also reported for vanadium antidiabetic action is through the inhibition of PTP and the activation of PTK's leading to signal transduction pathways including apoptosis, inhibition of cell proliferation, invasion, metastasis and the lowering of drug resistance. Reproduced from Critical Reviews in Oncology/Hematology, Evangelou.*[129]* Vanadium in Cancer Treatment, 42, 249-265, copyright 2002, with permission from Elsevier.....28

Figure 1.14: Protein secondary structures; a) α-helix and; b) β-pleated sheet. 31

Figure 1.15: Three types of spectral data acquisition used in FTIR microspectroscopy: a) point scanning; b) line or grid mapping; and c) focal plane array (FPA) detector, which uses a two-dimensional array of detector elements of specified size.....33

Figure 1.16: Description of two modes of data collection used in FTIR microspectroscopy. Incident radiation is focussed by the microscope to the user defined region of interest (ROI) where it penetrates the cell membrane and is either reflected back towards the direction of the incident radiation (reflectance) or is transmitted through the sample (transmission).....33

Figure 1.17: Comparison of the intensity and beam spot of SR compared to typical Globar® sources of laboratory-based FTIR microspectrometers, which shows the increased brilliance (intensity) of synchrotron light sources and the broad dispersion of the Globar® source. Reproduced from Kimura, S. and Okamura, H. Infrared and Terahertz Spectroscopy of Strongly Correlated Electron Systems Under Extreme Conditions, J. Phys. Soc. Jpn. 82, 021004 (2013). © 2013.....37

Figure 1.18: Experimental strategies: a) the OFAT approach holds all variables constant except for the one under investigation constant while optimising the response based on changing the single variable; b) the orthogonal factorial design covers the maximum experimental design space in a minimum number of experimental runs. The contours represent the actual, but initially unseen response surface, which is dependent on both variables simultaneously. As shown, the OFAT approach can easily miss the optimal response using a one-dimensional approach to experimentation.....40

Figure 1.19: A 2^3 full factorial design in two-levels with a centre point (*cp*). The design space is defined as a cube and the volume enclosed by the cube is exactly modelled using linear regression methodology.[223,225] In this figure, standard DoE terminology is used to label the experimental runs that define each point of the cube. This terminology is defined in the in the text.....41

Figure 1.20: The Box-Behnken (BB) design in three experimental factors; a) shown in cartesian coordinates; and b) shown as the points on a sphere. 44

Figure 1.21: Conceptual t_1 vs. t_2 scores plot showing four clusters of objects. The four clusters show tight within cluster grouping, which demonstrates small interclass variability and strong separation from other classes. This situation represents an ideal situation in which every class can be uniquely interpreted through analysis of the loadings (*p*). 47

Figure 1.22: Example p_1 loadings line plot showing the inverse relationship between the two highly weighted bands at 1743 cm^{-1} (lipid ester, C=O) and 1650 cm^{-1} (C=O, α-helix protein secondary structures). The lipid band is highly positively weighted, while the protein band is negatively weighted.....48

Figure 1.23: Joint interpretation of; a) scores; b) loadings and; c) reconstructed **X**. The two clusters in the scores plot are described by the inverse relationship of the loadings at 1743 cm^{-1} and 1650 cm^{-1}. Since the data are second derivatised, the higher the content of a particular component, the more negative the band. Cluster 1 is defined by negative t_1

values, therefore, negative scores × positive loading at 1743 cm^{-1} results in a more negative lipid band in the reconstructed **X** data. The inverse situation occurs for Cluster 1 at the 1650 cm^{-1} loading, negative scores × negative loadings result in a more 'positive' protein band when added to the mean spectrum. The reverse situation occurs for Cluster 2. 48

Figure 1.24: Example of a PLSR overview plot showing; a) explained **Y**-variance plot, indicating the number of optimal PLSR factors to interpret; b) PLSR scores showing the object relationships as related to the *y*-response; c) the predicted vs. reference plot showing the quality of the model for a selected number of PLSR factors; and d) the regression coefficient plot showing the important variables used to predict the *y*-response for a selected number of PLSR factors. 51

Figure 1.25: PLS-DA predicted vs. reference plot showing discrimination of classes based on a binary class variable. When more than two class variables are being modelled, there is one predicted vs. reference plot per class. If the predicted result is close to 1 and within the 95% confidence interval, the object is considered to be a member of that class. If it is not a member of the class, it will either lie close to 0 (for objects with classes defined by the model) or in the ambiguous classification zone, for objects with no classes defined by the model. 53

Figure 1.26: Representation of the pseudo-three-way data structure associated with chemical mapping and hyperspectral imaging; a) representative data structure showing the pixel directions as one plane and the variables as a second independent direction; b) an example of a hyperspectral cube showing the data structure. 55

Figure 1.27: The process of developing a hyperspectral image analysis (HIA): a) the original data are represented by a pseudo-three-way data cube; b) matricising the data along the variable direction results in a long table of (pixel 1 × pixel 2 direction) × variables; c) analysis of the long, two-way data table using PCA or other multivariate methods; and d) mapping of the scores back to the original image space. 56

Figure 1.28: The process of masking in HIA; a) original scores image using all pixels for the calculation of the PCA model; b) masking the region of interest (ROI) based on the sample outline; and c) recalculation of the model without the unimportant pixels. 57

Figure 3.1: *x*-*y*-*z*-optical stage of the Bruker Hyperion 3000 FTIR microscope with a 36× Cassegrain microscope objective installed. The stage has a slotted sample holder wide enough to capture reliable spectra of cells fixed to CaF_2 substrate and small enough to

minimise the risk of the sample dropping into the microscope condenser, located underneath the stage. 74

Figure 3.2: Schematic diagram of a Cassegrain microscope objective used for FTIR microspectroscopy. Various cell lines can be chemically fixed to a substrate, e.g., CaF_2, where cell densities naturally vary from very sparse to dense colonies. 75

Figure 3.3: a) Digital image of a CaF_2 substrate with chemically fixed HepG2 cells and; b) optical micrograph of the region of interest (ROI) as viewed under the microscope of the Bruker Hyperion 3000 system at 36× magnification. The red grid in b) represents a single cell either measured as a single-point spectrum by setting the aperture to the size of the cell, or mapped over a predefined grid of appropriate aperture and step size. 75

Figure 3.4: Detectivity vs. wavenumber (cm^{-1}) of commonly used MCT detectors in mid-infrared spectroscopy. Adapted from Application Note AN M161, Bruker Optiks, GmbH.[264] 77

Figure 3.5: Optical micrographs of 3T3-L1 adipocytes chosen to optimise data acquisition parameters on a Bruker Hyperion 3000 FTIR Microscope at 36× magnification..... 78

Figure 3.6: Averaged spectra acquired from the selected positions of 3T3-L1 adipocyte cells 1 and 2. **Table 3.2**. details the justification of the selection and description of cell biochemistry. Spectra were acquired using 128 coadditions at a resolution of 4 cm^{-1} with the large mechanical pinhole inserted (~0.6 mm). 80

Figure 3.7: Raw spectra acquired from four points on two 3T3-L1 adipocyte cells (**Table 3.2**); a) small pinhole; b) medium pinhole and; c) large pinhole. Pinhole sizes correspond to those listed in **Table 3.4**..... 82

Figure 3.8: PCA scores and loadings plots for spectral data collected from four repeated positions using; a) small; b) medium; and c) large pinholes. Three PC models for each pinhole accounted for >90% of the **X**-variance in each case. 84

Figure 3.9: t_1 vs. t_2 vs. t_3 scores plot of FTIR spectra collected on four cell positions using a small mechanical pinhole and grouped by number of coadditions. Cell positions marked based on their cluster. 85

Figure 3.10: PCA of two 3T3-L1 cells measured at four positions using a large pinhole, processed using the Savitzky-Golay second derivative (13-point smooth) then SNV over

the wavenumber region 3000-1050 cm^{-1}; a) t_1 vs. t_2 scores; b) p_1 loadings; c) p_2 loadings; and d) p_3 loadings. 89

Figure 3.11: a) raw spectra; and b) processed spectra of 3T3-L1 adipocytes over the wavenumber region 3650-2640 cm^{-1}. 90

Figure 3.12: a) t_1 vs. t_2 scores; and b) p_1, p_2 loadings of a PCA model of 3T3-L1 spectra collected at four positions using a large pinhole over the wavenumber region 1800-750 cm^{-1}. Spectra were collected at 16, 32, 64, 128 and 256 coadditions and processed using second derivative (13-point smooth) and SNV over the defined wavenumber region. .. 92

Figure 3.13: Comparative PCA models for data assessed over; a) 1800-1050 cm^{-1}; b) 1800-1100 cm^{-1}; and c) 1800-1150 cm^{-1}. Data were acquired using a large pinhole and processed using a second derivative (13-point smooth) then SNV over the selected wavenumber regions. 93

Figure 3.14: Comparative PCA of a) 13-point second derivative, SNV; and b) nine-point second derivative, SNV preprocessed spectra acquired using a small pinhole over the wavenumber region 1800-1200 cm^{-1}. 94

Figure 3.15: Comparison of spectra acquired using a) large pinhole; b) small pinhole; and c) combined data with 16, 32, 64, 128 and 256 coadditions (13-point second derivative spectra) over the wavenumber region 1800-750 cm^{-1} for Cell 2, Position 1. 95

Figure 3.16: Optimisation spectral coaddition for; a) large; b) medium; and c) small pinholes calculated over specified wavenumber regions. The *x*-axis (1800-X) represented the wavenumber region from 1800 cm^{-1} to the value listed on the axis, e.g., the first point on the *x*-axis represented the wavenumber region 1800-750 cm^{-1}. 96

Figure 3.17: Spatial resolution and oversampling in SR-FTIR microspectroscopy using mechanical pinholes; a) large pinhole using a 3.5 μm step size; b) large pinhole using a 7 μm step size; c) small pinhole using a 4 μm step size; and d) small pinhole using a 2 μm step size. 98

Figure 3.18: Integrated false colour maps (3.5 μm step size) and blended images of a 3T3-L1 adipocyte, acquired using a large pinhole at a resolution of 4 cm^{-1} and 16 coadditions in a 14×10-pixel grid; a) contour plot integrated at 1743 cm^{-1}; b) pixel map integrated at 1743 cm^{-1}; c) blended map at 1743 cm^{-1}; d) contour plot 1654 cm^{-1}; e) pixel map 1654 cm^{-1}; and c) pixel map of 1654 cm^{-1} region blended with the optical micrograph. 99

Figure 3.19: Scores images and associated loadings plots for a single 3T3-L1 cell acquired using a large pinhole and a 3.5 μm step size for the first two PCs only; a) image collected using 16 coadditions, PC1; b) 16 coadditions, PC2; c) 128 coadditions, PC1; and d) 128 coadditions, PC2. Spectra were collected in the wavenumber region 3000-1000 cm^{-1}. Map size, 14×10. 100

Figure 3.20: Scores images and associated loadings plots for a single 3T3-L1 cell acquired using a large pinhole and a 7 μm step size for the first two PCs only; a) image collected using 16 coadditions, PC1; b) 16 coadditions, PC2; c) 128 coadditions, PC1; and d) 128 coadditions, PC2. Spectra were acquired over the wavenumber range 3000-1000 cm^{-1}. Map size, 7×5. 102

Figure 3.21: Energy throughput of; a) aligned; and b) offset condenser focus of a 3T3-L1 adipocyte. 103

Figure 3.22: Comparsion of FTIR spectra collected when the condensor was aligned and offset according to the settings shown in **Figure 3.21**. The inset shows the region between 1100-900 cm^{-1}. 103

Figure 3.23: Integrated false colour maps and blended images (4 μm step size) of a 3T3-L1 adipocyte, acquired using a small pinhole at a resolution of 4 cm^{-1} and 256 coadditions in a 12 × 8 grid. See **Figure 3.18** for a description of this figure. 104

Figure 3.24: Scores maps and associated loadings plots for a single 3T3-L1 cell acquired using a small pinhole and a 4 μm step size for the first two PCs only; a) map collected using 16 coadditions, PC1; b) 16 coadditions, PC2; c) 256 coadditions, PC1; and d) 256 coadditions, PC2. Spectra were acquired over the wavenumber range 3000-1000 cm^{-1}. Map size, 12×8. 105

Figure 3.25: Integrated band, scores maps and associated loadings plots for a single 3T3-L1 cell acquired using a small pinhole and a 2 μm step size, with 256 coadditions for the first two PCs only; a) integrated map at 1743 cm^{-1} (lipid); b) 256 coadditions PC1 scores map; c) 256 coadditions PC2 scores map; d) 128 coadditions, PC2; d) integrated map at 1654 cm^{-1} (amide I); e) PC1 loadings; and f) PC2 loadings. Spectra were anaysed over the wavenumber range 3000-1000 cm^{-1}. Map size, 23×15. 106

Figure 3.26: Depth profiling experiment showing how the *x*-*y*-*z*-stage was moved in the *z*-direction in 5 μm steps from the substrate surface (defined at 0 μm). 107

Figure 3.27: Depth profiling optical micrographs of a 3T3-L1 cell defocussed at; a) 0 μm; b) 5 μm; c) 10 μm; and d) 15 μm from the substrate surface. The circles represent a grid of nine measurement points taken at the same position of the single cell for comparison. 108

Figure 3.28: PCA scores and loadings for the depth profile study; a) t_1 vs t_2 scores plot showing how the measurements gradually increase in variability with focus from the substrate; b) t_1 vs. t_2 vs. t_3 scores plot; c) p_1 loadings; and d) p_2 loadings. 109

Figure 3.29: Depth profiling study performed using a small pinhole at 0- and 15 μm focus to substrate; a) raw spectra; and b) processed spectra..... 109

Figure 3.30: Optical micrograph with acquisition points of a representative HepG2 cell (~25×25 μm^2) grown in supplemented media and chemically fixed to a CaF_2 substrate using cold methanol. 110

Figure 3.31: Raw FTIR spectra of a single HepG2 cell shown in **Figure 3.30** acquired in transmission mode at 4 cm^{-1} resolution; a) spectra grouped by number of coadditions; and b) spectra grouped by aperture size. Five replicate positions were scanned for each experiment. 112

Figure 3.32: t_1 vs t_2 scores for PCA models of HepG2 spectra acquired using various coadditions and aperture sizes. The data were colour grouped by aperture size; a) nine-point second derivative; b) 13-point second derivative; c) nine-point second derivative, SNV; and d) 13-point second derivative, SNV. The 30×30 μm aperture points were difficult to observe in figures a) and b), respectively and lie in the centre of the ellipses located around the (0,0) scores values. 113

Figure 3.33: t_1 vs. aperture size grouped by; a) aperture size, where it was observed that spectral variance was minimised from an aperture size of 16×16 μm; and b) number of coadditions, where two processes are described by the piecewise straight-line fits. These linear fits are a function of both aperture size and number of coadditions. 114

Figure 3.34: t_1 vs. aperture size colour grouped by number of coadditions between 12×12 to 30×30 μm. 114

Figure 3.35: a) Diagrammatic representation of the 6×6 μm aperture defined by the Bruker OPUS software; and b) comparison of the Globar® beam spot with respect to the aperture size. The actual aperture size is 12×12 μm. 114

Figure 3.36: FBSD vs. aperture size for 128 and 256 spectral coadditions. Beyond the 20×20 μm aperture, there was a marked decrease in spatial resolution due to the size of the aperture being of similar size to the cell dimensions. 116

Figure 3.37: 64×64 FPA image of a 3T3-L1 adipocyte; a) optical micrograph; and b) false colour image integrated at the lipid band ~1743 cm^{-1}. 117

Figure 3.38: a) 10×5-pixel ROI of a 3T3-L1 adipocyte for optimisation study; and b) extracted raw FTIR spectra from the ROI, colour grouped by number of coadditions. Spectra were acquired at 4 cm^{-1} resolution and were displayed in the wavenumber region 3000-1000 cm^{-1}. 117

Figure 3.39: a) t_1 vs. t_2 scores; and b) FBSD plot of selected spectra acquired by FPA FTIR microspectroscopy at 128, 256 and 512 coadditions for the ROI shown in **Figure 3.38**. The PCA and FBSD assessment confirm that 256 or 512 coadditions were required to collect images with low spectral variability. 118

Figure 3.40: FPA images of a 3T3-L1 adipocyte integrated in the lipid region 1743 cm^{-1} and amide I region 1654 cm^{-1} for images acquired at; a) 128; b) 256; and c) 512 coadditions. 119

Figure 3.41: Focussed beamlines at the Australian Synchrotron to match the optical pupil of the Bruker Vertex FTIR spectrometer and Hyperion 3000 Microscope for use with an FPA detector; a) inner 32×32 pixel array highlighted; b) expanded 32×32 region before fine adjustment of focussing mirrors and; c) energy distribution after adjustment of the focussing mirrors. Figure adapted with permission, from Tobin, *et al*,[255] and, Dynamic full field infrared imaging with multiple synchrotron beams, Stavitski, *et al*.[282] Copyright, 2013, American Chemical Society. 119

Figure 3.42: Optical micrographs of 3T3-L1 adipocytes showing the morphology of; a) Control; b) Glucose; c) Fructose; and d) Glucose-Fructose treatments. Cells were fixed to the to 0.5 mm thick CaF_2 substrate using cold methanol. Treatment conditions are listed in **Table 3.11**. 120

Figure 3.43: Raw FTIR spectra collected on a control 3T3-L1 adipocyte using the four-beam synchrotron FPA microspectrometer. 121

Figure 3.44: Integrated FPA images of a 3T3-L1 adipocyte; a) optical micrograph; b) lipid ester region; c) amide I; d) membrane fatty acids and lipids; e) amide II; and f)

glycogen and phosphates. The amide band images highlighted the effects of coherent aberrations. 122

Figure 3.45: FPA images of a differentiated 3T3-L1 adipocyte with no contrasting applied; a) integrated at 1654 cm^{-1} (amide I); and b) 1550 cm^{-1} (amide II)..... 122

Figure 3.46: a) optical micrograph of a differentiated 3T3-L1 adipocyte fixed to a 0.5 mm thick CaF_2 substrate; and b) t_1 scores image for Savitzky-Golay second derivative (nine-point smooth) data. 123

Figure 3.47: HSI analysis of a FPA image acquired on a differentiated 3T3-L1 adipocyte chemically fixed to a CaF_2 substrate; a) t_1 scores image and associated loadings; and b) t_2 scores image and associated loadings. 123

Figure 4.1: 3T3-L1 adipocyte cell morphology as observed in; a) culture media using an upright light transmission microscope (Olympus CKX31/CKX41 Phase Contrast and Fluorescence Inverted Microscope, 20x magnification); b) a round cell with partially resolved features; and c) a high-quality image clearly showing the multilocular structure. Images b) and c) were aquired from adipocytes chemically fixed to the CaF_2 substrate prior to image acquisition in transmission mode using the Hyperion 3000 microscope. 129

Figure 4.2: Experimental design for investigating the effects of sugars, vanadate and insulin resistance using the orthogonal 2^4 full factorial design in 20 runs, (Chapter 1, Section 1.7.1). The design is based on two blocks defined by insulin sensitivity/resistance. Low levels of factors are defined by (-1) and high levels by (+1), while centre points are defined by (0). 131

Figure 4.3: ^{51}V NMR spectrum of 1.0 mM Na_3VO_4 in cell culture medium (16 h pre-incubation + 72 h incubation at 310 K). Data courtesy of Dr. Aviva Levina. 132

Figure 4.4: a) raw; and b) processed FTIR spectra of individual insulin-sensitive 3T3-L1 cells treated with various concentrations of vanadate. The prominent absorbance bands (in the negative direction only) are listed in the figure with assignments in **Table 1.1**. (Chapter 1). The legend defines the treatment concentrations used in the study..... 133

Figure 4.5: t_1 vs. t_2 scores plot for insulin-sensitive 3T3-L1 vanadate study; a) scores coloured by vanadate treatment concentration; and b) separated into three arbitrary groups labelled; low 0-15 μM; medium 31-125 μM; and high 250-1000 μM. Local Hotelling's T^2 ellipses were drawn at 95% confidence. 134

Figure 4.6: $t_1 - t_3$ scores vs. [V(V)] for insulin-sensitive 3T3-L1 adipocytes as all data and interval plots: a) t_1 scores plot; b) t_2 scores plot; and c) t_3 scores plot. Dotted lines represent the observed trends in the data. Intervals were drawn at 95% confidence.... 135

Figure 4.7: a) p_1; b) p_2; and c) p_3 loadings plots for the insulin-sensitive 3T3-L1 adipocytes treated with vanadate. 137

Figure 4.8: Ratio of processed FTIR band intensities at 2922 and 2957 cm^{-1} vs. [V(V)] for insulin-sensitive adipocytes. Intervals are displayed for each treatment at the 95% confidence level. 138

Figure 4.9: Ratio of processed FTIR band intensities at 1146 and 2957 cm^{-1} vs. [V(V)] for insulin-sensitive adipocytes. Intervals are displayed for each treatment at the 95% confidence level. 139

Figure 4.10: a) raw; and b) processed FTIR spectra of insulin-resistant 3T3-L1 adipocytes treated with various concentrations of vanadate. The prominent band assignments are listed in **Table 1.1**..... 141

Figure 4.11: t_1 vs. t_2 scores plot for insulin-resistant 3T3-L1 vanadate study: a) scores coloured by vanadate treatment concentration; and b) separated based on three groups labelled; low range, 0-15 μM; medium range, 31-125 μM; and high range 250-1000 μM. Local Hotelling's T^2 ellipses were drawn at the 95% confidence level..... 142

Figure 4.12: $t_1 - t_3$ scores vs. [V(V)] as individual data and interval plots for insulin-resistant 3T3-L1 adipocytes: a) t_1 scores plot; b) t_2 scores plot; and c) t_3 scores plot. The dotted lines represent the trends observed in the data..... 143

Figure 4.13: a) p_1; b) p_2; and c) p_3 loadings plots for the insulin-resistant 3T3-L1 vanadate treatment model..... 144

Figure 4.14: Ratio of processed FTIR bands at 1146 and 2957 cm^{-1} vs. [V(V)] for insulin-resistant adipocytes. Intervals are displayed for each treatment at the 95% confidence level..... 145

Figure 4.15: Intensity ratio of processed FTIR bands at 2922 and 2957 cm^{-1} vs. [V(V)] for insulin-resistant adipocytes. Intervals are displayed for each treatment at the 95% confidence level. 146

Figure 4.16: t_1 vs. t_2 scores for the PCA model of combined insulin-sensitive and -resistant 3T3-L1 cells treated with various concentrations of vanadate. This data showed that there was no separation in the first two PCs at the 95% confidence level..... 147

Figure 4.17: t_1 vs. t_2 PLS-DA scores for insulin-sensitive and -resistant adipocytes grown in normal supplemented media only. Local Hotelling's T^2 ellipses were drawn at the 95% confidence level. 147

Figure 4.18: w_1 PLS-DA loading weights showing the main spectral differences between insulin-sensitive and -resistant 3T3-L1 adipocytes. 148

Figure 4.19: Projection of spectra acquired on a separate test set of control insulin-sensitive and -resistant 3T3-L1 adipocytes onto the PLS-DA model shown in **Figure 4.17**. The original model samples were designated as Trial 1, while the new samples were designated Trial 2. The dotted line represents a linear discriminator between the data along Factor 1 (difference between insulin-sensitive and -resistant adipocytes) and Factor 2 (difference between cultures). 149

Figure 4.20: Definition of blocks as applied to the analysis sections in this chapter. The design was split by factor D (insulin-resistance) as per usual conventions; however, Blocks 1-4 were defined by the presence or absence of vanadate (C) in the treatments. Factors A and B represent glucose and fructose, respectively. 150

Figure 4.21: PLS-DA scores plots of Block 1 treatments of insulin-sensitive 3T3-L1 adipocytes assessed by FTIR microspectroscopy; a) t_1 vs. t_2 scores plot; and b) t_1 vs. t_2 vs. t_3 scores plots. Local Hotelling's T^2 ellipses were drawn in a) for each treatment at 95% confidence. 150

Figure 4.22: PLS-DA loading weight directions w_1-w_3 for Block 1 treatments of insulin-sensitive 3T3-L1 adipocytes; a) w_1 loading weights; b) w_2 loading weights; and c) w_3 loading weights. 152

Figure 4.23: PLS-DA scores plots of vanadate-sugar treatments (Block 2) of insulin-sensitive 3T3-L1 cells assessed by FTIR microspectroscopy; a) t_1 vs. t_2 scores plot; and b) t_1 vs. t_2 vs. t_3 scores plots. Local Hotelling's T^2 ellipses are drawn in a) for each treatment at 95% confidence. 153

Figure 4.24: Comparison of the processed FTIR spectra for the vanadate only treatment *c* and the fructose-vanadate treatment *bc* conditions for Block 2 insulin sensitive 3T3-L1 cells. 153

Figure 4.25: PLS-DA loading weight directions w_1-w_3 for Block 2 treatments of 3T3-L1 adipocytes; a) w_1 loading weights; b) w_2 loading weights; and c) w_3 loading weights. 155

Figure 4.26: t_3 vs t_2 scores plot of the Block 2 treatments glucose-vanadate (*ac*) and glucose-fructose-vanadate (*abc*) only for insulin-sensitive cells and showed separation of the treatments along the w_3 direction. 156

Figure 4.27: PLS-DA scores plots of sugar treatments of insulin-resistant 3T3-L1 adipocytes (Block 3) assessed by FTIR microspectroscopy; a) t_1 vs. t_2 scores plot; and b) t_1 vs. t_2 vs. t_3 scores plots. Local Hotelling's T^2 ellipses are drawn in a) for each treatment at 95% confidence. 157

Figure 4.28: t_2 vs. t_3 PLS-DA scores for Block 3 insulin-resistant 3T3-L1 adipocytes grouped by treatment conditions. 157

Figure 4.29: PLS-DA loading weight directions w_1-w_3 for Block 3 treatments of insulin-resistant 3T3-L1 adipocytes. a) w_1 loading weights; b) w_2 loading weights; and c) w_3 loading weights. 158

Figure 4.30: PLS-DA scores plots of vanadate-sugar treatments of insulin-resistant 3T3-L1 adipocytes assessed by FTIR microspectroscopy; a) t_1 vs. t_2 scores plot; and b) t_1 vs. t_2 vs. t_3 scores plot. Local Hotelling's T^2 ellipses were drawn in a) for each treatment at 95% confidence. 160

Figure 4.31: PLS-DA loading weight directions w_1-w_3 for Block 4 treatments of insulin resistant 3T3-L1 adipocytes; a) w_1 loading weights; b) w_2 loading weights; and c) w_3 loading weights. 161

Figure 4.32: PLS-DA scores of the entire DoE and Block comparisons; a) all treatment Blocks; b) Blocks 1 and 2 scores; and c) Blocks 3 and 4 scores. Colour grouping was defined in plot b). 163

Figure 4.33: Definition of centre point treatments in the experimental design of **Figure 4.2**. 164

Figure 4.34: PLS-DA model of centre point data showing the separation of the insulin-sensitive and -resistant treatments; a) t_1 vs. t_2 vs. t_3 scores; b) predicted vs. reference plot with discriminating line; c) w_2 loading weights; and d) w_3 loading weights. Samples grouped as per the legend in plot b). 164

Figure 4.35: Postulated four-step process of low concentration vanadate action on insulin-sensitive 3T3-L1 adipocytes: 1) Insulin binds to the insulin-receptor inducing phosphorylation of the receptor β-subunits;[299] 2) activation of pathways that induce GLUT4 translocation for glucose uptake[325]; 3) induction of other biochemical pathways

by normal insulin activated cascade; and 4) insulin-activity enhanced by V(V) inihibition of PTPs with detoxification of excess V(V) by reduction to V(IV) by GSH, which is oxidised to GSSG.[111] Created with BioRender.com. 166

Figure 4.36: Postulated four-step process of low concentration vanadate action on insulin-resistant 3T3-L1 adipocytes: 1) induction of insulin resistance and oxidative stress;[75] 2) vanadate acting as an insulin-mimetic;[111,299] 3) vanadate activation of pathways that induce GLUT4 translocation for glucose uptake;[104] and 4) induction of other biochemical pathways by enhanced peroxidovanadate production.[312] Created with BioRender.com..... 167

Figure 4.37: Postulated four-step process of cytotoxic vanadate action on insulin-sensitive and -resistant 3T3-L1 adipocytes: 1) redox cycling induced by excess vanadate entering into cells;[129,299] 2) increased ROS generated resulting in FFA oxidation and other stresses in the endoplasmic reticulum (ER); 3) mitochondiral damage induced by metabolism of oxidised fatty acids inducing lipotoxicity;[146] and 4) loss of integrity in membrane lipids induced by lipid peroxidation.[195] Created with BioRender.com. 170

Figure 4.38: Postulated model of fructose metabolism in adipocytes for higher than physiological concentrations showing; 1. Fructose entry into adipocytes via the GLUT5 transporter;[33] 2. TAG and FFA synthesis induced by pyruvate, including production of VLDL and protein synthesis;[11,352] and 3. Oxidative stress induced by fructose metabolism. Created with BioRender.com. 173

Figure 4.39: Postulated model of vanadate action towards insulin-resistant adipocytes in the presence of high sugar concentrations. The cell is already under high oxidative stress induced by insulin-resistance and represented by the ROS symbol;[75] 1. Vanadate entry into adipocytes via phosphate or sulfate ion channels; 2. Glucose uptake stimulated by vanadate;[110] 3. Synthesis of glycogen and lipids from glucose; 4. Fructose uptake through GLUT 5 transporter; 5. Increased oxidative stress leads to mitochondrial and ER damage and synthesis of TAGs and FFAs.[361] 178

Figure 5.1: Experimental design for investigating the effects of sugars and vanadate using the orthogonal 2^3 full factorial design in 11 runs. Standard notation for experimental runs was used as described by Montgomery.[226] The design was based on two blocks defined by treatments with and without vanadate. 183

Figure 5.2: MTT assay results for cell viability of HepG2 cells treated with; a) sodium orthovanadate; b) cisplatin; and c) doxorubicin serially diluted by factors of two from the

maximum concentration. The curves in all treatments were modelled using a sigmoidal curve fit, for experiments performed in triplicate. Error bars were drawn at the 95% confidence level for six replicate wells per treatment. 185

Figure 5.3: Raw and processed FTIR spectra of HepG2 cells treated with; a) vanadate; b) cisplatin; and c) doxorubicin. The processing applied to the data was atmospheric correction,[372] followed by Savitzky-Golay second derivative (second order polynomial, 13-point smoothing) and normalisation using standard normal variate (SNV) over the wavenumber region 3000-2800 and 1800-1000 cm^{-1}. The individual spectra were coloured according to the legend in c). 186

Figure 5.4: Optical micrographs of HepG2 cells; a) In the absence of, or at low concentrations of vanadate (0-15.6 μM); b) in the concentration range 31-125 μM vanadate (at the IC_{50} point); and c) at 1000 μM. 187

Figure 5.5: Optical micrographs of HepG2 high vanadate concetration treatment and reproliferation experiment; a) 62.5 μM; b) 250 μM; and c) 1000 μM. Top row; fixed vanadate treated cells; and bottom row, cells after re-proliferation (72 h in normal glucose suplemented vanadate-free medium). 187

Figure 5.6: t_1 vs. t_2 scores plot for HepG2 vanadate study; a) scores grouped by vanadate treatment concentration; and b) separated into groups based concentration ranges identified in the MTT assay curve; cell proliferation range 0-15 μM; cell death range 31-125 μM; and almost complete cell death range 250-1000 μM, with data from surviving cells. Local Hotelling's T^2 ellipses were drawn at 95% confidence. 188

Figure 5.7: t_1 -t_3 scores vs. [V(V)] as all data and interval plots. a) t_1; b) t_2; and c) t_3 scores. Data coloured by legend in a). Error bars represent standard deviations of scores values at the 95% confidence level. 190

Figure 5.8: PCA loadings plots for vanadate cytotoxicity experiment; a) p_1 loadings; b) p_2 loadings; and c) p_3 loadings plots. Important bands have been marked on each plot. 191

Figure 5.9: PCA scores plots for cisplatin treated HepG2 cells; a) t_1 vs. t_2 scores grouped by treatment concentration; b) t_1 vs. t_2 scores grouped by three phases; c) t_2 vs. t_3 scores grouped by treatment concentration; and d) t_2 vs. t_3 scores grouped by three phases. Plots a) and c) grouped by legend in plot c) and plots b) and d) grouped by legend in plot d). 192

Figure 5.10: t_1 to t_3 scores vs. [cisplatin] as all data and interval plots. a) t_1 scores indicating the possibility of the 12.5 μM treatment being an outlier; b) t_2 scores showing high resemblance to the MTT assay curve; and c) t_3 scores, again showing that the 12.5 μM treatment may be an outlier. 193

Figure 5.11: PCA loadings plots for cisplatin cytotoxicity experiment; a) p_1 loadings; b) p_2 loadings; and c) p_3 loadings plots. Important bands have been marked on each plot. 194

Figure 5.12: t_1 vs. t_2 scores plots for HepG2 doxorubicin study; a) scores grouped by doxorubicin treatment concentration; and b) separated into groups based on the three phases; 0-0.16 μM; rapid cell death between 0.31-1.25 μM; and 2.5-10 μM. Local Hotelling's T^2 ellipses were drawn at 95% confidence. 196

Figure 5.13: t_1 and t_2 scores vs. [doxorubicin] as all data and interval plots; a) t_1 scores; and b) t_2 scores vs. [doxorubicin]. The 1.25 μM treatment in b) may be an outlier. The dotted lines indicate the best fit of the data and in particular, the dotted curve in b) does not take into account the 1.25 μM treatment. 197

Figure 5.14: PCA loadings plots for doxorubicin cytotoxicity experiment; a) p_1 loadings; and b) p_2 loadings. Important bands have been marked on each plot. 197

Figure 5.15: a) t_1 vs. t_2; and b) t_1 vs. t_2 vs. t_3 scores plots for PLS-DA model of HepG2 cells treated with three cytotoxic agents. Hotelling's T^2 ellipses were drawn at the 90% confidence level. Sample grouping was performed as per the legend at the bottom of plot b). 198

Figure 5.16: t_1 vs. t_3 scores plot of all treatments highlighting the control points for each cytotoxic agent studied. This arrangement of scores clearly showed that all control points were similar in the t_1 direction. Local Hotelling's T^2 ellipses drawn at the 90% confidence level. 199

Figure 5.17: t_1 vs. t_2 scores of HepG2 cells treated with vanadate, cisplatin and doxorubicin. This plot was grouped by vanadate concentrations over the ranges 0-15 μM; 31-125 μM and 250-1000 μM. Cisplatin and doxorubicin treatments were groups as overall treatments. 199

Figure 5.18: PLS-DA loading weights for cisplatin, doxorubicin and vanadate treated HepG2 cells; a) w_1 loading weights; b) w_2 loading weights; and c) w_3 loading weights. Important bands are marked in each plot. 201

Figure 5.19: Experimental design of the factorial design cell viability assay. The edge wells were left blank resulting in six replicates of the ten treatments of the designed experiment. Two centre points (*cp1* and *cp2*) were run as a measure of design repeatability. Three replicate plates were run to determine the reproducibility of the design. The terminology of the experimental runs was previously described in Chapter 1, Section 1.7 and also in **Figure 5.1**. 203

Figure 5.20: Cell viability assay results obtained using a modification of the MTT assay and the experimental design in **Figure 5.1**. Each variable in the interval plot represented an experimental run and the intervals represented the variability within results of three replicates of the design. Block 1 described treatments *1, a, b* and *ab* and Block 2 described treatments *c, ac, bc* and *abc*. The centre points (*cp's*) represented the mid-points of all treatment concentrations. 204

Figure 5.21: Response surface plot of HepG2 designed experiment model. The centre points represent treatments at 2.5 mM glucose and fructose and 25 μM vanadate. For the linear model to be valid, the centre point should ideally lie close to the plane of the model. In this case, the linear model was not the best fit to the data and a quadratic model provided a better fit. 205

Figure 5.22: Response surfaces of a simulated Box-Behnken analysis of cell viability showing the quadratic surface associated with the promotion of cell growth at vanadate concentration values less than the IC_{50} value; a) 0 μM; b) 25 μM; c) 50 μM [V(V)]; and d) The Box-Behnken (BB) design used to generate the results. These plots are indicative only, based on results generated from a PLS model. 206

Figure 5.23: a) Raw FTIR point spectra; and b) normalised, second derivative spectra of HepG2 cells over the wavenumber region 3000-1000 cm^{-1}. Plots were colour grouped by the legend in plot b)..... 207

Figure 5.24: t_1 vs. t_2 vs. t_3 PLS-DA scores plot of HepG2 cells treated with sugars and assessed by FTIR microspectroscopy. Local Hotelling's T^2 ellipses are drawn for each treatment at 75% confidence. 208

Figure 5.25: PLS-DA loading weights for Block 1 treatments of HepG2 cells; a) w_1 loading weights; b) w_2 loading weights; and c) w_3 loading weights. Important bands are marked in each plot. 209

Figure 5.26: t_1 vs. t_2 vs. t_3 PLS-DA scores plot of HepG2 cells treated with sugars and assessed by FTIR microspectroscopy. Local Hotelling's T^2 ellipses are drawn for each treatment at 75% confidence. 211

Figure 5.27: PLS-DA loading weights for Block 2 treatments of HepG2 cells; a) w_1 loading weights; b) w_2 loading weights; and c) w_3 loading weights. Important bands are marked in each plot. 212

Figure 5.28: t_1 vs. t_3 scores plot of Block 2 treatments. The t_1 direction separated the frutose-vanadate treatment (*bc*) while the t_3 direction described the differences between the glucose-fructose-vanadate (*abc)*, the glucose-vanadate (*ac*) and the vanadate-only (*c*) treatments. The *ac* and *bc* treatments were defined by scores centred around zero in the t_3 direction..... 213

Figure 5.29: a) t_1 vs t_2; and b) t_1 vs. t_2 vs. t_3 PLS-DA scores plots of Block 1 and Block 2 HepG2 sugar and vanadate treatments. Calibration scores were marked by a circle and validation by a rectangle in the t_1 vs. t_2 plot. Blocks coloured by legend in plot b). 213

Figure 5.30: PLS-DA loading weights for Block 1 and Block 2 comparison of HepG2 cell treatments; a) w_1 loading weights; b) w_2 loading weights; and c) w_3 loading weights. Important bands are marked in each plot. 214

Figure 5.31: Projection of centre points onto the Block 1 and 2 PLS-DA model of HepG2 cells treated with sugars and vanadate. Hotelling's T^2 ellipses drawn at the 90% confidence level. 216

Figure 5.32: Postulated growth phase action of vanadate towards HepG2 at low concentrations (0-15 μM); 1) transport of amino acids into HepG2 cells via AATs provides precursors for GSH production and protein synthesis;[399] 2) vanadate transport into cells via phosphate or sulfate ion channels promotes PTP inhibition at the insulin receptor substrate and triggers downstream processes to result in protein synthesis;[401] 3) insulin receptor activation and signalling of PI3K-Akt pathways;[398-399,402] 4) uptake of glucose via GLUT1 or GLUT3 independent of insulin;[398] 5) depletion of cellular defences by high ROS already induced in cancer cells;[391] 6) activation of mTOR/mTORC1 pathways results in cell proliferation and protein synthesis;[399] and 7) decreased glycogen synthesis in favour of protein synthesis.[311] Created with BioRender.com. 221

Figure 5.33: Postulated cell death pathways due to vanadate towards HepG2 over the concentration range 31-250 μM; 1) Uptake of vanadate, redox cycling and production of peroxidovanadate species inhibit PTPs;[111] 2) inhibition of PI3K/Akt/mTOR pathways and

activation of pentose phosphate pathway (PPP) diverting glucose from glycolysis to synthesis of NADPH;[408] 3) uptake of glucose via GLUT1 and GLUT3 transporters for metabolism;[398] 4) inhibition of fatty acid oxidation (FAO);[311] 5) ROS induced DNA damage to nucleus and mitochondria induced by H_2O_2 and other ROS;[409] 6) AMPK/p53 pathways induced by DNA damage resulting in cell cycle arrest and repair;[340] 7) neutral lipid synthesis induced by apoptosis;[311] and 8) lipid peroxidation induced by increased oxidative stress.[195,202,205] Created with BioRender.com. 224

Figure 5.34: Postulated fibrosis/phenotype change model of vanadate action towards HepG2 over the concentration range 125-1000 μM; 1) inititally, HepG2 cells show a cobblestone, epithelial structure; 2) increased oxidative stress leads to changes in protein secondary structures that results in an increase in β-sheet protein;[175] 3) induction of the p38MAPK pathway results in the formation of amyloid structures, including Aβ-like peptides;[415] 4) Aβ-like peptides induce pathways such as TGF-β and HSP27 that result in the breakdown of actin and the formation of actin stress fibres;[416-417] and 6) when complete breakdown of actin occurs in surviving cells, cell adhesion is lost in favour of a phenotype that is better able to migrate.[411] Created with Biorender.com. 227

Figure 5.35: Modes of action towards DNA of; a) cisplatin;[379] and b) doxorubicin.[140] 229

Figure 6.1: Images of four beam spots focussed onto an FPA detector at the Brookhaven National Laboratory. This image was adapted with permission from, Dynamic full field infrared imaging with multiple synchrotron beams, Stavitski, *et al*.[282] Copyright, 2013, American Chemical Society..... 239

Figure 6.2: Spatial resolution (Δx) vs wavenumbers calculated for a 36× Cassegrain objective with NA = 0.5. The red dotted line is the pixel width for the FoV. 240

Figure 6.3: FPA images of a single 3T3-L1 adipocyte integrated at a number of wavenumber positions related to the main functionality in the cell; a) optical micrograph captured at 36× magnification; b) integrated for fatty acids (~2850 cm^{-1}); c) integrated for lipid esters (~1740 cm^{-1}); and d) integrated for amide I protein (~1650 cm^{-1}). 242

Figure 6.4: HIA assessment of a single 3T3-L1 adipocyte; a) PC1 related to membrane lipids and fatty acids; b) PC2 related the internal lipids and fatty acids; c) PC3 again related to lipids and fatty acids that are different to those of PC2 and; d) PC4 related to complex lipid and protein structures. 244

Figure 6.5: Optical micrographs of selected insulin sensitive 3T3-L1 adipocytes; a) treatment *1*, no-sugar; b) treatment *a*, glucose; c) treatment *b*, fructose; and d) treatment *ab*, glucose-fructose. For treatment terminology, refer to **Figure 4.2**. Scale bar for all images is shown in figure d.....246

Figure 6.6: PC1 scores and loadings for insulin sensitive 3T3-L1 adipocytes, treated according to **Figure 4.2**, Block 1 treatments; a) treatment *1*, no-sugar; b) treatment *a*, glucose; c) treatment *b*, fructose; and d) treatment *ab*, glucose-fructose. Important loadings are highlighted in this figure.....247

Figure 6.7: PC2 scores and loadings for insulin sensitive 3T3-L1 adipocytes, treated according to **Figure 4.2**. Block 1 treatments; a) treatment *1*, no-sugar; b) treatment *a*, glucose; c) treatment *b*, fructose; and d) treatment *ab*, glucose-fructose. Important loadings are highlighted in this figure.....249

Figure 6.8: PC3 scores and loadings for insulin sensitive 3T3-L1 adipocytes, treated according to **Figure 4.2** Block 1 treatments; a) treatment *1*, no-sugar; b) treatment *a*, glucose; c) treatment *b*, fructose; and d) treatment *ab*, glucose-fructose. Important loadings are highlighted in this figure.....250

Figure 6.9: Optical micrographs of selected insulin sensitive 3T3-L1 adipocytes; a) treatment *c*, no-sugar and vanadate; b) treatment *ac*, glucose and vanadate; c) treatment *bc*, fructose and vanadate; and d) treatment *abc*, glucose-fructose and vanadate. For treatment terminology, refer to **Figure 4.2**. Scale bar for all images is shown in figure d. 251

Figure 6.10: PC1 scores and loadings for insulin sensitive 3T3-L1 adipocytes, treated according to **Figure 4.2**. Block 2 treatments; a) treatment *c*, no-sugar-vanadate; b) treatment *ac*, glucose-vanadate; c) treatment *bc*, fructose-vanadate; and d) treatment *abc*, glucose-fructose-vanadate. Important loadings are highlighted in this figure.....252

Figure 6.11: PC2 scores and loadings for insulin sensitive 3T3-L1 adipocytes, treated according to **Figure 4.2** Block 2 treatments; a) treatment *c*, no-sugar-vanadate; b) treatment *ac*, glucose-vanadate; c) treatment *bc*, fructose-vanadate; and d) treatment *abc*, glucose-fructose-vanadate. Important loadings are highlighted in this figure.....254

Figure 6.12: PC3 scores and loadings for insulin sensitive 3T3-L1 adipocytes, treated according to **Figure 4.2** Block 2 treatments; a) treatment *c*, no-sugar-vanadate; b) treatment *ac*, glucose-vanadate; c) treatment *bc*, fructose-vanadate; and d) treatment *abc*, glucose-fructose-vanadate. Important loadings are highlighted in this figure.....255

Figure 6.13: Optical micrographs of selected insulin resistant 3T3-L1 adipocytes; a) treatment *d*, no-sugar; b) treatment *ad*, glucose; c) treatment *bd*, fructose; and d) treatment *abd*, glucose-fructose. For treatment terminology, refer to **Figure 4.2**. Scale bar for all images is shown in figure d.....257

Figure 6.14: PC1 scores and loadings for insulin resistant 3T3-L1 adipocytes, treated according to **Figure 4.2**. Block 3 treatments; a) treatment *d*, no-sugar; b) treatment *ad*, glucose; c) treatment *bd*, fructose; and d) treatment *abd*, glucose-fructose. Important loadings are highlighted in this figure.....258

Figure 6.15: PC2 scores and loadings for insulin-resistant 3T3-L1 adipocytes, treated according to **Figure 4.2**. Block 3 treatments; a) treatment *d*, no-sugar; b) treatment *ad*, glucose. Important loadings are highlighted in this figure.....259

Figure 6.16: PC3 scores and loadings for insulin resistant 3T3-L1 adipocytes, treated according to **Figure 4.2**. Block 3 treatments; a) treatment *d*, no-sugar-vanadate; b) treatment *ad*, glucose-vanadate; c) treatment *bd*, fructose-vanadate; and d) treatment *abd*, glucose-fructose-vanadate. Important loadings are highlighted in this figure.....261

Figure 6.17: Optical micrographs of selected insulin-resistant 3T3-L1 adipocytes; a) treatment c*d*, no-sugar-vanadate; b) treatment *acd*, glucose-vanadate; c) treatment *bcd*, fructose-vanadate; and d) treatment *abcd*, glucose-fructose-vanadate. For treatment terminology, refer to **Figure 4.2**. Scale bar for all images is shown in figure d.....262

Figure 6.18: PC1 scores and loadings for insulin-resistant 3T3-L1 adipocytes, treated according to **Figure 4.2**. Block 4 treatments; a) treatment *cd*, no-sugar-vanadate; b) treatment *acd*, glucose-vanadate; c) treatment *bcd*, fructose-vanadate; and d) treatment *abcd*, glucose-fructose-vanadate. Important loadings are highlighted in this figure. ...263

Figure 6.19: PC2 scores and loadings for insulin resistant 3T3-L1 adipocytes, treated according to **Figure 4.2**. Block 4 treatments; a) treatment *cd*, no-sugar-vanadate; b) treatment *acd*, glucose-vanadate; c) treatment *bcd*, fructose-vanadate; and d) treatment *abcd*, glucose-fructose-vanadate. Important loadings are highlighted in this figure. ...265

Figure 6.20: PC3 scores and loadings for insulin resistant 3T3-L1 cells, treated according to **Figure 4.2**. Block 4 treatments; a) treatment *cd*, no-sugar-vanadate; b) treatment *acd*, glucose-vanadate; c) treatment *bcd*, fructose-vanadate; and d) treatment *abcd*, glucose-fructose-vanadate. Important loadings are highlighted in this figure. 267

Figure 6.21: Optical micrograph and PCA scores images of a single 3T3-L1 adipocyte chemically fixed to a 0.2 mm CaF_2 substrate; a) optical micrograph; b) t_1 scores image; c) t_2 scores image; and d) t_3 scores image. 268

Figure 6.22: PCA loadings for FPA images of a 3T3-L1 adipocyte treated with glucose and chemically fixed to a 0.2 mm CaF_2 substrate; a) p_1 loadings; b) p_2 loadings; and c) p_3 loadings. 269

Figure 6.23: a) t_4 scores image; and b) p_4 loadings for a 3T3-L1 adipocyte treated with glucose and chemically fixed to a 0.2 mm CaF_2 substrate..... 269

Figure 6.24: Optical micrograph and PCA scores images of a single 3T3-L1 adipocyte chemically fixed to a 0.5 mm CaF_2 substrate; a) optical micrograph; b) t_1 scores image; c) t_2 scores image; and d) t_3 scores image. 270

Figure 6.25: PCA loadings for FPA images of a 3T3-L1 adipocyte treated with glucose and chemically fixed to a 0.5 mm CaF_2 substrate; a) p_1 loadings; b) p_2 loadings; and c) p_3 loadings. 271

Figure 6.26: Masked PCA scores images and loadings for a single 3T3-L1 adipocyte chemically fixed to a 0.5 mm CaF_2 substrate. Scores image and loadings for; a) PC1; b) PC2; and c) PC3. 272

Figure 6.27: Optical micrograph and PCA scores images of a single 3T3-L1 adipocyte chemically fixed to a 1.0 mm CaF_2 substrate; a) optical micrograph; b) t_1 scores image; c) t_2 scores image; and d) t_3 scores image. 273

Figure 6.28: PCA loadings for FPA images of a 3T3-L1 adipocyte treated with glucose and chemically fixed to a 1.0 mm CaF_2 substrate; a) p_1 loadings; b) p_2 loadings; and c) p_3 loadings. 274

Figure 6.29: a) t_3 scores image; and b) p_3 loadings for a 3T3-L1 adipocyte treated with glucose and showing the fringing pattern induced by the 1.0 mm CaF_2 substrate. 274

Figure 7.1: Preliminary AFM-IR images and spectra collected from an MV extracted from a sugar treated 3T3-L1 adipocyte; a) AFM topographic image; b) infrared intensity map; c) spectra collected from four locations on the vesicle and; d) the average spectrum of the four positions. Data courtesy of Dr Adrian Cernescu, NeaSpec GmbH..... 294

List of Tables

Table 1.1: Mid-infrared assignment table of typical bands frequently found in biological materials. 34

Table 1.2: Definition and terminology associated with the 2^3 full factorial design with a centre point. 42

Table 1.3: Example responses of a PLS-DA model for a three-class classification problem. 52

Table 1.4: Common terminology used in multivariate (chemometric) modelling. 54

Table 2.1: General reagents used in this study. 61

Table 2.2: Cell Culture Media and Reagents 62

Table 2.3: Cell lines used in this study. 63

Table 2.4: High and low levels of experimental factors used in designed experiments for assessing the effects of sugar and vanadate treatments on the three cell lines investigated in this study. 66

Table 3.1: Main spectral data acquisition parameters of the Hyperion 3000 FTIR microscope (excluding sample coadditions). 76

Table 3.2: Selection and description of cellular biochemistries in **Figure 3.5**. Refer to **Table 1.1** for band assignments relevant to each position. 79

Table 3.3: Experimental conditions employed for FTIR repeatability and reproducibility study. 81

Table 3.4: Pinhole sizes and calculated beam focus sizes used at the Australian Synchrotron*. 83

Table 3.5: Processing methods and parameters applied to spectral data prior to application of multivariate data analysis methods*. 88

Table 3.6: Effect of SNV normalised second derivative spectra on PCA explained variance when applied to different wavenumber segments in the 1800-950 cm^{-1} region. Data are for small and large pinholes acquired using 128 and 256 coadditions only. 91

Table 3.7: Experimental parameters used to evaluate mechanical pinhole, spatial resolution (step size and oversampling) and spectral coadditions when mapping single cells with SR-FTIR spectroscopy. 97

Table 3.8: Experimental design used to evaluate the optimised scanning conditions of the laboratory-based Hyperion 3000 FTIR microspectrometer. 111

Table 3.9: Processing combinations applied to HepG2 point spectra acquired using different numbers of coadditions and various aperture sizes. 112

Table 3.10: Summary of FBSD results obtained from the aperture and coaddition experimental design. 115

Table 3.11: Treatment conditions used to prepare 3T3-L1 adipocyte samples for SR-FTIR-FPA study. 120

Table 3.12: Comparison of instrumental optimisation parameters for Globar®, synchrotron and FPA spectral data acquisition between the literature and this study. . 125

Table 5.1: Experimental factor levels defined for the design shown in **Figure 5.1**. 183

Table 5.2: ANOVA table for HepG2 experimental design; glucose, fructose and vanadate treatments. 205

List of Equations

1.1 43

1.2 43

1.3 46

1.4 46

1.5 49

1.6 49

1.7 49

1.8 50

1.9 50

1.10 50

1.11 51

3.1 76

3.2 86

3.3 87

3.4 94

3.5 95

Abbreviations

2FI	Two Factor Interaction
3FI	Three Factor Interaction
AAT	Amino Acid Transporter
Abs	Absorbance
ACC	Acetyl-CoA Carboxylase
Acetyl-CoA	Acetyl Coenzyme A
ADC	Analogue to Digital Converter
ADP	Adenosine Diphosphate
AFM	Atomic Force Microscopy
Akt	Protein Kinase B
AMP	Adenosine Monophosphate
AMPK	Adenosine Monophosphate Kinase
Ang II	Angiotensin II
AP-1	Activator Protein 1
AS	Australian Synchrotron
ATCC	American Tissue Culture Collection
ATM	Ataxia Telangiectasia Mutated Protein
ATP	Adenosine Triphosphate
ATR	Attenuated Total Reflectance or Ataxia Telangiectasia and Rad3
BAX	bcl-2-like protein 4
BB	Box-Behnken Design
BSA	Bovine Serum Albumin
CCD	Central Composite Design
C_H	Constitutional Heterogeneity

Cp	Centre Point
CVD	Cardiovascular Disease
DAG	Diacylglyceride
DAHP	Dihydroxyacetone Phosphate
D_H	Distributional Heterogeneity
DLS	Diamond Light Source
DMEM	Dulbecco's Modified Eagle Medium
DNA	Deoxyribonucleic Acid
DNL	De Novo Lipogenesis
DoE	Design of Experiments
EDA	Exploratory Data Analysis
elF-4E	Eukaryotic Translation Initiation Factor 4E
EMA	European Medicines Agency
EMSC	Extended Multiplicative Scatter Correction
EMT	Epithelial to Mesenchymal Transition
ER	Endoplasmic Reticulum
ERK	Extracellular Signal Regulated Kinase
ET-1	Endothelin-1
EV	Extracellular Vesicle
F-1-P	Fructose-1-phosphate
F-6-P	Fructose-6-phosphate
F-1,6-P	Fructose 1,6-biphosphate
FAO	Fatty Acid Oxidation
FAS	Fatty Acid Synthase
FBSD	Fixed Block Standard Deviation

FCS	Foetal Calf Serum
FK	Fructokinase
FoV	Field of View
FFA	Free Fatty Acids
FFT	Fast Fourier Transform
FPA	Focal Plane Array
FTIR	Fourier Transform Infrared
G-6-P	Glucose-6-phosphate
GA	Glyceraldehyde
GA-3-P	Glyceraldehyde-3-phosphate
GLUT	GLUT proteins
GSIS	Glucose Stimulated Insulin Secretion
HCC	Human Hepatocarcinoma
HFCS	High Fructose Corn Syrup
HIA	Hyperspectral Image Analysis
HK	Hexokinase
HSI	Hyperspectral Imaging
IC_{50}	Half-Maximum Inhibitory Concentration
ICH	International Conference on Harmonisation
ICS	International Chemometrics Society
IDF	International Diabetes Foundation
IGF	Insulin Like Growth Factor
IL-6	Interleukin-6
IR	Infrared
IRe	Insulin Resistance

IRENI	Infrared Environmental Imaging
IRM	Infrared Microspectroscopy
IRS	Insulin Sensitive Substrate
JNK-1	c-Jun N-Terminal Kinase
LPL	Lipoprotein Lipase
MAPK	Mitogen Activated Protein Kinase
MBSD	Moving Block Standard Deviation
MCR	Multivariate Curve Resolution
MCT	Mercury Cadmium Telluride
ME-EMSC	Mie Extinction Extended Multiplicative Scatter Correction
MEK-1	Mitogen Activated Protein Kinase Kinase
MIR	Mid Infrared
MLR	Multiple Linear Regression
MSC	Multiplicative Scatter Correction
mTOR	Mammalian target of rapamycin
MTT	3-(4,5-dimethylthiazol-2-yl)-2,5-diphenyltetrazolium bromide
MV	Microvesicle
MVDA	Multivariate Data Analysis
N.A.	Numerical Aperture
NADHP	Nicotinamide adenine dinucleotide phosphate
NAFLD	Non-Alcoholic Fatty Liver Disease
NEFA	Non-Esterified Fatty Acids
NF-κB	Nuclear Factor Kappa-Light-Chain-Enhancer of Activated B Cells
NIRS	Near Infrared Spectroscopy
OFAT	One Factor at a Time

PAI	Plasminogen Activator Inhibitor
PARP	Poly (ADP-ribose) polymerase
PBS	Phosphate Buffered Saline
PC	Principal Component
PCA	Principal Component Analysis
PCNA	Proliferating Cell Nuclear Antigen
PDK-1	Pyruvate Dehydrogenase Lipoamide Lipase Isozyme 1
PFK-1	Phosphofructokinase
PGE2	Prostaglandin E2
PI3K	Phosphatidylinositol-3-kinase
PIP_3	Phosphatidylinositol (3,4,5)-triphosphate
PK	Pyruvate Kinase
Phen	1,10-phenanthroline
PHI	Phosphohexose Isomerase
PLS-DA	Partial Least Squares Discriminant Analysis
PLSR	Partial Least Squares Regression
PPP	Pentose Phosphate Pathway
PSD	Particle Size Distribution
PTK	Protein Tyrosine Kinase
PTP	Protein Tyrosine Phosphatase
QbD	Quality by Design
QCL	Quantum Cascade Laser
RCS	Reactive Chlorine Species
RMieS	Resonance Mie Scattering
RNA	Ribonucleic Acid

ROI	Region of Interest
RNS	Reactive Nitrogen Species
ROS	Reactive Oxygen Species
S6K1	Ribosomal Protein S6 Kinase 1
SNV	Standard Normal Variate
SOD	Superoxide Anion Dismutase
Sr-FTIR	Synchrotron Fourier Transform Infrared
T1DM	Type I Diabetes Mellitus
T2DM	Type II Diabetes Mellitus
TAG	Triacyl glycerides
TCA	Tricarboxylic Acid
TGF	Transforming Growth Factor
TNF	Tumour Necrosis Factor
ToS	Theory of Sampling
USD	United States Dollars
VCAM-1	Vascular Cell Adhesion Molecule 1
VEGF	Vascular Endothelial Growth Factor
VLDL	Very Low-Density Lipoprotein
WHO	World Health Organisation
XIAP	X-linked Inhibitor of Apoptosis Protein

Abstract

Metabolic disorders such as Diabetes Mellitus are reaching epidemic proportions in societies that have incorporated the Western diet. Much research has focussed on the detrimental effects of added sugars in the diet and in particular, the effects of fructose and high fructose corn syrup (HFCS). Better understanding on how these sugars are metabolised and the signalling pathways they induce at the cellular level is required. Prevention through improved diet and exercise are always the best approach to minimising lifestyle diseases, however, for individuals who have a metabolic disorder, non-pharmaceutical intervention is always desired. The use of vanadium-derived complexes as dietary supplements or used in food fortification offer one such alternative due to their purported antidiabetic and anti-cancer effects; however, their mode(s) of action are still not completely understood.

This study used vibrational spectroscopic techniques such as Fourier-transform infrared (FTIR) microspectroscopy to gain insights into biochemical changes induced by sugars and treatments with sodium orthovanadate. Treatments were applied to the insulin-responsive cell lines 3T3-L1 mouse adipocyte (fat cells) and HepG2 (human hepatocarcinoma, HCC) as they have been reported to be representative models for understanding biochemical changes induced by diet and treatment. FTIR spectra were collected on multiple cells treated with increasing concentrations of vanadate in a similar manner to standard cytotoxic assays, where strong correlations were found between the standard cell viability curves and principal component scores plotted versus vanadate concentration. It was also found that the combined FTIR/chemometrics (multivariate) models developed in the cytotoxic assay studies provided deeper insights into the biochemical processes induced by vanadate where its anti-diabetic effects were interpreted, followed by its transition to cytotoxic effects. The cytotoxic assay method and chemometrics models allowed the estimation and verification of IC_{50} values that could be used to further assess vanadates cytotoxic effects with the use of rational design of experiments (DoE).

Analysis of the FTIR spectra acquired from the DoE study further confirmed the findings of the cytotoxicity studies and provided insights into the unique metabolic pathways induced by fructose, particularly its ability to induce protein synthesis, which is a hallmark of fructose metabolism. Combined vanadate-fructose treatments were shown to increase oxidative stress in all cell types studied, consistent with the literature, and

resulted in apoptotic pathways that were characterised by lipid synthesis and subsequent peroxidation, resulting in lipotoxicity.

In the HepG2 cell line, low concentrations of vanadate were observed to increase cell viability in the presence of glucose and unexpectedly, viability was induced through protein synthesis rather than *de novo* lipid synthesis. It was found that lipid synthesis in HepG2 cells was a characteristic of induced apoptotic pathways, however, when vanadate reached a critical concentration, protein aggregation and the possible transition of HepG2 cells from an epithelial to a mesenchymal phenotype occurred. When the new phenotype was treated with normal supplemented media, it was observed that the cells reverted back to their epithelial phenotype, however, more work is required to verify this observation.

Hyperspectral imaging and chemometrics were used to investigate the effects of the DoE treatments on 3T3-L1 adipocytes using laboratory-based FTIR imaging systems and a special four-beam synchrotron based focal-plane-array (FPA) system to better understand compositional and morphological changes induced in single cells. These studies revealed a common pattern in all treatments where membrane and interior lipid compositions could be partitioned into the first principal component of all images, while the second principal component images revealed lipid and fatty acid compartmentalisation, providing insights into the way adipocytes store lipids and fatty acids into specialised compartments.

Overall, the investigations performed in this study have established improved protocols for optimising FTIR spectral acquisition parameters, leading to the reduction of noise, and the acquisition of spectra that provided detailed insights into the biochemical processes occurring within treated cells that can be used to compliment standard biochemical assay techniques. FTIR is an averaging method and is not specific in terms of being able to identify individual proteins or specific pathways, however, it was able to provide detailed average environmental changes that were consistent with known biochemical pathways, which have provided new insights into the biochemical mechanisms induced by vanadium compounds in terms of their anti-diabetic and anti-cancer action.

Chapter 1 Spectroscopic and Chemometric Investigations into the Modes of Action of Vanadium Prodrugs for Better Understanding of the Metabolic Syndrome

1.1 Introduction: The Sugar Epidemic

"Fructose is a poison that is slowly killing us" is a big claim made by David Gillespie in the book Sweet Poison.[1] Fructose is a naturally occurring simple sugar, primarily found in fruits (the name fructose is derived from the words "fruit sugar') and its major delivery source to the body is either through the consumption of table sugar (sucrose), fruit/fruit juices, or a product known as High Fructose Corn Syrup (HFCS).[2] Sucrose is a disaccharide (two sugar groups chemically bonded) of glucose and fructose,[3] rapidly hydrolysed in the body into its monomers (monosaccharides). **Figure 1.1** provides the cyclic chemical structures of sucrose and its hydrolysis into D-glucose and D-fructose.

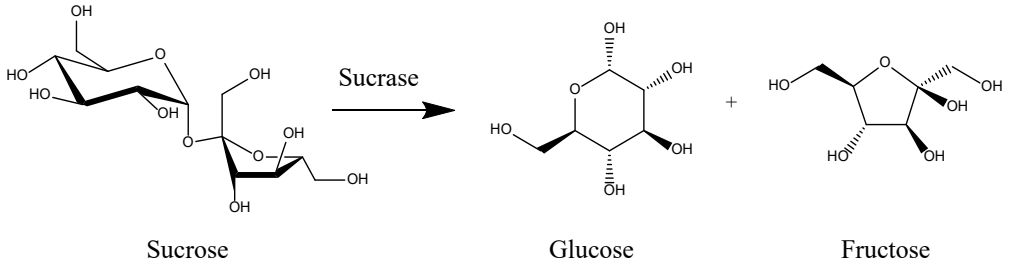

Figure 1.1: The structure of the disaccharide sucrose, glucose and fructose (only the predominant chemical structures are given).

The consumption of foods and food supplements with moderate to large amounts of added sucrose has been claimed to have deleterious effects on the health and wellbeing of many people worldwide.[4] However, bodies such as Nutrition Australia have refuted the claims made in the Sweet Poison book that sugars such as fructose are detrimental to health stating "Sweet Poison is based on gross misinterpretations of key aspects of the scientific literature, and entirely ignores others".[5] A number of scientific papers cited within the Sweet Poison book, takes a contrary stance to this assessment.[2-4,6] However, an evidence-based review of the effect of normal dietary intake of fructose on obesity in healthy individuals found when fructose was delivered in a normal dietary manner, the incidence of hyperlipidaemia and obesity did not increase and biologically relevant changes in triacyl glycerides (TAGs) or body weight did not occur.[7]

The key point is in the statement "normal dietary manner". Prior to recent modernisation (mid to late 1800's), humans consumed between 16-24 g of fructose daily in the form of fruits and honey. Today, daily fructose consumption is in the range of 8-100 g due to refined foods and processed fructose.[2,8] A higher than average intake of added sugars is linked to the onset of metabolic diseases such as type 2 diabetes mellitus (T2DM),[2-4] cardiovascular disease (CVD),[3,9] obesity and cancer.[8] Such consumption levels are also

strongly linked to fructose not being regulated by the body's insulin pathway,[10-11] in the same way it regulates glucose.

Figure 1.2 provides a schematic illustrating glucose and fructose metabolism in the liver. Post ingestion of sucrose through the stomach leads to molecule breakdown into its component monosaccharides, in the duodenum. In the case of HFCS, fructose is already available for metabolism. Food nutrients, such as amino acids and simple sugars, are transported to the liver through the portal vein where metabolism starts. Hepatocytes transform the nutrients into fuels and precursors required by other parts of the body that are removed from the liver via blood.[12]

In healthy individuals, glucose is utilised by skeletal (muscular) and adipose tissue, then converted into energy reserves regulated through the secretion of the hormone insulin and transported into cells through the glucose transporter proteins (GLUTs) in particular GLUT1 and predominantly GLUT4.[13-14] A major role of adipose tissue is lipid storage as fuel reserves in the form of TAGs.[15] During fasting or increased energy demand, fuel stored in adipose tissue is used to provide energy to other tissues throughout the body. Adipose tissue mainly consists of adipocytes, which until recently were thought to only store energy; however, they are now recognised to have other important functionality in key physiological processes as discussed in Chapter 4, which are important to the development of obesity and metabolic syndrome.[16]

In complex signalling pathways postulated to originate in the hypothalamus, specific hormones moderate food intake and control glucose and energy homeostasis. Ghrelin is a fast-acting hormone produced in the gastrointestinal tract with many functions including its orexigenic function (i.e., stimulation of hunger), ability to regulate glucose homeostasis through insulin inhibition, regulation of energy expenditure through thermogenesis and cardio-protective functionality.[17] It is a key regulator of obesity, insulin resistance and diabetes and these functions are independent of its orexigenic effects, possibly through a mechanism of energy dysregulation.[17]

Leptin is primarily produced in adipose tissue and to a lesser extent in the stomach and is released into the circulatory system as a function of adipocyte energy stores.[18] It functions as a feedback mechanism for the reduction of food intake, thus regulating body weight and energy homeostasis. Leptin secreted in the stomach is stimulated by insulin released during food intake, supressing appetite and producing a sense of satiety.[19]

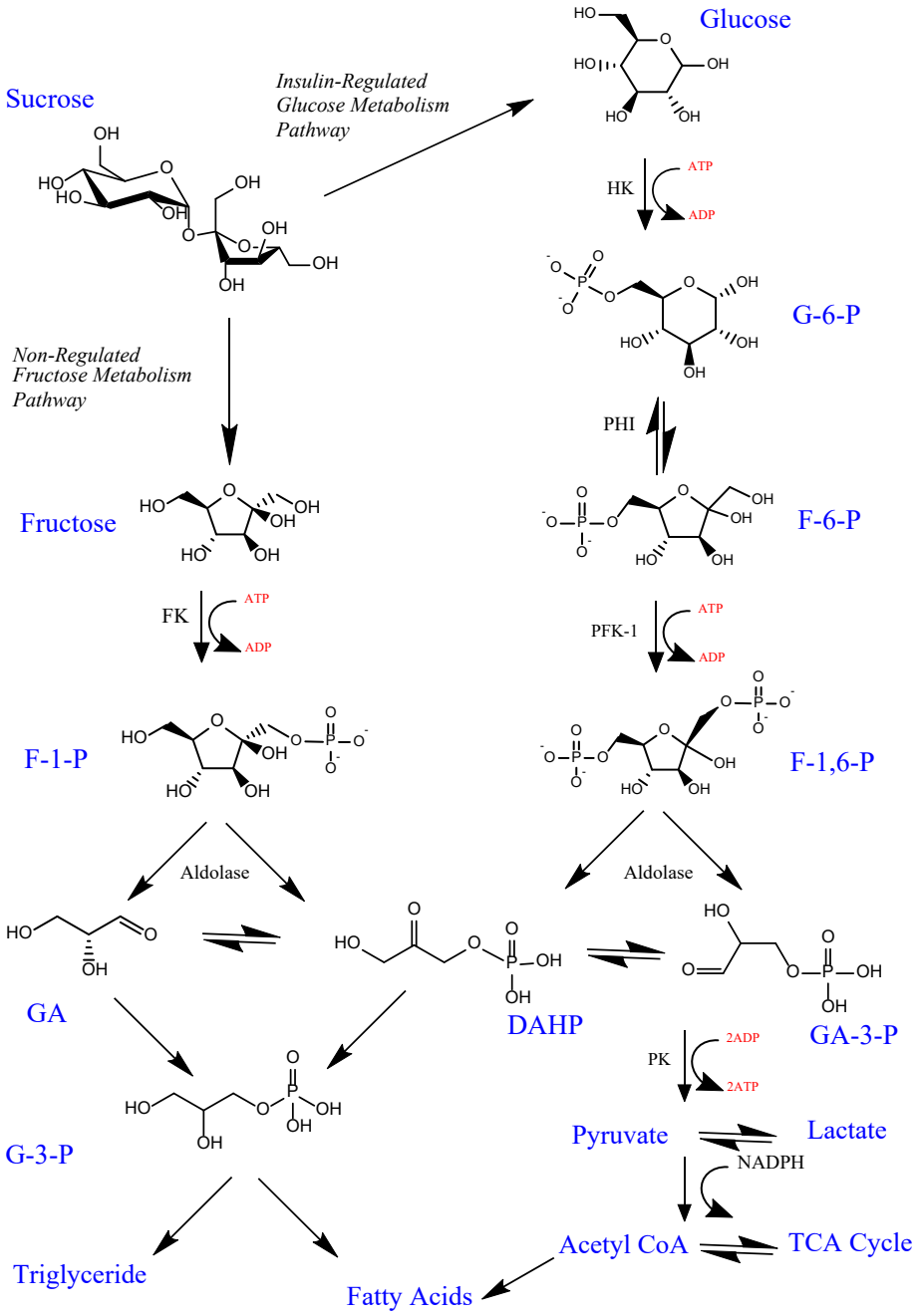

Figure 1.2: Sugar metabolism in the liver. Sucrose is cleaved in the small intestine into glucose and fructose. Glucose metabolism is regulated by the insulin pathway, whereas fructose metabolism is unregulated. In this figure, the following definitions are: HK, hexokinase; FK, fructokinase; ADP, adenosine diphosphate; ATP, adenosine triphosphate; PHI, phosphohexose isomerase; F-1-P, fructose-1-phosphate; G-6-P, glucose-6-phosphate; F-6-P, fructose-6-phosphate; F-1,6-P, fructose 1,6-biphosphate; PFK-1, phosphofructokinase; GA, glyceraldehyde; G-3-P, glycerol-3-phosphate; DAHP, dihydroxyacetone phosphate; GA-3-P, glyceraldehyde-3-phosphate; PK, pyruvate kinase; Acetyl-CoA, acetyl coenzyme A; NADHP, nicotinamide adenine dinucleotide phosphate; and TCA, tricarboxylic acid cycle (citric acid or Kreb's cycle). Each enzyme plays its role in converting glucose and fructose into energy stores for utilisation by the various tissues in the body. Adapted from Port, *et al*. Curr Opin Endocrinol Diabetes Obesity, 2012, 19:367-374, with permission Wolters Kluwer Health, Inc.[20]

Excessive food intake, induced by hyperphagia, results in overexpression of circulating leptin, which is believed to lead to long term leptin and insulin resistance.[21-22] The mechanisms of leptin resistance are unclear and there is no consensus whether abnormalities in ghrelin and leptin signalling are a cause or consequence of obesity, however, it is established that obese patients are leptin resistant.[23] **Figure 1.3** describes the ghrelin, insulin and leptin pathways in sugar metabolism used in cells and tissues to maintain glucose and energy homeostasis.

1.2 Fructose Metabolism

Fructose is not regulated by the insulin pathway (**Figure 1.2**) but it uses the GLUT5 transporter in the small intestine where it is absorbed at a slower rate than glucose. Fructose is cleared at a rate >70% from portal circulation and transported to the liver[8,20,24] where it is phosphorylated by fructokinase,[10] to fructose-1-phosphate (F-1-P), which is then cleaved by aldolase-B into triose phosphates where it promotes *de-novo* lipogenesis (DNL) in hepatocytes. This leads to the production of TAGs that circulate through the blood, as shown in the fructose metabolism pathway in **Figure 1.2** and conceptualised in **Figure 1.3**. When excessive uptake of TAGs occurs, such as in adipocytes,[25] the cells become enlarged, which can result in obesity, insulin resistance and metabolic disorders through a process known as hypertrophy. Adipocyte hypertrophy is associated with dysfunctional adipose tissue induced by cellular stress, decreased metabolic flexibility and diabetes, as the cells attempt to adapt to excessive nutrient levels to protect other tissues from lipotoxicity.[26] In adipocytes, GLUT5 expression is confined to the plasma membrane, where it is responsible for cellular uptake of fructose from the blood.[27]

Hypoxia increases GLUT5 expression nine-fold in humans, which is an interesting finding given that hypoxia becomes more common in obese individuals.[28] When the adipocyte cell diameter exceeds 100 μm, hypoxia may ensue because the tissue diffusion distance of O_2 is exceeded, resulting in the release of hypoxic-response genes, endoplasmic reticulum and oxidative stress conditions, inflammation and metabolic dysfunction.[26,29] By deduction, GLUT5 expression induced by higher serum fructose content, increases TAG production and hypertrophy that leads to leptin dysfunction, insulin resistance and metabolic syndromes, and the processes that regulate adipocyte hypertrophy are poorly understood.[26]

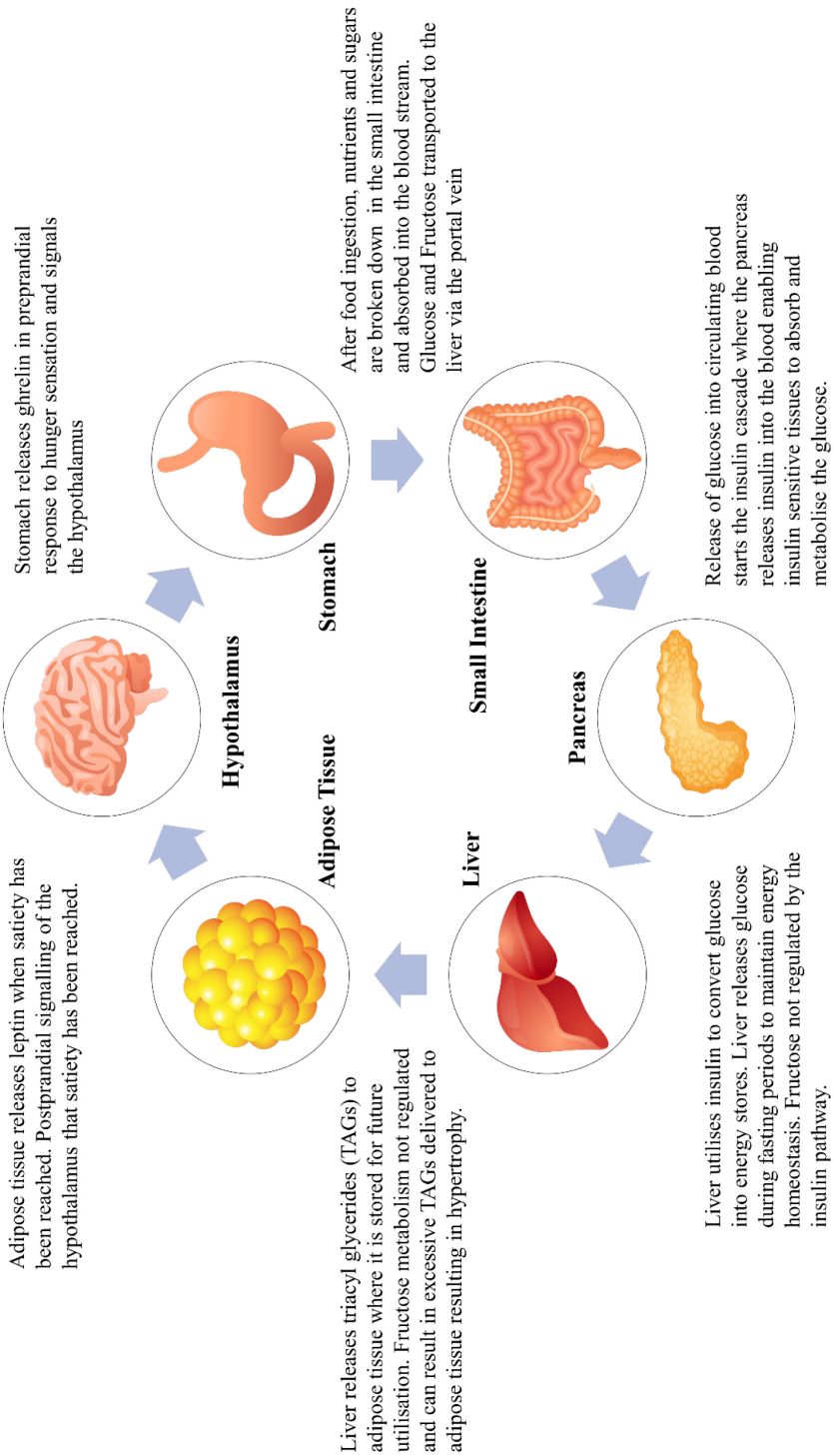

Figure 1.3: Conceptualisation of the ghrelin, insulin and leptin cascade. Preprandial signalling through ghrelin results in the feeling of hunger. After food ingestion and breakdown, nutrients, including sugars such as glucose and fructose are metabolised, primarily in the liver until a feeling of satiety has been reached. Adipose tissue then releases leptin which crosses the blood brain barrier and signals the hypothalamus to limit the intake of more food.[17]

Adipocytes are approximately 90% lipid,[30] consistent with the optical micrograph (**Figure 1.4**) fixed to a calcium fluoride (CaF_2) window. The optical micrograph shows the multilocular morphology of the cell associated with the lipid droplets and when these

become too large, hypertrophy can restrict O_2 entry, resulting in the release of toxic cytokines (adipokines) that can trigger biochemical pathways associated with inflammatory responses and disease.[31-32]

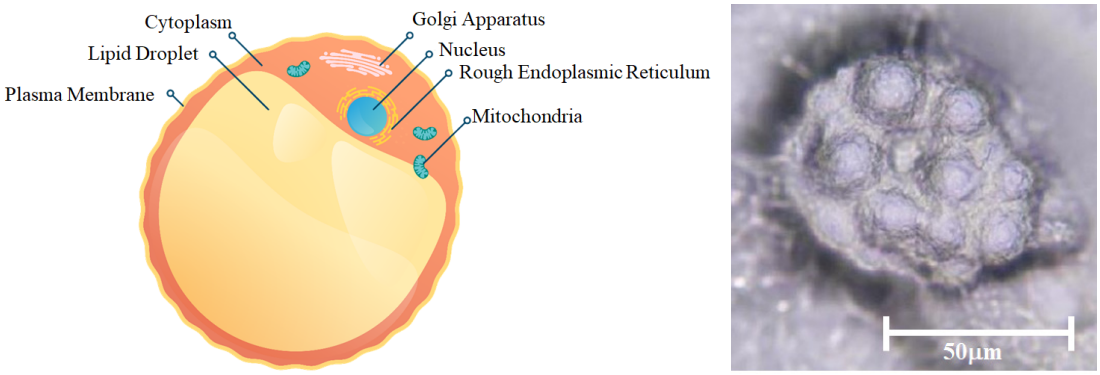

Figure 1.4: Diagrammatic and optical micrograph of a single 3T3-L1 mouse adipocyte cell collected during this work.

Even though high levels of fructose are cleared by portal circulation, significant amounts escape into circulation following a large fructose load, which is taken up primarily by the kidney, muscle and adipose.[20] Studies have shown that serum fructose concentrations increase 50-100-fold (2-4 mM) over basal levels (0.04 mM),[33] with oral loads of 0.5 g/kg.[34-35]

The rapid depletion of adenosine triphosphate (ATP) and phosphate reserves increases adenosine monophosphate (AMP) with ADP/ATP ratio, which leads to an increase in purine nucleotide degradation to produce uric acid to restore balance.[20] Uric acid is a possible biomarker of impaired hepatic function[29] and excess production can lead to a condition known as hyperuricaemia. However, fructose overconsumption impairs this balance leading to irregular ATP homeostasis in obese diabetics with a corresponding increase in unregulated TAG production,[10,29] The increased uric acid production results in proinflammatory and oxidative effects which have been inferred in the development of non-alcoholic fatty liver disease (NAFLD).[36]

When aldolase-B cleaves F-1-P into glyceraldehyde (GA) and dihydroxyacetone phosphate (DAHP), these can enter glycolysis. DAHP and glyceraldehyde-3-phosphate (GA-3-P) are produced during the regulated metabolism of glucose in the liver and all three intermediates are in equilibrium. Therefore, fructose metabolism bypasses two major rate limiting steps of the insulin pathway, glucokinase and PFK1,[10] enabling fructose-derived intermediates to enter the glycolytic pathway downstream of these enzymes. Fructose overrides the PFK1 termination of glycolysis resulting in ATP

production that downregulates mitochondrial oxidative respiration, leading to DNL and nucleotide biosynthesis and, therefore, the consumption of high doses of fructose can result in unregulated TAG production.[20]

Increased DNL promotes dyslipidaemia, impairs insulin sensitivity, increases endoplasmic reticulum stress, induces mitochondrial dysfunction, increases apoptotic activity and visceral adiposity.[37] This is because there is no feedback mechanism regulating fructose phosphorylation, which when left unchecked, depletes hepatic ATP regardless of cellular energy status.[20] This depletion is associated with an arrest in hepatic protein synthesis and induces inflammatory and pro-oxidative hepatic cell damage,[29] with an unfavourable energy balance that is different from a maintained energy state via insulin-regulated glucose metabolism.

In insulin-regulated glucose metabolism, a decrease in ATP favours mitochondrial respiration over glycolysis, however, unchecked fructose phosphorylation promotes glycogen synthesis and glycolysis to initiate hepatic glucose disposal but antagonises the usual insulin-regulated feedback mechanisms.[20] Continued exposure to fructose upregulates the GLUT5 fructose transporter and fructokinase, thus self-perpetuating DNL. Typically, in insulin-regulated metabolism of glucose, AMP is re-phosphorylated to ATP by adenosine monophosphate kinase (AMPK) in a balanced manner to maintain glucose and energy homeostasis. Insulin decreases glucagon levels and AMPK activation, hypothesised to increase fatty acid oxidation, reduce adiposity, and improve mitochondrial function in skeletal muscle.[38] Individuals with insulin resistance, diabetes or obesity experience greater impairment in energy homeostasis compared to healthy individuals.[39]

1.3 Metabolic Syndrome; its Causes, Complications and Effects

According to the World Health Organisation (WHO) and the International Diabetes Federation (IDF), from 1980 to 2014, diabetics increased 390% from 108 to 422 million[40] and this number is expected to reach 700 million by 2045.[41] The IDF estimates that in 2019 the health expenditure of diabetes was USD 760 billion.

The question arises, what is the major contributor to the rapid increase in these diseases, particularly over the past half century? The dominant theory links increases in obesity, diabetes and its complications to the increase in sugars added to foods and beverages available to the everyday consumer and increased consumption of processed foods common to the "Western Diet".[4] In the USA, where obesity, T2DM and other related

diseases are almost at epidemic levels,[2] the corn industry is highly subsidised for production of High Fructose Corn Syrup (HFCS).[42] The background of how corn became a food staple and the origins of its widespread incorporation into the diet is well described.[43-44] Gross, *et al.*[2] provides a short history about the discovery and production of HFCS and, in particular, its positive correlation to T2DM (at the 0.038 significance level).

Changes in carbohydrate quality in processed food and the risk of T2DM are yet to be quantified.[2] Refined foods have increased carbohydrate content and subsequently decreased dietary fibre has paralleled the upward trend in the prevalence of obesity and T2DM. Viscous, non-fermentable dietary fibres have positive metabolic effects, such as reduction of post-prandial glucose and insulin concentrations, reduction of adiposity through reduced glucose diffusion in the small intestine, increased mitochondrial biogenesis and fatty acid oxidation in skeletal muscle.[38] While there is some consensus that high carbohydrate diets may exacerbate the occurrence of insulin resistance and metabolic syndrome, it is the type of carbohydrate and its intake that is a contributing factor, with dietary fibre having an overall positive effect on health and wellbeing.[45]

Gillespie[1] discusses the work of T.L Cleave, captain-surgeon of the Royal British Navy, where the term 'saccharine disease' was coined. Cleave observed that a large number of modern diseases were the result of the refinement of raw grains and fruits/vegetables into energy-dense, highly palatable foods, produced through the removal of the majority of its dietary fibre content. This was one of the main outcomes of the review by Gross, *et al.*[2]

The Adult Treatment Panel III of the National Cholesterol Advisory Panel defines metabolic disorder as the "constellation of lipid and non-lipid risk factors of metabolic origin".[46] This metabolic syndrome is linked to biochemical and physiological abnormalities associated with the development of obesity, insulin resistance, hypertension, CVD, dyslipidaemia and T2DM.[2-3,9-10] The non-regulation of hepatic fructose metabolism may lead to metabolic syndrome and T2DM.[3] Although this type of diabetes is manageable using a strict diet, it is currently not fully curable using non-invasive means[47] and eventually leads to a decline in the health of the individual.[25] T2DM is characterised by chronic hyperglycaemia (elevated blood sugar) and insulin resistance typically induced by poor diet and sedentary lifestyles. This results in ineffective insulin utilisation damaging the nervous system and blood vessels (epithelium) and sets it apart from Type I diabetes, where insulin is not produced by the body at all.[48]

The cascading effect of obesity to metabolic syndrome and increased risk of diabetes, CVD and cancers through elevated levels of circulating insulin, fructose and glucose leading to inflammation and oxidative stress (Section 1.5.3), has been well documented.[49-50] Non-regulated fructose metabolism in the liver increases levels of TAGs, which results in higher blood viscosity and the deposition of a higher than normal fat and lipid content into the body.[6] Non-alcoholic fatty liver disease (NAFLD) and the rise of T2DM parallels an increase in fructose consumption, particularly in the USA where many foods and beverages are sweetened with HFCS. Diabetic obese individuals have a more severe form of NAFLD.[29]

Hyperphagia and elevated levels of insulin and leptin are common features in obese individuals.[22] This is paradoxical as leptin inhibits food intake and is expected to reduce insulin levels;[51] however, obesity impairs both actions by inducing leptin and insulin resistance. This dual resistance is most detrimental for those predisposed to weight gain or diabetes as the adipostat is impaired for such individuals.[22]

Cancer cells undertake anaerobic glycolysis with a large glucose flux, even in the presence of oxygen to fuel growth, known as the Warburg effect.[52] In the liver, when glycolysis and mitochondrial respiration are uncoupled, fructose may favour a Warburg-type phenotype in proliferating cells.[20,53] Oxidative stress and compromised antioxidant defence caused by DNL may also be a risk factor because the nature and composition of the lipids are related to the onset of insulin resistance, NAFLD, T2DM, and kidney disease.[29,37]

Cancer cells use the less energetically favourable and slower anaerobic glycolysis route of fructose metabolism, whereby lactate production is minimised to result in less acidic conditions and promotion of metabolite generation for protein synthesis.[54-55] Individuals with obesity and diabetes have an increased cancer risk, mainly as a consequence of increased circulating insulin and blood glucose. Diabetics have four times the amount of fructose-derived advanced glycation end products in their serum, higher fasting fructose levels and increased GLUT5 expression in the intestine and muscles relative to healthy individuals, putting them at higher risk of developing cancers with more aggressive phenotypes.[56-57]

There is considerable interest in the development of pharmaceuticals for adiposity reduction,[38] but current pharmaceuticals only manage short-term symptoms. Drugs such as Metformin and thiazolidinediones treat acute symptoms of T2DM by improving

glycaemic control and decreasing endogenous insulin secretion.[56] However, they may also suppress fibrosis, which is believed to regulate the reciprocal balance between adipocyte hypertrophy and preadipocyte hyperplasia.[26] Alternative non-pharmaceutical approaches are based on food fortification and better agricultural practices that help with glucose and fructose clearance from the circulatory system after eating.[38] Vanadium based pro-drugs are one particular option (Section 1.5).

1.4 Insulin and Insulin Resistance

1.4.1 Insulin

Insulin facilitates glucose cellular uptake; regulates carbohydrate, lipid and protein metabolism; promotes cell division through mitogenic effects; and inhibits ketogenesis and gluconeogenesis and glycolysis, glucose storage, lipid synthesis and storage (**Figure 1.2**).[15,58] It binds to insulin receptors located mainly on cell membranes and when insulin binds to the extracellular α-subunit of the receptor, conformational changes to enable ATP binding to the intracellular β-subunit initiates phosphorylation and confers tyrosine kinase activity.[59-60] This results in phosphorylation of insulin responsive substrates (IRS), which initiates a series of signalling processes that further induce intracellular insulin activity. The activation of phosphatidylinositol-3-kinase (PI3K) mediates metabolic effects of insulin by promoting the translocation of the glucose transporter proteins (GLUTs) in muscle and adipocytes, glycogen, lipid and protein synthesis, anti-lipolysis and the control of hepatic gluconeogenesis.[60]

In muscle and fat (adipocyte) cells, insulin-stimulated translocation of the glucose transporter (GLUT4) to the plasma membrane reduces glucose levels in plasma,[13] by providing an aqueous pore across the membrane (**Figure 1.5**). Insulin also stimulates the production of glycogen, a long-term energy store composed of polymers of glucose.[59,61] In the liver, insulin suppresses the hepatic glucose output and lipogenesis, and it inhibits lipolysis. Lipogenesis refers to the biosynthesis of fatty acids whereas lipolysis refers to the breakdown of lipids into free fatty acids. Unregulated DNL is associated with negative health consequences such as insulin resistance, diabetes and cancer by elevating levels of insulin, circulatory glucose, inflammation and oxidative stress.[20]

Figure 1.6 provides a diagrammatic representation of hepatic glucose metabolism. Increased circulating glucose levels are the primary stimulus for insulin secretion from pancreatic β-cells, which increases intracellular ATP and closes K^+-ATP channels.[46] Insulin secretions are also induced by neural stimuli, adrenergic pathways, peptide

hormones such as leptin and adiponectin, and amino acids.[46] The counter-regulatory hormone to insulin is glucagon, which regulates blood glucose concentrations.[62]

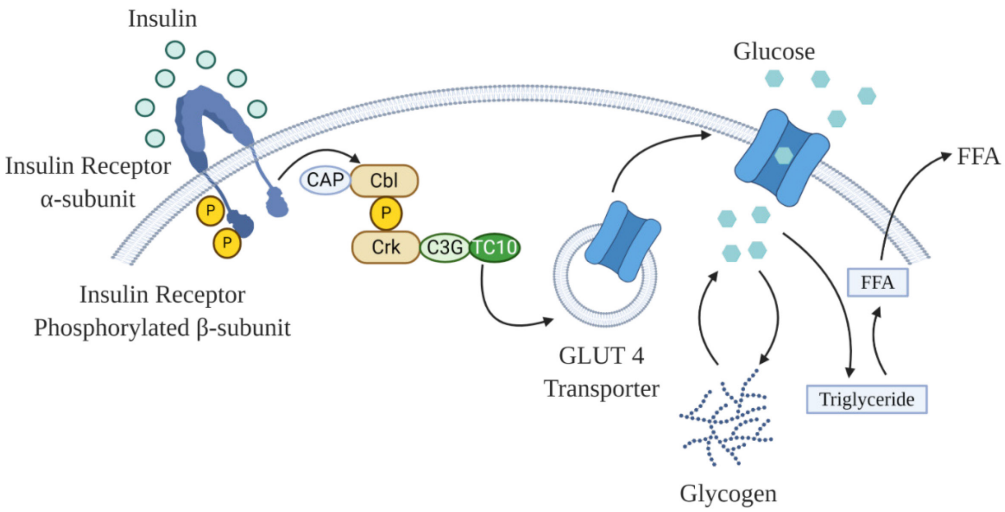

Figure 1.5: Circulatory insulin binds to the α-subunit of the insulin receptor (tyrosine kinase), which then autophosphorylates at the trans-membrane β-subunit to activate its catalytic activity. This triggers a complex sequence of cascades, including activation of PI3K and PIP_3 to TC10 activation and translocation of GLUT4 to the cell membrane, to facilitate glucose entry into the cell for metabolism. Glucose is converted into glycogen for storage and excess glucose can also be converted into TAGs and free fatty acids (FFA).[60,63] Adapted by permission from Springer Nature, Saltiel and Kahn, Insulin signalling and the regulation of glucose and lipid metabolism, copyright, 2001.[60] Created with BioRender.com.

Under tight regulatory control, fasting insulin levels prevent uncontrolled hydrolysis of TAGs and limits gluconeogenesis, thereby maintaining normal fasting blood glucose levels.[46] Non-esterified fatty acids (NEFA) are released from the liver, adipocytes or small intestine from excess carbohydrate loads, which in turn, increases liver hepatic glucose output, reduces peripheral insulin sensitivity and may also modify glucose stimulated insulin secretion (GSIS).[64]

Insulin production based on food intake and that induced by exercise draw on GLUT4 from distinct intracellular compartments, indicating that exercise may be an effective therapy in relieving metabolic disease based on the differential action of exercise and insulin on GLUT4 traffic.[14,65] Better understanding of the action of GLUT4 and insulin resistance is the subject of ongoing research, particularly in light of the notion that GLUT4 defects in one part of the body could act as a signalling system to the rest of the body. The pancreas does not contain GLUT5 transporters, so when fructose is consumed, it does not release insulin, nor does fructose stimulate the release of gastric inhibitory peptide, which also induces insulin[10] and leptin[66] secretion.

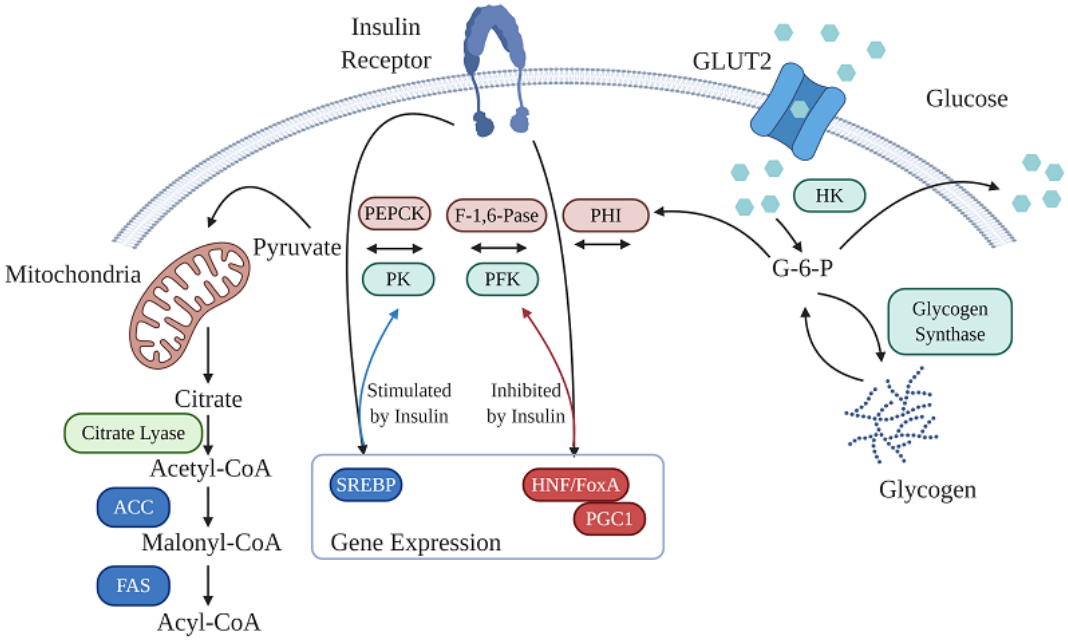

Figure 1.6: GLUT2 transports glucose into the liver for metabolism, energy storage (glycogen) and its subsequent release through the process of gluconeogenesis. It can also use glucose for gene expression, or mitochondrial processing of pyruvate via the Kreb's cycle into Acyl-CoA for further conversion into fatty acids. For acronyms see **Figure 1.2** in addition to: F-1,6-Pase, fructose 1,6-biphosphate kinase; PEPCK, phosphoenolpyruvate carboxykinase; SREBP, sterol regulatory element binding protein; HNF, hepatic nuclear factor; FoxA, forkhead protein; PGC1, PPARγ-co-activator 1; ACC, acetyl-CoA carboxylase; and FAS, fatty-acid synthase. Adapted by permission from Springer Nature, Saltiel and Kahn,[60] Insulin signalling and the regulation of glucose and lipid metabolism, copyright, 2001. Created with BioRender.com.

1.4.2 Insulin Resistance

Insulin resistance is defined as dysfunctional glucose uptake into muscle and adipose tissue along with glucose oversupply from the liver. In this condition, insulin is unable to produce its responses such as increasing glycogen synthesis and decreasing gluconeogenesis,[10] which results in hyperinsulinemia. The actions of insulin are influenced by many other hormone related processes in the body, including interactions with growth hormones that act to prevent hypoglycaemia.[46] Where insulin promotes glycogen synthesis and inhibits its breakdown, hormones such as glucagon promotes hepatic glycogenolysis, gluconeogenesis and ketogenesis. The ratio of insulin to glucagon determines the degree of phosphorylation or dephosphorylation of relevant enzymes and, therefore, nutrients flux into or out of storage.[67]

The origins of human insulin resistance are still unclear and have been associated with post-receptor defects in insulin signalling, including deficiencies or changes in tyrosine phosphorylation of IRS proteins, or abnormalities in GLUT4 function.[65] The primary sites of insulin resistance are muscles, adipose tissue and the liver. In adipocytes, glucose is transported into to the cell by GLUT4 in an insulin-dependent manner where it is estimated that adipose tissue accounts for 10% of insulin stimulated whole body glucose uptake.[68] Adipocytes influence glucose disposal through the production of FFAs and they secrete a number of cytokines that have systemic effects on insulin resistance. These include interleukin-6 (IL-6), tumour necrosis factor (TNFα), plasminogen activator inhibitor (PAI-1), angiotensinogen and leptin.[69] Increased plasma FFA concentrations induce insulin resistance through inhibition of glucose transport activity, thought to be a consequence of decreased IRS-1 associated PI3K activity.[68-69] Overall, dyslipidaemia occurs long before glucose tolerance becomes impaired[70] and decreased IRS-1 expression and downstream signalling events are associated with insulin resistance.[68]

The resulting hyperinsulinemia in insulin resistant individuals is also related to the onset of hypertension.[10] Somatostatin release reduces blood pressure along with pharmaceuticals, such as Metformin (through the stimulation of AMP-activated protein kinase[71]), thiazolidinediones (through changes in TNFα, FFAs and resistin[72]) and pro-drugs based on vanadium (Section 1.5.1).[73] Insulin resistance within the endothelium may result in endothelium dysfunction, which may then lead to hypertension through increased vascular resistance.[10] Endothelial dysfunction also leads to insulin resistance in skeletal muscle tissue from decreased blood flow.[74] Increased endothelin-1 (ET-1) release induced by fructose is related to hyperinsulinemia which is a contributor to blood pressure,[10] and while regulated secretion of ET-1 can promote GLUT4 translocation and stimulate glucose uptake, chronic treatment induces insulin resistance in adipocytes.[75-77]

Other mechanisms by which insulin resistance leads to hypertension include elevation in angiotensin II (Ang II), a known vasoconstrictor that reduces blood flow and glucose uptake into insulin sensitive tissues,[78] nitric oxide (NO) defects,[79] oxidative stress,[10] and uric acid production.[80] These conditions produce reactive oxygen species (ROS) to reduce production of vasodilators, increased inactivation of NO and increased production of vasoconstrictors.[10,65]

Studies in T2DM patients show an inverse relationship between oxidative stress and insulin action,[81] and leads to a reduction in GLUT4 translocation, thus impairing the

insulin signalling pathway.[82] The increased production of ROS as superoxide has been observed in individuals with insulin resistance and highly correlates with the development of atherosclerosis in these individuals.[83] Acute antioxidant treatments have been shown to improve insulin sensitivity and endothelial function through the reduction of ROS with a corresponding decrease in CVD.[84-85]

For CVD and atherosclerosis, insulin action on vascular cells is mediated by two pathways, the IRS/PI3K/Akt pathway, which is anti-inflammatory, reduces antioxidant stress and promotes antiatherogenic activity through the release of NO, the expression of heme oxygenase 1 (HO-1) and vascular endothelial growth factor (VEGF) and reduction of vascular cell adhesion molecule 1 (VCAM-1). The Grb/Shc/MAPK pathway may stimulate mitogenic or chronic actions of insulin, which is proatherogenic resulting in the expression of ET-1 and PAI-1.[86] Insulin also has an antiatherogenic action on vascular cells, which indicates that insulin may act in a protective manner towards the vascular wall. The protective effect induced by the IRS/PI3K/Akt pathway can be reversed by the MAPK pathways, which is not inhibited in diabetes by hyperinsulinemia and FFAs where it may activate a different set of signalling pathways, including the atherogenic pathway.[87] The impairment of insulin mediated glucose metabolism in the heart in insulin-resistant and diabetic individuals results in increased use of FFAs released into circulation and a corresponding elevation in ROS, decreased cardiac mitochondrial function and, in some cases, apoptosis.[88]

The liver does not require insulin for glucose uptake; however, it accounts for 30% of whole-body insulin mediated glucose disposal where it is required to facilitate key metabolic processes.[89] Impaired hepatic insulin utilisation results in increased glucose output via gluconeogenesis and as a result, the corresponding hyperinsulinemia promotes mitogenic effects, particularly on endothelial smooth muscle cell proliferation, which are believed to contribute to atherosclerosis.[65] In insulin resistance, increased FFA flux in the liver tends to promote hepatic very low-density lipoprotein (VLDL) production.[90] This is believed to result in the observed hypertriglyceridemia and impaired glucose uptake observed in individuals with insulin resistance and these effects may be mediated through inhibition of IRS-associated PI3K activity.[69] **Figure 1.7** provides a model of insulin resistance in endothelial cells.

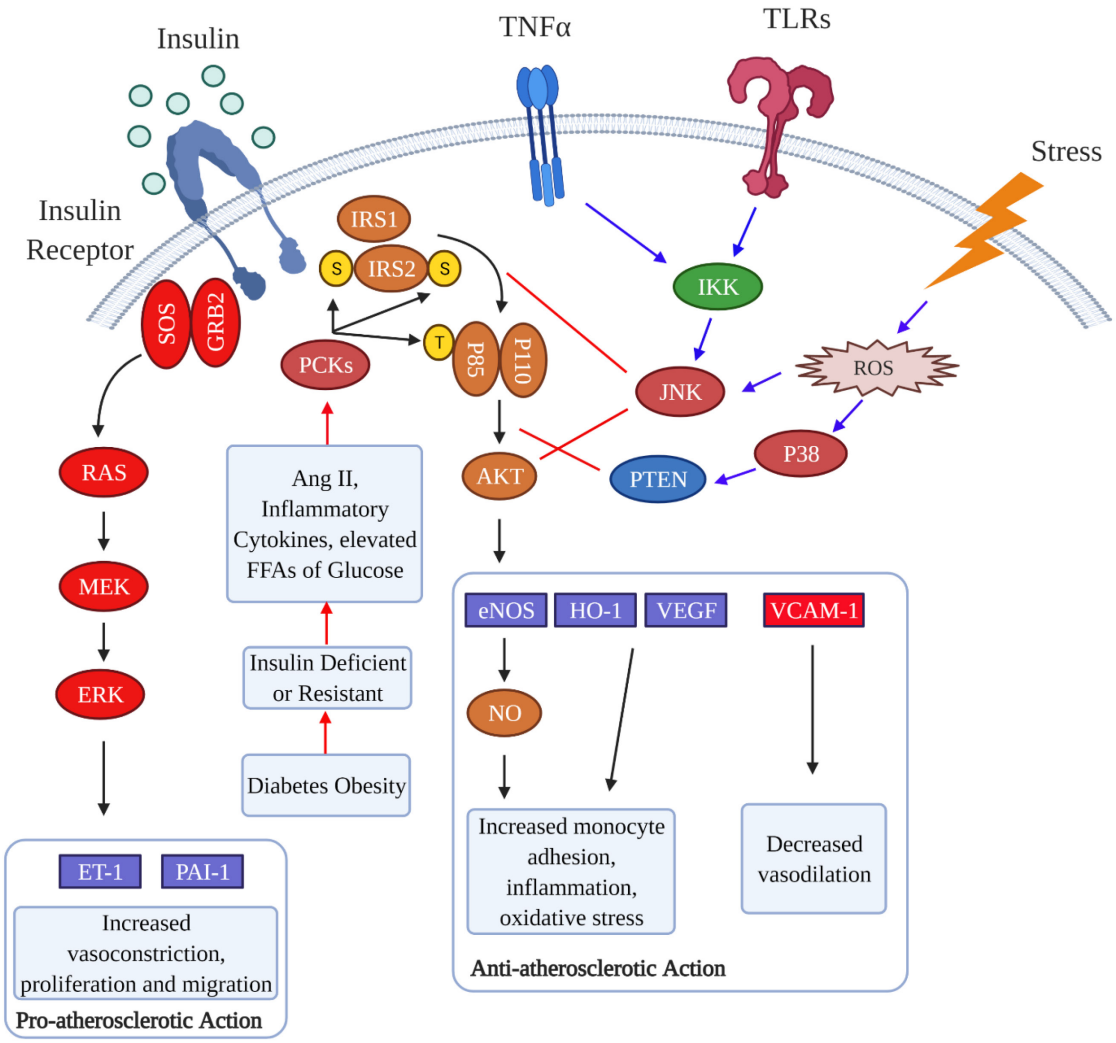

Figure 1.7: Model of insulin resistance in endothelial cells. Elevated levels of Ang II, FFAs, glucose, and proinflammatory cytokines induced by insulin resistance and diabetes result in the stimulation of PKC isoforms to phosphorylate IRS1/2 and PI3K and inhibition of the IRS/PI3K/Akt pathway. The stimulation of the SOS/Grb2/MAPK pathway by insulin is unaffected or even enhanced. The selective loss of insulin activity via the IRS/PI3K/Akt pathway causes the reduction of its antiatherosclerotic action and contributes to acceleration of atherosclerosis and other cardiovascular pathologies in diabetes. PTEN, phosphatase and tensin homolog. Adapted from the American Diabetes Association, King, *et al.* Selective Insulin Resistance and the Development of Cardiovascular Diseases in Diabetes: The 2015 Edwin Bierman Award Lecture, 2016, copyright, all rights reserved.[86] Created with BioRender.com.

1.4.3 Fructose Induced Insulin Resistance

Since fructose metabolism in the liver is unregulated, rapid and depletes ATP levels, this acts like ischemia and can cause production of inflammatory proteins, endothelial dysfunction and oxidative stress.[39] Furthermore, fructose stimulates triglyceride production and fat deposition in the liver and the production of uric acid in a

concentration-dependent manner,[91-92] which are all reported to be responsible for its ability to induce metabolic syndrome (**Figure 1.8**).[39]

Insulin mediated endothelial NO release accounts for one third of the action of insulin in increasing blood flow to muscle and peripheral tissues to enhance their uptake of glucose.[93] However, in both cell and animal studies, uric acid reduces endothelial NO bioavailability and an increase in ROS through a mechanism involving uric acid oxidant production, which further induces oxidative modifications of proteins and lipids.[94] Evidence also exists that insulin resistance is affected by uric acid in adipocytes through inflammation and oxidative stress.[95]

Lowering uric acid levels reduces key features of metabolic syndrome including hypertension, hypertriglyceridemia, hyperinsulinemia, insulin resistance, renal vasoconstriction and renal microvascular disease.[39] Antioxidants, such as vitamin C, block the actions of uric acid in a number of cell types and in fructose fed rat models, which are believed to be a direct blocking of the effects of fructose. Uric acid can have a dual role, depending on the physiological state, where it can act as an antioxidant,[96] or can induce oxidative stress as previously mentioned with adipocytes, through stimulation of NADP oxidase.[94]

Therefore, compelling evidence exists that excessive fructose intake leads to the onset of pathophysiological effects resulting in insulin resistance, metabolic syndrome, T2DM, CVD and cancer. The aetiology of the metabolic syndrome is not well understood and its elucidation is complex given the myriad potential pathways the disease progression can take in terms of demographics and predisposition to disease. The symptoms of T2DM are typically not the root cause of its origins and the many models developed to date have only found some of the pieces required to fully understand the full metabolic pathway. Prevention is always better than cure, however, for those with T2DM and its complications, the search for safe and effective treatments may be the only hope to maintain a reasonable lifestyle until full understanding of the disease is made.

1.4.4 Endothelin Induced Insulin Resistance

Endothelin-1 (ET-1) is a vasoconstrictor produced by endothelial cells to result in hypertension and also inhibits insulin-stimulated glucose uptake in adipocytes.[97] ET-1 is one of three isopeptides ET-1, ET-2 and ET-3, that act on different receptors to result in a variety of pathophysiological responses in various cell types including the inhibition of glucose uptake mentioned above.

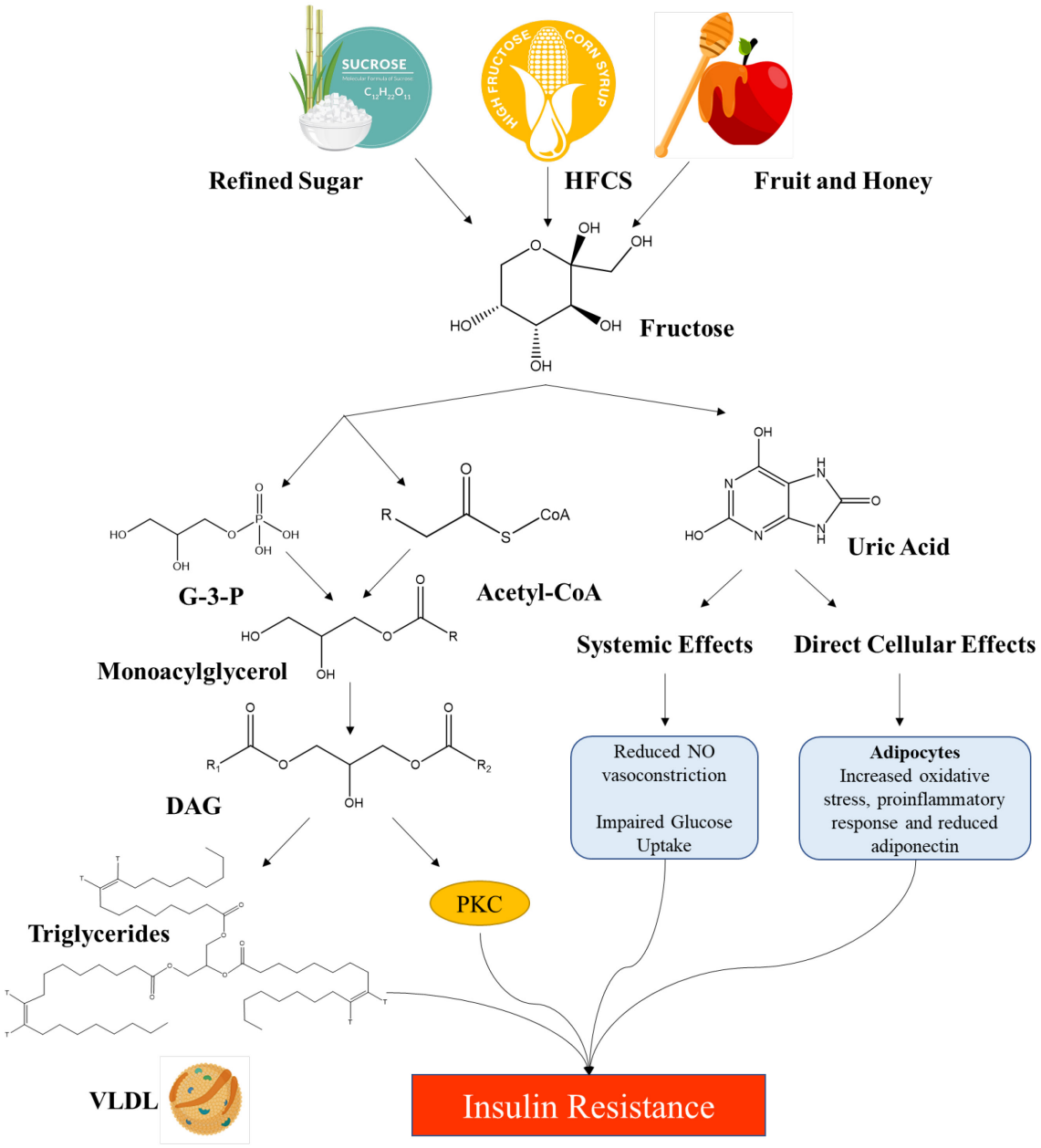

Figure 1.8: Fructose induces insulin resistance through the overproduction of TAG/VLDL and through the uric acid pathway. GLUT5 fructose transport leads to phosphorylation by F1K in an unregulated manner to result in rapid depletion of ATP. This activates the uric acid pathway leading to a reduction in insulin-dependent NO-mediated vascular dilation and other cellular effects in adipocytes. *De novo* lipogenesis (DNL) produces intracellular triglycerides that can induce insulin resistance. Adapted from Johnson, *et al.*[39] Hypothesis: Could Excessive Fructose Intake and Uric Acid Cause Type 2 Diabetes? *Endocrine Reviews*, 2009, 30(1):96-116, by permission of Oxford University Press.

ET-1 (**Figure 1.9**) is present in higher levels in individuals with insulin resistance, T2DM, obesity and hypertension.[97-98] The pathway to ET-1 overproduction, leading to pro-atherosclerotic activity is via the RAS/MEK/ERK pathway (**Figure 1.7**).[86,99]

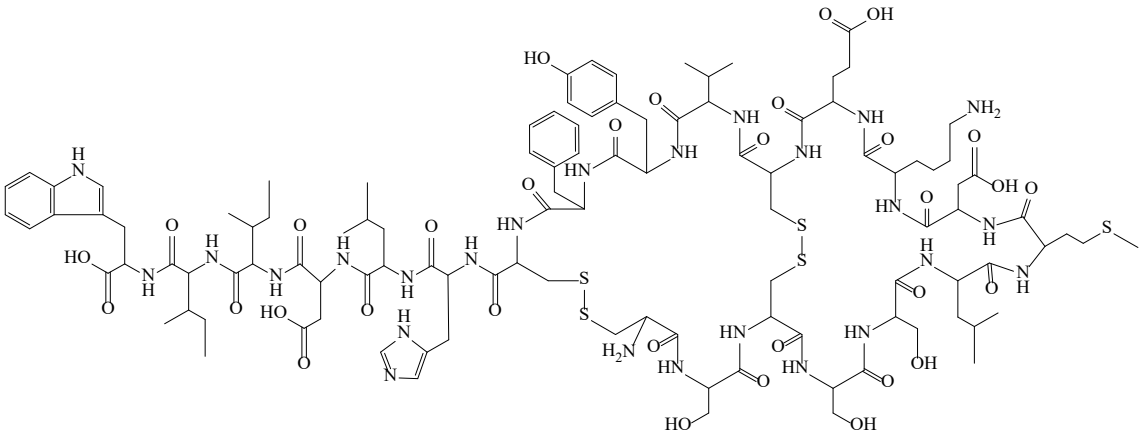

Figure 1.9: Chemical structure of Endothelin-1 (ET-1) a potent vasoconstrictor with pro-atherosclerotic activity.

Ishibashi, *et al.*[75] reported that chronic treatment of adipocytes with ET-1 results in the desensitisation of the metabolic and mitogenic actions of insulin, possibly through reduced tyrosine phosphorylation of the insulin receptor substrates IRS-1, SHC and Gαq/11. In this manner, insulin stimulated glucose uptake is inhibited in a manner similar to ET-1 suppression of lipoprotein lipase (LPL), which inhibits insulin stimulated heparin releasable LPL activity.[100] This suggests that elevated circulating ET-1 levels are a marker of insulin resistance and although the mechanism of action has yet to be elucidated, it is thought to be a result of its interference of insulin's ability to dephosphorylate GLUT4, thus reducing glucose transport.[101]

1.5 Insulin Mimetics and Insulin Enhancers

An insulin mimetic is any moiety that demonstrates insulin-like regulation of glucose metabolism in the complete absence of insulin. A drug is described as functionally insulin mimetic when it can replace insulin, whereas a drug is described as insulin-enhancing when it needs a small amount of insulin present to be effective.[102]

In individuals with type I diabetes (T1DM), the pancreas does not produce insulin[48] and requires a subcutaneous insulin injection directly into the blood stream to regulate glucose metabolism, usually in a postprandial manner.[103] For individuals with T2DM, the pancreas produces insulin, however, due to insulin resistance mainly in adipose tissue, circulatory glucose cannot be used, in a controlled manner by the body, which results in high concentrations of insulin and glucose in the circulatory system.[104]

Metal complexes of d-block elements have attracted much interest over the past two decades as potential anti-diabetic agents and in particular, most attention has been directed towards vanadium (V), molybdenum (Mo), tungsten (W), chromium (Cr) and

zinc (Zn).[105-121] The comparative potency observed for glucose metabolism and inhibition of alkaline phosphate activity was vanadate > tungstate > molybdate.[122] Peroxidovanadates were two orders of magnitude more potent in protein tyrosine phosphatase (PTP) inhibition compared to Mo and W, however, the higher hydrolytic stability of Mo and W compounds, along with other factors,[110] has been a driver of their further research as insulin mimetics.[123] Zinc compounds have also shown potential as insulin mimetics as zinc appears to play an essential role in the maintenance of glucose metabolism.[124]

A large body of literature describes the effects of these agents on diabetic animals (i*n vivo*) and *in vitro* cell culture studies, but information is limited on their exact mechanism(s) of action as insulin mimetics and warrants further investigation.[125] For metal complexes to be useful as biomimetic agents, they must be able to cross biological membranes, preferably by passive diffusion, be of low molecular weight, have moderate stability and have a balance of hydro- and lipophilicity, with thermodynamic and hydrolytic water stability.[104,123] In the case of V, Mo, W and Cr, ions of these metals can enter a cell via ion channels.[110]

Together with a reasonable window of optimal pharmacological effect, the abovementioned properties contribute to high bioavailability of potential insulin mimetics. Delivery of these insulin mimetics to target sites of action, *in vivo*, should proceed via slow kinetics of decomplexation to avoid rapid homeostatic removal of metal ions, such as vanadium as vanadyl, V(IV) and vanadate, V(V). In the treatment of T2DM, the insulin mimetic compound should not induce the secretion of insulin, should not exacerbate existing oxidative stress and should act as a substitute for the hormone.[126]

Although the use of metal complexes as dietary supplements may promote their widespread use, without the need for regulatory approvals associated with pharmaceutical therapeutics, the Lay group published a recent article on the potential deleterious effects of taking chromium (Cr) dietary supplements.[127] The ability of Cr to be oxidised to the known carcinogenic Cr(VI) state represents a situation where these supplements may be detrimental to the long-term health of those using such supplements. Fortunately, V(IV) and V(V) are not carcinogenic at biologically relevant concentrations and although they can be cytotoxic at higher concentrations, they represent a class of supplements with low risk to the end user,[105] but there is insufficient information on what levels are beneficial without side effects.

1.5.1 Vanadium as an Insulin Mimetic

Vanadium is a trace element in the human diet and is typically taken up by crops in vanadium rich soils and is in a number of grains, fruits, vegetables, herbs and spices.[105] Other sources of dietary vanadium are meat, fish, nutrient supplements and through inhalation of environmental pollutants.[128-129] Historically, vanadium complexes were mainly studied as potential anti-diabetic agents[105,118] and their benefits have been recognised for over a century, particularly their ability to lower plasma glucose levels in models of T2DM.[125] Since the 1980's much research has focussed on better understanding of their mode(s) of action, particularly for improving carbohydrate and lipid metabolism, glucose transport, glycogen synthesis and its inhibition of gluconeogenesis and lipolysis.[115] Recent literature has also provided evidence of their potential for use as anti-cancer, anti-parasitic drugs, wound healing, CVD and for neuroprotection.[105,111,129] The anti-cancer properties of vanadium complexes is discussed in detail in Section 1.5.2.

In an excellent review by Crans,[102] the history of vanadium salts and complexes is discussed and the current understanding of the action of vanadium compounds as insulin mimetics or insulin enhancers is presented. Since vanadium is approved for human use as a dietary supplement, the need for extensive clinical trials when evaluating its anti-diabetic actions is reduced to some extent. One of the major benefits of using vanadium compounds over pharmaceutical drug products is that they can be used to fortify foods, by growing crops in vanadium rich soils, or as previously mentioned, added to health supplements. In this way, the costly and time consuming process of new drug substance regulatory approvals can be avoided and greater access to the public is the result.[105]

Air-stable vanadium compounds in the higher oxidation states (IV and V) have the greatest benefits to health. The vanadate ion (VO_4^{3-}) has been reported to exist under physiological conditions and is similar in structure and action to the phosphate ion (PO_4^{3-}).[130] The vanadate-phosphate analogue is important because of its interactions with proteins such as PTP, where V(V) binds to the active site of the enzyme and, therefore, inhibits phosphatase activity.[131] This inhibitory action is postulated to be responsible for the beneficial actions of vanadate as an anti-diabetic treatment.[130,132] The pK_a values for monomeric vanadate are 3.5, 7.8 and 12.5, which compare to the corresponding pK_a values for phosphate, 2.1, 7.2 and 12.7. Therefore, the main species at pH 7 is $H_2VO_4^-$.[102] **Figure 1.10** shows the similarities between the structures of the phosphate and monomeric vanadate groups.

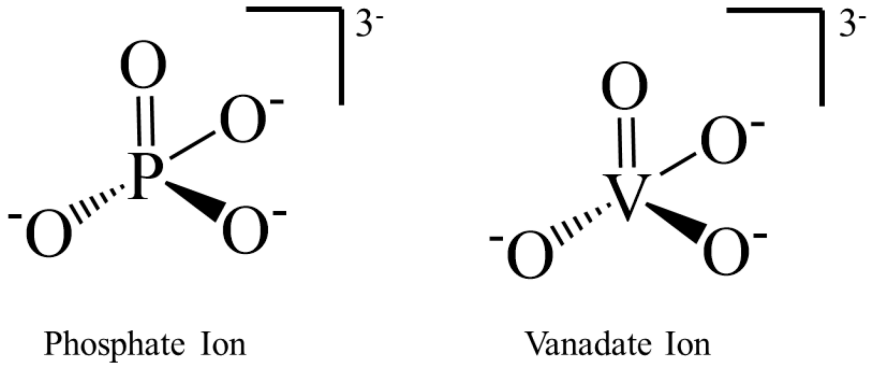

Figure 1.10: The chemical structures of the phosphate and vanadate groups are similar. The V-O bond lengths in vanadate are not much longer than those of the P-O bond lengths (1.7 vs 1.54 Å).[133-134]

In normal insulin signalling, autophosphorylation of the insulin receptor β-subunits is susceptible to substitution by vanadium compounds, with much research dedicated to the use of V(IV) and V(V) complexes as potential insulin mimetics,[135] although the active form of the vanadium species *in vivo/in vitro* remains elusive.[102] Changes in the coordination geometry of a particular vanadium species has a marked impact on the manner in which it acts *in vivo/in vitro* and warrants further research at the molecular level to fully understand its actions.[110,129]

Figure 1.11 provides a simple overview of the potential action of vanadium complexes as insulin mimetics and **Figure 1.12** provides a schematic of the different ways vanadium can enter a cell in order to impart its insulin mimetic/enhancing or cytotoxic actions. Vanadium can enter a cell by three mechanisms; (i) through ion channels as vanadate (V(V)), representing the most likely route of transport *in vitro*;[111] (ii) by endocytosis through binding with transferrin; and (iii) by diffusion. Intracellular vanadate can act to inhibit PTP through binding to the active site cysteine residue.[111] The intracellular vanadate ion undergoes reduction to the vanadyl ion (V(IV)) in the presence of glutathione, and V(IV) is a weaker inhibitor of PTPs than V(V).[129] This allows phosphate to bind to the intracellular site of the insulin receptor, which signals GLUT4 transporters to translocate to the cell membrane and allow glucose into the cell for metabolism.

Oral ingestion of most vanadium compounds is ineffective since they are converted into insoluble $VO(OH)_2$ in the gastrointestinal tract,[111,136] therefore, complexes were designed to facilitate uptake (including the bis(maltolato)oxovanadium(IV) complex, BMOV).[105] In circulation, ingested vanadium compounds are likely to be bound to transferrin where they are transported to the sites of action.[112] It is possible that vanadium is delivered to a cell via the processes of endocytosis through binding to transferrin or albumin, or through

the process of diffusion.[111] The mechanisms of vanadium release from transferrin into the cell are not well understood.[102] It has been proposed that the nature of the ligand used in the metallocomplex may play a role in delivery by transferrin and can explain the higher doses responsible for their anti-diabetic behaviour.[112]

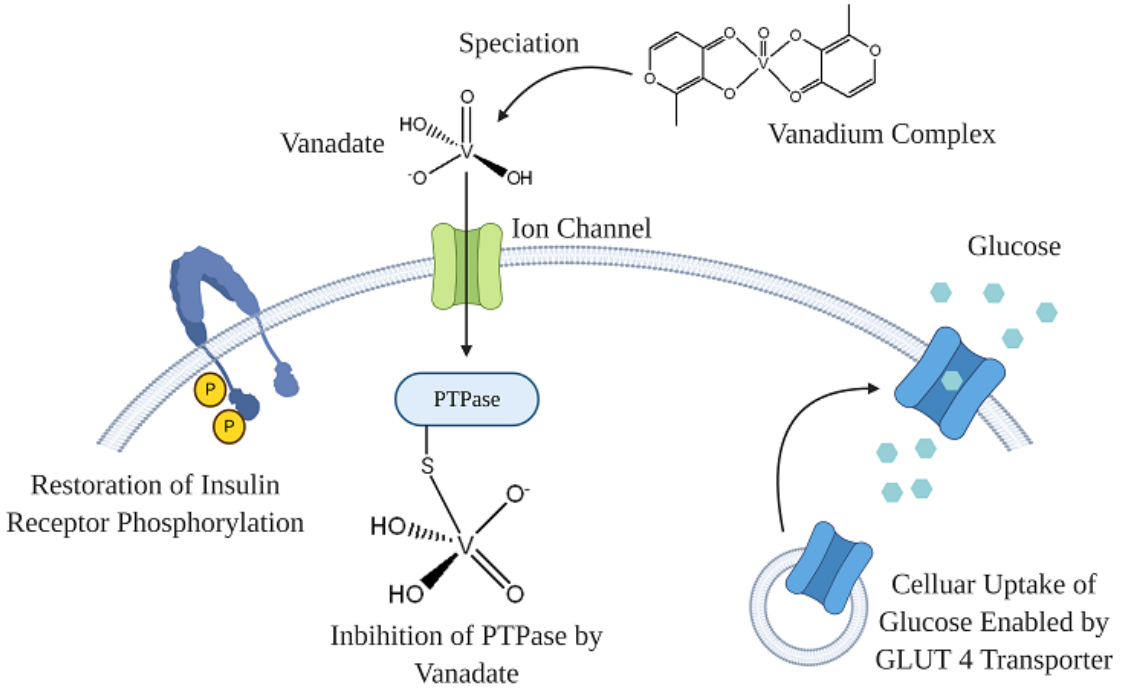

Figure 1.11: PTP inhibition by vanadate. Bis(maltolato)oxovanadium(IV) (BMOV) is used as an example. BMOV is orally ingested and is postulated to remain intact until it reaches its target site of action. Physiological conditions promote the oxidation of the V(IV) complex to V(V) as the vanadate ion. Adapted by permission from Springer Nature, Rehder.[136], Vanadium in Health Issues, copyright, 2001. Created with BioRender.com.

Sodium orthovanadate (Na_3VO_4) and vanadyl sulfate ($VOSO_4$) have been carried forward into clinical trials based on the effects observed in animal studies.[102] While both showed promise, side effects such as gastrointestinal discomfort limited their clinical application.[125] BMOV and its analogue bis(ethylmaltalato)oxidovanadium(IV) (BEOV) are more effective *in vivo*, than vanadate due to their increased oral absorption, higher potency, lower toxicity and improved tolerance.[125]

The exact oxidation state of intracellular vanadium is also a topic of continued research and Evangelou,[129] reports that both V(V) and V(IV) complexes, inhibit PTPs, but may be acting with different mechanisms.[110-113] It is possible that the antidiabetic effects of vanadium are a combination of its ability to adapt to its environment (given its complex pH dependent chemistry) and its ability to generate ROS and inhibition of downstream

enzymes, including phosphorylases.[102] Levina, *et al.*[113] performed a series of experiments where vanadium compounds were pre-treated with simulated gastrointestinal media with and without the addition of food nutrients into culture media prior to analysis by X-ray near edge structure (XANES) spectroscopy. V(V) was the predominant intracellular species and this finding supported the mechanism proposed by Rehder,[136] (**Figure 1.11**).

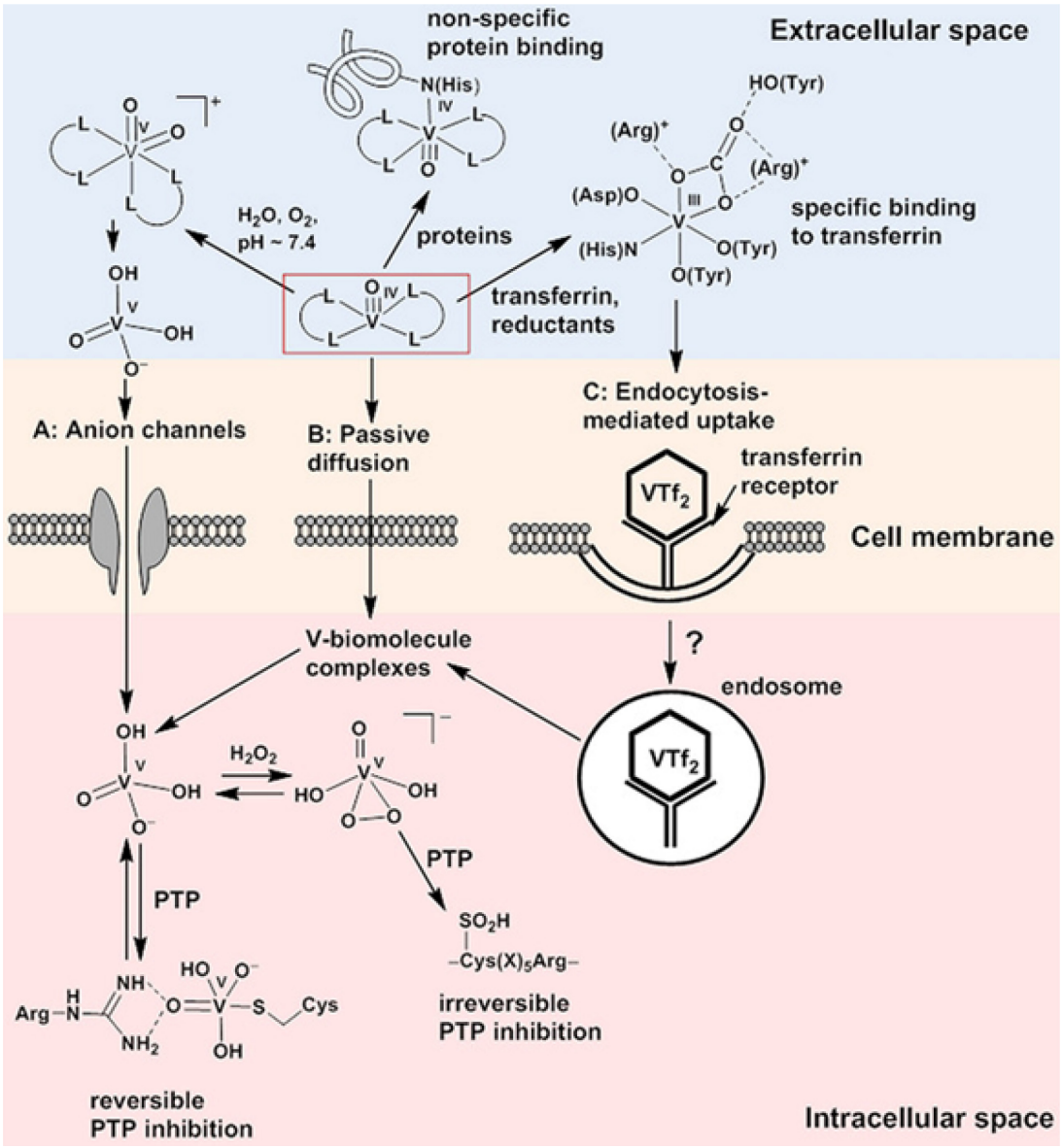

Figure 1.12: Modes of cellular uptake of anti-diabetic/anti-cancer vanadium compounds. Reproduced by permission from John Wiley and Sons, Levina, A. and Lay, P. A.,[111] Stabilities and Biological Activities of Vanadium Drugs: What is the Nature of the Active Species? Chemistry - An Asian Journal, copyright, 2017.

In vitro studies on vanadium compounds have been performed over the concentration range of several μM to mM, which are much higher than typical physiological concentrations (0.3 μM averaged over all tissues and an order of magnitude less in blood

serum concentrations),[136] raising doubts over the therapeutic relevance of vanadium compounds.[125] These findings do not exclude the continued research into vanadium compounds as insulin mimetics or anti-cancer drugs, where most attention has been shifted compared to anti-diabetic effects.[111] Further research is warranted, particularly studies related to vanadium's glucoregulatory actions and its interactions with several enzymes in the insulin-signalling pathway, including MAP and S6 kinases, which are defective in diabetes, but could be rectified with vanadate treatment.[137]

In Section 1.4.2, the link between insulin resistance and hypertension was established. Poucheret, *et al.*[137] performed trials on spontaneous hypertensive rats (SHR) and fructose hypertensive rats where $VOSO_4$ and BMOV were assessed for their antihypertensive activity. The study findings indicate that vanadium compounds are capable of lowering blood pressure, strengthening the link between hyperinsulinemia, insulin resistance and hypertension, which demonstrated vanadium's ability to act as an antihypertensive.

1.5.2 Vanadium as an Anti-Cancer Therapeutic.

Cancer is the second leading cause of death globally and was responsible for 9.6 million deaths in 2018.[138] To better understand how to treat cancer, knowledge of the various phenotypes of the disease is imperative. Eight hallmarks of cancer must be considered when developing anti-cancer therapies; proliferation, growth suppression evasion, apoptosis evasion, replication of immortality, induction of angiogenesis, invasion and metastasis, energy metabolism and immune destruction evasion.[139] Targeted drug development is focussed on disturbance of energy production, respiration or mitochondrial structure and function disorders as observed in the Warburg effect.[52]

According to the World Health Organisation (WHO), cancer is defined as a large group of diseases that can originate in any organ and is hallmarked by abnormal and uncontrolled cell growth.[140] The uncontrolled cell proliferation and genetic instability of cancer cells is associated with deregulation of the cell cycle process.[141] Tumours are comprised of two parts; the proliferating cells and the stroma, or supporting cells that comprise blood vessels and connective tissue.[140] Metastases occur when the host tissue integrity is broken down and tumour cells enter circulation to establish themselves in distant parts of the body with the ability to induce angiogenesis. At this stage, the tumours can proliferate via a similar mechanism and establish at secondary sites.[142]

As discussed in Section 1.3, Port, *et al.*[20] observed that during periods where glucose is not available for metabolism, fructose may also be metabolised via a Warburg-type

process. In the presence of a carbohydrate source, such as glucose and fructose, cancer cells rapidly upregulate glucose (fructose) uptake and undergo glycolysis, which is uncoupled from the mitochondrial TCA cycle and oxidative phosphorylation.[143] The produced pyruvate is utilised in lactate fermentation, where it is kept away from oxidative metabolism.[52] The Warburg metabolic phenotype is widespread in many cancers, and vanadium compounds have the ability to modulate the metabolic processes associated with the Warburg effect.[144] Such factors must be taken into account when evaluating the efficacy of vanadium compounds, particularly given the fact that the anti-tumorigenic actions imparted by these compounds may be working under a similar mechanism to those observed when vanadium acts as an anti-diabetic agent.

Levina, *et al*,[110-111] Evangelou,[129] Kioseoglou, *et al.*[144] and Kowolski *et al.*[145] have reviewed the role of vanadium compounds used in anti-cancer studies. The modes of action of tumour growth suppression have been classified as those that inhibit tumour cell growth that leads to apoptosis and those that minimise the invasiveness and metastatic potential of cancer cells. These reviews state that the V(V) species are the main cytotoxic species and their actions may be specific to tumour cells. The trigonal bipyramidal complexes may act in a similar way as they act in anti-diabetic activities of vanadium as this coordination geometry resembles a transition state with high reactivity.[132]

Metallodrugs, such as cisplatin and its derivatives, have been approved by world regulatory authorities for the treatment of cancer for well over 30 years and most anti-cancer research into metallodrugs has stemmed from cisplatin.[128] Like cisplatin, some vanadium complexes activate the p53 protein, a tumour suppressor protein that normally functions in the regulation of apoptosis.[129] Orthovanadate induces DNA fragmentation, loss of mitochondrial membrane potential, production of ROS and activation of caspase-3, all of which induce apoptotic pathways in cells.[146] The potential of vanadium compounds as PTP enzyme inhibitors, reviewed by Irving, *et al*,[147] recognised that phosphotyrosine signalling is implicated in almost all aspects of cancer biology due to its widespread influence over cell signalling pathways.

The ability of intracellular vanadium to produce ROS can be used to good effect in the treatment of cancer, as high levels of ROS can induce cytotoxicity and result in apoptosis.[129] After transport of vanadate ions into a cell through phosphate or sulfate ion channels, intracellular glutathione can reduce V(V) to V(IV).[148-149] Zhao, *et al.* has studied the glucose uptake effect of $VOSO_4$, *in vitro*, using the HepG2 cell line,[150] which is the subject of Chapter 5. It was reported that $VOSO_4$ could stimulate glucose uptake

and IR/Akt phosphorylation in the range 0-50 μM, where at the upper limit, both effects started to decrease. At this stage, vanadium may be changing from a growth promoter to being cytotoxic.

In order to counter cytotoxic effects, cellular processes such as autophagy are used to remove waste build up and damaged organelles from the cellular interior, thus maintaining cell homeostasis.[151] However, in a tumour cell, autophagy can also be used to maintain cell homeostasis and its inhibition can decrease a cancers ability to use fatty acids to promote growth.[152] Wu, *et al.* showed that Na_3VO_4 modulates autophagy in tumour cells to promote apoptosis in the HepG2 cell line.[153] These researchers report similar results to Zhao, *et al.*[150] that V(IV) concentrations of up to 50 μM stimulated glucose uptake, a result that was also observed for V(V).[153]

The effective uptake of these drugs orally, or intravenously in a stable and active form is dependent on the ligands of the vanadium complexes and also, in the co-action of the ligand and the vanadium species.[102] Recently, the use of vanadium nanoparticles has been investigated for the targeted and sustained treatment of cancer.[154] These considerations are particularly important for *in vivo* studies, however, for *in-vitro* studies, the simple inorganic vanadium salts have proven useful in the understanding of the anti-cancer properties of vanadium in general.[144]

In the case of vanadium complexes of 1,10-phenanthroline (Phen), enhanced cytotoxicity was observed, but this is related to the high cytotoxicity of the dissociated Phen ligand.[155] Phen is an active DNA intercalator and deforms the DNA double helix structure, rendering it susceptible to attack by the vanadium species. Zhang, *et al.*[156] performed an *in vitro* study of a mixed-ligand oxovanadium complex investigating the cytotoxicity towards the HepG2 cell line with a Phen group. The cytotoxicity was attributed to the vanadium species; however, it is more likely, based on the results of Le, *et al.*[155] that the observed cytotoxicity of these complexes is related to the dissociation of the Phen ligand from the complex. This again highlights the important co-activity of the ligand system in terms of its flexibility and ability to adapt in the tumour microenvironment when these drugs perform their action *in vivo*.

Vanadium complexes, including *in vitro* treatments using Na_3VO_4,[153] inhibit the epithelial mesenchymal transition (EMT) process, which is mainly responsible for the invasive and metastatic cancer phenotypes.[157] EMT results in epithelial cells becoming mesenchymal, with loss of cell adhesion, thus changing their shape and intracellular

properties. Mesenchymal cells migrate to other tissues, or are transported via circulation to other parts of the body where they can metastasise. In this current research project, the use of sodium orthovanadate, Na_3VO_4, was used for all *in vitro* studies as it is believed this is the active species that acts as an insulin mimetic and a cytotoxic agent.[110-111] Evangelou[129] has summarised the possible actions of anti-cancer vanadium *in vivo* and *in vitro* as shown in **Figure 1.13**.

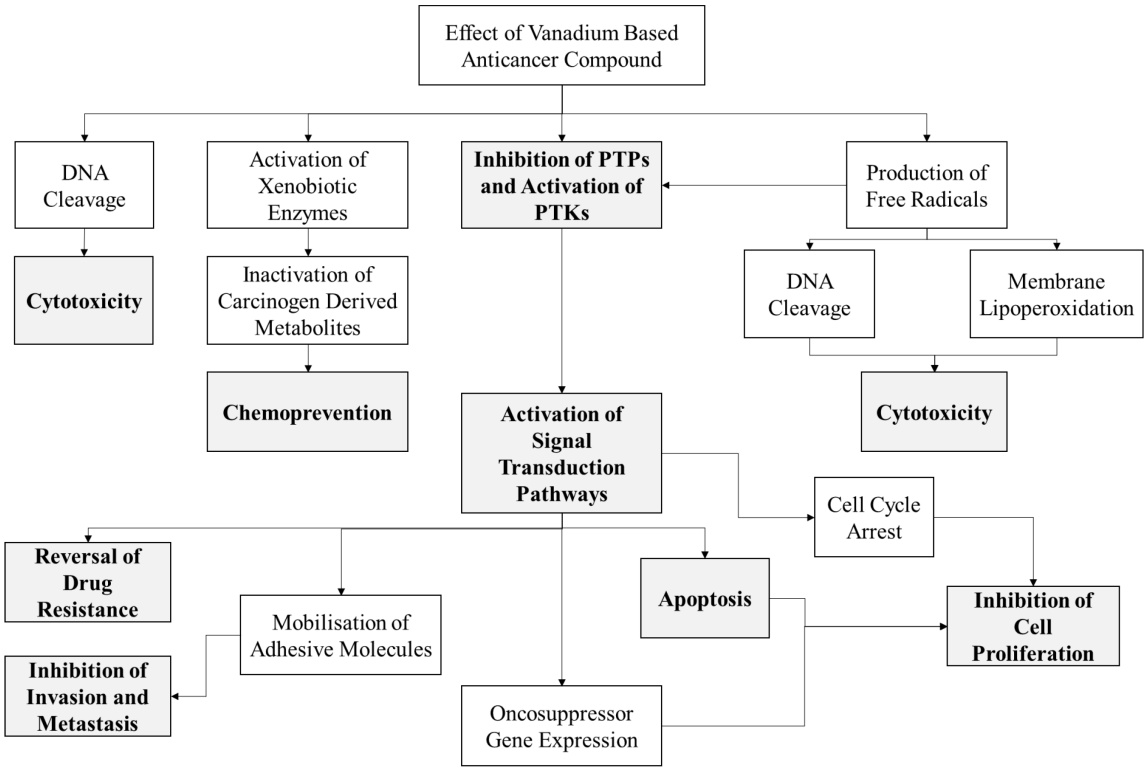

Figure 1.13: The complex pathways of action of vanadium compounds as anticancer therapeutics. Cytotoxic effects are induced via DNA cleavage pathways or via cell membrane degradation through lipoperoxidation. Chemoprevention is induced via pathways that minimise the production or inactivate carcinogen derived metabolites (possibly extracellular vesicles come into this category). The most common pathway, as also reported for vanadium antidiabetic action is through the inhibition of PTP and the activation of PTK's leading to signal transduction pathways including apoptosis, inhibition of cell proliferation, invasion, metastasis and the lowering of drug resistance. Reproduced from Critical Reviews in Oncology/Hematology, Evangelou.[129] Vanadium in Cancer Treatment, 42, 249-265, copyright 2002, with permission from Elsevier.

1.5.3 Oxidative Stress and Reactive Oxygen, Nitrogen and Chlorine Species

Reichmann, *et al.*[158] published an excellent review of oxidative stress and its effects on the proteome. Oxidative stress is defined as the imbalance between oxidants and antioxidants in favour of the former.[159] Minor disturbances in this balance do not constitute conditions of oxidative stress and it is only when the levels of pro-oxidants

(such as hydrogen peroxide H_2O_2) increase with a corresponding decrease in glutathione that conditions can become conducive to cellular damage.[160]

The generation of reactive oxygen, nitrogen and chlorine species (ROS, RNS and RCS, respectively), results in protein unfolding and irreversible aggregation due to reactions with highly reactive protein amino acid side chains. The accumulation of misfolded proteins in the cellular environment results in toxic conditions that can disrupt proteome homeostasis (proteostasis).[161] Prolonged toxic environments induced by accumulation of protein mis-folding and lipid peroxidation products[162] ultimately result in the condition of oxidative stress.

Hydroxyl radicals (•OH) have been postulated to be the most reactive ROS and are responsible for most of the protein, lipid and DNA damage induced under oxidative stress conditions and lipid peroxides generated as a result of •OH can further lead to cellular damage.[163] However, there is dispute as to whether hydroxyl radicals are produced under physiological conditions since their existence is based on indirect evidence, and metal complexes in high oxidation states cause the same products.[164]

In normal cell homeostasis, an imbalance in favour of pro-oxidants is undesirable; however, for abnormal cells, such as cancer cells, a shift to localised pro-oxidant conditions is an advantage, particularly in the design and development of anti-cancer therapies. Under conditions of lower pH (anticipated in cancer cells through the Warburg effect and generation of lactate)[52] combined with an altered state of antioxidants and increased H_2O_2 levels, the generation of ROS by vanadate species is postulated to occur according to the following proposed chemical reactions.[129]

$$VO^{2+} + H_2O \longrightarrow VO_2^+ + H^+ + \bullet OH$$

$$VO^{2+} + O_2^{2-} + H_2O \longrightarrow VO_2^+ + OH^- + \bullet OH$$

V(IV) in the presence of water may lead to the generation of highly cytotoxic hydroxyl radicals or the production of the benign superoxide anion radical, which is spontaneously dismutated by superoxide anion dismutase (SOD) to oxygen and H_2O_2.[129] It has been shown that peroxido- and hydroperoxide V(IV) radicals can be formed intracellularly by a superoxide generated by NADPH-oxidase as described in the following reaction.[165]

$$2V(V) + NADPH \longrightarrow 2V(IV) + NADP^+ + H^+$$

$$V(IV) + O_2 \longrightarrow V(V) + \bullet O_2^-$$

$$V(V) + \bullet O_2^- \longrightarrow [V(IV) - OO^\bullet]$$

In this redox cycling reaction, the superoxide radical results in the formation of the vanadyl hydroperoxide radical, which decomposed in the presence of H^+ to produce vanadate and H_2O_2 as follows.

$$[V(IV) - OOH] + H^+ \longrightarrow V(V) + H_2O_2$$

NADPH is necessary for the maintenance of the thioredoxin-glutaredoxin systems that restore cellular redox homeostasis.[166] Cells that undergo high levels of oxidative stress have up to 50% less ATP than non-stressed cells as a result of oxidative inactivation of redox-regulated metabolic enzymes involved in ATP generation.[167] These pathways redirect glucose metabolism from glycolysis to the pentose phosphate pathway (PPP), reducing ATP synthesis and generating NADPH. In the presence of vanadium species, increased NADPH results in the generation of more H_2O_2 and, therefore, to higher levels of oxidative stress described by the chemical reactions above.[129]

The formation of peroxides activates pathways that inhibit PTP, causing tyrosine phosphorylated proteins to accumulate, and promotes further formation of ROS, regenerates V(IV) peroxides and, hence perpetuates the cycle of ROS generation. This inhibition of PTP with corresponding PTK activation, MAPK-dependent signal transduction, and DNA cleavage is postulated to be the major mechanism for the cytotoxic action of intracellular vanadium species.[129] Overall, the ROS generated by vanadium species leads to membrane lipid peroxidation, protein denaturation and DNA damage,[168] fundamental properties of anti-cancer therapies.

To combat the effects of ROS, cellular glutathione and vitamins scavenge free radicals in order to restore the oxidant/antioxidant balance.[169] In the detoxification process, cells such as macrophages release large amounts of peroxide and RCS during an event known as oxidative burst.[170] It is believed that RCS are more likely to result in protein aggregation due to their ability to react rapidly with amino acid side chain residues during protein unfolding events.[171]

Redox sensitive proteins undergo either local or global conformational rearrangements under conditions of oxidative stress, which directly affect the functionality of the protein.[158] FTIR and Raman spectroscopy, reveal changes in protein secondary structure induced by oxidative stress and other stimuli.[172] Two protein conformations of particular interest are the α-helix and β-sheet conformations (**Figure 1.14**).

a) α-helix structure

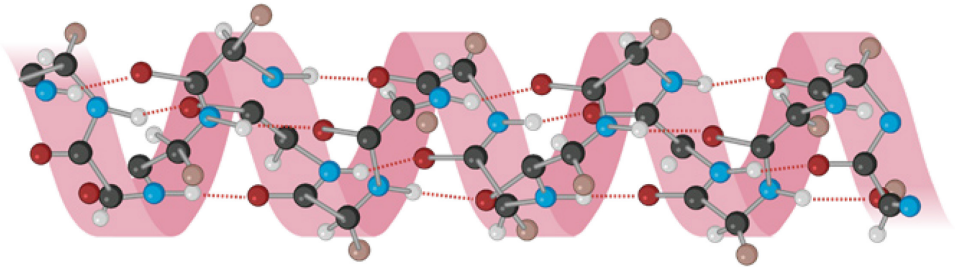

b) β-(pleated) sheet structure

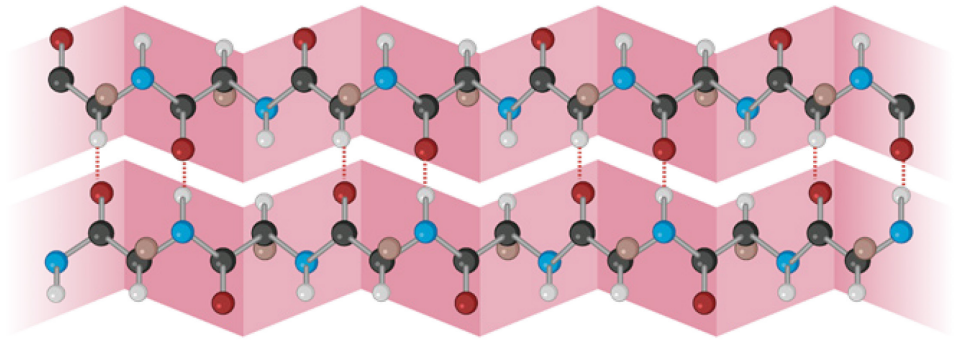

Figure 1.14: Protein secondary structures; a) α-helix and; b) β-pleated sheet.

Secondary structures of proteins are key factors of their biological functions and consist of α-helix, β-sheet, β-turns and random coil structures.[173] The folding and unfolding of this secondary structure in a regulated manner determines the biological activity towards a specific target.[173] Protein folding is guided by chaperones and folding catalysts that require energy in the form of ATP to maintain full efficiency. Loss of structural fidelity induced by misfolding is a common feature of a wide range of diseases, including some types of cancer and T2DM.[173-174]

Neurodegenerative diseases such as Alzheimer's and Parkinson's, are characterised by the formation of protein aggregates (amyloid fibrils) that deposit in tissues and organs.[173] Shivu, *et al.*[175] used vibrational spectroscopic methods to confirm that these aggregates are of β-sheet structure and under stress conditions, α-helix to β-sheet transition can be observed using vibrational spectroscopy for a number of protein types.[176-177] Oxidative stress is also believed to be a trigger of the aggregation process and the onset of diseases such as T2DM, where amyloid deposits in the pancreas have been found.[178] This information is relevant to the results reported in this thesis to better understand the modes of action of vanadate complexes on adipocytes and hepatocytes.

1.6 Vibrational Spectroscopy

While vibrational spectroscopy covers the wavelength region 700–1,000,000 nm encompassing the near, mid and far-infrared regions,[179] the mid-infrared (MIR) region (4000-400 cm^{-1}, 2500-25000 nm) provides information about stretching and bending modes of chemical bonds. The chemical composition and conformations of biomolecules from FTIR can be deduced from assignment tables,[180-183] such as **Table 1.1**. This table was compiled based on an extensive search of the literature and provides a general overview of the common band assignments, including much cited articles by Movisaghi, *et al.*[181] on general biological materials; Wood[182] and Dovbeshko, *et al.*[184] focussed on DNA and nucleic acids; Barth[180] focussed on proteins; and Bader, *et al.*[185] focussed on lipids. Assignments are general to wavenumber regions for specific chemical groups and Naumann[172] states that the detection of a single component within complex biological matrices is intrinsically problematic. Therefore, group frequency tables should be used as a guide, given the complex nature of cells and their internal heterogeneity and changes in wavenumbers of bands due to effects of hydrogen bonding and other environmental factors on structure.[180] **Table 1.1** was used as a general reference point for band assignments observed in the multivariate data analysis procedures discussed in Chapters 3-6.

1.6.1 Fourier Transform Infrared Microspectroscopy

Fourier transform infrared (FTIR) microspectroscopy combines the spectral data acquisition of an FTIR spectrometer with the magnifying power of a microscope. The theory of vibrational spectroscopy is covered in authoritative articles and textbooks.[172,179,186-190] Only instrumental and sampling aspects associated with infrared microspectroscopy are discussed with relation to single cell (bulk) scanning, mapping and imaging (**Figure 1.15** and **Figure 1.16**). A highly precise mechanical *x*-*y*-*z* stage is used to position samples under a Cassegrain or Schwarzschild objective[191] of selected magnification power. For chemical mapping, this objective moves in a predefined grid pattern in increments, therefore, any extraneous movement or stage imprecision motions result in misaligned maps and may lead to incorrect interpretations.

There are two types of acquisition mode; reflectance (specular), where incident light is directed to the sample and the reflected radiation is collected by the microscope optics and directed to the detector and; transmission, where incident radiation is transmitted through the sample and is collected using a transmission detector arrangement. Where the

substrate used to mount cell or tissue samples is reflective, the incident light may penetrate through the sample and reflect off the substrate where it is directed towards the detector. In this situation, the process of transflection may occur.[192]

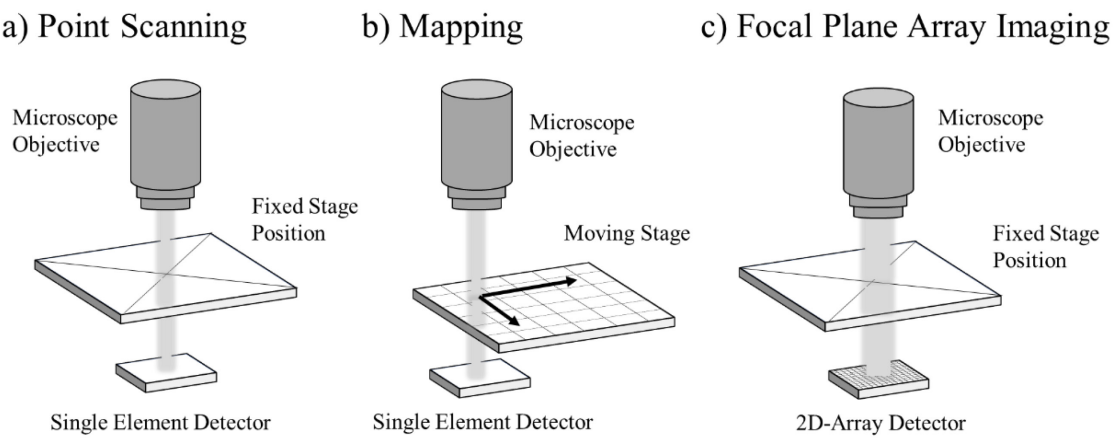

Figure 1.15: Three types of spectral data acquisition used in FTIR microspectroscopy: a) point scanning; b) line or grid mapping; and c) focal plane array (FPA) detector, which uses a two-dimensional array of detector elements of specified size.

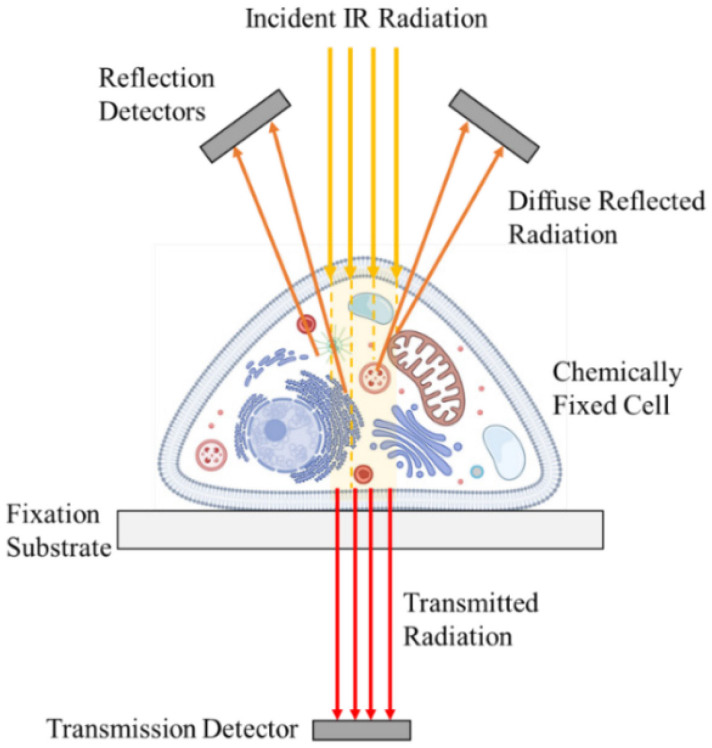

Figure 1.16: Description of two modes of data collection used in FTIR microspectroscopy. Incident radiation is focussed by the microscope to the user defined region of interest (ROI) where it penetrates the cell membrane and is either reflected back towards the direction of the incident radiation (reflectance) or is transmitted through the sample (transmission).

With reference to **Figure 1.15**, point scanning involves isolation of a single feature, either a single cell, cluster of cells or a tissue section, and using the microscopes entire field of view (FoV) (or reducing the FoV with mechanical apertures) obtaining a single spectrum of the region of interest (ROI). In line or grid mapping, a larger area than the FoV can be defined by the step size of the sampling grid. The grids can be spaced with no overlap between adjacent scans (optimal sampling), or a degree of overlap can be defined (oversampling). The mechanical *x-y-x* stage moves the sample according to the defined line or grid dimension until a spectral map is obtained of the ROI.

Table 1.1: Mid-infrared assignment table of typical bands frequently found in biological materials.

Wavenumber (cm^{-1})	Assignment	Reference
3006	ν (=C-H) *cis*-conformation lipids and fatty acids	Guillén and Cabo[193]
2958	ν_{as} (CH_3) acyl chains of fatty acids and cellular lipids	Junhom, *et al.*[194] Ricciadi, *et al.*[195] Guillén and Cabo[193]
2934-2925	ν_{as} (CH_2) cholesterol	Ami, *et al.*[196] Dreissig, *et al.*[197]
2918	ν_{as} (CH_2) acyl chains of fatty acids and membrane lipids	Junhom, *et al.*[194] Ricciadi, *et al.*[195] Naumann[183]
2898	ν (C-H) amino acids	Davis and Mauer.[198]
2870	ν_s (CH_3) cellular lipids and proteins	Ricciadi, *et al.*[195]
2850	ν_s (CH_2) chains of fatty acids and membrane lipids	Naumann,[183] Ricciadi, *et al.*[195]
2810	ν_s (CH_2) aliphatic fatty acid chains	Sukprasert, *et al.*[199]
1745	ν (C=O) lipid ester, protonated phosphatidylserine	Movasaghi, *et al.*[181], Bader *et al.*[185], Wood.[182] Gomez-Fernandez, *et al.*[200]
1725	ν (COOH) protonated free fatty acids	Gomez-Fernandez, *et al.*[200] Gazi, *et al.*[201]
1715	ν (C=O and C=N) B-DNA base pairing vibration	Wood.[182]
1712	ν (COOH) protonated free fatty acids	Oleszko, *et al.*[202]
1708	ν (C=O and C=N) A-DNA base pairing vibration	Wood.[182]
1695	ν (C=O and C=N) Z-DNA base pairing vibration	Wood.[182]
1690	ν_{as} (C=O) RNA	Wood.[182]
1688	ν (C=O) Amide I, β-turns	Buijs, *et al.*[203]
1660	ν (C=O) Amide I, β-turns	Buijs, *et al.*[203]
1656	ν (C=O) Amide I α-helix conformation	Barth.[180], Nevskaya, *et al.*[204]
1654 and 1648	ν (C=C) *cis*-conformation lipids and fatty acids	Guillén and Cabo[193]
1639	ν (C=O) Amide I random coils	Zelig, *et al.*[205]

Table 1.1 (*cont*): Mid-infrared assignment table of bands frequently found in biological materials.

Wavenumber (cm-1)	Assignment	Reference
1623	ν (C=O) Amide I β-sheet, β-strands (protein aggregates)	Buijs, *et al*.[203] Shivu, *et al*.[175] Ami, *et al*.[196]
1620	ν (COO^-) unprotonated carboxyl groups in lipids	Gomez-Fernandez, *et al*.[200]
1612	Tyrosine and arginine side chains	Chirgadze, *et al*.[206]
1590	δ N-CH_3 Choline group	Oleszko, *et al*.[202]
1578	ν (C=N) DNA and RNA, imidazole ring	Wood.[182]
1550	δ (N-H) and ν (C-N) Amide II	Barth.[180]
1515	Tyrosine band	Naumann.[172] Davis and Mauer.[198]
1481	δ $(N-CH_3)_3$ Choline and Cholesterol	Ami, *et al*.[196]
1465	δ (CH_2) of lipid and fatty acids	Barth.[180], Naumann.[183] Fukuyama.[207] Oleszko, *et al*.[202]
1450	δ (CH_2 /CH_3) lipids and proteins	Naumann.[183]
1425, 1418 and 1408	A-DNA, B-DNA Z-DNA Deoxyribose	Wood.[182]
1418	ν (=C-H) *cis*-conformation lipids and fatty acids	Guillén and Cabo[193]
1415	δ (C-O-H) carbohydrates, DNA/RNA backbone, proteins, short chain fatty acids.	Frigneli and Günthard,[208] Davis and Mauer.[198] Koca, *et al*.[209]
1400	δ (COO^-) lipids	Ricciadi, *et al*.[195]
1379	δ (COO^-) fatty acids and amino acid side chain groups, δ (CH_3) lipids	Lozano, *et al*.[210] Arrondo and Goni.[211]
1365	δ (CH_2) fatty acids	Dreissig, *et al*.[197]
1296	Amide III	Ricciadi, *et al*.[195]
1240	ν_{as} (-PO_2) phosphodiester DNA	Wood.[182]
1238	ν (C-O) and δ (CH_2) lipids	Guillén and Cabo[193]
1185	A-DNA, ribose	Wood.[182]
1178	δ (CH_2), fatty acid chains	Dovbeshko, *et al*.[184] Dreissig, *et al*.[197]
1173	ν (C-OH) serine, threonine, tyrosine	Ami, *et al*.[196]
1163	ν (C-O) and δ (CH_2) lipids	Guillén and Cabo[193]
1160	ν (C=O) ribose, RNA	Wood.[182]
1150	ν (CO-O-C) and (C-O) lipids and DNA	Ricciadi, *et al*.[195]
1127	ν (C-O) lactate	Petibois, *et al*.[212]

Table 1.1 (*cont*): Mid-infrared assignment table of bands frequently found in biological materials.

Wavenumber (cm-1)	Assignment	Reference
1120	ν (C=O) Ribose, RNA	Wood.[182]
1118	ν (C-O) lipids	Guillén and Cabo[193]
1112	P-O-C band phospholipid	Dovbeshko, *et al*.[184]
1097	ν (C-O) lipids	Guillén and Cabo[193]
1085	ν_s (-PO_2) phosphodiester DNA	Ricciadi, *et al*.[195]
1070	ν_s (-SO_3) Sulfatides	Dreissig, *et al*.[197]
1060, 1050	ν (C=O) Ribose, DNA, RNA	Wood.[182]

s- symmetric, as- asymmetric, ν- stretching, δ- bending.

A focal plane array (FPA) detector is a two-dimensional array of detector elements of specified size. Typical FPA grid sizes include 32 × 32, 64 × 64 and 128 × 128 elements. Even though the physical dimensions of the 64 × 64 FPA detector are 72 × 72 μm, the theoretical pitch of the detect pixels of 1.1 μm^2 do not translate to the true spatial resolution in the infrared images obtained.[213] The true spatial resolution of an image depends on a number of parameters including the numerical aperture (NA) of the objective used and the instrument specific coupling optics. This is described in more detail in Section 3.2.

Griffiths and Miseo[213] discuss the various types of detectors used in FTIR microspectroscopy where the cryogenically cooled, narrow band mercury cadmium telluride (MCT) photoconductive detectors result in high sensitivity at the expense of a shorter wavenumber region (cut-off at ~750 cm^{-1}). When calcium fluoride (CaF_2) is used as the substrate to fix samples onto, this cut-off does not result in any real information loss in the spectra as the substrate becomes less infrared transparent at wavenumbers < 1000 cm^{-1}.[214-215]

Cryogenically cooled MCT FPA detectors operate in photovoltaic mode, which has a similar sensitivity, per pixel, as the narrow band single MCT detectors, however in the case of the FPA detector there is a higher cut-off limit ~ 850 cm^{-1}.[213] This is still below the 1000 cm^{-1} cut-off limit of CaF_2 substrates and therefore, does not impose further any practical limitations to the analysis of cells fixed to this substrate.

1.6.2 Synchrotron Based FTIR Microspectroscopy

Synchrotrons accelerate electrons to close to the speed of light through the use of strong magnetic and electric fields to produce focussed electron beams of high energy.[216] The

synchrotron light produced by these electron beams as they change direction are collected down beamlines to provide photons from the X-ray to the far infrared regions of the electromagnetic spectrum. The brilliance of synchrotron radiation (SR) enables IR radiation to be focussed through small apertures compared to conventional blackbody sources of laboratory-based spectrometers,[216] to enhance its spatial resolution (10-20 μm) while maintaining a high signal-to-noise ratio.[217] A comparison of the synchrotron light beam intensity with a standard blackbody (Globar®) source is presented in **Figure 1.17**. The overall advantage of SR-FTIR microspectroscopy is, therefore, an improvement in spatial resolution and sensitivity when used in mapping mode.

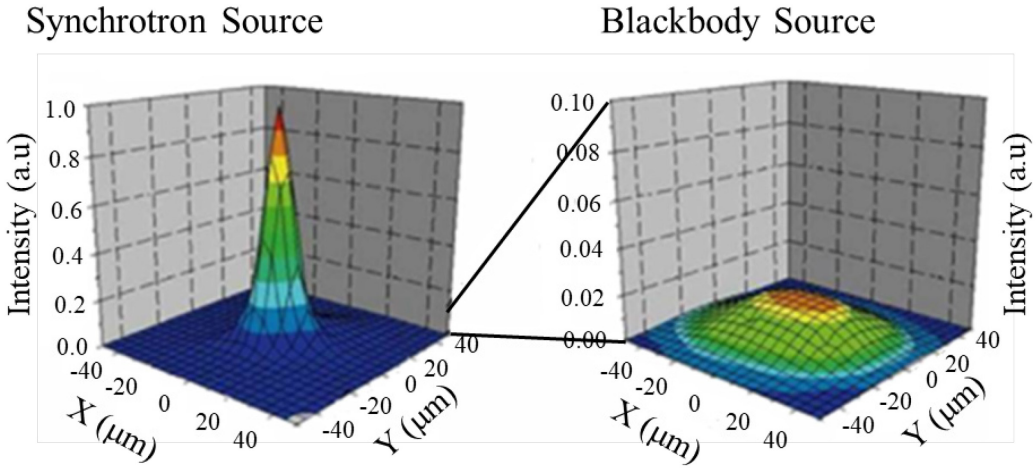

Figure 1.17: Comparison of the intensity and beam spot of SR compared to typical Globar® sources of laboratory-based FTIR microspectrometers, which shows the increased brilliance (intensity) of synchrotron light sources and the broad dispersion of the Globar® source. Reproduced from Kimura, S. and Okamura, H. Infrared and Terahertz Spectroscopy of Strongly Correlated Electron Systems Under Extreme Conditions, J. Phys. Soc. Jpn. 82, 021004 (2013). © 2013.

Diem, *et al*,[218] have reviewed the application of infrared spectral imaging to individual cells and have coined the term 'spectral cytopathology' as the combined use of microspectroscopy and chemometrics to provide objective assessment of cell disease state.[219] While it is recognised that synchrotron-based measurements are superior to those generated from an instrument utilising a thermal light source, comparison of spectra from next generation conventional FTIR instruments showed that data of similar quality can be obtained in reduced timeframes.[220]

Practical limitations are associated with higher spatial resolution and larger area maps, and are mainly due to mercury cadmium telluride (MCT) detectors, which require cryogenic cooling with liquid nitrogen Dewars that only maintain working detector temperatures for up to 8 hr. For a 12x12 grid map of pixels with a spectral resolution of

4 cm^{-1} and using 128 coadditions per spectrum, a total of 144 spectra are collected for the map. This results in a map collection time of ~3 hr. Doubling this map size, with corresponding doubling of oversampling results in map collection time that exceed the time the detector can remain at its working temperature. New generation infrared spectrometers based on quantum cascade lasers (QCL) and QCL combined atomic force microscopy (AFM) are currently available.

While the QCL spectrometers can generate large FPA images of 480 × 480 pixels in a fraction of the time of Globar® and synchrotron based FTIR spectrometers, the spatial resolution is still diffraction limited. AFM based mapping systems can provide images up to three orders of magnitude less than the diffraction limit, however, these systems are much slower than the QCL based FPA bolometers.[221-222] The QCL and AFM systems also typically have limited spectral ranges of 900-1800 cm^{-1}.

1.7 Design of Experiments (DoE) and Multivariate Data Analysis (MVDA)

Reliable and reproducible experimental data require careful planning and experimental designs to enable extraction of maximum information. Rational design of experiments (DoE) is possibly the best known approach for the design of systematic experiments.[223] DoE results are analysed using exact mathematical models, whose results can be validated and more importantly, interpreted to a high level of confidence.

Multivariate data analysis (MVDA) can be applied to both designed (DoE) and non-designed data sets, including time series and trend data. MVDA typically deals with complex data sets, including FTIR spectra to detect meaningful and interpretable patterns that often cannot be observed by visualising the data as line plots, or simple scatter plots. MVDA outputs usually provide data maps to detect patterns, trends, similarities or differences between groups in a specified data set in either a supervised, or unsupervised manner.[223]

1.7.1 Rational Design of Experiments (DoE)

Traditional experimental design involves the process of changing one independent variable (**X**) while keeping all other variables constant and measuring the response(s) or dependent variable (**Y**). In this approach, once the optimal conditions are determined for the first variable, it is held constant and the next variable is changed, while holding all other variables constant. This process is continued until all variables are ‘optimised’ and the final set of variable values is assumed to be the best conditions for measuring the response.

While labelled the 'scientific approach', or the one-factor-at-a-time (OFAT) approach it is not only unscientific, but it rarely ever leads to the optimised response.[223] For all but the simplest systems, OFAT rarely leads to parameters that describe the system completely and usually results in localised minima/maxima rather than absolute maxima/minima in multivariate space. The OFAT approach typically requires more experiments compared to those required for the DoE approach.[223]

Simple algorithms enable DoE methods to generate a maximum amount of information from a minimum number of experiments.[224] The DoE methodology is a key driver behind the pharmaceutical industry's Quality by Design (QbD) initiatives and organisations, such as the International Conference on Harmonisation (ICH), who have developed guidance documents on the use of DoE and MVDA methods for drug development and drug product manufacturing. DoE for the pharmaceutical and other regulated industries is summarised in a chapter by Swarbrick.[225]

1.7.1.1 Design Types

There are three main types of designed experiments, in which experimental factors and variables can be used interchangeably.

1. **Screening Designs:** Screening of important factors from many potential variables is used to determine whether only a few factors (2-5) are influential when the number of potential factors is large (10-20). Design types include the Plackett-Burman or low resolution fractional factorial designs.[226]
2. **Factor Influence Studies:** Detailed investigation of a small number of factors, either isolated during a screening design, or used when the number of experimental factors is manageable (typically 2-5). Design types include the full factorial designs or high resolution fractional factorial designs.[226]
3. **Optimisation Designs:** Detailed understanding of a small region of the design space where optimal conditions have been determined in the factor influence study. These designs typically use 2-4 factors to understand the stability of the optimal conditions towards small, but deliberate changes to the experimental factors. Design types include central composite designs (CCD) and Box-Behnken (BB) designs.[226]

The simplest experimental designs are factorial in two levels (represented as 2^k, where k is the number of controllable experimental factors, or independent variables). Using this approach, two experimental factors can be assessed in 2^2 = four experimental runs if all

experiments are performed as single replicates. Factorial designs are orthogonal in structure, a property that imparts independence on the factors and allows the experimental design space to capture the largest possible area/volume. The designs are generated at two-levels defined by the experimenter as the low (-1) and high (+1) levels. **Figure 1.18** provides a simple comparison of the OFAT and factorial design spaces for a two-factor situation. It shows conceptually how important relationships can be missed in the OFAT approach due to its highly one-dimensional approach.

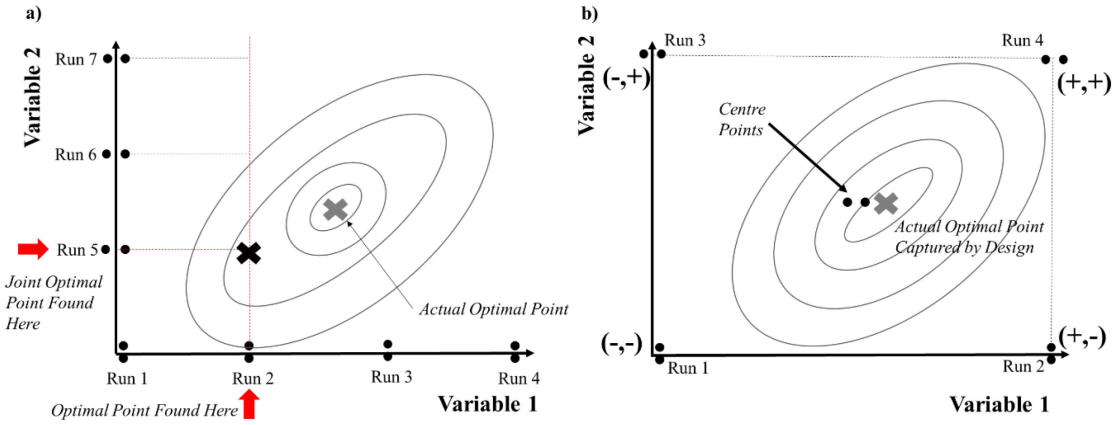

Figure 1.18: Experimental strategies: a) the OFAT approach holds all variables constant except for the one under investigation constant while optimising the response based on changing the single variable; b) the orthogonal factorial design covers the maximum experimental design space in a minimum number of experimental runs. The contours represent the actual, but initially unseen response surface, which is dependent on both variables simultaneously. As shown, the OFAT approach can easily miss the optimal response using a one-dimensional approach to experimentation.

For a two-factor problem, the experimental points define the corners of a square and the square defines an experimental boundary defined by the high and low levels of the factors. When a third factor is added to the design, the design space becomes a cube (**Figure 1.19**).

1.7.1.2 Design Construction and Terminology

Specific rules and terminology associated with the construction of designed experiments is described in detail in an authoritative text.[226] The terminology provides descriptive shorthand details of the design and is described briefly as follows.

Using the definition of the low level (-1) and the high level (+1) for each experimental factor, the first level for all factors in the design is set to (-1). The first factor is designated as (A) and there are 2^k experimental runs in total. When $k = 3$, there are eight experimental runs to be defined. For factor (A), the experiments are designated as alternate (-1) and

(+1) until all eight runs have been assigned. The next factor is (B) and the sequence of experimental runs is (-1), (-1), (+1), (+1) until all runs are designated.

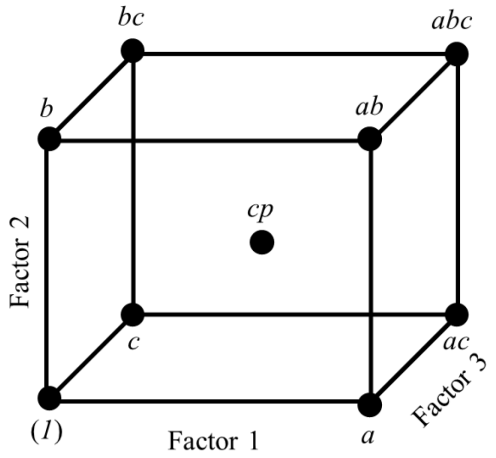

Figure 1.19: A 2^3 full factorial design in two-levels with a centre point (*cp*). The design space is defined as a cube and the volume enclosed by the cube is exactly modelled using linear regression methodology.[223,225] In this figure, standard DoE terminology is used to label the experimental runs that define each point of the cube. This terminology is defined in the in the text.

A similar sequence for factor (C) is continued (**Table 1.2**), where the experimental factors are listed in their defined sequence as ±1. When a factor has a (+1) assigned to a main factor, the experimental run contains the name of the factor as a lowercase letter. For example, the second run is designated (*a*) since factor A is the only factor with a (+1) and the eighth run is (*abc*) since all factors have the level (+1). The first run has only (-1) for all factors and this run is defined as (*1*) by default.

A centre point (*cp*) is the mid-level of the factor levels in the design and is designated as (0). This is because centre points are not used as part of the regression model calculation and are used as a source of experimental error determination and to check whether a linear model is appropriate at the centre of the design. It is common practice in DoE not to replicate the entire design, but only to replicate the centre of the design so as to keep the number of experimental runs to a minimum.[223] The main assumption made when using centre points as a source of determining experimental error is that the variance at the centre of the design is the same as the design points.[226]

Also shown in **Table 1.2** are the interaction terms associated with the design. One of the failings of the OFAT approach is its inability to reliably detect the interaction between two (or more) factors, thus resulting in an incomplete description of the system under investigation. Interaction terms describe the synergistic or antagonistic relationships

between the main factors. For as many factors in the design, there will always be a *k*-factor interaction term.

Table 1.2: Definition and terminology associated with the 2^3 full factorial design with a centre point.

Run	Experimental Factors (Main Effects)			Interaction Terms (*2FI* and *3FI*)			
	A	B	C	AB	AC	BC	ABC
1	-1	-1	-1	+1	+1	+1	-1
a	+1	-1	-1	-1	-1	+1	+1
b	-1	+1	-1	-1	+1	-1	+1
ab	+1	+1	-1	+1	-1	-1	-1
c	-1	-1	+1	+1	-1	-1	+1
ac	+1	-1	+1	-1	+1	-1	-1
bc	-1	+1	+1	-1	-1	+1	-1
abc	+1	+1	+1	+1	+1	+1	+1
cp	0	0	0	0	0	0	0

In most practical situations, two-factor interactions (*2FI*) are likely to occur, three-factor interactions (*3FI*) are less likely to occur and so on. The 2^3 full factorial design is capable of determining all interactions up to *3FI*. When the settings of the factors in the design are run for all of the combinations, a response is measured for each experimental run. The response can be a univariate outcome, such as yield, pH, etc, or can be a spectrum collected on a sample after the conditions have been applied.

1.7.1.3 Regression Model for DoE

The orthogonality condition imparts unique properties to the analysis methods used to understand the relationships between the factors and the response (y) and a model can be developed that describes the entire experimental space using multiple linear regression (MLR).[223,225] The MLR algorithm is an extension of simple linear regression and enables the calculation of main effects of the experimental factors and their interactions. The

MLR equations for a two- and three-factor design are shown in Equations 1.1 and 1.2, respectively.

$$\hat{y} = b_0 + b_1x_1 + b_2x_2 + b_{12}x_1x_2 + \varepsilon \quad 1.1$$

$$\hat{y} = b_0 + b_1x_1 + b_2x_2 + b_3x_3 + b_{12}x_1x_2 + b_{13}x_1x_3 + b_{23}x_2x_3 + b_{123}x_1x_2x_3 + \varepsilon \quad 1.2$$

The model associated with the 2^3 full factorial design has seven terms and the intercept term (b_0) resulting in a total of eight model terms (**Table 1.2**). This requires eight experimental runs in the design in order to uniquely calculate each term in the model. This is a requirement of the orthogonal MLR model.[223] The DoE equations above can become very complex for a relatively small number of factors, i.e., a design with five experimental factors, $2^5 = 32$ experimental runs results in an equation with 31 terms for main effects and interactions and the intercept term b_0. Main effects of the individual factors are defined by terms, such as b_1x_1, where b represents the regression coefficient or importance of the factor, and x represents the factor being modelled. Synergistic effects have positive *b*-coefficients and antagonistic effects have negative *b*-coefficients.

In the case of the 2^5 factorial design, if only *2FIs* are to be considered, 26 redundant terms in the MLR equation will be calculated, including the highly unlikely five-factor interaction term. Simpler designs, known as fractional factorial designs exist to handle this type of redundancy, however, these are outside of the scope of the present study and are discussed in detail in the pioneering texts of Box, Hunter and Hunter,[224] and Montgomery.[226]

1.7.1.4 The Box-Behnken Design

The simplest of a class of designs called the optimisation designs is the Box-Behnken (BB) design.[223] Unlike more complex optimisation designs, the BB design only fits a quadratic model to account for curvature in the design points and requires the minimum number of points to run. Each point can be considered to lie on the surface of a sphere, providing each point with equivalent variance properties and three levels to fit a quadratic model. **Figure 1.20** shown an example BB design in three experimental factors.

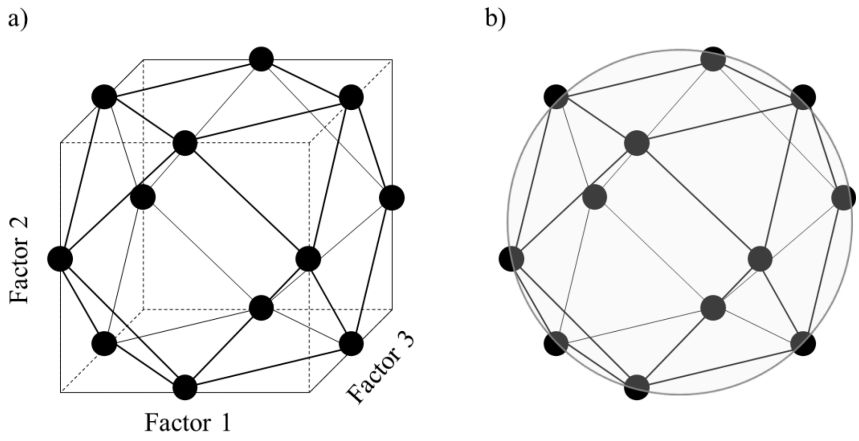

Figure 1.20: The Box-Behnken (BB) design in three experimental factors; a) shown in cartesian coordinates; and b) shown as the points on a sphere.

1.7.2 Multivariate Data Analysis (MVDA)

By definition, multivariate data analysis (MVDA) refers to the simultaneous analysis of more than one variable. Bivariate analysis requires an extension of the simple linear model to the MLR models described in Section 1.7.1.3. However, when the number of variables to be assessed becomes large (typically >10), the MLR and associated linear discrimination methods become less effective, mainly because of the exactness of the MLR model, that requires a single run for every variable measured. For a spectrometer generating 2000 variables per spectrum, the object set would require 2000 objects. The terminology 'object' is used to describe the points in a MVDA unless the object can be defined as a sample according to the criteria of representativity of the theory of sampling (ToS).[223,227-229]

When applied to chemical data, including spectroscopic and chemical imaging data, MVDA was first coined as chemometrics by Svante Wold in 1971.[230] The International Chemometrics Society (ICS) defines chemometrics as follows, "the chemical discipline that uses mathematical and statistical methods to: (a) design or select optimal measurement procedures and experiments; and (b) provide maximum chemical information by analysing chemical data."[231] Although the term chemistry is used in the definition, it is easily translated to the understanding of chemical processes that occur in biological systems, particularly cell cultures and their treatments.

Chemometrics is applied widely to spectroscopic data, including FTIR spectroscopy, which can benefit from such analysis particularly when applied to hyperspectral images. Chemometric methods objectively distinguish subtle changes in lipid, protein and other

biologically active molecules when analysing the large numbers of spectra generated by a mapping or imaging experiment.[190,218,232]

Chemometrics methods can be grouped into three main strategies.[233]

1. **Exploratory Data Analysis (EDA)**: This group are unsupervised classification methods used to investigate the internal structures (patterns, or natural groupings) of complex data sets. The main workhorse of EDA is principal component analysis (PCA, Section 1.7.2.1).
2. **Multivariate Calibration**: These methods are used to model a response (**Y**) from multivariate data (**X**), to provide predictive models of constituents/properties of interest. The process is a two-stage operation where a set of calibration objects with known reference values, measured using a reliable reference method, are measured on, for example, a spectrometer and a model is developed relating spectral bands to the constituent or property of interest. These models can be applied to spectra collected on new objects and quantitative values can be generated, non-destructively, in real time. The method of partial-least-squares-regression (PLSR) is described in Section 1.7.2.2.
3. **Multivariate Classification**: Using EDA as a basis for identifying interpretable classes from spectroscopic or other data types, local class models are developed and saved into a library of classes. The library is then applied to newly collected data in order to establish class membership. This is known as supervised classification or supervised pattern recognition and is used extensively in industries, such as the pharmaceutical industry, or in research to classify new and existing objects. The main classification algorithm used in this research was the method of partial least squares discriminant analysis (PLS-DA, Section 1.7.2.3).

1.7.2.1 Principal Component Analysis (PCA)

PCA is a multivariate clustering technique that describes an initial data set (**X**) in terms of its object relationships, known as scores (*t*) and the variable correlations, known as loadings (*p*). The loadings describe the variable contributions associated with any clustering observed in the scores and works on the premise that objects and variables are not mutually exclusive, i.e., objects cannot be described without variables and *vice versa*. PCA uses linear algebraic methods to decompose the original data set into informative components known as principal components (PCs) based on variance maximisation.[233]

The PCs describe a set of linear combinations, that when summed, reconstruct the original data (**X**). Mathematically, this can be described in matrix notation in Equation 1.3.

$$\mathbf{X} = \mathbf{TP^t} + \mathbf{E} \qquad 1.3$$

Where **X** is the original data, **T** is the combination of the *a* most important scores, **P** are the *a* loadings associated with the scores and **E** is a matrix of residuals. The residuals are the part of the original data that cannot be described by the model $\mathbf{TP^t}$. In expanded notation, the PCA model is a linear combination of PCs (Equation 1.4).

$$X = t_1 p_1^t + t_2 p_2^t + \cdots + t_a p_a^t + E = \sum_{a=1}^{A_{opt}} t_a p_a^t + E \qquad 1.4$$

There are two constraints placed upon a PCA model:

1. Each PC is orthogonal (independent) of the others and thus describes a unique set of variances in multivariate space; and
2. The variance described by each successive PC cannot be larger than the previous PC.

This means that the information contained in a PC diminishes as the number of PCs becomes large. Typically, in an information rich data set, the number of PCs required to describe the data is relatively low (2-5 PCs) and this is known as the rank, or dimension of the data set and is represented by A_{opt}. The maximum number of PCs cannot be greater than the minimum of the number of objects/variables used to describe the data.

Since PCs are orthogonal, scores and loadings can be plotted on a set of cartesian coordinates as scatter plots in two- and three-dimensions, or as line plots that best describe the data situation. For example, the loadings of spectra are best plotted as a line plot of loadings vs. wavenumbers in order to identify the important wavenumber(s) that describe the object patterns in the scores.

When scores are plotted as scatter plots, objects may be observed to cluster together as they have similar properties and are, therefore, similar in their original data. Objects that separate into new clusters have unique properties with respect to other clusters and their loading patterns describe these differences. The simplest way to plot scores is as a pairwise scatter plot of one PC vs. another. When PC1 scores are plotted against PC2 scores, this is called the t_1 vs. t_2 plot (**Figure 1.21**).

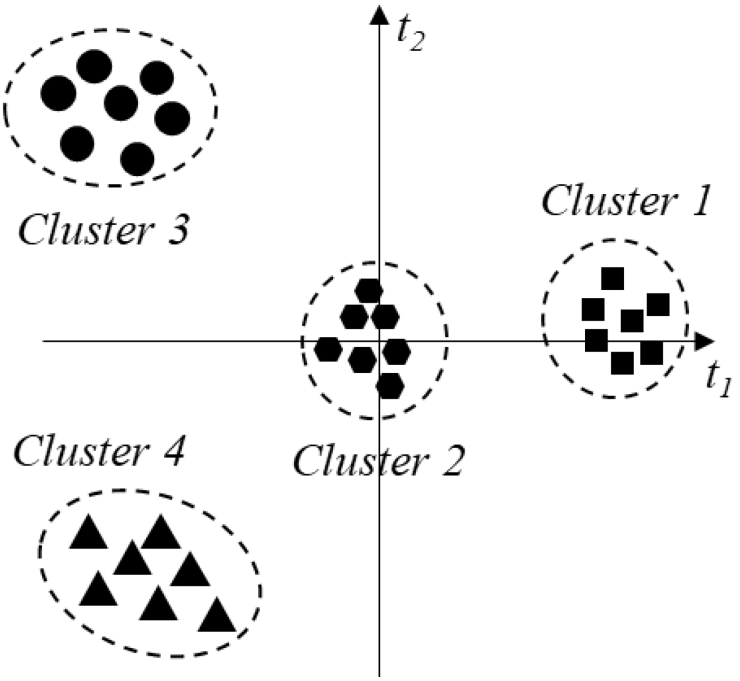

Figure 1.21: Conceptual t_1 vs. t_2 scores plot showing four clusters of objects. The four clusters show tight within cluster grouping, which demonstrates small interclass variability and strong separation from other classes. This situation represents an ideal situation in which every class can be uniquely interpreted through analysis of the loadings (p).

In the scores plot (**Figure 1.21**), the following general interpretations can be made.

1. Cluster 1 lies exclusively along the t_1 direction and its properties are interpreted solely by the p_1 loading direction.
3. Cluster 2 lies at the intersection of t_1 and t_2 (at 0,0). This cluster represents minimal variability with respect to the other clusters and the objects in this cluster can be considered as 'average' objects.
4. Clusters 3 and 4 are separated from each other in the t_2 direction and from Cluster 1.

The loadings plots describe the variable correlations to the defined PC direction. Loadings can take both positive and negative values and can be used to describe the relationships between the variables, particularly when interpreting spectral changes relative to chemical functionality. For example, a positive loading associated with the lipid bands in the spectra may be inversely correlated to a negative loading associated with protein bands. This can be interpreted as, when the lipid content of the measured object is high, its associated protein content is low, and *vice versa*. **Figure 1.22** shows a typical **X**-loadings plot for direction p_1. When the original data are mean centred, the loadings are centred around zero and scaled such that their sum adds to 1 (normalised).

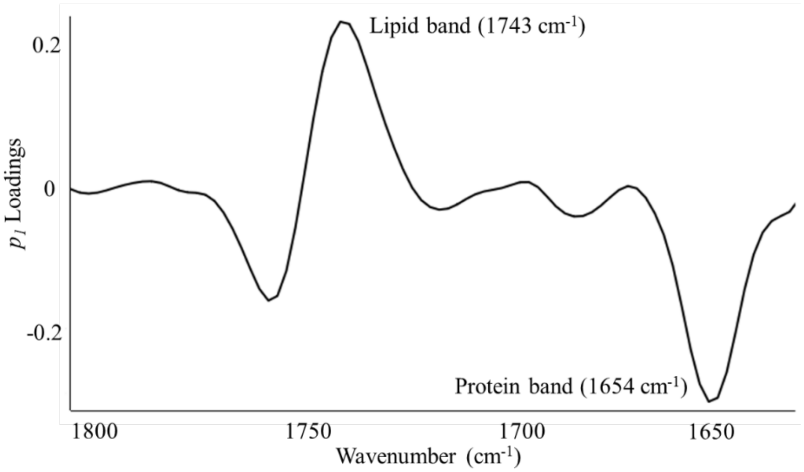

Figure 1.22: Example p_1 loadings line plot showing the inverse relationship between the two highly weighted bands at 1743 cm^{-1} (lipid ester, C=O) and 1650 cm^{-1} (C=O, α-helix protein secondary structures). The lipid band is highly positively weighted, while the protein band is negatively weighted.

PCA scores and loadings must be interpreted together as demonstrated in **Figure 1.23**, using an example from the current study.

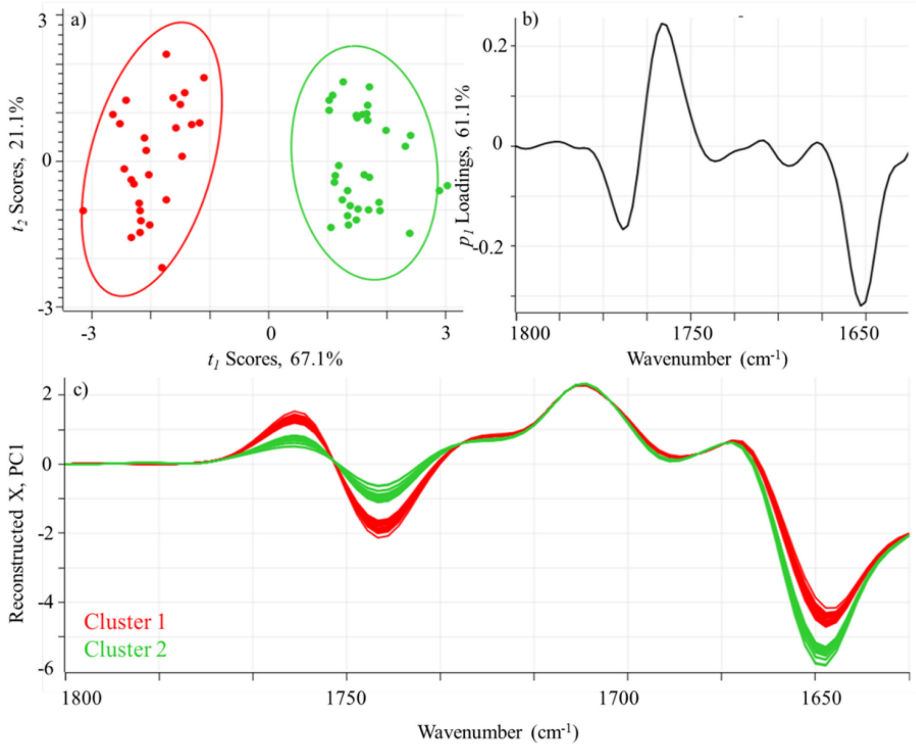

Figure 1.23: Joint interpretation of; a) scores; b) loadings and; c) reconstructed **X**. The two clusters in the scores plot are described by the inverse relationship of the loadings at 1743 cm^{-1} and 1650 cm^{-1}. Since the data are second derivatised, the higher the content of a particular component, the more negative the band. Cluster 1 is defined by negative t_1 values, therefore, negative scores × positive loading at 1743 cm^{-1} results in a more negative lipid band in the reconstructed **X** data. The inverse situation occurs for Cluster 1 at the 1650 cm^{-1} loading, negative scores × negative loadings result in a more 'positive' protein band when added to the mean spectrum. The reverse situation occurs for Cluster 2.

These data were collected on fixed HepG2 cells measured as single point spectra, therefore, each point in the scores plot represents a single cell. There are two distinct classes in the t_1 vs. t_2 scores plot (Cluster 1 and Cluster 2) separated along the t_1 direction and accounting for 67.1% of the total variability of the data set. The spectra were processed using a Savitzky-Golay second derivative[234-235] followed by the standard normal variate (SNV) algorithm of Barnes, *et al.*[236] The loadings represent the profile expected of second derivatised data.

The reconstructed **X** plot generated from the t_1 scores and the mean spectrum shows that the two clusters are separated based on intensity changes in the bands at 1743 and 1650 cm^{-1}. The reconstructed **X** data were calculated using Equation 1.5, where $\bar{X}$ is the mean spectrum,

$$X_{t_1} = \bar{X} + t_1 p_1^t \qquad 1.5$$

1.7.2.2 Partial Least Squares Regression (PLSR)

Multivariate regression methods are used to model an external and dependent response variable (**Y**) using a set of independent variables (**X**). In chemometrics, **X** is generated data, which contain the chemical information of the objects measured. Using regression techniques, a model (**B**) is generated such that the general least-squares model of Equation 1.6 holds,

$$\mathbf{Y} = \mathbf{XB} \qquad 1.6$$

This model states that the predicted value **Y** can be predicted from **X**, provided a reliable and interpretable model **B** can be generated from the available data. In an expanded form, the Equation 1.7 represents a form of the MLR model,

$$\hat{y} = b_0 + b_1 x_1 + b_2 x_2 + \cdots + b_n x_n + \varepsilon \qquad 1.7$$

Where $\hat{y}$ is a predicted value of the response y when the model **B** is applied to new data, b_0 is the intercept term in the equation, b_n are the regression coefficients that weight each of the independent **X** variables and ε is the residual term. The MLR equation uses individual variables to model the response; however, when n becomes large, this model becomes unreliable due to collinearity between the variables and the requirement for large numbers of objects to evaluate the terms in the equation.[223]

Multivariate methods of regression eliminate the collinearity problem through the calculation of latent variables such, as principal components (Section 1.7.2.1). A

requirement of the MLR model is independence of variables and by calculating PCs from the original data set, these have the property of orthogonality. Therefore, replacing the individual **X** variables with the first few important PCs leads to an exact MLR solution of Equation 1.8,

$$\hat{y} = b_0 + b_1 t_1 + b_2 t_2 + \cdots + b_a t_a + \varepsilon \qquad 1.8$$

Where t_a are the PCA scores summed up to the optimal number of PCs (A_{opt}). This is called the principal component regression (PCR) model and uses the condensed information of PC scores to model the response. While this model is exact mathematically, in practice, PCA describes the major sources of variability in the data. In some cases, the first few PCs may not be related to the variance in the *y*-response and this can lead to models with inflated **Y**-variance for the first components used in the model. As more PCs are added to the model, the variance in **Y** is explained, to result in a model that is more complex than expected. To overcome this issue, the partial least squares regression (PLSR) method was developed by Wold[237] to allow for faster convergence of the regression model to the optimal solution. To achieve this, the first step in PLSR is to find the highest correlation between the response **Y** and the **X** variables and in this manner, the decomposition of **X** into latent variables is guided by the response **Y**, this leads to the calculation of the first loading weight (*w*), Equation 1.9.

$$w_1 = \frac{X^t y}{|X^t y|} \qquad 1.9$$

The denominator normalises the loading weight and represents the largest correlation between **X** and **Y**. From there, the first PLSR score (t_1) is calculated using Equation 1.10.

$$t_1 = X w_1 \qquad 1.10$$

Importantly, PLSR scores are different from PCA scores and must be interpreted in a different way. This is because PLSR scores are the object relationships of **X** as they relate to **Y**. The remainder of the non-iterative partial alternating least squares (NIPALS) algorithm is outside of the scope of the current study and the algorithm is discussed in Esbensen and Swarbrick[223] and Swarbrick and Westad.[233] The final regression model resembles the classical least-squares equation; however, to overcome the collinearity issues, the model contains latent variables derived from both **X**- and **Y** in the calculation of Equation 1.11.

$$\mathbf{B} = \mathbf{W}(\mathbf{P}^{\mathbf{t}}\mathbf{W})^{-\mathbf{1}}\mathbf{Q}^{\mathbf{t}} \quad 1.11$$

Where **W** are the loading weights, **P** are the PLSR loadings and **Q** are the **Y**-loadings. Additionally, the PLSR model is unlike PCA, since loading weights, not loadings are orthogonal and are used to interpret the model.

The directions of a PLSR model are known as Factors rather than PCs to reflect the fact that PLSR scores are related to the **X**- and **Y**-data. The output of a PLSR model is similar to that of a PCA model with scores and loading weights for interpretation; however, PLSR also provides regression coefficients (b) that are displayed for the optimal number of factors (A_{opt}) and these summarise the important **X**-variables used to predict the response **Y**. The other important plot associated with PLSR is the predicted versus reference plot that displays the straight line fit between the predicted and reference values for the optimal number of PLSR factors. An example PLSR overview is shown in **Figure 1.24**.

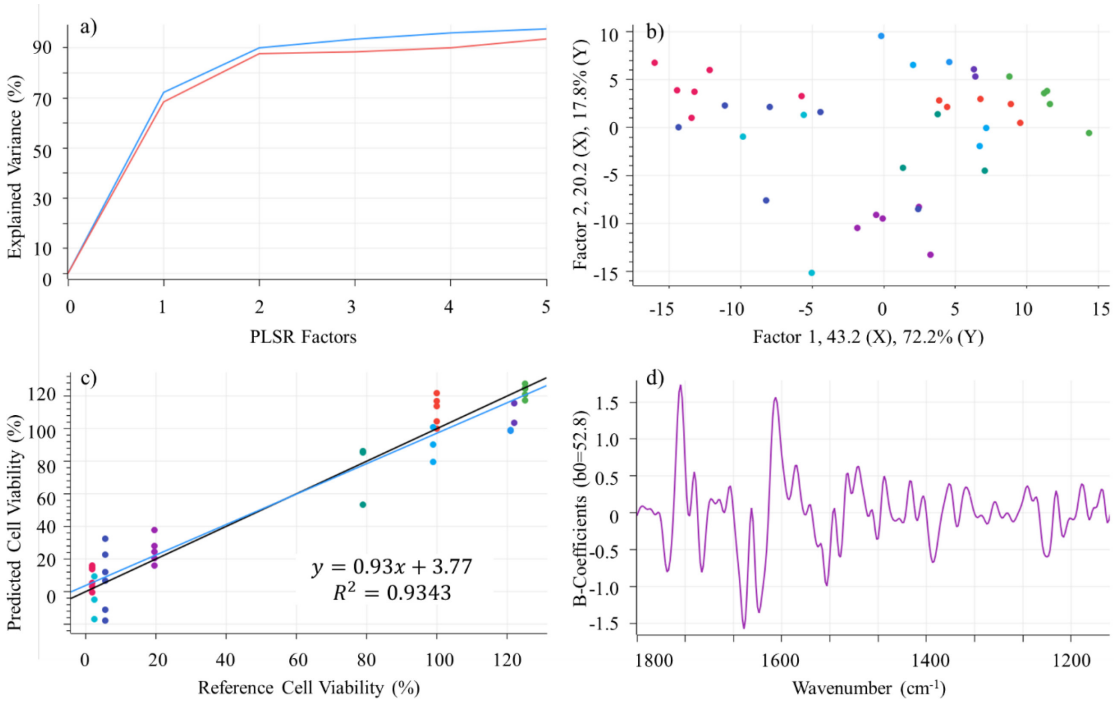

Figure 1.24: Example of a PLSR overview plot showing; a) explained **Y**-variance plot, indicating the number of optimal PLSR factors to interpret; b) PLSR scores showing the object relationships as related to the *y*-response; c) the predicted vs. reference plot showing the quality of the model for a selected number of PLSR factors; and d) the regression coefficient plot showing the important variables used to predict the *y*-response for a selected number of PLSR factors.

1.7.2.3 Partial Least Squares Discriminant Analysis (PLS-DA)

Partial least squares discriminant analysis (PLS-DA) is an extension of the PLSR method where the *y*-response is replaced with a binary descriptor of class, typically 0/1 or -1/+1.

In this way, a predicted value of 1 represents class membership and 0 (or -1) represents non-membership to the selected class. When there are more than two classes to be modelled, the PLS-2 algorithm is used to model multiple **Y**-responses.[223] **Table 1.3** lists a PLS-DA model for a three-class example. The columns represent a class and for each response, the objects defined as that class are designated the value 1 and all other objects with the value 0 (or -1).

This process is continued for all classes and this table serves as the training set used to build the classification method.

Table 1.3: Example responses of a PLS-DA model for a three-class classification problem.

Object	Class 1	Class 2	Class 3
1	1	0	0
2	1	0	0
3	1	0	0
4	0	1	0
5	0	1	0
6	0	1	0
7	0	0	1
8	0	0	1
9	0	0	1

By treating a categorical variable as a binary response, the PLSR model results in a binary regression situation as conceptualised in **Figure 1.25**. One of the limitations of the PLS-DA method is that it cannot reliably predict an objects class when the class has not been defined in the model. To overcome this limitation, some chemometric software packages provide confidence intervals around the classes to either reject extreme objects, or objects that do not fit any class.

Herein, the PLS-DA method was used to guide the decomposition of spectral data collected on individual cells using designed experiments. The full factorial designs described in Section 1.7.1 are orthogonal in construction and in the studies undertaken, individual spectra represent the **X**-variables acquired at each point in the design. The treatment conditions were then used as the responses. In this way, the large biological

variability in the objects can be effectively 'filtered' out by guiding the decomposition of the spectral data based on external knowledge. Consequentially, the results can be explicitly obtained, rather than implicitly sorted out by exploratory data analysis, such as PCA, that only look for the highest sources of variability in the data, that may not be related to the responses. In this way, a scientifically justified approach to information extraction and interpretation is achieved.[238]

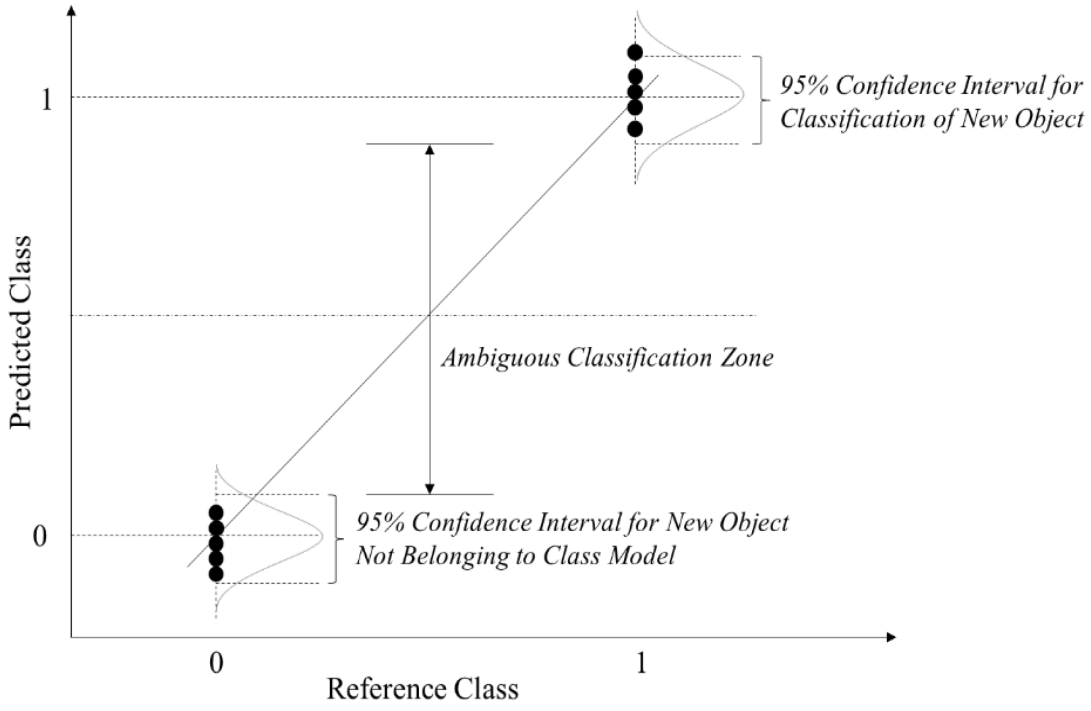

Figure 1.25: PLS-DA predicted vs. reference plot showing discrimination of classes based on a binary class variable. When more than two class variables are being modelled, there is one predicted vs. reference plot per class. If the predicted result is close to 1 and within the 95% confidence interval, the object is considered to be a member of that class. If it is not a member of the class, it will either lie close to 0 (for objects with classes defined by the model) or in the ambiguous classification zone, for objects with no classes defined by the model.

1.7.2.4 MVDA Terminology

MVDA (chemometrics) has its own unique terminology and definitions, many of which were derived in the 1930's in the field of psychology.[239] Terms such as scores relate to patient scores recorded after application of certain stress factors and the loadings refer to the intensity of the factor.[240] Much of this terminology is still in use in modern chemometrics and the most important definitions and symbols used in this thesis are summarised in **Table 1.4**.

Table 1.4: Common terminology used in multivariate (chemometric) modelling.

Symbol	Name	Definition*
X or (x)	Independent Variable	Variables measured on a set of objects used to model the characteristics of those objects, typically spectra and chromatograms.
Y or (y)	Dependent Variable	Response data measures on an object set that defines the reference values to be correlated to the independent (**X**) values. **Y**-responses can be quantitative and qualitative.
T or (t_a)	Scores	Scores are the object relationships calculated in PCA or PLSR models. **T** describes the total scores in matrix notation, while t_a describes the individual scores in a model up to $a = A_{opt}$., where A_{opt} is the optimal number of principal components, or PLSR factors determined by validation of the model.
P or (p_a)	Loadings	In PCA, loadings represent the directions in multivariate space capturing the greatest source of variability in the set of objects measured. They describe the correlation between variables and their importance. **P** describes the total loadings in matrix notation, while p_a describes the individual loadings in a model up to A_{opt}.
W or (w_a)	Loading Weights	In PLSR and PLS-DA, loading weights are orthogonal and are used for model interpretation instead of the loadings also generated by PLSR. Loadings weights represent the correlations in **X** most related to **Y**. This also means that PLSR scores must be interpreted differently from PCA scores. **W** describes the total loading weights in matrix notation, while w_a describes the individual loading weights up to A_{opt}.
B or (b)	Regression Coefficients	Regression coefficients are specific to regression models and describe the variable importance for the optimal number of factors used in a model, $A_{opt,}$ for reliable predictions of new data using the model.

Table 1.4 (*cont*): Common terminology used in multivariate (chemometric) modelling.

Symbol	Name	Definition*
E *or* (ε)	Residuals	Residuals describe the part of a data set (**X** or **Y**) that cannot be explained by the fitting of the optimal number of principal components or PLSR factors.

*In this thesis, the terms multivariate analysis and chemometrics are used interchangeably.

1.8 Hyperspectral Image Analysis (HSI)

When spectra are collected on cells in a grid manner (**Figure 1.15b** and **c)**, the result is a pseudo-three-way data table with dimensions *pixels* × *pixels* × *variables*, where variables are the absorbance values of the wavenumbers of the spectral data collected for each pixel. This results in the data cube represented in **Figure 1.26**.

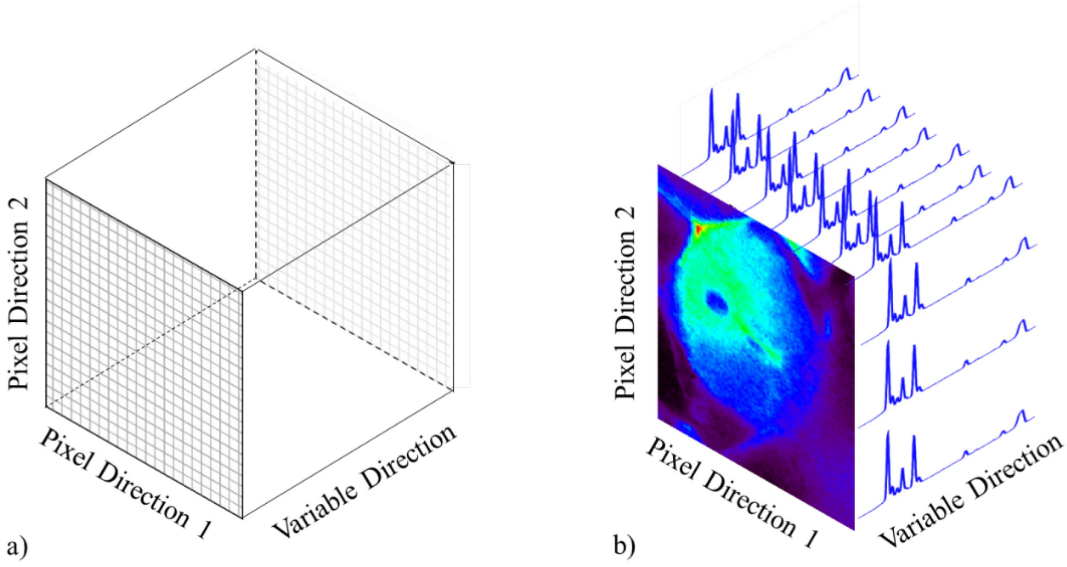

Figure 1.26: Representation of the pseudo-three-way data structure associated with chemical mapping and hyperspectral imaging; a) representative data structure showing the pixel directions as one plane and the variables as a second independent direction; b) an example of a hyperspectral cube showing the data structure.

The term pseudo-three-way is used for this type of data structure, as opposed to the regular definition of a three-way table as the pixel directions are not independent.[241-242] This enables the table to be matricised along the variable direction, to generate a two-way data table that is analysed using the regular multivariate methods (Section 1.7.2).

The process of matricising (sometimes incorrectly called un-folding) is shown in **Figure 1.27**. Maintenance of the order of the matrix is important because the scores from a PCA/PLSR model applied to the matricised data are remapped to pixel space, thus

providing a false colour image of the data represented by the information described in selected scores. Each score image has an associated loadings plot that describes the intensity of the scores value in the image and can be used to investigate cell morphology and compartmentalisation.

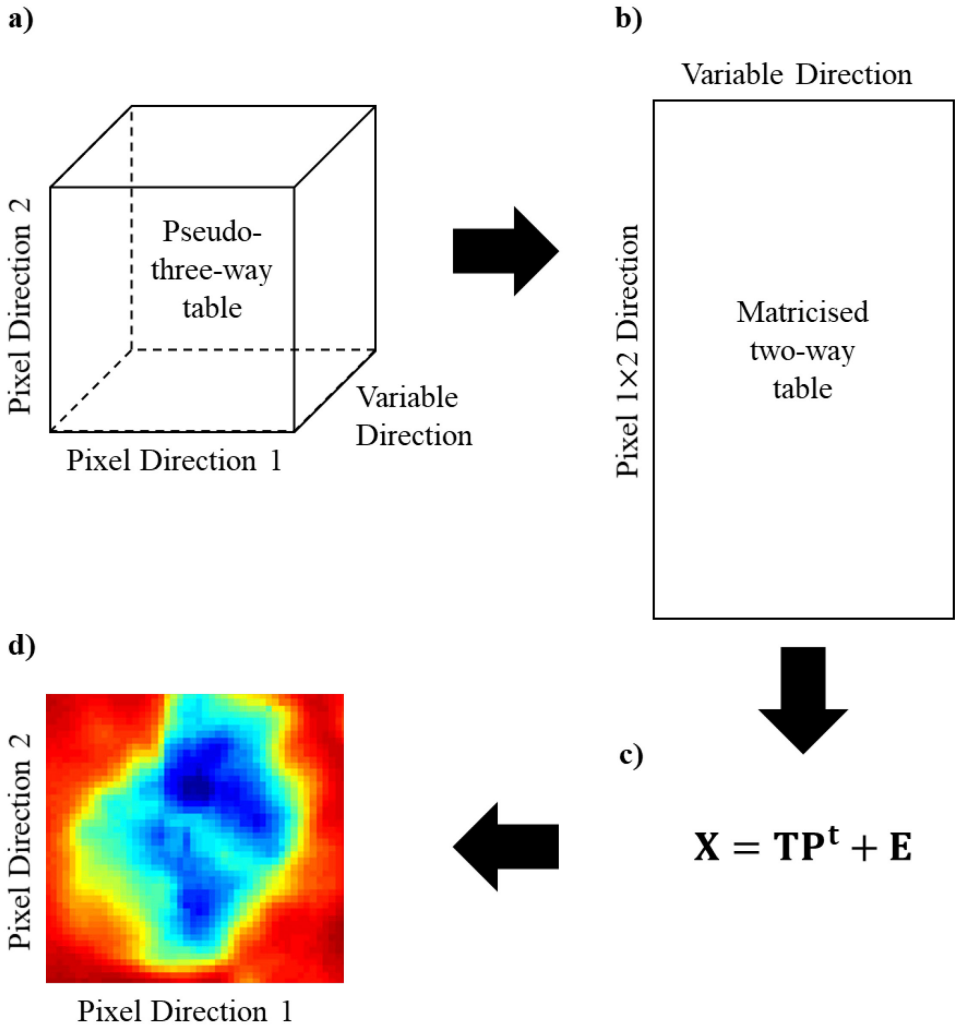

Figure 1.27: The process of developing a hyperspectral image analysis (HIA): a) the original data are represented by a pseudo-three-way data cube; b) matricising the data along the variable direction results in a long table of (pixel 1 × pixel 2 direction) × variables; c) analysis of the long, two-way data table using PCA or other multivariate methods; and d) mapping of the scores back to the original image space.

After data acquisition parameters are optimised, the scores image ideally show the sample outline and highlights the internal structure. The data exterior to the region of interest (ROI) can add noise to the calculated model by adding information that is not sample related. Most multivariate and hyperspectral imaging software packages provide an option for masking unimportant regions. **Figure 1.28** shows the process of masking for the scores image in **Figure 1.27** along with the resulting scores image after calculation without the unimportant regions.

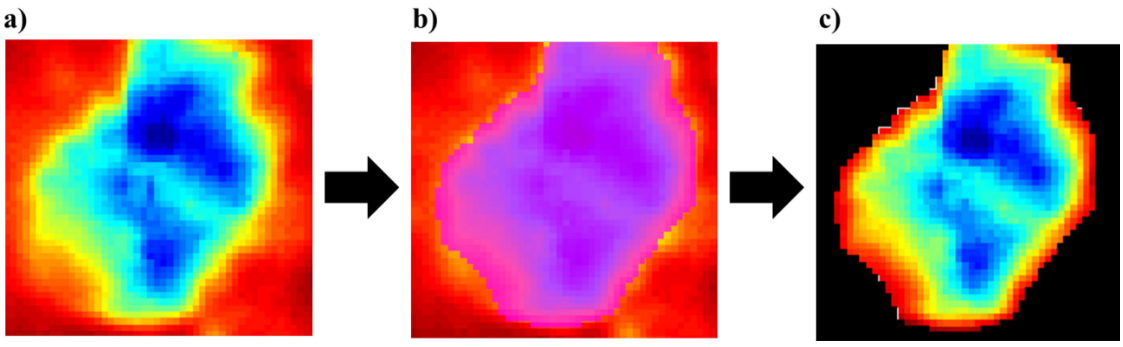

Figure 1.28: The process of masking in HIA; a) original scores image using all pixels for the calculation of the PCA model; b) masking the region of interest (ROI) based on the sample outline; and c) recalculation of the model without the unimportant pixels.

Simple, univariate approaches to identify morphological features in hyperspectral images also exist based on integration of areas under specified bands in the original, or processed spectra. Such images are useful as a rough guide to locating specific ROIs but do not take advantage of the power of multivariate analysis and in many cases, lead to limited conclusions made from the complex data.

This process of matricising, analysis and masking were used to assess the multivariate images generated in this thesis, along with optimisation of processing methods used to extract meaningful information from the images. The use of band integration was used as a method to initially locate ROIs and to confirm the finding of any hyperspectral image (HSI) models developed.

1.9 Aims and Thesis Outline

With particular focus on the biochemical processes involved in sugar uptake and metabolism and the actions of vanadium pro-drugs as insulin mimetic/cytotoxic agents, the research outlined in this thesis aims to use vibrational spectroscopic and chemometrics methods to elucidate and better understand the biochemical processes associated with the treatments applied to insulin-sensitive and -resistant cell types. Individual chapters provide additional details of experimental methods, including the optimisation of spectroscopic parameters for reliable data acquisition. The following outlines the general procedures described in the chapters that follow.

Chapter 2 describes the general *in vitro* cell culture and fixation methods used to prepare cells onto calcium fluoride (CaF_2) substrates for vibrational spectroscopic analysis. General spectroscopic instrument configurations are discussed along with an overview of the software used to generate results.

Chapter 3 describes the optimisation of data acquisition parameters and sampling methodology used to collect spectra generated by synchrotron and laboratory-based FTIR instrumentation. Using method validation procedures employed in the pharmaceutical and related industries, spectral data acquisition parameters including coadditions, reduction of additive and multiplicative effects (processing) and measurement repeatability were investigated and optimised. Optimisation experiments were performed for single point, raster scan mapping and focal-plane-array (FPA) imaging on adipocytes and hepatocarcinoma cells, including a unique experimental setup at the Australian Synchrotron using four focussed beams in an FPA arrangement.

Chapter 4 describes the application of FTIR single point scanning applied to chemically fixed 3T3-L1 adipocytes treated with sugars and vanadate using a design of experiments (DoE) approach. Initial work focusses on establishing the action of vanadate on insulin-sensitive and -resistant cells to understand the insulin-mimetic/enhancing and cytotoxic effects of vanadate, followed by a combined glucose, fructose and vanadate study to investigate the main effects and interactions of the experimental factors. Acquired spectral data were assessed using chemometric approaches to gain greater insights into biochemical changes induced by the factors and to better understand the modes of action of vanadate. A number of models describing the action of vanadate were proposed based on the information obtained from the FTIR spectra and available biochemical literature.

Chapter 5 describes a study performed on the HepG2 hepatocarcinoma cell line as a model of insulin-sensitive hepatocytes that investigated the action of vanadate and two commonly used anti-cancer treatments, cisplatin and doxorubicin. Using point scanning and chemometrics methods, individual models for each cytotoxic agent were developed and compared to the results of common cytotoxic assay methods to determine whether any correlations between the FTIR spectra acquired and the assay methods exist. This was followed by the development of a combined model to comparatively evaluate the modes of action of each agent.

A similar DoE approach to that performed in Chapter 4 investigated the actions of glucose, fructose and vanadate on HepG2 cells to investigate the main effects and interactions of the factors and the data were evaluated using chemometrics approaches to gain further insights into the mode of action of vanadate as a cytotoxic agent. Models were developed that described the observed spectral changes as related to biochemical pathways induced by the treatments.

Chapter 6 outlines a short feasibility study of FPA images acquired on 3T3-L1 adipocytes using synchrotron and laboratory-based FTIR microspectrometers and using hyperspectral imaging (HSI) methods. Single cells were selected for this analysis based on visible morphological characteristics in order to determine whether such analyses could provide better understanding of biochemical changes induced in single cells on a compositional and morphological basis.

Chapter 7 provides a summary of the results and conclusions obtained and also discusses future work and new technological advances that can improve on the studies performed in this thesis.

Chapter 2 Experimental

2.1 Chapter Overview

Two cell lines were investigated as models for various diseases associated with metabolic syndrome. The 3T3-L1 cell line (murine adipocytes) is a widely used model of mammalian white adipose tissue particularly in the study of diabetes.[243] This makes them highly suitable for investigations related to the uptake of sugars commonly consumed in the Western diet, such as glucose and fructose. The HepG2 cell line is an epithelial-like human hepatocarcinoma (HCC) cell line that exhibits properties similar to normal hepatocytes in terms of drug uptake and metabolism.[244] In addition, they are an epithelial model of insulin sensitive tumour cell, which serves as a reference point regarding the action of vanadate to the results obtained from the 3T3-L1 cell line.

2.2 Materials

General reagents are listed in **Table 2.1**. All reagents, except for Sodium orthovanadate, were used without further purification. Water was purified using the Milli-Q technique (Millipore, Billerica, MA, USA).

Table 2.1: General reagents used in this study.

Material	Grade/Purity	Source	Catalogue Number
Sodium Orthovanadate ($Na_3[VO_4]$)	99.98%	Aldrich	450243
D-(+)-glucose	>99.5%	Sigma	G7528
D-(-)-fructose	>99.5%	Sigma	F2543
Methanol (absolute)	HPLC grade	Ajax Chemicals	
Ethanol (absolute)	HPLC grade	Ajax Chemicals	
Dimethyl Sulfoxide (DMSO)	Analytical grade	Ajax Chemicals	
cis-Diamineplatinum(II) dichloride (cisplatin) $[Pt(NH_3)_2Cl_2]$	>99.9%	Aldrich	479306
Doxorubicin Hydrochloride	>98.0%	Sigma	D1515

Cell culture media and reagents are listed in **Table 2.2**

Table 2.2: Cell Culture Media and Reagents

Material	Source	Catalogue Number
Dulbecco's modified Eagle's medium – base (DMEM, without glucose L-glutamine, phenol red, sodium pyruvate, and $NaHCO_3$)	Thermo Fisher Scientific	A1443001
Dulbecco's modified Eagle's medium – Non-Advanced,		11965092
Dulbecco's modified Eagle's medium – Advanced, High Glucose.		12491015
Foetal Bovine Serum (FBS)		10099141
Glutamax		35050061
TrypLE		12605028
Phosphate buffer saline (PBS)		70011069
Insulin from bovine pancreas, human insulin (recombinant, expressed in yeast)	Sigma-Aldrich	16634
Dexamethasone		D4902
3-iso-butyl-1-methylxanthine (IBMX)		I5879
Antibiotic-antimycotic mixture (100 U/mL penicillin, 100 U/mL streptomycin, and 0.25 μg/mL amphotericin B)		A5955
Endothelin-1		E7764
Tetrazolium dye MTT 3-(4,5-dimethylthiazol-2-yl)-2,5-diphenyltetrazolium bromide	Alfa Aesar	L11339

Cell lines used in this study are listed in **Table 2.3**.

Table 2.3: Cell lines used in this study.

Cell Line	Source	Catalogue Number
3T3-L1 Pre-adipocyte (mouse embryonic fibroblast-adipose like cell line)	American Type Culture Collection (ATCC, Manassas, VA)	CL-173
HepG2 Liver hepatocellular carcinoma		HB-8065

2.3 Cell Culture Protocols

2.3.1 Culture of 3T3-L1 Adipocytes

3T3-L1 pre-adipocytes of low passage were removed from liquid N_2 storage and thawed, then transferred into a 25 cm^2 culture flask and Non-Advanced DMEM/10% FCS (5 mL) was added. The culture was incubated for 24 h at 37 ˚C in a 5% CO_2/95% air atmosphere. The initial growth media was removed, washed with PBS (5 mL) and TrypLE (0.05%, 2 mL) was added. The culture flask was incubated at 37 ˚C for 3-5 min until cell detachment from the flask was observed. DMEM/10% FCS (2 mL) was added to the flask to terminate the action of trypsin, and the contents were transferred to a 15 mL centrifuge tube and centrifuged for 3 min at 2000 rpm to produce a small pellet. The supernatant was removed and the pellet was resuspended and dispersed in DMEM high glucose (containing 4.5 g/L glucose), supplemented with antibiotic-antimycotic mixture (100 U/mL penicillin, 100 U/mL streptomycin, and 0.25 U/mL amphotericin B), L-glutamine (2.0 mM), and 10% foetal calf serum, for the purposes of seeding the preadipocytes onto IR transparent substrates (Section 2.5.1) in 24-well plates (typically 1mL of suspension per plate). The preadipocytes were then incubated until 70-80% confluency.

Two days post confluency, 3T3-L1 pre-adipocytes were incubated with differentiation medium containing 10% FCS, and adipogenesis cocktail (1.0 µg/mL bovine insulin, 1.0 µM dexamethasone, and 0.50 mM IBMX) for 3 d (this time point was designated day 0). Post-differentiation medium (DMEM/high glucose, containing 10% FCS, 1 µg/mL insulin) was added at day 3, after removal of the differentiation media and incubated for 2 d. The culture was then maintained using DMEM containing 10% FCS every 2-3 d,

until such time that the cells were fully differentiated (typically 8-12 d post confluency).[245]

2.3.2 Culture of HepG2 Cells

HepG2 cells were cultured in an identical manner in Advanced Dulbecco's Modified Eagle Medium (DMEM) supplemented with 2% FCS, 100 U/mL penicillin, 100 U/mL streptomycin, and 0.25 U/mL amphotericin B (anti-biotic and anti-mycotic mixture) and L-glutamine (2.0 mM) in 5% CO_2/air at 37 ˚C. Cell media was changed every 3 d until cells were >80% confluent and, at this stage, they were further split or used in viability assay or spectroscopic studies.

2.4 Cell Counting

Prior to seeding cells onto CaF_2 substrates, cell counting was performed using an automated cell counting system (Countess, Invitrogen). After trypsinisation of cells, the resulting suspensions were centrifuged at 2000 rpm for 3 min (Labofuge 400, Thermo Fisher Scientific). The medium was removed by pipetting and the resulting pellet was redispersed in supplemented media with aspiration using a 1 mL pipette.

A 15 μL aliquot of the cell suspension was transferred to an Eppendorf tube, and 15 μL of Trypan Blue stain was added to the suspension, which was transferred into the Countess cuvette for cell counting. Results were provided as cell counts/mL and a % viability measurement was also provided. Cell counts were based on the number of live cells detected during the analysis.

2.5 General Cell Seeding and Fixation Protocol onto Calcium Fluoride Substrate

2.5.1 3T3-L1 pre-adipocyte seeding protocol

3T3-L1 pre-adipocytes were washed once with PBS and trypsin (4 mL) was added to the cell culture. The fibroblasts were incubated for 10 min until fully detached and DMEM/10% FCS was added to stop trypsinisation. Fibroblasts were counted as described in Section 2.4 and the fully dispersed cells were diluted to result in a final aliquoted volume containing 15×10^4 cells per well of a 24 well plate with a CaF_2 substrate.

CaF_2 substrate (0.5 mm, Crystran, UK) was prepared as 5 × 5 mm windows (plates), sterilised with 80% ethanol, washed with PBS to remove the ethanol and preconditioned by dipping in supplemented media before being placed into the wells of a 24-well plate. Each window was covered with the appropriate amount of cell suspension and incubated

overnight until cell attachment occurred. Differentiation of seeded pre-adipocytes (Section 2.3.1) proceeded until the desired confluence and were then ready for the treatment protocols (Section 2.6).

2.5.2 HepG2 seeding protocol

The HepG2 cells were grown to confluence, detached by trypsinisation and seeded at 15×10^4 cells per well on CaF_2 substrate. Counting and seeding of HepG2 was performed in a similar manner to those described (Section 2.5.1). Once the desired confluence was achieved (incubation at 37 °C, 5% CO_2/air), they were treated according to specific cell type protocols described (Section 2.6).

2.5.3 Cell Fixation Protocol

The chemical fixation of all cell types onto CaF_2 substrates was performed according to the cold methanol fixation method of Carter, *et al*.[243] The substrate was removed from the well plate and washed in PBS and blotted to remove as much PBS as possible. The cells were then fixed by immersion of the substrate into methanol (cooled to dry ice, 253 K) once for 1-2 s. Excess methanol was removed from the plates and the samples were air-dried then stored in Eppendorf tubes in an anhydrous environment prior to spectroscopic analysis. Although methanol can result in the extraction of lipids from cells,[218] the morphological images provided in Chapter 4 show that this fixation method kept the multilocular structure of adipocytes intact.

2.6 Cell Treatment Protocols

A standard treatment regime of glucose, fructose and sodium vanadate Na_3VO_4 was devised for the treatment of insulin sensitive and resistant 3T3-L1 cells based on a two-level full factorial design. Treatment levels in the design included a no-treatment (starvation) run and included treatment at the physiological level of glucose reported in the bloodstream to be 3.8-7.8 mM and as high as 11 mM postprandial.[246] The concentration was defined as 5.0 mM for the trials utilising glucose in the treatment regime.[247] Although fructose is present in much lower physiological concentrations in the bloodstream under normal conditions (0.060 mM), after consumption of a large fructose load, circulation concentrations of 1.0 mM were observed.[248] Fructose concentrations in excess of 1.0 mM could be expected for individuals who consume more than the daily average soft drink and processed food loads and concentrations of up to 5 mM can be expected at the portal vein as the liver consumes ~50-80 of blood fructose levels.[249] Therefore, fructose concentration was also fixed at 5.0 mM,[11] in order to induce cellular

response during the treatments and represents an upper limit of postprandial portal venous concentration.[249]

The concentration of Na_3VO_4 was different for each cell line studied and the particular concentration used was determined using the cell viability assay method described in Section 2.7. The individual maximum concentrations of vanadate used are reported in the chapters for the individual cell lines. The following describe the general reagent preparation protocols.

2.6.1 Preparation of Glucose, Fructose and Vanadate Stock Solutions

Stock solutions (10 mM) of D-(+)-Glucose and D-(-)-fructose were prepared in glucose-free DMEM supplemented media. Each solution was sterilised by filtration through a 0.22 μm syringe filter (Merck Millipore) prior to use. Dilutions of each stock solution were made according to the treatment conditions of the experimental design.

Na_3VO_4 (100 mM) stocks were prepared in Milli-Q water by heating until boiling.[250] The pH value was adjusted to 10 with 1.0 M NaOH/HCl and boiled until the yellow colour of the solution dissipated. The process of pH value adjustment and boiling was repeated until the pH value remained constant and no evidence of yellow colouration, due to polyvanadates,[251] was observed. The cooled solution was volume adjusted with Milli-Q water to final concentration.

2.6.2 General Sugar-Vanadate Treatment Protocols

Individual cell lines were treated based on a full factorial DoE approach (Section 1.7.1). The high (+1) and low (-1) levels of glucose and fructose were defined in Section 2.6. Vanadate was set at a low value of 0 μM and high levels from IC_{50} values defined in each chapter. **Table 2.4** provides an overview of the factor levels used in the designed experiments of this study.

Table 2.4: High and low levels of experimental factors used in designed experiments for assessing the effects of sugar and vanadate treatments on the three cell lines investigated in this study.

Concentration	Low Level (-1)	High Level (+1)	Centre Point (0)
Glucose (mM)	0	5	2.5
Fructose (mM)	0	5	2.5
Vanadate (mM)	0	Cell line specific, refer to individual chapters	

For the treatment of the 3T3-L1 cell line, four experimental factors were assessed. These include the three listed in **Table 2.4** and a fourth factor, insulin resistance. Insulin resistance is a binary factor (yes/no) and was induced according to the protocol described in Section 2.6.3. The designs used for HepG2 included only the factors listed in **Table 2.4**.

2.6.3 Inducement of Insulin Resistance in 3T3-L1 cells

Fully differentiated 3T3-L1 cells grown on CaF_2 substrates were incubated for 24 h at 37 °C, 5% CO_2/air in the presence of 1.0×10^{-8} M endothelin-1, according to the procedure described by Ishibashi, *et al*.[75] which renders 3T3-L1 adipocytes insulin-resistant. Further testing of insulin resistance was not performed as part of this investigation and the treated cells were assumed to be rendered insulin-resistant, based on similar results obtained previously on 3T3-L1 cells.[252]

2.6.4 Cisplatin Treatments of HepG2 Cells

A 1.0 mM stock solution of cisplatin was prepared in PBS. Aliquots were prepared, stored at -20 °C and thawed for use immediately before cell treatments. For cell viability assay experiments (Section 2.7), HepG2 cells were treated with twofold serial dilutions of cisplatin, with the highest concentration at 100 μM. Dilutions were performed using cell culture medium.

2.6.5 Doxorubicin Treatments of HepG2 Cells

A 0.5 mM stock solution of doxorubicin was prepared in PBS. Aliquots were prepared, stored at -20 °C and thawed for use immediately before cell treatments. For cell viability assay experiments (Section 2.7), HepG2 cells were treated with two-fold serial dilutions of doxorubicin, with the highest concentration at 10 μM. Dilutions were performed using cell culture medium.

2.7 Cell Viability Assay

The 3-(4,5-dimethyl-2-thiazolyl)-2,5-diphenyl-2H-tetrazolium bromide (MTT) assay was performed according to the method of Mosmann[253] and reviewed by Stockert, *et al*,[254] for HepG2 cells only. However, under the conditions used, the high metabolic activity of 3T3-L1 adipocytes produced a saturated response in MTT assays and cell viability could not be reliably measured. Cells were seeded onto 96-well plates at a density of 2×10^3 cells per well and allowed to attach for 24 h, then the selected treatment regimen was applied, and the cells were allowed to incubate at 37 °C, 5% CO_2/air for 72 h. The cell

media was removed and replaced with media containing 1.0 mg/mL MTT and the cells were incubated for 3 h. The media was removed and the cells were lysed with DMSO (100 μL/well) to generate the characteristic purple formazan colour formed by mitochondrial dehydrogenases. Absorbance was measured at 600 nm using a Victor^{3}V 1402 Multilabel Counter (Perkin Elmer, Boston, MA) and the results were expressed as percentage cell viability, assuming the viability of control cells (cultured in high glucose DMEM, 2% FCS) was 100%. Cell viability calculations were presented as plots of cell viability vs. log[concentration].

2.8 Spectroscopic and Hyperspectral Imaging Methodology

2.8.1 Laboratory Based FTIR Measurements

Single-point spectra or focal-plane-array (FPA) images were acquired in transmission mode on a Tensor 27 FTIR spectrometer coupled to a Hyperion 3000 IR microscope with either a 36× or 15× Cassegrain objective (Bruker Optics, Ettlingen, Germany) at Sydney Analytical. The microscope was equipped with a trinocular viewer, which accommodates a video camera allowing direct viewing of the sample. The microscope was fitted with a motorized *x-y-z* mapping stage, a motorised knife-edge aperture and a narrow-band detector or an FPA detector. Both the microscope stage and optics area are enclosed in a Perspex box, which was constantly purged with dry N_2. Atmospheric moisture was controlled through the use of desiccants that were constantly maintained in the spectrometer optics train.

The wavelength range covered was dependent on the detector used with a maximum range of 4000-400 cm^{-1}. Due to optical constraints imposed by the CaF_2 substrate and the rapid loss of sensitivity below 1000 cm^{-1}, spectra were only assessed over the region 3050-1050 cm^{-1} at a spectral resolution of 4 cm^{-1}. The N-H and O-H bands in the wavenumber region 3300-3700 cm^{-1} were observed as prominent bands in the raw spectra, however, when the second derivative processing method was applied, these bands diminished to weak signals compared to the C-H bands in the region 3000-2800 cm^{-1} (refer to Chapter 3), therefore, this justified the upper cut-off limit for spectral analysis of 3050 cm^{-1}. Optimisation of the data acquisition parameters, including number of coadded scans, aperture sizes and Fourier transform parameters were dependent on the cell type (Chapter 3). Background spectra were typically collected before the collection of single spectra, per line during mapping or before a 64×64 FPA image was collected to give 4096 individual spectra per image. The sampling area covered by the FPA detector was 170×170 μm, with an

approximate pixel resolution of 7 μm^2 (lateral resolution = 2.65 μm). Reference is made to **Figure 6.2** in Section 6.1.3 for a complete description of the spatial resolution obtained by photovoltaic FPA detectors in this work using a 36× Cassegrain objective with a numerical aperture of 0.5.

In all cases, single cell spectra were acquired by adjusting the knife edge apertures of the microscope such that the maximum area of the cell was scanned and the extracellular matrix was minimised. FPA spectra were acquired by selecting a region of interest (ROI) containing the cell and then moving the region in the OPUS software such that the FPA detector captured the entire centred cell image.

2.8.2 Synchrotron Based FTIR Measurements

2.8.2.1 Point- and Raster-Scanning

Synchrotron FTIR (SR-FTIR) spectroscopic data acquisition was performed at the Australian Synchrotron IRM beamline (2BM1), operating at a beam energy of 3 GeV with a maximal beam current of 200 mA. Spectra were collected in transmission mode using a Vertex V80v FTIR spectrometer coupled to a Hyperion 3000 IR microscope with a 36× objective (Bruker Optics, Ettlingen, Germany). The microscope was fitted with a motorized *x*-*y*-*z* mapping stage, a motorised knife-edge aperture and an MCT detector.

Prior to data collection, an optimisation protocol was developed to determine the settings that provided the least variable spectral data while at the same time, keeping the spectral data acquisition time to a minimum. This protocol used three mechanical pinhole settings available on the microscope, along with adjusting the number of co-added spectra for the assessment of spectral quality (Chapter 3).

Single spectra were obtained in the same manner as described for the laboratory-based instruments in Section 2.8.1.

2.8.2.2 Four Beam Synchrotron FPA Imaging

The Bruker Hyperion 3000 microscope (2BM1) was equipped with a mid-IR focal plane array detector with 64×64 active pixels. The microscope was equipped with a combination of a 20× (0.6 Numerical Aperture) condenser (Bruker Optik GmbH, Germany) and a 52× (0.65 Numerical Aperture) objective (Edmund Optics, Singapore), with a detector pixel pitch of 0.77 μm×0.77 μm. The detector was operated at the full frame size of 64×64 pixels. Detector readout rates were 5 kHz for the FPA (actual integration time used = 0.2146 ms). The FPA detector had a long wavelength cut-off of

850 cm^{-1}, whereas the single element MCT used had a cut-off of 750 cm^{-1}. FPA images were acquired at 4 cm^{-1} resolution using 256 coadditions for background and sample scans.[255]

2.8.3 Spectral Data Acquisition and Processing

The spectrometer and microscope were controlled using the OPUS software package (version 8.2.9, Bruker Optics, Ettlingen, Germany). The FPA measurements at the Australian Synchrotron were collected using OPUS software (version 7.2). Spectral data were saved in OPUS formats that were imported into chemometrics and multivariate image analysis software.

Image files required extraction of spectra prior to importation into third party software packages using the extract function of OPUS software. The OPUS software package also has a number of options for assessing integrated peak areas on raw and processed spectra.

2.9 ^{51}V NMR Spectroscopy

^{51}V NMR of 1.0 mM Na_3VO_4 in cell culture medium was acquired after cytotoxicity assay with HepG2 cells (16 h pre-incubation + 72 h incubation at 310 K). D_2O (10% vol.) was added to the medium immediately before acquiring the spectra to lock the NMR signal. Spectra were recorded at 300 K on a Bruker Avance 400 MHz spectrometer at 26.35 MHz[256] in the −1000 to 500 ppm spectral window (2560 scans; total scan time, 23 min), and were externally referenced using 100 mM Na_3VO_4 solution in 1.0 M NaOH ($[VO_4]^{3-}$ signal at −541 ppm).[256]

2.10 Data Analysis Methodology

Experimental design generation and analysis was performed using the Design Expert software package (version 13, Statease, MN, USA). General univariate statistical analyses were performed using Minitab (version 19, Minitab LLC PA, USA). IC_{50} calculations were performed using Origin software (version 6.1, OriginLab Corporation, MA, USA).

Multivariate analysis (MVDA) of single point spectra was performed using the VEKTOR DIREKTOR software package (version 1.0. KAX Group, Australia). Spectra were imported as the proprietary OPUS file format for visualisation, preprocessing and exploratory analysis. VEKTOR DIREKTOR provides functionality for exploratory data analysis, multivariate regression and multivariate classification and hyperspectral image analysis (HIA).

HIA was performed using PLS-Toolbox Solo + MIA (Solo, version 8.9.1, Eigenvector Research, WA, USA) and VEKTOR DIREKTOR. Image files extracted from OPUS were saved in ASCII (.csv) format in numerical order and imported into the respective software package. The 2D-file was converted into an image format and analysed using the preprocessing methods and multivariate analysis tools available for HIA. Unimportant regions of the image space were manually masked and models were calculated using the region of interest (ROI) only.

Chapter 3 Optimisation of Fourier Transform Infrared (FTIR) Microspectroscopic Point Scanning and Focal Plane Array (FPA) Imaging

3.1 Introduction

Baker, *et al.*[257] provide an excellent protocol for addressing sample preparation, the optimisation of spectral data acquisition and data processing methods for use with FTIR microspectroscopy. The protocol is applicable to the Globar® (silicon carbide) light sources commonly used in benchtop instrumentation or for instrumentation interfaced to a synchrotron light source, such as the infrared microspectroscopy (IRM) beamline at the Australian Synchrotron (AS). This protocol contains a wealth of general information, but little detail on the practical aspects for optimisation of spectral acquisition parameters such as number of coadded spectra, mechanical spot size restrictions and depth profiling. Such parameters affect the quality of spectral data obtained, minimise extraneous noise so that simpler processing methods can be applied, which result in multivariate analyses which better partition noise into higher order components.[223]

Laboratory and synchrotron-based FTIR (SR-FTIR) spectroscopies are excellent tools to probe biochemical changes in fixed and live cell cultures,[257-258] and when coupled to a high magnification microscope (**Figure 3.1**),[259] both spatial (morphological) and chemical information of intact cells is provided. Such information can be used to assess the inherent heterogeneity within individual cells and locate cellular components such as the nucleus, lipid droplets and cell membrane boundaries.[189,217-218,260]

FTIR spectrometers require continual referencing against a constant non-absorbing background to account for changes in atmospheric moisture and carbon dioxide levels. Even in the presence of a dry nitrogen purging system and regular desiccant recharging that are used to maintain a constant environment, regular re-referencing is an absolute requirement. Lasch and Petrich[189] showed that when water vapour is not completed purged from the instrumentation, important chemical information can be distorted or concealed for lipids, proteins and DNA (Wood,[182] has reviewed the influence of hydration levels on DNA band positions).

3.2 Parameters, Protocols and Spatial Resolution

Typically, a reference (background) scan is re-recorded after the completion of a single point scan, or at the end of a line array where a mechanical *x*-*y*-*z* stage is moved to either a point on an infrared transparent substrate, where there is minimal to no contamination of cellular matter, or a clean substrate in close proximity to the substrate containing the cells. In line or raster scanning, the stage is positioned at the start of the next array to complete another line scan and this process is repeated until an entire grid of predefined

size is mapped. The precision of stage positions is, therefore, a critical parameter to investigate to ensure that the spectral data acquired is aligned to the optical micrographs recorded before a chemical map is collected.

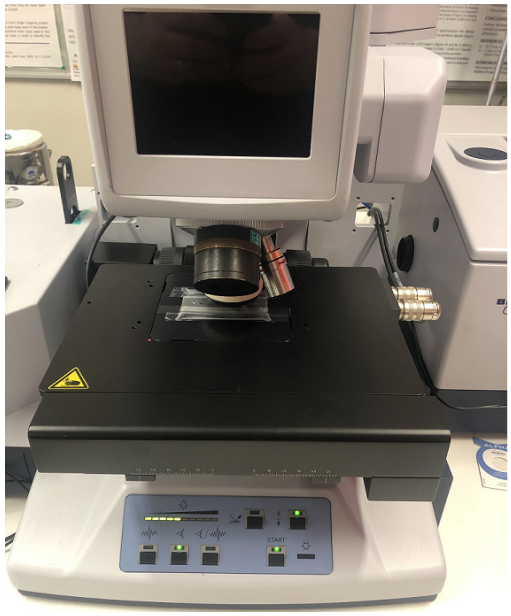

Figure 3.1: *x*-*y*-*z*-optical stage of the Bruker Hyperion 3000 FTIR microscope with a 36× Cassegrain microscope objective installed. The stage has a slotted sample holder wide enough to capture reliable spectra of cells fixed to CaF_2 substrate and small enough to minimise the risk of the sample dropping into the microscope condenser, located underneath the stage.

A schematic (**Figure 3.2**) of the operation of the FTIR microscope shown in **Figure 3.1**, highlights why the precision of the *x*-*y*-*z* stage is critical to the quality of obtained spectra. Chemically fixed cells on the substrate are either sparsely or densely populated, depending on the confluence of the cells and the treatment conditions. In many situations, the selection of single, isolated cells is desired to provide unique biochemical information free from interactions with other cells in more dense colonies.[258]

The regular instrument re-referencing required during chemical mapping that takes ~2-4 hr to complete for a small map, e.g., a 12×12 grid, means the *x*-*y*-*z* stage constantly moves to and from the cell to the background position. This constant movement increases the potential for misalignment; therefore, it is important to ensure that the stage is calibrated each day of operation and that an alignment study is performed on a regular basis to ensure that when single images are collected to create a montage, they are stitched together in a manner that reduces the risk of misalignment. The daily stage calibration is typically a macro check of the entire stage range. A repeatability test should also be performed to assess the micro control of the stage.

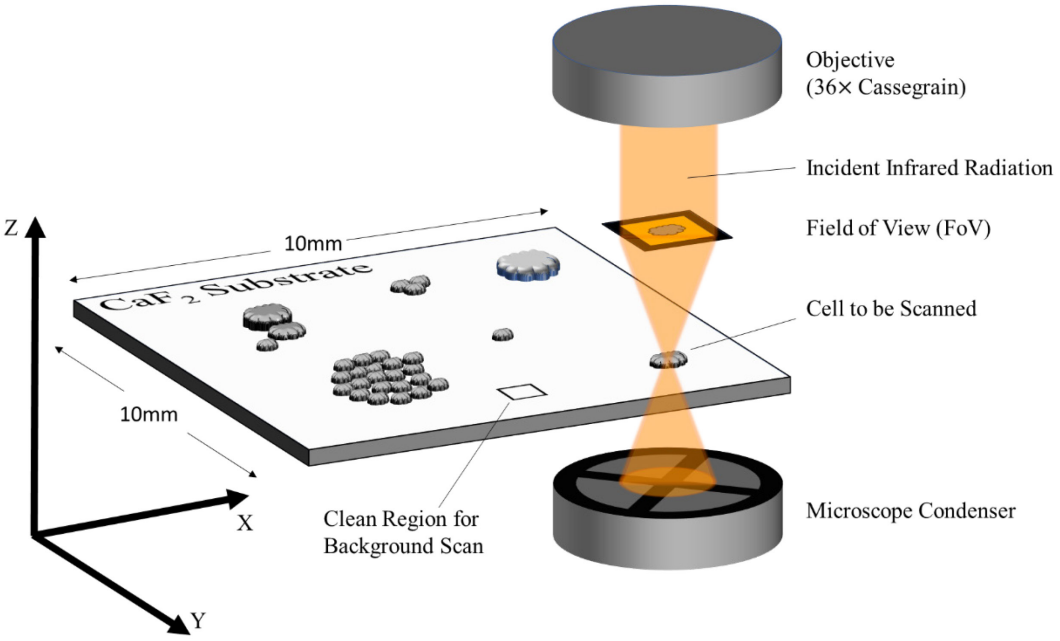

Figure 3.2: Schematic diagram of a Cassegrain microscope objective used for FTIR microspectroscopy. Various cell lines can be chemically fixed to a substrate, e.g., CaF_2, where cell densities naturally vary from very sparse to dense colonies.

In single-point scanning, the stage is moved in the *x*-*y* direction over the object of interest and a mechanical knife-edge aperture is used to define the field of view (FoV) with the aid of a microscope objective (**Figure 3.2** and **Figure 3.3a**). During raster scanning, the stage is moved to the object of interest and a rectangular grid array is defined in *x*-*y* space over the microscopic image, therefore, the area of each partition in the grid will be one spectrum (**Figure 3.3b**) and as can be observed in this figure, a single spectrum would be comprised of multiple cellular components.

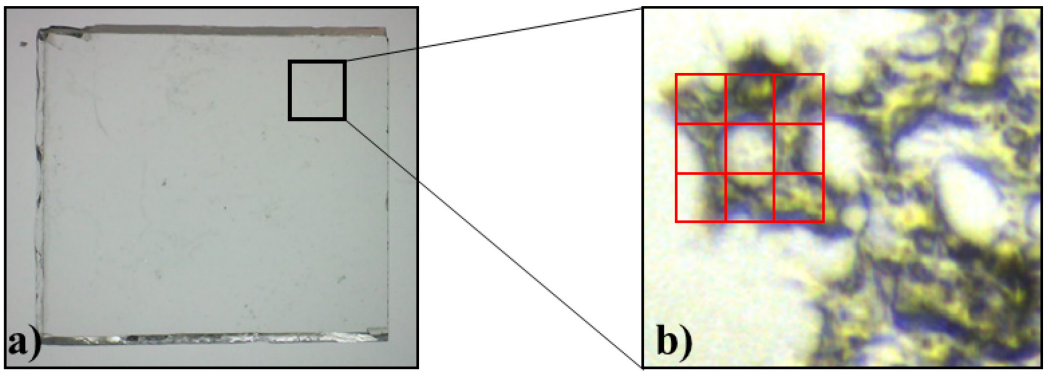

Figure 3.3: a) Digital image of a CaF_2 substrate with chemically fixed HepG2 cells and; b) optical micrograph of the region of interest (ROI) as viewed under the microscope of the Bruker Hyperion 3000 system at 36× magnification. The red grid in b) represents a single cell either measured as a single-point spectrum by setting the aperture to the size of the cell, or mapped over a predefined grid of appropriate aperture and step size.

Spatial resolution is restricted by the diffraction limit.[217,261-262] The high light flux intensity (brightness) of synchrotrons provided enhanced signal-to-noise ratio spectra using apertures approaching the diffraction limit. However, for a focal-plane-array (FPA) detector, the light is dispersed over a larger area and the benefits of the high intensity cannot be exploited, unless multiple beamlines are combined (Section 3.8). The diffraction limit is expressed as Equation 3.1

$$\Delta x \geq 0.61 \frac{\lambda}{n sin\theta} \qquad 3.1$$

Δx is the distance separating two objects; n is the refractive index of the medium between the objective and the object; θ represents the acceptance angle of the objective and together, $n\sin\theta$ is the numerical aperture (NA) of the objective. NA measures the range of angles that an objective can accept or emit light. This equation is consistent with Rayleigh's criterion that two points can be resolved as long as the centre of one Airy disc coincides with the first minima of the second Airy pattern.[217,263] While the spatial resolution of infrared microscopes will always be inferior to visible microscopes, what is lost in resolution is gained in the chemical information contained within the spectra.[217]

In the current study, spatial resolution was evaluated using a highly heterogeneous cell line with a Bruker Hyperion 3000 system in transmission mode, where a spatial resolution of 2.4 μm has previously been reported with a 36× Cassegrain objective (with NA_{36x} of 0.5).[217] It is noted, however, that such resolution is applicable at 5000 cm^{-1} and is not relevant to the work conducted in this study. In general, the shorter the wavelength, the higher the contrast as predicted by Abbe's theory for diffraction limited optical systems in Equation 3.1.[217] **Table 3.1** lists the main data collection parameters, (other than spectra coadditions), which were set in this study to obtain high quality spectra.

Table 3.1: Main spectral data acquisition parameters of the Hyperion 3000 FTIR microscope (excluding sample coadditions).

Parameter	Setting
Spectral resolution	4 cm^{-1}
Apodisation	Blackman-Harris 3-term
Zero Filling Factor (ZFF)	2
Spectral Range (D316 MCT Detector)	4000-650 cm^{-1}

3.3 Substrates

CaF_2 is routinely used as an optical substrate as it is water insoluble, colourless, and transparent over most of the infrared region.[214-215] However, it displays fringing and chromatic aberration characteristics, particularly below 950 cm^{-1}.[214-215,255] Even though the MCT D316 detector has a cut off at 600 cm^{-1} (**Figure 3.4**), the CaF_2 aberrations limit the amount of useful information obtainable below 1000 cm^{-1}.[214] Fabian, *et al*.[214] has suggested that the wavenumber region 1800-1000 cm^{-1} is most suited for biological samples analysis, however, the high lipid content in 3T3-L1 adipocytes and changes in lipid biochemistry of HepG2 cells, investigated in this study, required the inclusion of the 3050-2800 cm^{-1} range.[195,202]

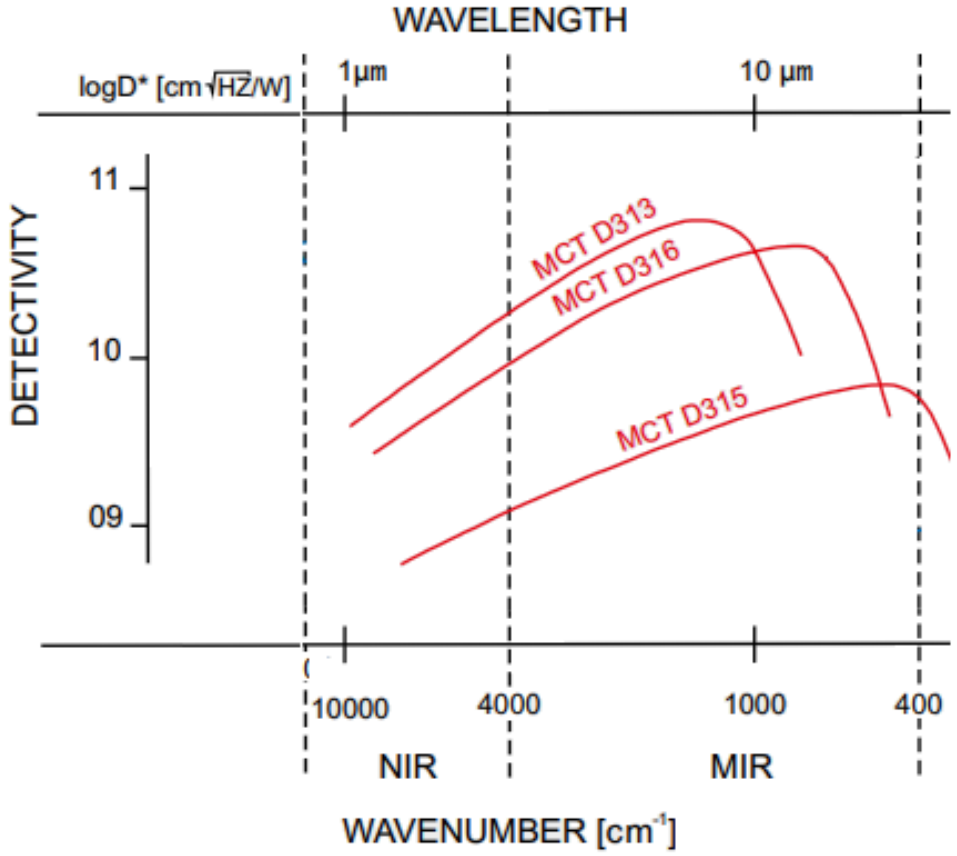

Figure 3.4: Detectivity vs. wavenumber (cm^{-1}) of commonly used MCT detectors in mid-infrared spectroscopy. Adapted from Application Note AN M161, Bruker Optiks, GmbH.[264]

To optimise scanning conditions, 3T3-L1 adipocytes were used as they represent a physically large cell type with high heterogeneity due to distinct lipid droplets dispersed on a protein monolayer. Epithelial HepG2 cells with less heterogeneity, a smaller diameter and tending to grow in clusters, were used as a comparison to the 3T3-L1 adipocytes for the optimisation experiments.

3.4 Optimisation of Point and Raster Scanning Data Acquisition Parameters of the Bruker Hyperion 3000 Microscope at The Australian Synchrotron.

3.4.1 Sample Selection and General Instrument Setup

The repeatability and reproducibility of data obtained from SR-FTIR microspectroscopy was investigated using 3T3-L1 mouse adipocyte cells fixed to a CaF_2 substrate. 3T3-L1 adipocyte cells represent a highly challenging sample for evaluation and optimisation of FTIR microspectroscopy acquisition parameters (Section 3.1) due to their high heterogeneity, large size (18-24 μm in diameter[258] and in some cases up to 300 μm),[32] and thickness (~30-50 μm) thus allowing reliable depth profiling studies to be performed. Cell interface boundaries also exhibit high refractive indices, that result in artefacts, including Mie scattering effects.[265]

Two cells in close proximity were selected and measured multiple times, which required the mechanical stage to move between the background and sample positions to evaluate spectral repeatability. **Figure 3.5** provides the optical micrograph of the cells together with the points where spectra were acquired.

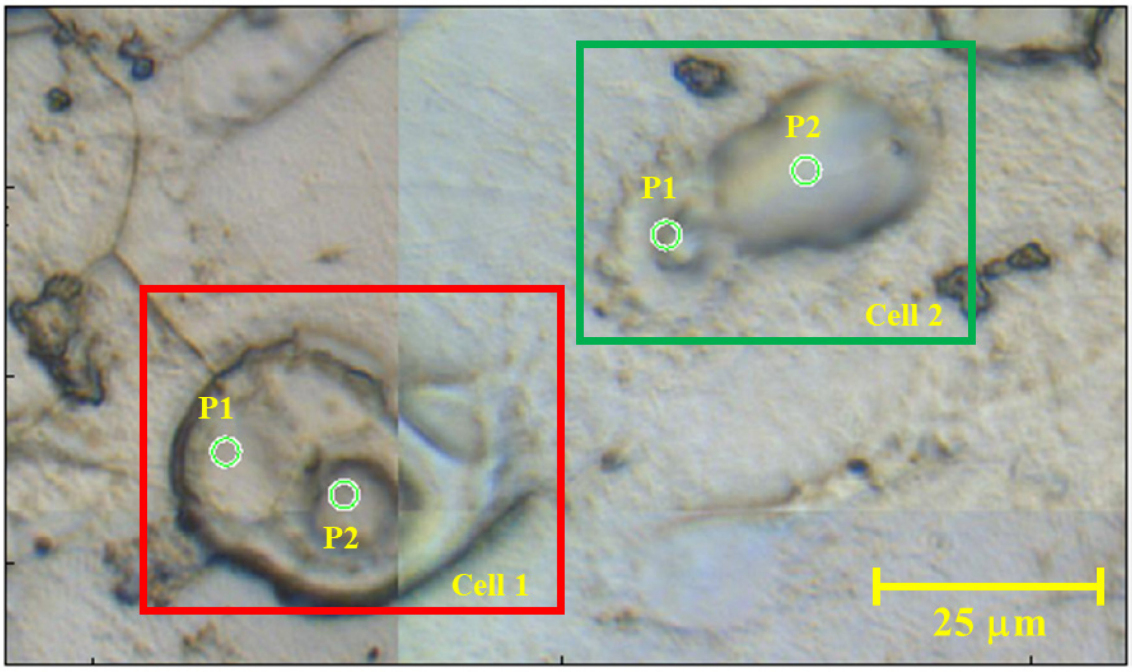

Figure 3.5: Optical micrographs of 3T3-L1 adipocytes chosen to optimise data acquisition parameters on a Bruker Hyperion 3000 FTIR Microscope at 36× magnification.

This experiment was designed to evaluate the following data acquisition parameters:

- Optimal number of scans (coadditions);
- Optimal mechanical pinhole size for single-point scans and mapping;

- Consistency of the microscope stage position; and
- The effect of data processing and the definition of suitable wavenumber ranges to apply processing methods.

A random selection was considered to be representative due to the large cell numbers seeded on the substrate and each cell had an equal probability of being chosen. The large constitutional and distributional heterogeneity (C_H and D_H respectively) also ensured that biological variability was captured within the assessment.[227-228] The cell morphologies are very different as was observed in the optical micrographs (**Figure 3.5**) and **Table 3.2** provided justification for their selection.

Table 3.2: Selection and description of cellular biochemistries in **Figure 3.5**. Refer to **Table 1.1** for band assignments relevant to each position.

Cell Number	Position	Biochemical Description
1	1	Chosen for its combined intense lipid and protein bands.
	2	Chosen for its predominant lipid character.
2	1	Chosen for its distinct protein features and lack of lipid features.
	2	Chosen for its combined high lipid and protein bands.

Representative spectra from each position (**Figure 3.6**) illustrated the diversity within a single 3T3-L1 cell, in particular, Cell 2, Position 1 had a weak lipid band at ~1740 cm^{-1} and increased amide absorbances ~3300 cm^{-1} (protein N-H), ~1650 cm^{-1} (C=O amide I) and ~1550 cm^{-1} (N-H amide II), respectively (refer to **Table 1.1** for band assignments). The other three cell positions varied mainly in lipid content. Therefore, this data set was representative of diverse biochemical information, which allowed an optimisation study of scanning acquisition parameters to be performed and validated using multivariate data analysis.

The shadows around the averaged spectra (**Figure 3.6**) represent the spectral variability, i.e., the sampling bias.[227] This figure also highlighted the spectral noise below 1000 cm^{-1}, which was attributed to the decreasing detector sensitivity in this region (**Figure 3.4**), the CaF_2 substrate cut-off and restriction of incident radiation by the mechanical pinhole placed between the objective and the sample.

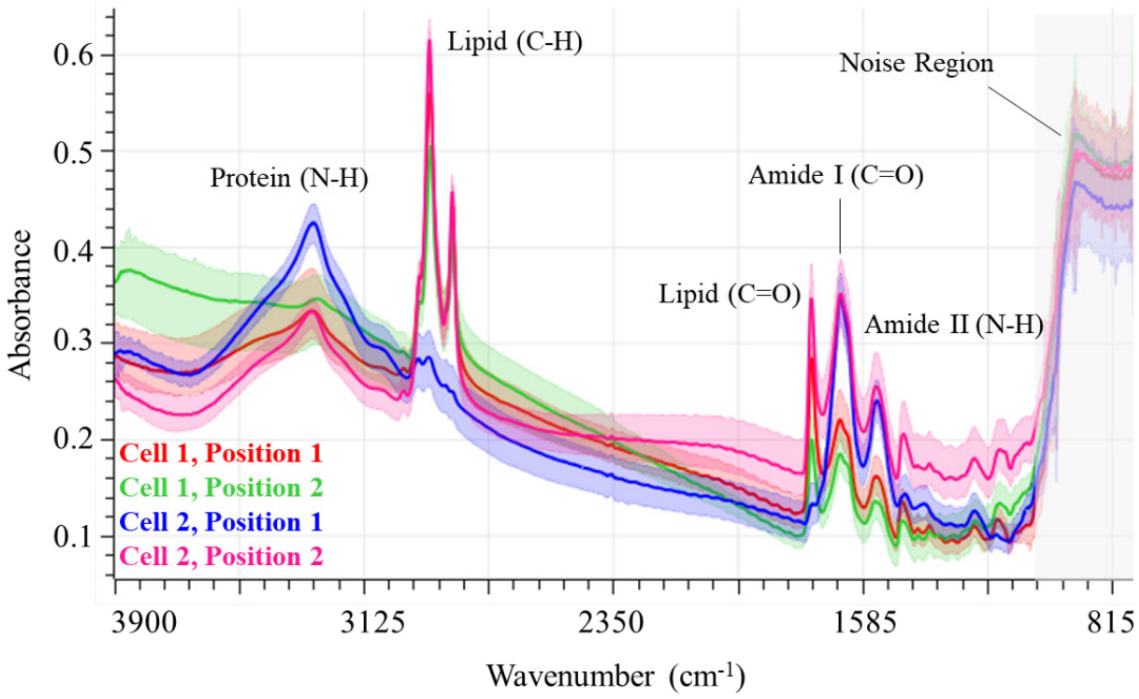

Figure 3.6: Averaged spectra acquired from the selected positions of 3T3-L1 adipocyte cells 1 and 2. **Table 3.2**. details the justification of the selection and description of cell biochemistry. Spectra were acquired using 128 coadditions at a resolution of 4 cm^{-1} with the large mechanical pinhole inserted (~0.6 mm).

3.4.2 Optimisation of Spectral Coadditions

The International Conference on Harmonisation (ICH) publishes guidance documentation regarding the development of analytical procedures for use in the pharmaceutical and other regulated industries (including medical devices).[266-267] This current study used the principles of the ICH guidance document Q2(R1)[266] on analytical method development to evaluate the optimal number of spectral coadditions for reliable acquisition of spectra and corresponding hyperspectral images. The study protocol (**Table 3.3)** was used to evaluate the repeatability/reproducibility of acquired spectral data for defined cell positions (**Table 3.2**).

Other guidelines exist for optimisation of spectral data acquisition parameters in regulatory environments. In particular, the European Medicines Agency (EMA) guidance for method development using near infrared spectroscopy (NIRS) provides detailed procedures required for development of quantitative and qualitative methods.[267] The EMA guidance is not limited to NIRS applications since Gouveia, *et al*.[268] has stated that the principles described in this guideline are equally applicable to data acquired using FTIR and Raman spectroscopy.

Table 3.3: Experimental conditions employed for FTIR repeatability and reproducibility study.

Parameter	Experimental Conditions
Number of cell positions measured	4 based on compositions of lipid and protein content (**Figure 3.5** and **Figure 3.6**).
Spectral Range	3897 – 650 cm^{-1}.
Coaddition of spectra	16, 32, 64, 128 or 256. The medium pinhole was assessed for 16, 128 and 512 coadds only.
Pinhole size	Small ~ 0.2 mm; medium ~0.45 mm; and large ~0.6 mm.
Spectral resolution	4 cm^{-1}.
Depth profiling	0, 5, 10 and 15 μm from substrate surface.

According to Miller and Dumas[269] microscopes that operate in a confocal arrangement, improve the spatial resolution ~λ/2 compared to the diffraction-limited spatial resolution of ~2λ/3 for a single objective.[270] An FTIR microscope is confocal when a second aperture (i.e., a mechanical pinhole) is used after the sample to define the region being sensed by the IR detector. The mechanical pinholes used as a second aperture in the Hyperion 3000 microscope at the Australian Synchrotron are listed in **Table 3.4**. along with the projected aperture size. Spectra from identified positions (**Figure 3.5**) were acquired by successively moving the microscopes mechanical stage to each position for a total of five replicate measurements at each position (**Figure 3.7**) with each replicate using three mechanical pinhole sizes.

Each measured position exhibited highly repeatable and unique information for this assessment. The following observations were made regarding the data in **Figure 3.7**.

- A larger spectral region is available for analysis when the large pinhole is used compared to the small pinhole (increased light flux).
- The small pinhole results in spectra with higher repeatability because of the smaller area scanned by the incident radiation, a highly desirable characteristic for investigating specific regions in cells and tissues.
- The shaded region between 1150-650 cm^{-1} defined the noise range for the small pinhole data acquisition and this region was projected to the spectra collected from

medium and large pinholes in **Figure 3.7b** and **c**. This region represented a practical cut-off limit for the small pinhole and band interpretation below this point was unreliable. The corresponding cut-off for the large pinhole was from 1050-650 cm^{-1}, representing a 100 cm^{-1} information gain compared to the small pinhole. The medium pinhole was intermediate between the small and large pinholes.

- The larger the number of coadditions, the lower the noise as would be expected due to the "multiplex" or "Fellgett Advantage".[271] Even at higher coadditions, the ability to interpret bands below 1000 cm^{-1} was limited by the CaF_2 substrate, which exhibits intense absorptions below this cut-off point.[214]

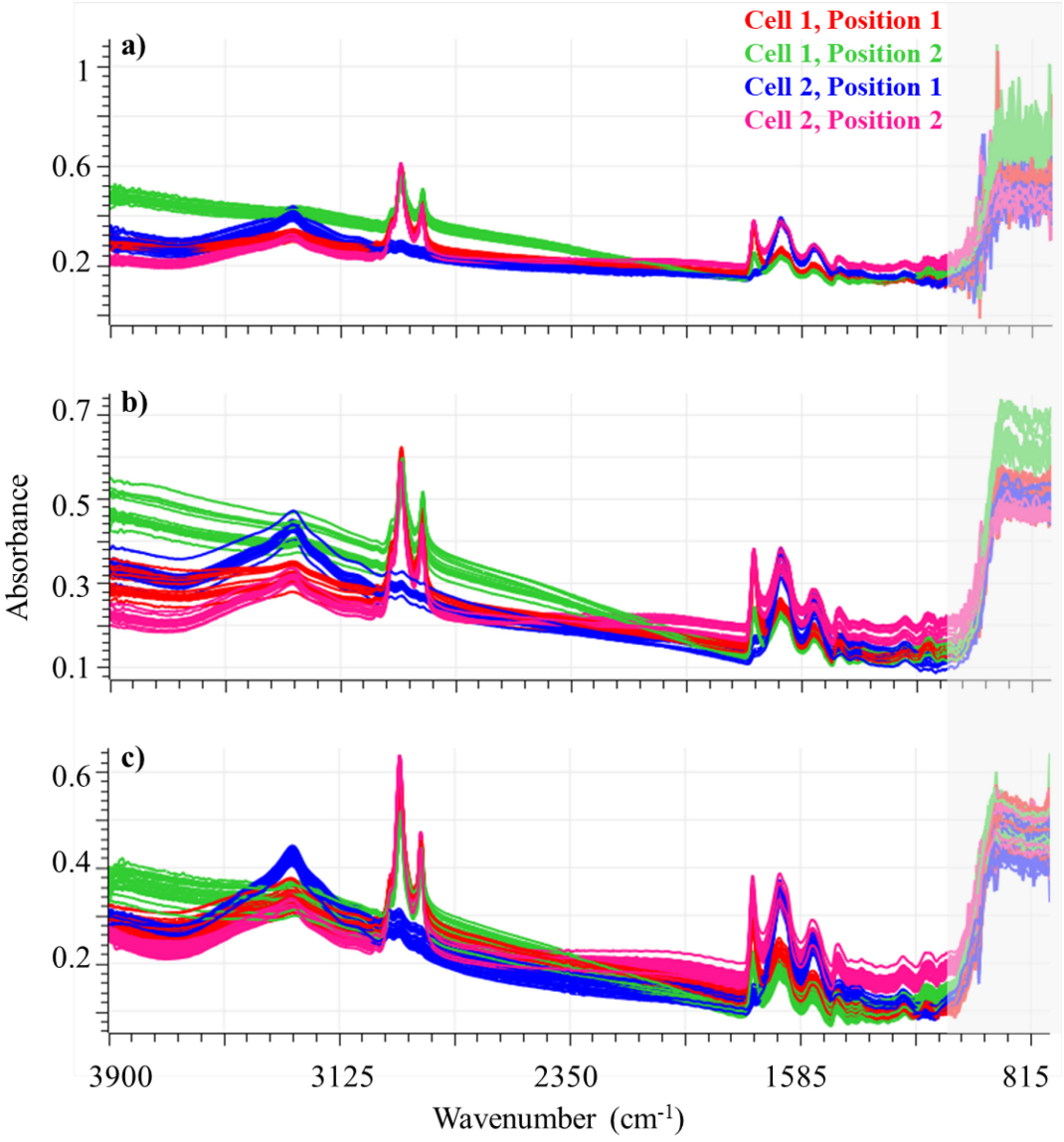

Figure 3.7: Raw spectra acquired from four points on two 3T3-L1 adipocyte cells (**Table 3.2**); a) small pinhole; b) medium pinhole and; c) large pinhole. Pinhole sizes correspond to those listed in **Table 3.4**.

Table 3.4: Pinhole sizes and calculated beam focus sizes used at the Australian Synchrotron*.

Pinhole Name	Pinhole Size (mm)		Objective: 36 × Transmission (μm)
	Labelled Size	Actual Size	
Small	0.20	0.20	5.56
Medium	0.45	0.42	11.67
Large	0.60	0.60	16.67

* Data courtesy of Dr. Pimm Vongsvivut, IR Beamline, Australian Synchrotron.

To compensate for the decreased flux of IR radiation incident from the small pinhole, a larger number of coadditions was required to achieve improved signal to noise (S/N) ratios. However, when a 15×15 map was collected from a single cell, it took ~1 min to collect 128 scans and ~ 1.5 min to collect 256 scans and the corresponding maps required 4 hr or 6 hr, respectively. The effective cooling period of cryogenic MCT detectors was ~8 hr, therefore, a compromise between spectral S/N and acquisition times was required for mapping.

The small pinhole (**Table 3.4**) provided a projected beam spot of 5.56 μm compared to the actual beam spot size of 8 μm. The two-dimensional light intensity distribution of the incident beam (**Figure 1.17**) is not collimated and dispersion of the incident beam may diminish the advantage gained from improved spatial resolution.[272] Based on the noise characteristics induced by the small pinhole, information below 1200 cm^{-1} has too much noise for reliable application of multivariate methods. Therefore, the large pinhole is a better option for long maps of larger areas based on improved S/N ratio and larger wavelength range. The small pinhole, with a high degree of oversampling and more coadditions provided improved spatial resolution for smaller regions of interest (ROI) identified from a large area mapping study of the sample, which initially used a large pinhole to identify the ROI.

Principal component analysis (PCA, **Figure 3.8**) was applied to the entire raw SR-FTIR data set to determine whether separation of the positions was possible. The t_1 vs. t_2 vs. t_3 scores plots with associated loadings line plots (p_1-p_3) showed that the data was grouped by cell position using local Hotelling's T^2 ellipses at the 95% confidence interval. The scores plot can be considered a visual analysis of variance (ANOVA) plot showing that the variability was smaller within a cluster than between clusters. These data also verified the *x*-*y*-*z* stage precision for producing repeatable spectral data. **Figure 3.8** showed that for all pinholes used, >90% of the spectral features were described by three PCs.

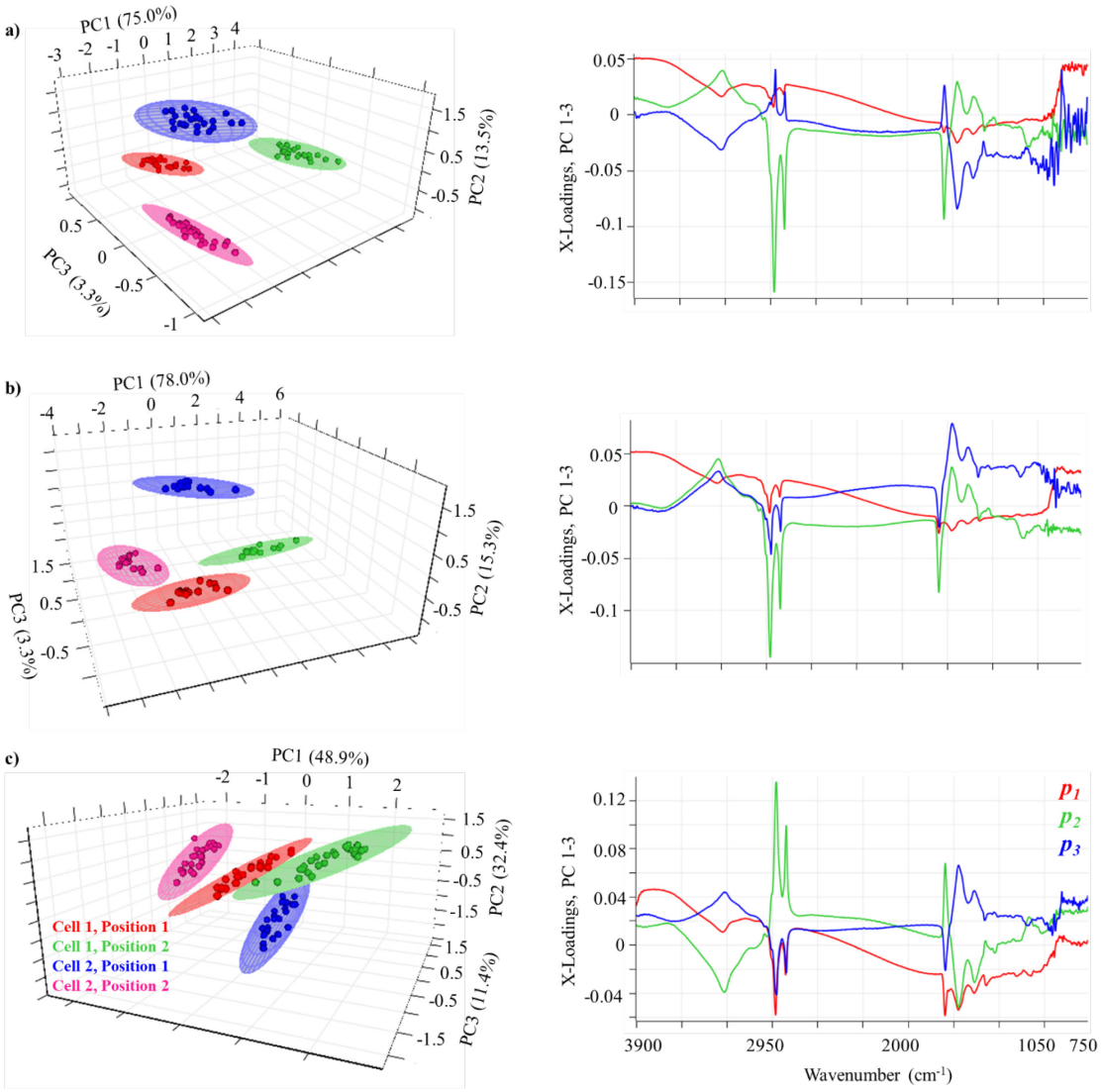

Figure 3.8: PCA scores and loadings plots for spectral data collected from four repeated positions using; a) small; b) medium; and c) large pinholes. Three PC models for each pinhole accounted for >90% of the **X**-variance in each case.

The following observations were made regarding the PCA models for these data.

- As expected, the spectral noise was greatest for the small pinhole and was prominent in the p_3 direction from about 1150 cm^{-1}, (**Figure 3.8**). Noise was less prominent below 1050 cm^{-1} in the data acquired with the medium and large pinholes, (**Figure 3.8b** and **c**).
- Separation of cell positions in the scores plots were less pronounced when comparing data acquired from the small and large pinholes, (**Figure 3.8a** and **c)**. This was expected due to the more localised spectral information obtained from a small spot size in highly heterogeneous 3T3-L1 cells.

- The profile of all three PC loadings were similar for each pinhole and resembled the mean spectra of the raw data set. This indicated that PCA of the raw spectra was dominated by physical density and scattering effects rather than being specific to biochemical changes.[223]

The dispersion in the scores plots was not a systematic effect of coadditions as evidenced in **Figure 3.9**, which showed that within the clusters, the category variable 'scan count' was randomly dispersed. The points representing 16 coadditions (red) showed the greatest variation within the clusters, a result of the low S/N for this number of coadditions. Although the PCA models were discriminatory, they were not informative at the chemical or biological level and thus the spectra required a suitable processing strategy to be applied in order to extract the biochemical information.

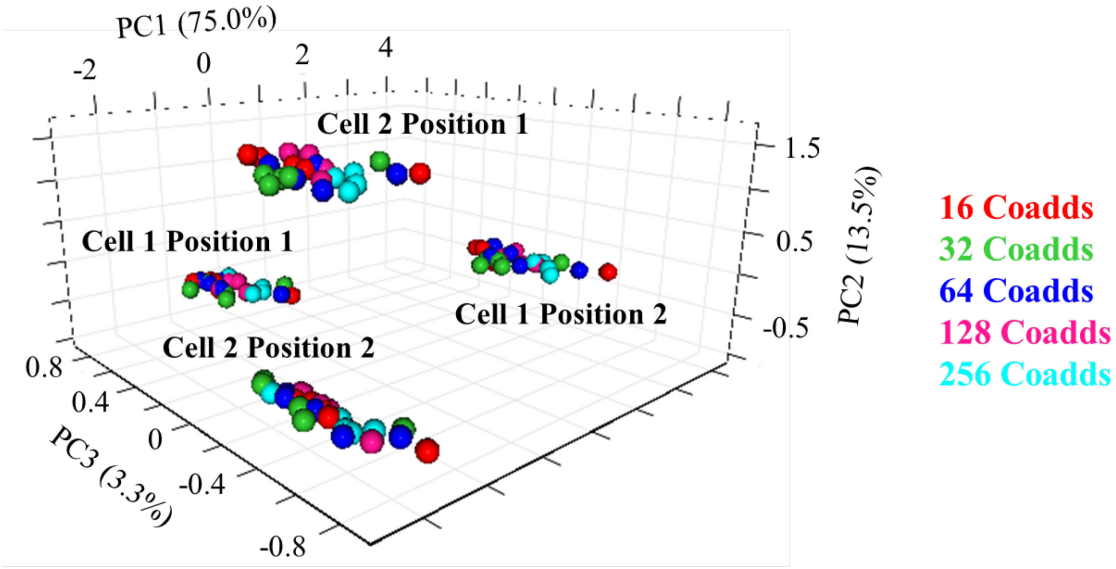

Figure 3.9: t_1 vs. t_2 vs. t_3 scores plot of FTIR spectra collected on four cell positions using a small mechanical pinhole and grouped by number of coadditions. Cell positions marked based on their cluster.

3.4.3 Optimisation of Spectral Processing of SR-FTIR Data

Vibrational spectroscopic data are typically influenced by physical phenomena associated with density, thickness and light scattering from the cell surface (or any other biological medium). Spectra are influenced by two major physical effects:[223,233,273]

- **Additive effects** arise from sample thickness and density characteristics. They usually present as offsets, i.e., the spectra do not overlay directly on top of each other.

- **Multiplicative effects** result from light scatter off the sample surface and can be associated with changes in size, shape and refractive index. These effects are commonly observed in spectra as sloping or curved baselines.

Appropriate spectral processing methods are required prior to multivariate analysis to minimise the impact of these artefacts and to reveal the underlying chemical/biochemical information in the data.[223]

3.4.3.1 Multiplicative Scatter Correction (MSC)

The MSC algorithm[274] is a linear model of physical and chemical affects (Equation 3.2).

$$Z_{app} = \mathbf{1}a + bZ_{ref} + \varepsilon \qquad 3.2$$

Equation 3.2 uses the terminology of Solheim, *et al*.[275] where an apparent spectral vector is defined as Z_{app}, which combines the 'true' spectral profile contaminated with physical effects to be corrected. This approach to spectral normalisation requires a training set of data to generate the reference spectrum, Z_{ref}, followed by linear regression to correct all spectra to the reference spectrum according to the linear model $\mathbf{1}a + bZ_{ref}$, where a is the additive effect and b is the multiplicative effect. By removing the additive and multiplicative components in the raw spectra, the residual ε should be a representation of the 'true' biochemical information with a minimum of extraneous effects. Algorithms exist that extend the MSC model for correction of Mie scatter effects.[275-278] The use of resonant Mie scatter (RMieS)[276] and the Mie extinction extended multiplicative scatter correction (ME-EMSC)[275] resulted in overcorrections in the lipid and protein spectral regions for 3T3-L1 cells and, hence was not pursued any further. For the large amount of spectral data generated by chemical mapping and imaging, alternative procedures were investigated, while future work may enable optimisation of the RMieS and ME-EMSC parameters.

3.4.3.2 Normalisation and Derivatives

Processing methods for SR-FTIR spectra include normalisation,[257] which is vital prior to multivariate analysis and normalisation after derivatisation is recommended to correct for residual pathlength effects not fully minimised by the derivative.[273] Such corrections are equally applicable to non-synchrotron-based methods, whereby derivatives are commonly used for correcting additive effects in FTIR spectra.[223] The algorithm proposed by Savitzky and Golay[234] (including the reported correction made by Steiner, *et al*.[235]) is

one of the first processing steps applied due to its ability to be used as both a smoothing and a derivative filter.[189,223,279]

3.4.3.3 Standard Normal Variate (SNV)

The optimal normalisation method for this data set was the standard normal variate (SNV) algorithm.[236] (sometimes incorrectly referred to as vector normalisation). Unlike MSC (Section 3.4.3.1), which requires a training set, or a target spectrum to normalise spectra, the SNV algorithm is a row-wise normalisation that corrects the spectrum to its own centre of gravity and then standardises each wavenumber to the variability of the spectrum. The SNV algorithm is defined in Equation 3.3.

$$Z_{corr\ i,j} = \frac{Z_{app,j} - \bar{Z}_i}{s_i} \qquad 3.3$$

Where $Z_{corr\ i,j}$ is the SNV corrected spectrum i corrected over j wavenumbers, $Z_{app,j}$ the apparent (uncorrected) spectrum at wavenumber j and $\bar{Z}_i$ is the mean spectrum i calculated over a defined wavenumber region j and represented as a scalar. s_i is the standard deviation of the *y*-scale calculated for spectrum i over the wavenumber region j and represents a single measure of variance of Z_{app}. While SNV is one of the simplest multiplicative scatter correction techniques, Barnes, *et al.*[236] suggested the use of the detrend algorithm after the application of SNV to correct for non-linear baselines. However, this is usually optional and the purpose of SNV was to normalise the derivatised data to account for residual pathlength effects in the spectra.[273]

3.4.3.4 Spectral Analysis: 3000-1000 cm^{-1} Region

The range of conditions investigated (**Table 3.5**) for optimal spectral processing for both large and medium pinholes was over the wavenumber range 3000-1050 cm^{-1} when combined second derivative (13-point smoothing) and SNV was applied to result in PCA models with only two PCs that explain > 90% of the total **X**-variance. The small pinhole region was optimised over the range 3000-1100 cm^{-1} and a two-PC model described 89% of the total **X**-variance.

Since the SNV used information from a specified wavenumber range to calculate the mean spectrum $\bar{Z}_i$ and the standard deviation s_i, the inclusion of noisy spectral regions into the normalisation calculations propagated this noise across the entire corrected spectrum.[280] This is one reason why the wavenumber regions listed in **Table 3.5** for the derivative-SNV processing methods were smaller than the corresponding derivative-only

data, as the noise transmitted between 1050-1000 cm^{-1} had detrimental effects on the separations observed in PCA.

Table 3.5: Processing methods and parameters applied to spectral data prior to application of multivariate data analysis methods*.

Pinhole	Processing Method**	Smoothing Window (pt)	Wavenumber region (cm^{-1}) ***	Explained Variance (%)	
				PC1	PC2
Small	Savitzky-Golay Second Derivative	9	3000-1050	68.6	12.2
		11	3000-1030	69.2	9.8
		13	3000-1030	77.1	8.9
	Savitzky-Golay Second Derivative + SNV	9	3000-1100	61.8	12.0
		13	**3000-1100**	**78.0**	**9.7**
Medium	Savitzky-Golay Second Derivative	9	3000-1000	66.5	11.1
		11	3000-1000	73.0	9.5
		13	3000-1000	82.1	8.7
	Savitzky-Golay Second Derivative + SNV	9	3000-1050	69.8	12.3
		13	**3000-1050**	**83.6**	**9.3**
Large	Savitzky-Golay Second Derivative	9	3000-1000	72.9	15.4
		11	3000-1000	80.7	13.1
		13	3000-1000	84.4	11.2
	Savitzky-Golay Second Derivative + SNV	9	3000-1050	78.3	14.3
		13	**3000-1050**	**87.4**	**9.7**

*The values listed are for 128 and 256 coadditions only (medium pinhole 128 and 512 coadditions). The noise in the region 1100-750 cm^{-1} for 16-64 scans was too high and resulted in lower cut-off values. When normalisation was applied to noisy regions, it had a detrimental effect on multivariate analysis results.

**The Savitzky-Golay derivatives used a 2^{nd} order polynomial fit to the data.

***The wavenumber region was determined post PCA based on removal of highly noisy loadings from the analyses, or by setting the wavenumber range of the SNV processing to exclude noisy regions.

The PCA overview of the 13-point, second derivatised, SNV data over the 3000-1050 cm^{-1} region is shown in **Figure 3.10** for spectra acquired using a large pinhole.

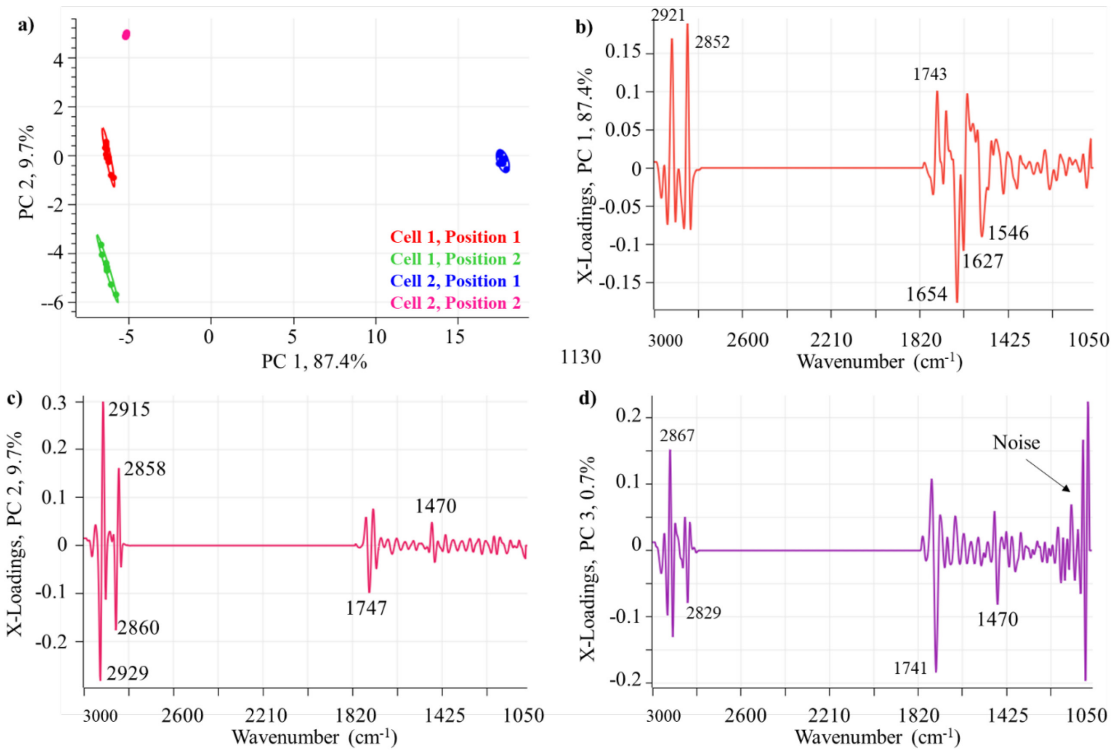

Figure 3.10: PCA of two 3T3-L1 cells measured at four positions using a large pinhole, processed using the Savitzky-Golay second derivative (13-point smooth) then SNV over the wavenumber region 3000-1050 cm^{-1}; a) t_1 vs. t_2 scores; b) p_1 loadings; c) p_2 loadings; and d) p_3 loadings.

The t_1 vs. t_2 scores plot (**Figure 3.10a**) showed that each cell position was well separated. The t_1 direction described why Cell 2, Position 1 was different from the others with corresponding p_1 loadings showing an inverse relationship between the lipid and fatty acid bands at 2921, 2852 and 1743 cm^{-1} and the protein bands at 1654, 1627 and 1546 cm^{-1} (**Table 1.1**). Cell 2, Position 1 was chosen for its high protein and low lipid character (**Table 3.2**), as confirmed by the p_1 loadings (**Figure 3.10b**). The t_2 direction described lipids as evidenced by the loadings at 2929, 2915, 2858, 2846, 1747 and 1470 cm^{-1} (**Figure 3.10c**). PC3 (**Figure 3.10d**) described <1% of the explained **X**-variance and the p_3 direction was dominated by large loadings between 1100-1050 cm^{-1}, which described a combination of diffraction effects, CaF_2 related aberrations and refractive index induced changes in the 3T3-L1 cells.[214,262]

The broad N-H band (3450-3050 cm^{-1}) in the raw spectra was very weak after derivatisation (**Figure 3.11b**) and was not used in subsequent analyses due to its low signal and similar biochemical information can be found within the range 1690-1500 cm^{-1}.[214]

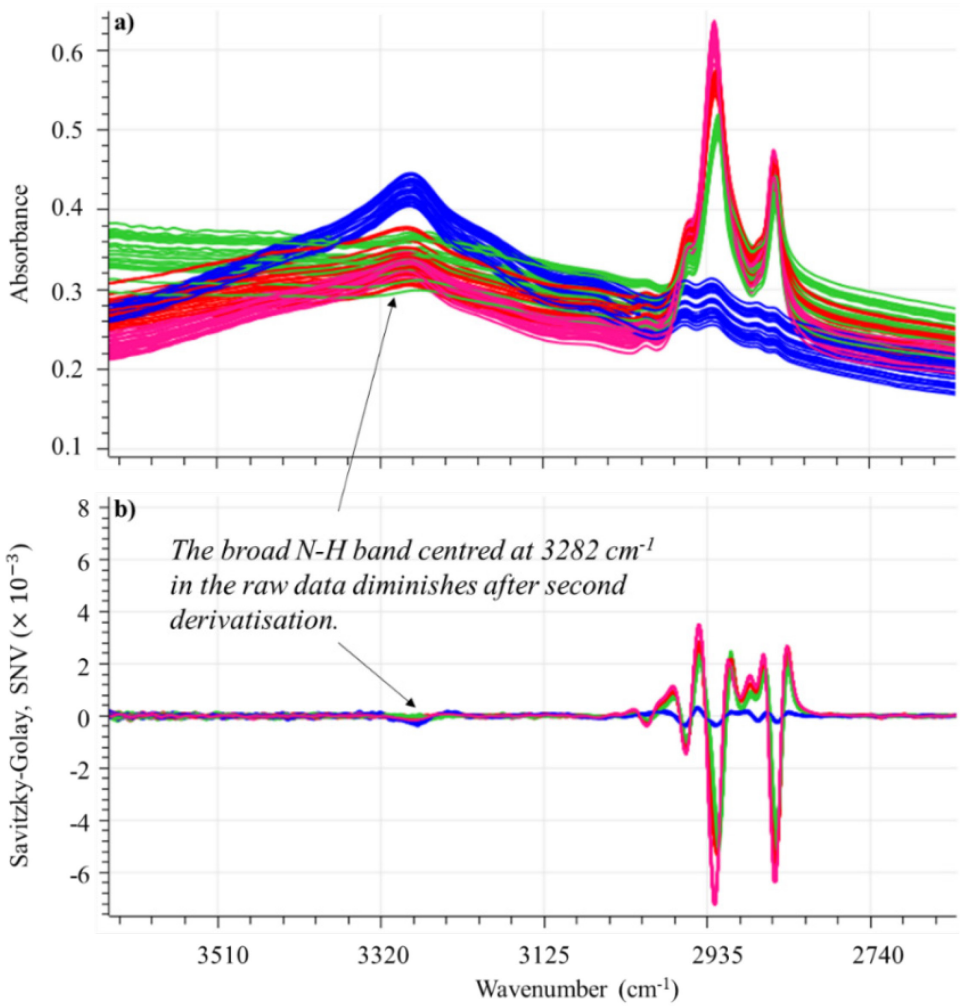

Figure 3.11: a) raw spectra; and b) processed spectra of 3T3-L1 adipocytes over the wavenumber region 3650-2640 cm^{-1}.

The 2800-1800 cm^{-1} region is where atmospheric CO_2 is detected and the intensity of bands around 2360 cm^{-1} were an indicator of the effectiveness of the nitrogen purging of the sampling area and optics. As this spectral region did not include any relevant biochemical information, it was discarded during multivariate analysis.

3.4.3.5 Spectral Analysis: 1800-1000 cm^{-1} Region

The assessed data in **Table 3.5** included the ν (C-H) modes between 3000-2800 cm^{-1}, which provided information on lipid and fatty acids and lipoproteins in cell membranes.[195,205] PCA was performed on spectra acquired on the four cell positions to determine whether similar separation could be obtained using the limited 1800-950 cm^{-1} region for large and small pinholes. **Table 3.6** lists the findings from the application of PCA to SNV normalised, second derivative (13-point smooth) data over various ranges between 1800-950 cm^{-1}.

Table 3.6: Effect of SNV normalised second derivative spectra on PCA explained variance when applied to different wavenumber segments in the 1800-950 cm^{-1} region. Data are for small and large pinholes acquired using 128 and 256 coadditions only.

Pinhole Size	Segment (cm^{-1})	% Explained Variance Using PCA					
		All Coadditions			128 and 256 Coadditions Only		
		PC1	PC2	Total	PC1	PC2	Total
Small	**1800-1200**	**62.8**	**3.9**	**66.7**	**85.2**	**3.8**	**89.0**
	1800-1150	55.3	4.8	60.1	81.1	4	85.4
	1800-1100	46.6	5.8	52.4	72.8	5.8	78.6
	1800-1050	33.3	11.8	45.1	58.5	10.8	69.3
	1800-1000	19.4	16.5	35.9	33.6	16.2	49.8
	1800-950	20.8	19.4	40.2	24.7	18.0	42.7
Large	**1800-1200**	**90.2**	**4.7**	**94.9**	**93.5**	**4.7**	**98.2**
	1800-1150	88.1	5.0	93.1	92.8	5.0	97.8
	1800-1100	85.6	4.9	90.5	92.0	5.0	97.0
	1800-1050	79.5	5.0	84.5	89.8	5.0	94.8
	1800-1000	54.8	12.9	67.7	78.8	6.2	85.0
	1800-950	30.0	20.2	50.2	43.4	20.2	66.6

Examination of **Table 3.6** revealed that the largest percentage of explained variance using PCA was achieved when data analysis was limited to the range 1800-1200 cm^{-1} for the small pinhole. As spatial resolution is improved by $\sim\lambda/2$,[269] the small pinhole should produce high quality spectra up to 1000 cm^{-1} (10 μm). However, investigation of **Figure 3.7a** showed that the spectra were noisy in this region. Therefore, the decreasing detector sensitivity, the reduced transmission of IR radiation through CaF_2 beyond 1000 cm^{-1} and the propagation of noise by normalisation were the combined factors most likely attributing to information loss when using the small pinhole.

To illustrate the effect of including data below 1000 cm^{-1}, a PCA model over 1800-750 cm^{-1}, processed by second derivative (13-point smooth) and SNV over 1800-750 cm^{-1} with the large pinhole (**Figure 3.12**) showed a large anomaly in the p_1 loading at 985 cm^{-1}. This was most likely introduced by the normalisation method, or coherent aberrations associated with CaF_2 substrates, where the use of substrates > 1 mm in thickness can result in < 10% transmission at 1000 cm^{-1}.[215] This effect was reduced through the use of 0.5 mm thick substrates,[215] which were used for the spectral data collected in subsequent chapters.

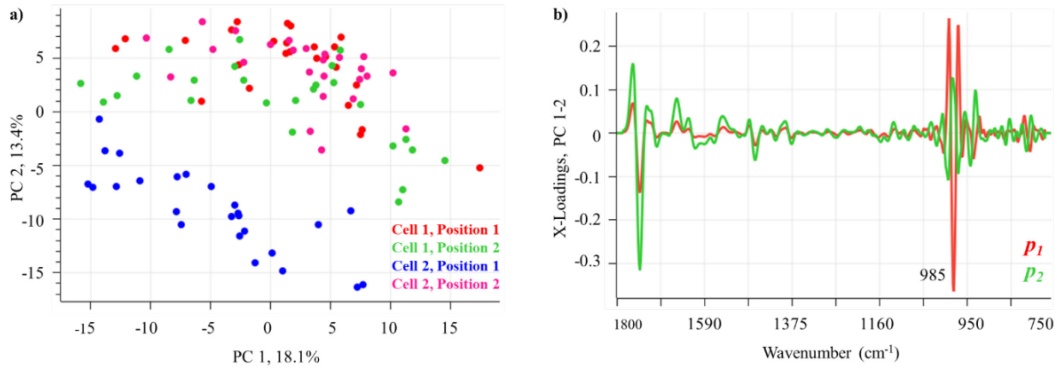

Figure 3.12: a) t_1 vs. t_2 scores; and b) p_1, p_2 loadings of a PCA model of 3T3-L1 spectra collected at four positions using a large pinhole over the wavenumber region 1800-750 cm^{-1}. Spectra were collected at 16, 32, 64, 128 and 256 coadditions and processed using second derivative (13-point smooth) and SNV over the defined wavenumber region.

3.4.3.6 Reduced Wavenumber Region Comparison of Small and Large Pinholes

PCA models were developed over the regions 1800-1050, 1800-1100 and 1800-1150 cm^{-1} acquired using 128 and 256 coadditions for the large pinhole only (**Figure 3.13**). A comparison of the first two PCs for each model showed almost identical separation of the cell positions compared to the results obtained from the broader wavenumber range (**Figure 3.10**). These data confirm the observation made by Fabian, *et al.*[214] that the spectral region between 1800-1000 cm^{-1} contained the majority of biochemical information.

As such, the data processing adopted for the spectra collected from 3T3-L1 adipocytes, using large apertures (pinholes) was application of the Savitzky-Golay second derivatives (13-point smoothing) and second order polynomial fit, then SNV, which was applied to either the combined 3050-2800 and 1800-1050 cm^{-1} regions, or to the 1800-1050 cm^{-1} region only. The use of a nine-point smoothing window was also considered and it may be possible that the vector normalisation (2-Norm) method could be used instead of SNV as the normalisation method.

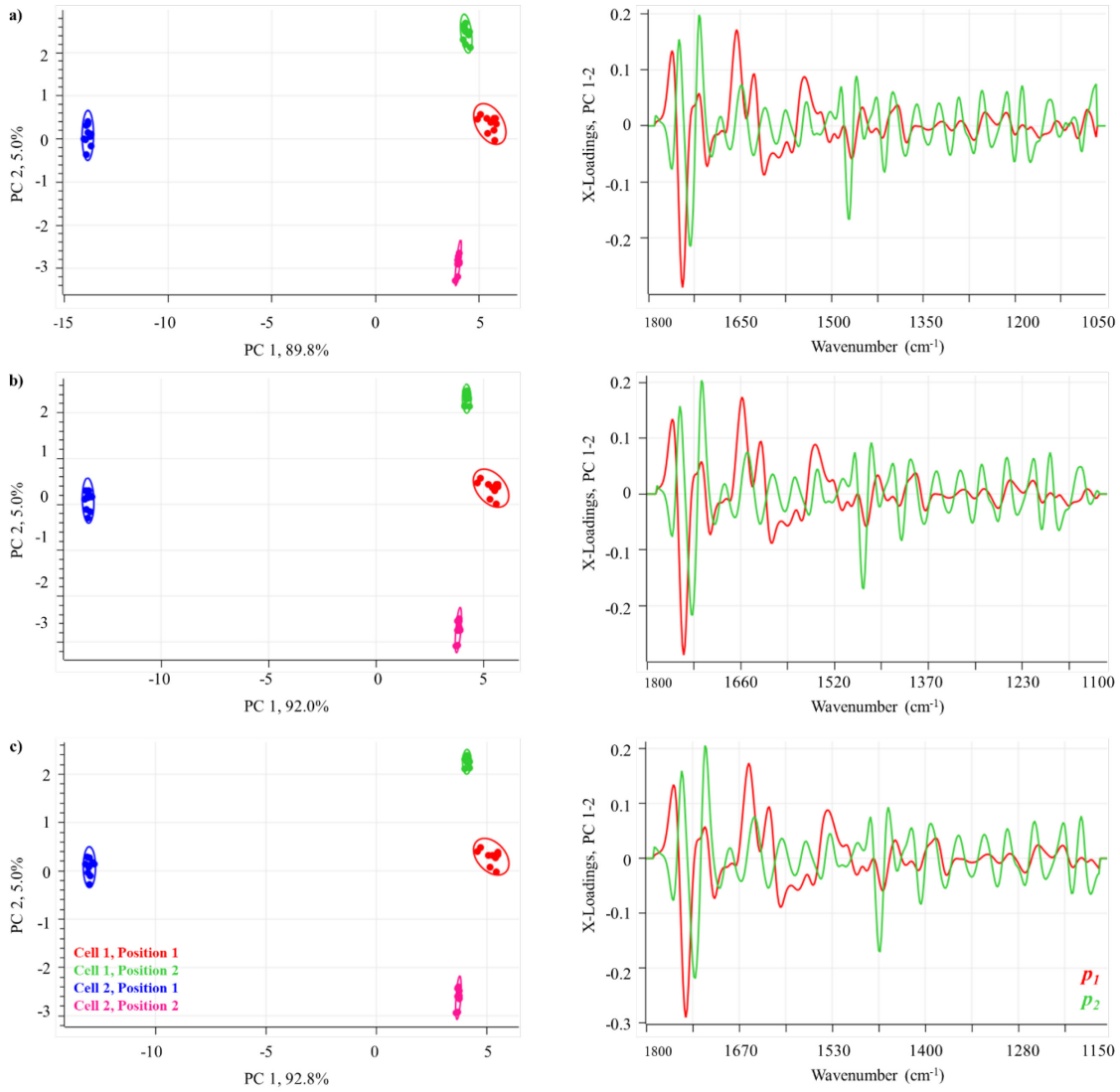

Figure 3.13: Comparative PCA models for data assessed over; a) 1800-1050 cm^{-1}; b) 1800-1100 cm^{-1}; and c) 1800-1150 cm^{-1}. Data were acquired using a large pinhole and processed using a second derivative (13-point smooth) then SNV over the selected wavenumber regions.

PCA (**Figure 3.14**) showed that the nine-point and 13-point second derivative smoothing and SNV for the small pinhole separated the spectral data into their respective groups, however, this was at the expense of a loss of information over the 1200-1050 cm^{-1} region, where phosphodiester bands of DNA, proteins and lipids occur.[172] Second derivatives with nine-point smoothing did not correct for the data noise as well as the 13-point smoothing. This was evidenced in the lower explained variance observed in the PCA model (**Figure 3.14b)**. Therefore, for 3T3-L1 adipocytes, 13-point smoothing was used when applying second derivatives.

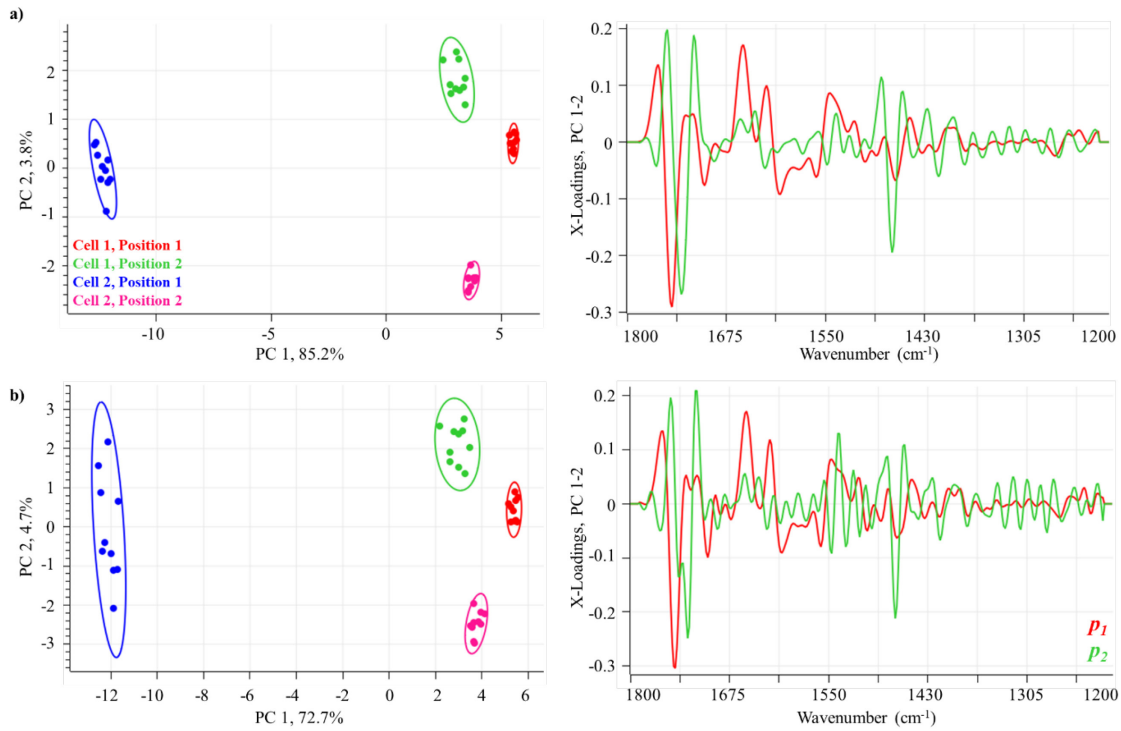

Figure 3.14: Comparative PCA of a) 13-point second derivative, SNV; and b) nine-point second derivative, SNV preprocessed spectra acquired using a small pinhole over the wavenumber region 1800-1200 cm^{-1}.

3.4.4 Justification of Coadditions Used to Acquire Spectral Data

Figure 3.15 presents the Savitzky-Golay second-derivative spectra (13-point smooth, second-order polynomial) over the 1800-750 cm^{-1} region acquired using small and large pinholes from Cell 2, Position 1, for all coadditions. These data showed the marked impact of noise amplification below 1000 cm^{-1} by the second-derivative processing. **Figure 3.15c** showed the full extent of noise coverage by the small pinhole up to 1200 cm^{-1}, as verified by the PCA results (**Table 3.6**).

To objectively validate the optimal number of coadditions for spectral data acquisition, the fixed block standard deviation (FBSD), was used based on an adapted calculation[281] as a measure of spectral variability (SV). Spectral variability was calculated using Equations 3.4 and 3.5:

$$SV_{ij}^2 = \frac{1}{M-1}\sum_{i=1}^{M}(x_{i,j} - \bar{x}_{i,j})^2 \qquad 3.4$$

where SV_{ij}^2 is the spectral variation for a block of M spectra at each of j wavenumbers, $x_{i,j}$ is the i^{th} spectrum in the block of M spectra and $\bar{x}_{i,j}$ is the average spectrum of the block.

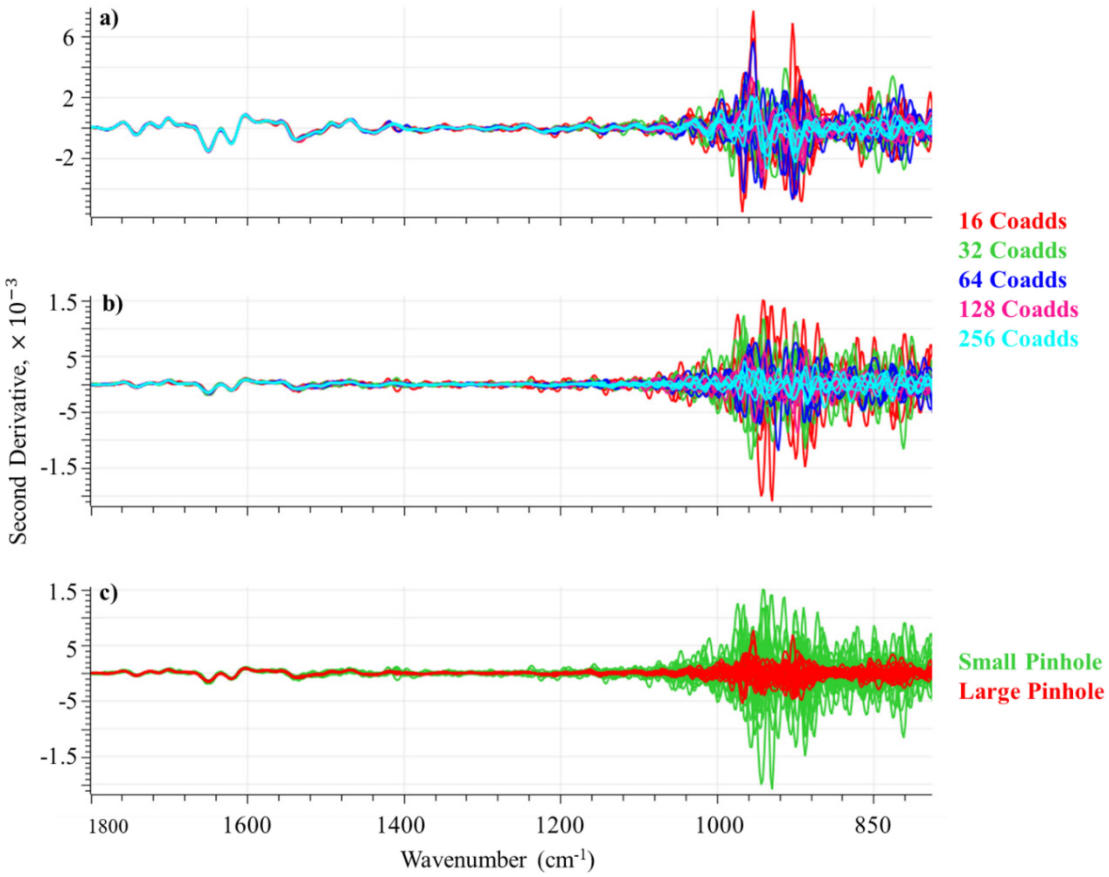

Figure 3.15: Comparison of spectra acquired using a) large pinhole; b) small pinhole; and c) combined data with 16, 32, 64, 128 and 256 coadditions (13-point second derivative spectra) over the wavenumber region 1800-750 cm^{-1} for Cell 2, Position 1.

The sum of the variances at each wavenumber, divided by the number of wavenumbers provides a measure of the fixed block standard deviation (FBSD) defined in Equation 3.5:

$$FBSD_i = \frac{1}{p}\sum_{j=1}^{p} SV_{i,j} \qquad 3.5$$

where $FBSD_i$ is the fixed block standard deviation for the selected block of spectra calculated over p wavenumbers defined in the block. A block in this case represented five replicate spectra acquired for each number of coadditions investigated. A representative summary of the optimised conditions for spectral data acquisition for the large, medium and small pinholes (**Figure 3.16**) used experimental conditions defined in **Table 3.3**.

It was concluded that 128 coadditions represented a balance between acquisition time reduction and spectral quality, while the use of 256 coadditions was optimal for the small pinhole. In a published protocol[257] 256 coadditions were recommended for synchrotron-based IR spectral data acquisition in transmission mode.

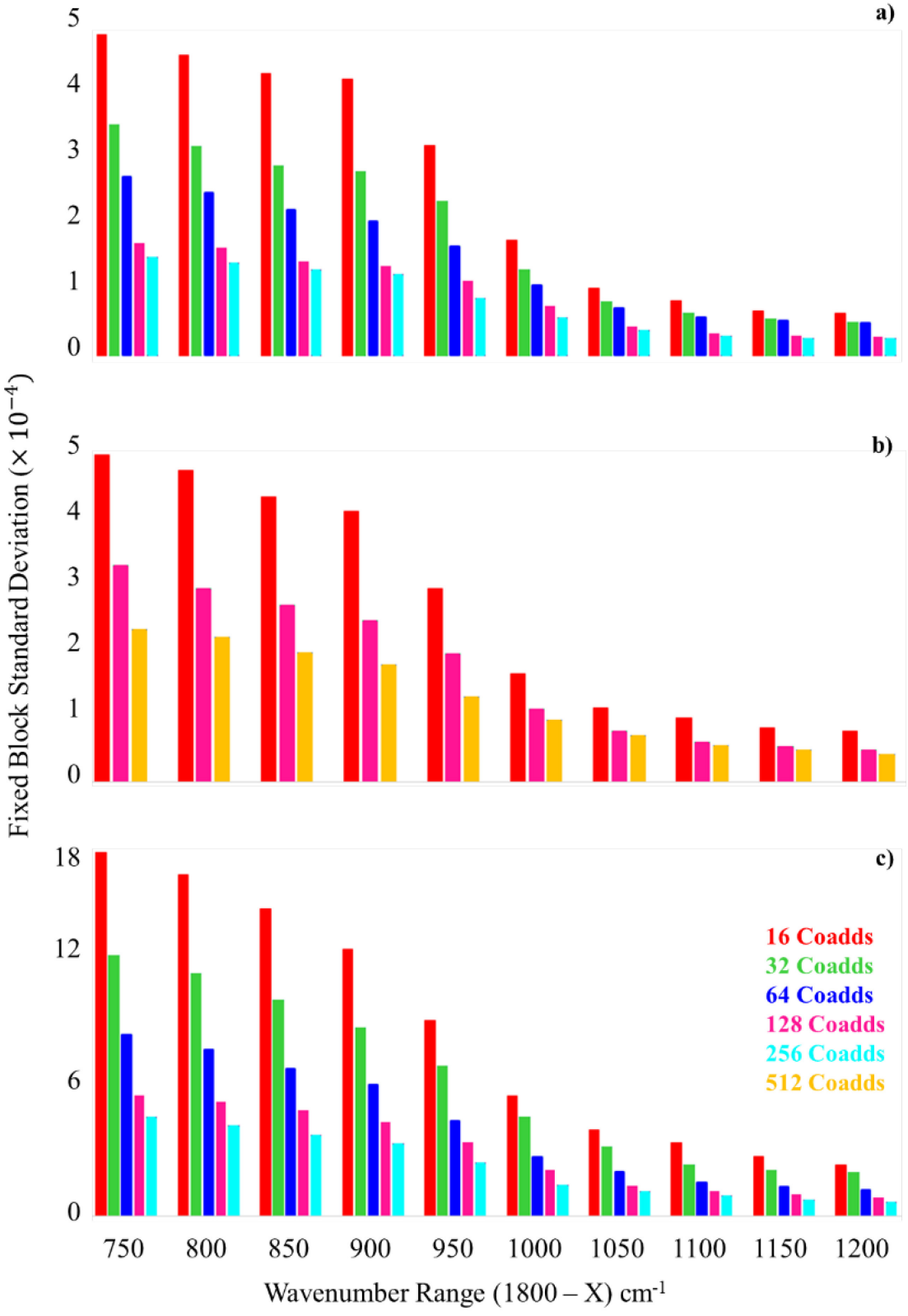

Figure 3.16: Optimisation spectral coaddition for; a) large; b) medium; and c) small pinholes calculated over specified wavenumber regions. The *x*-axis (1800-X) represented the wavenumber region from 1800 cm^{-1} to the value listed on the axis, e.g., the first point on the *x*-axis represented the wavenumber region 1800-750 cm^{-1}.

3.5 Infrared Chemical Mapping at the Australian Synchrotron

Section 3.4 evaluated optimal data acquisition conditions for point spectra that were translated to the acquisition of chemical maps. Large and small pinholes were used to probe the effects of spectral coadditions and processing on chemical maps acquired at different spatial resolution settings (**Table 3.7**).

Table 3.7: Experimental parameters used to evaluate mechanical pinhole, spatial resolution (step size and oversampling) and spectral coadditions when mapping single cells with SR-FTIR spectroscopy.

Pinhole	Step Size (μm)	Spectra Coadditions
Large	3.5	16
		128
	7	16
		128
Small	2	16
	4	16
		256

A 36× objective resulted in a beam spot with a diameter of 5.56 μm for the small pinhole and a 16.67 μm spot for the large pinhole (**Table 3.4**). The beam spot size of the Australian synchrotron light source is 8 μm, therefore, it is not restricted by the large pinhole (**Figure 3.17a**) as shown by the large pinhole sampling area (large open circles) and the beam (filled circles).

The intensity distribution of the incident beam (**Figure 1.17**) is such that the majority of the intensity lies within a 6 μm diameter and that rapidly disperses. Using a 3.5 μm step size produced an oversampling factor of 8 μm/3.5 μm = 2.3. Even with oversampling, the large pinhole leads to lower spatial resolution than the small pinhole in the *x*-*y*-direction.[282] When the step size was doubled to 7 μm, oversampling was minimised (**Figure 3.17b)**, however, the spatial resolution was not adequate enough to produce fine detail chemical maps.

Maps produced by the small pinhole benefit from the synchrotron radiation focussed intensity. A 4 μm step size resulted in minimal overlap in the *x*-*y*-direction and a map of the entire cell was acquired using an 8 × 5 grid. When the step size was reduced to 2 μm, a higher degree of oversampling was observed and the entire cell was mapped in a 13 × 9 grid. Stelzer[263] reviewed the impact of contrast, resolution, pixilation, dynamic range and signal-to-noise ratios in confocal and wide-field fluorescence microscopes and

postulates that oversampling relative to the beam size leads to improvements in spatial resolution up to an oversampling level of four times. The resolution improvement also results in an increase in noise due to a reduction of the number of photons detected when the sampled area and volume was reduced,[263] because pinholes and apertures reduce the amount of incident radiation. When the point-spread function was reduced by a factor of two, the observation period was increased to four to maintain signal-to-noise ratio,[263] (see **Figure 3.16a** and **c**, differences in *y*-scale (variance)).

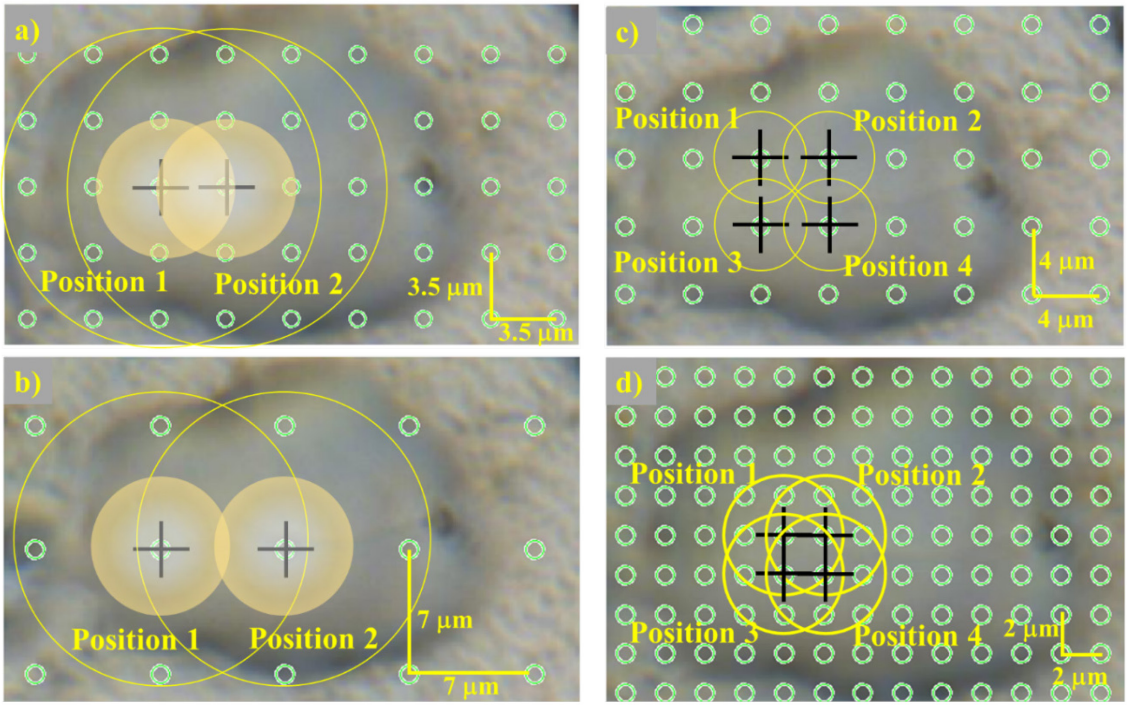

Figure 3.17: Spatial resolution and oversampling in SR-FTIR microspectroscopy using mechanical pinholes; a) large pinhole using a 3.5 µm step size; b) large pinhole using a 7 µm step size; c) small pinhole using a 4 µm step size; and d) small pinhole using a 2 µm step size.

3.5.1 Large Pinhole Assessment

The large pinhole map acquired using 16 coadditions and a 3.5 µm step size (second derivative processing) is shown in **Figure 3.18**, integrated in the lipid region (1743 cm^{-1}) and amide I region (1654 cm^{-1}). Also presented with the integrated false colour and pixel maps in **Figure 3.18** are blended images showing the optical micrograph of the cell with the integrated pixels overlaid. In the pixel map, the resolution achieved in terms of cellular structure was very poor, but rendering of the contour plots showed that reasonable detail was obtained from the low-resolution pixel imaging, even though it was artificial. The blended image showed that the chemical information in the integrated image aligned with

the composition of the cell and also confirmed the repeatability of the mechanical stage movement (variance study of Section 3.4).

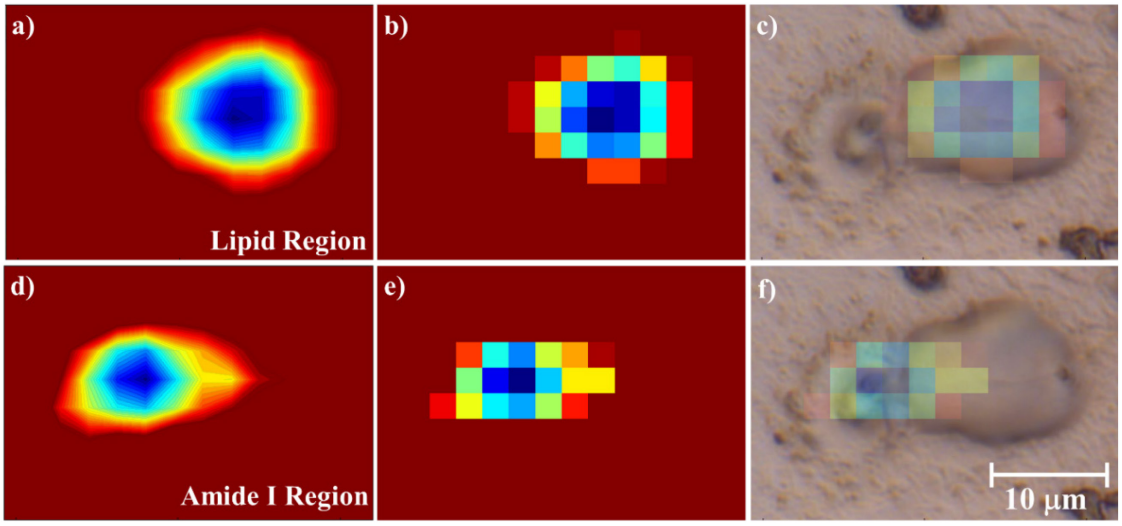

Figure 3.18: Integrated false colour maps (3.5 µm step size) and blended images of a 3T3-L1 adipocyte, acquired using a large pinhole at a resolution of 4 cm^{-1} and 16 coadditions in a 14×10-pixel grid; a) contour plot integrated at 1743 cm^{-1}; b) pixel map integrated at 1743 cm^{-1}; c) blended map at 1743 cm^{-1}; d) contour plot 1654 cm^{-1}; e) pixel map 1654 cm^{-1}; and c) pixel map of 1654 cm^{-1} region blended with the optical micrograph.

PCA was applied to the large pinhole spectra (acquired at 16- and 128 coadditions) and the scores and loadings are shown in **Figure 3.19**. Surprisingly, the t_1 scores maps (false colour maps) were similar for 16 and 128 coadditions and their loadings revealed inverse relationships between lipid (2920, 2850 and 1743 cm^{-1}) and protein content (1656 and 1625 cm^{-1}) in the cell. In **Figure 3.19b** and **d**, the t_2 scores maps did not show any detail for 16 coadditions and very little definition for 128 coadditions. The p_1 plot in **Figure 3.19a** for 16 coadditions highlighted increased noise levels in the 1200-1050 cm^{-1} region due to the low signal-to-noise (SN) ratio associated with a low number of coadditions, which was absent in the corresponding p_1 loadings plot for 128 coadditions (**Figure 3.19c**) The p_2 loadings for 16 coadditions was not interpretable due to the large noise loadings in the region 1150-1050 cm^{-1} as a result of the low number of coadditions and chromatic aberration effects induced by CaF_2.

Although the p_2 loadings improved with respect to noise in the 1150-1050 cm^{-1} region, there were large fringing effects and the ROI was not associated with the cell (**Figure 3.19d**). This either indicated that the acquisition parameters were not fully optimised, or these anomalies are sampling induced and need to be considered as part of a multivariate analysis strategy. Further work is required to better understand these effects.

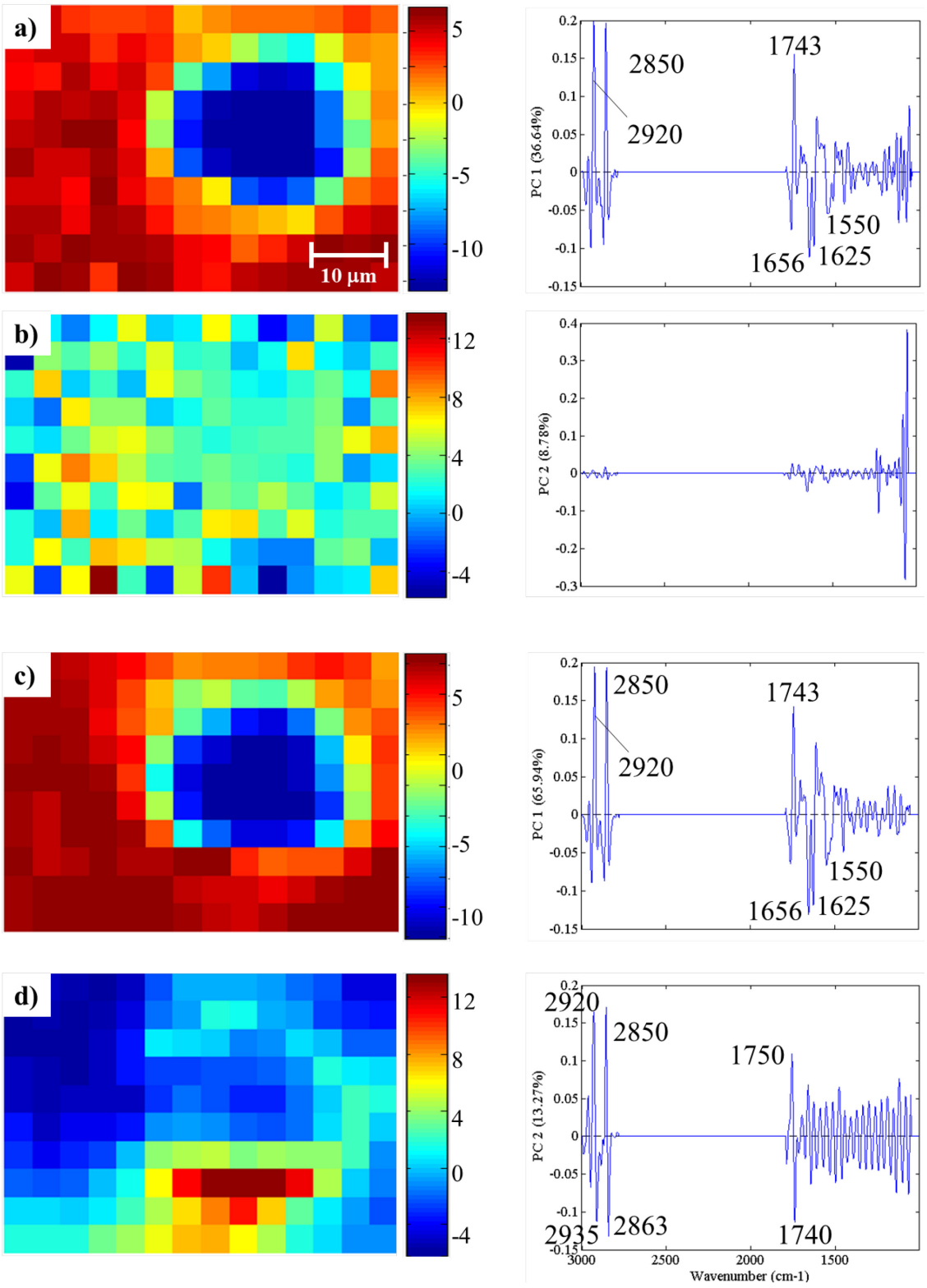

Figure 3.19: Scores images and associated loadings plots for a single 3T3-L1 cell acquired using a large pinhole and a 3.5 µm step size for the first two PCs only; a) image collected using 16 coadditions, PC1; b) 16 coadditions, PC2; c) 128 coadditions, PC1; and d) 128 coadditions, PC2. Spectra were collected in the wavenumber region 3000-1000 cm^{-1}. Map size, 14×10.

3.5.1.1 Effect of Step Size

To investigate the effect of step size on spatial resolution, data was acquired with a step size of 7 μm to assess the quality of information when compared to a 3.5 μm step size. The corresponding scores maps and loadings for the first two PCs (**Figure 3.20**) for the large pinhole at 16 and 128 coadditions showed a distinct lack of detail in the scores maps with respect to the cell morphology. With reference to **Figure 3.17b**, it was not surprising that these sampling parameters did not lead to the spatial resolution required for morphological and chemical understanding of the cell. A comparison of the p_1 loadings in **Figure 3.19** and **Figure 3.20** showed that the same chemical information was being modelled in the maps, only the increased step size resulted in a loss of spatial information.

The t_2 scores maps (**Figure 3.20**) for both conditions did not reveal any distinct information about the cells. A large anomaly at 1230 cm^{-1} was observed in the p_2 loadings for the 16 coaddition measurement, which was attributed to a combination of low SN ratio, the enhancement of an aberration effect in CaF_2 and the normalisation procedure propagating noise across the spectrum. This was consistent with the data in Section 3.4, where 16 coadditions resulted in the need to truncate spectra to a smaller wavenumber range. The p_2 direction for the 128 coaddition measurements showed enhanced chemical information in the 1800-1050 cm^{-1} region; however, spectral fringing was reduced in comparison to the data from the 3.5 μm step size in the corresponding p_2 loadings (**Figure 3.19**). Overall, the use of the large pinhole and step size combination does not achieve the required correlations between biochemical information and morphology.

3.5.1.2 Effect of Condenser Focus

Carr,[270] reported that chromatic aberrations can lead to focus shifts comparable to or larger than the region under investigation and result in reduction of spatial resolution, signal throughput, or both. Recent work at the Australian Synchrotron has demonstrated that adjustment of the condenser focus can reduce the effects of chromatic aberrations and energy throughput at lower wavenumbers.[283]

The energy profiles obtained from the OPUS software package when the condenser was aligned and offset from optimal focus (**Figure 3.21a** and **b**, respectively) showed that over the wavenumber region 3000-2500 cm^{-1}, the aligned condenser signal was maximised (**Figure 3.21a**) and below 1500 cm^{-1} the signal rapidly decreased to zero. When the condenser focus was offset from the optimised position in the *z*-direction, the

energy throughput in the region 1800-1000 cm^{-1} was maximised, with a corresponding decrease over the 3000-2500 cm^{-1} region (**Figure 3.21b**).

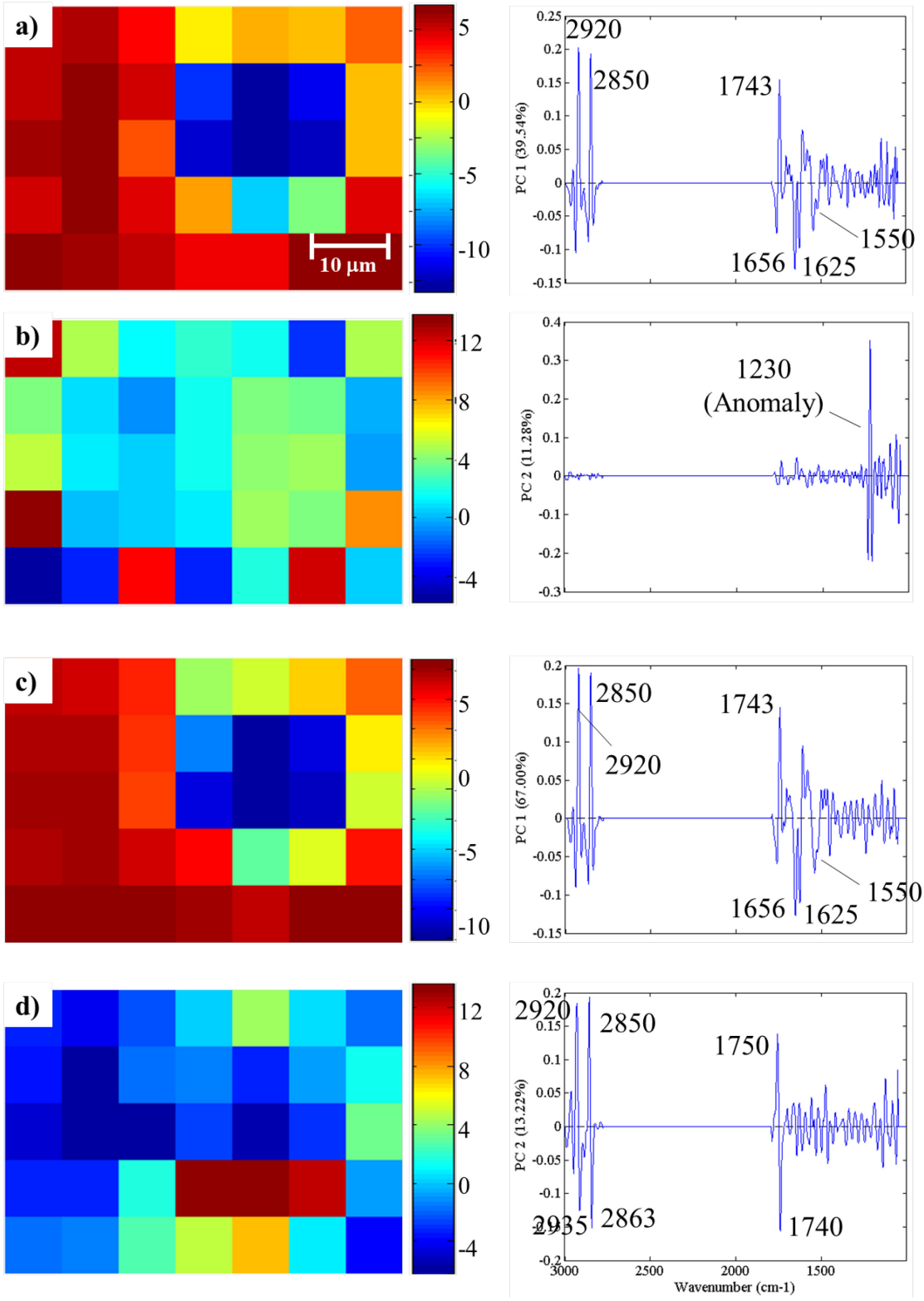

Figure 3.20: Scores images and associated loadings plots for a single 3T3-L1 cell acquired using a large pinhole and a 7 µm step size for the first two PCs only; a) image collected using 16 coadditions, PC1; b) 16 coadditions, PC2; c) 128 coadditions, PC1; and d) 128 coadditions, PC2. Spectra were acquired over the wavenumber range 3000-1000 cm^{-1}. Map size, 7×5.

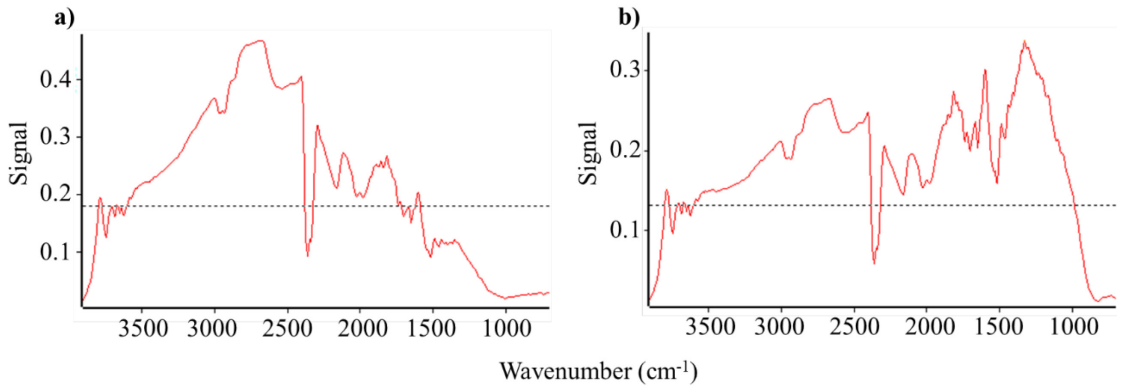

Figure 3.21: Energy throughput of; a) aligned; and b) offset condenser focus of a 3T3-L1 adipocyte.

A chemical map was collected over the wavenumber region 3895-750 cm^{-1} using the condenser alignment conditions shown in **Figure 3.21b** with a large pinhole inserted. Selected spectra from the lipid droplet region (**Figure 3.17**) were extracted and compared to spectra collected when the condenser was aligned (**Figure 3.22**).

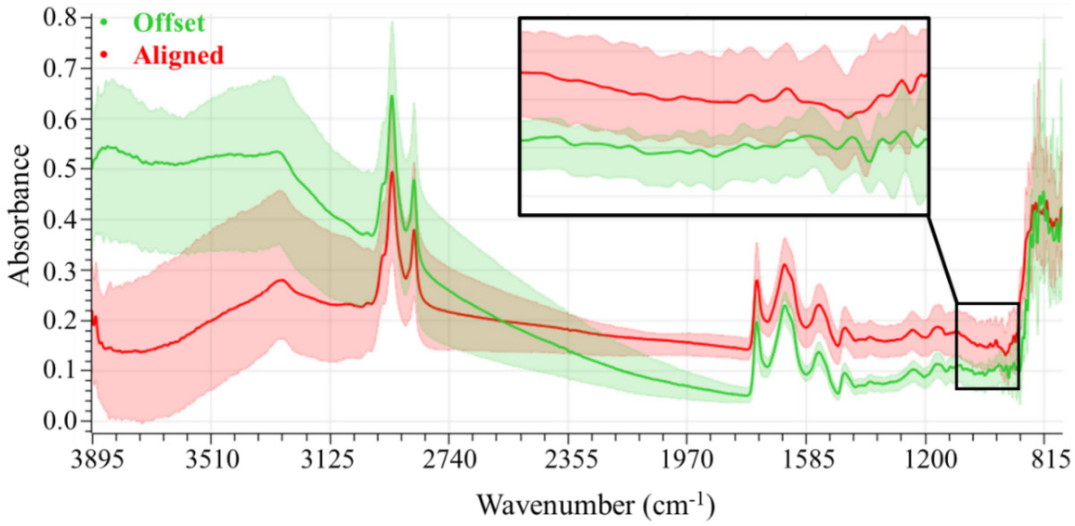

Figure 3.22: Comparsion of FTIR spectra collected when the condensor was aligned and offset according to the settings shown in **Figure 3.21**. The inset shows the region between 1100-900 cm^{-1}.

Higher absorbances between 3895-2800 cm^{-1} for the offset (green) spectra were consistent with the lower energy intensity in this region (**Figure 3.21b**), however, the inset in **Figure 3.22** between 1100-900 cm^{-1} did not show any visual improvement of spectral information as a result of the offset. Due to the limited time available for this experiment, the aligned condenser position was used for chemical map acquisition, however, future work will be performed to assess the condenser positioning to determine whether enhanced data quality over the range of 1000-900 cm^{-1} can be achieved and what effect it has on other spectral regions.

3.5.2 Small Pinhole Assessment

A map was acquired using the small pinhole (**Figure 3.23**) and resulted in only a slight improvement in spatial resolution compared to the results of **Figure 3.18**, however, these conditions did not enhance the visualisation of cell morphology and was most likely due to the synchrotron beam focus being smaller (8 μm) than the large pinhole but only somewhat larger than the small pinhole (5.56 μm).[284]

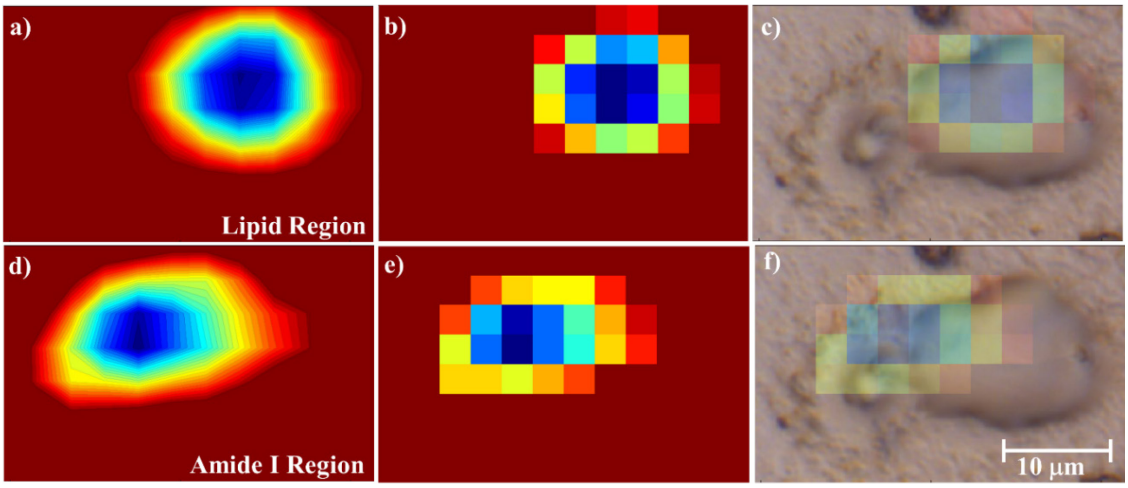

Figure 3.23: Integrated false colour maps and blended images (4 μm step size) of a 3T3-L1 adipocyte, acquired using a small pinhole at a resolution of 4 cm^{-1} and 256 coadditions in a 12 × 8 grid. See **Figure 3.18** for a description of this figure.

Scores maps and loadings for the first two PCs (**Figure 3.24**) were assessed for the same cell measured using a small pinhole, with a 4 μm step size at 16 and 256 coadditions. The map collected using 16 coadditions showed higher noise in the 1200-1050 cm^{-1} regions and the t_1 scores map did not exhibit as strong a spatial definition of biochemical information as observed for 256 coadditions. As with the large pinhole maps, the ν (C-H) lipid region between 2950-2800 cm^{-1} and the C=O lipid band ~1743 cm^{-1} were highly weighted in the p_1 direction. The intensity of the mainly noise loadings around 1000 cm^{-1} was of similar magnitude to the fatty acid and lipid bands (2950-2800 cm^{-1}), which verified that the noise in this region was inflated with respect to the usual band intensity observed in raw and processed data.

When the number of coadditions was increased to 256, the biochemical information in the t_1 scores map was better resolved spatially, compared to the 16 coaddition map and the noise in the loadings between 1200-1050 cm^{-1} was greatly reduced. The p_1 direction for the 256 coaddition map showed an inverse relationship between fatty acids/lipids and proteins. These loadings were much more correlated with biochemical information and

less noisy compared to those for the 16 coaddition map. The p_2 loadings showed a similar fringing pattern as observed in previous analyses that was enhanced in the 1200-1100 cm^{-1} region and was mainly an extracellular artefact, with only a small overlap with the cell morphology.

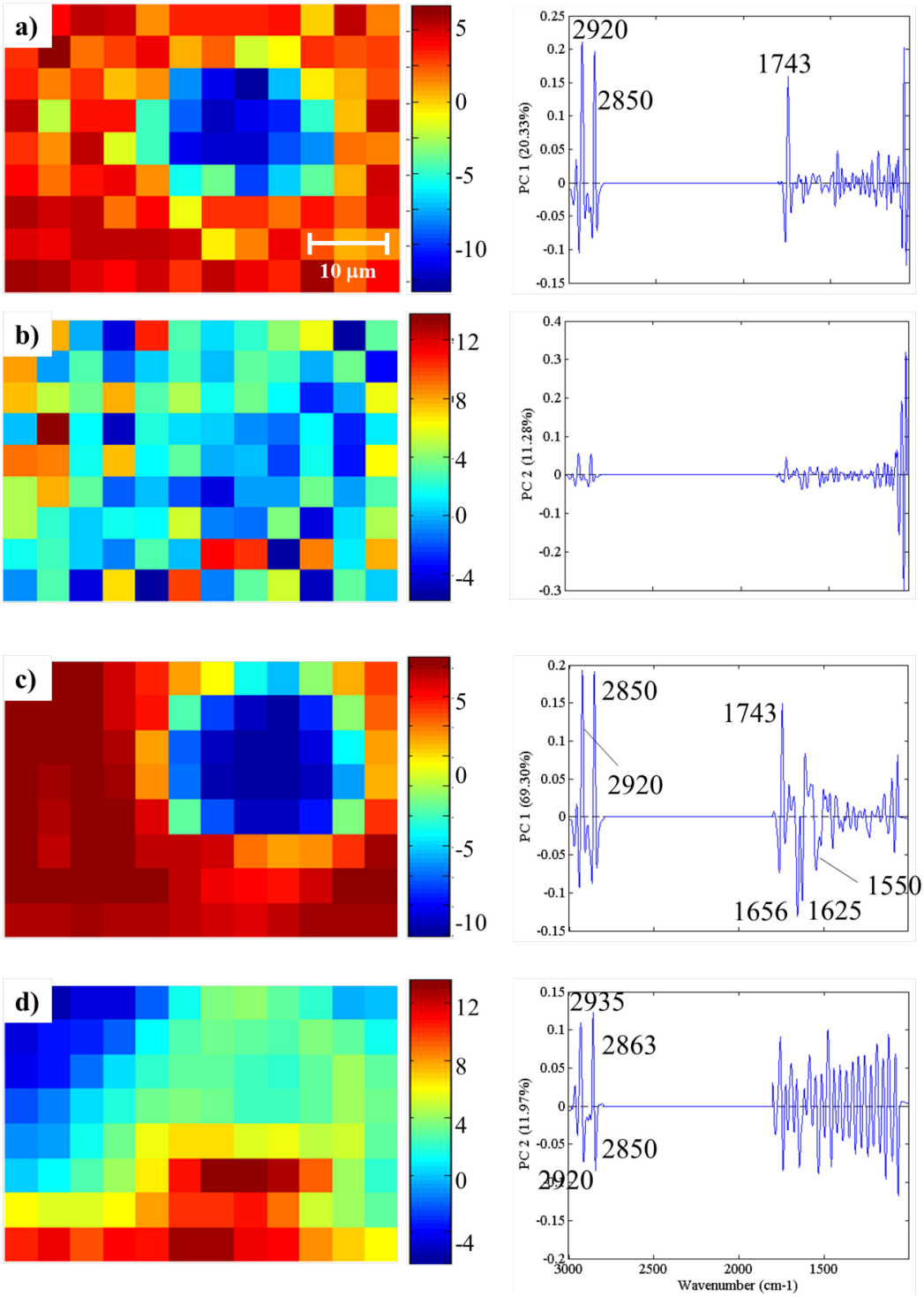

Figure 3.24: Scores maps and associated loadings plots for a single 3T3-L1 cell acquired using a small pinhole and a 4 µm step size for the first two PCs only; a) map collected using 16 coadditions, PC1; b) 16 coadditions, PC2; c) 256 coadditions, PC1; and d) 256 coadditions, PC2. Spectra were acquired over the wavenumber range 3000-1000 cm^{-1}. Map size, 12×8.

A 4 μm step size resulted in very small overlap between successive points (**Figure 3.17c)** but a 2 μm step size resulted in a high degree of oversampling (**Figure 3.17d)**. This enabled image rendering programs to make images more informative; however, the lack of independence did not impart a completely scientific justification for interpreting the information. Oversampling led to improved lateral resolution to push the achieved resolution closer to the optical diffraction limit, depending on the wavenumber.[263] These integrated peak maps at 1743 cm^{-1} (lipid) and 1654 cm^{-1} (α-helical protein) along with hyperspectral image (HSI) scores and loadings for the cell (small pinhole, 256 coadditions and 2 μm step size), **Figure 3.25** and **Figure 3.17a** and **d**, respectively, showed well-defined morphology consistent with the fact that the smaller pinhole and smaller steps resulted in improved spatial resolution.

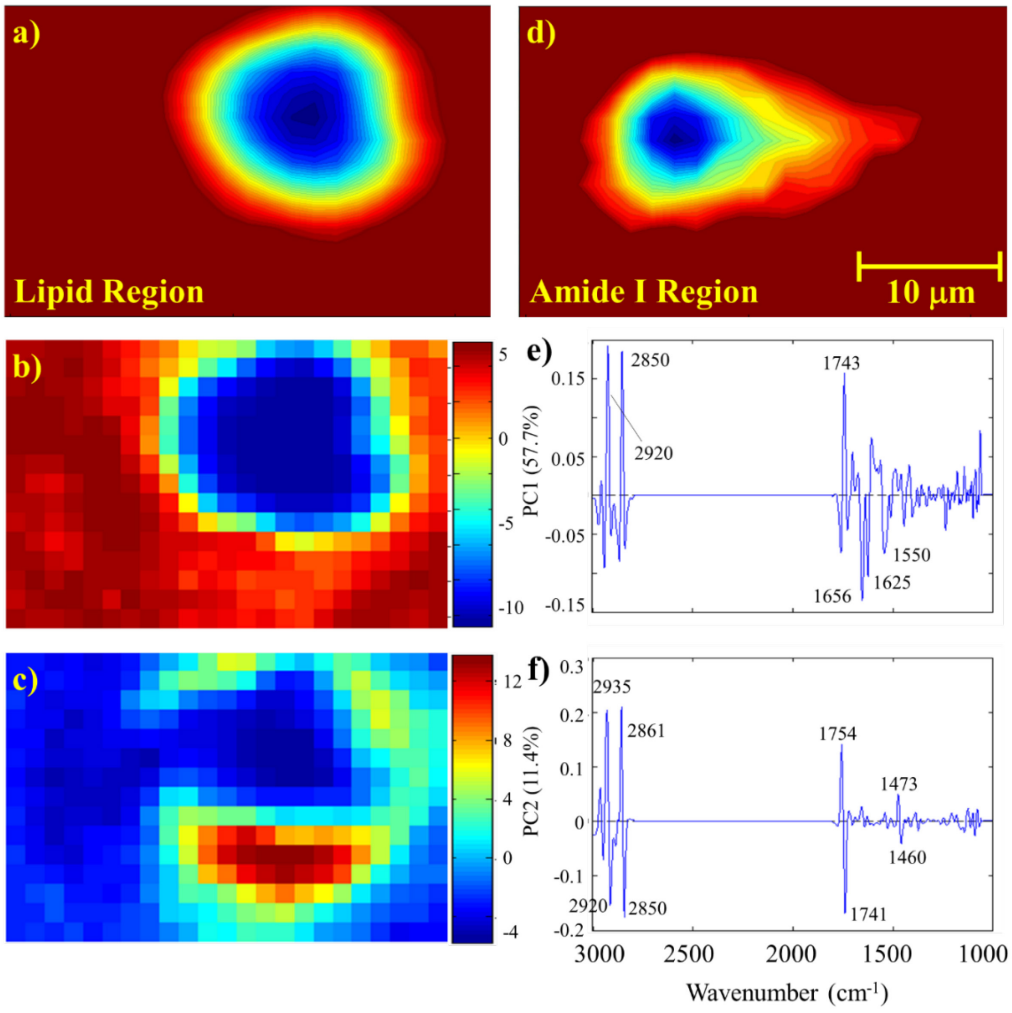

Figure 3.25: Integrated band, scores maps and associated loadings plots for a single 3T3-L1 cell acquired using a small pinhole and a 2 μm step size, with 256 coadditions for the first two PCs only; a) integrated map at 1743 cm^{-1} (lipid); b) 256 coadditions PC1 scores map; c) 256 coadditions PC2 scores map; d) 128 coadditions, PC2; d) integrated map at 1654 cm^{-1} (amide I); e) PC1 loadings; and f) PC2 loadings. Spectra were anaysed over the wavenumber range 3000-1000 cm^{-1}. Map size, 23×15.

The t_1 and t_2 scores maps, **Figure 3.25b** and **c**, respectively, were well-defined and exhibited distinct segmentation of biochemical information in corresponding loadings (**Figure 3.25e**), which showed resolution of the cell membrane from the main lipid/fatty acid content. The t_2 scores map (**Figure 3.25c)** provided chemical information free of noise with an inverse relationship between fatty acid/lipid C-H content and lipid content at 2920 and 2850 cm^{-1},[195] and the C=O lipid ester band ~1740 cm^{-1},[200] similar to that observed with FPA FTIR spectroscopy described in Section 3.8. The extracellular artefact observed in **Figure 3.24** was better resolved in **Figure 3.25**.

In summary, the large pinhole is appropriate for the collection of a single spectrum from a larger area in the cell, whereas the smaller pinhole, with oversampling is better for mapping. The major drawback with the small pinhole and oversampling conditions is that these maps take approximately 8 h to collect and the spatial information obtained is very pixelated and broad in spatial resolution of chemical features. In addition, the oversampling results in dispersion of information over pixels; however, the use of artificial rendering techniques produced maps of a quality to broadly interpret the data.

3.6 Depth Profiling Study

To test the effects of small- and large-scale defocussing of the microscope objective (as opposed to the condenser) and its impact on spectral data quality, a depth profiling study was performed (**Figure 3.26**). The focussed micrograph at the substrate surface was designated as the 0 µm position in the *z*-direction. This was refocussed in 5 µm steps up to 15 µm from the substrate surface as shown in the optical micrographs (**Figure 3.27**).

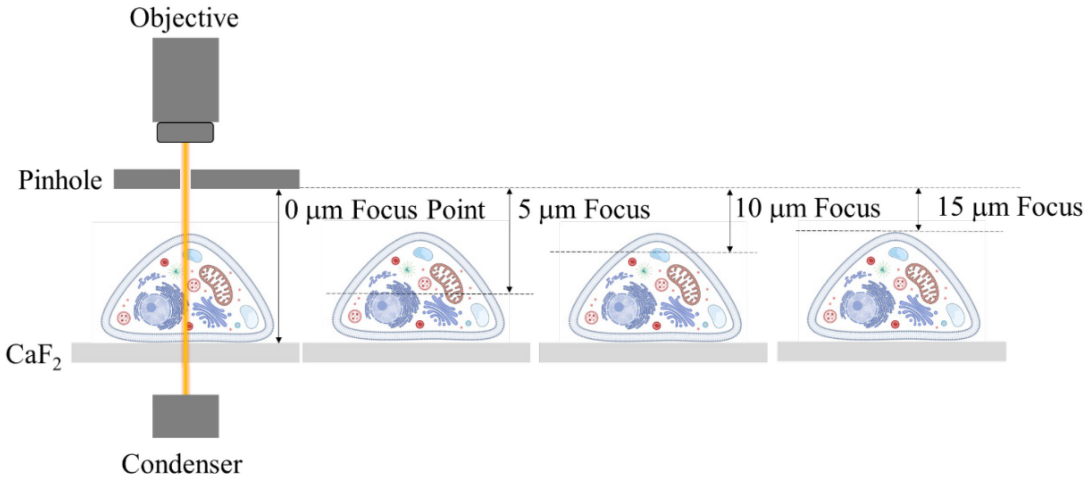

Figure 3.26: Depth profiling experiment showing how the *x*-*y*-*z*-stage was moved in the *z*-direction in 5 µm steps from the substrate surface (defined at 0 µm).

Nine spectra, with 256 coadditions in a grid (**Figure 3.27**) were measured at different focal points then processed using Savitzky-Golay second derivative (13-point smooth) followed by SNV over the wavenumber region 3000-2800 and 1800-1050 cm^{-1}.

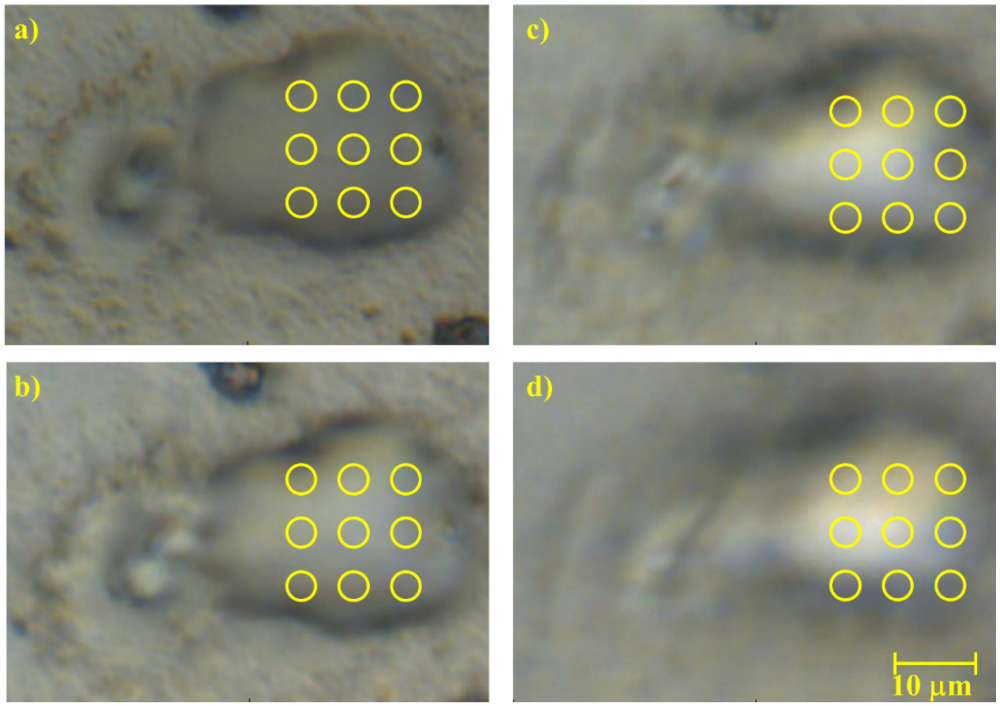

Figure 3.27: Depth profiling optical micrographs of a 3T3-L1 cell defocussed at; a) 0 µm; b) 5 µm; c) 10 µm; and d) 15 µm from the substrate surface. The circles represent a grid of nine measurement points taken at the same position of the single cell for comparison.

The optical micrographs showed different morphological features when the focus was changed due to the thickness of 3T3-L1 adipocytes, being much thicker than other cell types.[32] **Figure 3.27a** showed the cell morphology focussed CaF_2 substrate surface and progressing in 5 µm steps; **b** showed enhanced lipid droplet features, while **c** and **d** were focussed on the top of the cell, with a much smaller area in focus.

A three-PC model (**Figure 3.28**) was truncated to the wavenumber region 3000-1150 cm^{-1} to account for the noise introduced by the small pinhole below 1150 cm^{-1} and described 92.3% of the data. The t_1 vs. t_2 plot (**Figure 3.28a**) showed how the spectral variance increased as the focus moved further from the substrate surface. For each successive step in the *z*-direction, the size of the local Hotelling's T^2 ellipses for each group increased. At 0 µm focus, a maximum area of the cell was being scanned and as the focus was changed between 5-15 µm, the information obtained was more localised and, therefore, a more diverse biochemistry was being measured, particularly for the 15 µm compared to the 0 µm spectra.

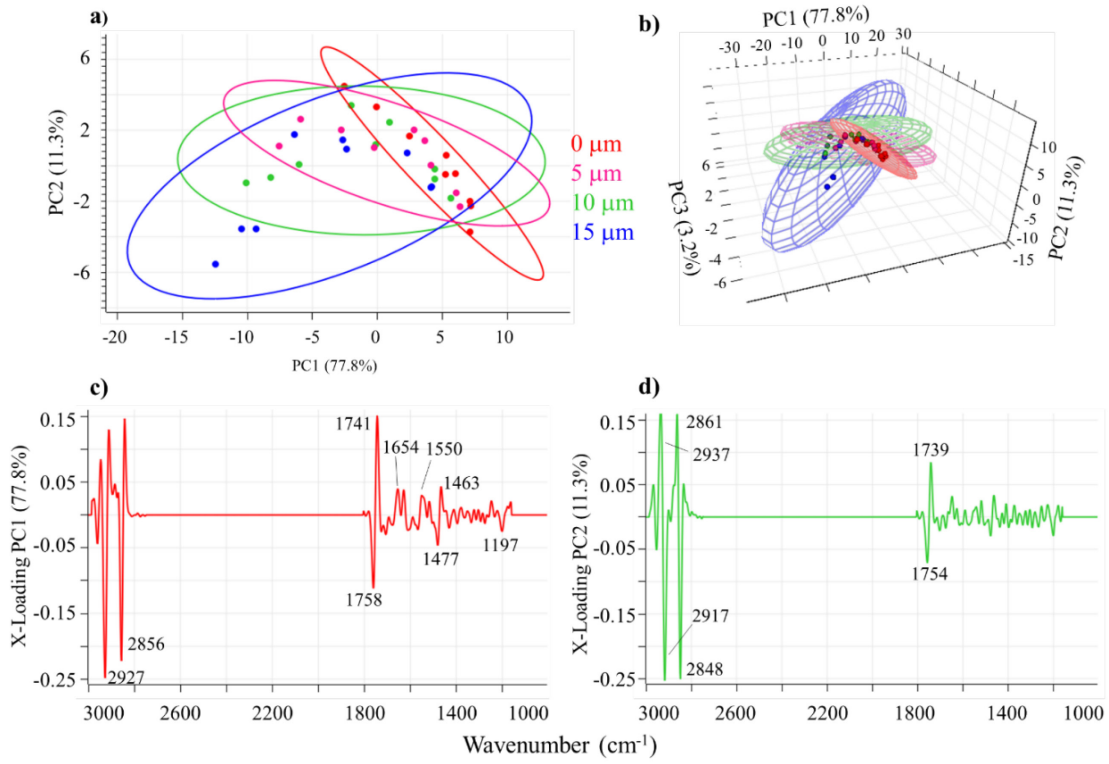

Figure 3.28: PCA scores and loadings for the depth profile study; a) t_1 vs t_2 scores plot showing how the measurements gradually increase in variability with focus from the substrate; b) t_1 vs. t_2 vs. t_3 scores plot; c) p_1 loadings; and d) p_2 loadings.

The spectra obtained from the depth profile study are available in Appendix 1. A comparison of the raw and processed spectra acquired at 0- and 15 µm (**Figure 3.29**) showed the scattering artefacts between 2800-1800 cm^{-1} were more prominent for the 15 µm measurements as evidenced by the highly curved profiles induced by Mie scattering.[276] It was also observed in the region 3000-2800 cm^{-1}, band intensities for the 0 µm spectra were higher, consistent with a larger area/volume of sample scanned.

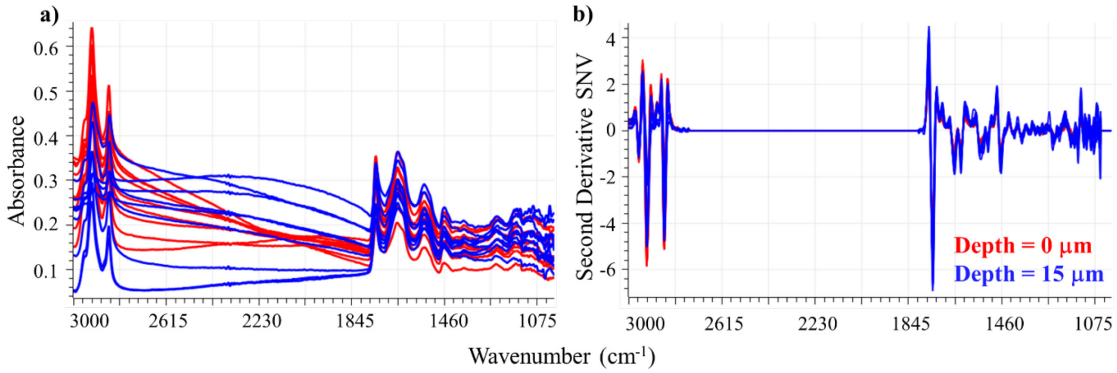

Figure 3.29: Depth profiling study performed using a small pinhole at 0- and 15 µm focus to substrate; a) raw spectra; and b) processed spectra.

The results of the depth profiling study showed that when the microscope was focussed on the substrate, or close to it, the biochemical information obtained was more consistent between scans, which indicated that similar biochemistry was being measured and became more diverse with less focus. This represented the challenge of measuring large cells such as adipocytes as the cell contour changes rapidly in the *z*-direction, especially when performing mapping experiments. Therefore, mapping the entire cell by focussing on or close to the substrate provided the compromise between balanced cell focus with quality of spectra obtained and is applicable to both SR-FTIR and non-synchrotron (Globar®) light sources.

3.7 Optimisation of Raster Scanning Data Acquisition Parameters for the Bruker Hyperion 3000 Microscope at Sydney Analytical.

3.7.1 Optimisation of Aperture Size and Spectral Coadditions.

The processing parameters defined for the SR-FTIR system (Section 3.4) were used for spectra acquired on a similar benchtop FTIR microspectrometer at Sydney Analytical, except, mechanical knife edge apertures rather than pinholes were used to restrict the scanned area. For the purposes of this assessment, the HepG2 cell line (studied in detail in Chapter 5) was used. **Table 3.8** summarises the experimental conditions used with the laboratory-based Hyperion 3000 FTIR microspectrometer to determine the optimised spectral data acquisition parameters.

A single HepG2 cell was randomly selected from a culture grown in normal supplemented media onto a 0.5 mm thick CaF_2 substrate chemically fixed using cold methanol.[258] An optical micrograph of the cell showed the spectral acquisition points (**Figure 3.30**).

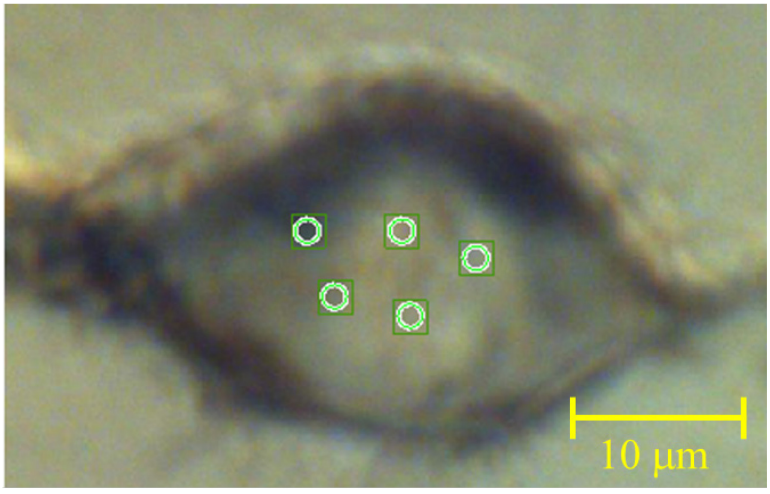

Figure 3.30: Optical micrograph with acquisition points of a representative HepG2 cell (~25×25 µm^2) grown in supplemented media and chemically fixed to a CaF_2 substrate using cold methanol.

Table 3.8: Experimental design used to evaluate the optimised scanning conditions of the laboratory-based Hyperion 3000 FTIR microspectrometer.

Parameter	Experimental Conditions
Number of cell positions measured	5 positions collected in close proximity to each other (**Figure 3.30**).
Spectral Range	3997-650 cm^{-1}.
Coaddition of spectra	128, 256 or 512, with 1028 scans also used for the 4×4 μm aperture only.
Aperture size	4×4, 8×8, 12×12, 16×16, 20×20, 24×24 and 30×30 μm.*
Spectral resolution	4 cm^{-1}.

*The OPUS software package defines the aperture size as half the value indicated, i.e., a 4×4 μm aperture corresponds to a true aperture size of 8×8 μm. The values listed in the table were the doubled values shown in the OPUS Software package. Refer to **Figure 3.35** for more details.

Raw spectra (**Figure 3.31**) over the 3000-1000 cm^{-1} region were corrected using the atmospheric compensation function in the Bruker OPUS software package prior to plotting. The data were grouped by number of coadditions and aperture size. Raw spectra showed high levels of noise associated with scans collected using smaller apertures and low numbers of coadditions. The smaller aperture scans showed more intense CO_2 bands around 2350 cm^{-1}. Processing combinations listed in **Table 3.9** were applied to the spectra prior to PCA.

Figure 3.32 shows the t_1 vs. t_2 scores plots for the processed data sets corresponding to the conditions listed in **Table 3.9**. The second derivative alone showed decreased spectral variance that converged at the 30×30 μm aperture size, i.e., the variance was modelled by the t_1 vs. t_2 direction (**Figure 3.32a** and **b**), whereas the normalised, derivative data modelled the variance in the aperture sizes along the t_1 direction (**Figure 3.32c** and **d**). This was an important justification for the use of normalisation after derivatisation as the normalisation was able to account for one source of unwanted variability explicitly, without the model trying to account for it implicitly.[238] There was no apparent difference between the use of a nine-point or a 13-point smoothing window in the derivatives and the use of one or the other depends on the specific cell type. During the modelling, wavenumbers below 1050 cm^{-1} were removed from the analyses similar to the analysis in Section 3.4.

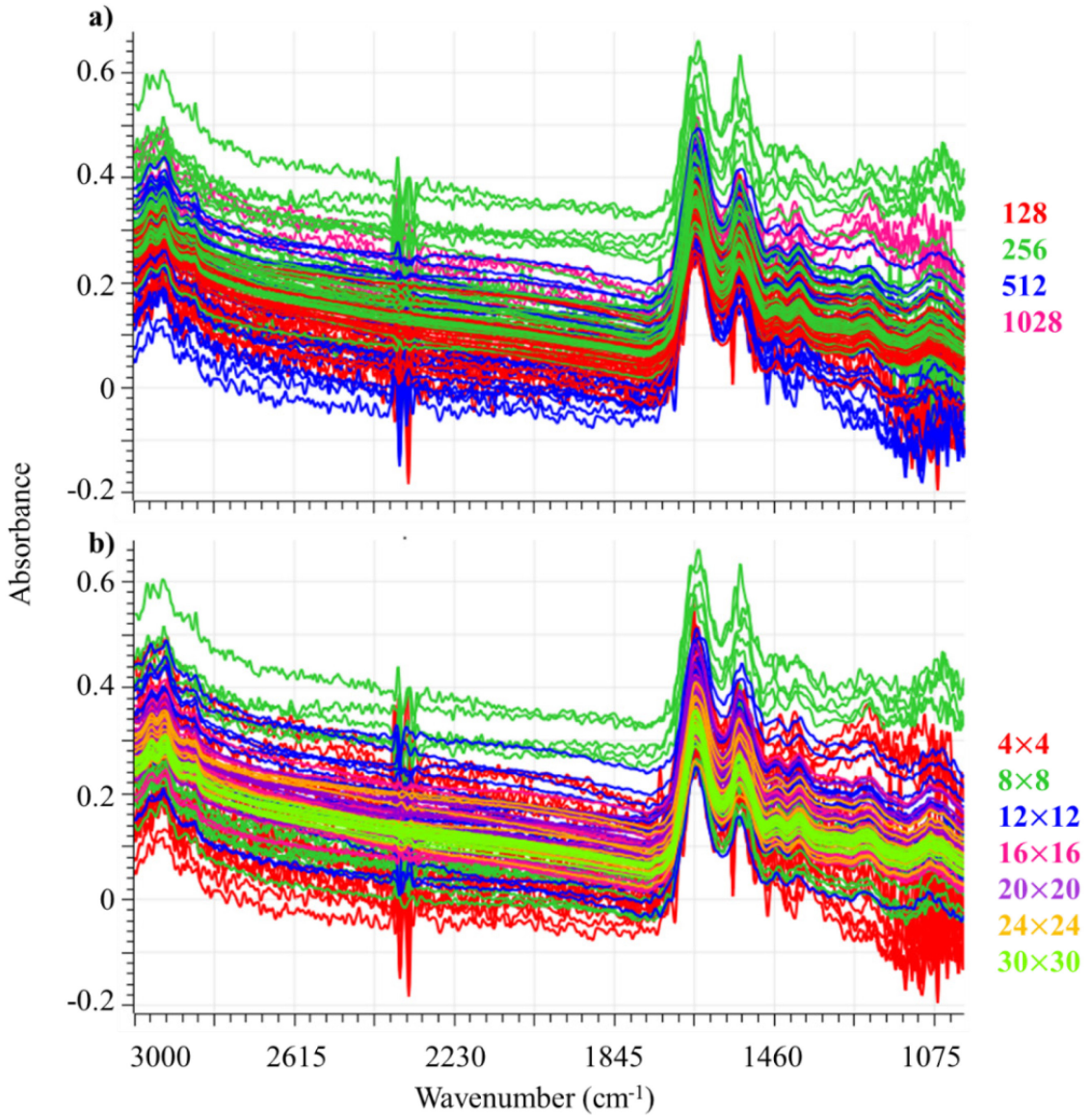

Figure 3.31: Raw FTIR spectra of a single HepG2 cell shown in **Figure 3.30** acquired in transmission mode at 4 cm^{-1} resolution; a) spectra grouped by number of coadditions; and b) spectra grouped by aperture size. Five replicate positions were scanned for each experiment.

Table 3.9: Processing combinations applied to HepG2 point spectra acquired using different numbers of coadditions and various aperture sizes.

Processing Method	Smoothing Points	Wavenumber Region (cm^{-1})
Savitzky-Golay Second Derivative	9 13	3000-1000
Savitzky-Golay Second Derivative and SNV	9 13	Derivative 3000-1000, SNV 3000-2800 and 1800-1050

The t_1 scores were plotted against aperture size for the nine-point derivative, SNV data and coloured by aperture and spectral coadditions (**Figure 3.33**), which showed that spectral variance was minimised from an aperture size of 16×16 µm. This represented a practical limit regarding spectral quality obtained from the laboratory-based FTIR microspectrometer. **Figure 3.33b** showed two straight-line fits to the data. The first line between 4×4 and 16×16 µm showed how spectral variance was minimised over this range until 16×16 µm where it started to plateau. The t_1 vs. aperture size scores plot (**Figure 3.34**) showed at the 12×12 aperture, 512 coadditions produced the same spectral variability as the 16×16 µm aperture acquired using 128 coadditions. Therefore, for smaller maps, finer detail can be achieved for a smaller aperture, with a four-times increase in acquisition time, consistent with the literature.[263]

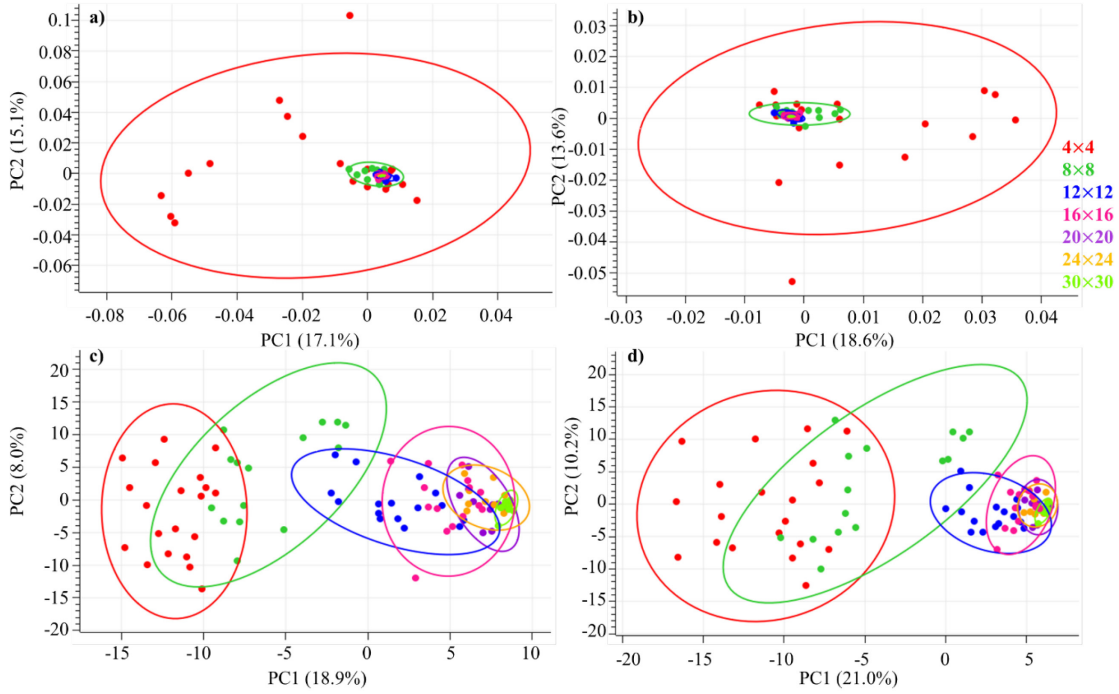

Figure 3.32: t_1 vs t_2 scores for PCA models of HepG2 spectra acquired using various coadditions and aperture sizes. The data were colour grouped by aperture size; a) nine-point second derivative; b) 13-point second derivative; c) nine-point second derivative, SNV; and d) 13-point second derivative, SNV. The 30×30 µm aperture points were difficult to observe in figures a) and b), respectively and lie in the centre of the ellipses located around the (0,0) scores values.

The OPUS software sets an aperture size as shown in the enclosed box of **Figure 3.35a**. **Figure 3.35b** is an adaptation of the Globar® energy intensity distribution as a two-dimensional contour distribution[270] and indicated that most of the high intensity beam reached the sample with a 20 µm spot size compared to the 8 µm beam size of the synchrotron.

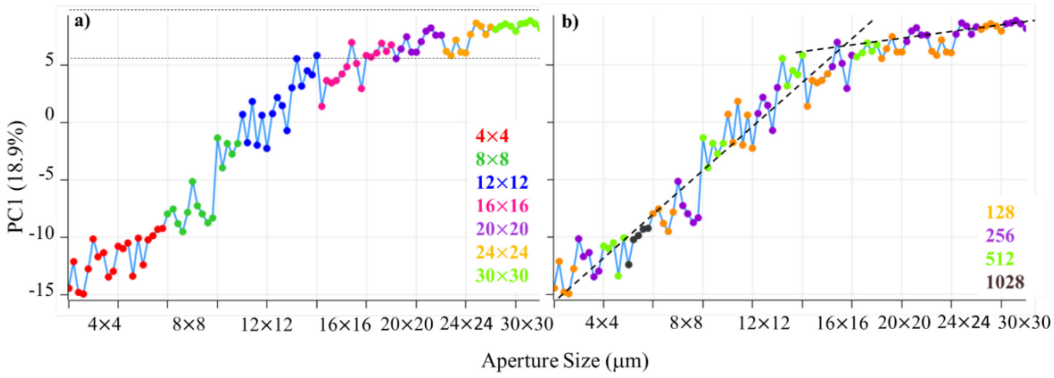

Figure 3.33: t_1 vs. aperture size grouped by; a) aperture size, where it was observed that spectral variance was minimised from an aperture size of 16×16 µm; and b) number of coadditions, where two processes are described by the piecewise straight-line fits. These linear fits are a function of both aperture size and number of coadditions.

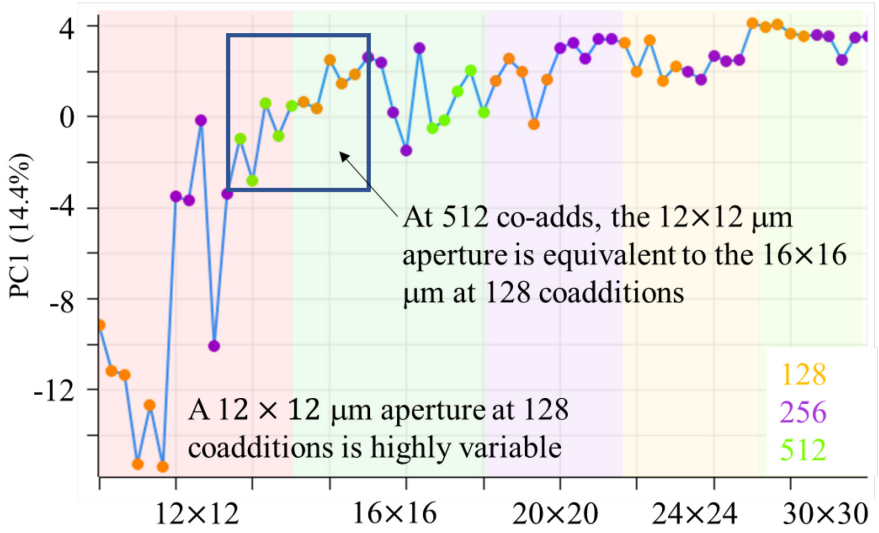

Figure 3.34: t_1 vs. aperture size colour grouped by number of coadditions between 12×12 to 30×30 µm.

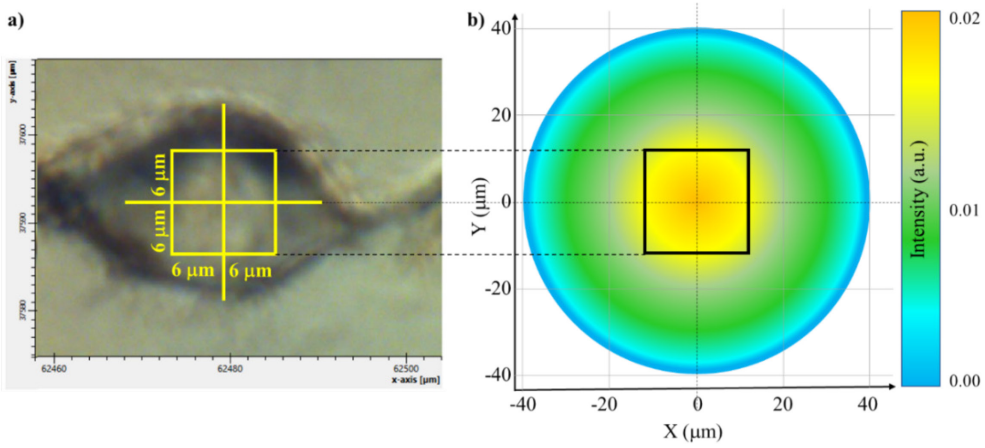

Figure 3.35: a) Diagrammatic representation of the 6×6 µm aperture defined by the Bruker OPUS software; and b) comparison of the Globar® beam spot with respect to the aperture size. The actual aperture size is 12×12 µm.

In practical terms, at the 12×12 μm aperture, 512 coadditions per step was required with a high degree of oversampling to achieve the level of detail required for biochemical mapping of a cell of dimensions 30×30 μm. This map required ~7 hr of scanning time to complete.

3.7.2 Assessment of Spectral Variability.

As an independent assessment, the PCA scores results were compared to those from FBSD (Section 3.4.4). **Table 3.10** summarises the FBSD results with the spectra being processed using the Savitzky-Golay second derivative (nine-point smoothing, SNV over the 3000-1050 cm^{-1} region.

Table 3.10: Summary of FBSD results obtained from the aperture and coaddition experimental design.

Number of Coadditions	Aperture Size (μm)						
	4×4	8×8	12×12	16×16	20×20	24×24	30×30
128 scans	0.5604	0.5441	0.4936	0.3903	0.2997	0.2649	0.1475
256 scans	0.6180	0.6210	0.4843	0.3354	0.2167	0.1763	0.1148
512 scans	0.5354	0.4270	0.3767	0.2595			
1028 scans	0.6088						

FBSD captures the spectral variance over a defined wavenumber region and in **Table 3.10**, the only variables assessed were aperture size and number of coadditions. For a selected number of coadditions, the spectral variability (*SV*) was averaged over the total wavenumber range to result in a single value of variance (FBSD). Using the 128 coaddition data, the FBSD values were listed for all apertures. These data showed that as the aperture size increased, the spectral variability was minimised and when the values plateaued, the aperture was deemed optimal for that number of spectral coadditions.

The data in **Table 3.10** were summarised in **Figure 3.36** for 128 and 256 coadditions only. Beyond an aperture size of 8×8 μm, the variance in the spectral data decreases, particularly for the data collected at 256 coadditions. This plot showed the trade-off between precision and time as the larger apertures are best suited for scanning the entire cells, but are not adequate for chemical mapping.[261]

These data showed that larger apertures only required 128 coadditions. Aperture sizes 15×15 to 150×150 μm with 512 coadditions have been suggested for Globar® light sources.[257] The results in **Table 3.10** showed that for the smaller apertures, this may be

the case; however, for aperture sizes > 16×16 µm, 128 or 256 coadditions result in spectral data of low variability.

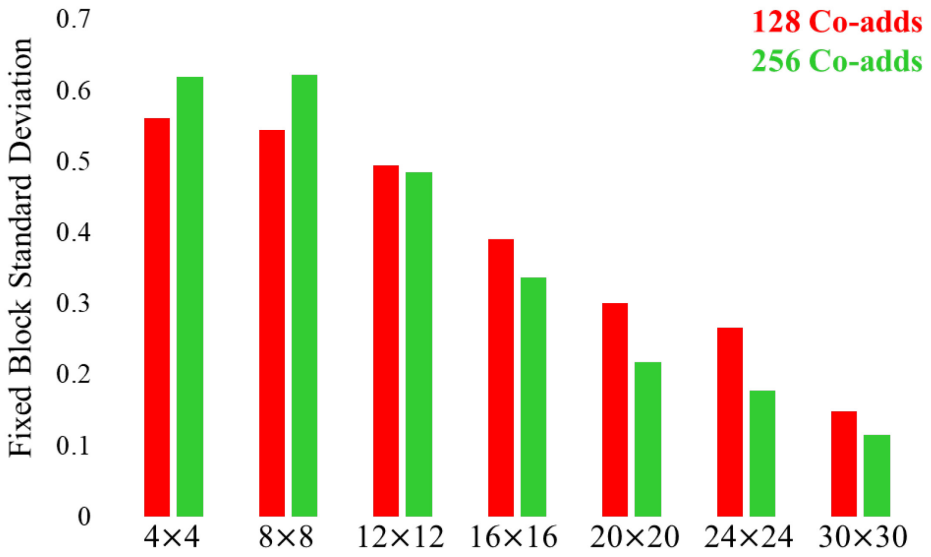

Figure 3.36: FBSD vs. aperture size for 128 and 256 spectral coadditions. Beyond the 20×20 µm aperture, there was a marked decrease in spatial resolution due to the size of the aperture being of similar size to the cell dimensions.

3.8 Focal Plane Array IR Imaging

3.8.1 Laboratory based FPA Imaging

To obtain high quality spatial and morphological information from single cells in a much shorter acquisition time than mapping, required the use of focal-plane-array (FPA) FTIR microspectroscopy (Section 1.6). A 64×64 element detector acquires 4096 spectra and a pixel size of 1.1 µm using a 36× objective.[213] Such pixel sizes are well below the diffraction limit for radiation in the MIR region (Equation 3.1). Kimber, *et al*.[285] state that as the FPA is spatially discrete, it is necessary to oversample the imaged area to avoid aliasing effects and obtain true diffraction limited images.

A 64×64 FPA image of a 3T3-L1 adipocyte collected using 256 coadditions, generating 4096 spectra in only 10 min is shown in **Figure 3.37**. Three parameters associated with FPA image acquisition; frame time, frame rate and integration time,[262] were optimised. Adjustment of the integration time was critical to avoid detector pixel saturation. Balancing the integration time to achieve high quality images without saturation was a challenge throughout the study. A small optimisation study was performed where images were acquired at 128, 256 and 512 coadditions at a resolution of 4 cm^{-1} on the same 3T3-L1 cell, using the same stage position.

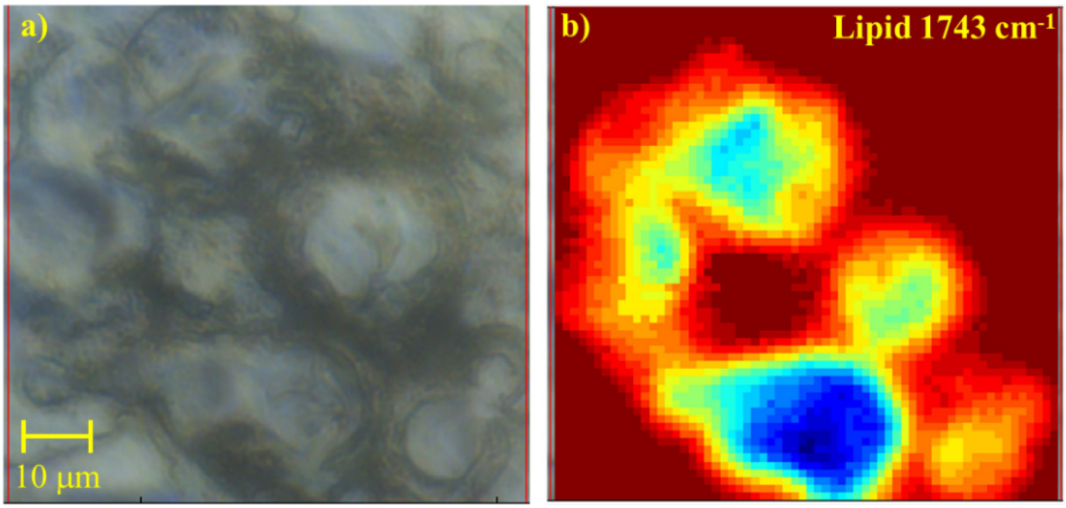

Figure 3.37: 64×64 FPA image of a 3T3-L1 adipocyte; a) optical micrograph; and b) false colour image integrated at the lipid band ~1743 cm^{-1}.

PCA was applied to spectra extracted from the 10×5 grid ROI (**Figure 3.38**) and processed using a Savitzky-Golay second derivative (13-point smooth) followed by SNV applied to the regions 3000-2800 and 1800-1050 cm^{-1}. A three-PC model described 69% of the **X**-variance and the t_1 vs. t_2 scores plot and FBSD plot are shown in **Figure 3.39a** and **b**, respectively. These plots confirm that 128 coadditions produced spectra of much higher variability than those from 256 or 512 coadditions. There was no difference statistically at the 95% confidence interval between images obtained at 256 and 512 coadditions. The FPA images in Chapter 6 were acquired using 256 coadditions and when a high-definition confirmation image was required, 512 coadditions were used for these images. **Figure 3.40** shows integrated FPA images for the cell in **Figure 3.38** acquired at 128, 256 and 512 coadditions.

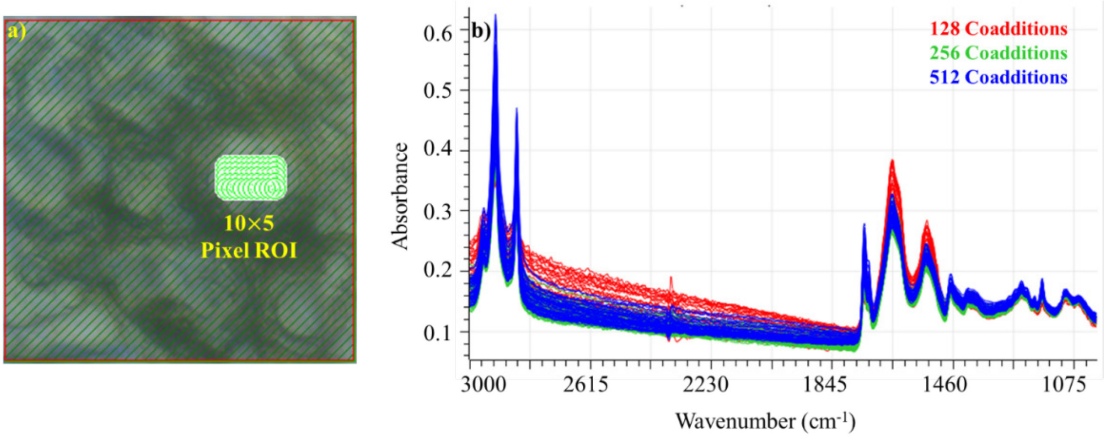

Figure 3.38: a) 10×5-pixel ROI of a 3T3-L1 adipocyte for optimisation study; and b) extracted raw FTIR spectra from the ROI, colour grouped by number of coadditions. Spectra were acquired at 4 cm^{-1} resolution and were displayed in the wavenumber region 3000-1000 cm^{-1}.

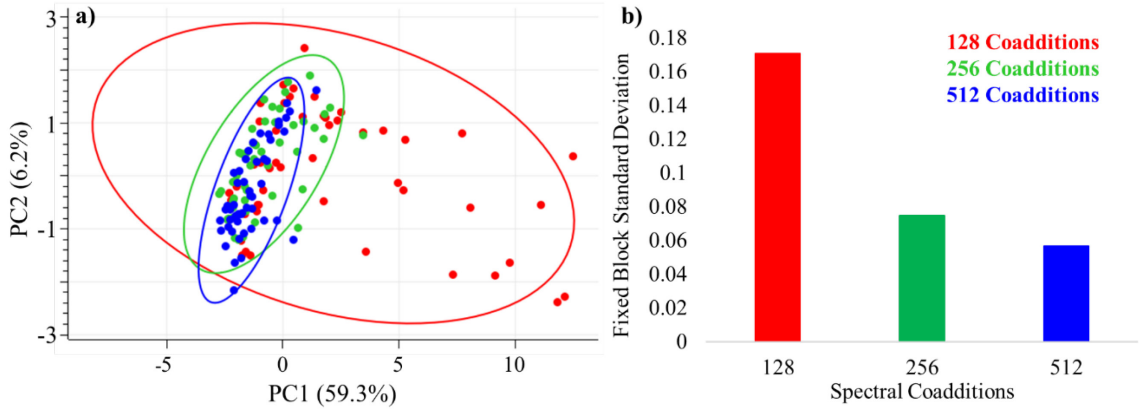

Figure 3.39: a) t_1 vs. t_2 scores; and b) FBSD plot of selected spectra acquired by FPA FTIR microspectroscopy at 128, 256 and 512 coadditions for the ROI shown in **Figure 3.38**. The PCA and FBSD assessment confirm that 256 or 512 coadditions were required to collect images with low spectral variability.

3.8.2 Four Beam Synchrotron Radiation FPA Imaging

During May 2017, the optical light train from the beam to the Hyperion 3000 microscope at the Australian Synchrotron was reconfigured by splitting multiple beams and spatially reconfiguring them to match the aperture of the FTIR instrumentation[255] prior to the experiment. The purpose of the reconfiguration was to gain the synchrotron advantage of brightness over a wider area of the FPA detector compared to a single beam. The field-of-view (FoV) of the detector for this objective configuration was approximately 50×50 µm. The beam spot of the synchrotron radiation had a diameter of 8 µm and when four beams were aligned, edge-to-edge, this resulted in an optimised illumination area of approximately 16×16 µm (**Figure 3.41**). The inner 32×32 µm section of the FPA detector (**Figure 3.41a-c**) showed that the illumination is more intense in the centre compared to the edges of the FoV.

Due to the limited available beamtime for this study, a complete optimisation of the settings was not possible. Images were collected using a 52× magnification objective over a 64×64 array detector and 256 coadditions per image. At this magnification, the pitch of the pixels of the FPA detector corresponds to 0.77×0.77 µm^2.[255] 3T3-L1 adipocytes were treated as per the conditions of the 2^2 full factorial design in **Table 3.11**. After treatment, cells were fixed to CaF_2 substrates of three different thicknesses; 0.2, 0.5 and 1.0 mm, respectively.

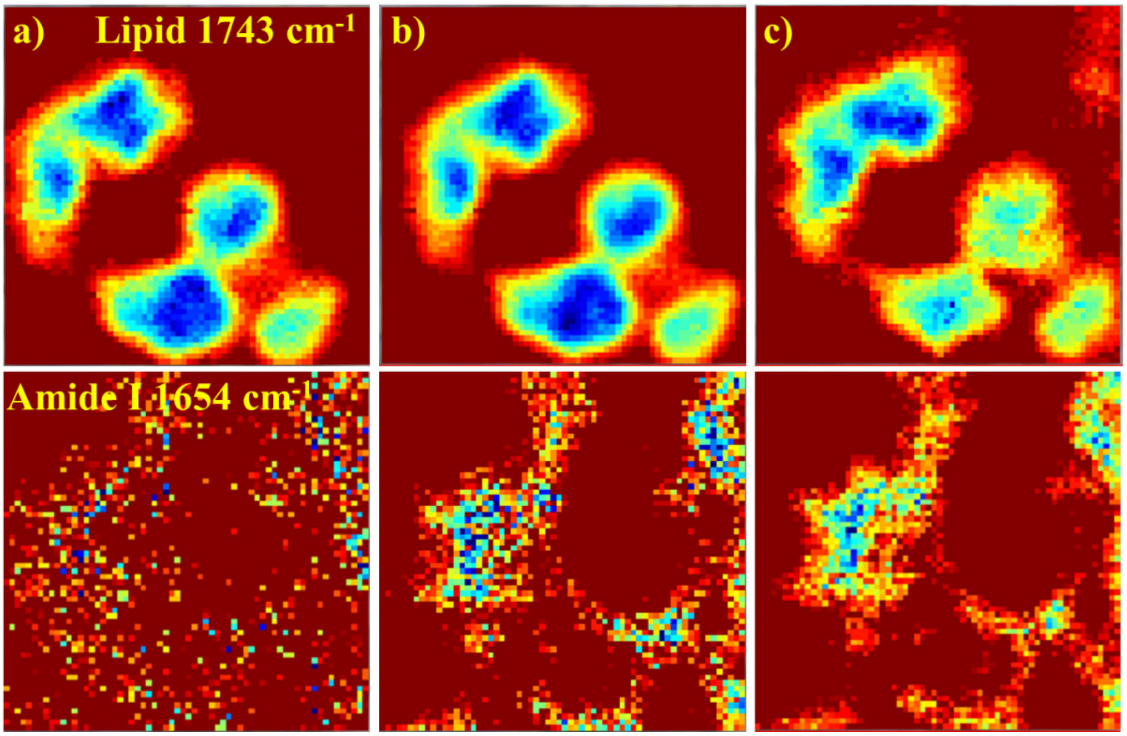

Figure 3.40: FPA images of a 3T3-L1 adipocyte integrated in the lipid region 1743 cm^{-1} and amide I region 1654 cm^{-1} for images acquired at; a) 128; b) 256; and c) 512 coadditions.

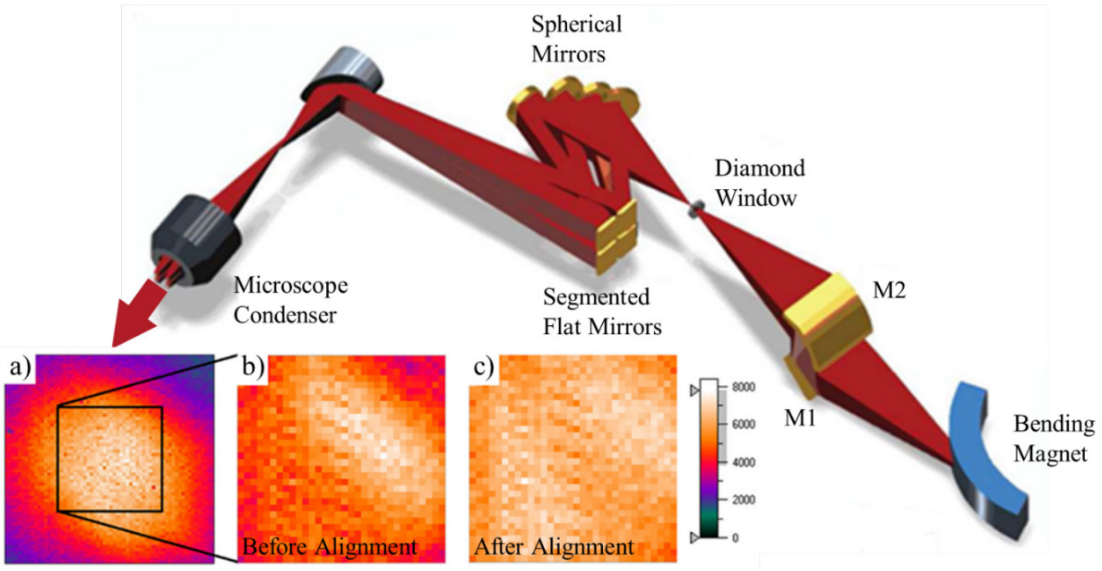

Figure 3.41: Focussed beamlines at the Australian Synchrotron to match the optical pupil of the Bruker Vertex FTIR spectrometer and Hyperion 3000 Microscope for use with an FPA detector; a) inner 32×32 pixel array highlighted; b) expanded 32×32 region before fine adjustment of focussing mirrors and; c) energy distribution after adjustment of the focussing mirrors. Figure adapted with permission, from Tobin, *et al*,[255] and, Dynamic full field infrared imaging with multiple synchrotron beams, Stavitski, *et al*.[282] Copyright, 2013, American Chemical Society.

Table 3.11: Treatment conditions used to prepare 3T3-L1 adipocyte samples for SR-FTIR-FPA study.

Sample ID	Sugar Treatment (mM)		CaF_2 Substrate Thickness
	Glucose	Fructose	
Control	0	0	0.2, 0.5 and 1.0 mm for each treatment
Glucose	5	0	
Fructose	0	5	
Glucose-Fructose	5	5	

Optical micrographs collected on single adipocytes fixed to 0.5 mm thick CaF_2 substrates (**Figure 3.42**) showed the lipid structures in the cells and the stromal cells in the background on which the adipocytes propagate.[201]

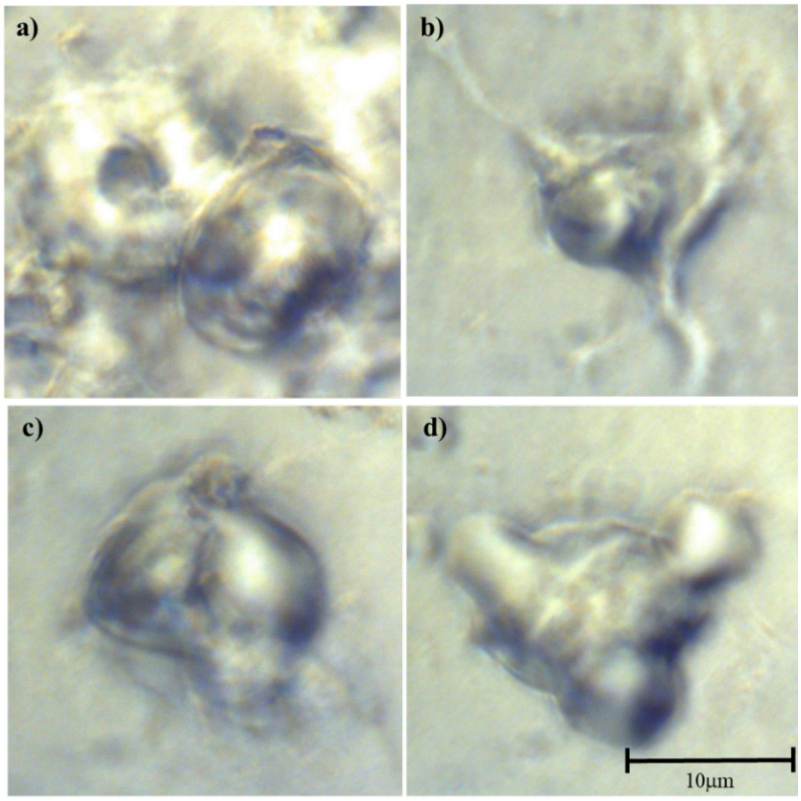

Figure 3.42: Optical micrographs of 3T3-L1 adipocytes showing the morphology of; a) Control; b) Glucose; c) Fructose; and d) Glucose-Fructose treatments. Cells were fixed to the to 0.5 mm thick CaF_2 substrate using cold methanol. Treatment conditions are listed in **Table 3.11**.

The raw spectra of the control cell (**Figure 3.43)** was processed using the RMieS and ME-EMSC approach but did not result in adequate corrections. This may be due to not fully understanding the procedure and will be investigated in the future, therefore, processing was undertaken using the Savitzky-Golay second derivative (nine-point smooth).

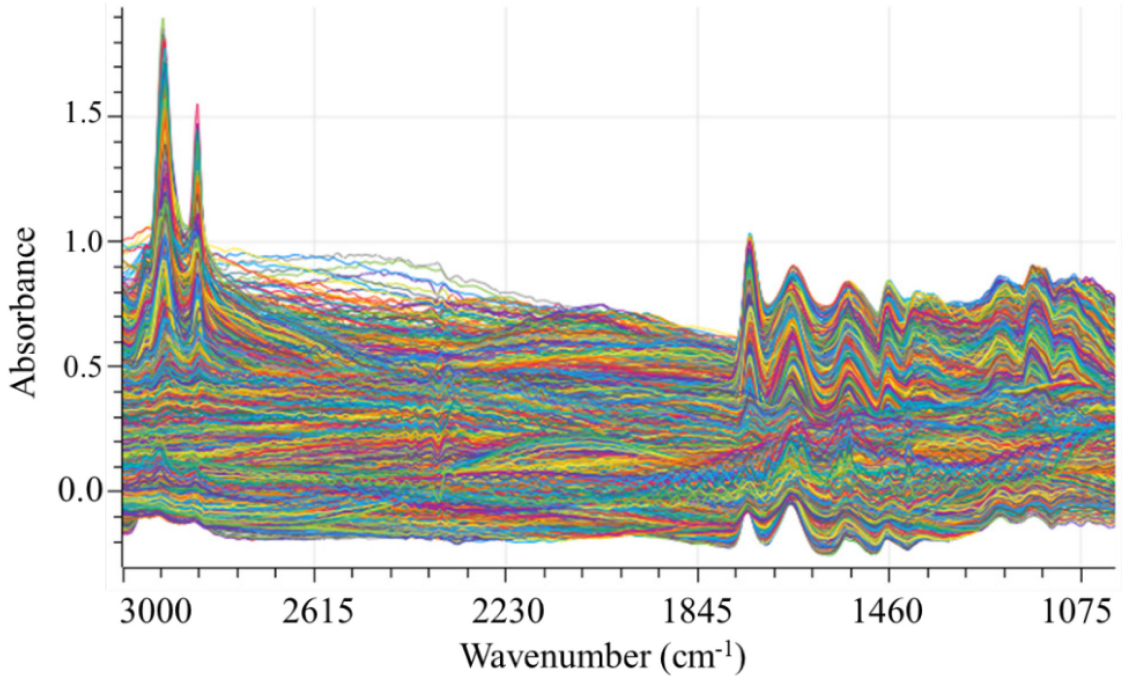

Figure 3.43: Raw FTIR spectra collected on a control 3T3-L1 adipocyte using the four-beam synchrotron FPA microspectrometer.

Selected FPA contrasted images (**Figure 3.44**) showed various levels of fringing (aberrations) from coherent interference,[255] which were particularly noticeable in some of the amide band images. Findlay, *et al*.[286] observed similar aberrations which they referred to as Moire-like patterns for images collected on tissue samples using the multiple-beam FPA setup at IRENI.[287] This pattern was attributed to scattering from small crystals present in the sample or artefacts generated by the multiple beam overlap.

Amide I and amide II regions integrated with no colour bar contrasting performed highlighted the effects of fringing (**Figure 3.45**). These aberration effects introduced high frequency features in the spectral data and an attempt to deresolve the spectra using a triangular kernel function,[288] reduced the aberrations in some cases, however, this was at the expense of information loss through reduced spectral resolution. No further attempts were used to process these data. A comparison of the optical micrograph and the unmasked t_1 scores image (**Figure 3.46**) for a PCA model calculated over the range 3000-1000 cm^{-1}, showed that the scores resembled the outline of the control 3T3-L1 adipocyte to a high level of definition without correction for the background.

The PCA scores images and loadings for the first two PCs after background masking (**Figure 3.47**) revealed most of the morphology of the cell, while PC3 and beyond captured the effects of aberrations. These images were further studied in Chapter 6, with the complete scores images and loadings provided in Appendix 2. This showed how PCA

implicitly corrected the images by removing the aberrations as noise contributing PCs. A future study will aim to investigate other correction methods to explicitly remove these effects before HSI analysis.

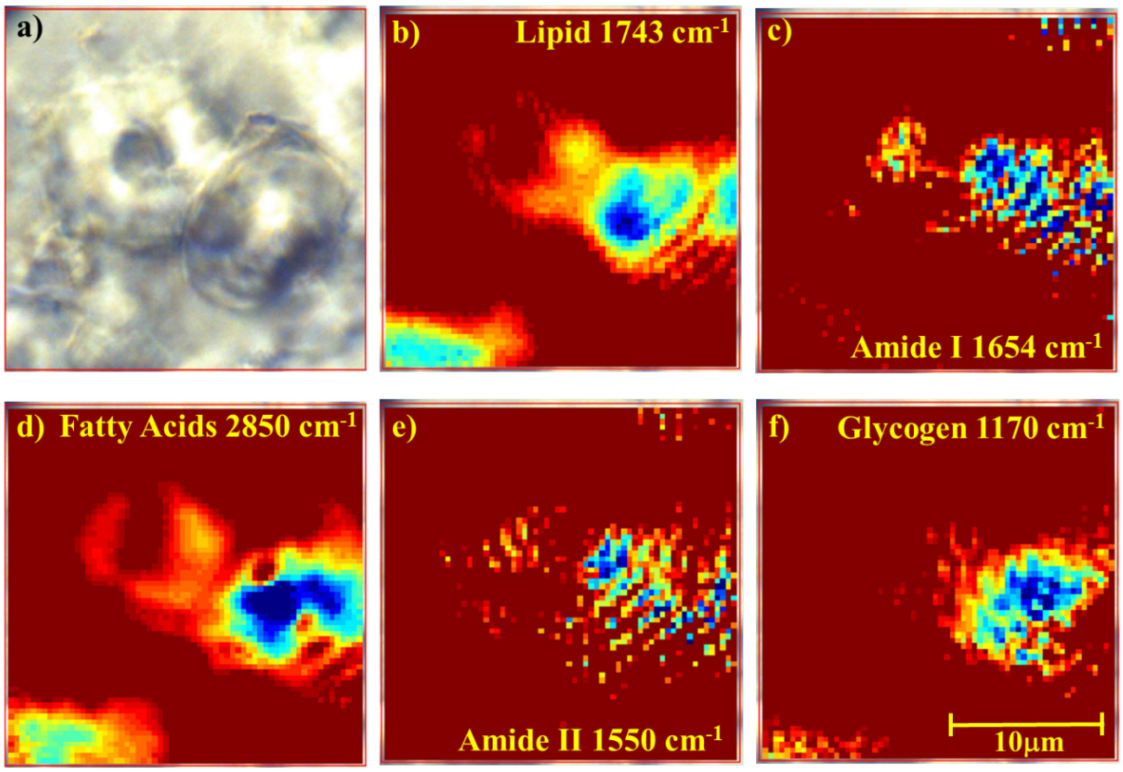

Figure 3.44: Integrated FPA images of a 3T3-L1 adipocyte; a) optical micrograph; b) lipid ester region; c) amide I; d) membrane fatty acids and lipids; e) amide II; and f) glycogen and phosphates. The amide band images highlighted the effects of coherent aberrations.

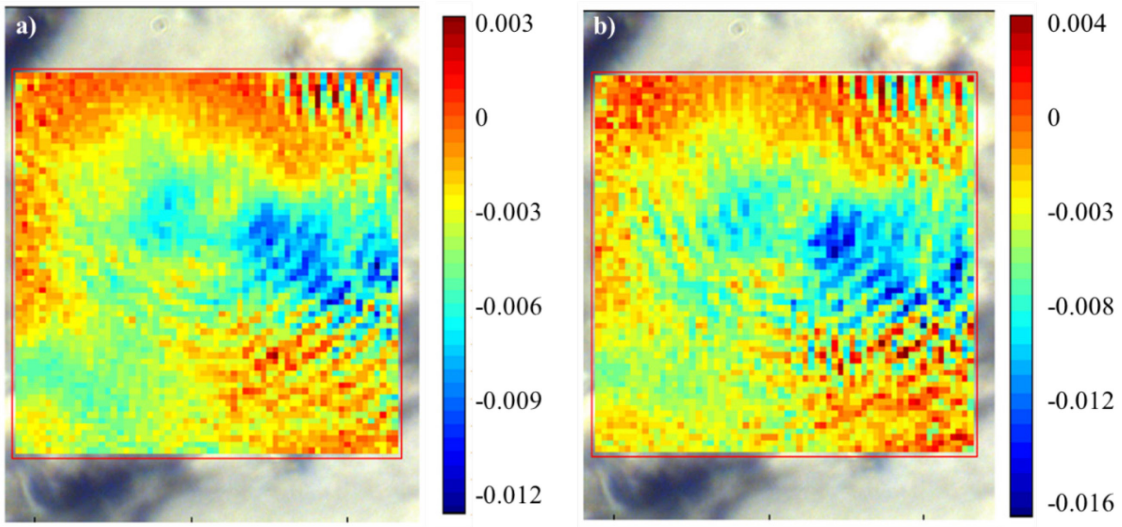

Figure 3.45: FPA images of a differentiated 3T3-L1 adipocyte with no contrasting applied; a) integrated at 1654 cm^{-1} (amide I); and b) 1550 cm^{-1} (amide II).

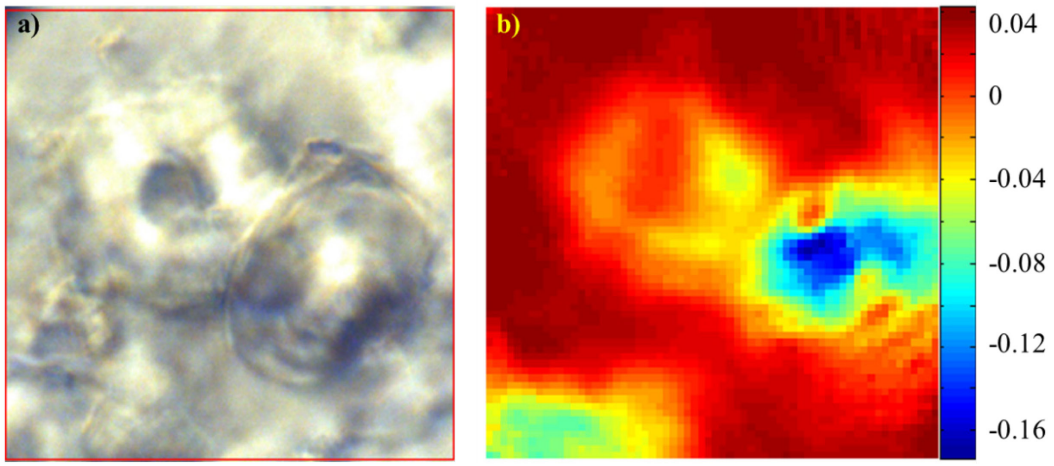

Figure 3.46: a) optical micrograph of a differentiated 3T3-L1 adipocyte fixed to a 0.5 mm thick CaF_2 substrate; and b) t_1 scores image for Savitzky-Golay second derivative (nine-point smooth) data.

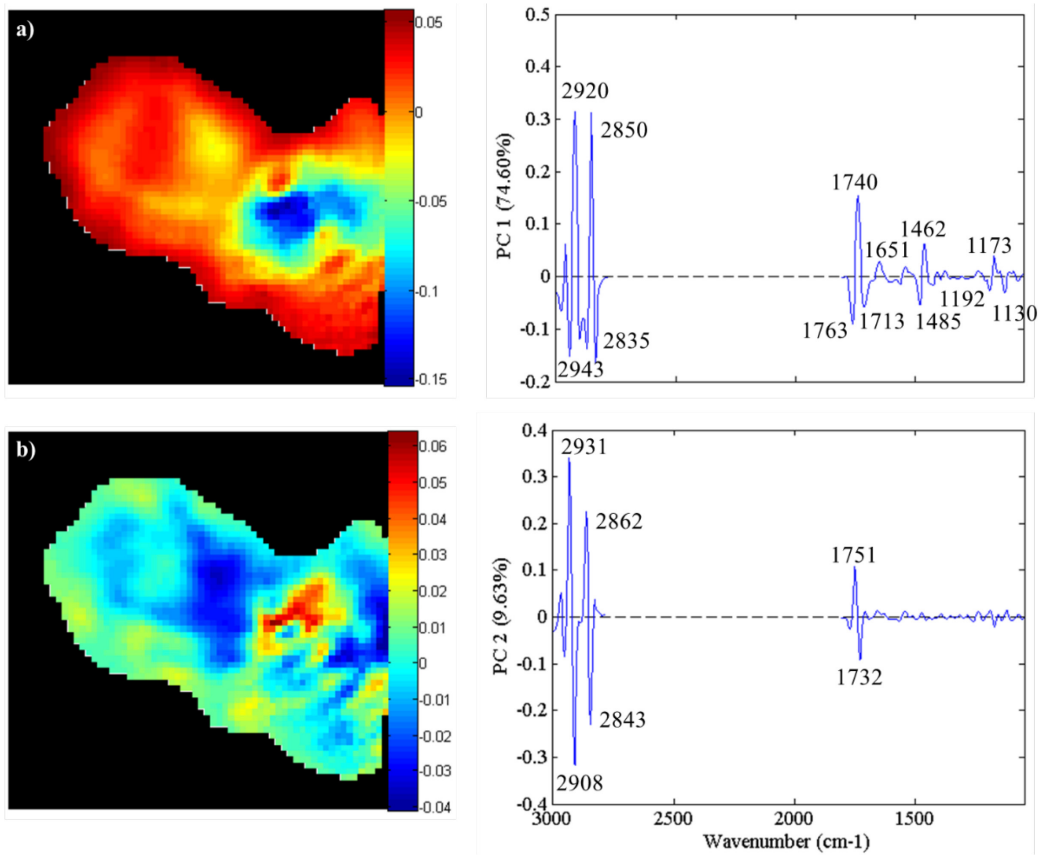

Figure 3.47: HSI analysis of a FPA image acquired on a differentiated 3T3-L1 adipocyte chemically fixed to a CaF_2 substrate; a) t_1 scores image and associated loadings; and b) t_2 scores image and associated loadings.

Unlike univariate analysis used in integrating the area under band regions, the multivariate approach showed the relationships between the biochemical content over the entire cell. The p_1 loadings had positive correlations among 2920, 2862, 1740, 1462 and 1173 cm^{-1} bands, which were negatively correlated to those at 2943, 2835, 1763, 1713,

1485 and 1130 cm^{-1}. These bands all represent the predominant lipid character in adipocytes and in particular indicate how diverse the lipid structures are within a single cell (see **Table 1.1** for band assignments).

The ν (C=O) band at 1740 cm^{-1} was assigned to TAGs, however, the loadings indicate that there may be a number of different lipid types, particularly the band at 1763 cm^{-1} is an upper value for the C=O lipid ester band and the smaller band at 1713 cm^{-1} has been attributed to protonated carboxyl groups of free fatty acids.[202] Gazi, et al.[201] has shown that any band intensities in the region below 1725 cm^{-1} increases as the relative ratio of FFA to glycerol-bound lipids increases. This data set was analysed in detail in Chapter 6, where the sugar treatment conditions listed in **Table 3.11** were compared to each other to gain a better understanding of the effects of the combined sugar and vanadate treatments on 3T3-L1 adipocytes.

3.9 A Note on Spectral Variability

Biological variability is a major challenge in any studies performed on single cells or tissue samples. This variability is captured in the spectral data obtained as a result of the cell cycle stage, phenotypes/genotypes, the individual growth characteristics and the general health of the culture, thus resulting in differences within in a single culture and between different cell cultures.[218-219]

Heterogeneity, in the biological and statistical sense, is a major challenge associated with the assessment single cells an there are no statistical distributions that adequately describe heterogeneity in the theory of sampling (TOS).[227-228] However, the challenge is not to assess the homogeneity (or lack of) in a population samples, but rather to determine which components of the observed cellular heterogeneity contain meaningful information, i.e., which cell-to-cell differences are important and which differences can be ignored.[289] In spectral cytopathology studies performed by Diem, *et al*.[218] > 10,000 cells were assessed using next generation FTIR microspectrometers which provided sample sizes where reliable statistical assessment could be performed.

In this study, the generation of the large data sets described in the spectral cytopathology literature was not possible due to instrumental constraints, however, to compensate for smaller sample sets, the use of rational experimental design (DoE, Section 1.7.1) was employed as described in Chapter 4-Chapter 6. This was done to increase the statistical power of the analysis and allow the treatment effects induced by application of the design parameters to be modelled using exact mathematical techniques. In this manner, the

important treatment differences were anticipated to isolate from those effects that are not important, particularly when assessed in closed systems of single cell cutures.[223] The results and conclusions obtained from this approach are expected to form the basis of future studies based on larger populations where spectral variability will be assessed on multiple cultures.

3.10 Chapter Summary

This chapter provided an in-depth study of the instrumental parameters deemed critical for reliable spectral data and image acquisition. These parameters were used as a basis for the spectral data acquisitions performed in subsequent chapters. Sample preparation in terms of cell culturing and fixation was not investigated as part of the optimisation study and the method of cold methanol fixation was used for all studies. In the protocol by Baker, *et al*.[257] a table of optimised spectral acquisition parameters was provided. The information in **Table 3.12** compares the published optimisation parameters[257] and the results from the current study.

Table 3.12: Comparison of instrumental optimisation parameters for Globar®, synchrotron and FPA spectral data acquisition between the literature and this study.

Detector	**Single Element**				**Focal Plane Array (FPA)**	
Light Source	**Globar®**		**Synchrotron**		**Global® FPA**	
Reference	**Literature***	**This Study**	**Literature***	**This Study**	**Literature***	**This Study**
Aperture (μm)	15×15 to 150×150	12× 12 to 30×30	5×5 to 20×20	5×5 to 20×20	700×700 (FOV)	700×700 (FOV)
Number of Coadditions	512	256	256	256	64 or 128	256-512
Spectral Resolution	4 or 8 cm^{-1}	4 cm^{-1}	4 or 8 cm^{-1}	4 cm^{-1}	4 or 8 cm^{-1}	4 cm^{-1}

*Baker, *et al*.[257]

The results obtained were in close agreement with the literature and provided a more in-depth procedure on how to verify optimal coaddition numbers in an objective manner. The 3T3-L1 adipocyte cell line presented a challenge compared to other cell lines due to their high heterogeneity, large diameter and thickness and the large changes in refractive index as a result of the multilocular structure, particularly the boundaries between lipid droplets. While processing methods exist that minimise these effects, including the correction of Mie scattering effects, these were not found to improve the spectra obtained from 3T3-L1 adipocytes. Standard preprocessing methods based on derivatives and simple normalisation techniques were found to produce acceptable data for multivariate

analysis. These simple processing methods translated from synchrotron point spectra to chemical mapping and point spectra acquisition using laboratory-based Globar® instruments.

FPA spectra acquired on laboratory-based FTIR microspectrometers produced adequate images that could also be processed using simple methods revealing enhanced compositional and morphological detail in images acquired on single cells. When four-beams of the Australian Synchrotron were combined and focussed onto the aperture of the Hyperion 3000 microscope, this configuration introduced a number of aberration effects that could be minimised using simple spectral processing methods and the use of multivariate methods was able to partition residual noise effects into higher order PCs. Further assessment of the laboratory-based and synchrotron-based FPA images is provided in Chapter 6.

Chapter 4 Vibrational Spectroscopic Investigations of Adipocytes as Models of Diabetes and Metabolic Syndrome.

4.1 Introduction

Adipose tissue is one of three insulin sensitive tissues in mammals and is composed of a number of different cell types, predominantly adipocytes.[32,290] Initially adipose tissue was postulated to have simple energy storage, insulation and thermoregulation properties, but it is now known to play a role in key physiological processes, including: reproduction, apoptosis, inflammation, angiogenesis, hypertension, atherogenesis, coagulation, fibrinolysis, immunity, and vascular homeostasis.[16] Secretion of adipocytokines including leptin, adiponectin, Interleukin-6 (IL-6), adipsin, adiponectin, tumour necrosis factor α (TNFα) retinol-binding protein-4, transforming growth factor-β (TGFβ), prostaglandin E2 (PGE2), insulin-like growth factor-1 (IGF-1) and IGF-binding proteins (IGFBPs), have a role in obesity development, pathogenesis of the metabolic syndrome, and the aetiopathogenesis of insulin resistance and cardiovascular disease.[291] Secretion of free fatty acids (FFAs) and adipokines from adipose tissue induce signalling processes between the various organs to affect whole body metabolism.[32]

The 3T3-L1 mouse adipocyte cell line is used extensively as an *in vitro* model to probe the effects of factors and environmental conditions related to T2DM.[292] *In vivo*, adipocytes originate from multipotent mesenchymal stems cells that develop into adipoblasts (or pre-adipocytes),[16] which develop during the gestational period until they differentiate via the accumulation of lipids into adipocyte cells with distinct lipid droplets. Adipocytes are highly heterogeneous in terms of cell morphology and composition. Typically they have a nucleus surrounded by lipid droplets, referred to as a multilocular morphology.[16] These lipid droplets are a complex mixture of polar and neutral lipids including phospholipids, TAGs (mainly oleic and palmitic acids)[16] and cholesterol esters, which are involved in many aspects of cell biology, including membrane architecture/compartment formation, cell signalling, hormone regulation, energy storage and metabolism.[32] Alterations in lipid transport and metabolic processes are involved in human diseases including T2DM, obesity, CVD and neurodegenerative disorders.[32,293]

In obese individuals, adipocytes fail to regulate excess nutrients, and as a result, circulating fatty acids and glucose increase along with altered adiponectin secretion and dysregulated metabolism. These factors are postulated to contribute to the onset of insulin resistance and related complications that follow.[294] Hypertrophy of adipocyte cells (i.e., size expansion) is correlated with the release of inflammatory cytokines and then insulin resistance.[295] Hypoxic conditions can result from cell enlargement to limit dioxygen availability to the cell, promoting a Warburg-type metabolism.[20,26]

De novo synthesis of lipids (DNL) originates from FFA production via acetyl-CoA in an enzymatic process (**Figure 1.6**).[60] Adipocytes store energy as TAGs during lipogenesis and mobilise stored energy via lipolysis when needed in an insulin and epinephrine regulated manner.[32] Neutral lipids are stored for future uptake by muscle tissue and other processes in the body that require access to energy reserves. Phospholipids are polar in nature and are synthesised from neutral lipids and are involved in the formation of structural membranes.[296]

Under a brightfield microscope, cultured adipocytes range in shape, size and complexity (**Figure 4.1a)**. The cells in **Figure 4.1b** and **c** were chemically fixed to a CaF_2 substrate prior to spectroscopic imaging and optical micrographs were acquired using the microscope of the Bruker Hyperion 3000 system. These images showed a different morphology compared to live cells (**Figure 4.1a)**; however, the multilocular morphology was highly preserved. The compartments are rich in lipid esters/fatty acids and the use of vibrational spectroscopic techniques provide chemical and biological insights into the composition and distribution of the various lipids/fatty acids within a cell.[185,293]

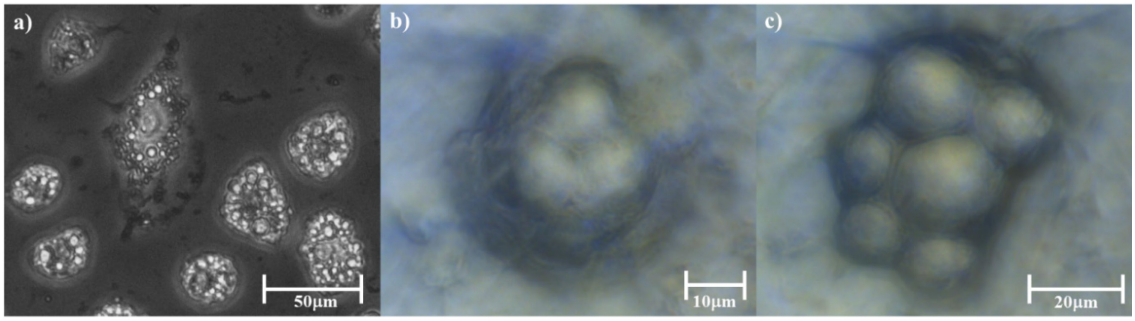

Figure 4.1: 3T3-L1 adipocyte cell morphology as observed in; a) culture media using an upright light transmission microscope (Olympus CKX31/CKX41 Phase Contrast and Fluorescence Inverted Microscope, 20x magnification); b) a round cell with partially resolved features; and c) a high-quality image clearly showing the multilocular structure. Images b) and c) were aquired from adipocytes chemically fixed to the CaF_2 substrate prior to image acquisition in transmission mode using the Hyperion 3000 microscope.

Two of the major challenges associated with spectroscopic analysis of adipocytes are fixation and the heterogeneous morphology. As discussed in Section 3.6, focussing the microscope to obtain the highest quality image and spectral data was challenging and this was observed in **Figure 4.1b**, which is typical of a very thick adipocyte, where most of the cell was in focus, however, the base of the cell was out of focus. The adipocyte in **Figure 4.1c** was not as thick as the one in **Figure 4.1b** and was in complete focus for spectral data acquisition.

Adipocytes are highly susceptible to cell rupture during fixation conditions where the osmotic pressure is not maintained, or under harsh separation techniques that include centrifugation. This results in the release of TAGs from ruptured cells that can be detrimental to the entire cell population.[32] The cold methanol fixation method described by Carter, *et al*.[258] was used in this study and resulted in intact cellular morphology (**Figure 4.1b** and **c**).

Gazi, *et al*.[201] recommended against formalin fixation as it contains methanol, which permeates the cell membrane and extracts intracellular lipids. Methanol-free paraformaldehyde fixation was used as an alternative to preserve lipid structure, followed by osmium tetroxide (OsO_4). One of the disadvantages of the use of OsO_4 is that the fixation occurs through reactions with the lipid double bonds.[201] Even though the fixation method employed in this study uses methanol, the process is performed at 195 K (dry ice) temperature with minimal exposure time, followed by rapid blotting and air drying, minimising the risk of lipid extraction.

Another common fixation method uses paraformaldehyde as the fixing agent and this method has also come under scrutiny because it cross-links proteins to the substrate; however, Diem, *et al*.[218] stated that the level of cross-linking is below the limit of detection by FTIR and will not result in any detectable changes. The SurePath method of fixation, which uses a mixture of methanol, ethanol, 2-propanol and water is another alternative.[297] This protocol was attempted, without success and based on the optical micrographs presented in **Figure 4.1b** and **c**, the cold methanol procedure resulted in acceptable morphology of fixed cells.

4.2 Experimental Design and Objectives

Reported herein are biochemical changes induced by sodium orthovanadate (Na_3VO_4 or V(V)) towards 3T3-L1 adipocytes in supplemented culture media to produce an MTT type cytotoxicity assay based on changes in FTIR spectra. A [V(V)] in the cytotoxic range was then used in a two-level factorial design to investigate the effects of glucose, fructose, vanadate and insulin resistance on adipocyte metabolism (**Figure 4.2**). The factors glucose, fructose and vanadate are continuous variables and insulin resistance is a category (binary) variable, i.e., insulin-sensitive or insulin-resistant. The response for each run was generated as a spectrum, or hyperspectral image for multivariate assessment. The overall objective of this study was to determine whether point spectra of single cells, acquired after treatment, could be used as molecular probes to better understand the action

of vanadate as an anti-diabetic/cytotoxic agent. Spectra acquired in this study were from single cells using the methodology described in Section 2.8.1. A similar study using the design in **Figure 4.2** and FPA imaging is described in Chapter 6.

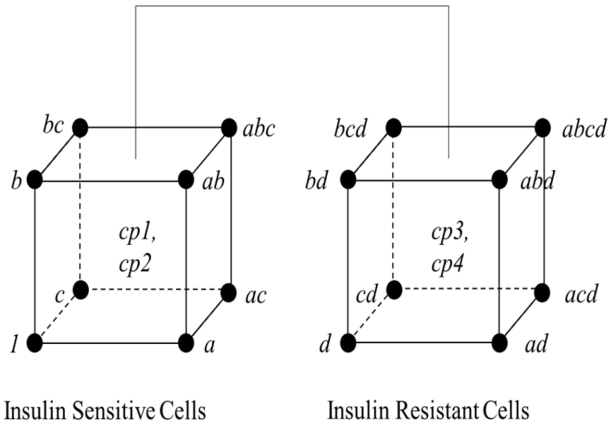

Run	Glucose (A)	Fructose (B)	Vanadate (C)	Insulin Resistant (D)
1	-1	-1	-1	-1
a	+1	-1	-1	-1
b	-1	+1	-1	-1
ac	+1	+1	-1	-1
c	-1	-1	+1	-1
ac	+1	-1	+1	-1
bc	-1	+1	+1	-1
abc	+1	+1	+1	-1
d	-1	-1	-1	+1
ad	+1	-1	-1	+1
bd	-1	+1	-1	+1
abd	+1	+1	-1	+1
cd	-1	-1	+1	+1
acd	+1	-1	+1	+1
bcd	-1	+1	+1	+1
abcd	+1	+1	+1	+1
cp1	0	0	0	0
cp2	0	0	0	0
cp3	0	0	0	0
cp4	0	0	0	0

Figure 4.2: Experimental design for investigating the effects of sugars, vanadate and insulin resistance using the orthogonal 2^4 full factorial design in 20 runs, (Chapter 1, Section 1.7.1). The design is based on two blocks defined by insulin sensitivity/resistance. Low levels of factors are defined by (-1) and high levels by (+1), while centre points are defined by (0).

4.3 Results

4.3.1 Vanadate Cytotoxicity

Vanadate cytotoxicity studies were performed on insulin-sensitive and -resistant cells. Insulin resistance was induced using Endothelin-1 (ET-1), which is a potent vasoconstrictor produced by endothelial cells that is preferentially released towards smooth muscle cells.[75] In response to insulin, activity of ET-1 and its receptor ETA are increased,[75] which leads to chronic hyperinsulinemia.[10]

3T3-L1 preadipocytes were seeded directly onto a CaF_2 substrate and differentiated before half of the cultures were treated with ET-1 for 24 h.[75] Cells were then treated according to the design in **Figure 4.2**. The release of CO_2 (amongst other metabolites, including lactate) during treatment increased the acidity of the medium, which resulted in the phenol red indicator changing colour from pink to orange when the cells were metabolising nutrients. In a cell culture medium supplemented with 10% FCS,

Glutamax^{TM} and antibiotic-antimycotic solution, a ^{51}V NMR spectrum of a 1.0 mM vanadate solution (**Figure 4.3**) showed the predominance of deprotonated VO_4^{3-} species (-541 ppm). Under physiological conditions, $[HVO_4]^{2-}/[H_2VO_4]^-$ was expected to be the predominant species, however, outside of the CO_2 environment of the incubator and Na_3VO_4 increased the media pH value to 8 and probably explained why $VO_4^{3-}$and not the protonated $[HVO_4]^{2-}/[H_2VO_4]^-$ species was dominant.[256]

Evidence of the divanadate species $[HV_2O_7^{3-}]$ was observed at -564 ppm[256] but in lower concentrations than VO_4^{3-} and a likely peroxidovanadium species was observed at even lower concentration at -624 ppm.[256] These data indicated that in cell culture medium, the main active species is V(V), however, as V(IV) and V(III) are paramagnetic, ^{51}V NMR cannot be used to detect these species.[298-299] **Figure 4.3** showed that V(IV) was only present in trace amounts since it broadens peak shapes, which were relatively sharp in the spectrum. The presence of V(III) is also unlikely as it is extremely oxygen sensitive at neutral pH values.[298] The observed orange colour of the media at lower concentrations of V(V) indicate that the 3T3-L1 cells were metabolising glucose in the presence of up to 62.5 μM V(V). In the range 125-250 μM V(V), the medium pH value was unchanged, which indicated the cells were no longer metabolising glucose via glycolysis. Based on this information, the IC_{50} value of vanadate for 3T3-L1 cells was expected to lie in the range 125-250 μM.

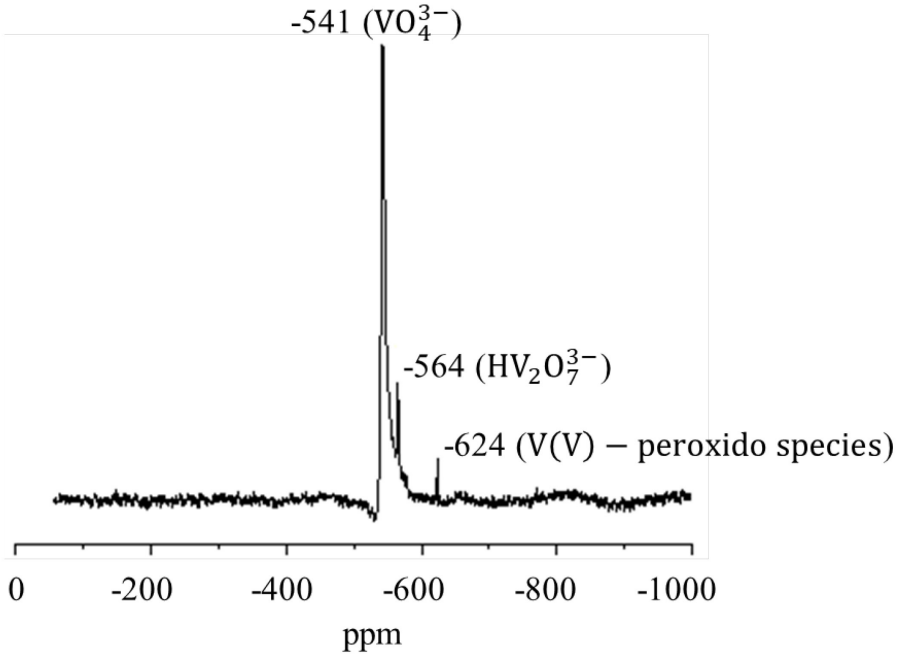

Figure 4.3: ^{51}V NMR spectrum of 1.0 mM Na_3VO_4 in cell culture medium (16 h pre-incubation + 72 h incubation at 310 K). Data courtesy of Dr. Aviva Levina.

4.3.2 FTIR Chemometric Assessments of Insulin Sensitive Single Cells

Raw FTIR spectra of the insulin-sensitive 3T3-L1 cells (**Figure 4.4a**) were processed over the 3050-1050 cm^{-1} region as second derivative (13-point smooth), then SNV over the 3050-2800 and 1800-1050 cm^{-1} regions (**Figure 4.4b**). Characteristic lipid, fatty acid and protein bands associated with adipocytes were present in the wavenumber regions 3010-2800 and 1750-1550 cm^{-1}.[194,300] While examination of the raw and processed data revealed some changes in relative band intensities, multivariate analysis methods were required to decipher relevant information.

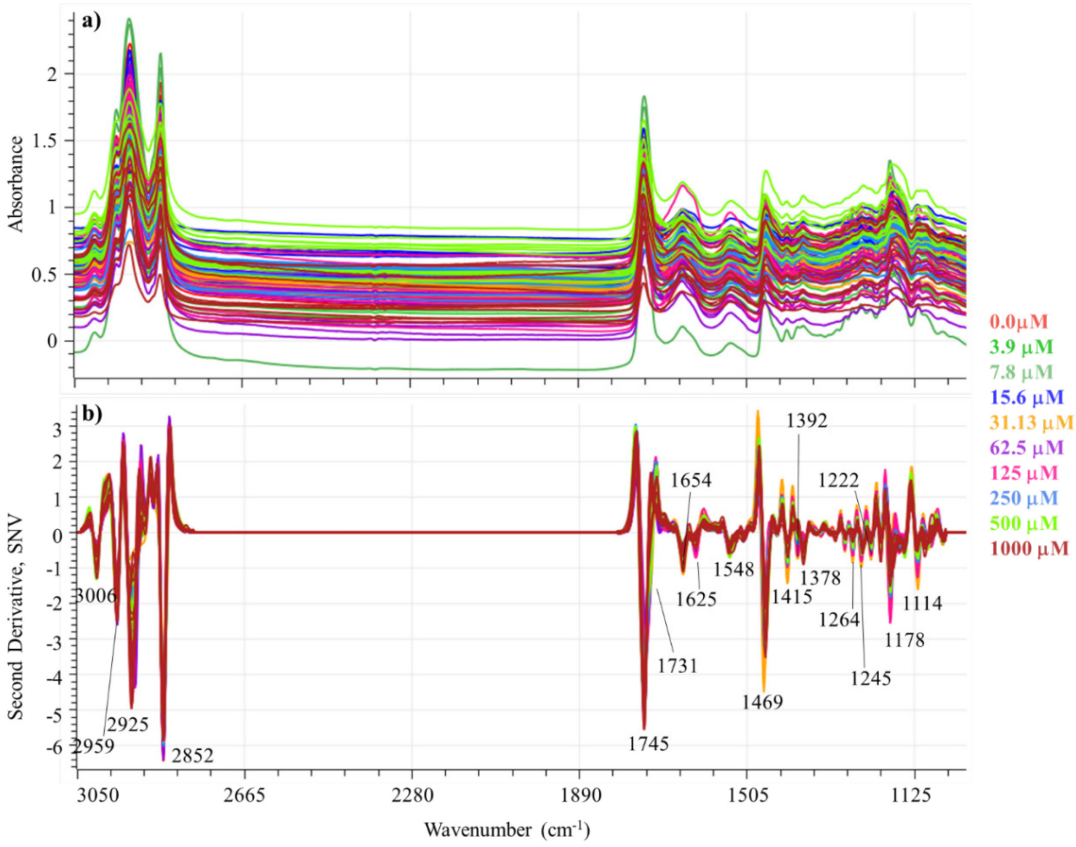

Figure 4.4: a) raw; and b) processed FTIR spectra of individual insulin-sensitive 3T3-L1 cells treated with various concentrations of vanadate. The prominent absorbance bands (in the negative direction only) are listed in the figure with assignments in **Table 1.1**. (Chapter 1). The legend defines the treatment concentrations used in the study.

PCA was applied to the processed data over the 3050-1050 cm^{-1} region to evaluate vanadium dose-dependent changes in the FTIR spectra on insulin-sensitive 3T3-L1 cells (**Figure 4.5**). This PCA model described 86.5% of the **X**-variance in four PCs with 82.3% in three PCs. These data did not show any discernible trends related to treatment. However, when the treatments were grouped based on an arbitrary low (0-15 µM), medium (31.5-125 µM) and high (250-1000 µM) treatment grouping, a small trend was

observed in the t_2 direction when the data were grouped using local Hotelling's T^2 ellipses at the 95% confidence interval (**Figure 4.5b**).

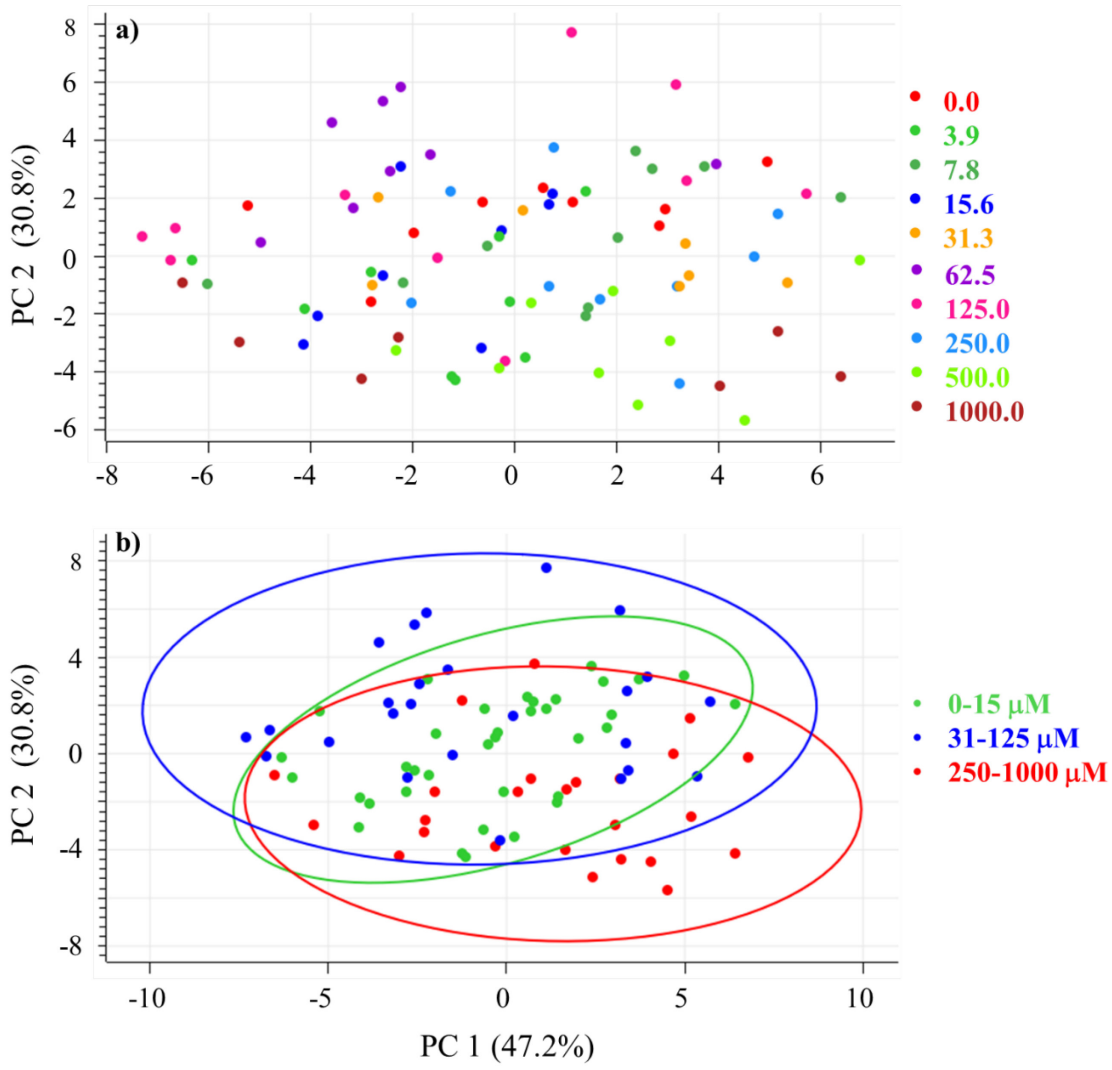

Figure 4.5: t_1 vs. t_2 scores plot for insulin-sensitive 3T3-L1 vanadate study; a) scores coloured by vanadate treatment concentration; and b) separated into three arbitrary groups labelled; low 0-15 µM; medium 31-125 µM; and high 250-1000 µM. Local Hotelling's T^2 ellipses were drawn at 95% confidence.

The scores vs. [V(V)] plots for the first three PCs are shown in **Figure 4.6** as individual point plots and interval plots. The t_1 scores plotted against [V(V)] showed that beyond 31.3 µM, a linear increase in scores values were observed (**Figure 4.6a)**. Thus, the t_1 direction most likely described the insulin-mimetic/enhancing action of vanadate between 0-31.3 µM, followed by a change in biochemistry between 62.5-1000 µM.

The t_2 direction, displayed a similar trend in the data after 31.3 µM, this time a negative linear trend in scores was observed. (**Figure 4.6b)**. The t_3 vs. [V(V)] plot (**Figure 4.6c)** exhibited three separate linear relationships. The linear trend between 0-15.6 µM V(V)

showed that the cells responded in a linear manner to vanadate before a negative linear trend was observed over the range 15.6-62.5 µM. A step in the positive t_3 direction occurred at 125 µM followed by a second linear decrease between 125-1000 µM.

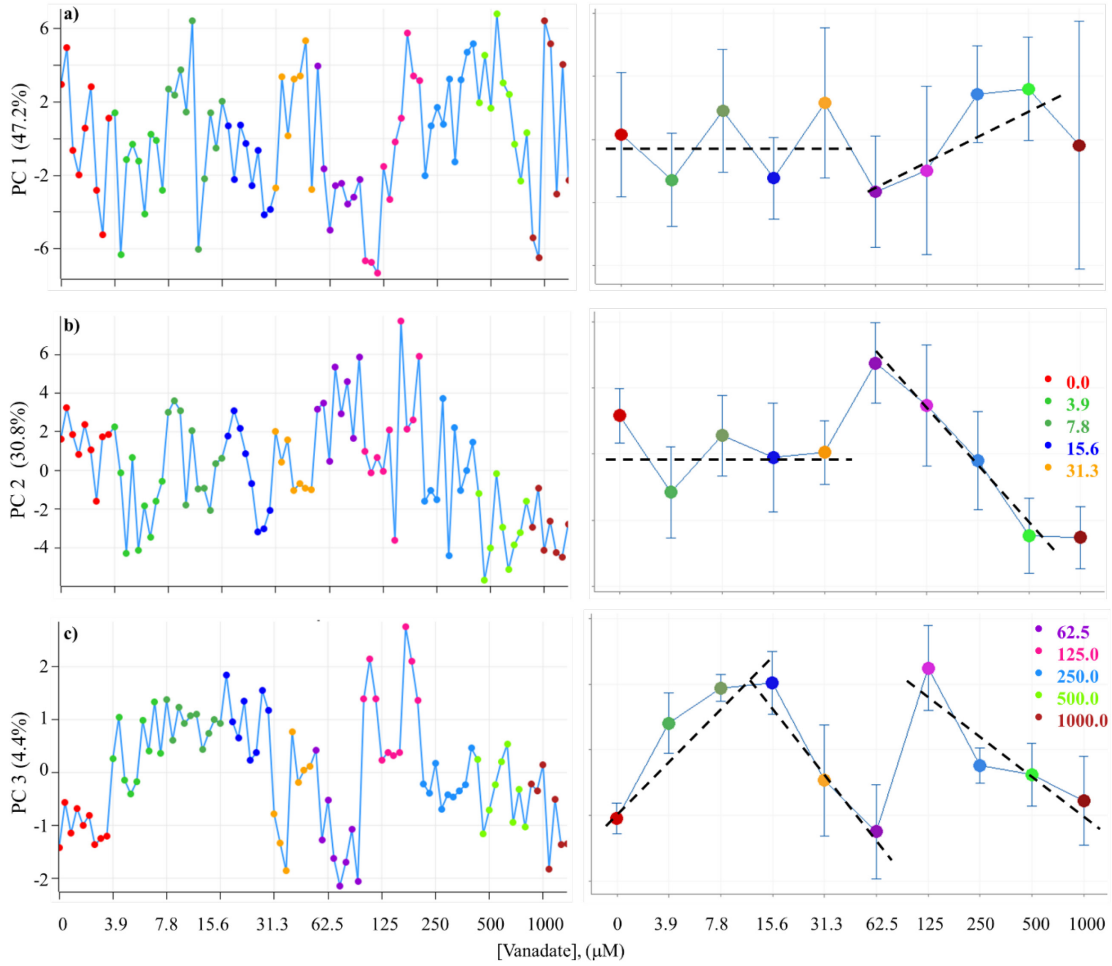

Figure 4.6: $t_1 - t_3$ scores vs. [V(V)] for insulin-sensitive 3T3-L1 adipocytes as all data and interval plots: a) t_1 scores plot; b) t_2 scores plot; and c) t_3 scores plot. Dotted lines represent the observed trends in the data. Intervals were drawn at 95% confidence.

These data were consistent with a number of dose-dependent biochemical changes induced by vanadate and indicated that insulin-sensitive adipocytes may be tolerant to V(V) treatment up to 31.3 µM. The t_1 and t_2 vs, [V(V)] plots indicated that a change in biochemistry occurred in a linear manner beyond this concentration point up to 500 µM. The t_3 vs. [V(V)] plot indicated that a smaller, more complex, biochemical process was occurring concurrent with the changes described by the t_1 and t_2 directions. Over the 72 hr treatment protocol, there was an associated pH change in the media, observed visually as colour changes over 0-62.5 µM consistent with reduced glucose metabolism induced by higher [V(V)]. During glycolysis, cells generate CO_2 under aerobic conditions according to the general reaction,[12]

$$\text{Glucose} \xrightarrow{Glycolysis} 2\ \text{Pyruvate} \xrightarrow{-CO_2} 2\ \text{Acetyl} - \text{CoA} \xrightarrow{Citric\ Acid\ Cycle} 4CO_2 + 4H_2O$$

The generated CO_2 lowers the pH of the media, possibly through the formation of carbonic acid.[301] The lack of this colour change in the media at [V(V)] > 62.5 μM was attributed to reduced cell viability and the onset of cell death.

Although there were clear trends observed, this experiment was based on a relatively small number of spectra collected on individual cells and future studies would require a much larger sample set to be studied over a number of cell cultures to fully understand the observed variability. However, this study was sufficient to gain an initial understanding of the system to plan subsequent experiments. Scores for PCs > 3 did not reveal any further trends and each described < 2% of the total **X**-variance.

In summary, these data showed at least four dose-dependent biochemical changes. Those observed over 0-15 μM, were postulated to be the known insulin mimetic effect of vanadate,[150,153] which was observed as the linear trend in t_3 vs. [V(V)] (**Figure 4.6c)** compared to the lack of trending in the t_1 and t_2 plots. Beyond 31.3 μM, vanadate was expected to transition into a cytotoxic agent, as evidenced in Chapter 5, Section 5.3.2, where concentrations ranges > 50 μM induced cytotoxic effects in the insulin-sensitive HepG2 cell line.

The corresponding PC loadings plots (**Figure 4.7**) are shown with wavenumbers of prominent bands marked. The p_1 loadings were dominated by bands associated with lipids and free fatty acids (**Table 1.1**). The band around 3010 cm^{-1} was assigned to *cis*-conformations of ν (=CH_2) modes in unsaturated fatty acids and lipids.[193] Bands at 2920 and 2850 cm^{-1} were assigned to ν_{as} and ν_s (CH_2) modes of membrane lipids and fatty acids,[195] and in the p_1 loadings, these bands showed splitting into positive and negative loading contributions. In particular, the nominal 2920 cm^{-1} band was split into two bands at 2923 and 2909 cm^{-1} and the nominal 2850 cm^{-1} band was split into bands at 2855 and 2844 cm^{-1}, respectively. This observed splitting was attributed to diverse changes in cell membrane integrity or fluidity induced over the range of vanadate treatments[302] and may be an indication of chemical modification due to lipid peroxidation.[95,160,165,202,303-305]

The bands at 2909 and 2844 cm^{-1} showed strong positive correlations with those at 1754, 1731, 1469, 1415 and 1180 cm^{-1} associated with the lipid character of the cells. The band at 1754 cm^{-1} corresponded to ν (C=O) in lipid esters including TAGs,[181] while bands at

1731 and 1415 cm^{-1} were associated with FFAs.[193,198,200,208-209,306] The band at 1470 cm^{-1} was assigned to δ ($-CH_2$) modes in lipids, aliphatic chains of fatty acids and proteins.[202]

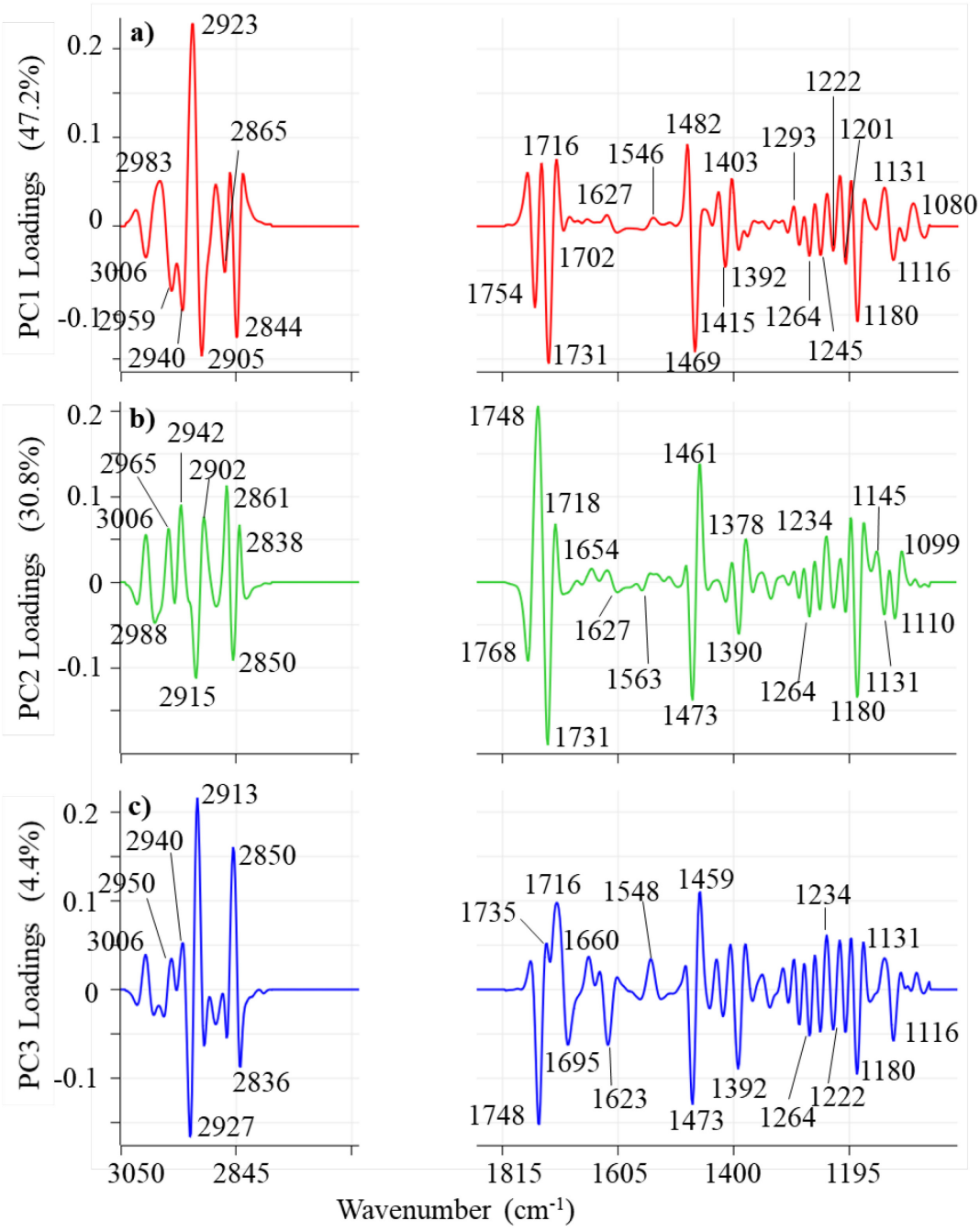

Figure 4.7: a) p_1; b) p_2; and c) p_3 loadings plots for the insulin-sensitive 3T3-L1 adipocytes treated with vanadate.

Bands around 1400 cm^{-1} were associated with bending modes in deprotonated $-COO^-$ groups in lipids while those between 1180-1150 cm^{-1} to stretching modes of C-O groups related to lipids, DNA and possibly tyrosine groups in cell proteins.[195,307] Wood,[182] also assigned bands around 1180 cm^{-1} to A-DNA and ribose, however, this band could also be attributed to lipid content given that adipocytes are mainly lipid in composition.[30] The

bands between 1120-1080 cm^{-1} were assigned to $(RO)_2PO_2^-$ bands associated with DNA and phospholipids.[182,184,193,197,306]

The PC1 direction showed that beyond 31.3 µM, vanadate induced biochemical changes that increased lipid and fatty acid content in the cells and resulted in a change in membrane lipids, as evidenced by the decrease in the band at 2923 cm^{-1} with a corresponding increase in the bands at 2909 and 2844 cm^{-1}. Ricciardi, *et al.*[195] reported that the ratio of the bands at 2922 cm^{-1} (ν_{as} CH_2) and 2957 cm^{-1} (ν_{as} CH_3) related to changes in membrane lipids associated with apoptosis. The ratio of these band intensities vs. [V(V)] for insulin-sensitive cells (**Figure 4.8**) showed that the profile closely resembled the inverse profile of the t_1 vs. [V(V)] plot in **Figure 4.6a** and indicated that the PC1 direction mainly described changes in membrane lipids in adipocytes cells due to the action of increasing [V(V)].

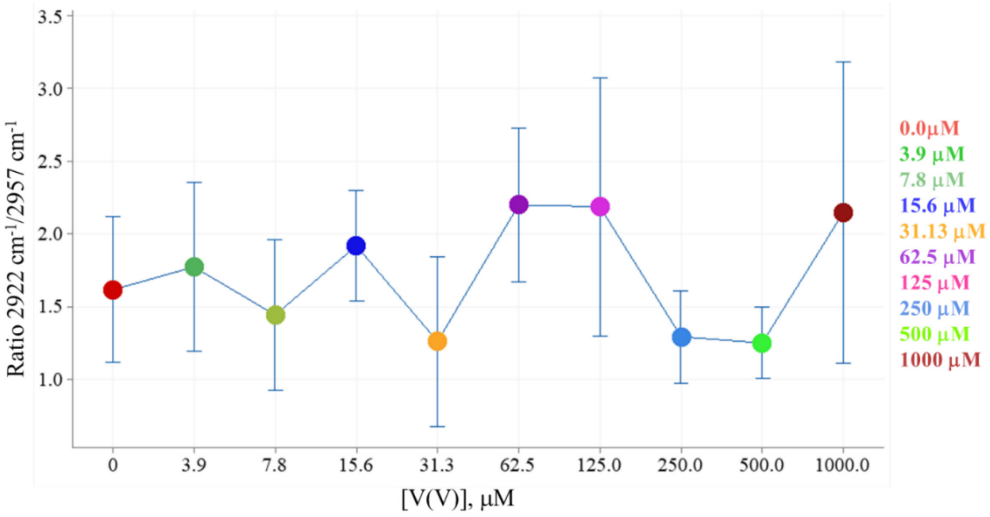

Figure 4.8: Ratio of processed FTIR band intensities at 2922 and 2957 cm^{-1} vs. [V(V)] for insulin-sensitive adipocytes. Intervals are displayed for each treatment at the 95% confidence level.

The t_2 scores displayed a negative trend between 62.5-500 µM compared to the positive trend observed in the t_1 scores over this range. This trend was consistent with the large loadings observed at 1731, 1473 and 1180 cm^{-1} attributed to fatty acids and smaller contributions from the loadings at 1390, 1264, 1131 and 1110 cm^{-1} mainly associated with $(RO)_2PO_2^-$ bands of phospholipids, DNA and RNA.[172,202] The p_2 loadings showed a positive correlation between the bands at 2915 and 2850 cm^{-1}, associated with membrane lipids,[195,202,205] which were also positively correlated to the bands listed above. These bands were negatively correlated to those at 1748, 1718, 1464, 1378, 1234 and 1099 cm^{-1} also associated with lipids (**Table 1.1**). The p_2 loadings also showed what may

be a small contribution from proteins at 1654 and 1627 cm^{-1}, associated with amide I α-helix and β-sheet secondary structures, respectively.[172] The band at 1654 cm^{-1} may also have contributions from ν (C=C) modes,[193] however, the presence of the 1627 cm^{-1} band indicated that this was most likely a protein band. These bands were positively correlated to the 1748, 1464, 1378, 1234 and 1099 cm^{-1} bands listed above. This observation may be associated with vanadate induced changes in intracellular TAG/phospholipid and fatty acid content. Ricciardi, *et al.*[195] reported that the ratio of the band intensities at 1146 cm^{-1} ν (C-O) and 2957 cm^{-1} ν_{as} (CH_3) was related to lipid peroxidation induced in cells due to oxidative stress. The 1145 cm^{-1} band was also correlated to the band at 1748 cm^{-1}, also consistent with lipid peroxidation.[202] **Figure 4.9** provides a plot of the intensity ratio 1146/2957 cm^{-1} vs. [V(V)] for insulin-sensitive cells.

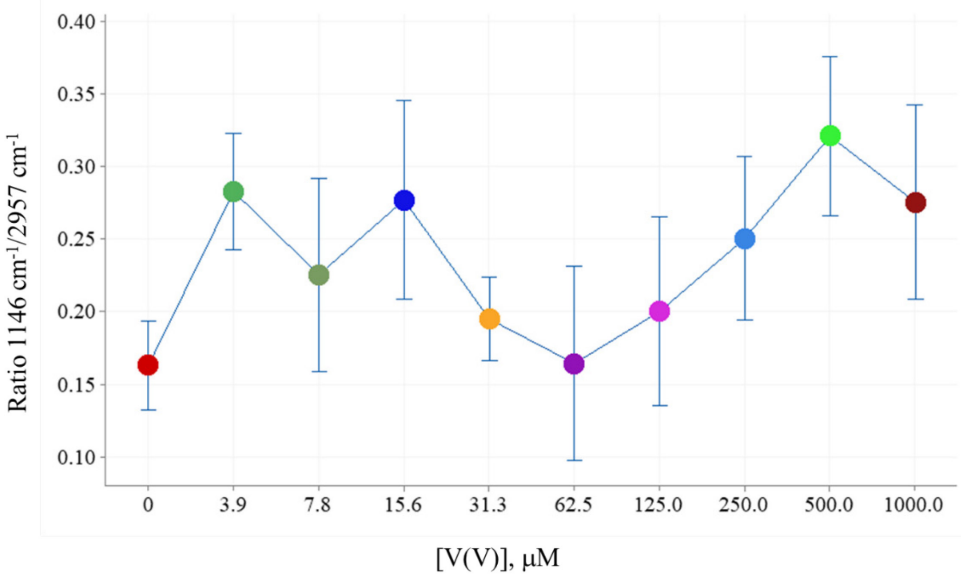

Figure 4.9: Ratio of processed FTIR band intensities at 1146 and 2957 cm^{-1} vs. [V(V)] for insulin-sensitive adipocytes. Intervals are displayed for each treatment at the 95% confidence level.

The profile in **Figure 4.9** closely resembles the inverse profile of the t_2 vs. [V(V)] plot in **Figure 4.6b** and indicated that the PC2 direction was mainly describing lipid peroxidation in adipocytes cells due to the action of increasing [V(V)]. In Chapter 6, FPA images of 3T3-L1 cells showed that regions close to the cell membrane contained the highest intensities of the 2920 and 2850 cm^{-1} bands and was consistent with the observation made here that the p_2 loadings were differentiating between membrane changes and changes in the cell interior. The FPA images in Chapter 6 also showed compartmentalisation of lipids and fatty acids into specific lipid droplets and this may be an indication of redistribution of these species under oxidative stress.[308]

The p_3 direction (**Figure 4.7c**) described three distinct biochemical processes displayed in the t_3 vs. [V(V)] plot. The changes modelled by this PC were minor (4.4%) compared to the first two PCs (78%). The first biochemical process occurred between 0-15 μM and was associated with a positive trend in t_3 values associated with increases in band intensities at 2927, 1748, 1473, 1392 (lipids), 1695, 1623, 1264 (α-helix, β-sheet and amide III respectively), 1222, 1180 and 1116 cm^{-1} (DNA and $(RO)_2PO_2^-$) changes (**Table 1.1**). Increases in the protein band at 1623 cm^{-1} (amide I, β-sheet) were associated with protein aggregation,[175,203] and increased β-sheet protein generation has also been associated with tyrosine phosphorylation,[309] which is an essential mechanism of insulin action for stimulating glucose uptake.[310]

The negative trend in the scores between 15.6-62.5 μM corresponded with a decrease in intensity in the bands listed above and an increase in band intensities at 3006, 2950, 2913, 2850, 1716, 1660, 1548 and 1459 cm^{-1}, and in particular, changes in membrane lipids and β-turns (1660 cm^{-1}) and the band around 1716 cm^{-1} were related to changes in DNA content in cells.[182] A discontinuous rise in score values from 62.5 to 125 μM was observed in the t_3 vs. [V(V)] plot and was followed by a linear trend towards negative values over the concentration range 125-1000 μM. These may be related to cellular defence mechanisms producing lipid stores to overcome oxidative stress during apoptosis.[311] Between 125-1000 μM, cellular lipid content was decreased and the high loadings at 2913 and 2850 cm^{-1} indicated lipid peroxidation was affecting the integrity of cellular membranes, which induced the onset and progression of apoptosis, consistent with the literature.[195,202]

4.3.3 FTIR Chemometric Assessments of Insulin Resistant Single Cells

Insulin resistance was induced by ET-1 (24 hr, 37 °C, 5% CO_2) in 3T3-L1 adipocytes, then treated with increasing concentrations of vanadate (Section 4.3.2). The raw spectra of the insulin-resistant cells (**Figure 4.10a**) were processed by second derivative, followed by SNV normalisation (**Figure 4.10b**) over the wavenumber region 3050-1050 cm^{-1}. These spectra had similar spectral profiles to those from insulin-sensitive cells (**Figure 4.4**). Main features included lipid ester/fatty acid bands associated with adipocytes at 3006, 2960, 2923, 2852, 1740, 1731, 1467 1413 and 1180 cm^{-1}, proteins at 1656, 1625 and 1546 cm^{-1}, and DNA/phosphodiester bands at 1708, 1264-1199 and 1080 cm^{-1} (**Table 1.1**).

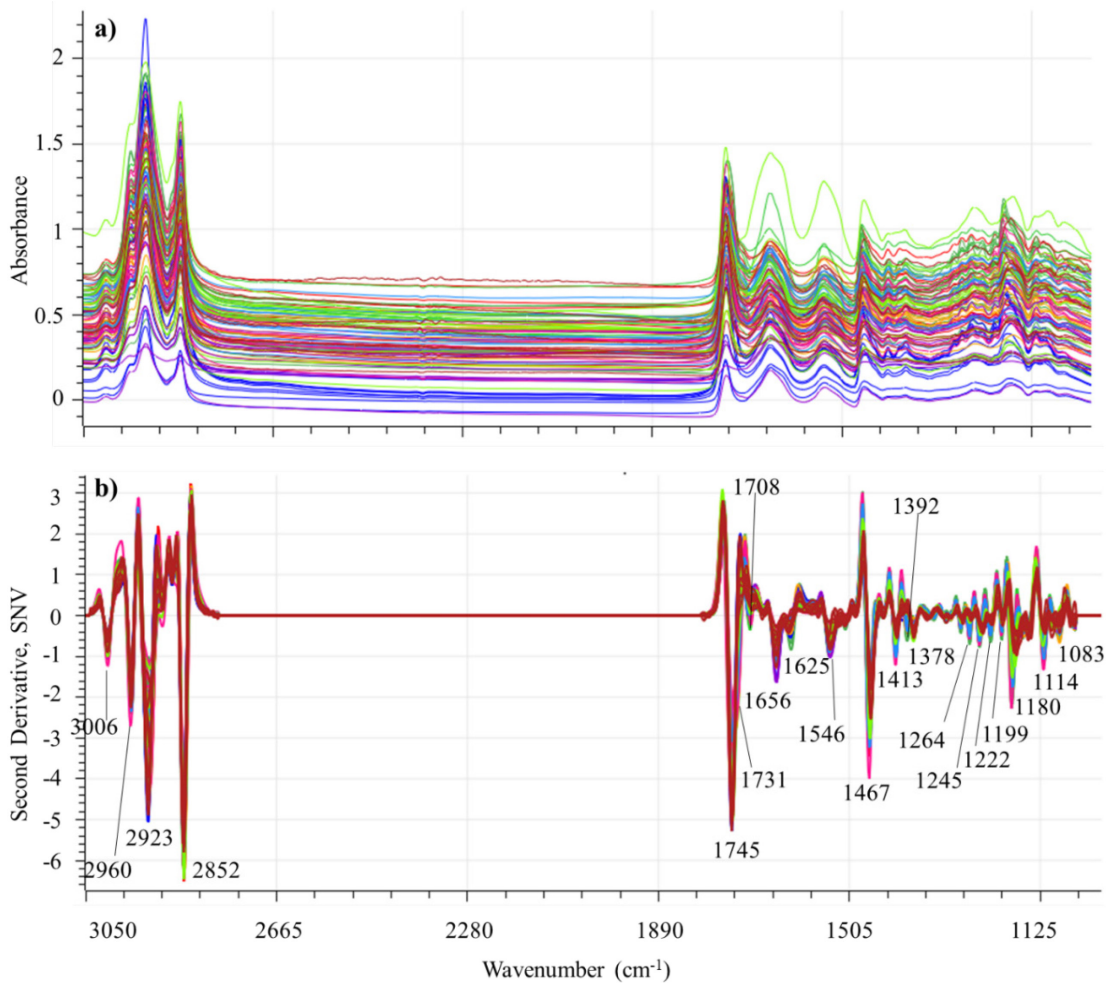

Figure 4.10: a) raw; and b) processed FTIR spectra of insulin-resistant 3T3-L1 adipocytes treated with various concentrations of vanadate. The prominent band assignments are listed in **Table 1.1**.

The t_1 vs t_2 plot for a PCA model generated from processed data over the 3050-1050 cm^{-1} range (**Figure 4.11**) showed that 74.9% of the **X**-variance was described in two PCs and 79.3% in three PCs. The points in the scores plots were coloured by [V(V)] into arbitrary low, medium and high vanadate concentrations, but did not show any distinct clustering of the treatment types (**Figure 4.11b**). The t_1 vs. [V(V)] plot indicated three dose-dependent biochemical processes (**Figure 4.12a)**. There was no effect observed until a step change from positive to negative scores at 15.6 µM vanadate concentration, followed by an increasing linear trend over 15.6-125 µM and a decreasing linear trend over 125-1000 µM. These data may be a first indication that insulin-resistant adipocytes are tolerant of vanadate over the range 7-15 µM compared to the 31.3 µM observed for insulin-sensitive cells.

The t_2 direction showed a linear trend from negative to positive score values over the entire concentration range 0-1000 µM. The t_3 direction showed a similar trend to the

corresponding t_3 scores for insulin-sensitive cells (**Figure 4.6c**) over the concentration range 0-15 µM, which may be an indication of the insulin-mimetic/enhancing action of vanadate. A similar step change occurred at 31.3 µM, however, unlike the t_3 scores for insulin-sensitive cells, the same increase in score values, followed by the negative linear trend was not observed for insulin-resistant cells. This may be a result of the high levels of oxidative stress in these cells and their inability to induce pathways to minimise cellular damage.[312]

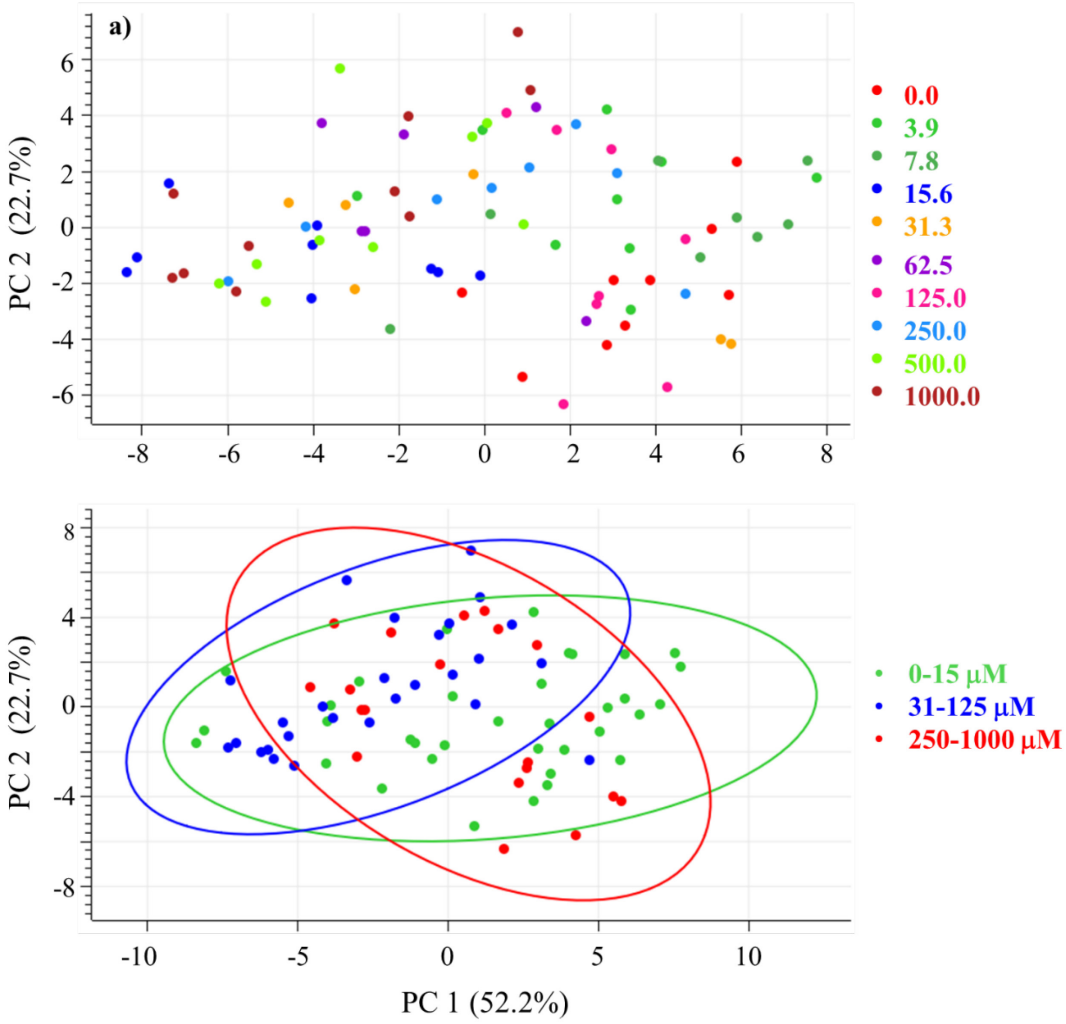

Figure 4.11: t_1 vs. t_2 scores plot for insulin-resistant 3T3-L1 vanadate study: a) scores coloured by vanadate treatment concentration; and b) separated based on three groups labelled; low range, 0-15 µM; medium range, 31-125 µM; and high range 250-1000 µM. Local Hotelling's T^2 ellipses were drawn at the 95% confidence level.

The corresponding p_1-p_3 loadings plots (**Figure 4.13**) showed that the p_1 direction was very similar to corresponding p_1 direction for insulin-sensitive cells, however, they were describing different biochemical processes.

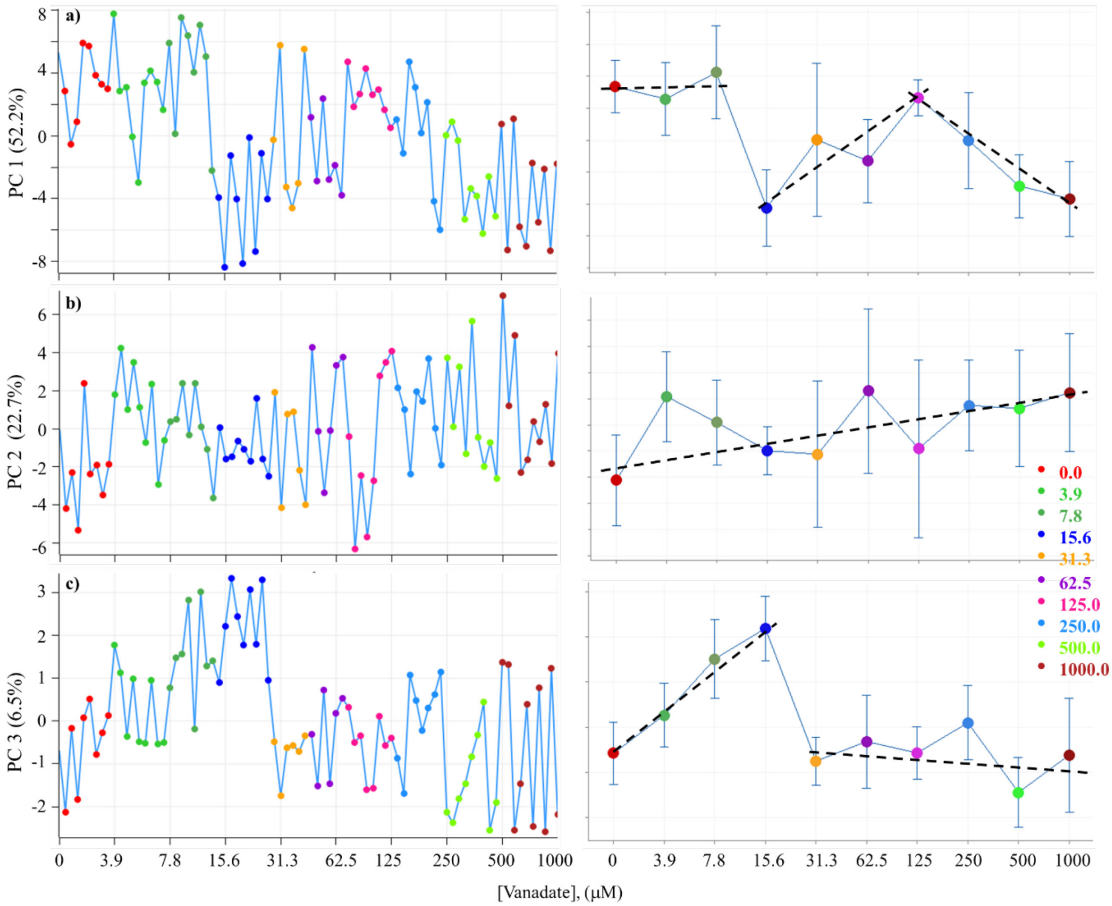

Figure 4.12: t_1 – t_3 scores vs. [V(V)] as individual data and interval plots for insulin-resistant 3T3-L1 adipocytes: a) t_1 scores plot; b) t_2 scores plot; and c) t_3 scores plot. The dotted lines represent the trends observed in the data.

Over the range 0-7.9 μM, insulin-resistant cells have lower band intensities at 1745 cm^{-1} for lipid esters and higher band intensities for fatty acids (1731 and 1715 cm^{-1}). These data indicate that there is already a higher content of fatty acids within insulin-resistant cells in this range.[60] At 15 μM, a step change to negative scores corresponded with increased production of TAGs and a reduction in the fatty acid content, which may be an indication of DNL. A linear increase towards positive score values followed over the range 15-125 μM, which corresponded to decreases in TAGs and increased fatty acid content. Increased production of TAGs was observed again over the range 125-1000 μM. The lack of the band at 3006 cm^{-1} ν (C-H) for *cis*-alkenes in the p_1 direction indicated that the biochemical processes described by this direction were associated with saturated fatty acids.[313-314] The observations made for the p_1 direction indicate that very complex biochemical changes were occurring in response to oxidative stress induced by increasing [V(V)].

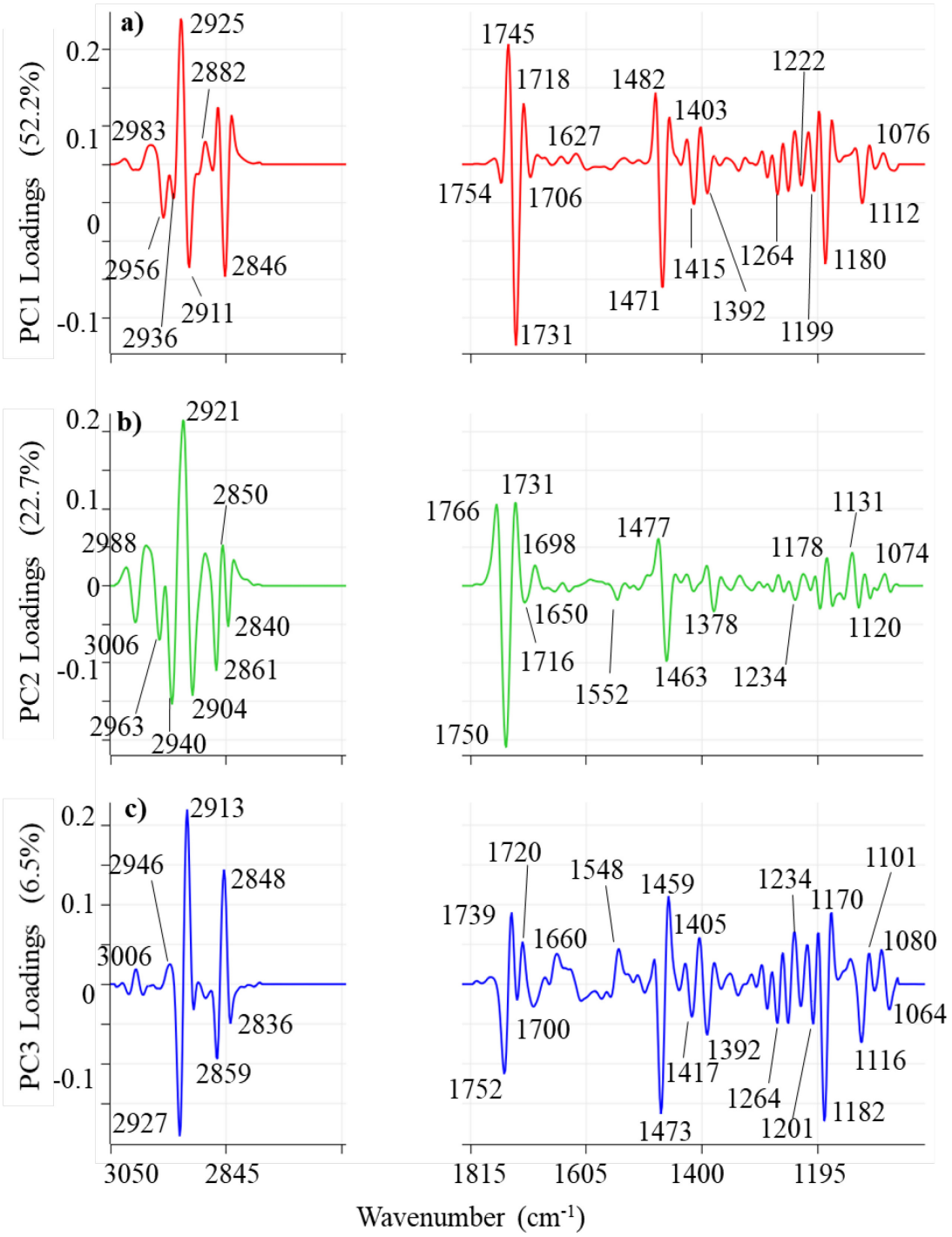

Figure 4.13: a) p_1; b) p_2; and c) p_3 loadings plots for the insulin-resistant 3T3-L1 vanadate treatment model.

The ratio of the absorbance bands at 1146 cm^{-1} ν (C-O) and 2957 cm^{-1} ν_{as} (CH_3) was related to lipid peroxidation induced in cells due to oxidative stress (Section 4.3.2).[195] **Figure 4.14** provides a plot of the ratio of these absorbances vs. [V(V)] for insulin-resistant adipocytes and showed an inverse relationship to the t_1 vs. [V(V)] plot of **Figure 4.12a**, therefore, these two plots were describing lipid peroxidation induced by vanadate.

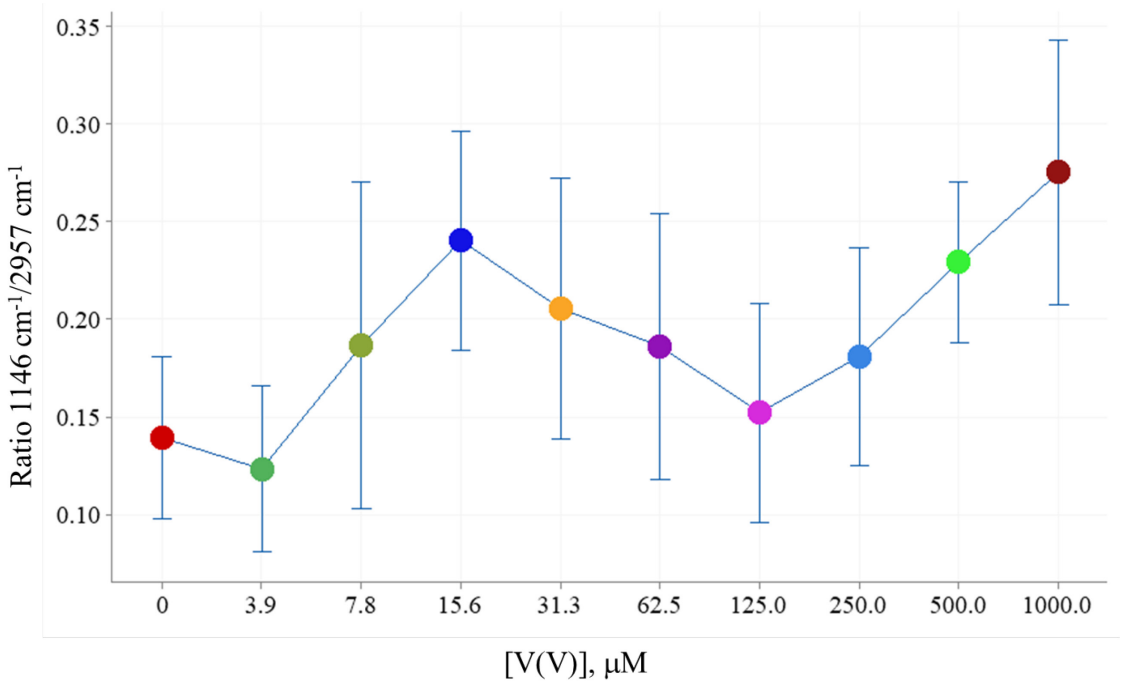

Figure 4.14: Ratio of processed FTIR bands at 1146 and 2957 cm^{-1} vs. [V(V)] for insulin-resistant adipocytes. Intervals are displayed for each treatment at the 95% confidence level.

The p_2 direction for insulin-resistant adipocytes is markedly different from the corresponding p_2 direction for insulin-sensitive cells (**Figure 4.7b**). The main difference was related to the prominent band at 2921 cm^{-1} associated with membrane lipids,[195,202,205] which decreased with increasing [V(V)] over the entire range. This corresponded with an increase in TAGs as evidenced by the bands at 1750, 1463, 1378, 1234 and 1120 cm^{-1}. At lower concentrations of vanadate, the bands at 1731 and 1178 cm^{-1} were assigned to cells containing more fatty acid content in the p_1 direction. [197,315] Also, the band at 1131 cm^{-1} showed increased band intensity and was assigned to lactate production, typical of increased glucose metabolism.[212]

The ratio of the bands at 2922/2957 cm^{-1} vs. [V(V)] (**Figure 4.15**) showed a positive linear trend and was attributed to changes in membrane lipids.[195] Except for the potential outlier at 15.6 µM, this plot resembled the p_2 vs. [V(V)] plot (**Figure 4.12b**) and along with the high loading of the 2921 cm^{-1} band, these data indicate that the p_2 direction was describing lipid membrane changes in a dose-dependent manner with increasing [V(V)]. The observed loading band at 3006 cm^{-1} indicated that this PC also described the production of unsaturated lipids,[316] corresponding to an increase in band intensity at 1750 cm^{-1}.

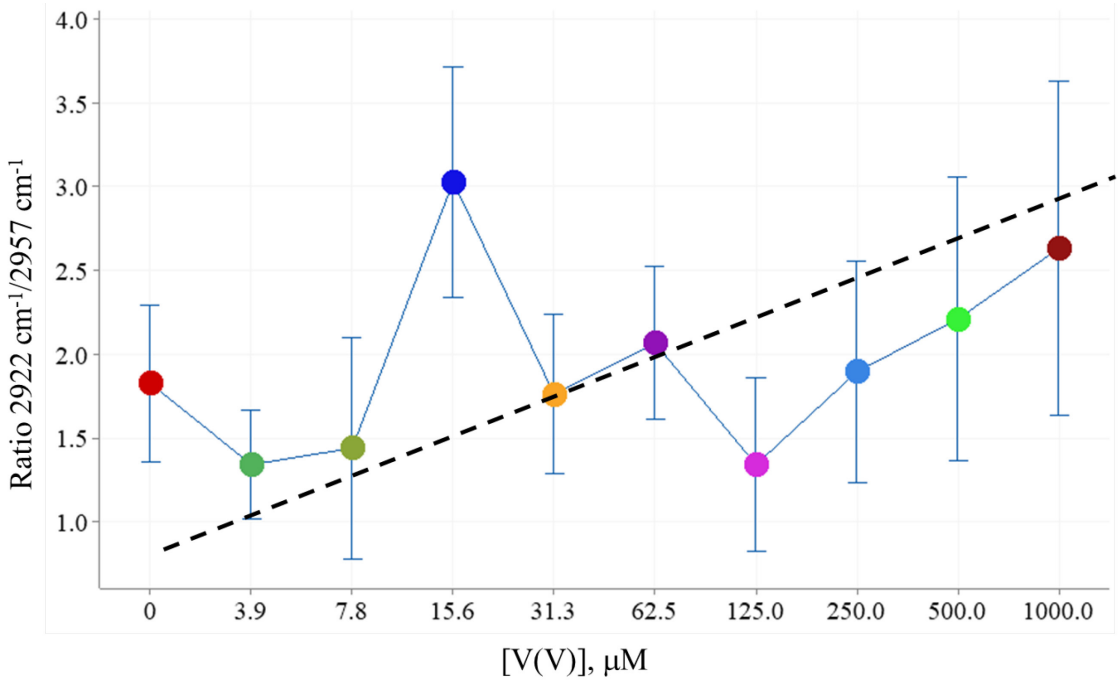

Figure 4.15: Intensity ratio of processed FTIR bands at 2922 and 2957 cm^{-1} vs. [V(V)] for insulin-resistant adipocytes. Intervals are displayed for each treatment at the 95% confidence level.

Unlike the corresponding p_3 loadings for insulin-sensitive cells, the insulin-resistant treatment loadings did not show the same two-step biochemical process and only showed a single step change to negative scores over the range 31-1000 µM. This change corresponded to an increase in the band intensities at 2913 and 2848 cm^{-1}, which have been attributed to membrane changes associated with apoptosis,[195] and protein secondary structural changes between 1660 cm^{-1} (β-turns),[182,203] and 1548 cm^{-1} (amide II).[180] Other contributions observed were the highly complex loadings between 1480-1392 cm^{-1} associated with bending vibrations in lipids and proteins,[172] and bands between 1180-1080 cm^{-1} associated with DNA and C-O stretching bands.[182]

4.3.4 Comparison of Insulin Sensitive and Insulin Resistant Cells

A PCA model of all data was performed and colour grouped by insulin-sensitive and -resistant cells. The t_1 vs t_2 scores for this model (**Figure 4.16**) showed no separation between data obtained from the two cell types. Analysis of other combinations of PCs did not reveal any separation in the treatment groups. To verify insulin-resistance was induced by the ET-1 treatment, a partial least squared discriminant analysis (PLS-DA) model of the controls (0 µM V(V)) was performed on insulin-sensitive and -resistant cells. A simple two-factor PLS-DA model separated the insulin-sensitive and -resistant cells (**Figure 4.17**).

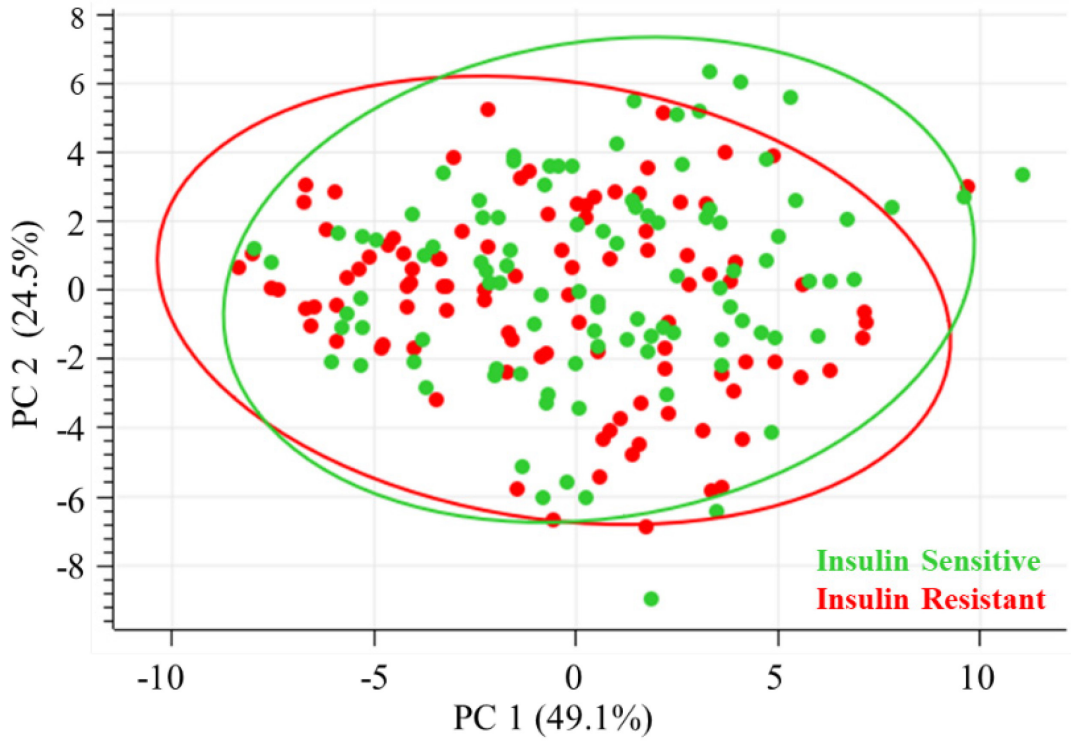

Figure 4.16: t_1 vs. t_2 scores for the PCA model of combined insulin-sensitive and -resistant 3T3-L1 cells treated with various concentrations of vanadate. This data showed that there was no separation in the first two PCs at the 95% confidence level.

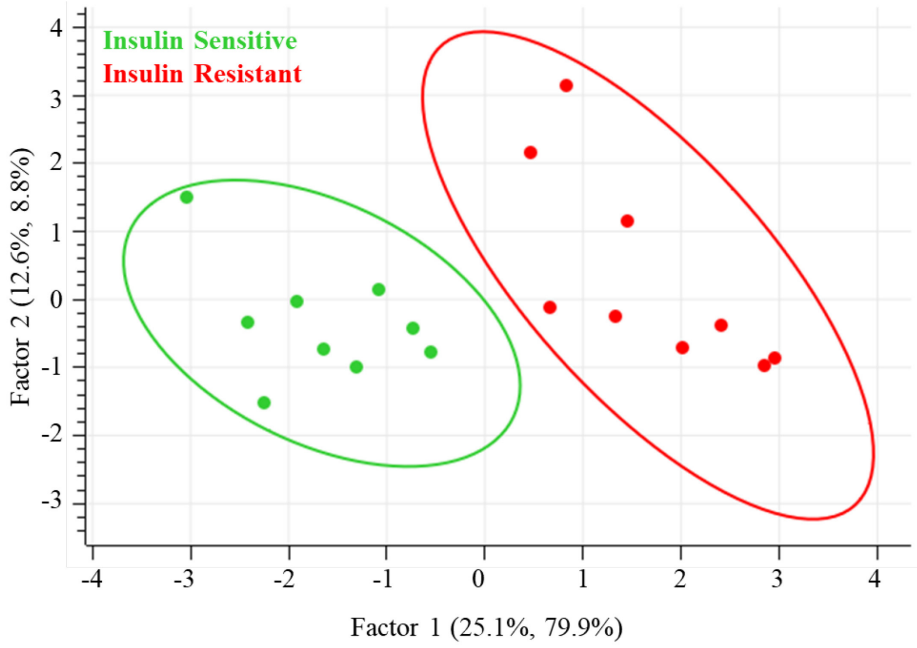

Figure 4.17: t_1 vs. t_2 PLS-DA scores for insulin-sensitive and -resistant adipocytes grown in normal supplemented media only. Local Hotelling's T^2 ellipses were drawn at the 95% confidence level.

The w_1 loading weights described the main differences between the two controls (**Figure 4.18**). Although the PLS-DA scores separation was small, the information in the w_1 loading weights were consistent with the difference between insulin-sensitive and -resistant cells. The former showed higher lipid content at 1747 cm^{-1} and lower fatty acid and protein content, 2917, 2844, 1731, 1654, 1629 and 1548 cm^{-1}. The increased intensities of the bands at 2917, 2844 and 1731 cm^{-1} were indicative of lipid membrane changes and lipid peroxidation[195] and these bands were associated with the insulin-resistant cells. Higher order PCs did not reveal any separation between the two treatment types.

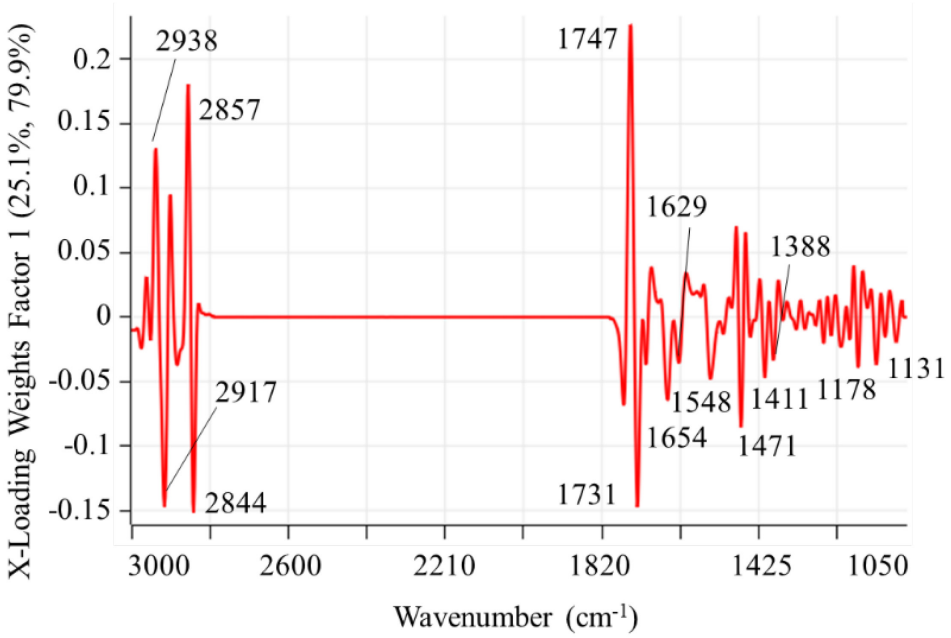

Figure 4.18: w_1 PLS-DA loading weights showing the main spectral differences between insulin-sensitive and -resistant 3T3-L1 adipocytes.

In Section 4.3.5, two of the design points, namely glucose (*a*) and glucose/insulin-resistant (*ad*), cultured in glucose media (**Figure 4.2**). FTIR spectra acquired on these treatments were projected onto the model in **Figure 4.17** and their location in PC space was within their expected class membership, which was also consistent with insulin-resistance being induced in these cells. The projected data is shown in **Figure 4.19**.

Factor 1 (**Figure 4.19**) described the difference between insulin-sensitive and -resistant cells and factor 2 described the differences between the natural variation of the two cultures used. Trial 1 cells were sub-divided from the same culture prior to differentiation, treatment, and fixation onto CaF_2 substrates. The trial 2 cells were sub-divided treated

and fixed from a different culture. Therefore, the w_2 loading weights provide test set validated information on the biological differences between cultures in this analysis.

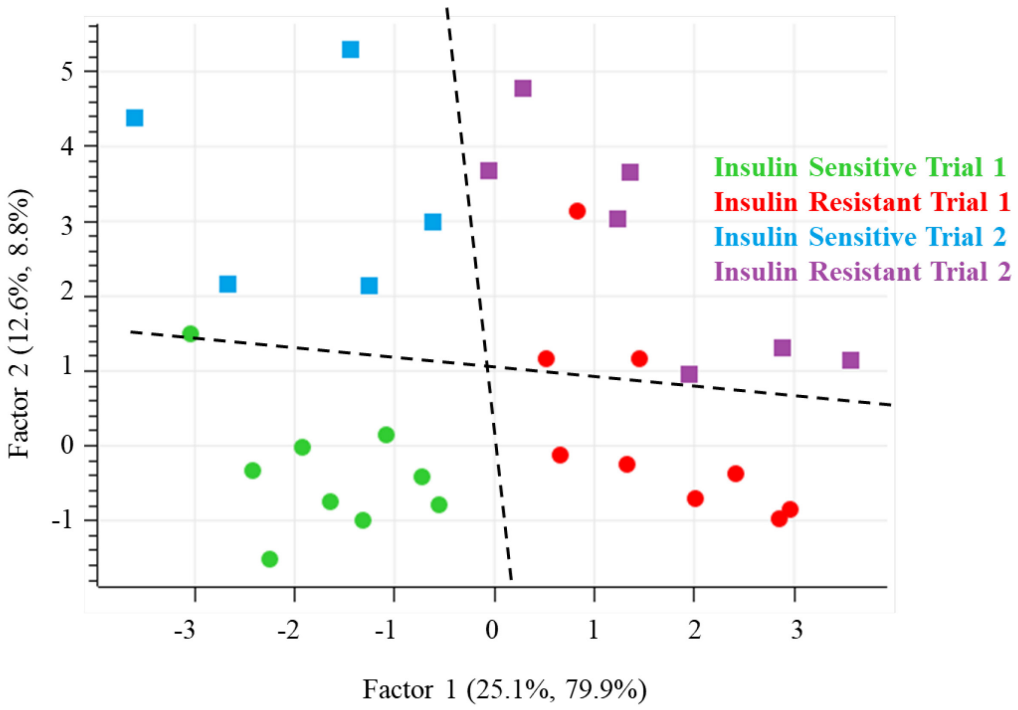

Figure 4.19: Projection of spectra acquired on a separate test set of control insulin-sensitive and -resistant 3T3-L1 adipocytes onto the PLS-DA model shown in **Figure 4.17**. The original model samples were designated as Trial 1, while the new samples were designated Trial 2. The dotted line represents a linear discriminator between the data along Factor 1 (difference between insulin-sensitive and -resistant adipocytes) and Factor 2 (difference between cultures).

4.3.5 Effects of Sugars and Vanadate on Insulin Sensitive and Resistant 3T3-L1 Adipocytes Using Single Cell Point Spectra FTIR Microspectroscopy.

The vanadate cytotoxicity results indicated that studies of relevance to diabetes (insulin-mimetic action) should be performed in the 0-10 μM range, whereas those associated with chemotherapy, e.g., direct injection,[317-318] would be appropriate at 150 μM to examine the effects on adipocytes when vanadate is used as an anti-cancer treatment. Time limitations only allowed the latter. The experimental design in **Figure 4.2** has exact mathematical properties regarding orthogonalisation (Chapter 1, Section 1.7). These properties include the ability to break the design down into blocks, which result in a design that does not measure every point, but captures the maximum volume of the design space in a minimum number of experimental runs.[223,225-226] This is the formal definition of blocking in the DoE literature; however, in the following sections, the term block was defined based on treatments containing vanadate and those not containing vanadate. **Figure 4.20** presents

a diagrammatic representation of how blocks were defined in the following sections and the experimental runs associated with each of the blocks.

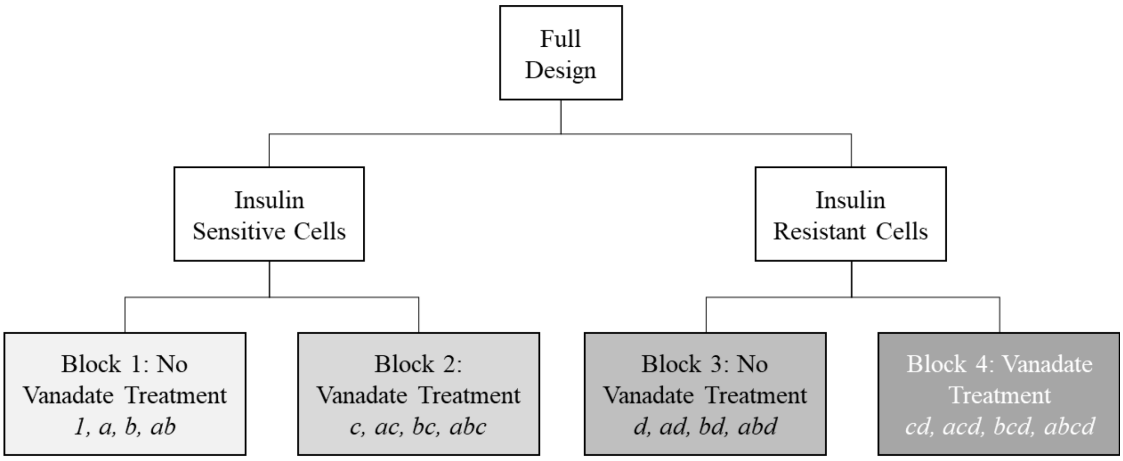

Figure 4.20: Definition of blocks as applied to the analysis sections in this chapter. The design was split by factor D (insulin-resistance) as per usual conventions; however, Blocks 1-4 were defined by the presence or absence of vanadate (C) in the treatments. Factors A and B represent glucose and fructose, respectively.

4.3.5.1 Analysis of Sugar Treatments, Insulin Sensitive 3T3-L1 Adipocytes (Block 1)

Processed FTIR spectra from the first four runs (Block 1) were assessed using PLS-DA. Due to the exploratory nature of the analysis, the method of random cross validation was used to validate the model. A five factor PLS-DA model explained 60.4% of the **Y**-response (calibration variance) and only 19.5% (validation variance), which indicated that only subtle differences were being modelled. The t_1 vs. t_2 and the t_1 vs. t_2 vs. t_3 scores plots are shown in **Figure 4.21**.

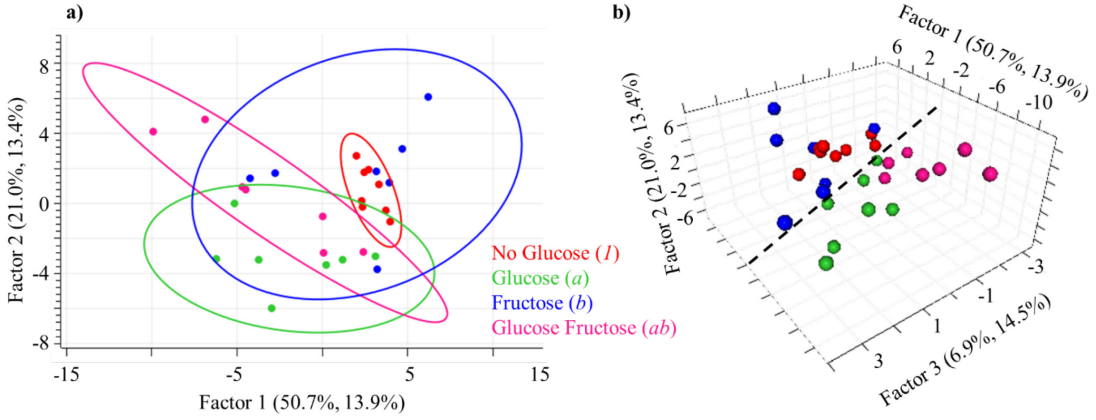

Figure 4.21: PLS-DA scores plots of Block 1 treatments of insulin-sensitive 3T3-L1 adipocytes assessed by FTIR microspectroscopy; a) t_1 vs. t_2 scores plot; and b) t_1 vs. t_2 vs. t_3 scores plots. Local Hotelling's T^2 ellipses were drawn in a) for each treatment at 95% confidence.

The t_1 vs. t_2 scores plot showed high variability except for the no-sugar treatment (*1*). Even though there was little separability, which was attributed to variability induced by the highly heterogeneous 3T3-L1 adipocytes, there was natural grouping within the treatment classes. There was a trend in the data described by the joint t_1, t_2 direction and when the data were displayed as a t_1 vs. t_2 vs. t_3 scores plot, a grouping of glucose and non-glucose treatments was observed (dotted line in **Figure 4.21b**).

The w_1-w_3 loading weights (**Figure 4.22**) showed an inverse relationship in the w_1 direction at 2919 and 2852 cm^{-1} versus 1752, 1731, 1471 and 1182 cm^{-1} bands. This showed differences in the membrane fatty acid and lipid contents attributable to the glucose versus non-glucose treatments.[195] In particular, these data showed that adipocytes preferentially use glucose for TAG synthesis and fructose for DNL of fatty acids.[319]

The w_2 direction showed the relationships between two pairs of fatty acid/lipid bands. The first described the 2925/1752 cm^{-1} correlation and the second the 2848/1729 cm^{-1} correlation. The two pairs of correlations were inversely correlated to each other, which showed that the different treatments induced different distributions of lipid and fatty acid ratios. In particular, the fructose and no-sugar treatments had more fatty acid content as observed in an increase in the bands at 1729, 1471, 1415, 1390 and 1176 cm^{-1} along the t_2 direction. The band around 1131 cm^{-1} was attributed to an increase in lactate production and was also associated with changes induced in the no-sugar and fructose treatments.[212]

The w_3 direction showed a large contribution induced by changes in protein secondary structures between 1660-1540 cm^{-1}. The amide I α-helix band at 1654 cm^{-1} was correlated with a change in the amide II band at 1548 cm^{-1} and these bands were negatively correlated with the amide I β-sheet band at 1621 cm^{-1}. The t_3 scores showed that this direction mainly separated glucose treatments (*a*) and glucose-fructose treatments (*ab*) with higher intensities in the protein bands consistent with fructose inducing protein production, through metabolic pathways such as mechanistic target of rapamycin (mTOR).[20,320]

An increase in β-sheet proteins may also be an indication of increased tyrosine phosphorylation[309] and as observed in the w_3 loading weights, this may be attributed to the glucose treated cells using insulin to promote metabolism. This was supported by the phosphodiester/DNA loading weight observed at 1240 cm^{-1}, which increased with an increase in β-sheet band at 1621 cm^{-1}.[182,193]

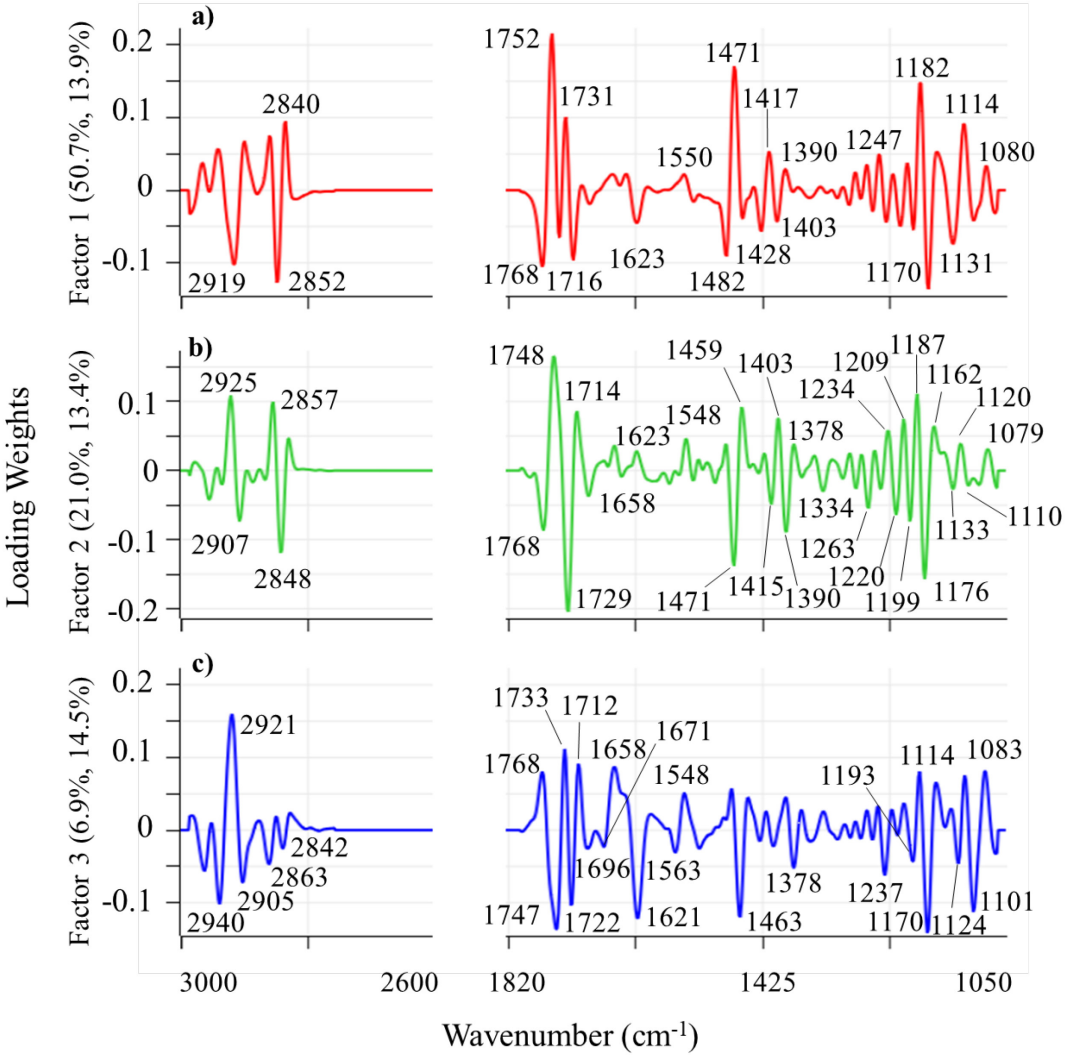

Figure 4.22: PLS-DA loading weight directions w_1-w_3 for Block 1 treatments of insulin-sensitive 3T3-L1 adipocytes; a) w_1 loading weights; b) w_2 loading weights; and c) w_3 loading weights.

4.3.5.2 Analysis of Vanadate Sugar Treatments, Insulin Sensitive 3T3-L1 Cells (Block 2)

PLS-DA scores for the Block 2 model (**Figure 4.23**) separated the vanadate only treatment (*c*) into two groups. As the chosen vanadate concentration of 150 µM was postulated to be the IC_{50} value, the two cell sub-populations were attributed to a population of cells resistant to the cytotoxic effects of vanadate and the other where the action of vanadate was cytotoxic. To confirm these findings, the processed FTIR spectra for the vanadate only treatment (*c*) and the fructose-vanadate treatment (*bc*) were compared (**Figure 4.24**). It was observed that treatment *bc* and half of the treatment *c* adipocytes showed a lack of the lipid ester band at 1743 cm^{-1} and an increase in the protein bands at 1654 and 1623 cm^{-1}.

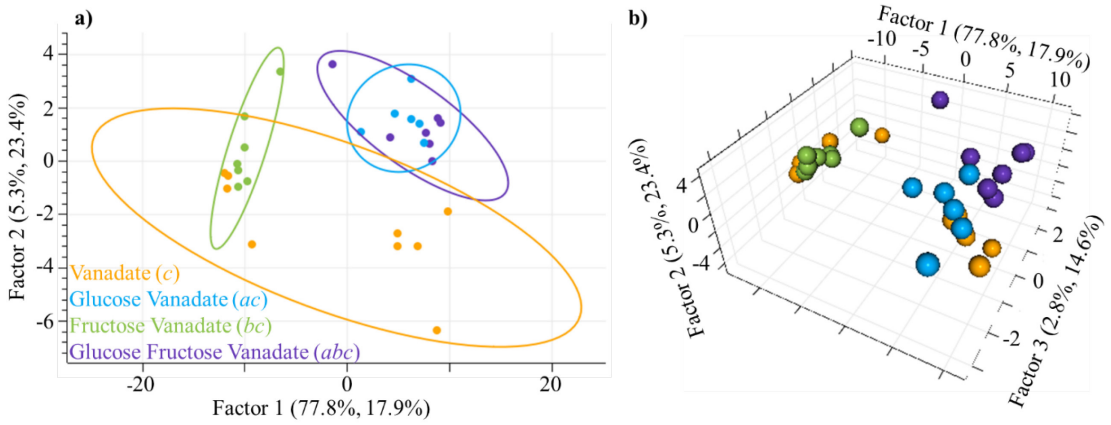

Figure 4.23: PLS-DA scores plots of vanadate-sugar treatments (Block 2) of insulin-sensitive 3T3-L1 cells assessed by FTIR microspectroscopy; a) t_1 vs. t_2 scores plot; and b) t_1 vs. t_2 vs. t_3 scores plots. Local Hotelling's T^2 ellipses are drawn in a) for each treatment at 95% confidence.

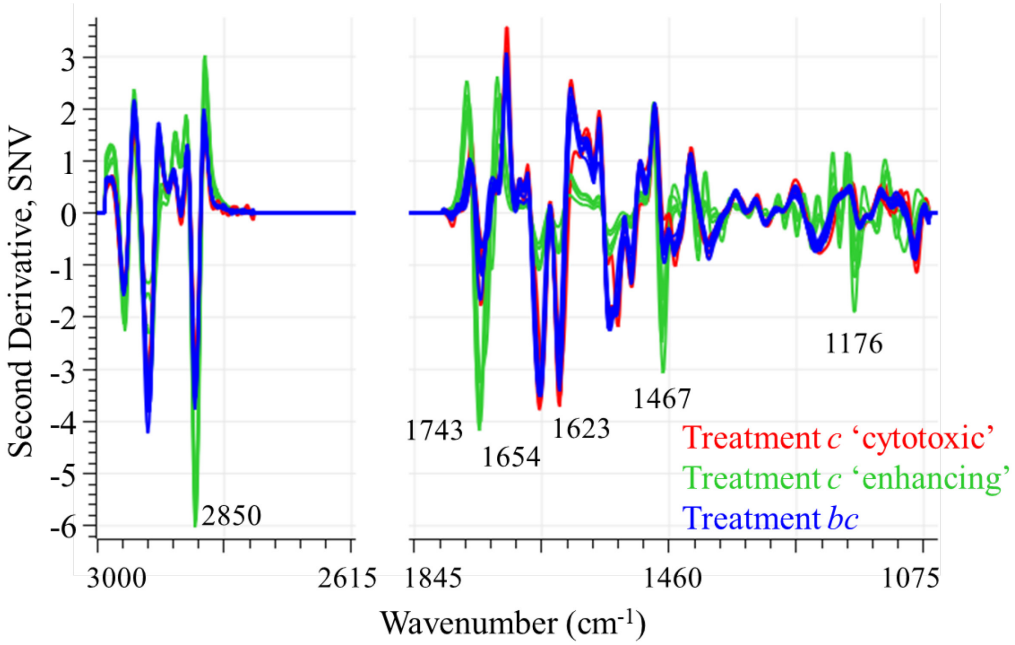

Figure 4.24: Comparison of the processed FTIR spectra for the vanadate only treatment *c* and the fructose-vanadate treatment *bc* conditions for Block 2 insulin sensitive 3T3-L1 cells.

The lack of lipid bands observed in the *bc* and 'enhancing, *c*' treatments had the effect of increasing the band intensities of protein secondary structures in the spectra, particularly the large β-sheet band at 1621 cm^{-1} for the *bc* treatment. These observations were consistent with the findings in Sections 4.3.1 and 4.3.5.1 that fructose and vanadate induce oxidative stress and with subsequent transition of protein conformation to β-sheet, indicative of protein agglomeration.[175] A second type of spectra associated with treatment *c* (vanadate only) displayed clear lipid associated bands at 2850, 1743, 1467 and 1176 cm^{-1} and were labelled 'enhancing' in **Figure 4.24**. This was an indication that these cells

were resistant to vanadate at this concentration and, as stated above, may be a confirmation that 150 μM V(V) was the IC_{50} value of vanadate towards 3T3-L1 adipocytes.

As was observed in the analysis of the Block 1 data, there was also a separation of treatments based on glucose in the Block 2 data, with the glucose-vanadate (*ac*) and glucose-fructose-vanadate (*abc*) treatments tightly grouped. This separation was associated with the t_1 and t_2 directions and the w_1-w_3 loading weights (**Figure 4.25**) showed increased band intensities in the w_1 and w_2 directions for lipid esters at 1747 and 1469 cm^{-1} and a decrease in FFA bands at 1733 and 1716 cm^{-1}.[202] The grouping of the glucose containing treatments was an indication that the presence of vanadate may enhance glucose metabolism in adipocytes.

The fructose-vanadate (*bc*) treatment may, therefore, relate to the least favourable conditions for cell survival, consistent with increased oxidative stresses induced by the combination of treatments, particularly with vanadate at its IC_{50} value. The w_1 loading weights described the combined action of fructose and vanadate induced changes with respect to the glucose containing treatments and were associated with changes in proteins secondary structure. These data indicated that in the presence of vanadate, glucose was the preferred metabolite, as evidenced by increased lipid synthesis in the presence or absence of fructose. Although the concentration of vanadate was high (IC_{50}), the PLS-DA model in **Figure 4.23** indicated that it may be acting as an insulin-mimetic under the Block 2 conditions. Further studies are required to investigate whether this effect is large or small compared to adipocytes treated without vanadate using a larger sample size and multiple cultures.

The w_2 direction was consistent with an apoptosis hypothesis because positively weighted bands at 2909, 2846, 1733, 1615, 1131 and 1083 cm^{-1} are markers of apoptosis[195,205] and correspond to the vanadate only and the fructose-vanadate treatments *c* and *bc*, respectively. Bands at 2925, 2859, 1750, 1658, 1546 and 1461 cm^{-1} were all correlated and corresponded to normal lipid synthesis and α-helix protein structures. Although Zelig, *et al.*[205] attribute changes in the 2920 and 2850 cm^{-1} bands to a biomarker of apoptosis, the splitting of these bands in the w_2 loadings may indicate that many types of lipids with similar bands were present, some indicative of pro-apoptotic activity and some with anti-apoptotic properties.

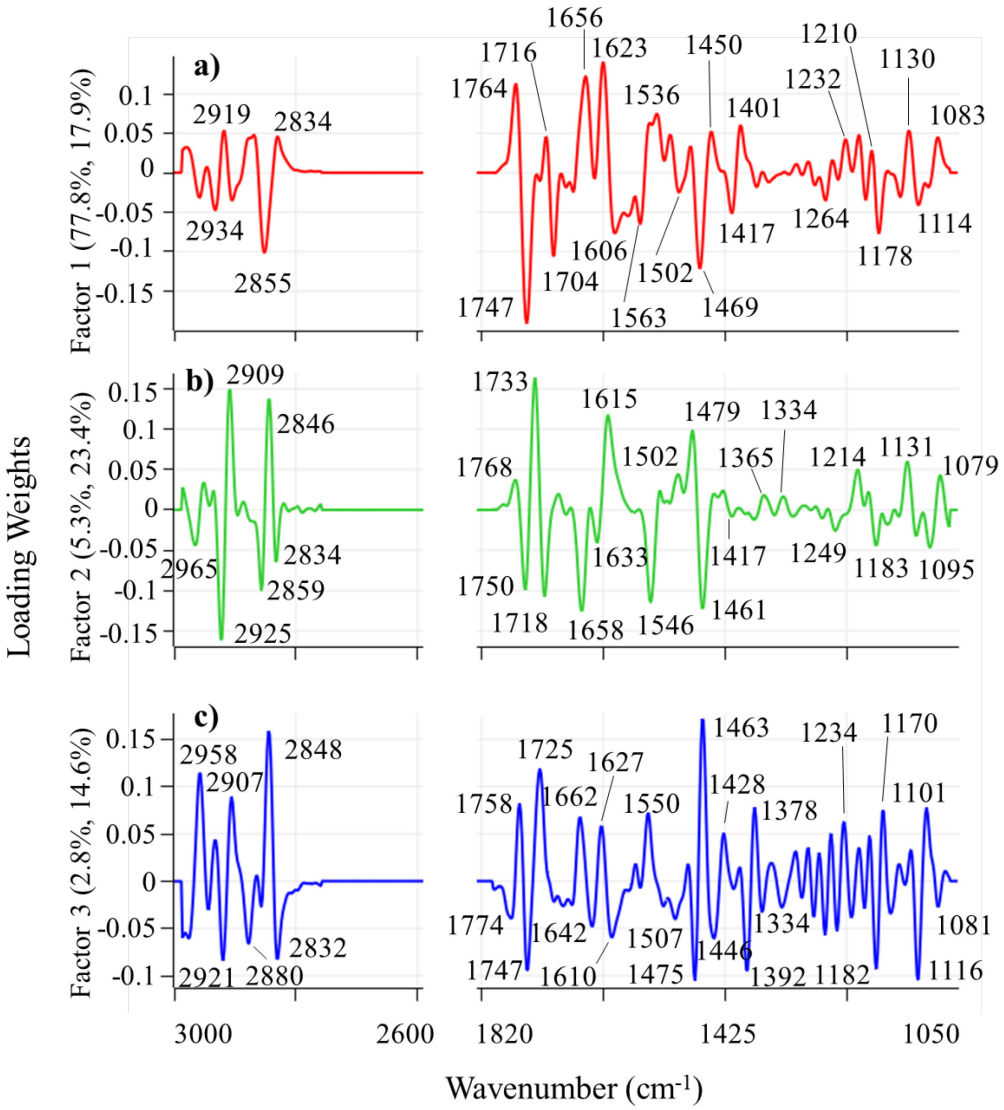

Figure 4.25: PLS-DA loading weight directions w_1-w_3 for Block 2 treatments of 3T3-L1 adipocytes; a) w_1 loading weights; b) w_2 loading weights; and c) w_3 loading weights.

The w_3 direction described the separation between the glucose-vanadate (*ac*) and glucose-fructose-vanadate (*abc*) treatments (both contained glucose and vanadate) with the addition of fructose resulting in positive scores (*abc* treatments) in the t_3 vs. t_2 scores plot (**Figure 4.26**). A similar separation was also observed in the t_3 direction for the Block 1 analysis (**Figure 4.21b**). For the w_3 loading weights, the bands at 2958, 2909, 2848, 1725, 1662 and 1627 cm^{-1} were all positively correlated and were associated with the treatments containing fructose. These data showed that fructose in high concentration had a detrimental effect on cell viability, even in the presence of glucose, but to a lesser extent than the fructose-vanadate treatment, i.e., the *bc* treatment. This loading weight only accounted for 14.6% of the explained **Y**-variance and is commensurate with the smaller effect of fructose, and further indicated that glucose was preferentially metabolised.

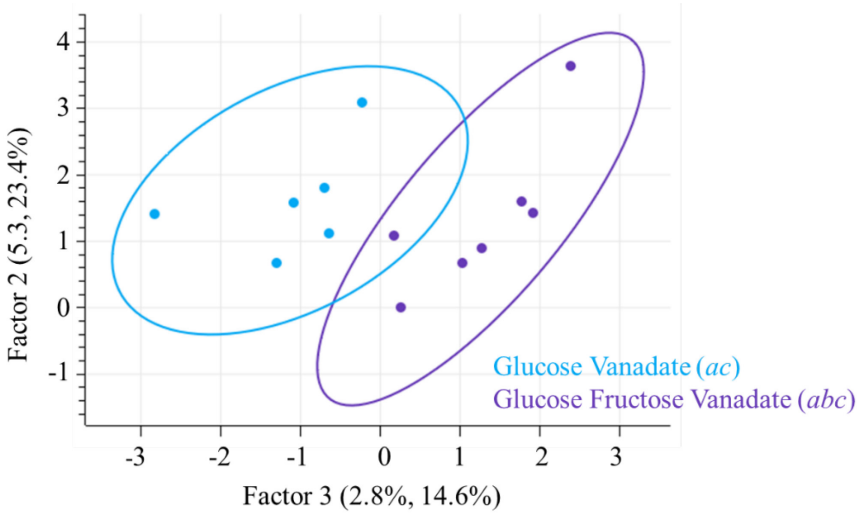

Figure 4.26: t_3 vs t_2 scores plot of the Block 2 treatments glucose-vanadate (*ac*) and glucose-fructose-vanadate (*abc*) only for insulin-sensitive cells and showed separation of the treatments along the w_3 direction.

Overall, these data verified the observations made in the Block 1 treatments that glucose and fructose were metabolised differently even in the presence of vanadate for insulin-sensitive cells. The expected increase of ROS induced by vanadate and fructose-vanadate[20,129] was attributed to the separation of these treatments from the glucose containing treatments and indicated that glucose may have a protective effect in the presence of fructose and vanadate.

4.3.5.3 Analysis of Sugar Treatments, Insulin Resistant 3T3-L1 Adipocytes (Block 3)

The PLS-DA scores for the Block 3 model (**Figure 4.27**) showed separation of the treatments along the t_1 direction in the order: (i) no-sugar *d*; (ii) glucose *ad*; and (iii) treatments containing fructose, *bd* and *abd*, where *d* represented induce insulin resistance in Block 3 treatments. The fructose treatment (*bd*) separated from the other treatments along the t_2 direction and was visually distinct from the other treatments in the t_3 direction (**Figure 4.27b**).

The t_1 direction showed a general separation of fructose containing treatments along positive scores values and non-fructose treatments along negative scores values. The fructose treatment (*bd*) was located closer to the zero scores values along t_1 but was separated into negative scores along the t_2 direction. These data indicate that the t_1 direction described a combined glucose-fructose effect, while the t_2 direction was attributed to the main effect of fructose. Therefore, the w_2 loadings could be interpreted as fructose induced changes in insulin-resistant cells. The t_3 direction separated the

treatments in the order glucose (*ad*), glucose-fructose (*abd*) and no-sugar (*d*) with the fructose treatment (*bd*) separated the from the other treatments along the t_2 direction (**Figure 4.28**).

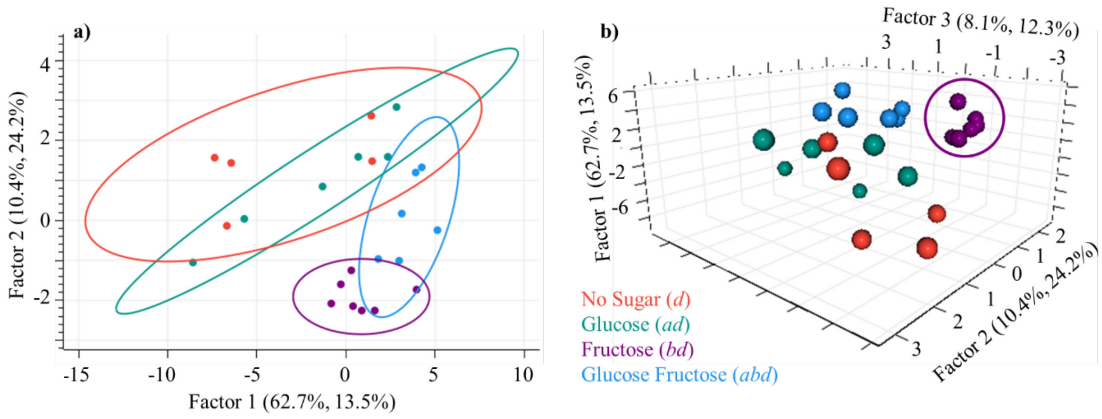

Figure 4.27: PLS-DA scores plots of sugar treatments of insulin-resistant 3T3-L1 adipocytes (Block 3) assessed by FTIR microspectroscopy; a) t_1 vs. t_2 scores plot; and b) t_1 vs. t_2 vs. t_3 scores plots. Local Hotelling's T^2 ellipses are drawn in a) for each treatment at 95% confidence.

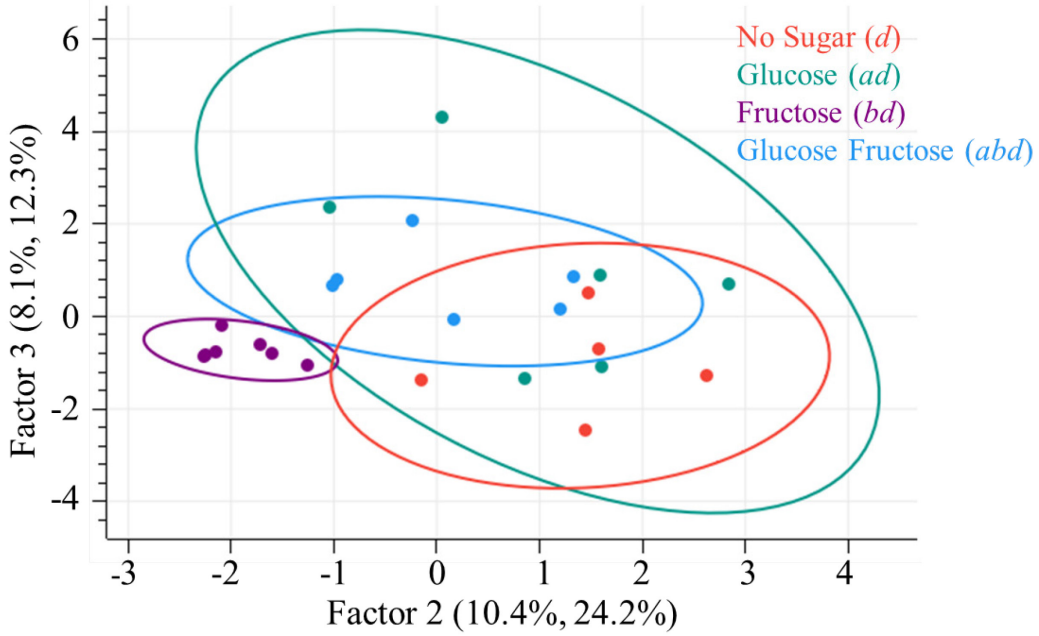

Figure 4.28: t_2 vs. t_3 PLS-DA scores for Block 3 insulin-resistant 3T3-L1 adipocytes grouped by treatment conditions.

The w_1 direction (**Figure 4.29a**) indicated that increases in lipid band intensities (1745 and 1482 cm^{-1}) were associated with the glucose-fructose treatment (*abd*) and were lowest for the no-sugar (*d*) and glucose treated (*ad*) cells. This was consistent with the insulin-resistance induced in these cells by the lack of glucose metabolism and indicated that fructose may be preferentially up-taken and metabolised by these cells.

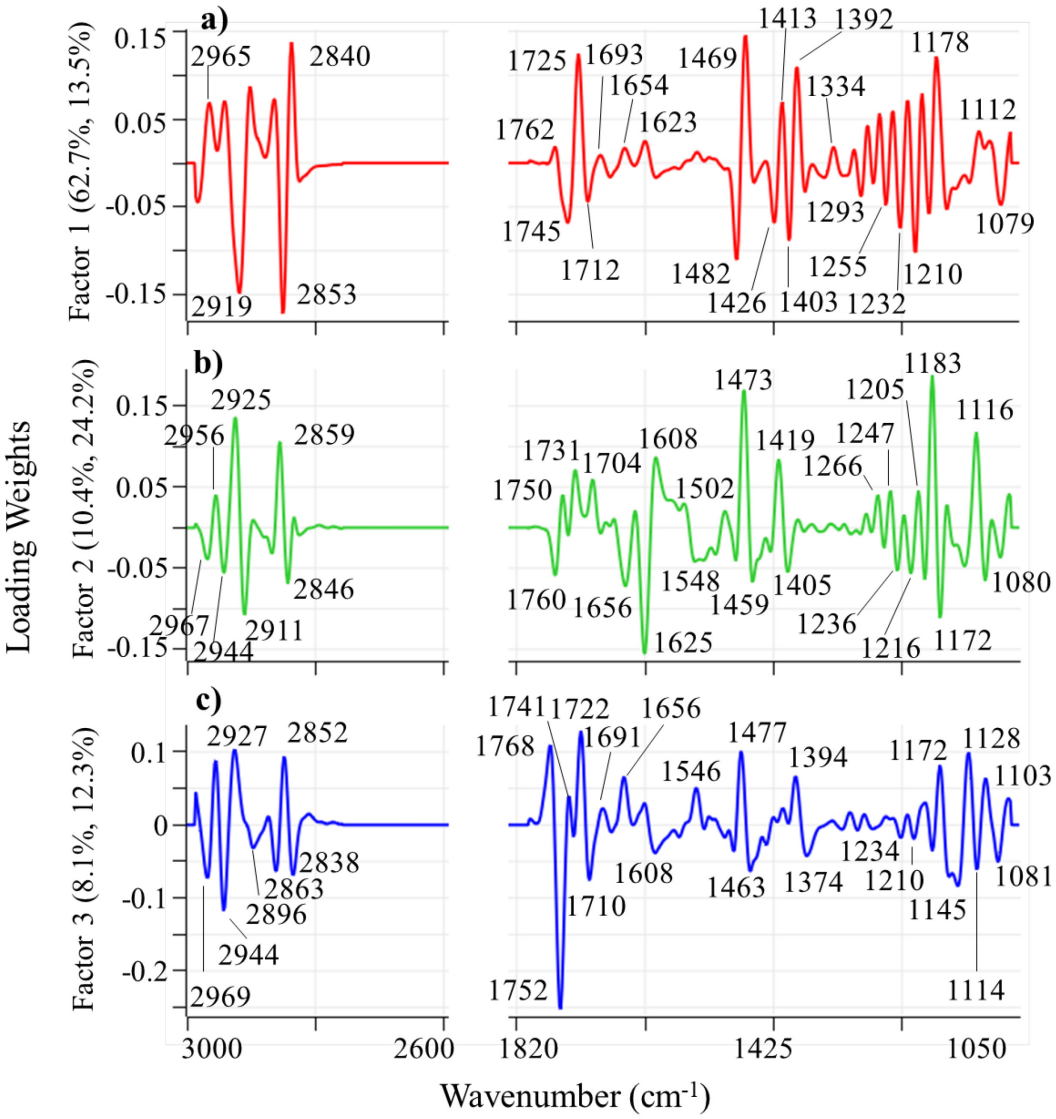

Figure 4.29: PLS-DA loading weight directions w_1-w_3 for Block 3 treatments of insulin-resistant 3T3-L1 adipocytes. a) w_1 loading weights; b) w_2 loading weights; and c) w_3 loading weights.

The uptake of fructose may be enhanced by glucose as the glucose-fructose treatment (*abd*) had larger loading weights at 1745 cm^{-1}, while the glucose and no-sugar treatments showed higher levels of FFAs at 1725, 1469, 1413 and 1178 cm^{-1}. Associated with the fructose containing treatments were increased band intensities at 2919 and 2853 cm^{-1}, which were also observed for fructose treatments in the Block 1 loading weights, associated with membrane lipid changes and possibly related to fructose induced oxidative stress.[195,202,205] A large splitting of the band around 2850 cm^{-1} into two components at 2853 and 2840 cm^{-1} was also observed, with the band at 2840 cm^{-1} associated with changes in the no-sugar (*d*) and glucose (*ad*) treatments.

Szalontai, *et al.*[321] reported that a spitting of the band around 2850 cm^{-1} (**Figure 4.29a**) was indicative of a conformational change in the acyl side chains of fatty acids, with the

higher wavenumber positions related to a *trans* (ordered) conformation and the lower wavenumber shift to a *gauche* (disordered) conformation. This conformation switching between ordered and disordered fatty acyl chains is in balance as the total number of -CH_2 groups is constant. Therefore, the 'first derivative' profile of the band around 2850 cm^{-1} was attributed to changes in the membrane structures induced by fructose containing treatments.

The w_2 direction was attributed to biochemical changes induced in insulin-resistant adipocytes by fructose containing treatments. Increased band intensities at 2925, 2859, 1731, 1473, 1419, 1183 and 1116 cm^{-1} were correlated with the fructose treatment (*bd*), through increased DNL. This was evidenced by the large band at 1419 cm^{-1},[193] associated with fructose metabolism.[319] The bands at 2925 and 2859 cm^{-1}, associated with ordered fatty acid side chains were also correlated with the fructose treated adipocytes. Other important bands associated with this direction were those at 1704 cm^{-1}, related to A-DNA base pairing,[182] 1608 cm^{-1} related to tyrosine and arginine side chains,[206] 1473 cm^{-1} related to bending vibrations in proteins and lipids, and 1183 and 1116 cm^{-1} related to phospholipids and DNA.[182]

The non-fructose containing treatments displayed a marked increase in the band intensity at 1625 cm^{-1} typically associated with β-sheet proteins and in particular, protein agglomeration.[175,196,203] An increase in β-sheet proteins may also be an indication of increased tyrosine phosphorylation,[309] Muir, *et al*.[26] report that fibrosis is an adaptive feature of adipose tissue to protect adipocytes against hypertrophy, therefore, it was most likely that the β-sheet protein bands were associated with protein agglomeration/ fibrosis/amyloid structures, which have been reported in individuals with T2DM.[173]

The w_3 direction had a large loading weight at 1752 cm^{-1} associated with TAG related lipids and did not contribute to any groupings of treatments. Due to the complex nature of this loading weight and the lack of separation observed in the t_3 scores direction, a complete interpretation of this loading weight was not possible and was possibly related to stored lipids associated with glucose treated cells.

4.3.5.4 Analysis of Vanadate-Sugar Treatments, Insulin Resistant 3T3-L1 Adipocytes (Block 4)

The t_1 vs. t_2 scores plot of the PLS-DA Block 4 model for insulin-resistant cells (**Figure 4.30**) showed that the t_1 direction separated the vanadate only treatment (*cd*) from the other treatments. The remainder of the treatments separated along the t_2 direction and the

joint t_2, t_3 direction; i.e., the vanadate-only (*cd*) and glucose-fructose-vanadate (*abcd*) treatments separated from the glucose-vanadate (*acd*) and fructose-vanadate (*bcd*) treatments. Factor *d* represented induced insulin-resistance.

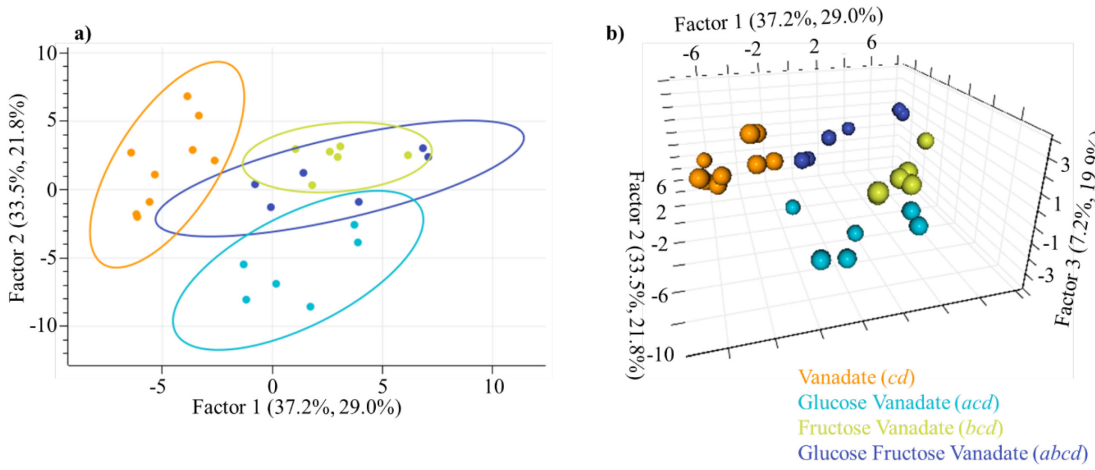

Figure 4.30: PLS-DA scores plots of vanadate-sugar treatments of insulin-resistant 3T3-L1 adipocytes assessed by FTIR microspectroscopy; a) t_1 vs. t_2 scores plot; and b) t_1 vs. t_2 vs. t_3 scores plot. Local Hotelling's T^2 ellipses were drawn in a) for each treatment at 95% confidence.

The w_1-w_3 loading weights (**Figure 4.31**), showed the w_1 direction was dominated by the band at 2919 cm^{-1} associated with membrane lipids.[195,202] This band was positively correlated with the B-DNA base pairing or FFA band at 1716 cm^{-1}, the amide I bands at 1654 and 1623 cm^{-1} and the amide II band at 1546 cm^{-1}. Since adipocytes are typically 90% lipid in content,[16] it was most likely that the band at 1716 cm^{-1} was associated with FFAs. These data were consistent with increased oxidative stress induced by vanadate and insulin resistance, which induced membrane lipid changes and changes in protein/DNA. The above listed bands were negatively correlated with bands at 1745, 1471, 1415, 1178 and 1116 cm^{-1}, which were assigned to TAGs and changes in phospholipids (**Table 1.1**). These bands were associated with the treatments glucose-vanadate (*acd*), fructose-vanadate (*bcd*) and glucose-fructose-vanadate (*abcd*) and were attributed to the insulin mimetic effect of vanadate and DNL fatty acid synthesis promoted by fructose.[319]

The t_2 scores showed a separation of the sugar containing treatments in order of positive to negative scores values fructose-vanadate (*bcd*), glucose-fructose-vanadate (*abcd*) and glucose-vanadate (*acd*), which correlated to the combined fructose-vanadate effect. The vanadate only (*cd*) treatment also displayed positive t_2 scores values and occupied a space similar to the *bcd* treatment, which was a similar result observed in the Block 2 treatments

(**Figure 4.23a**). The w_2 loading weights showed that the major band associated with the glucose-vanadate treatment (*acd*) was the band at 1747 cm^{-1}, which increased in intensity consistent with glucose metabolism in to TAGs and with vanadates insulin-mimetic activity, even though [V(V)] was cytotoxic in this treatment protocol. Comparison of these results to the t_1 vs. [V(V)] results of **Figure 4.6a**, was consistent with glucose possibly promoting growth around 125 µM, before the next biochemical process occurred > 125 µM postulated to be early stages of apoptosis.

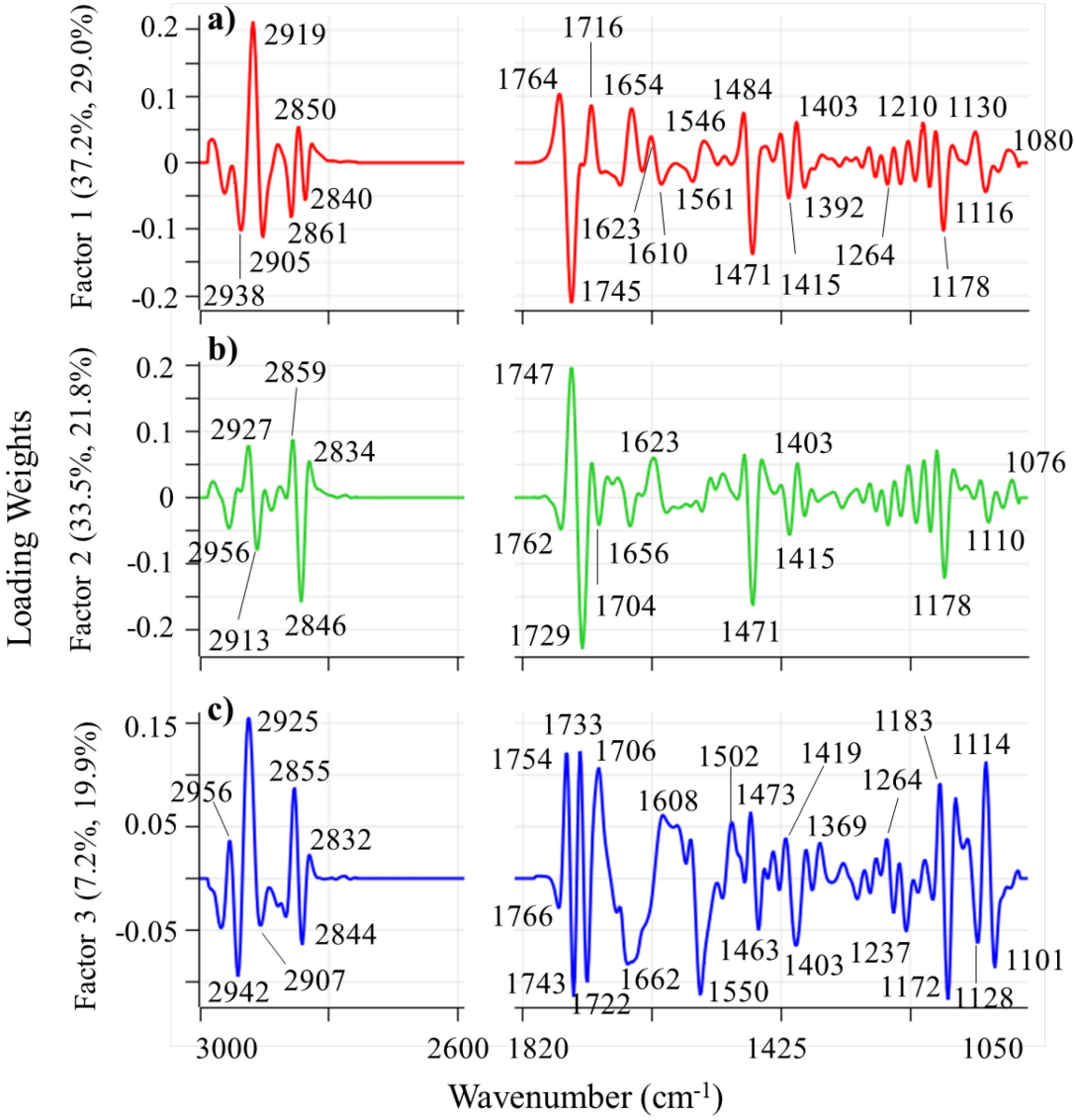

Figure 4.31: PLS-DA loading weight directions w_1-w_3 for Block 4 treatments of insulin resistant 3T3-L1 adipocytes; a) w_1 loading weights; b) w_2 loading weights; and c) w_3 loading weights.

The fructose-vanadate treatment (*bcd*) was associated with increased band intensities at 1729, 1471, 1415, 1178 and 1110 cm^{-1} related to DNL of fatty acids consistent with fructose metabolism.[20,184,197,200,208] The insulin-sensitive fructose-vanadate treatment (*bc*)

and corresponding insulin-resistant fructose-vanadate treatment (*bcd*) also exhibited similarities consistent with changes in membrane lipids at 2913 and 2844 cm^{-1}, possibly related to the onset of apoptosis.[195,205]

The w_3 direction showed a highly complex relationship between lipid and protein bands, however, two bands, 1706 cm^{-1} (DNA) and 1608 cm^{-1} associated with tyrosine and arginine bands,[206] were positively correlated. The t_3 direction separated the glucose-fructose-vanadate (*abcd*) treatment, from the other treatments and was attributed to the combined effects of glucose metabolism into TAGs (1743 cm^{-1}), and fatty acid synthesis (1722 cm^{-1}) and changes in protein secondary structure induced by the synergistic action of fructose and vanadate.

4.3.5.5 Comparison of Block Treatments

A comparison of all treatments was performed as a PLS-DA model using Blocks 1-4 as the *y*-response (**Figure 4.32**). The scores plot in **Figure 4.32a** showed that except for Block 2, there is very little difference between the treatments. Block 2 data was already discussed in Section 4.3.5.2 with regard to the no-sugar-vanadate and fructose-vanadate treatments, *c* and *bc*, respectively. These differences were also apparent for the combined Blocks 1 and 2 analyses (**Figure 4.32b**).

Block 3 and 4 treatments separated along the t_1, t_2 direction (**Figure 4.32c)** and this was consistent with the pronounced effect of vanadate on insulin-resistant cells compared to its action on insulin-sensitive cells (Blocks 1 and 2). The w_2 loading weights for the Block 3 and 4 model were consistent with an increase of TAGs and fatty acid band intensities (1743 and 1729 cm^{-1}) for vanadate treatments and an increase in DNA and protein bands between 1710-1620 cm^{-1}. While the band at 1625 cm^{-1} may be related to tyrosine phosphorylation,[309] or it may be an indicator of protein synthesis and aggregation (fibrosis), with the latter being the most likely explanation associated with this band.[175,203]

4.3.5.6 Analysis of Centre Points

As part of the experimental design (**Figure 4.2**), centre points were defined as the mid-points of the factor treatment levels. In this study, mid-points represented glucose and fructose concentrations of 2.5 mM and vanadate concentration was set to 75 μM. The factor insulin sensitive/resistant was a binary categorical variable that does not have a logical centre point definition. In the DoE literature, when categorical variables are defined in the design, centre points are defined as the mid-point values of all continuous

variables for each categorical variable.[223,226] This resulted in two blocks of centre points, one for insulin-sensitive and one for insulin-resistant cells as described in **Figure 4.33**.

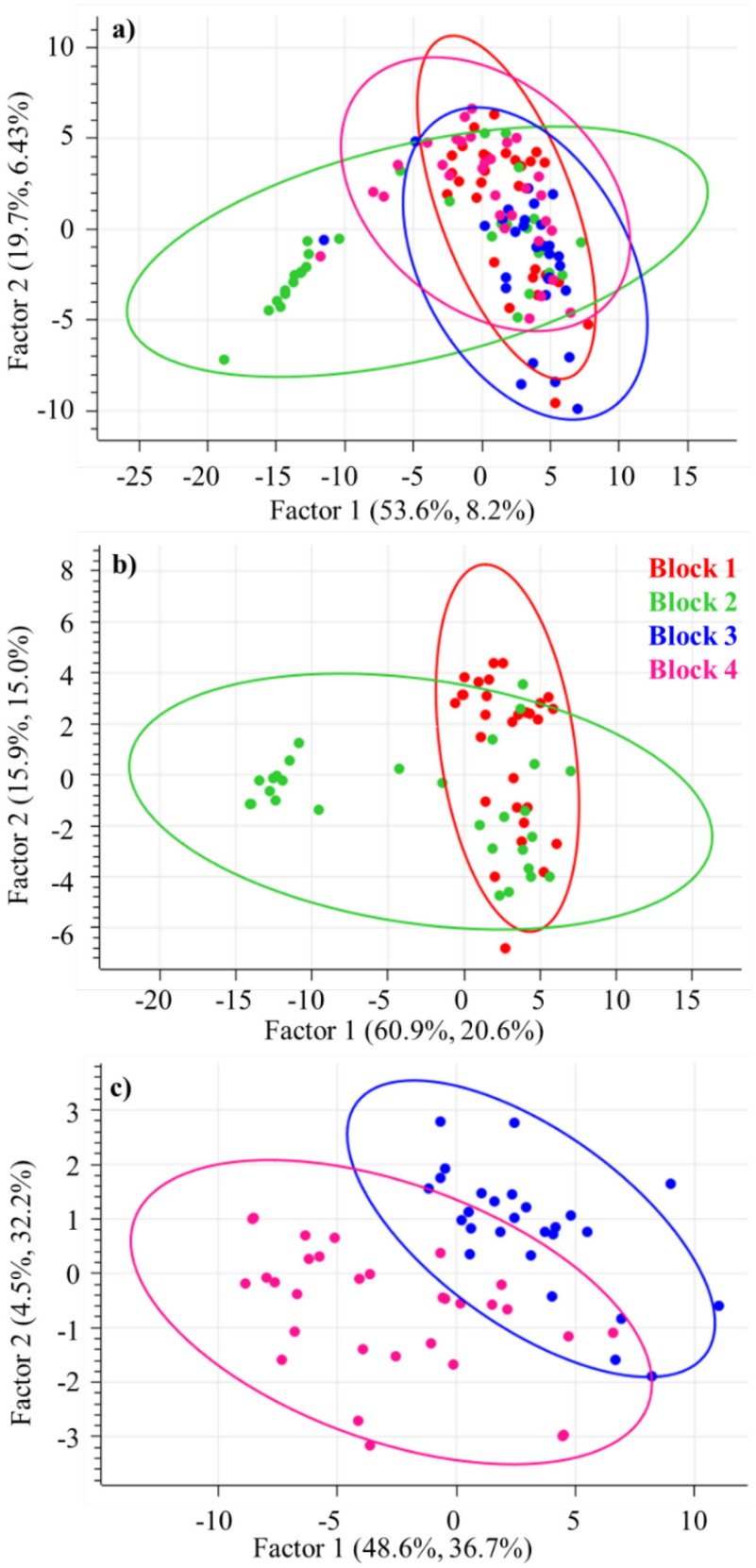

Figure 4.32: PLS-DA scores of the entire DoE and Block comparisons; a) all treatment Blocks; b) Blocks 1 and 2 scores; and c) Blocks 3 and 4 scores. Colour grouping was defined in plot b).

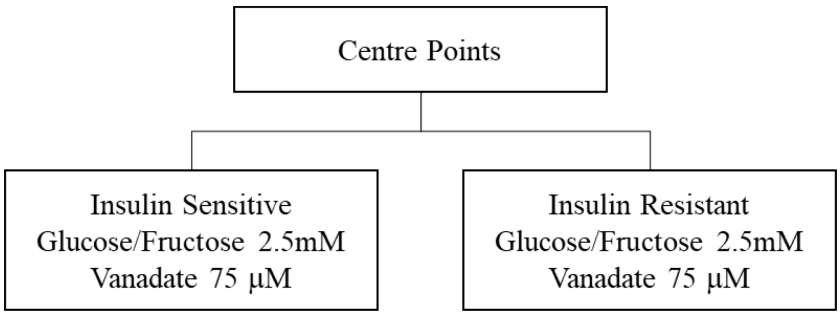

Figure 4.33: Definition of centre point treatments in the experimental design of **Figure 4.2**.

PLS-DA applied to the centre point spectra (**Figure 4.34**) showed that the w_2 direction described the main differences in the data. The separation of the insulin-sensitive and -resistant treatments was consistent with insulin-resistance induced by ET-1.

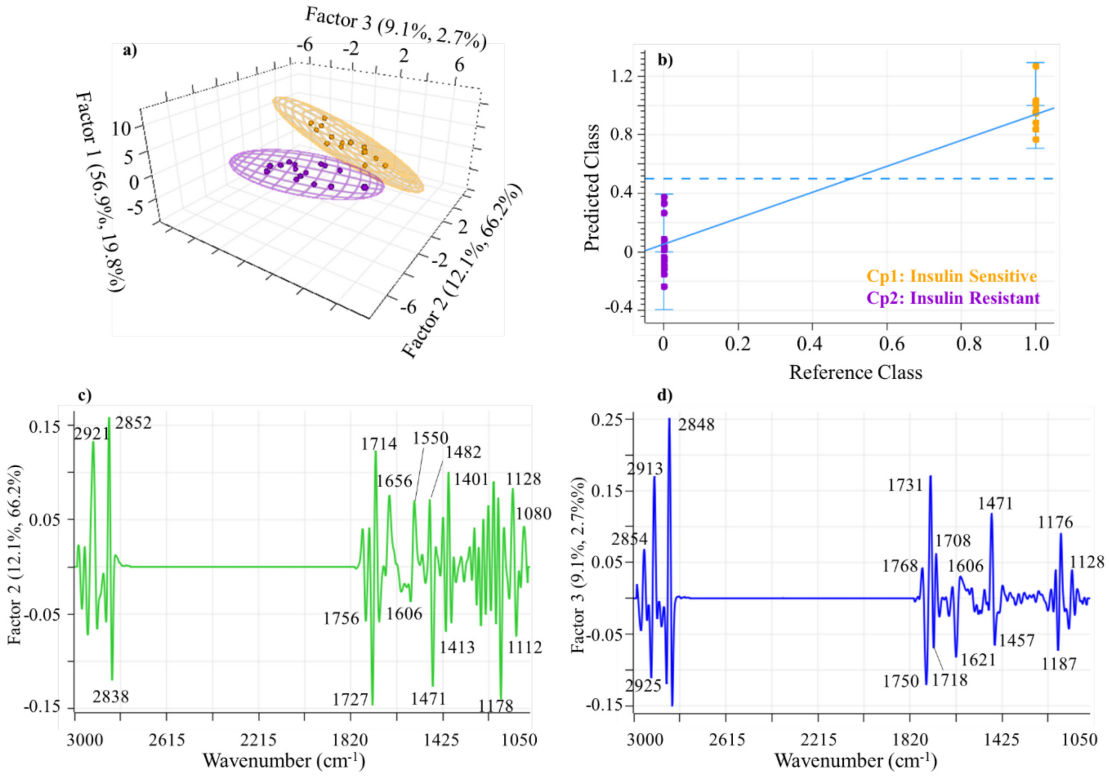

Figure 4.34: PLS-DA model of centre point data showing the separation of the insulin-sensitive and -resistant treatments; a) t_1 vs. t_2 vs. t_3 scores; b) predicted vs. reference plot with discriminating line; c) w_2 loading weights; and d) w_3 loading weights. Samples grouped as per the legend in plot b).

The Factor 1 direction did not contribute to this model, possibly due to the small number of spectra used to develop the model, however, Factor 2 described the majority of the differences between the insulin-sensitive and -resistant treatments. The w_2 loading weights indicated that the main difference between insulin-sensitive and -resistant cells were protein secondary structural changes and changes in the band at 1606 cm^{-1}, related to tyrosine.[206]

This led to the postulate that the insulin-sensitive cells were most likely using insulin in the supplemented media to induce tyrosine phosphorylation for metabolising glucose in the presence of vanadate and fructose. By contrast, the combined vanadate-fructose levels were inducing protein synthesis[20] (evidenced by the large loading weights at 1654 and 1550 cm^{-1}). As established in Section 4.3.3, the centre point concentration of vanadate, in combination with oxidative stress induced by fructose, may be inducing cytotoxic effects, rather than insulin mimetic effects in the treated cells.

4.4 Discussion

4.4.1 Vanadate as an Insulin Mimetic and Cytotoxic Agent

Cells cultured *in vitro* use supplemented media that is pH adjusted in the range 7.35-7.45 to best approximate physiological conditions expected *in vivo*. Glucose is the main *in vivo* energy source available for cell metabolism, where it is converted into lipids and fatty acids, essential for proper cell functioning, or stored as glycogen for later use as and when required (**Figure 1.2**.).[20] The cellular conversion of glucose into lipids and other products results in the production of CO_2 and lactate,[212] which increases the acidity (lower pH values) of the culture medium.[322] Culture media usually contains pH sensitive colour-based indicators to detect the depletion of glucose in the media as a result of increased cellular metabolism and acidity. Therefore, a change in colour in the media is an indirect measurement of cell metabolism and growth, but is also an indicator of pH-induced changes. Vanadium chemistry is highly diverse and the particular active species are dependent on the pH value, their concentration (low concentrations result in higher monomeric species) and reducing potential of the environment.[132,299]

At physiological pH the expected vanadium species is V(V) in non-reducing environments and V(III)/V(IV) in reducing environments.[129,323] Therefore, as media pH changes, a corresponding change in vanadium species is also expected, which could change its mode of action on treated cells. Insulin-sensitive 3T3-L1 adipocytes treated for 72 hr with increasing amounts of vanadate demonstrated changes in media pH values, indicative of glucose metabolism up to 125 μM for insulin-sensitive cells and lower for -resistant cells.

PCA models of FTIR spectra acquired on vanadate treated insulin-sensitive and -resistant cells, revealed two major biochemical processes associated with insulin-mimetic/enhancing and cytotoxic actions of vanadate. The models developed also showed that vanadate action differs for insulin-sensitive and -resistant cells and these observations

were consistent with differences in the onset of oxidative stress induced by higher vanadate concentrations. Designed experiments (DoE) with fructose resulted in biochemical changes consistent with the literature of increased oxidative stress, DNL and protein synthesis,[20] as described in more detail in the following sections.

4.4.1.1 Vanadate as an Insulin-Mimetic/Enhancer

Figure 4.35 presents a proposed mechanism for vanadate action on insulin-sensitive adipocytes cultured under normal conditions (in glucose supplemented media) over the range 0-31.3 μM V(V). Foetal calf serum (FCS) in supplemented media contains insulin,[324] which binds to the α-subunit of the insulin-receptor and resulted in phosphorylation of the β-subunit and subsequent translocation of the GLUT4 receptor to the cell membrane (**Figure 1.5**)[60] and insulin regulated glucose metabolism results.

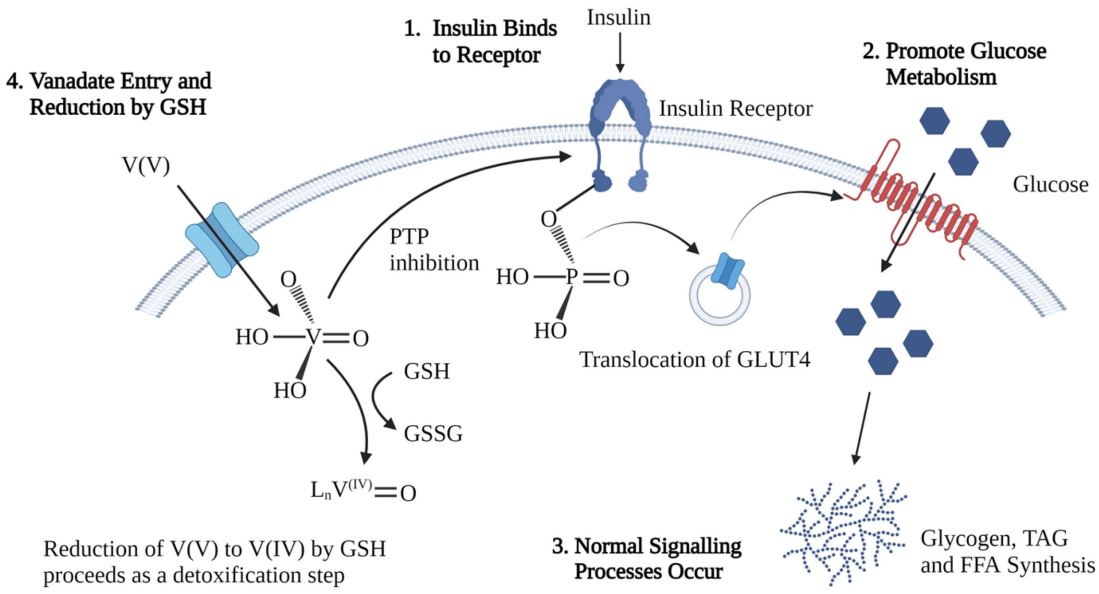

Figure 4.35: Postulated four-step process of low concentration vanadate action on insulin-sensitive 3T3-L1 adipocytes: 1) Insulin binds to the insulin-receptor inducing phosphorylation of the receptor β-subunits;[299] 2) activation of pathways that induce GLUT4 translocation for glucose uptake[325]; 3) induction of other biochemical pathways by normal insulin activated cascade; and 4) insulin-activity enhanced by V(V) inihibition of PTPs with detoxification of excess V(V) by reduction to V(IV) by GSH, which is oxidised to GSSG.[111] Created with BioRender.com.

Entry of vanadate into the cell through phosphate or sulfate ion channels induced insulin enhancing and mimetic activity by phosphatase inhibition.[116] Toxicity from excess V(V) was minimised through reduction by intracellular GSH to glutathione disulfide (GSSG) as a detoxification step, where generated vanadyl (V(IV)) can bind to proteins.[111,326]

Therefore, GSH protects cells from the effects of agents that generate ROS and its depletion has been associated with severe oxidative stress.[327]

At low concentrations, there are dynamic changes in V(V) and V(IV) in cancer cells and compared to insulin-resistant cells, which have higher levels of oxidative stress,[328] the higher tolerance of vanadate up to 31.3 μM in insulin-sensitive adipocytes can be explained by enhanced GSH reduction of cytotoxic V(V) to V(IV). At 31.3 μM, the level of GSH depletion is postulated to affect homeostasis of ROS where both increased ROS generation and increased intracellular V(V) leads to a transition to cytotoxic action, discussed further in Section 4.4.1.2.

Figure 4.36 presents a postulated four-step mechanism for the action of vanadate at concentrations between 0-10 μM for insulin-resistant cells. This is the typical concentration range of V(IV)/V(V) in treated mammalian tissues found to inhibit phosphatases with subsequent activation of kinases.[305] ET-1, used to induce insulin resistance,[75] was transported into cells by the receptor, ETA, and stimulated the production of ROS, primarily as superoxide anions ($O_2^{-\bullet}$) to induce oxidative stress.[299,329-330]

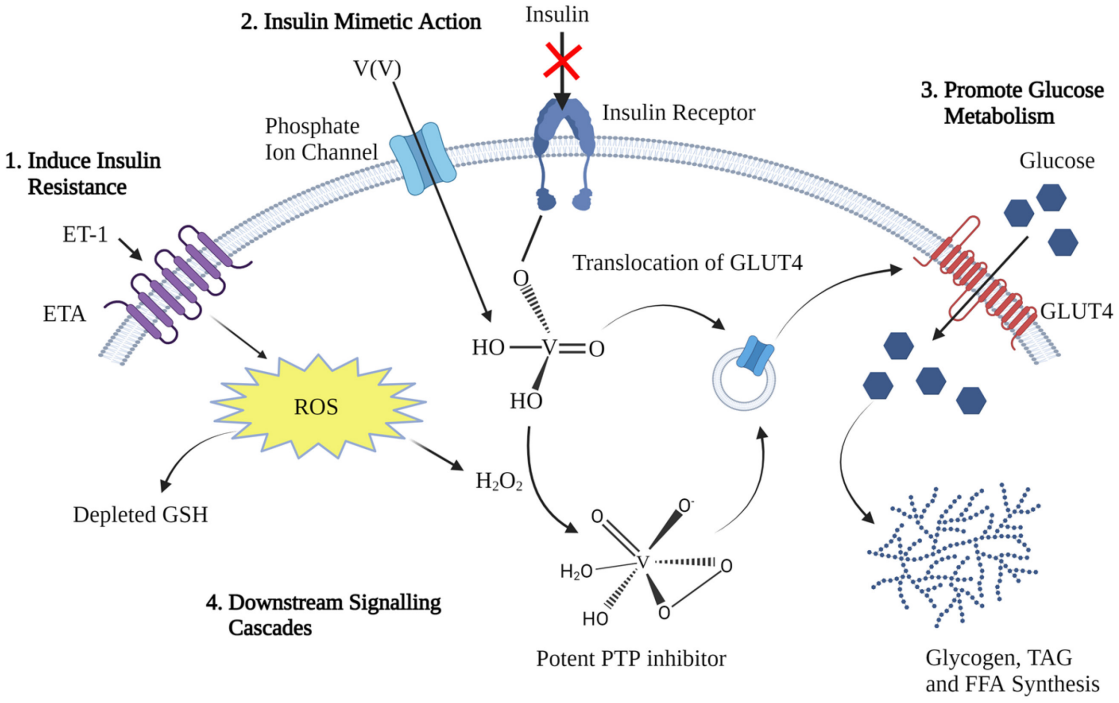

Figure 4.36: Postulated four-step process of low concentration vanadate action on insulin-resistant 3T3-L1 adipocytes: 1) induction of insulin resistance and oxidative stress;[75] 2) vanadate acting as an insulin-mimetic;[111,299] 3) vanadate activation of pathways that induce GLUT4 translocation for glucose uptake;[104] and 4) induction of other biochemical pathways by enhanced peroxidovanadate production.[312] Created with BioRender.com.

Generation of ROS is associated with lipid peroxidation and reduction of intracellular GSH.[330-331] As a consequence, in cells with depleted GSH levels, the insulin-mimetic and cytotoxic effects of V(V) are both enhanced.[299] Entry of vanadate into the cell via phosphate and sulfate ion channels can enhance phosphorylation of the insulin receptor substrate (IRS) β-subunits and many kinases by phosphate inhibition, where it acts as an insulin-mimetic.[111,299] This is followed by translocation of GLUT4 transporters to the cell surface, where glucose entry followed by its metabolism occurs.[104]

The induced oxidative stress in insulin-resistant cells and GSH depletion results in increased generation of H_2O_2[111] that increases the conversion of vanadate into peroxidovanadate species.[332] Peroxidovanadate species are even stronger and irreversible inhibitors of PTP compared to vanadate and act by oxidising active-site cysteine residues,[312,333] and enables strong activation of the PI3K and MAPK pathways, associated with cell proliferation and survival.[58,334] The stabilisation of H_2O_2 by peroxidovanadate formation, leads to it becoming a positive messenger in insulin signalling.[110,332]

Chemometrics models developed for the insulin-sensitive and -resistant adipocyte vanadate studies were consistent with an increase in TAG production over the concentration range 0-15.6 μM V(V) evidenced by the increase in the bands ~1743, 1473, 1182 and 1116 cm^{-1} (**Table 1.1**). Vanadate exhibited it cytotoxic action from 15.6 μM for insulin-resistant cells, therefore, an effective concentration range for vanadate insulin-mimetic activity was defined between 0-10 μM, with insulin-sensitive cells able to tolerate up to 31.3 μM before clear evidence of the onset of cytotoxicity. The low micromolar concentrations of V(V) were commensurate with other studies utilising vanadate as an insulin mimetic e.g., Germinario, *et al*.[335] reported that orthovanadate was most effective at 10 μM in 3T3-L1 adipocytes, *in vitro*. This has certain ramifications regarding the use of vanadium as a cytotoxic agent and its potential detrimental effects on insulin-sensitive adipocytes at higher concentrations that will affect essential biochemical processes.

The ROS generated by chronic ET-1 treatment has been used as a model to induce oxidative stress that is typically observed in T2DM patients,[336] and explained the reduction in cellular defences (such as GSH and NADPH levels). It is postulated that this lack of defence and the increased production of peroxidovanadate species enabled V(V) to enhance insulin-mimetic activity in the 10-15μM V(V) range compared to insulin-sensitive cells. Furthermore, Nakamura, *et. al*.[327] reported that at non-cytotoxic

concentrations of oxidants, changes in protein phosphorylation is an adaptive response to mitigate damage induced by oxidative stress. Thus, vanadate at low concentrations, may act to reduce oxidative stress in both insulin-sensitive and -resistant cells, through vanadylation of tyrosine residues.[104] In agreement with the results obtained in this current study, Ma, *et al*.[337] showed that transient ROS treatment of 3T3-L1 adipocytes (in the form of H_2O_2) can promote glucose uptake through oxidation of PTEN. This enhances Akt phosphorylation and increases GLUT4 translocation, however, when the levels of ROS become excessive, p53 can inhibit the Akt and mTOR pathways and activate PTEN leading to apoptosis.[311]

4.4.1.2 Vanadate as a Cytotoxic Agent

As previously stated, higher levels of GSH and other defensive mechanisms in insulin-sensitive adipocytes delay the onset of vanadate cytotoxicity up to 31.3 μM. Beyond this concentration, a number of concurrent biological processes were observed from chemometric modelling of FTIR data that could be associated with lipid membrane changes and lipid peroxidation processes.[195] Similar chemometric modelling on insulin-resistant adipocytes showed that these cells exhibited changes indicative of the onset of cytotoxic responses at [V(V)] > 15.6 μM and also revealed some specific actions different from those observed in insulin-sensitive adipocytes, alongside some common changes.

A general model of vanadate cytotoxic action was postulated for insulin-sensitive and -resistant adipocytes (**Figure 4.37**) after high levels of oxidative stress were induced that triggered apoptosis mechanisms. Vanadate is known to oxidise NADH by a free radical mediated process, depleting intracellular stores of NADH, NADPH and GSH.[165,338] The depletion of cellular defences results in the generation of ROS, inducing pathways that lead to lipid peroxidation, an aetiology that is associated with inflammation, insulin-resistance and other diseases.[303]

Keller, *et al*.[338] postulated that lipid peroxidation is mediated by V(IV) and is induced by hydroxyl radicals ($OH^{-\bullet}$), however, this assertion is contentious and Ding, *et al*,[339] reported a study on vanadate-induced AP-1 activation in mouse epidermal cells and, using $OH^{-\bullet}$ scavengers, showed that this radical does not alter AP-1 activity, rather superoxide ($O_2^{-\bullet}$) and H_2O_2 were the main species inducing lipoperoxidation. Byczkowski and Kulkarni,[165] have also presented evidence that the hydroxyl radical does not participate in vanadium induced lipoperoxidation.

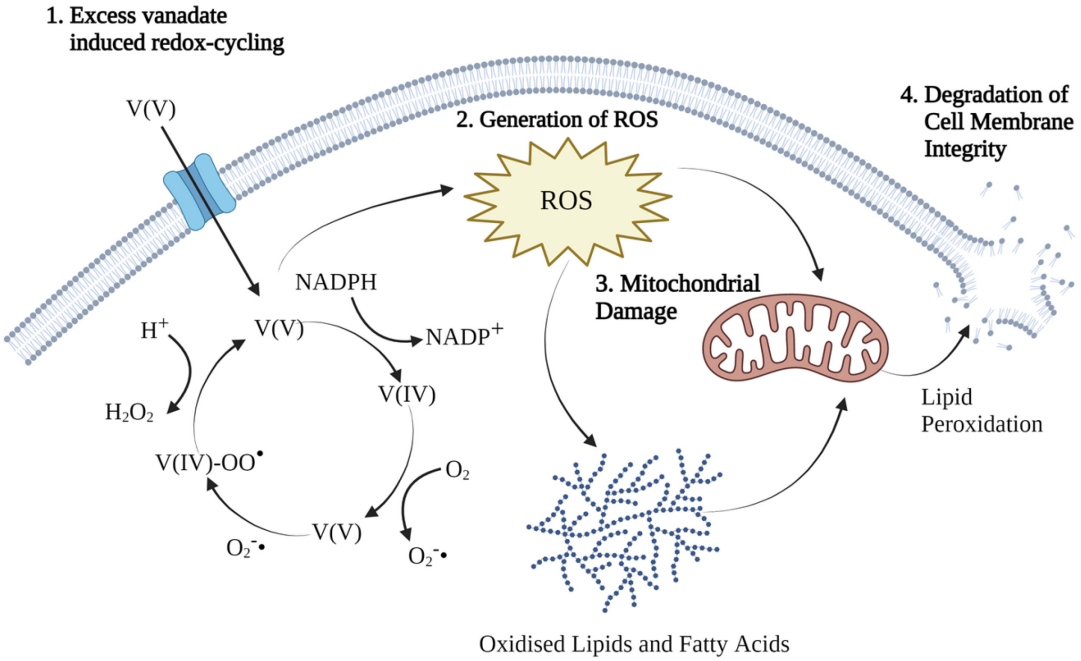

Figure 4.37: Postulated four-step process of cytotoxic vanadate action on insulin-sensitive and -resistant 3T3-L1 adipocytes: 1) redox cycling induced by excess vanadate entering into cells;[129,299] 2) increased ROS generated resulting in FFA oxidation and other stresses in the endoplasmic reticulum (ER); 3) mitochondiral damage induced by metabolism of oxidised fatty acids inducing lipotoxicity;[146] and 4) loss of integrity in membrane lipids induced by lipid peroxidation.[195] Created with BioRender.com.

Huang, *et al*.[340] demonstrated that vanadate activates p53 tumour suppressor proteins in response to H_2O_2 generation to induce apoptosis. Activation of the p53 protein depends on its phosphorylation and is induced by a number of mechanisms, mainly in response to DNA damage, which is one manner in which vanadium can impart its cytotoxic action along with lipid peroxidation.[129,340] Inhibition of tyrosine phosphatases and the extended duration of phosphorylation of proteins such as AP-1, MEK-1, ERK-1, JNK-1, PI3K and NF-κB are also associated with vanadate cytotoxicity and are all linked to pathways promoting ROS production and DNA damage.[129,339,341] Changes in DNA structure were observed in the FTIR spectra obtained in this current study and were correlated with changes in FTIR bands associated with increased lipid peroxidation and cell membrane changes.

In the model of vanadate insulin-mimetic action towards insulin-resistant adipocytes (**Figure 4.36**), H_2O_2 can further react with V(V) to form peroxidovanadate species to irreversibly inhibit PTPs, which is beneficial as an insulin-mimetic/enhancer at low concentrations, but cytotoxic at high concentrations.[111,250] Phosphorylated proteins are known to exist in a β−sheet conformation as evidenced by Raman spectroscopic

studies.[309] β-sheet structures were observed in FTIR spectra around 1625 cm^{-1} along with changes in β-turn structure around 1660 cm^{-1}, obtained from insulin-sensitive and -resistant cells treated with vanadate, particularly for insulin-sensitive cells. Changes in β-sheet structures were more prominent in the FTIR spectra of adipocytes when they were also treated with fructose (Section 4.4.2). This was most likely the result of fibrosis occurring as a means of protection against higher ROS and hypertrophy.[26]

Cytotoxic concentrations of vanadate induce mitochondrial dysfunction as a result of ROS, induce lipid peroxidation and activate the p53 pathway, via release of cytochrome *c* and caspase activation.[340,342-343] Mitochondria are mainly devoted to energy production and metabolism via synthesis of ATP through oxidation of carbohydrates, lipids and amino acids.[344] In a study of neurodegenerative diseases, Cenini, *et al*.[342] report that lipid peroxidation may induce p53 proteins to trigger apoptotic pathways that lead to amyloid structures, consisting of neurofibrillary tangles. These amyloid structure were reported to consist mainly of protein aggregates with β-sheet structures.[173] Shivu, *et al*.[175] have used attenuated-total-reflectance (ATR) FTIR spectroscopy to elucidate the structures of β-sheet proteins associated with amyloid fibrils assigned to bands around 1623 cm^{-1}.

Lipid peroxidation can be triggered by the one-electron oxidation of V(IV), critical in the mechanism of cytotoxicity and affecting bio-membranes, including those of the mitochondria.[165] This was an important finding in this study as the postulated redox-cycling mechanism of **Figure 4.37** is known to induce lipid peroxidation and cell membrane changes,[195] which were observed in the chemometrics models developed herein. The ability of vanadate to induce oxidative stress and generate free radicals can promote peroxidation in phospholipid peroxisomes[305] and in the presence of H_2O_2, can breakdown fatty acids during lipoperoxidation.[165,338]

Aon, *et al*.[345] postulated that the redox environment associated with altered mitochondrial function in response to ROS levels and increased lipotoxicity through either lack of, or incomplete β-oxidation, can result in increased H_2O_2 production and leads to insulin resistance. Oleszko, *et al*.[202] reported that H_2O_2 generated in blood as an immune response, rendered lipids and phospholipids more susceptible to peroxidation. In the postulated model of **Figure 4.37**, biochemical changes induced by ROS were associated with lipid and fatty acid bands in the FTIR spectra of treated adipocytes. These bands correlated with excessive production of H_2O_2 through vanadate redox cycling at higher concentrations and the increased production of H_2O_2 by the mitochondria, which induced

lipid peroxidation. Changes in neutral lipid synthesis to fatty acid production as responses to stress were consistent with observations reported in the literature, particularly in cancer cells, which are in a constant state of high oxidative stress.[147,346-349]

Metabolic changes induced by T2DM have been reported to result in uncontrolled degradation of fatty acids, which cannot be efficiently processed by the citric acid cycle and leads to the accumulation of harmful ketonic bodies.[104] A number of authors have reported two breakdown products of lipid peroxidation; 4-hydroxynonenal (4-HNE) and malondialdehyde (MDA), which can induce apoptotic pathways.[303,342] Patel, *et al*.[350] state that 4-HNE, when its production exceeds concentration that can be inactivated, can form adducts with proteins and detection by immunoassays have been used to study chronic oxidative stress. FTIR spectroscopy is sensitive to protein secondary structural changes and the effects of these ketonic bodies were found to manifest themselves in spectral changes in the region 1700-1600 cm^{-1}.

FTIR spectroscopy is sensitive to ν (C=O) modes in aldehydes, ketones and carboxylic acids. Mirghani, *et al*.[351] studied the formation of MDA as an oxidation product in palm oil in the region 1730-1680 cm^{-1} assigned to stretching bands of aldehydic C=O groups. These authors only detected the presence of MDA by difference spectra of MDA spiked palm olein. Aldehydes also exhibit bands between 2699-2695 cm^{-1},[351] however, assessment of the spectra in this study only revealed small changes in this region using normalised, second derivative spectra and assessment was difficult due to low band intensities. The lipid ester and fatty acid content in adipocytes would effectively mask any absorbances of generated aldehydes and therefore, the presence of lipid peroxidation was established through peak ratios as defined Ricciardi, *et al*.[195] The use of combined techniques, such as FTIR and mass spectrometry may be useful in future studies to determine any correlations between MDA/4-HNE and the bands between 1730-1680 cm^{-1}.

4.4.2 Fructose Metabolism and Induced Oxidative Stress

4.4.2.1 Fructose Metabolism in Insulin-Sensitive Adipocytes

The vanadate concentration study indicated that biochemical changes related to cytotoxicity were initiated in the range 15-30 μM for insulin-sensitive and -resistant cells. The IC_{50} value was estimated to occur over the range 125-250 μM, therefore, in the DoE study, a value of 150 μM was set as the high level [V(V)]. The DoE already included glucose and vanadate data and extended the study to include the effects of no-sugar and

fructose. In this manner, the effects of each treatment were compared using multivariate regression models to better understand the synergies between the treatments and reveal the mechanism of action of sugars and vanadate simultaneously.

Figure 4.38 presents a postulated model of fructose action on insulin-sensitive adipocytes in the absence of glucose, defined by the fructose only treatment (*b*) in the Block 1 DoE (Section 4.3.5.1). While circulating fructose is normally controlled in fasting conditions to 0.06 mM,[248] it is present at much higher concentrations when foods or drinks with high fructose levels are consumed that overwhelm normal homeostatic processes.[249] High fructose concentrations are relevant to the current studies and are known to induce oxidative stress in cells, through the process of DNL, that compromise cellular antioxidant defence mechanisms[20] and deplete adenine nucleotides, which promote pyruvate synthesis.[11] By entering glycolysis via the pentose phosphate pathway (PPP), fructose metabolism is unregulated by insulin, therefore, increased TAG and FFA synthesis result.[8,20,24] The PLS-DA model developed for Block 1 showed that glucose and fructose were metabolised differently as they clustered in opposite directions from each other in the joint t_1-t_2 direction (**Figure 4.21**). This model showed that adipocytes used glucose for TAG synthesis whereas fructose induced changes in membrane lipids as observed in the t_1 direction, however, the t_2 direction showed that fructose resulted mainly in FFA production (large weighing of bands at 1729, 1471, 1415, 1390 and 1178 cm^{-1}).

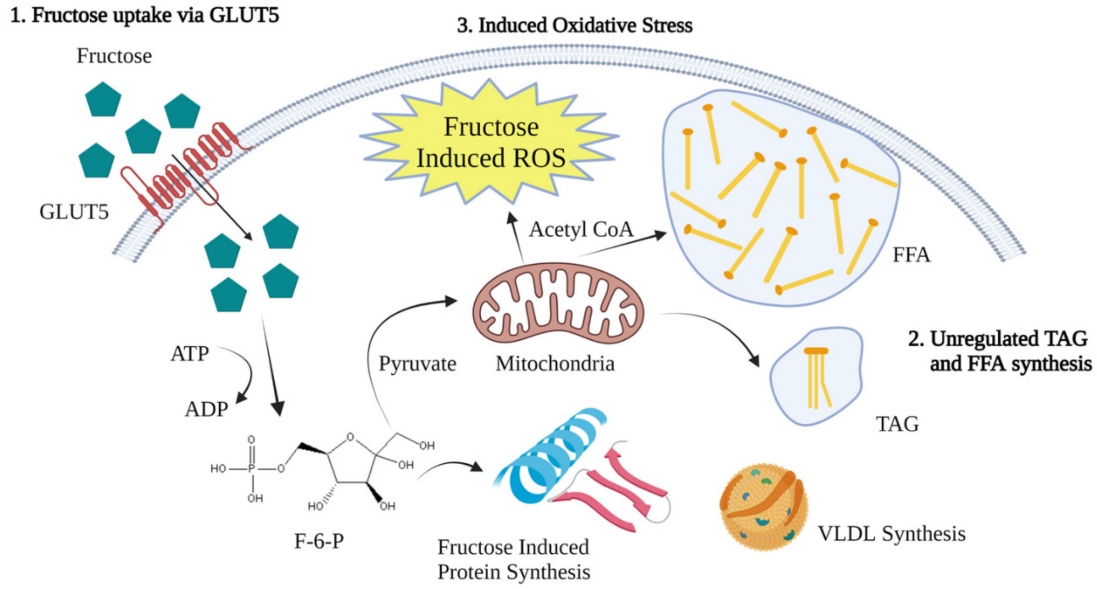

Figure 4.38: Postulated model of fructose metabolism in adipocytes for higher than physiological concentrations showing; 1. Fructose entry into adipocytes via the GLUT5 transporter;[33] 2. TAG and FFA synthesis induced by pyruvate, including production of VLDL and protein synthesis;[11,352] and 3. Oxidative stress induced by fructose metabolism. Created with BioRender.com.

Mayes[11] reported that fructose metabolism in adipocytes causes impaired glucose utilisation promoting the release of non-esterified fatty acids (NEFA) and VLDL production.[11] Froesch and Ginsberg,[353] reported that fructose is metabolised slower than glucose when fructose levels are low, but faster at high concentrations. The results obtained herein were consistent with these observations, as adipocytes treated with equal concentrations of glucose and fructose did not uptake glucose as readily as the glucose-fructose treatment (*ab)* and clustered in multivariate space in an intermediate level between the glucose (*a*) and fructose (*b*) treatments (**Figure 4.21a**). Fructose treated cells produced more FFA and lactate (1131 cm^{-1}), which indicated that its metabolism follows a different pathway to glucose metabolism. Unlike glucose, fructose enters adipocytes using the GLUT5 transporter for cellular uptake[27] and, unlike the liver, fructose is phosphorylated by hexokinase (HK),[353] which forms fructose-6-phosphate (F-6-P), thus entering pathways of lipid and fatty acid synthesis that deplete ATP levels.[11,354]

A no-sugar treatment (*1*) was also part of the design and clustered with the fructose treatments in the chemometric model. When no sugar was present for metabolism, the main nutrient available in the supplemented media was glutamine.[355] Glutamine enters the TCA cycle through glutaminolysis, which plays a key role in the regulation of inflammatory responses and acts to inhibit glycolysis.[356] These observations combined with the results obtained in this study indicate that native fructose uptake may be slower than glucose uptake and based on the chemometric models developed, its metabolism resembles that of glutamine rather than glucose.

As was stated in Section 1.2, *in vivo*, the liver processes the majority of fructose and metabolises it in an unregulated manner via DNL, which then releases TAGs and FFAs into circulation. These exogenous lipid sources are the main form utilised by adipocytes where they are stored as energy reserves for use by other organs when required.[11,20,357] In the *in vitro* cultures of this current study, fructose was delivered to adipocytes in its native form and was representative of a higher than physiological fructose load in circulation.[35,66,358] Therefore, native fructose may not be taken up by adipocytes rapidly and when it is transported into adipocytes, it favours the synthesis of FFAs and proteins rather than TAGs and glycogen.[11]

Block 2 treatments included vanadate at a concentration of 150 μM. An interesting finding was that the vanadate treatment alone (*c*) resulted in two populations of cells and one of these populations was observed to cluster with the fructose vanadate treatment

(*bc*). This may be a result of the IC_{50} [V(V)] resulting in cells that were vulnerable to vanadate action and those that were resistant, possibly through substantial depletion of GSH defences.[165,338] The population that clustered with the fructose-vanadate (*bc)* treatments were characterised by high protein content and low lipid content in their FTIR spectra. The observation that all of the (*bc)* treatments clustered together indicated that the additive oxidative stress induced by vanadate and fructose may have promoted the onset of more rapid apoptosis in these cells.

Cells treated with glucose (glucose-vanadate *ac* and glucose-fructose-vanadate *abc*) clustered together in the Block 2 treatments and this was associated with TAG production rather than FFA production. This indicated that glucose may have a protective effect in the presence of vanadate and fructose, where it may be preferentially metabolised in response to oxidative stress. Froesch and Ginsberg,[353] report that insulin can promote fructose uptake and metabolism only in the absence of glucose, however, in the presence of glucose and insulin, fructose uptake remains at baseline levels and is not suppressed. The results of this study indicated that vanadate, through inhibition of PTPs, promoted fructose metabolism in the presence of glucose.

4.4.2.2 Fructose Metabolism in Insulin-Resistant Adipocytes

ET-1 induced insulin-resistance of adipocytes results in a state of high oxidative stress[75] and when treated with higher concentrations of vanadate, the process of apoptosis is induced. The addition of fructose was expected to induce greater stresses on these cells and was representative of obese, insulin-resistant individuals consuming a large sugar load in the form of high sucrose or HFCS foods.[359] The Block 3 treatment protocols were used to replicate this situation *in vitro*.

Chemometric modelling of the Block 3 data revealed lower lipid and higher FFA content in no-sugar and glucose treated cells compared to fructose alone or the combined glucose-fructose treatment. This observation was consistent with insulin-resistance induced in these cells and showed that in the presence of fructose, insulin-resistant adipocytes may be using this sugar as an energy source. Also, glucose transport into the cells could be facilitated to a small extent by fructose as evidenced by the combined glucose-fructose treatment separating furthest from the no-sugar treatments in PLS-DA scores direction t_1. Mayes,[11] states that if fructose and glucose were administered equally, there is a likelihood of increased lipogenesis, particularly with an increase in insulin. Since the serum added to media contains insulin, the current data were consistent with this statement.

When insulin-resistant adipocytes were treated with fructose alone, a different mechanism of metabolism was observed in the FTIR spectra related to increases in TAGs and FFAs. Fructose induced membrane lipid changes were also observed at 2925 and 2859 cm^{-1}.[195,205] These results indicated that fructose alone may not be effectively taken up in insulin-resistant cells and further supports the postulate that fructose may be enhancing glucose uptake. The generation of H_2O_2 under conditions of high oxidative stress is also known to mimic insulin action on glucose transport in adipose tissue.[360] Whichever mechanism is occurring, these results indicate that during large fructose loads, adipocytes can use fructose as an energy source, however, the metabolism of fructose may be inducing ROS and the production of oxidised fatty acids and may also be promoting small amounts of glucose uptake. However, oxidised fatty acids and the generation of very low-density lipoproteins (VLDL) further induce and maintain insulin resistance in the cells and when released into circulation, result in detrimental effects in other organs.[20]

The no-sugar and glucose treatments were associated with higher protein FTIR band intensities as a result of lower lipid synthesis induced by insulin resistance. In particular, these treatments showed large loading weights at 1656, 1625 and 1548 cm^{-1} associated with α-helix, β-sheet and amide II bands, respectively. As discussed in Section 4.3.2, the increase of β-sheet proteins, particularly protein aggregates and a decrease in α-helix proteins was an indication of biochemical transformations associated mainly with disease state, possibly induced by oxidative stress and fibrosis,[26] as a result of insulin-resistance induced in these cells.

Block 4 treatments represented the situation of obese, insulin-resistant individuals on a high-sugar diet, treated with vanadate. The PLS-DA model showed a clear separation of the vanadate only treated cells from those treated with vanadate-sugar, and were described by lower lipid and higher protein content. The separation of the vanadate only treatment from the others was consistent with the cytotoxic action of vanadate, inducing changes in DNA, or FFAs observed at 1716 cm^{-1}.[110-111,129,182] The correlation of the 1716 cm^{-1} with the membrane lipid/fatty acid band at 2920 cm^{-1} makes band assignment to FFA the most likely outcome and was consistent with the lipid peroxidation argument presented earlier in this chapter.[195,202,205]

The sugar containing Block 4 treatments showed clustering in the order fructose-vanadate, glucose-fructose-vanadate and glucose-vanadate, respectively, and these

clusters were evidence of vanadates insulin-mimetic activity based on two observations; firstly, the glucose-vanadate treatment resulted in the highest intensity of the TAG band at 1747 cm^{-1}, while the fructose-vanadate treatment contained the highest FFA content described by bands at 1729, 1471, 1415, 1178 and 1110 cm^{-1}; and secondly, the order of treatment clusters was the inverse of the observations made in Block 3, providing evidence that vanadate was promoting cellular uptake and metabolism of glucose into the cells.

Hajduch, *et al*.[27] reported that insulin-resistant rats provided with 3.8 mM V(V) in drinking water, were able to restore fructose uptake in adipocytes via the GLUT5 transporter as insulin-resistance has also been shown to reduce fructose, as well as glucose uptake. A comparison of the Block 3 and 4 chemometric models (Sections 4.3.5.3 and 4.3.5.4) showed that in the presence of vanadate, insulin-resistant cells were able to use glucose as an energy source, and in the presence of fructose, the ability to utilise fructose was diminished. This was demonstrated by the glucose-fructose-vanadate treatment representing an intermediate condition in the Block 4 between the fructose-vanadate and the glucose-vanadate treatments and a similar conclusion was drawn for the Block 1 data where the glucose-fructose treatment represented an intermediate level between glucose- and fructose-only treatments (**Figure 4.21**).

Analysis of the centre point data showed distinct differences between insulin-sensitive and -resistant cells treated with glucose, fructose and vanadate. Chemometric analysis of these data showed that insulin-sensitive adipocytes process sugars differently than insulin-resistant cells. In particular, insulin-resistant adipocytes showed larger changes in membrane associated lipids, large changes in DNA/FFA and protein bands and lower TAG levels compared to insulin-sensitive cells. Therefore, the FTIR spectra were able to identify bands associated with increased oxidative stress, induced by insulin-resistance, fructose and vanadate that were attributed to lipid membrane integrity changes as a result of lipid peroxidation and changes in protein content and secondary structure, possibly as an indicator of DNA damage. **Figure 4.39** provides a postulated model for the combined action of glucose, fructose and vanadate on insulin-resistant cells based on the observations made on the Block 4 model.

The model in **Figure 4.39** represents a composite of all of the previous models describing combined sugar-vanadate action. Insulin-resistant adipocytes were already in a state of higher-than-normal oxidative stress, with lower GSH and NADPH levels.[357] Vanadate entry, via ion channels, mimics phosphorylation of the insulin receptor, binding to the β-

subunit of the receptor and activating PI3K/Akt pathways that translocate GLUT 4 to the plasma membrane, where glucose can be taken up and metabolised in the cell.[111] As observed in the FTIR spectra, an increase in lipid bands was an indication of glucose metabolism into TAGs, which was not observed in the Block 3 insulin-resistant adipocytes in the absence of vanadate.

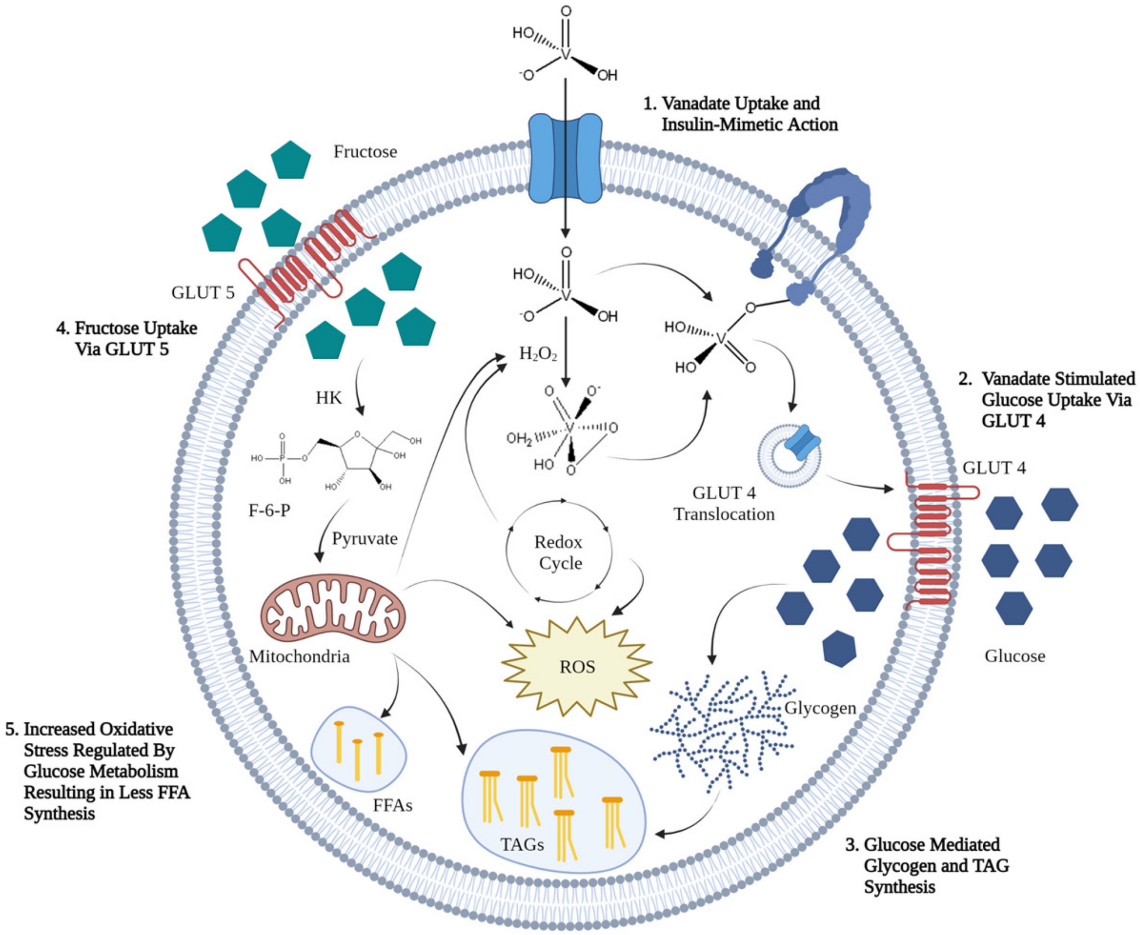

Figure 4.39: Postulated model of vanadate action towards insulin-resistant adipocytes in the presence of high sugar concentrations. The cell is already under high oxidative stress induced by insulin-resistance and represented by the ROS symbol;[75] 1. Vanadate entry into adipocytes via phosphate or sulfate ion channels; 2. Glucose uptake stimulated by vanadate;[110] 3. Synthesis of glycogen and lipids from glucose; 4. Fructose uptake through GLUT 5 transporter; 5. Increased oxidative stress leads to mitochondrial and ER damage and synthesis of TAGs and FFAs.[361]

Fructose metabolism, in the presence of an equal concentration of glucose resulted in a decrease in glucose metabolism consistent with the findings of Froesch and Ginsberg.[353] This was also observed in the Block 1 analysis of insulin-sensitive cells in the presence of equal concentrations of glucose and fructose. In treatments with glucose, fructose and vanadate, H_2O_2 already generated by oxidative stress resulted in peroxidovanadate species that promoted irreversible PTP inhibition.[111] This enhanced glucose metabolism

and may be representative of a protective mechanism of the cell against higher oxidative stresses induced by fructose.[20] The redox-cycling of vanadate can also result in higher H_2O_2 and at higher [V(V)], this would lead to vanadate exhibiting a greater cytotoxic action, rather than an insulin-mimetic behaviour. H_2O_2 induced by oxidative stress may also be mimicking insulin for glucose transport into adipocytes,[360] and further work is required to investigate whether this is a synergistic effect of vanadate induced ROS.

Chapter 5 Spectroscopic and Chemometric Investigations of the Effects of Vanadate, Cisplatin and Doxorubicin Towards the HepG2 Cell Line

5.1 Introduction – The HepG2 Cell Line as a Model of Insulin Resistance, Metabolic Disorders and Anti-Cancer Therapies

The HepG2 cell line is used widely for *in vitro* studies of drug metabolism, hepatotoxicity and various other treatments because it displays similar cell biology to normal hepatocytes found *in vivo*.[244,362] Insulin resistance in hepatocytes results in impairment of glucose metabolism, which leads to excess circulatory glucose that can interfere with cellular survival and proliferation.[363] The other main effect of hyperinsulinemia in hepatocytes is the over production of fatty acids to result in steatosis.[363] Overall, these conditions contribute to diseases, such as metabolic syndrome, T2DM and cancer.[20,364]

In Western diets, sucrose is processed at the jejunum where it is cleaved by the enzyme sucrase into glucose and fructose. These monosaccharides are transported to the liver via the portal vein, where they are processed into glycogens that can be used by other cells as energy stores.[20] In the USA, the food additive HFCS contains up to 55% fructose in its free form and is used as a substitute for sucrose in processed foods and carbonated beverages. It has been reported that fructose is mainly processed by the liver,[20] however, Jang, *et al.*[365] have shown that most dietary fructose is cleared by the intestine, while higher doses reach the liver and circulation. This finding indicates that the gastrointestinal tract also plays a major role in fructose homeostasis, but the liver is responsible for many of the features of metabolic syndrome.[143]

Vanadate drugs are insulin mimetics and are cytotoxic under the right conditions (Chapter 4). A number of comprehensive reviews describe in detail the chemistry and biology of many vanadium compounds synthesised as anti-diabetic and anti-cancer drugs.[102,105,129,132,144-145] Vanadium compounds are postulated to exert more potent anti-tumour potential on the initiation rather than the promotion stage of hepatocarcinogenesis, possibly through a mechanism that reduces intracellular concentrations of carcinogen-derived reactive intermediates.[366] This behaviour is dependent on the particular vanadium complex used.

This chapter describes studies using FTIR microspectroscopy to better understand the mechanisms of vanadate and sugar metabolism and to provide some key insights into the insulin-mimetic and cytotoxic effects of sodium orthovanadate on treated HepG2 cells as an *in vitro* model of the liver. FTIR microspectroscopy was used to investigate the biochemical mechanisms of cell viability and was compared to standard MTT cell viability assays. Vanadate cytotoxicity results were then compared to two well-known

chemotherapeutic agents, cisplatin[367] and doxorubicin[140] in order to gain insights into the molecular mechanisms of action at the single cell level.

5.2 Experimental Design and Objectives

The cytotoxicity of sodium orthovanadate, cisplatin and doxorubicin towards HepG2 cells in supplemented culture media was used to establish the IC_{50} values. An MTT type cytotoxicity study[253-254] was performed using FTIR spectra to gain further insights into the mode of action of vanadate, cisplatin and doxorubicin on HepG2. The critical concentration of vanadate once evaluated was used in a two-level factorial design (Chapter 1, Section 1.7) to investigate the effects of glucose, fructose and vanadate independently and in various combinations when treated according to the design shown in **Figure 5.1**.

Blocks (Section 4.3.5) are presented in **Figure 5.1**, with Block 1 describing the points no-sugar (*1*), glucose (*a*), fructose (*b*) and glucose-fructose (*ab*) and Block 2 describing the points vanadate only (*c*), glucose-vanadate (*ac*), fructose-vanadate (*bc*), and glucose-fructose-vanadate (*abc*). Centre points (*cp*'s) were used to evaluate the repeatability and reproducibility of the data collected at the design centre. Centre points are only applicable to continuous variables and are the mid-points of the levels defined for the factors. Use of *cp*'s is a standard validation method of an experimental design,[223,226] with the major assumption that the variability at the extremes of the design are statistically equivalent to the variance of the *cp*'s.

Cells were cultured onto CaF_2 substrates and allowed to fully attach before treatment. The treatments in **Figure 5.1** were applied using the conditions listed in **Table 5.1**. The glucose concentration used was 5.0 mM to mimic physiological concentrations in circulation[247] and the fructose concentration of 5.0 mM represented a large spike in circulation concentration after ingestion of foods containing high fructose content.[11,248]

The high (+1) level of vanadate was defined to be close to the IC_{50} value, therefore, the centre point vanadium concentration was well below the cytotoxic concentration and may provide information on its insulin mimetic action, while the high-level dose was used to evaluate cytotoxicity. In addition to the high level, low factor levels were defined by (-1) and centre points were defined by (0). Each run was an FTIR spectrum for single cells acquired on CaF_2 plates. Replication was performed by randomly acquiring spectra from multiple cells of each treatment attached to the CaF_2 substrates. Spectra acquired in this study were from single cells using the methodology described in Section 2.8.1.

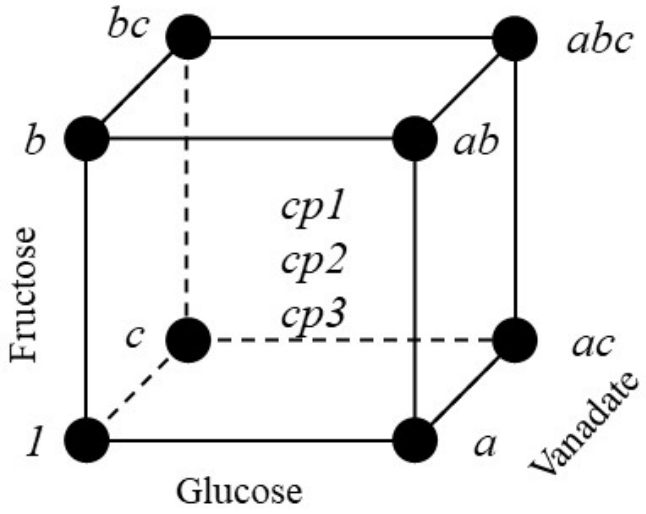

Run	Glucose (A)	Fructose (B)	Vanadate (C)	Block
1	-1	-1	-1	Block 1 (sugar treatments only)
a	+1	-1	-1	
b	-1	+1	-1	
ac	+1	+1	-1	
c	-1	-1	+1	Block 2 (sugar and vanadate treatments)
ac	+1	-1	+1	
bc	-1	+1	+1	
abc	+1	+1	+1	
cp1	0	0	0	Design Centre Points
cp2	0	0	0	
cp3	0	0	0	

Figure 5.1: Experimental design for investigating the effects of sugars and vanadate using the orthogonal 2^3 full factorial design in 11 runs. Standard notation for experimental runs was used as described by Montgomery.[226] The design was based on two blocks defined by treatments with and without vanadate.

Table 5.1: Experimental factor levels defined for the design shown in **Figure 5.1**.

Factor	Low Level (-1)	High Level (+1)	Centre Point (0)
Glucose (mM)	0	5.0	2.5
Fructose (mM)	0	5.0	2.5
Vanadate (μM)*	0	50	25

*The vanadate concentration was determined based on MTT assays described in section 5.3.1

5.3 Results

5.3.1 Cytotoxicity of Vanadate, Cisplatin and Doxorubicin towards HepG2 Cells Using MTT Assay

Standard MTT *in vitro* cytotoxicity assays[253-254] were performed on HepG2 cells. Cells were treated with either vanadate, (V(V)), cisplatin or doxorubicin for 72 h in supplemented culture media incubated at 37 °C and 5% CO_2, prior to the MTT assay. The treatment levels used were 0-1000, 0-100 and 0-10 μM for vanadate, cisplatin and doxorubicin, respectively (**Figure 5.1**). The concentration ranges for cisplatin and doxorubicin were chosen based on literature cytotoxic values.[368-370]

The cell viability was over 100% between 0 to 15 μM, for vanadate treated cells, therefore, vanadate may induce pathways that increase cell viability (**Figure 5.2a**). Beyond 15 μM, cytotoxicity ensues with an IC_{50} value of 68 ± 11 μM. The MTT assays for cisplatin (**Figure 5.2b**) gave an IC_{50} value of 6.4 ± 0.61 μM compared to literature values of 9.3-15.6 μM.[368-370] Although the calculated IC_{50} value was lower than the literature results, it was within the high variability in the MTT cytotoxicity assay.[371] The MTT assay for doxorubicin (**Figure 5.2c**) showed a linear, rather than a sigmoidal fit, however, the observed IC_{50} value of 1.0 ± 0.3 μM agreed with the literature value of 1.1 μM.[370]

5.3.2 Investigation of the Cytotoxicity of Vanadate, Cisplatin and Doxorubicin Towards HepG2 Cells Using FTIR Microspectroscopy.

HepG2 cells were seeded onto CaF_2 substrates and were treated as per Section 5.3.1. for 72 h prior to cell fixation and analysis using FTIR microspectroscopy. Single point-spectra were acquired using optimised scanning conditions (Chapter 3, Section 3.7). Raw and processed FTIR spectra of cells treated with three cytotoxic agents are provided in **Figure 5.3** over the 3000-1000 cm^{-1} region.

For the vanadate-treated cells (**Figure 5.3a**) the processed spectra showed two prominent bands at 2915 and 2847 cm^{-1} and two weaker bands at 2959 and 2872 cm^{-1}. These bands were assigned to membrane phospholipids and fatty acids.[195,205] The band at 1740 cm^{-1} was attributed to the ν (C=O) mode of lipid esters (**Table 1.1**). Increased lipid band intensities were observed over the range 31.3-125 μM, i.e., where cell viability rapidly decreased in the MTT assay curve (**Figure 5.2a**). At higher vanadate concentrations, the intensity of the lipid signal decreased again.

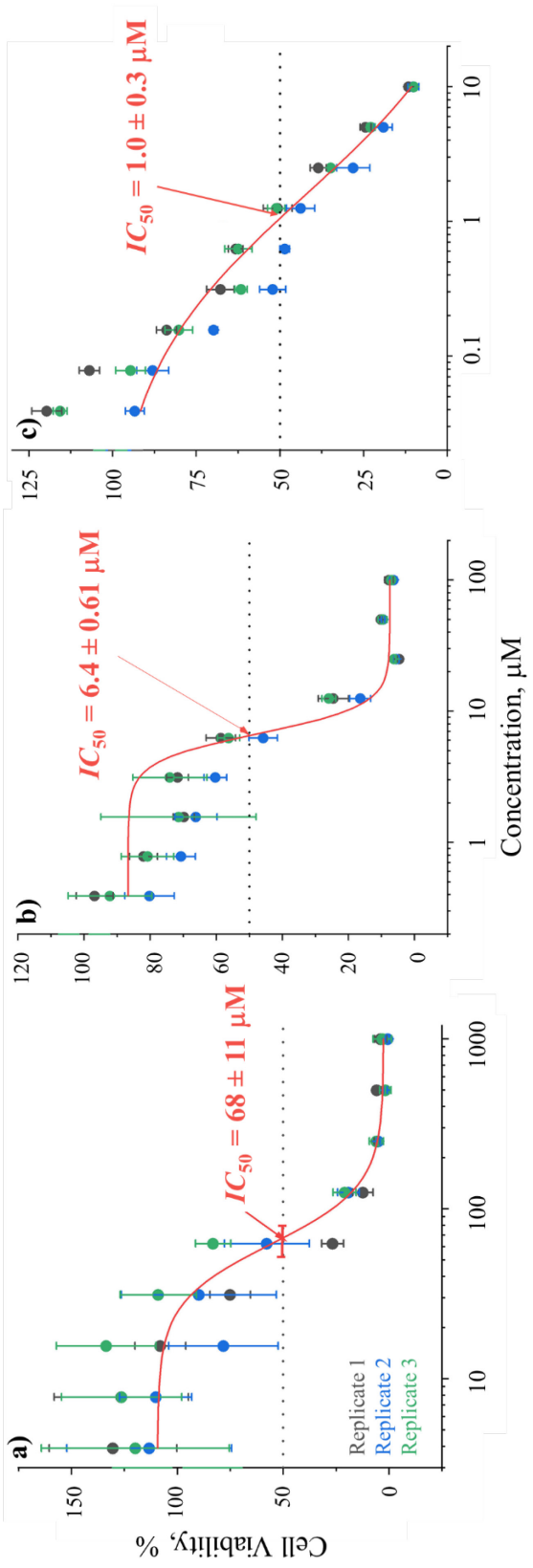

Figure 5.2: MTT assay results for cell viability of HepG2 cells treated with; a) sodium orthovanadate; b) cisplatin; and c) doxorubicin serially diluted by factors of two from the maximum concentration. The curves in all treatments were modelled using a sigmoidal curve fit, for experiments performed in triplicate. Error bars were drawn at the 95% confidence level for six replicate wells per treatment.

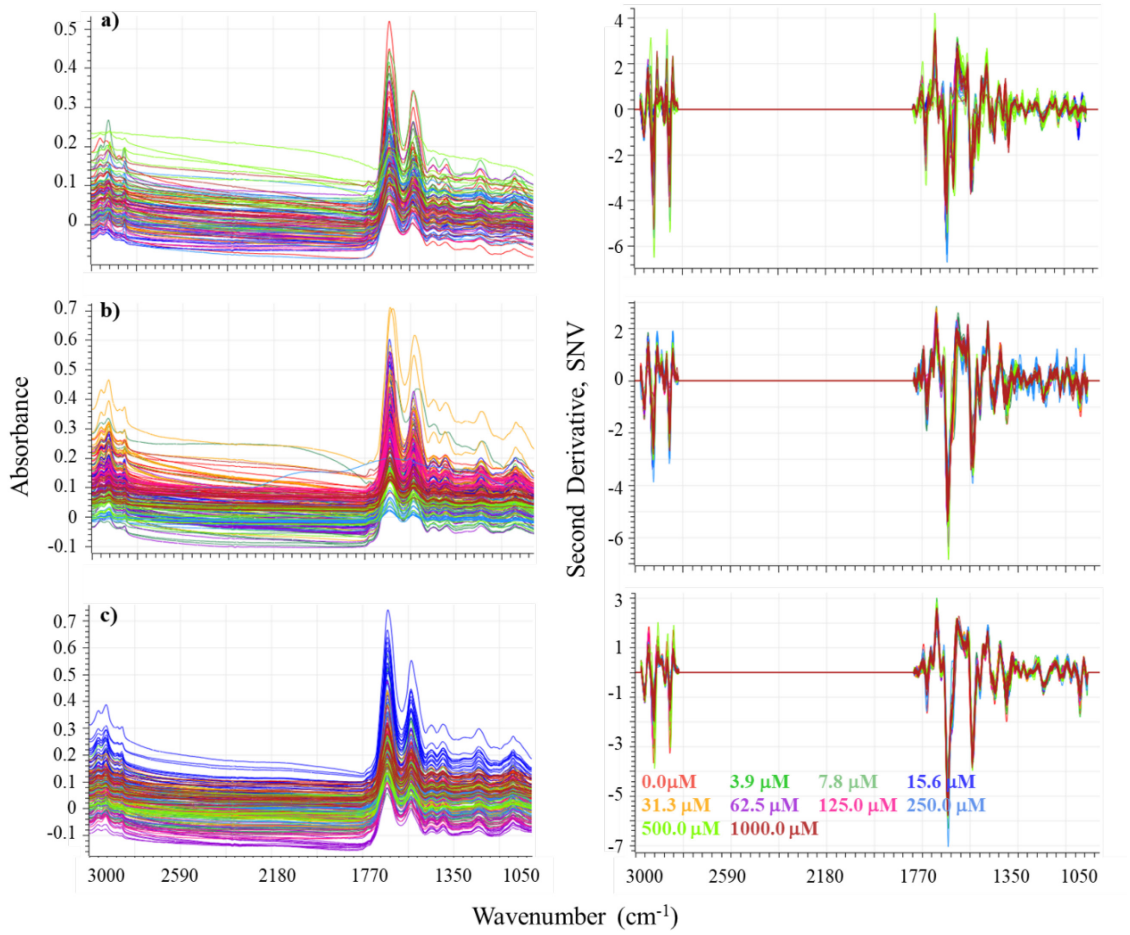

Figure 5.3: Raw and processed FTIR spectra of HepG2 cells treated with; a) vanadate; b) cisplatin; and c) doxorubicin. The processing applied to the data was atmospheric correction,[372] followed by Savitzky-Golay second derivative (second order polynomial, 13-point smoothing) and normalisation using standard normal variate (SNV) over the wavenumber region 3000-2800 and 1800-1000 cm^{-1}. The individual spectra were coloured according to the legend in c).

At low [V(V)], the lipid ester band at 1743 cm^{-1} was weak in intensity, which indicated that HepG2 cells store little lipid under favourable growth conditions compared to adipocytes (Chapter 4). As vanadate concentrations approached the IC_{50} value, the relative intensity of the lipid bands increased with increasing oxidative stress until 250 µM. Over the range 250-1000 µM, there was evidence of a protein conformational change with a change in the peak position from 1638 to 1623 cm^{-1}, which was consistent with changes in amide I secondary structures from random coils to protein aggregations.[175]

The changes in spectra with increasing vanadate treatment corresponded to changes in cellular morphology as observed in the optical micrographs (**Figure 5.4**). The control cells showed the cobblestone epithelial morphology typical of HepG2 cells[373] (**Figure 5.4a**). At 125 µM (**Figure 5.4b**), cells were less clustered and became more round, typical

of apoptosis.[327] At 1000 μM, most cells were dead and those remaining (**Figure 5.4c**) exhibit a fusiform stellate morphology typical of mesenchymal cells.[374]

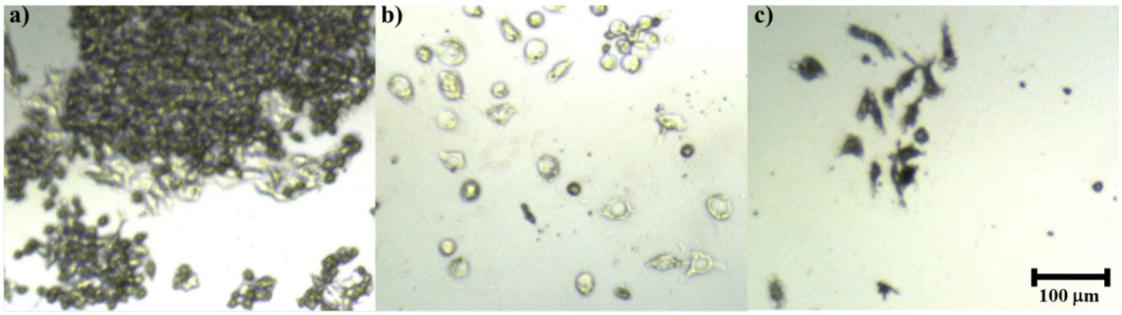

Figure 5.4: Optical micrographs of HepG2 cells; a) In the absence of, or at low concentrations of vanadate (0-15.6 μM); b) in the concentration range 31-125 μM vanadate (at the IC_{50} point); and c) at 1000 μM.

To determine whether the attached cells in **Figure 5.4c** were dead, a further study was performed where HepG2 cells were treated at higher vanadate concentrations (62.5-1000 μM), for 72 h at 37 °C and 5% CO_2. One set of cells were chemically fixed to CaF_2 substrates as a reference set and the remaining substrates were removed and incubated with normal supplemented culture media (72 h at 37 °C and 5% CO_2). The cells were chemically fixed to the substrates for FTIR microspectroscopic analysis. **Figure 5.5** compares the optical micrographs of the 62.5-, 250- and 1000-μM treatments before and after treatment and re-proliferation, respectively.

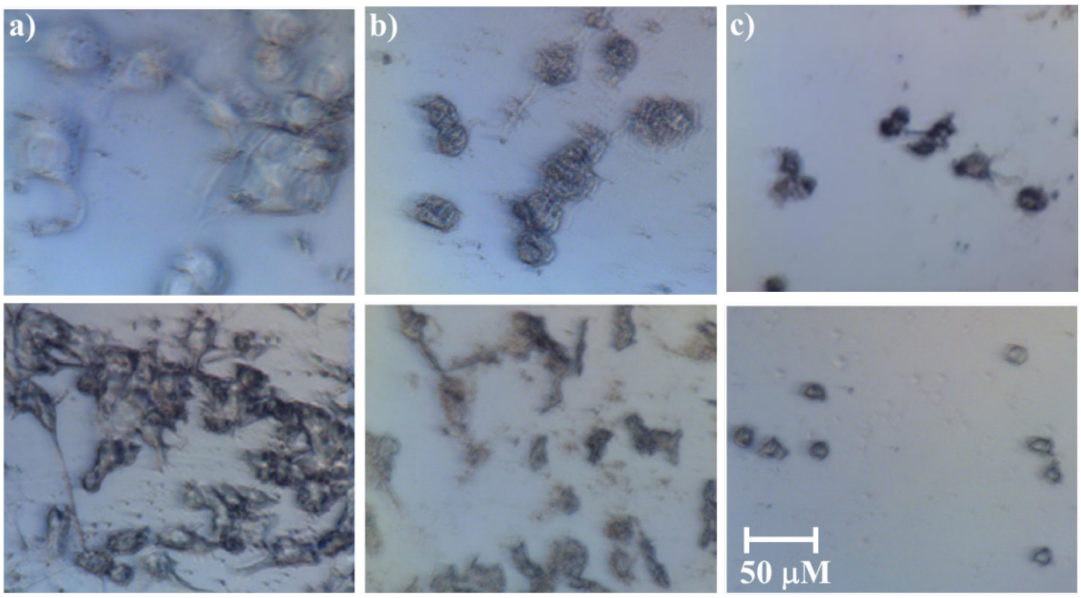

Figure 5.5: Optical micrographs of HepG2 high vanadate concetration treatment and reproliferation experiment; a) 62.5 μM; b) 250 μM; and c) 1000 μM. Top row; fixed vanadate treated cells; and bottom row, cells after re-proliferation (72 h in normal glucose suplemented vanadate-free medium).

The optical micrographs in **Figure 5.5** show that after treatment with high concentrations of V(V) followed by normal supplemented media, HepG2 cells re-proliferate or survive (**Figure 5.5a** and **b)**; these cells exhibit some fusiform shape and may be a different phenotype. In particular, at 1000 μM treatment (**Figure 5.5c**) the surviving cells were rounding and may be growing again as a new phenotype. Vileno, *et al.*[160] report that those cells remaining on the substrate may be those that are most treatment resistant, and this finding was supported by this current study. Due to time constraints no further work was undertaken on those cells, but will form the focus of future investigations.

5.3.2.1 Chemometric Assessment of Vanadate Treated HepG2 Cells Cytotoxicity Study

PCA was applied to processed spectra obtained from vanadate treated cells. Under the assumption that each cell scanned was a representative sample,[227] the method of random cross validation was used to validate the models. **Figure 5.6** shows the t_1 vs. t_2 scores plot for the analysis of the vanadate treated HepG2 cells.

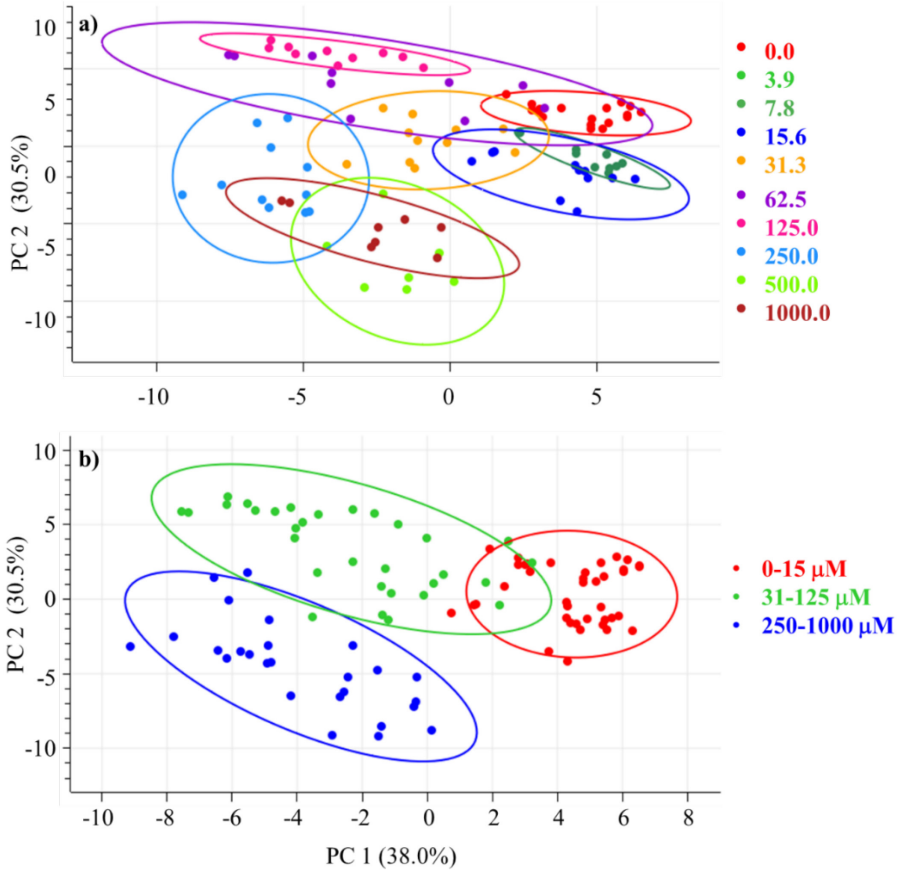

Figure 5.6: t_1 vs. t_2 scores plot for HepG2 vanadate study; a) scores grouped by vanadate treatment concentration; and b) separated into groups based concentration ranges identified in the MTT assay curve; cell proliferation range 0-15 μM; cell death range 31-125 μM; and almost complete cell death range 250-1000 μM, with data from surviving cells. Local Hotelling's T^2 ellipses were drawn at 95% confidence.

The data in **Figure 5.6a** were difficult to interpret; however, scores progressed from right to left with increasing vanadate concentration. Each treatment group formed local clusters and, in general, were observed to be distinct when grouped using local Hotelling's T^2 ellipses at 95% confidence. To improve interpretability, the scores were grouped based on the three concentration ranges observed in the MTT assay curve (**Figure 5.2a)**. Between 0-15 μM, vanadate may increase proliferation; between 31-125 μM, cell survival rapidly decreased; and between 250-1000 μM, most cells were dead and the surviving cells appeared to be a different phenotype (**Figure 5.4c** and **Figure 5.5**). A five PC model described 88% of the **X**-variance and the combined PC1-3 model described approximately 80% of the spectral changes (training and validation variance). The t_1 vs. t_2 scores plot showed that the biochemical changes induced by vanadate in HepG2 were described in two PCs.

Figure 5.7 presents the PCA scores vs. [V(V)] plots for t_1-t_3 as individual points and interval plots. The close resemblance of **Figure 5.7a** to the MTT assay curve (**Figure 5.2a)** indicated that the t_1 direction described cell viability. At 500 and 1000 μM an upward trend in t_1 scores indicated that a second biochemical process occurred at these concentrations.

The t_2 direction (**Figure 5.7b**) indicated that four different biochemical processes occurred with increasing [V(V)] over the ranges 0-15.6 μM; 15.6-125 μM; 125-500 μM; and 500-1000 μM; the first showed a linear decrease to 15.6 μM, then an increase to 125 μM, followed by a rapid decrease to 500 μM. The t_3 direction showed that the 1000 μM treatment was different to the other treatments. The tight grouping of the intervals indicated that these results were interpretable.

To evaluate the results in **Figure 5.7**, the p_1-p_3 loadings (**Figure 5.8**) were examined. The p_1 loadings exhibited an inverse correlation between lipid bands at 2920, 2850 and 1743 cm^{-1} and the β-sheet protein band at 1619 cm^{-1} vs. the protein bands at 1654 (α-helix), 1636 (random coil) and 1543 cm^{-1} (amide II). Minor contributions from the bands at 1714 cm^{-1} (DNA base pairing) were also observed,[182] however, this band may also be assigned to FFA,[202] 1479 cm^{-1}, δ (CH_2), 1397 cm^{-1} (amide III C-N), 1244 cm^{-1} (PO_2^- DNA) and 1080 cm^{-1} ($(RO)_2PO_2^-$ DNA) were also important for the interpretation of the t_1 scores pattern. At [V(V)] between 0-15 μM, the p_1 loadings indicated that the cellular protein content was highest and was mainly α-helix (1654 cm^{-1}) and random coil (1636 cm^{-1}) in structure. In the range over which cytotoxicity ensues (corresponding to the MTT assay

curve of **Figure 5.2a**), there was a transition of scores from positive to negative values, indicating that HepG2 cells were synthesising lipids during this phase (also refer to the transition of t_1 scores from positive to negative values for the 0-15 and 31-125 µM treatments, respectively, **Figure 5.6b**).

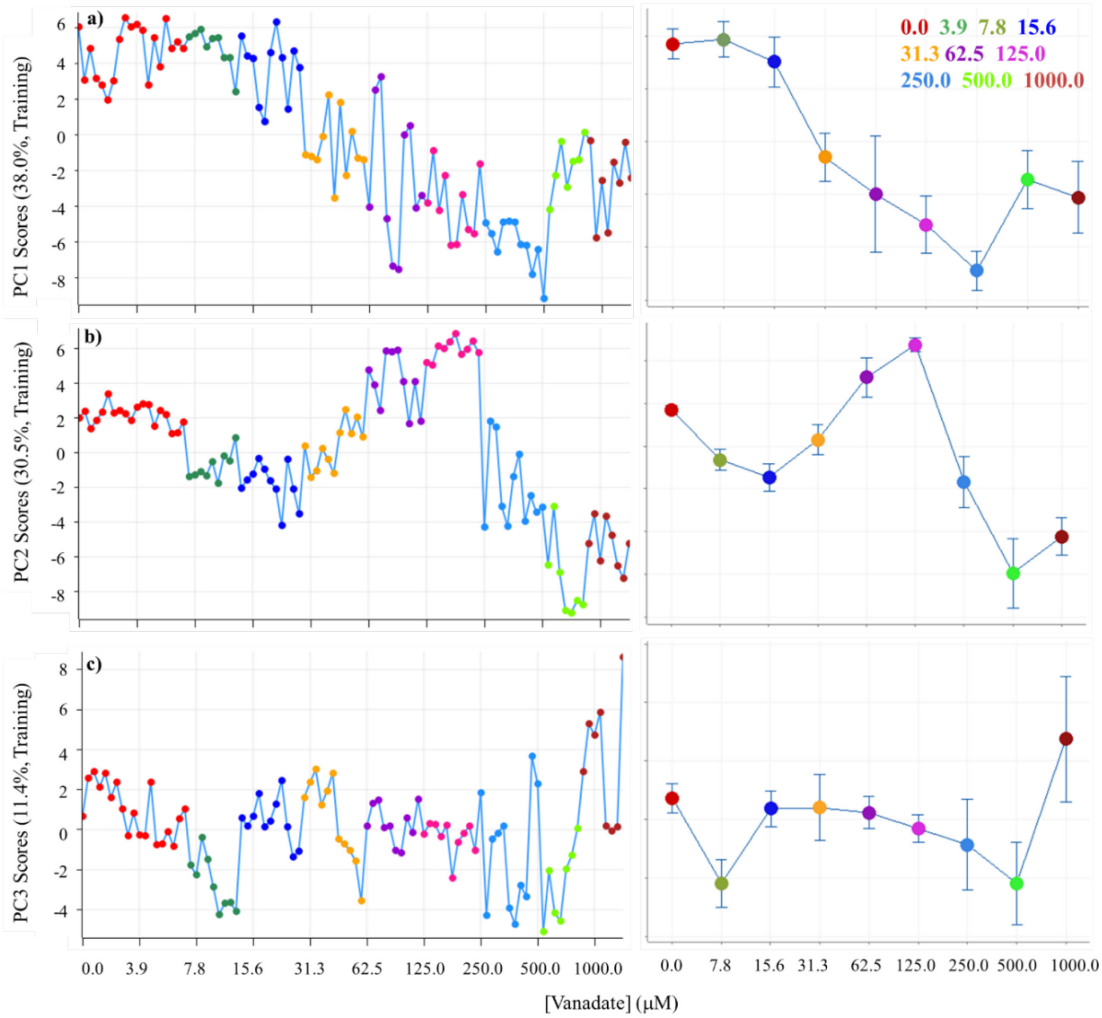

Figure 5.7: t_1 -t_3 scores vs. [V(V)] as all data and interval plots. a) t_1; b) t_2; and c) t_3 scores. Data coloured by legend in a). Error bars represent standard deviations of scores values at the 95% confidence level.

Beyond 250 µM [V(V)], the lipid content decreased and the cells had more relative protein content. The step observed in the t_1 scores between 250 and 500 µM may be an indication of a change in phenotype (consistent with the observed morphological changes in the optical micrographs in **Figure 5.5c**) as a change towards more positive scores was correlated to cell viability.

The t_2 scores vs. [V(V)] plot (**Figure 5.7b**) showed that a second biochemical process occurred after 125 µM. Beyond the IC_{50} value, a large decrease from positive to negative scores occurred and reference to the p_2 loadings showed that there was a strong negative

correlation between the membrane lipid bands at 2922 and 2850 cm^{-1} with the band at 1623 cm^{-1}, assigned to protein aggregation and also observed in the p_1 direction shifted to 1619 cm^{-1}.[175] Other important loadings in in the p_2 plot were associated with bands at 1704 and 1603 cm^{-1}, assigned to DNA modes,[182] consistent with a change in phenotype. With reference to **Figure 5.6b**, the p_2 loadings described changes induced by [V(V)] between the 31-125 μM and the 250-1000 μM treatments.

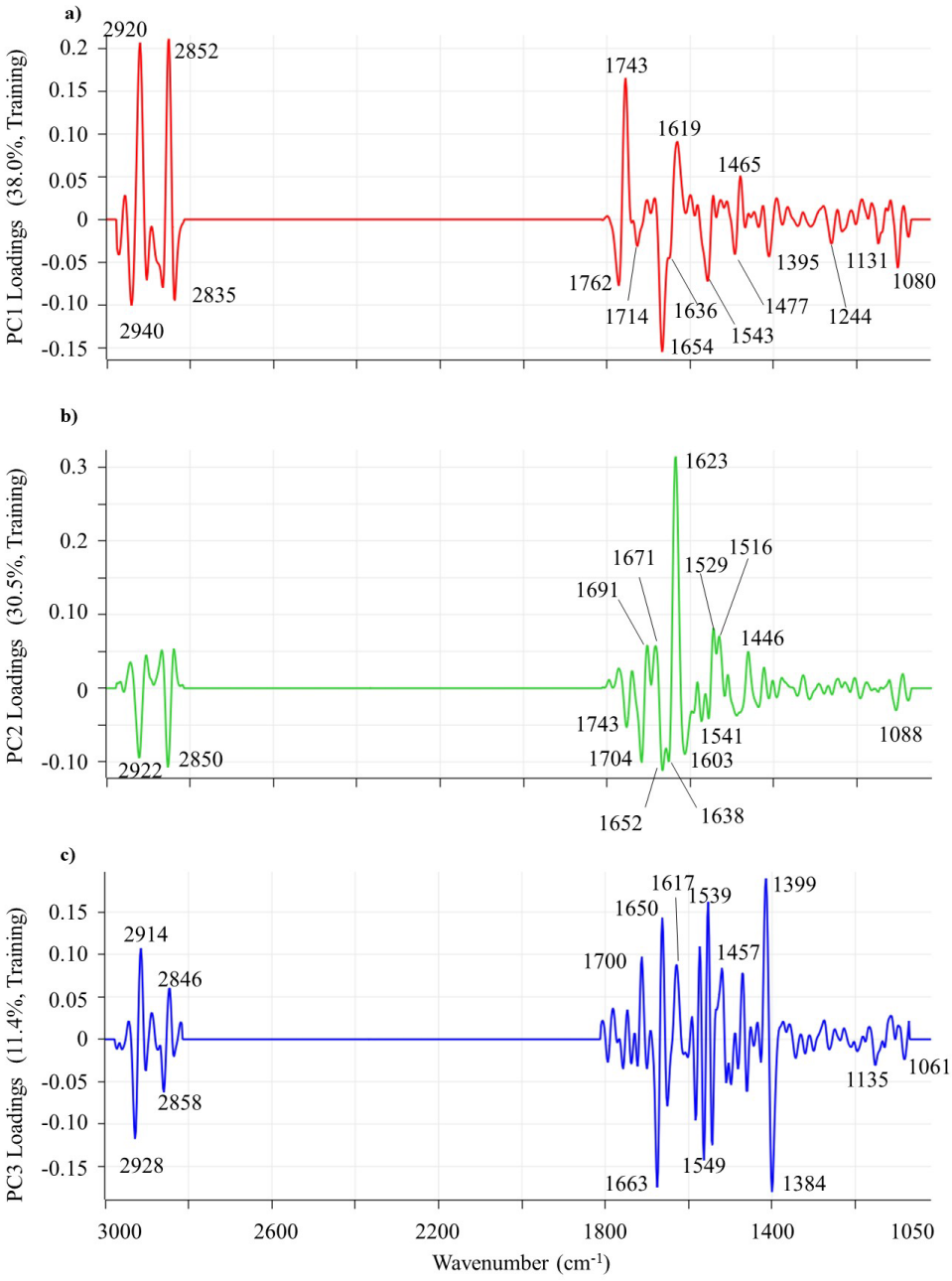

Figure 5.8: PCA loadings plots for vanadate cytotoxicity experiment; a) p_1 loadings; b) p_2 loadings; and c) p_3 loadings plots. Important bands have been marked on each plot.

In **Figure 5.8c**, the p_3 direction was associated with the 1000 μM treatment and was characterised by complex loading patterns associated with protein secondary structures

between 1690-1550 cm^{-1}. The band at ~1400 cm^{-1} split into two features at 1399 and 1384 cm^{-1}. This region was attributed to COO^- bands associated with fatty acids, or the side chains of amino acids.[195,214] Small contributions in the 3000-2800 cm^{-1} and 1740 cm^{-1} regions were consistent with changes in membrane lipid and lipoprotein structures and were most likely attributed to cell death, or changes in phenotype at 1000 µM [V(V)]. Assessment of higher order PCs did not reveal any further interpretable patterns in the data.

5.3.2.2 Chemometric Assessment of Cisplatin Treated HepG2 Cells

PCA scores were presented in several ways to show the overall effect of the cisplatin treatments (**Figure 5.9**). The t_1 vs. t_2 scores plot (**Figure 5.9b)** illustrate that the biochemical changes due to treatments between 0-12.5 µM were described by the t_1 direction and those between 25.0-100.0 µM by the t_2 direction.

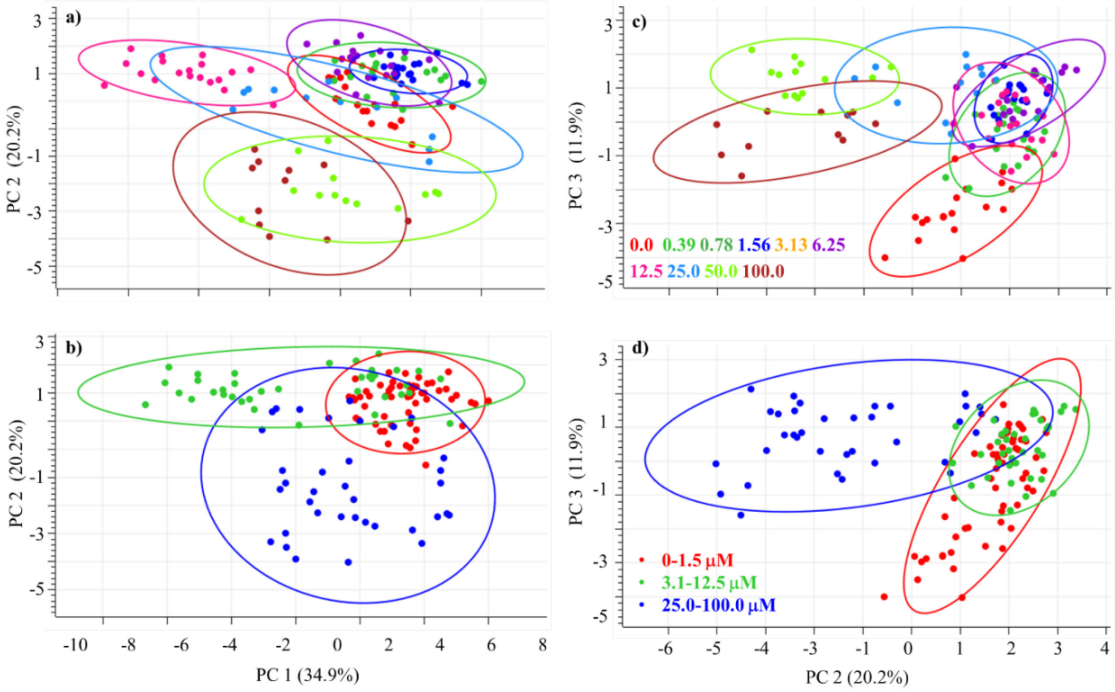

Figure 5.9: PCA scores plots for cisplatin treated HepG2 cells; a) t_1 vs. t_2 scores grouped by treatment concentration; b) t_1 vs. t_2 scores grouped by three phases; c) t_2 vs. t_3 scores grouped by treatment concentration; and d) t_2 vs. t_3 scores grouped by three phases. Plots a) and c) grouped by legend in plot c) and plots b) and d) grouped by legend in plot d).

Initially, a Savitzky-Golay second derivative (13-point smoothing) then SNV was applied, however, this processing combination did not result in a PCA model that adequately modelled the MTT response. Application of the second derivative alone and model redevelopment produced results that better described the MTT assay results in **Figure 5.2b**.

The t_2 vs. t_3 scores plot (**Figure 5.9c)** showed that the scores followed a curved path from low to high cisplatin concentrations, which started at negative t_2 values and progressed to positive t_2 values, followed by a progression to negative t_3 values. Such patterns are commonly observed in fermentation processes in the biopharmaceutical industry where spectroscopic tools based on vibrational spectroscopy are used for monitoring and determination of reaction endpoints.[375] The data in **Figure 5.9** can be interpreted in a similar manner since the increasing [cisplatin] represents a biological path model, describing the systematic changes induced by the treatments.

The t_1-t_3 scores vs. [cisplatin] plots (**Figure 5.10**) revealed that the treatment point 12.5 µM may have been an outlier in the t_1 direction, however, the t_2 direction closely resembled the MTT assay curve (**Figure 5.2b)** and the IC_{50} estimated by the t_2 scores, was similar to the literature value of 9.3-15.6 µM.[368-370]

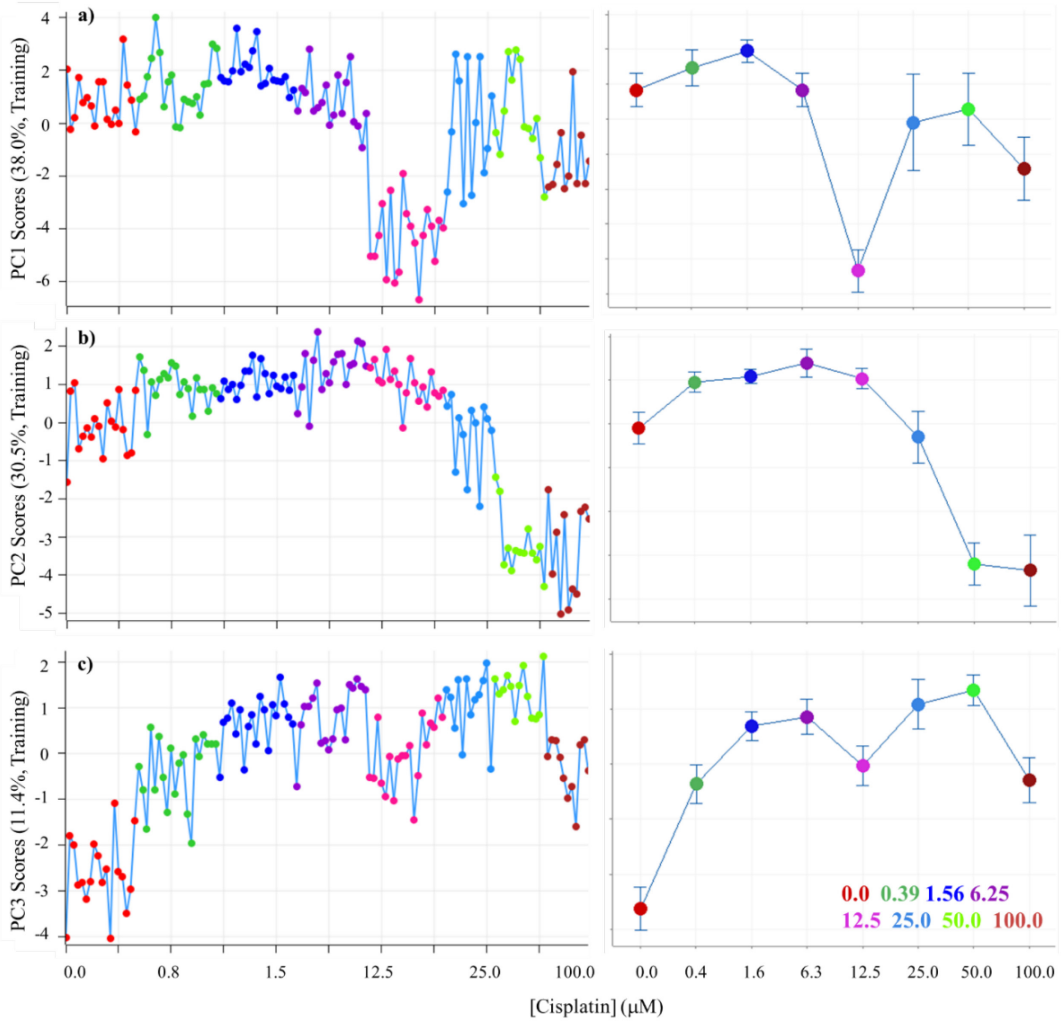

Figure 5.10: t_1 to t_3 scores vs. [cisplatin] as all data and interval plots. a) t_1 scores indicating the possibility of the 12.5 µM treatment being an outlier; b) t_2 scores showing high resemblance to the MTT assay curve; and c) t_3 scores, again showing that the 12.5 µM treatment may be an outlier.

The p_1-p_3 loadings (**Figure 5.11**) for the cisplatin PCA showed that the p_1 direction was associated mainly with changes in lipid bands at 2924, 2852 and 1741 cm^{-1}. The outlier identified lacked lipid associated bands and this observation was verified by visual inspection of the processed data for this treatment condition.

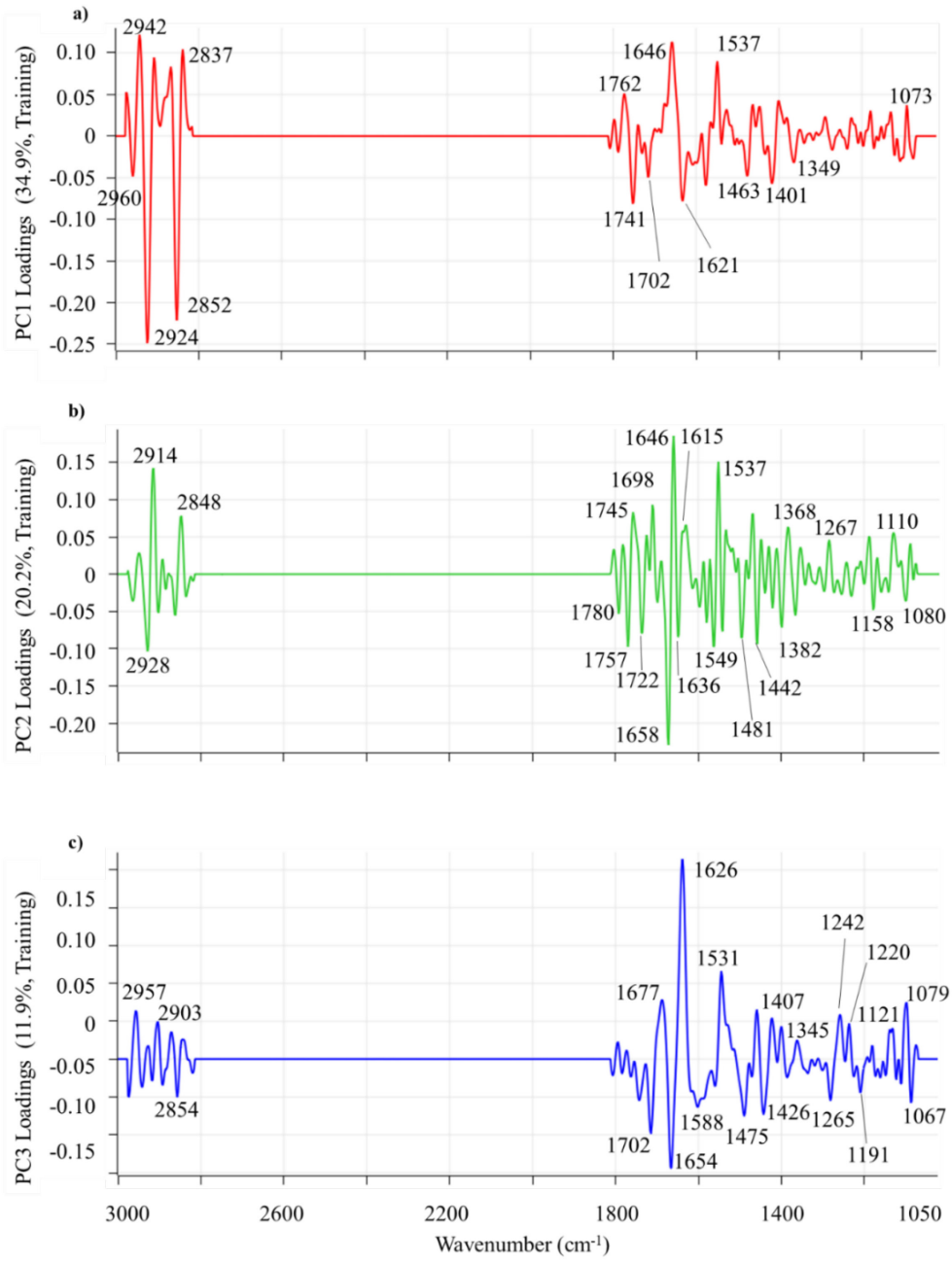

Figure 5.11: PCA loadings plots for cisplatin cytotoxicity experiment; a) p_1 loadings; b) p_2 loadings; and c) p_3 loadings plots. Important bands have been marked on each plot.

The p_2 loadings described cell viability as evidenced by the t_2 scores vs. [cisplatin] curve in **Figure 5.10b** and its close resemblance to **Figure 5.2b**. The observation that many of the DNA and protein bands in p_2 and p_3 loadings were important was interesting as cisplatin has been reported to crosslink with purine bases in DNA. Its action causes bends

in DNA strands that activate p53 proteins, and when the damage cannot be repaired, apoptotic pathways are triggered.[367] The region of the t_2 scores that illustrate a rapid decrease in cell viability, corresponding to the MTT assay curve over the concentration range 3.1-12.5 μM, was related to an increase in DNA band intensities at 1698 and 1615 cm^{-1}.[182] This mechanism was clearly distinct from mechanism of vanadate cytotoxicity.

The p_3 direction described the non-linear increase in the t_3 scores plot from negative to positive scores up to 50 μM. The largest loading was associated with the band at 1626 cm^{-1} assigned to β-sheet proteins, which were more abundant in cells at lower cisplatin concentrations and typically, these bands are associated with protein aggregation.[175,203] A number of bands associated with DNA at 1702, 1588, 1426, 1191 and 1067 cm^{-1} change with increasing [cisplatin] and were consistent with the DNA crosslinking action of cisplatin towards HepG2 cells leading to apoptosis, possibly through triggering of the p53 protein.[367]

5.3.2.3 Chemometric Assessment of Doxorubicin Treated HepG2 Cells

The t_1 vs. t_2 scores plots for doxorubicin-treated HepG2 cells (**Figure 5.12**) for a two PC model described 88.85% of the **X**-variance, with a three PC model describing 91.8% of the total spectral variability. **Figure 5.12b** indicated that both the t_1 and t_2 directions described cytotoxic changes induced by doxorubicin. Two PC's were used to interpret the model and **Figure 5.13** presents the t_1-t_2 scores vs. [doxorubicin] plots.

In **Figure 5.13**, the t_1 scores showed no effect of doxorubicin until 0.08 μM (dark green points) before they increased in a stepped manner to large positive scores values, which then decreased linearly to negative values until 5 μM then plateaued at 10 μM. The rapid linear decrease in the t_1 vs. [doxorubicin] plot was consistent with the rapid decrease in cell viability observed in the MTT assay (**Figure 5.2c)**. The t_1 direction was, therefore, attributed to biochemical changes associated with cell viability.

The t_2 direction displayed an exponential decrease in the scores over the 0.08-10 μM range. The data from the treatment condition 1.25 μM was postulated to be an outlier. However, it was not removed because models calculated with and without these treatment points were nearly identical, hence, these points had little influence on the analysis of the curve in **Figure 5.13b**. Like the t_1 direction, the t_2 direction was independent of [doxorubicin] up to 0.08 μM. This indicated that a critical concentration was required before doxorubicin produced its cytotoxic effects, as observed by FTIR spectroscopy.

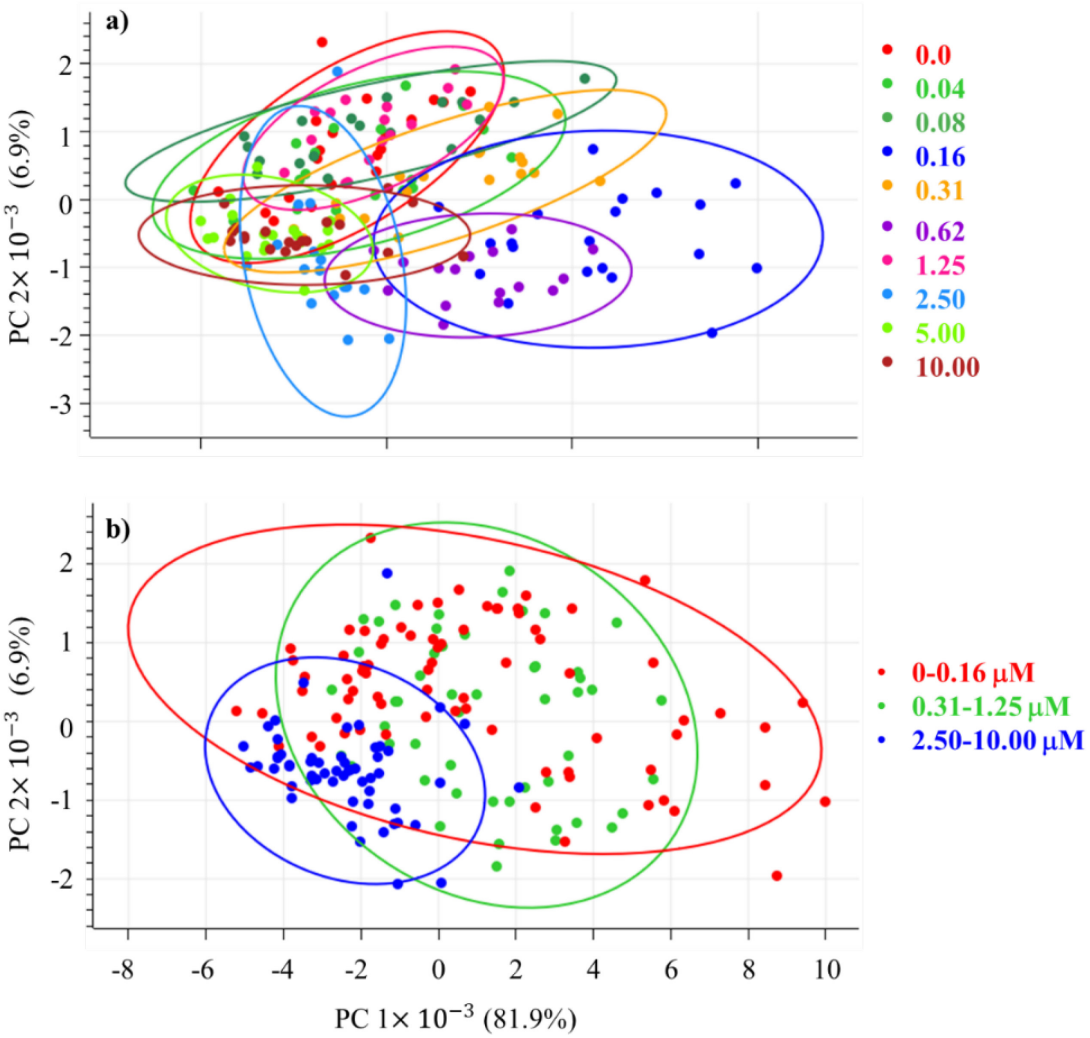

Figure 5.12: t_1 vs. t_2 scores plots for HepG2 doxorubicin study; a) scores grouped by doxorubicin treatment concentration; and b) separated into groups based on the three phases; 0-0.16 µM; rapid cell death between 0.31-1.25 µM; and 2.5-10 µM. Local Hotelling's T^2 ellipses were drawn at 95% confidence.

The p_1 and p_2 loadings for the doxorubicin model are presented in **Figure 5.14**. At the 0.16 µM treatment point, the p_1 loadings showed the highest cellular protein content which decreased as the concentration of doxorubicin increased, together with large changes in DNA bands at 1702, 1613 and 1580-1560 cm^{-1}.[182] As was the case for cisplatin, there were only small changes in lipid concentrations over the cytotoxic concentration range. Concurrent with the process described in PC1, the p_2 direction indicated that as the concentration of doxorubicin increased, the intensity of the membrane lipid bands at 2924 and 2852 cm^{-1} decreased and a number of changes in protein secondary structure and DNA bands were observed.[205] These data indicate that doxorubicin acts in a different manner to both vanadate and cisplatin. A comparison of the treatments was anticipated to provide more details into the action of all three treatment types as cytotoxic agents.

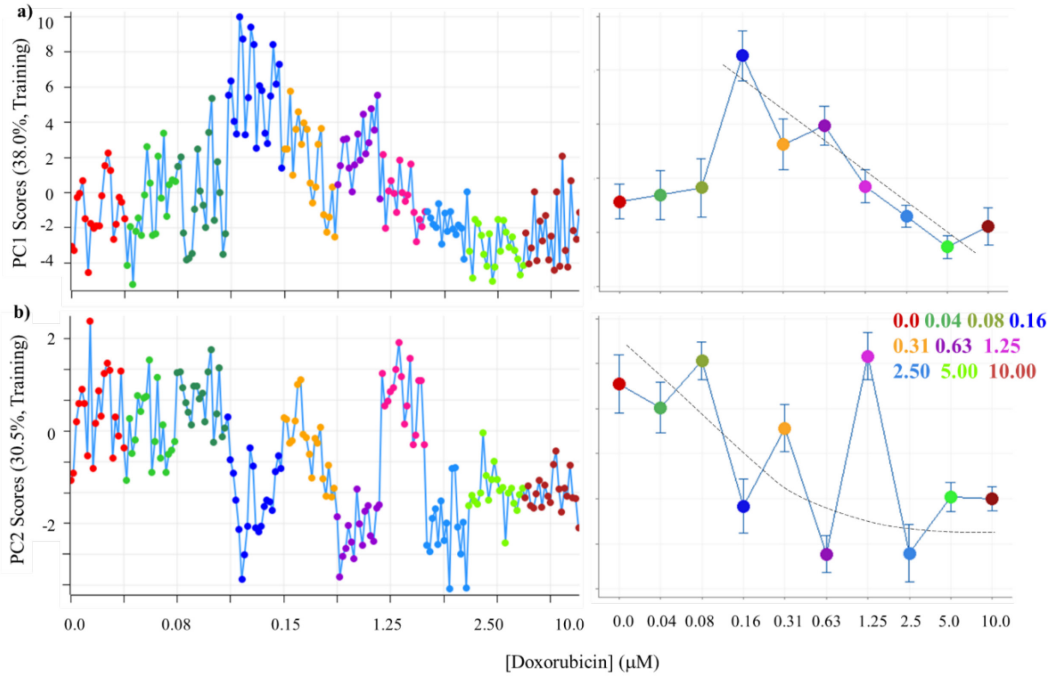

Figure 5.13: t_1 and t_2 scores vs. [doxorubicin] as all data and interval plots; a) t_1 scores; and b) t_2 scores vs. [doxorubicin]. The 1.25 μM treatment in b) may be an outlier. The dotted lines indicate the best fit of the data and in particular, the dotted curve in b) does not take into account the 1.25 μM treatment.

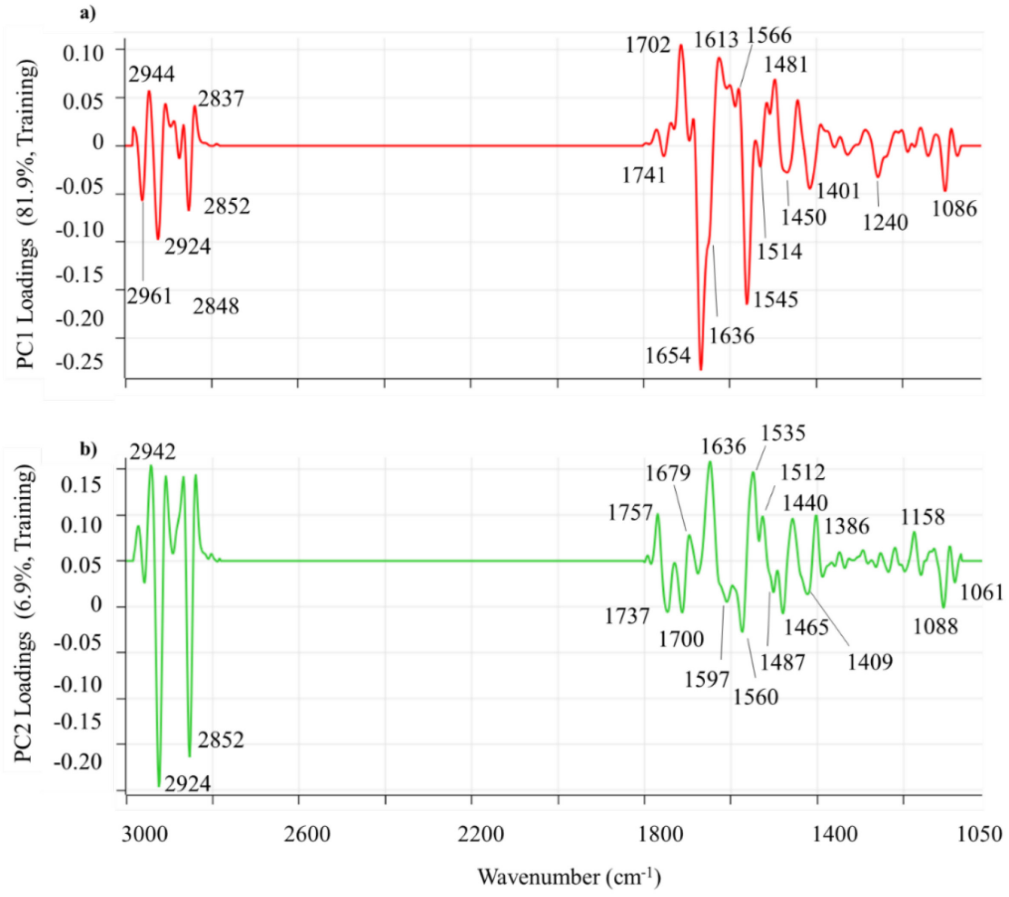

Figure 5.14: PCA loadings plots for doxorubicin cytotoxicity experiment; a) p_1 loadings; and b) p_2 loadings. Important bands have been marked on each plot.

5.3.2.4 Comparison of Vanadate, Cisplatin and Doxorubicin Treatments of HepG2

To gain further insights into the biochemical differences among the treatments, a combined PLS-DA model was developed and the scores plots are presented in **Figure 5.15**. The t_1 vs. t_2 scores plot (**Figure 5.15a)** showed a union of the three local Hotelling's T^2 ellipses drawn at 90% confidence for each treatment. In this union region lie the three control sets of spectra (i.e., no-treatment data), showing the validity of the comparison (**Figure 5.16**).

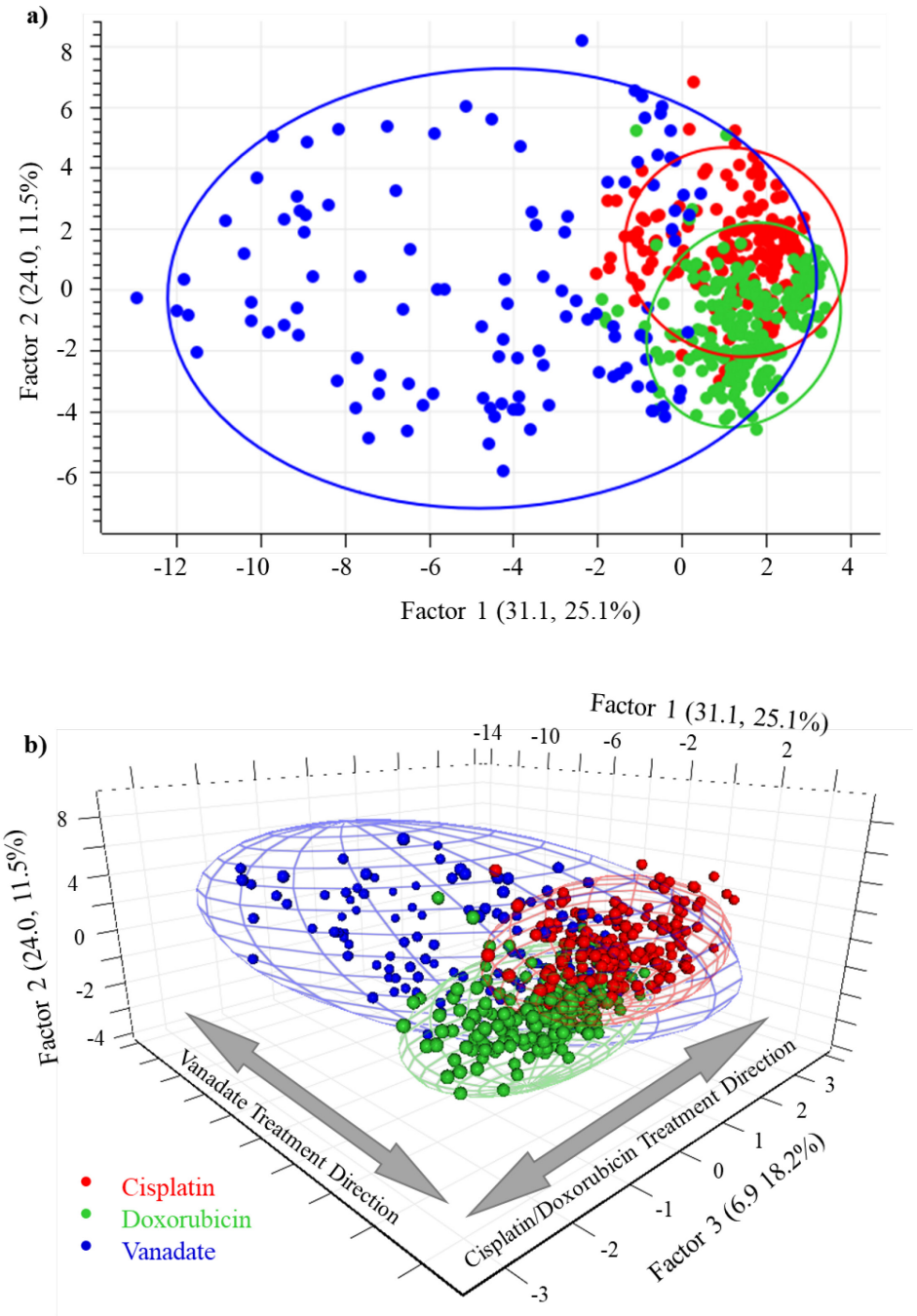

Figure 5.15: a) t_1 vs. t_2; and b) t_1 vs. t_2 vs. t_3 scores plots for PLS-DA model of HepG2 cells treated with three cytotoxic agents. Hotelling's T^2 ellipses were drawn at the 90% confidence level. Sample grouping was performed as per the legend at the bottom of plot b).

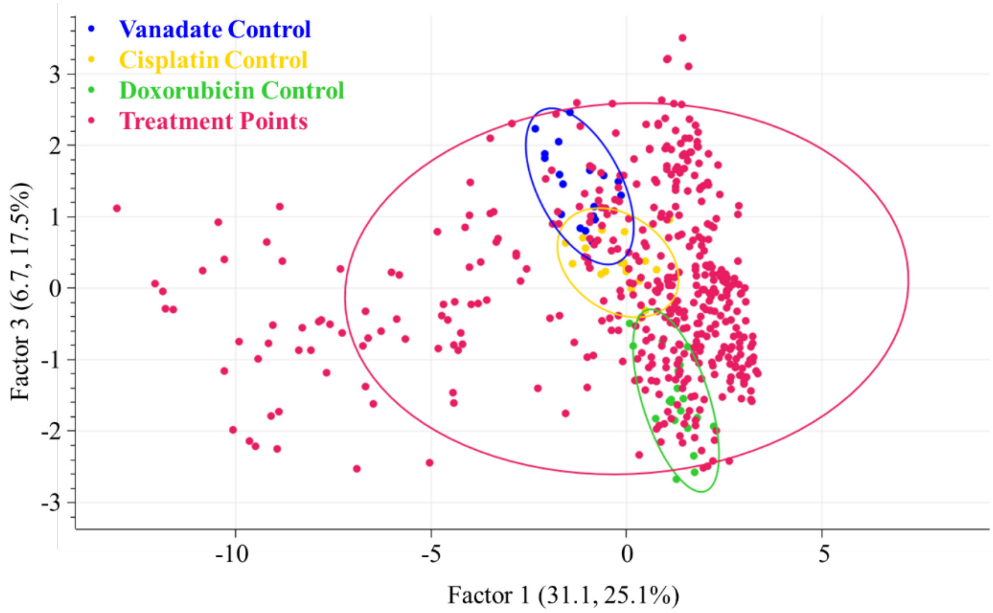

Figure 5.16: t_1 vs. t_3 scores plot of all treatments highlighting the control points for each cytotoxic agent studied. This arrangement of scores clearly showed that all control points were similar in the t_1 direction. Local Hotelling's T^2 ellipses drawn at the 90% confidence level.

Figure 5.16 presents the t_1 vs t_3 scores plot and highlights the control treatments for each cytotoxic agent studied, where t_3 described the biological variability between the three cultures of HepG2 cells used. None of the vanadate treatment points were located within the central clusters of the cisplatin and doxorubicin treatments (**Figure 5.17**).

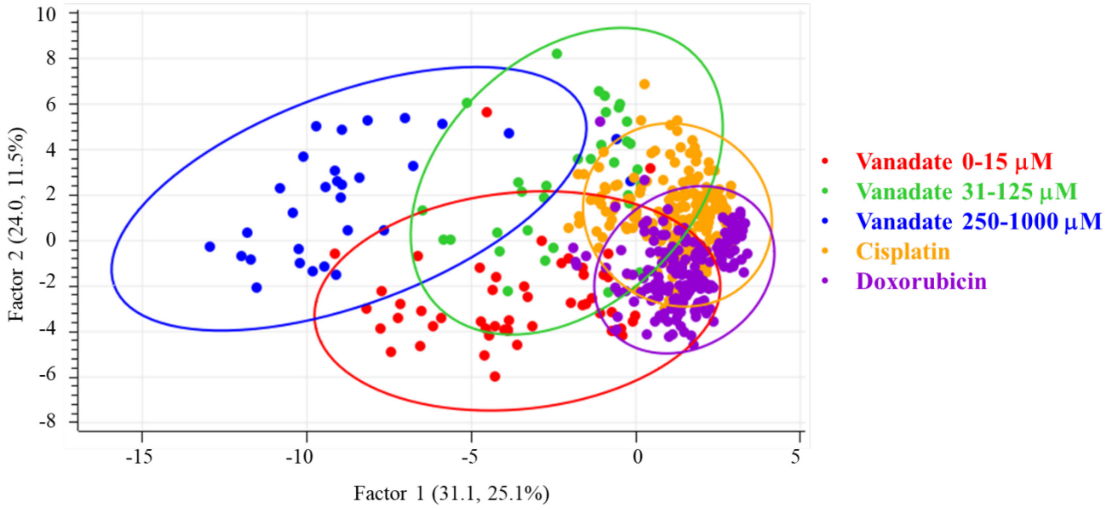

Figure 5.17: t_1 vs. t_2 scores of HepG2 cells treated with vanadate, cisplatin and doxorubicin. This plot was grouped by vanadate concentrations over the ranges 0-15 µM; 31-125 µM and 250-1000 µM. Cisplatin and doxorubicin treatments were groups as overall treatments.

The t_1 direction was attributed to the more prominent biochemical changes induced by vanadate compared to those induced by cisplatin and doxorubicin. The large spread of the

vanadate treatments indicated a wider range of concentration dependent biochemical effects, whereas the cisplatin and doxorubicin treatments were tightly clustered and therefore showed a more focussed mode of action. The t_2 direction did not provide distinct separation of any treatments, however, it was related to the variability within vanadate treatments. **Figure 5.17** also showed that the scores for the lower concentrations of vanadate (0-15 μM) lie in the negative t_2 region, while the higher concentrations lie towards the positive t_2 direction. Between 250-1000 μM, the treatments also occupy the negative t_1 direction. This direction, therefore, described the cytotoxic concentration effects of vanadate, as opposed to those of the cisplatin and doxorubicin treatments, which were located around the zero t_2 direction.

The w_1-w_3 loading weights for Factors 1 to 3 are shown in **Figure 5.18** with the important bands marked on these plots. As was the case in previous sections, loading weights were highly complex in the protein and DNA spectral regions. Factor 1 described the differences between the vanadate vs. the cisplatin/doxorubicin treated cells. The vanadate treatments were associated with negative t_1 scores and were described mainly by changes in the 1621 cm^{-1} band assigned to β-sheet protein structures. This observation was consistent with those made in Section 5.3.2.1, which also showed a large contribution of this band in the p_2 loading direction most likely related to PTP inhibition, which promoted lipid synthesis, with this hypothesis supported by the presence of the lipid band at 1745 cm^{-1}. The negative loading weights in the w_1 direction were attributed to the cisplatin/doxorubicin treatments and were associated with the bands at 1706, 1638, 1605, 1401 and 1080 cm^{-1}, related to changes in DNA and secondary protein structures.

Factor 2 described the varying biological changes across the three treatment types and showed a small separation of the cisplatin treatment in the positive t_2 direction and the doxorubicin treatment in the negative t_2 direction. The vanadate treatments were uniformly spread over the t_2 direction, which was related to [V(V)] (**Figure 5.17**).

With reference to the w_2 loading weights in **Figure 5.18b**, lower concentrations of vanadate resulted in lower lipid content, as evidenced by the reduced band intensity at 1737 cm^{-1} and more β-turn and amide II protein secondary structures (1661 and 1549 cm^{-1}, respectively). Over [V(V)] values of 31-125 μM, increases in the band intensities at 2922 and 2852 cm^{-1} were related to membrane lipids and proteins and an associated increase in lipid ester bands at 1737 cm^{-1}.[195] These changes were attributed to the action of vanadate transitioning from an insulin-mimetic agent to a cytotoxic agent at higher

concentrations and in the process, the cells were accumultaing lipids in response to the increased oxidative stress.[311] A number of bands were also present, that were indicative of DNA changes at 1698 cm^{-1} and a complex pattern of loading weights in the 1570-1400 cm^{-1} region.[182]

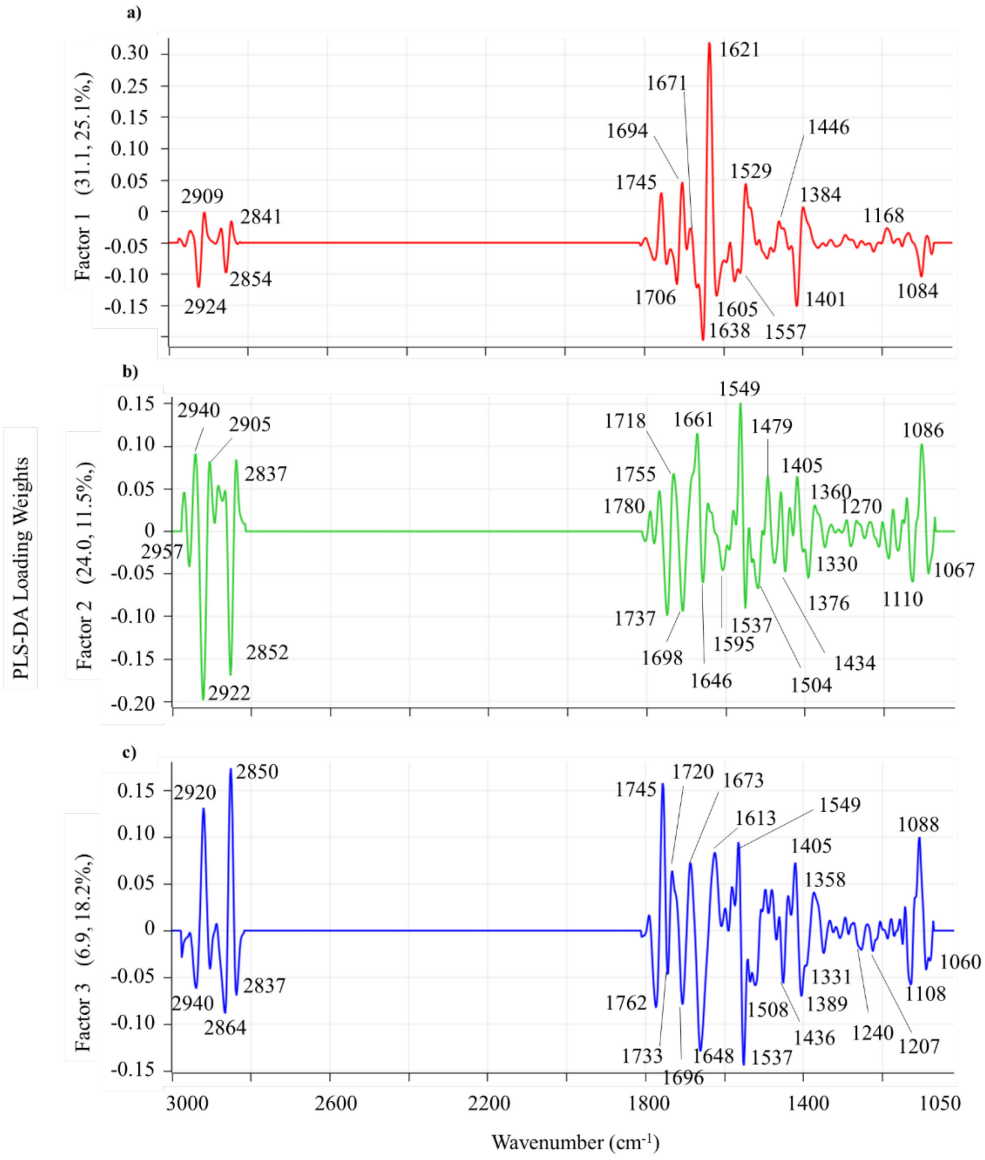

Figure 5.18: PLS-DA loading weights for cisplatin, doxorubicin and vanadate treated HepG2 cells; a) w_1 loading weights; b) w_2 loading weights; and c) w_3 loading weights. Important bands are marked in each plot.

Another important observation regarding the vanadate treatments was related to the 250-1000 μM treatments occupying the negative t_1 direction and the cisplatin/doxorubicin treatments occupying the positive t_1 direction. Important modes of action of cisplatin and doxorubicin involve DNA damage and these results revealed that higher concentrations of vanadate were not changing DNA structure,[140,367] and were mainly the result of changes in lipid and protein signalling.

The Factor 3 direction described the main differences between the cisplatin and doxorubicin treatments (**Figure 5.15b)** and the biological variability observed in the control points (**Figure 5.16**). Negative t_3 scores were associated with doxorubicin and positive t_3 scores described cisplatin treatments. For the cisplatin analysis, the p_1 loadings in **Figure 5.11a** had high band intensities at 2924 and 2850 cm^{-1}. These bands were also highly weighted in the w_3 direction associated with doxorubicin, which indicated that its mode of action altered the cell membrane lipids, fatty acids and proteins resulting in apoptosis.[195,205] Cisplatin showed more changes associated with DNA (1696 cm^{-1}) and associated protein secondary structures (1648 and 1537 cm^{-1}).[182]

These results demonstrate the diverse action of vanadate, compared to the more targeted actions of cisplatin and doxorubicin. In all cases, the lipid membrane bands at 2920 and 2850 cm^{-1} were highly influenced by the treatments and the results were consistent with the cytotoxic agents action leading to a reduction of cell membrane integrity.

5.3.3 Investigation of Vanadate Action on HepG2 Cells Using Full Factorial Design: Sugar and Vanadate Treatments.

A modified cell viability assay was performed based on the 2^3 full factorial design (**Figure 5.1** and **Table 5.1**). Briefly, three replicates of a 96-well plate were prepared where ten rows of the plate were defined as the treatments of the design. As there were only ten rows in the plate available for treatments, only two centre points were run per plate. The general design layout in the 96-well plate is shown in **Figure 5.19**.

A value of 50 μM [V(V)] was defined as the maximum concentration investigated in the sugar-vanadate experiments. This value induced a cytotoxic response in HepG2 cells and enabled synergistic or antagonistic glucose or fructose interactions with vanadate to be assessed to evaluate enhanced or reduce cell viability, respectively.

The following important observations were made with respect to the interval plot of cell viability vs. treatment condition (**Figure 5.20**),

- There was a distinct difference between treatments that do not contain vanadate (*1, a, b, ab*) and the treatments (*c, ac, bc, abc*) containing vanadate at the IC_{50} value.
- The centre points (*cp*'s) were consistent with each other and represented a situation where cell growth was promoted. This was attributed to vanadates insulin-mimetic effects at concentrations lower than the IC_{50} value.

- Fructose, rather than glucose, appeared to promote growth in the presence of vanadate at the IC_{50} concentration. However, fructose treatments only (*b* and *bc*), were associated with the highest variances in the design points, which indicated that the action of fructose induced a wide range of biochemical variability.

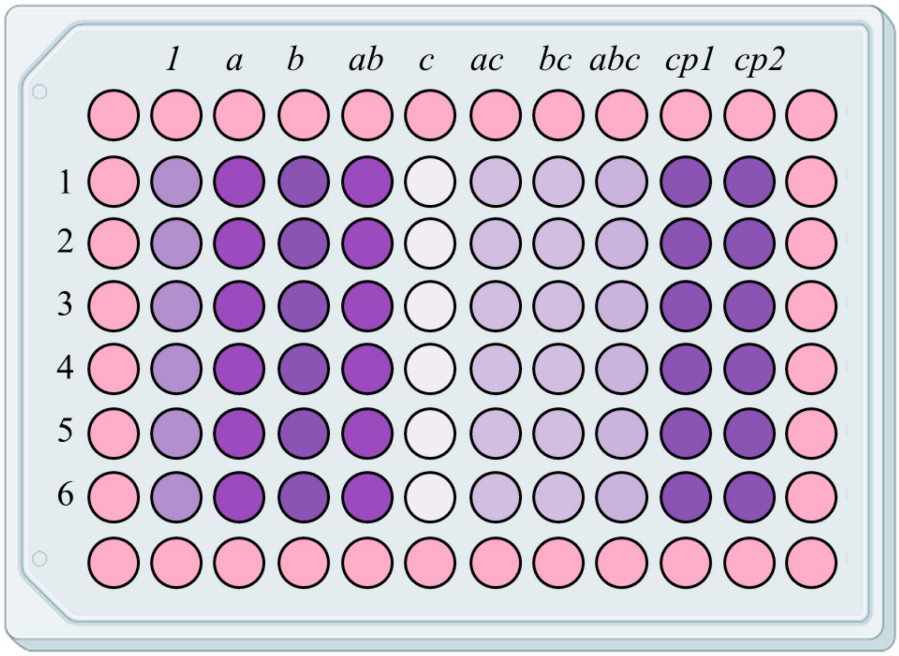

Figure 5.19: Experimental design of the factorial design cell viability assay. The edge wells were left blank resulting in six replicates of the ten treatments of the designed experiment. Two centre points (*cp1* and *cp2*) were run as a measure of design repeatability. Three replicate plates were run to determine the reproducibility of the design. The terminology of the experimental runs was previously described in Chapter 1, Section 1.7 and also in **Figure 5.1**.

The statistical significance of each treatment and its interactions were evaluated using analysis of variance (ANOVA in **Table 5.2**). This was only possible due to the orthogonality constraint imposed on the factorial design.[226] The cell viability model was significant at the 95% confidence level and vanadate (C) was the most significant contributor to the model ($p = 0.002$). There were also two important interaction terms: the AB (*glucose* × *fructose*) and the AC (*glucose* × *vanadate*) interactions.

ANOVA showed a large and significant curvature term in the model ($p = 0.003$), which accounted for 30% of the total variability and resulted in the centre points not fitting the plane of a linear model. This was visualised in the response surface plot (**Figure 5.21**) where the centre points were observed to lie above the plane of the model. This was the result of a synergistic effect of glucose, fructose and vanadate, observed as significant interactions, in promoting cell growth when the concentration of vanadate was below the IC_{50} value.

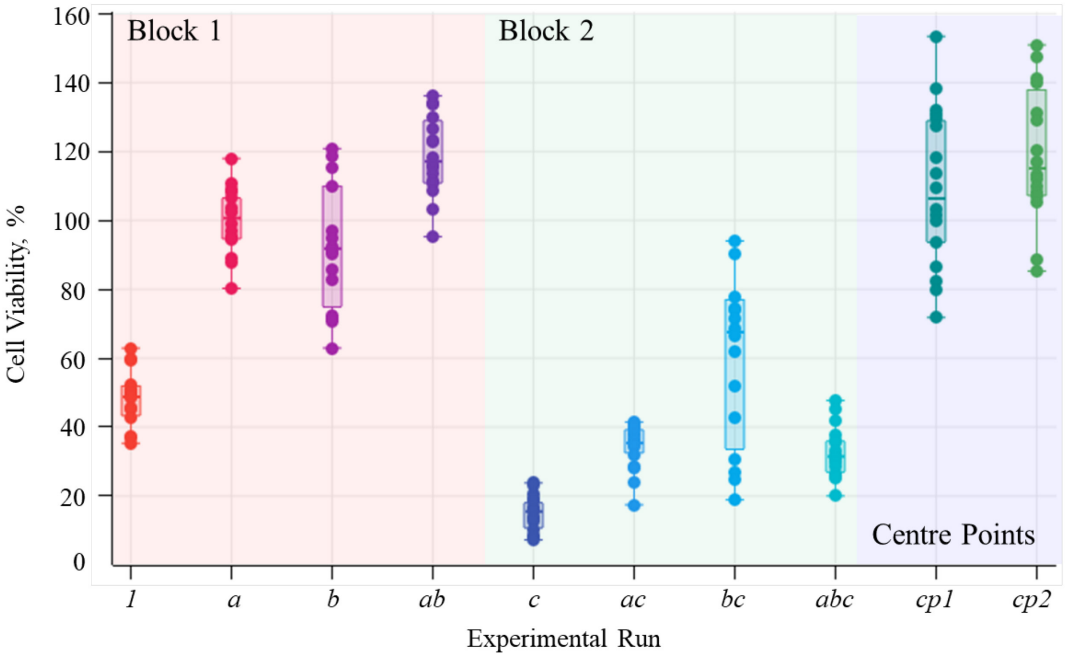

Figure 5.20: Cell viability assay results obtained using a modification of the MTT assay and the experimental design in **Figure 5.1**. Each variable in the interval plot represented an experimental run and the intervals represented the variability within results of three replicates of the design. Block 1 described treatments *1, a, b* and *ab* and Block 2 described treatments *c, ac, bc* and *abc*. The centre points (*cp's*) represented the mid-points of all treatment concentrations.

When the curvature term was removed, the model was no longer significant, which showed that the linear design was not an appropriate fit of the data. This was because the 2^3 factorial design did not have enough points to fit a quadratic model. Even though centre points were available, providing three levels to fit a non-linear model, the ANOVA table does not use these points in model calculations as design orthogonality would be lost.[223,226] An alternative approach used partial least squares regression (PLSR) including squared and interaction terms in the model to account for curvature. By adding such terms, the PLS model was used to generate predictions of the design points of the exact quadratic model (in this case, a design known as the Box-Behnken design).[223] The response surface for the Box-Behnken model based on PLSR simulated data (**Figure 5.22**) was anticipated to be representative of the actual design.

The response surfaces of **Figure 5.22** were produced at three levels: 0, 25 and 50 µM [V(V)], respectively. The clear quadratic surface showed the cytotoxic effect of vanadate at 50 µM compared to the 0 and 25 µM treatments on cell viability. The small increase in cell viability related to the centre points showed that insulin mimetic concentrations of V(V) could also promote cancer growth.

Table 5.2: ANOVA table for HepG2 experimental design; glucose, fructose and vanadate treatments.

Source	Sum of Squares	df	Mean Square	*F*-value	*p*-value	
Model	9737	5	1947	34.16	0.008	significant
A-Glucose	613	1	613	10.75	0.046	
B-Fructose	1458	1	1458	25.58	0.015	
C-Vanadate	6050	1	6050	106.14	0.002	
AB	648	1	648	11.37	0.043	
AC	968	1	968	16.98	0.026	
Curvature	4203	1	4203	73.73	0.003	
Residual	171	3	57			
Lack of Fit	121	2	61	1.21	0.541	not significant
Pure Error	50	1	50			
Cor Total	14110	9				

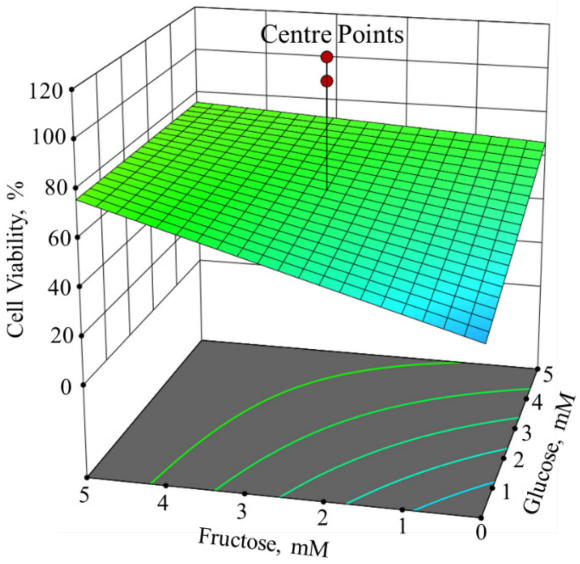

Figure 5.21: Response surface plot of HepG2 designed experiment model. The centre points represent treatments at 2.5 mM glucose and fructose and 25 μM vanadate. For the linear model to be valid, the centre point should ideally lie close to the plane of the model. In this case, the linear model was not the best fit to the data and a quadratic model provided a better fit.

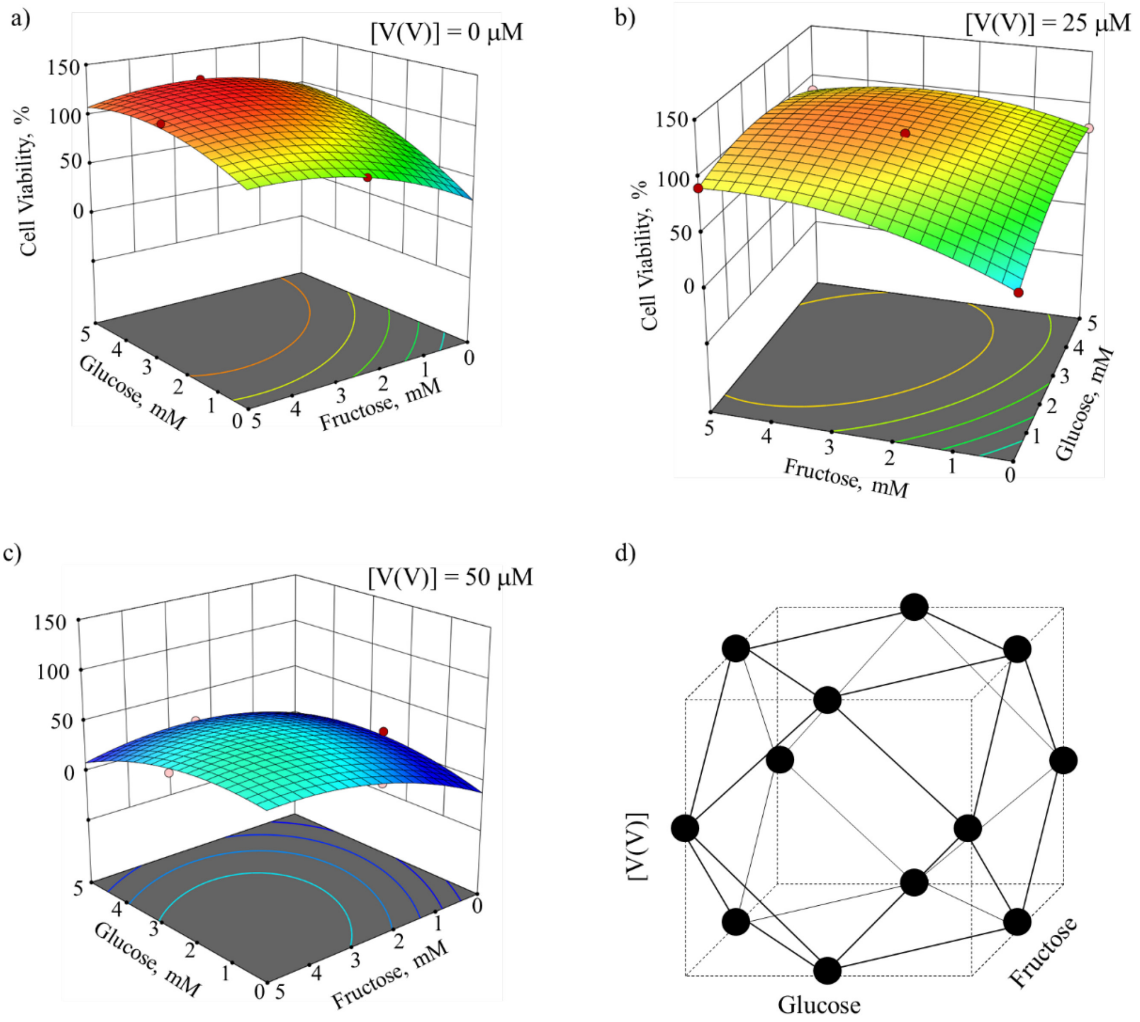

Figure 5.22: Response surfaces of a simulated Box-Behnken analysis of cell viability showing the quadratic surface associated with the promotion of cell growth at vanadate concentration values less than the IC_{50} value; a) 0 µM; b) 25 µM; c) 50 µM [V(V)]; and d) The Box-Behnken (BB) design used to generate the results. These plots are indicative only, based on results generated from a PLS model.

5.3.4 Analysis of Designed Experiment Using Single Point Spectra.

The full factorial design in **Figure 5.1** was assessed as two blocks (excluding centre points) where Block 1 was run as the 2^2 full factorial design in sugars only (*1, a, b* and *ab*) and Block 2 was assessed as the sugar-vanadate treatments (*c, ac, bc* and *abc*). FTIR point spectra were collected using a 15×15 µm^2 knife edge aperture from single cells fixed to CaF_2 substrates. The entire set of raw and processed spectra (**Figure 5.23**) were grouped based on blocks and centre points.

The Block 2 (vanadate treated cells) data exhibit an increased intensity of the lipid ester band at 1743 cm^{-1} (**Figure 5.23b)**,[181] consistent with the higher ROS generated promoting DNL.[20] A large shoulder between 1638 to 1623 cm^{-1} indicated a shift from random coil to β-sheet protein secondary structure and was consistent with the observations made in

the MTT assay study described in Section 5.3.2.1, **Figure 5.8b**. This was attributed to increased protein synthesis and aggregation in HepG2 associated with increased oxidative stress induced by vanadate and fructose resulting in DNL.

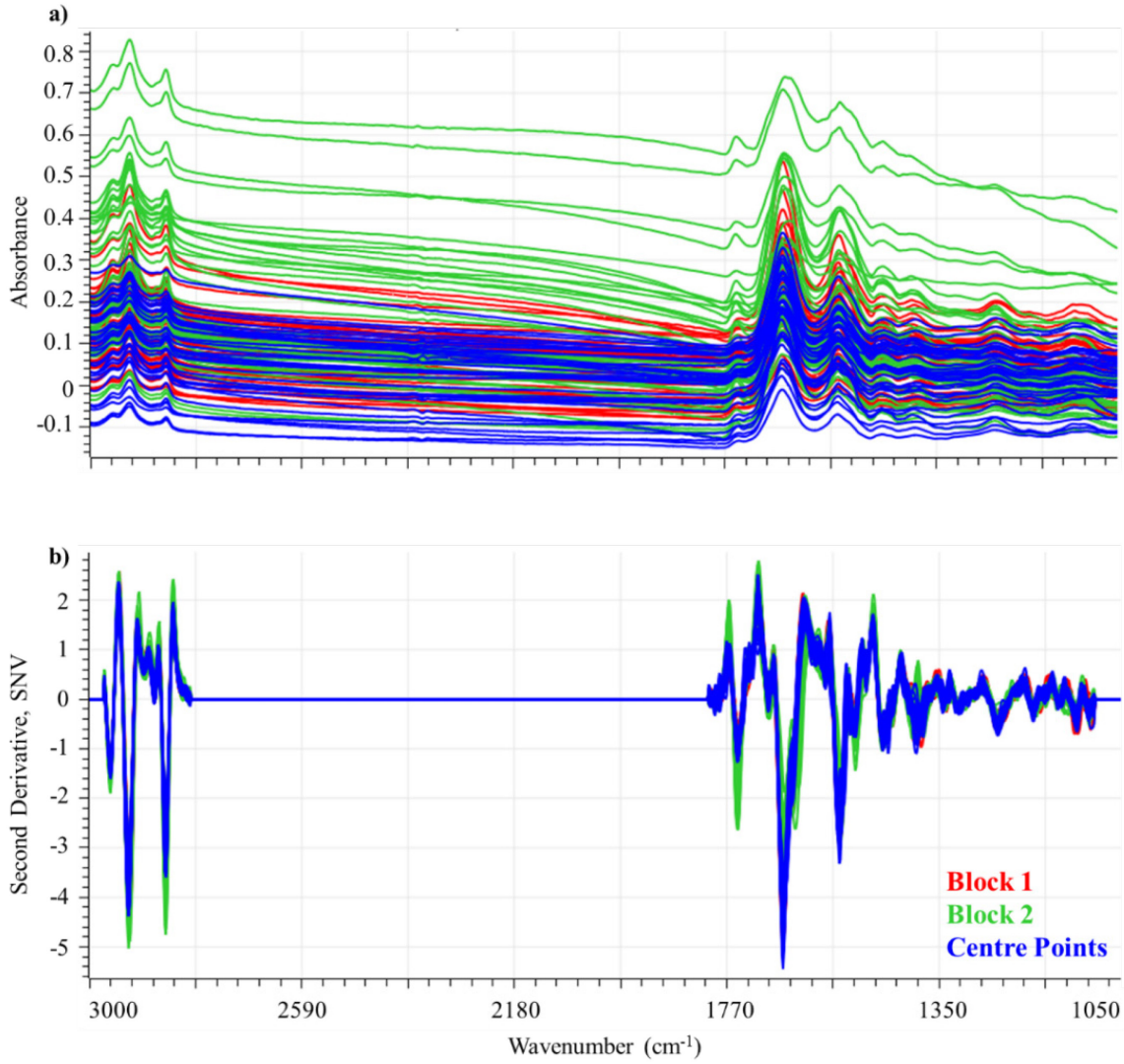

Figure 5.23: a) Raw FTIR point spectra; and b) normalised, second derivative spectra of HepG2 cells over the wavenumber region 3000-1000 cm^{-1}. Plots were colour grouped by the legend in plot b).

5.3.4.1 Analysis of Sugar Treatments (Block 1)

Processed spectra from the first four runs (Block 1) in the design (**Figure 5.1**) were analysed using the PLS-DA technique described previously in Section 1.7.2.3 (Chapter 1). Due to the exploratory nature of the analysis, the method of random cross validation was used to validate the model. A three factor PLS-DA model explained 66.2% of the **Y**-response (calibration variance) and 56.3% (validation variance). The t_1 vs. t_2 vs. t_3 scores plot is presented in **Figure 5.24**.

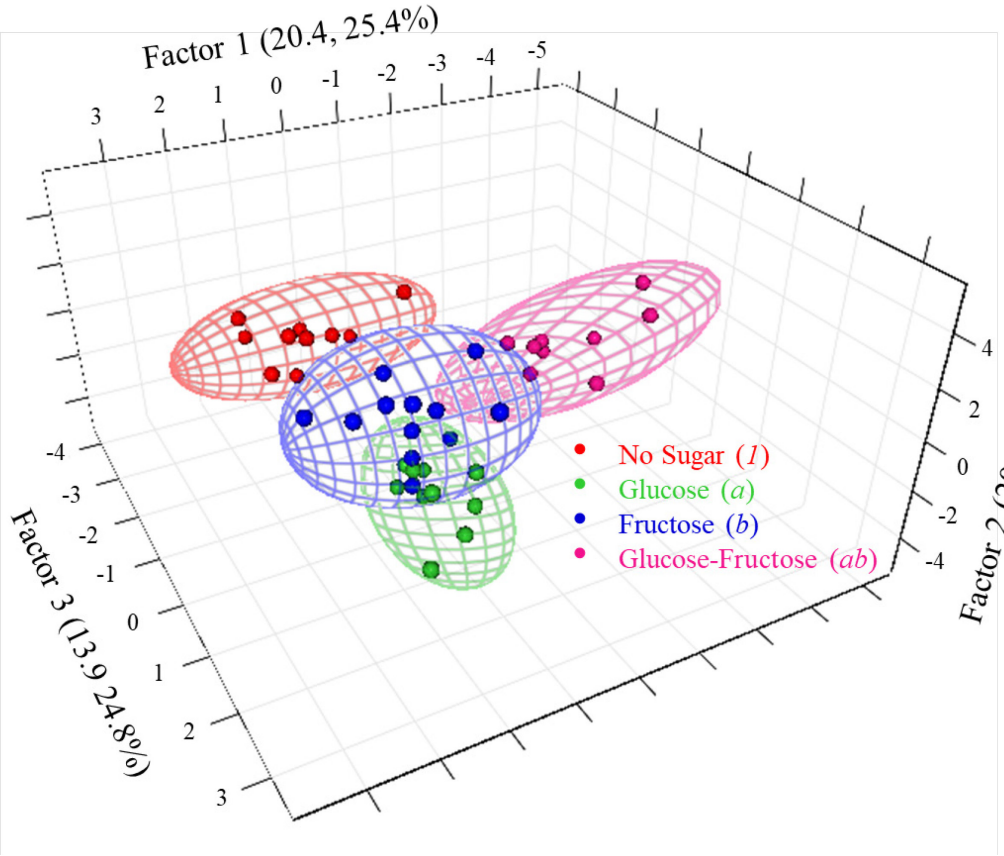

Figure 5.24: t_1 vs. t_2 vs. t_3 PLS-DA scores plot of HepG2 cells treated with sugars and assessed by FTIR microspectroscopy. Local Hotelling's T^2 ellipses are drawn for each treatment at 75% confidence.

Factor 1 described why the glucose-fructose treatment (*ab*) separated from the rest of the treatments. Factor 2 described the difference between the glucose treatments and the other treatments and Factor 3 described why the no-sugar treatment (*1*) separated from the other treatments. The w_1-w_3 loading weights are shown in **Figure 5.25**.

Negative scores in the t_1 direction were associated with the glucose-fructose treatment (*ab*). The w_1 loading weights described a complex pattern associated with many biochemical changes associated with membrane lipids, fatty acids and lipoproteins (2920 and 2850 cm^{-1}). Band splitting related to the *ab* treatment, indicated induced biochemical changes where these bands shifted to lower wavenumbers (2915 and 2845 cm^{-1}, respectively). The band at 1722 cm^{-1} was attributed to fatty acids.[200-201] The bands at 1706, 1693, 1572, 1220 and 1079 cm^{-1} were all associated with DNA/RNA changes[182] and were indicative of the combined glucose-fructose treatment, which resulted in a very different mechanism of metabolism compared to glucose alone.

The t_2 direction (**Figure 5.24b**) separated the glucose treatment (*a*) from the other treatments and was associated with negative score values. The w_2 loading weights, (**Figure 5.25b**) showed this treatment was described by increased band intensities at

1702, 1650, 1541 and 1399 cm^{-1} associated with DNA, α-helix protein secondary structures and COO^- bands in lipids/FFAs. The other treatments were described by increases in the intensity of bands at 2922, 2852, 1743, 1726, 1663, 1625, 1444 and 1378 cm^{-1}, which indicated that the fructose and no-sugar treatments may be triggering lipid synthesis pathways postulated to be in response to increased oxidative stress.[20,376]

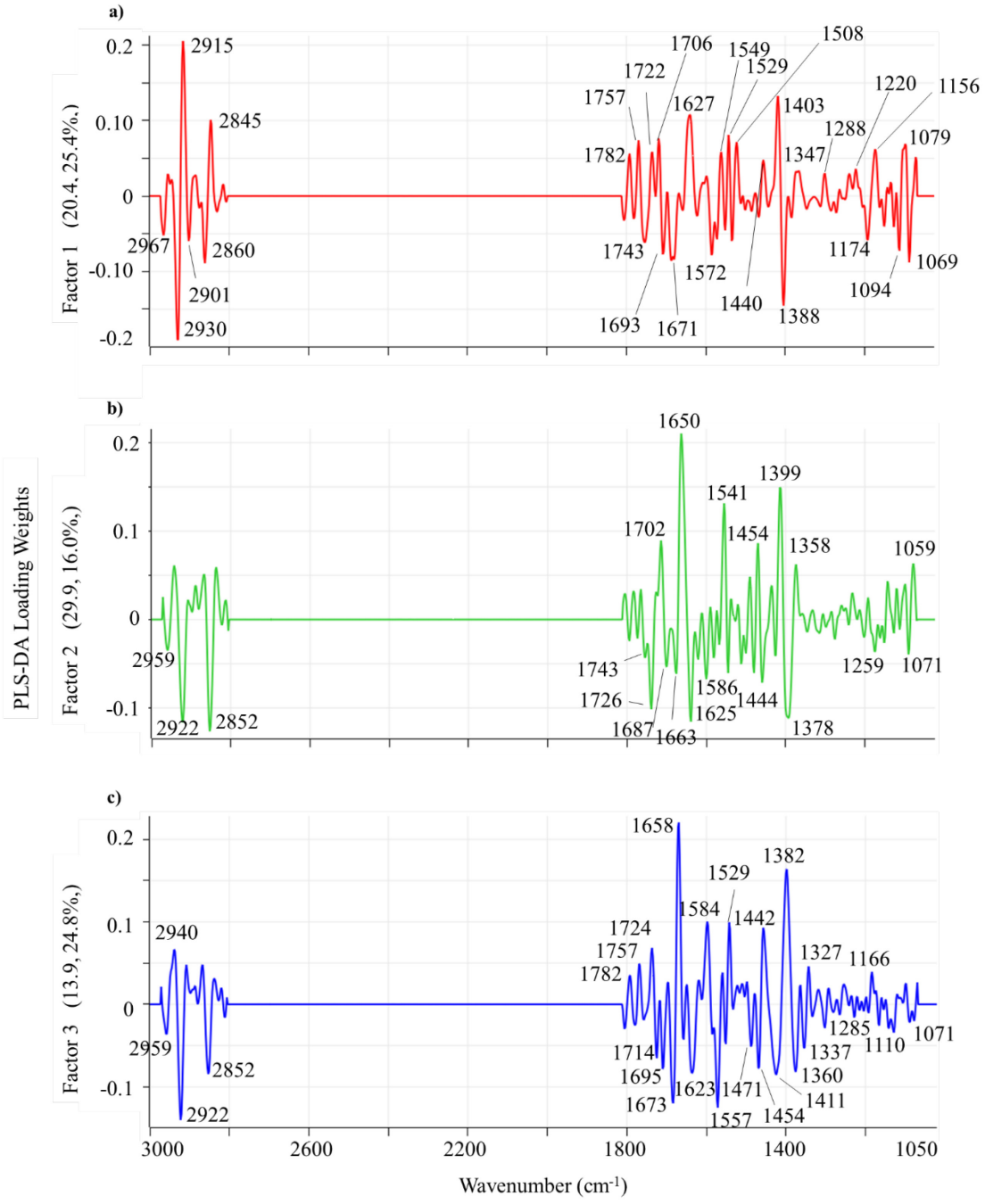

Figure 5.25: PLS-DA loading weights for Block 1 treatments of HepG2 cells; a) w_1 loading weights; b) w_2 loading weights; and c) w_3 loading weights. Important bands are marked in each plot.

The t_3 scores (**Figure 5.24**) separated the no-sugar treatment (*1*) from the other treatments in the negative t_3 direction. The w_3 loading weights were associated with increased band

intensities at 1658, 1584, 1529, 1442 and 1382 cm^{-1}, mainly associated with amide I and II protein secondary structure changes.[181] Positive scores in the t_3 direction were associated with increasing band intensities at 2922, 2850 and 1623 cm^{-1}, with very little contribution from the 1740 cm^{-1} region. This was attributed to a lower production of lipids by HepG2 cells in the absence of vanadate (as shown in **Figure 5.23b**).

Overall, these data showed that FTIR microspectroscopy separated the treatments into unique clusters and the loading weights provided information about the distinct biochemical processes induced by each treatment.

5.3.4.2 Analysis of Sugar-Vanadate Treatments (Block 2)

Block 2 of the experimental design in **Figure 5.1** contained the treatment conditions of sugars in the presence of 50 μM Na_3VO_4. These spectra were analysed in a similar manner as the sugar treatments described in Section 5.3.4.1. This resulted in a five factor PLS-DA model that explained 78.4% of the **Y**-response (calibration variance) and 62.2% (validation variance). A three-factor model described 72.6% and 61.6% of the calibration and validation variance respectively. The t_1 vs. t_2 vs. t_3 scores plot (**Figure 5.26**) showed that the fructose-vanadate treatment (*bc*) separated from the other treatments along the t_1 direction.

The t_2 direction described the difference between the treatments vanadate only (*c*), glucose-vanadate (*ac*) and glucose-fructose-vanadate (*abc*), in particular, it described the similarity between the *ac* and *abc* treatments and their dissimilarity from the treatment *c*. The t_3 scores described the difference of treatment *c* from the other treatments. The t_4 direction did not show any separation of the treatments and was not discussed further.

With reference to the w_1-w_3 loading weights plots (**Figure 5.27**), the w_1 loading weights for the Block 2 treatments were much simpler compared to the corresponding w_1 loading weights in Block 1 and described the main effect of the combined fructose-vanadate treatment (*bc*) compared to the other treatments. Treatment *bc* was associated with positive scores in the t_1 direction and was described by a decrease in the intensity of lipid associated bands at 2926, 2854 and 1745 cm^{-1} and the β-sheet protein band at 1619 cm^{-1}. This treatment was also associated with increased band intensities at 1656 and 1547 cm^{-1} associated with protein synthesis, which is a hallmark of fructose metabolism.[20]

The t_2 direction separated the glucose-vanadate treatment (*ac*) and was described by positive score values. The w_2 loading weights (**Figure 5.27b**) were associated with an increase in band intensity at 1627 cm^{-1}, assigned to protein aggregation and this was also

observed for this treatment in the w_1 loading weights at 1619 cm^{-1}. The other treatments had negative t_2 scores and were associated with increased band intensities at 2924, 2852, 1749, 1702, 1658, 1586, 1475, 1193, 1150 and 1094 cm^{-1}. These data indicated that a second type of lipid synthesis process occurred compared to the one described by the w_1 loading weights and was also associated with changes in DNA and protein structures as evidenced by bands at 1702, 1658 and 1586 cm^{-1}.[172,182]

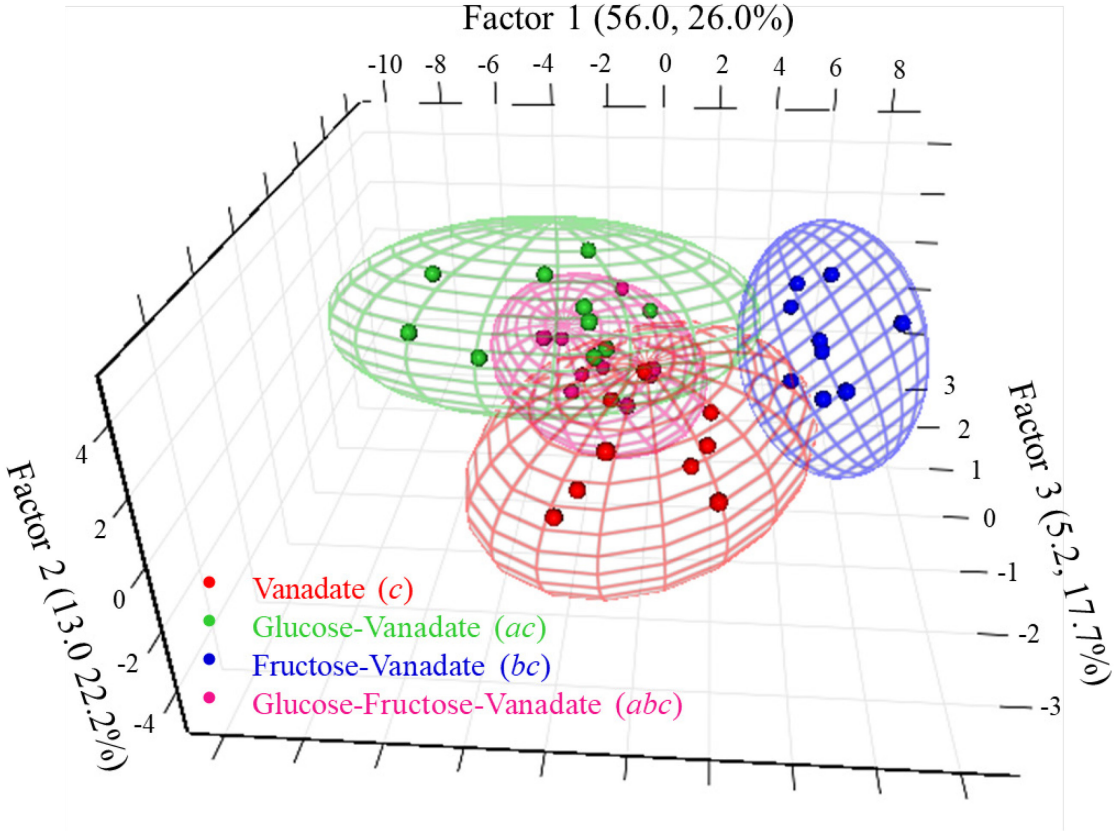

Figure 5.26: t_1 vs. t_2 vs. t_3 PLS-DA scores plot of HepG2 cells treated with sugars and assessed by FTIR microspectroscopy. Local Hotelling's T^2 ellipses are drawn for each treatment at 75% confidence.

The t_3 direction provided further insights into the differences between the vanadate only (*c*), glucose-vanadate (*ac*) and glucose-fructose-vanadate (*abc*) treatments, with treatment *c* described by negative t_3 scores, *abc* by positive scores and *ac* at the zero scores position. The *bc* treatment was also described by scores at the zero t_3 direction, therefore, the w_3 loadings (**Figure 5.27c**) described the differences between the *c* and *abc* treatments. **Figure 5.28** showed how the t_3 direction separated these treatments.

Vanadate only treatment (*c*, **Figure 5.27c**) was associated with increased band intensities at 2930, 2903, 1747, 1698, 1648, 1555, 1452 and 1339 cm^{-1} and a complex pattern of bands between 1250-1080 cm^{-1}, related to DNA and lipid changes. The glucose-fructose-vanadate treatment (*abc*) resulted in increased band intensities at 2913, 1757, 1683, 1634,

1545, 1442, 1250, 1156 and 1079 cm^{-1}. These bands were related to protein and lipid changes (**Table 1.1**) and the 1634 cm^{-1} band assigned to random coil protein structures.[205]

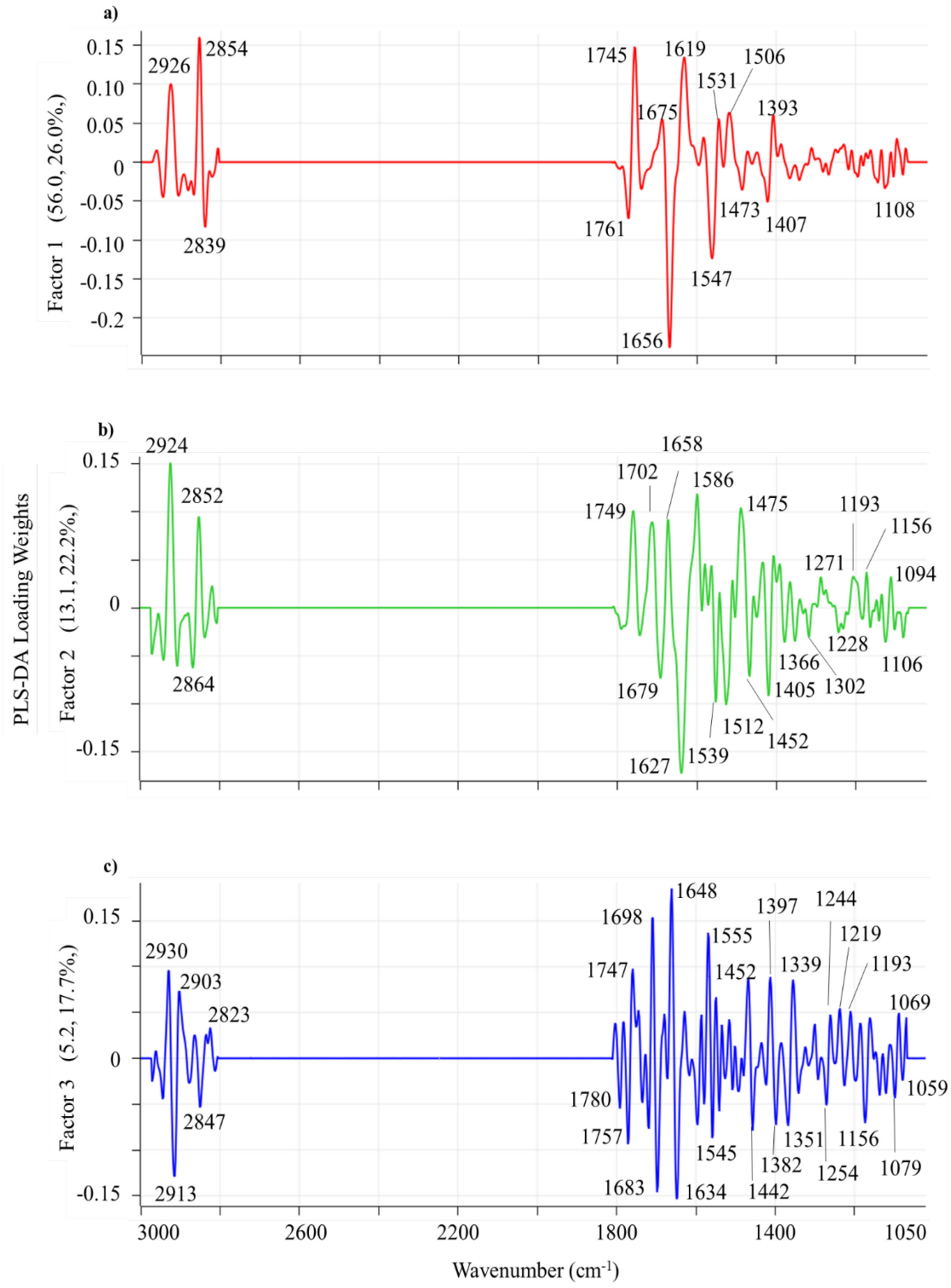

Figure 5.27: PLS-DA loading weights for Block 2 treatments of HepG2 cells; a) w_1 loading weights; b) w_2 loading weights; and c) w_3 loading weights. Important bands are marked in each plot.

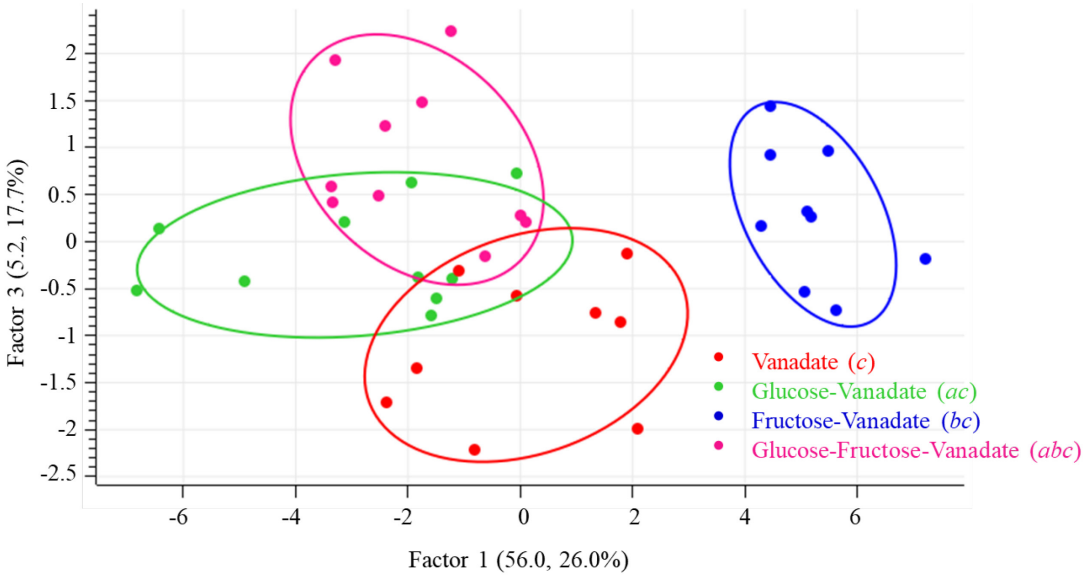

Figure 5.28: t_1 vs. t_3 scores plot of Block 2 treatments. The t_1 direction separated the frutose-vanadate treatment (*bc*) while the t_3 direction described the differences between the glucose-fructose-vanadate (*abc)*, the glucose-vanadate (*ac*) and the vanadate-only (*c*) treatments. The *ac* and *bc* treatments were defined by scores centred around zero in the t_3 direction.

5.3.4.3 Overall Factorial Design Analysis

The complete design in **Figure 5.1** in two blocks was assessed and resulted in a three-factor PLS-DA model that explained 89.6% of the **Y**-response (calibration variance) and 85.9% (validation variance). The t_1 vs t_2 and t_1 vs. t_2 vs. t_3 plots (**Figure 5.29**) described the main differences between the blocks of treatments. The validation scores were also drawn for the blocks in the t_1 vs t_2 plot as an indication of the predictive ability of the model.

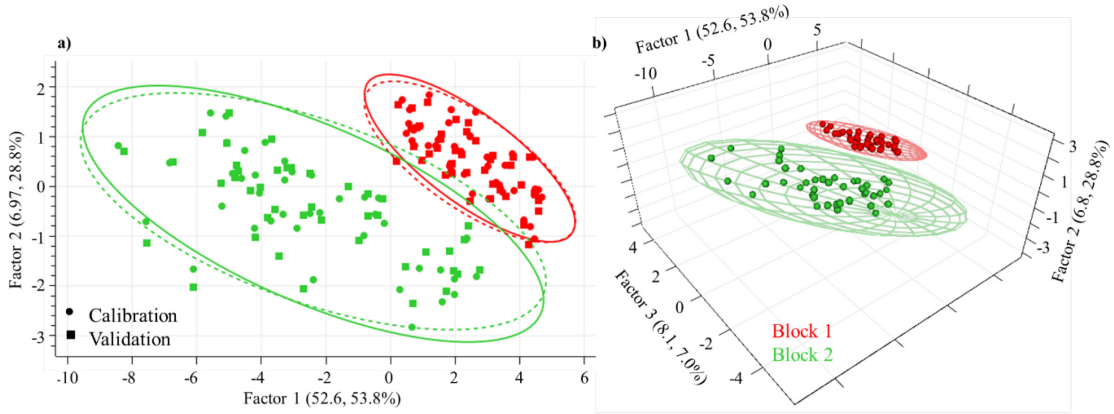

Figure 5.29: a) t_1 vs t_2; and b) t_1 vs. t_2 vs. t_3 PLS-DA scores plots of Block 1 and Block 2 HepG2 sugar and vanadate treatments. Calibration scores were marked by a circle and validation by a rectangle in the t_1 vs. t_2 plot. Blocks coloured by legend in plot b).

The t_1 and t_2 directions described a common trend in the treatments and the addition of the t_3 direction showed clear separation between the treatment groups. Higher order factors did not result in any further separation of the data, nor were any interpretable trends observed. The w_1-w_3 loading weights are presented in **Figure 5.30**.

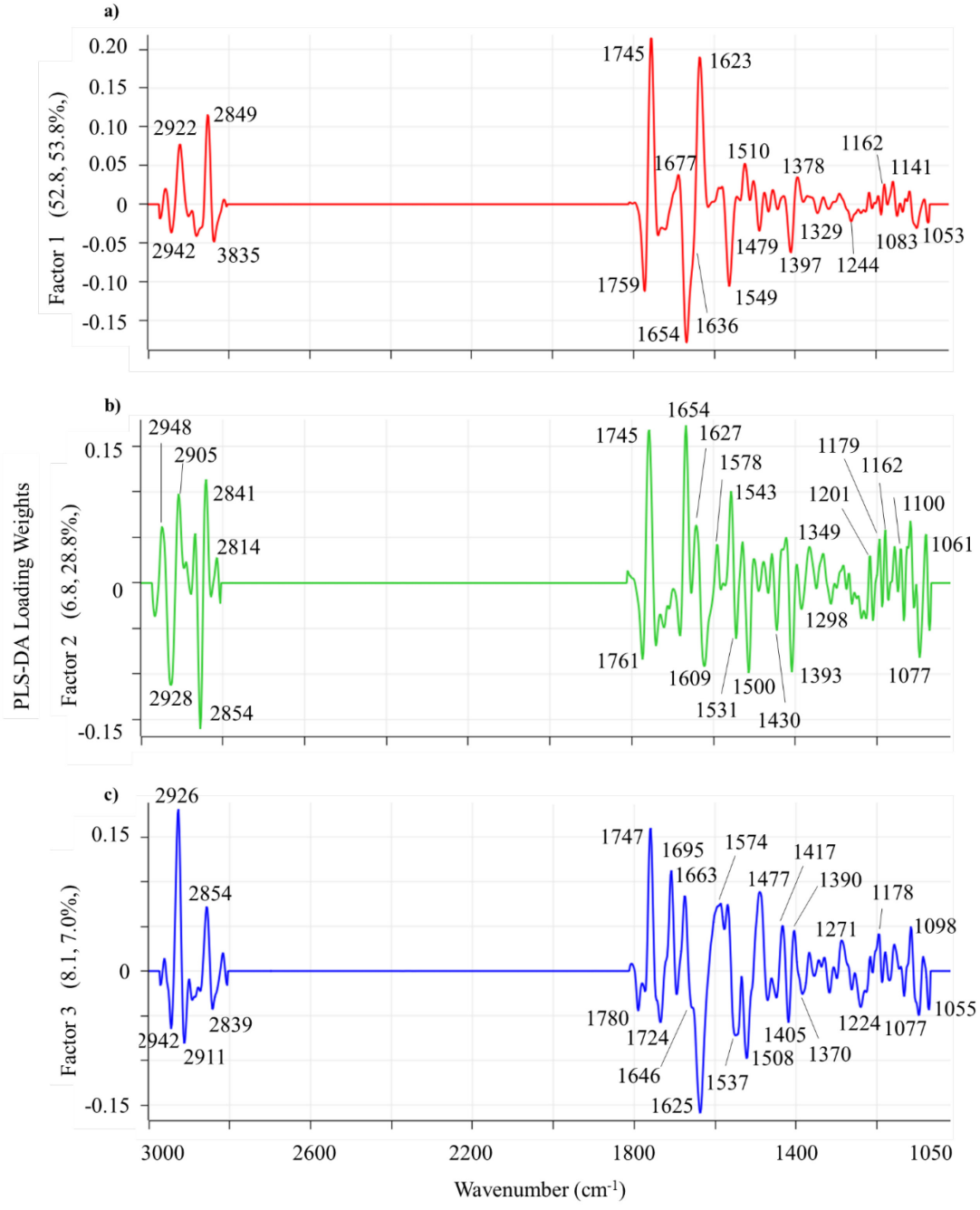

Figure 5.30: PLS-DA loading weights for Block 1 and Block 2 comparison of HepG2 cell treatments; a) w_1 loading weights; b) w_2 loading weights; and c) w_3 loading weights. Important bands are marked in each plot.

All of the t_1 scores for Block 1 (**Figure 5.29**) had positive scores values, while the majority of the Block 2 scores were negative. The w_1 loading weights showed that, in

general, Block 2 treatments had increased intensities of bands at 2922, 2849 and 1745 cm^{-1} attributed to increased lipid synthesis,[195] particularly for treatments containing both glucose and vanadate. The fructose-vanadate containing treatment (*bc*) was associated with positive t_1 values and cells for this treatment had less lipid content. An increase in intensity of the band at 1623 cm^{-1} (β-sheet) was also related to the Block 2 treatments, which could be associated with protein aggregation (fibril formation).[175] Alternatively, this finding further supported the hypothesis that in the presence of vanadate, protein tyrosine residues are phosphorylated and glucose containing treatments synthesise more lipids,[309] consistent with the results observed in Section 5.3.2.1 during decreased cell viability.[311]

The t_1 direction for Block 1 was associated with increased band intensities at 1654, 1636 and 1549 cm^{-1}, and was attributed to a relative increase in protein content compared to lipids. Positive t_2 scores were evident for all of the Block 1 treatments and a majority of the Block 2 treatments. The fructose-vanadate treatment (*bc*) was defined by negative t_2 scores and represented a different metabolic process associated with the fructose-vanadate treatments in the absence of glucose. Positive t_2 scores had increased band intensities at 2928 and 2854 cm^{-1}, which were inversely correlated to that for the lipid ester band at 1745 cm^{-1}. These changes were attributed to membrane lipid changes associated with apoptosis.[195,205]

The Factor 3 direction did not describe any separation in the treatment blocks, but in combination with Factors 1 and 2, allowed visual separation of the two blocks in the t_1 vs. t_2 vs. t_3 scores plot in **Figure 5.29b**. The w_3 loading weights described minor biochemical processes associated with protein structural changes and in particular, the inverse relationship between the bands at 1695 and 1663 cm^{-1} attributed to DNA and β-turns, respectively,[182,203] and the 1625 cm^{-1} band associated with β-sheet structures.[203] Overall, the combined Block 1 and 2 assessment revealed that vanadate induced biochemical changes were mainly characterised by increased lipid synthesis and protein secondary structural changes.

5.3.4.4 Assessment of Centre Points

The centre points (**Figure 5.1**) typically validate the analysis at the design centre, rather than replicating the entire design. This approach is commonly used in the analysis of DoE generated data.[223] The centre points were projected onto the model developed in Section 5.3.4.3 and are presented in the t_1 vs. t_2 vs. t_3 scores plot (**Figure 5.31**).

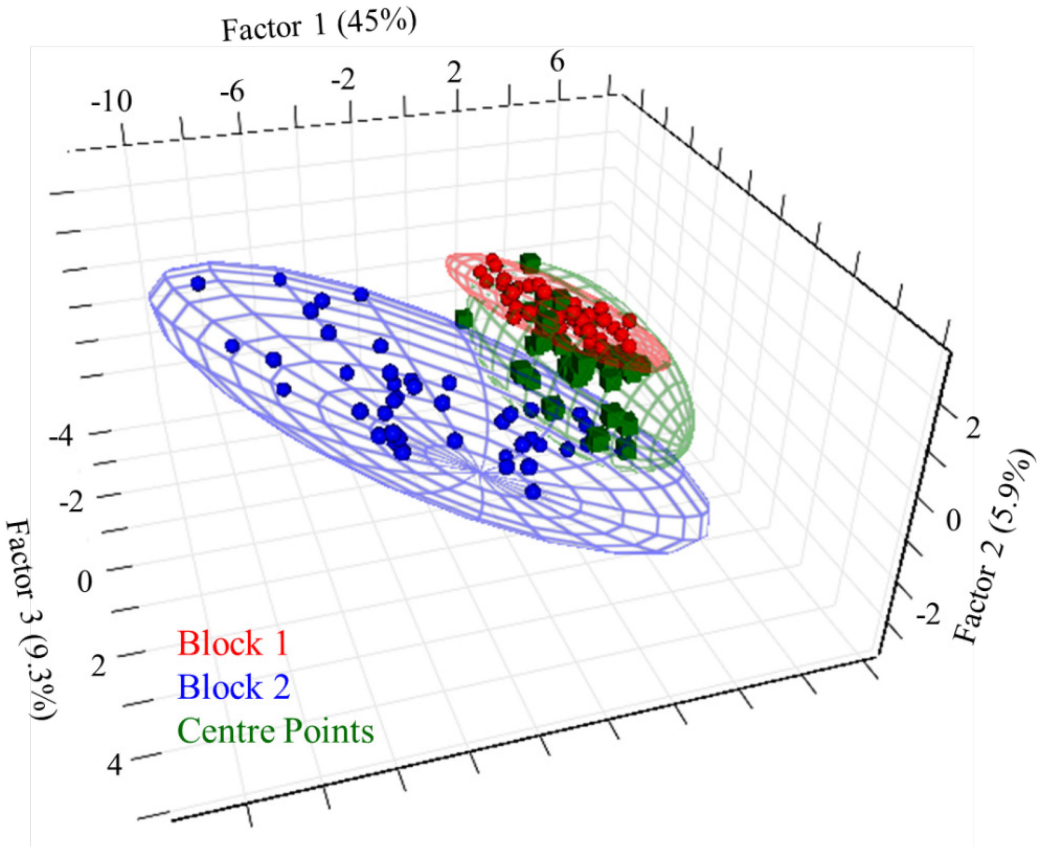

Figure 5.31: Projection of centre points onto the Block 1 and 2 PLS-DA model of HepG2 cells treated with sugars and vanadate. Hotelling's T^2 ellipses drawn at the 90% confidence level.

The projected scores, represented by green cubes, lie in the expected region between the two block treatments and further confirm the validity of the model. The projected points lie slightly above the Block 1 and Block 2 ellipses, which was also an indication of the increased cell viability induced by the centre point treatments (as was also observed in the interval plot in **Figure 5.20**). These results verify those in Section 5.3.3 where it was shown that the centre points resemble the Block 1 treatments and lower vanadate concentrations promotes cell growth. At these concentrations, vanadate was acting more as an insulin-mimetic, rather than a cytotoxic agent.

As was observed in the vanadate cytotoxic study (**Figure 5.6**) cells treated with vanadate over the concentration range 0-1000 μM covered a broad region of multivariate space compared to the more focussed cisplatin and doxorubicin treatments (**Figure 5.15** and **Figure 5.17**). **Figure 5.31** displays a similar trend that was concentration dependent, i.e., the Block 2 treatments (highest vanadate concentration) show the largest variability, followed by the centre points and then the Block 1 treatments (no vanadate). This was an indication of the diverse biochemical changes induced by vanadate, on proteins, lipids and DNA, particularly at cytotoxic concentrations.

5.4 Discussion

5.4.1 Modes of Action of Metallodrugs

The role of a cytotoxic agent is to induce selective apoptosis, or other cell death modes in target cells while minimising side effects. The complex nature of biological cells and the underlying biochemical processes that regulate cellular function can lead to positive outcomes towards the cytotoxic agent, or to negative effects, including resistance to the agent.[367] Mechanisms by which cytotoxins induce cell death and drug resistance are very active research topics and there is an abundance of literature aimed to understand the myriad roles of DNA, genes and proteins and their interactions in the proliferation and suppression of cancer cells.[105,110-112,114,129,146-147,333] In many cases, there are contrary literature results, making the need for non-destructive spectroscopic and more objective data analysis tools all the more important for providing new insights into mechanisms.[129,205]

Much research has focussed on the use of vanadium complexes as insulin-mimetics in the treatment of T2DM and other complications associated with metabolic syndrome, however, vanadium complexes also have promise as anti-cancer drugs,[105,129,132,144-145,377-378] (Chapter 1). When compared to the most commonly used anti-cancer drug therapies, vanadium complexes have much lower overall body toxicity and side effects,[129,145] making them attractive targets for future management of cancer and its proliferation. This type of therapy is also known as antineoplastic therapy and is used to either completely eliminate cancer, or used to suppress its growth, thus improving the patient's chance of survival and reducing their symptoms.[140] In this study, two benchmark antineoplastic therapies, cisplatin[367,379] and doxorubicin[140,380] were compared with the action of vanadate.

5.4.2 Vanadate Mode of Action

While there are many vanadium complexes with biological activities, all decompose in cells to form a mixture of V(IV)/V(V).[113] Therefore, vanadate was used as a general model of activity of vanadium complexes, mainly due to its analogy with inorganic phosphate.[130] The most likely mechanism of vanadate action as a cytotoxic agent is through the generation of reactive oxygen species (ROS) resulting in oxidative stress.[111,129,145] Oxidative stress shifts the balance from antioxidant to prooxidant behaviour, which leads to disruption of redox signalling and control to result in

biomolecular damage.[159,381] It is believed that induction of oxidative stress may lead to apoptotic cell death.[382]

A similar observation was made in the case of 3T3-L1 adipocytes in Chapter 4, where excess vanadate induced redox cycling between V(IV) and V(V). This balance of redox signalling is essential for regulating many of the important cellular processes and maintaining homeostasis, however, in the presence of sustained high levels of ROS, apoptotic pathways result from decreased mitochondrial membrane potential in HepG2 cells.[383] Sodium metavanadate and -orthovanadate have been reported to cause G2/M cell cycle arrest in prostate and hepatic cancer cell lines, as evidenced by the increased level of phosphorylated cdc2(cdk1) at its inactive Tyr-15 site in a mechanism believed to be caused by ROS mediated degradation of cdc2.[153,384-385] Sodium orthovanadate has been reported to induce apoptosis through DNA fragmentation, loss of mitochondrial membrane potential and activation of caspase-3.[145] Other vanadium complexes upregulate apoptotic precursors, such as BAX, PARP and caspase-3/9, as well as the upregulation of p53 with corresponding downregulation of Akt, mTOR and VEGF in human breast and hepatic cancer cell lines.[153,386]

Wu, *et al*.[385] recognised that vanadium complexes and salts represented a novel type of anti-cancer drug because of their effective anti-diabetic and anti-proliferative activity. These authors studied the pancreatic cancer line AsPC-1, known for its poor prognosis for patients with this phenotype and is a cancer type that may be correlated with T2DM.[387] Antiproliferative activity was exhibited through the induction of G2/M cell cycle arrest as a result of increased ROS levels and leads to the activation of the PI3K/Akt and MAPK/ERK pathways, however, cell cycle arrest was induced through the ERK pathway only.[385] The inhibition of the PI3K/Akt pathway has deleterious effects on insulin signalling and as a result of altered glucose metabolism, leads to undesired physiological consequences, such as hyperglycaemia.[388]

In response to higher levels of ROS induced by vanadate, increased glutathione (GSH) production has been reported to maintain ROS at a constant level[385] by intracellular reduction of V(V) to V(IV).[129] This interconversion between oxidation states in vanadium is postulated to be the mechanism responsible for the intracellular production of ROS, through mechanisms such as Fenton or Haber-Weiss reactions.[389-390] Cancer cells adapt metabolically during the initiation stage to high levels of oxidative stress and then adapt genetically to maintain these levels during proliferation, in order to avoid pathways that lead to apoptosis.[391] Cancer cells produce oxidants, such as H_2O_2, as a signalling molecule

to promote proliferation that activate antioxidant transcription factors, which then trigger the production of NADPH via the pentose phosphate pathway (PPP).[392]

Intracellular reduction of V(V) to V(IV) in the presence of GSH or NADPH generates H_2O_2 from the superoxide ion $O_2^{-\bullet}$ in the presence of superoxide dismutase, with the level of production being cell line specific.[250] At critical concentrations of V(V)/V(IV) and H_2O_2, redox cycling leads to generation of peroxidovanadium species, increasing the oxidative stress in the cell (Section 4.4.1.2). The generation of ROS also leads to oxidation of polyunsaturated fatty acids (PUFAs) resulting in lipid peroxidation and the generation of by-products, such as 4-HNE (Section 4.4.1.2), stimulate pathways leading to inflammation, apoptosis and ferroptosis.[303,391] Wu *et al*.[153] reported that sodium orthovanadate suppressed HepG2 cell proliferation, induced cell cycle arrest, autophagy and apoptosis. They also reported that vanadate induced apoptosis (>40% at 30 μM [V(V)]) and inhibited autophagy, and when autophagy was suppressed prior to vanadate treatment, apoptosis was enhanced. These observations were consistent with this current study where the IC_{50} value of vanadate towards HepG2 was 68 ± 11 μM, therefore, [V(V)] around 30 μM was expected to result in < 50% cell death. Interestingly, Gonclaves, *et al*. reported an IC_{50} value for vanadate towards TPC-1 papillary thyroid carcinoma around 50 μM, which is similar to that estimated for HepG2 in this study.[146]

Intracellular generation of ROS is an essential process for triggering insulin response and, in particular, activates Akt to promote cell growth and survival.[150,360] Vanadate has also been reported to promote cell viability in some cell lines, via the phosphorylation of tyrosine residues and activation of the PI3K/Akt/mTor pathway at low concentrations, followed by a decreased expression of PTEN.[111,146,250,391] However, as observed for 3T3-L1 cells (Chapter 4), once a critical concentration of vanadate was reached, increased levels of ROS generated by redox-cycling and production of H_2O_2 transitions vanadate from an insulin-enhancing agent into a cytotoxic agent.[150] This transition induced apoptotic pathways resulting from DNA fragmentation, mitochondrial membrane potential loss, p53 tumour suppressor and caspase-3 activation by high levels of ROS.[146,390]

5.4.3 Vanadate Cytotoxicity Towards HepG2

The present study indicated that vanadate acted via three distinct biochemical processes, associated with three regions of the MTT cytotoxicity assay curve. At low concentrations, 0-15 μM, vanadate promoted cell growth, then transitioned to a cytotoxic mechanism

over the concentration range 31-250 μM and, finally, over the range 250-1000 μM, protein aggregation associated with near complete cell death, or the transition into a new phenotype for cells that remained attached to the CaF_2 substrate. An interesting observation was the concentration at which vanadate transitioned to a cytotoxic agent in HepG2 was similar to that observed for insulin-resistant 3T3-L1 adipocytes (Section 4.3.3). This was consistent with the high levels of ROS present in cancer and insulin-resistant cells, which is known to deplete GSH levels in HepG2 cells, inducing cellular damage.[299,391]

5.4.3.1 Growth Phase Model

A model has been postulated for the growth phase over the vanadate concentration range 0-15 μM (**Figure 5.32**). Unlike adipocytes, normal hepatocytes use the GLUT2 transporter in a non-insulin dependent manner for glucose uptake and metabolism.[60,393] However, in HepG2 cells, GLUT2 is replaced with GLUT1 and GLUT3 and the number of plasma membrane amino acid transporters is increased.[362,394] GLUT1 is a tumour promoter because the enhanced rates of glycolysis in cancer cells requires increased glucose transport.[395-398] Proliferation of cancer cells by overexpression of GLUT1 has been proposed as a mechanism for increasing growth rates, while suppression of GLUT1 reduces glucose uptake and lactate secretion, particularly under hypoxia.[398] The expression of GLUT1 is a common observation in a wide range of tumours and is associated with an increased state of energy utilisation associated with aggressive, metastatic behaviour.[396-397]

Therefore, HepG2 cells preferentially metabolise glucose and amino acids,[362] which is a different mechanism to the β-oxidation of fatty acids observed in normal hepatocytes (**Figure 1.6**).[60] The MTT cytotoxic assay results and corresponding PCA scores for the vanadate toxicity study were consistent with the literature data that over the concentration range 0-15 μM, an increase in protein synthesis (evidenced by band intensities associated with α-helix and random coils) was observed and the lipid ester/fatty acid content was minimal.[150,153,399] Amino acids can serve as oxidative fuel for ATP generation and an alternative to glucose, fatty acids and ketone bodies.[399] The only source of amino acids available to cells was from cell culture medium, present in relatively high concentrations and in particular, culture medium contains glutamine as the major amino acid component.[400] Tumours utilise glutamine as a fuel source in a process known as glutaminolysis, leading to downstream production of pyruvate, lactate, NADH and ATP.[399]

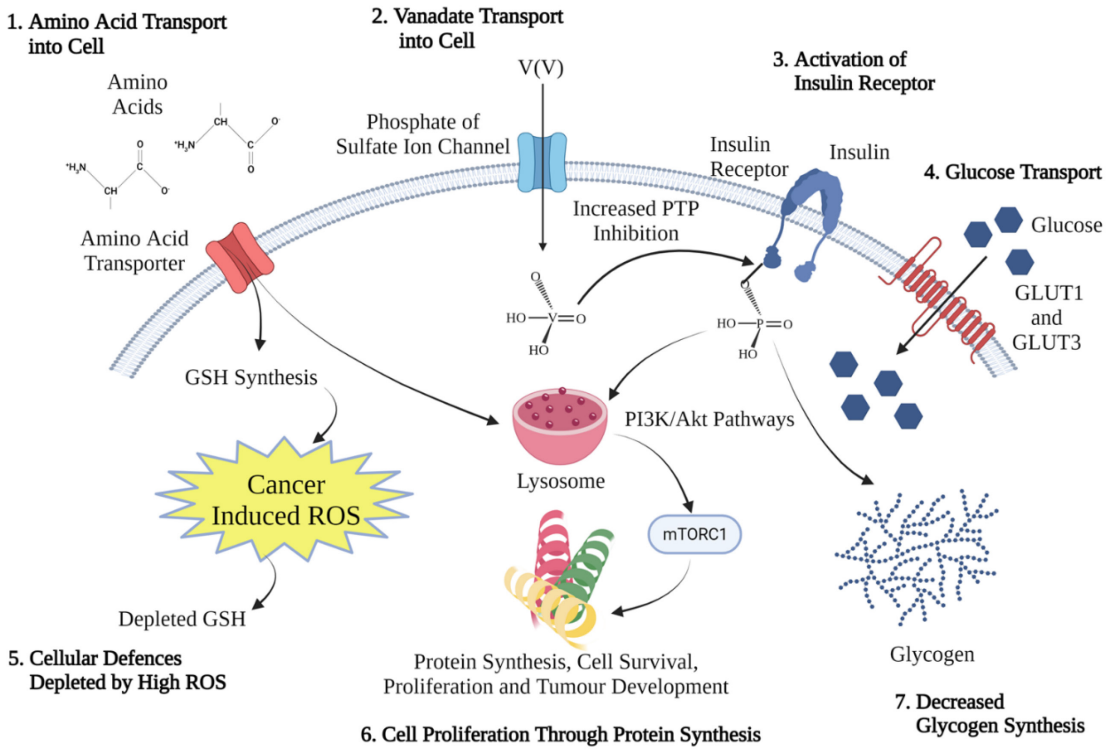

Figure 5.32: Postulated growth phase action of vanadate towards HepG2 at low concentrations (0-15 µM); 1) transport of amino acids into HepG2 cells via AATs provides precursors for GSH production and protein synthesis;[399] 2) vanadate transport into cells via phosphate or sulfate ion channels promotes PTP inhibition at the insulin receptor substrate and triggers downstream processes to result in protein synthesis;[401] 3) insulin receptor activation and signalling of PI3K-Akt pathways;[398-399,402] 4) uptake of glucose via GLUT1 or GLUT3 independent of insulin;[398] 5) depletion of cellular defences by high ROS already induced in cancer cells;[391] 6) activation of mTOR/mTORC1 pathways results in cell proliferation and protein synthesis;[399] and 7) decreased glycogen synthesis in favour of protein synthesis.[311] Created with BioRender.com.

Amino acid transporters (AATs) transport amino acids across cell and organelle membranes and regulate energy metabolism, protein synthesis, redox balance and cellular growth, while their dysregulation is linked to metabolic reprograming that can result in pathogenesis of cancer, obesity and T2DM.[399] Amino acids are positive regulators of mTORC1 through mTOR, which is activated through insulin like growth factor 1 (IGF-1). IGF-1 triggers the PI3K/Akt pathway and through phosphorylation of downstream effectors, such as ribosomal protein S6 kinase 1 (S6K1) and eukaryotic translation initiation factor 4E (elF-4E) binding, protein synthesis is promoted.[398-399] mTORC1, possibly stimulated by lysosomes, integrates stress signals, energy status and oxygen availability to induce both autophagy and protein synthesis and is also activated by upstream regulators, such as IGF-1 and MAPK.[399,403-404]

The observed increase in protein band intensity in the FTIR spectra with corresponding lack of bands due to lipid/fatty acid ester and glycogen synthesis for the growth phase (0-15 μM V(V)) were consistent with phosphorylation/vanadylation[104] of IGF-1 and other downstream processes that induced PI3K/Akt pathways. The further activation of the mTOR/mTORC1 pathways was postulated to result in protein synthesis consistent with cell proliferation and viability.[399,403] This was in contrast to GLUT1 being used as an alternative transporter to GLUT2 in HepG2 cells, which would be expected to result in glycogen synthesis.[398] Glycogen related bands were not found to increase in the same manner as protein bands. The band at 1078 cm^{-1}, assigned to glycogen,[405] could also be assigned to the $(RO)_2PO_2^-$ bands associated with DNA.[182] The protein synthesis pathway was also supported by the absence of the glycogen band at 1151 cm^{-1}.[181,405] This was consistent with the literature that in HepG2 cells, enzymes associated with glycogen degradation are reduced to the point that glycogen metabolism was negligible.[362]

Low doses of vanadate between 0-30 μM have also been reported to stimulate cell proliferation in a number of cell lines, including rat hepatoma cells.[406] Wu, *et al*.[153] observed decreasing cell viability after treatment with 7.5 μM vanadate in HepG2 cells; however, significant differences from control conditions were observed only at 15 μM, which were consistent with the current results. Zhao, *et al*.[150] also reported similar results, except using the V(IV) salt $VOSO_4$ where glucose uptake in HepG2 cells increased with increasing vanadyl concentration up to 25 μM and then diminished at 50 μM. These authors postulated that vanadyl-induced ROS promoted the IR/Akt pathway, stimulating glucose uptake to a point, where an excess of ROS triggered a cytotoxic pathway. This pathway could be the result of redox cycling to produce V(V), which is a more potent inhibitor of PTPs than V(IV)[299] and was consistent with the results observed in the cell death phase.

5.4.3.2 Apoptosis and Cell Death Phase

Cell death was defined as the sharp decrease in cell viability observed in the MTT assay curves (**Figure 5.2a** and **Figure 5.7a**). The PCA model developed for the vanadate MTT assay showed that two different concentration dependent biochemical processes were occurring. The first process, over the [V(V)] range 31-125 μM, coincided with a rapid synthesis of lipids, predominantly TAGs (as evidenced by the increased band intensity at 1743 cm^{-1}) and changes in membrane lipids/fatty acids. The second process over [V(V)] of 125-500 μM, was mainly associated with an increase in the band intensity at 1623 cm^{-1},

assigned to β-sheet proteins. This is discussed further in Section 5.4.3.3 for fibrosis/phenotype changes in HepG2 cells.

Oxidative stress in hepatocytes has been reported to induce mitochondrial and endoplasmic reticulum (ER) dysfunction to promote the accumulation of TAGs and liver steatosis.[402,407] It was postulated that the increased oxidative stress caused by increasing vanadate concentration triggered pathways that induced lipid synthesis. Boren and Brindle[311] reported that during apoptosis, cells rapidly accumulated cytoplasmic neutral lipid droplets and, using magnetic resonance spectroscopy, have shown that protein signals from membrane lipoproteins can be used as a non-invasive method of detecting cell death. These authors proposed that DNL results from inhibition of fatty acid oxidation (FAO) in the mitochondria, to result in increased mitochondrial membrane potential induced by increased ROS levels.[311]

Insulin-resistant adipocytes were postulated to have increased H_2O_2 production by redox cycling between V(IV) and V(V) and the production of peroxidovanadates, to result in decreased GSH levels and more potent PTP inhibition. This would turn on lipid synthesis machinery through activation of a number of pathways.[58] It was also postulated that reduction in GSH levels facilitated the induction of the PPP pathway to produce NADPH to counter the increasing ROS. This in turn would activate a mitochondrial glutaminase, which produced GSH,[311] in a cycle that continued until the oxidative stress in the cell became too high and the pathways discussed in Section 5.4.3.3 were induced.

Over the [V(V)] range 31-250 μM, cell viability decreased rapidly, as evidenced by the MTT assay curve and biochemical changes identified by PCA scores. The postulated cell death phase mechanistic processes are depicted in **Figure 5.33**. Chemometric analysis of FTIR spectra showed that under heightened cytotoxic and oxidative stress conditions, induced by higher [V(V)], HepG2 cells store neutral lipid reserves as a potential survival mechanism. When conditions were conducive to growth, (i.e., the absence of vanadate in the treatments, Section 5.3.2), these energy stores are available for cell proliferation, or in mechanisms that resist cell death.[129,144-145] During the cell death phase (31-250 μM V(V)) the p_2 direction (**Figure 5.7b**) in the PCA model of vanadate cytotoxicity showed a transition at 125 μM V(V) where, increased lipid synthesis (1743 cm^{-1}), protein aggregation (1623 cm^{-1}) and decreased DNA band intensity (1704 and 1080 cm^{-1}) were occurring simultaneously. Zelig, *et al*.[205] state that apoptosis can be characterised by three characteristics in FTIR spectra: increased lipid band intensity; decreased DNA band

intensity; and an increase in the total β-sheet protein secondary structures. These three characteristics were observed in FTIR spectra during the cell death phase.

The optical micrographs of HepG2 cells recorded over the concentration range 62.5 to 1000 μM showed a change from the usual epithelial cobblestone morphology to cells becoming less clustered and more round in morphology, which was an indication of apoptosis.[327] Changes in lipids and proteins in membrane structures are also an indication of apoptosis in cells and were observed in the FTIR spectra as increased band intensities at 2920 and 2850 cm^{-1},[160,195,202,205] with increasing [V(V)]. At these vanadate concentrations, increased lipid peroxidation, mitochondrial dysfunction and loss in cell membrane integrity ensue.[129]

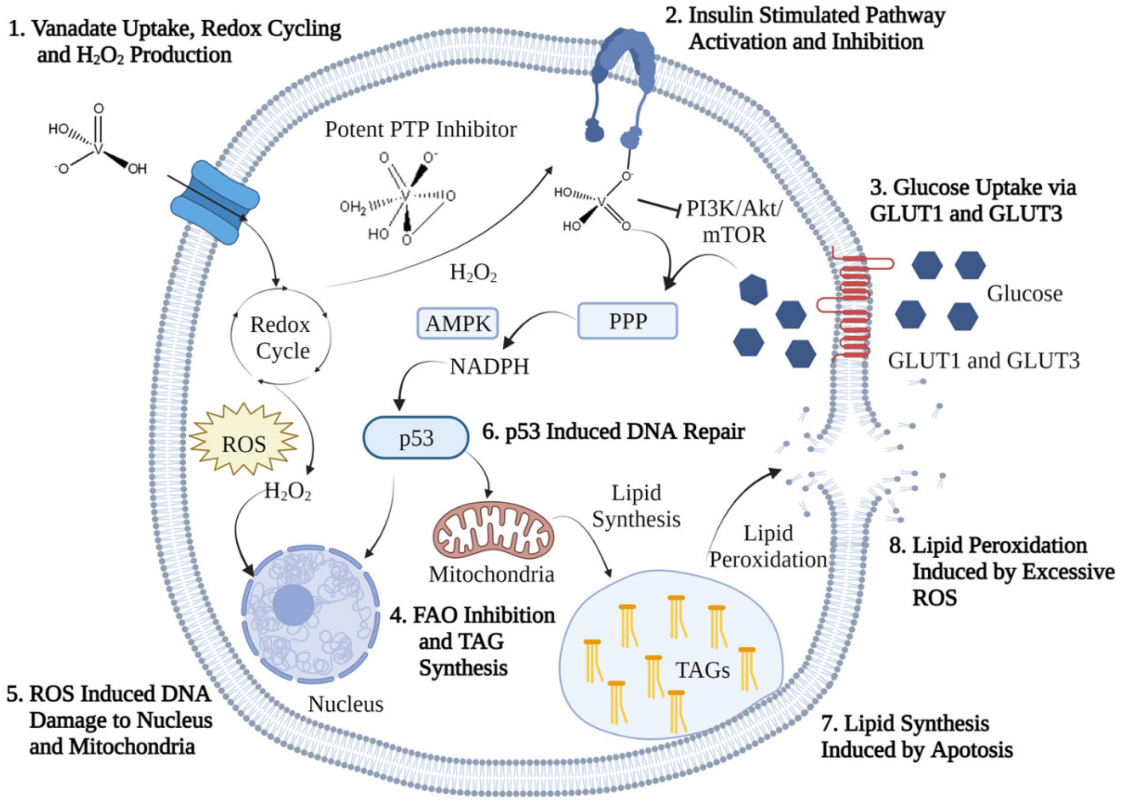

Figure 5.33: Postulated cell death pathways due to vanadate towards HepG2 over the concentration range 31-250 μM; 1) Uptake of vanadate, redox cycling and production of peroxidovanadate species inhibit PTPs;[111] 2) inhibition of PI3K/Akt/mTOR pathways and activation of pentose phosphate pathway (PPP) diverting glucose from glycolysis to synthesis of NADPH;[408] 3) uptake of glucose via GLUT1 and GLUT3 transporters for metabolism;[398] 4) inhibition of fatty acid oxidation (FAO);[311] 5) ROS induced DNA damage to nucleus and mitochondria induced by H_2O_2 and other ROS;[409] 6) AMPK/p53 pathways induced by DNA damage resulting in cell cycle arrest and repair;[340] 7) neutral lipid synthesis induced by apoptosis;[311] and 8) lipid peroxidation induced by increased oxidative stress.[195,202,205] Created with BioRender.com.

5.4.3.3 Protein Aggregation/Phenotype Change Phase

Beyond 250 μM V(V), the optical micrographs of the treated HepG2 cells started to show isolated cells with stellated, fusiform structures typical of mesenchymal cells.[349] These cells were either present in the main population, representing the challenges of effective cancer treatment due to the heterogeneous nature of cancer cells,[410] and were those that were most resistant to treatment,[160] or may be the result of an epithelial to mesenchymal transition (EMT).[349] EMT results in transcriptional and morphological changes in cells during the progression of diseases such as fibrosis and metastatic cancers, particularly observed as changes in actin structures that minimise cell adhesion and enhance the ability of cells to migrate and become invasive.[349]

EMT has been classified into three main types: type 1 associated with embryo and organ development; type 2 is associated with wound healing and the formation of scar tissue; and type 3 in neoplastic cells is associated with the dissemination of tumours.[411] Type 3 EMT, therefore, represents the manner in which actin filaments in epithelial cells (organised as cortical thin bundles) transition into thick, contractile stress fibres on the ventral cell surface of mesenchymal cells.[349,412]

The dominant 1623 cm^{-1} band particularly in spectra acquired over the concentration range 125-1000 μM indicated that protein aggregation was occurring,[175] consistent with the morphology changes observed in the optical micrographs. Zelig, *et al*.[205] reported similar findings for U937 human leukemic cells when treated with higher concentrations of the cytotoxic agents Ara-C and doxorubicin, which resulted from a gradual biochemical change in the cells with treatment concentration. This finding was consistent with the results in this study, where it was observed that increases in β-sheet protein structures occurred gradually over the vanadate concentration range 125-1000 μM. Haynes, *et al*.[349] observed slow and progressive changes in actin filament structures during EMT of mouse mammary epithelial (NMuMG) cells as a response to treatment with transforming growth factor-β (TGF-β). The TGF-β signalling pathway inhibits and promotes tumour growth,[413] and increases in liver cancer.[414] This pathway affects cell growth, cell cycle and apoptosis by regulating the protein expressions of proliferating cell nuclear antigen (PCNA), gankyrin, p115, X-linked inhibitor of apoptosis protein (XIAP) and survivin.[413]

Therefore, if TGF-β levels are increased in HepG2 cells as a mechanism of disease pathogenesis and it is also involved in the breakdown and reorganisation of actin into

stress fibres, this could potentially lead to EMT and the subsequent morphological changes observed in the optical micrographs of cells treated over the range 500-1000 μM V(V). Bracken, *et al*,[401] observed that in the epithelial bovine kidney cell line MDBK, at [V(V)] ~ 50 μM the cobblestone morphology was preserved, however, at concentrations > 50 μM, the cells become stellated in morphology and the intercellular contacts decreased. These observations were consistent with the optical micrographs of HepG2 cells treated with [V(V)] > 50 μM in this current study.

Bracken, *et al.* also observed a dose-dependent initial rapid uptake of vanadate,[401] which plateaued over time, and indicated a high affinity of vanadate, with uptake rates reported at approximately 90% in cultures that exhibited 30-70% cytotoxicity. This further supported the growth phase model in Section 5.4.3.1, where at low concentrations, vanadate is rapidly taken up by HepG2 cells and used to promote protein synthesis.[399] At higher vanadate concentrations, interference with cytoskeletal elements was reported to mediate the morphology changes in MDBK cells, however, vanadate's mitogenic and insulin-mimetic actions may also contribute to morphology changes.[401] Similar observations were also made for the HepG2 cells in this study and the changes in cytoskeletal components were attributed to the breakdown and rearrangement of actin to provide greater motility to the cells that result in their stellate morphology.[349]

Contrary to the EMT postulate, vanadium complexes, including *in vitro* treatment using Na_3VO_4, inhibit EMT in hepatocarcinoma cells.[144,153] Therefore, a plausible interpretation for the observations made on HepG2 cells could be somewhat similar to what occurs in neurodegenerative disorders, such as Alzheimer's disease, where increased levels of Aβ amyloid protein aggregates have been reported to result in the formation of actin stress fibres, through p38MAPK activation.[415] Increased oxidative stress in endothelial cells as a result of H_2O_2 production induces phosphorylation of heat-shock protein 27 (HSP27), which mediates actin polymerisation.[416] Kuordinova, *et al*. suggest that Aβ peptides also play other roles outside of neurodegenerative diseases and have studied the impact of an Aβ derivative on lipid synthesis in HepG2 cells.[417]

As discussed in Section 5.4.3.2, cytotoxic [V(V)] can induce DNA damage, which induces p53 proteins to repair mild to moderate damage, however, beyond a critical point, apoptotic pathways are induced.[311] The detailed loadings in the PCA model developed for the vanadate cytotoxicity range over the region 1500-1700 cm^{-1} revealed protein secondary structural changes that were attributed to a combination of the triggering of

p53 proteins that attempt to repair damaged DNA under physiological stress and changes induced by actin rearrangement. Changes in protein phosphorylation state were also observed at 1516 cm^{-1} and attributed to the 'tyrosine band'.[172,198] To explain the transition of HepG2 over the concentration range 500-1000 μM V(V) where cell viability plateaued to a very low level in the MTT assay curve, a postulated mechanism for fibrosis/phenotype change is shown in **Figure 5.34**.

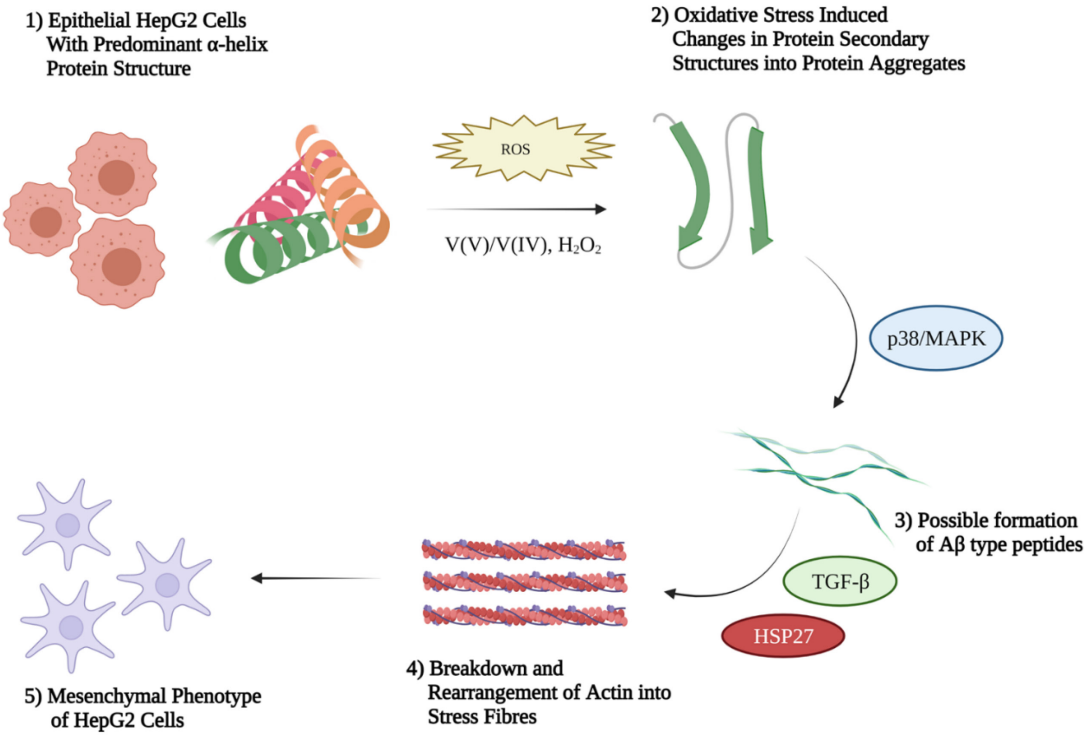

Figure 5.34: Postulated fibrosis/phenotype change model of vanadate action towards HepG2 over the concentration range 125-1000 μM; 1) initially, HepG2 cells show a cobblestone, epithelial structure; 2) increased oxidative stress leads to changes in protein secondary structures that results in an increase in β-sheet protein;[175] 3) induction of the p38MAPK pathway results in the formation of amyloid structures, including Aβ-like peptides;[415] 4) Aβ-like peptides induce pathways such as TGF-β and HSP27 that result in the breakdown of actin and the formation of actin stress fibres;[416-417] and 6) when complete breakdown of actin occurs in surviving cells, cell adhesion is lost in favour of a phenotype that is better able to migrate.[411] Created with Biorender.com.

5.4.4 Comparison of Vanadate to Cisplatin and Doxorubicin Modes of Action

Cisplatin (*cis*-diamminedichloridoplatinum(II)) is one of the most commonly used antineoplastic drugs and is classified as an 'alkylating' agent that directly damages DNA to inhibit cell division.[379] The lesions induced by cisplatin in DNA trigger intercellular pathways that either result in DNA repair, or apoptosis.[145,418] The pathways induced include ataxia telangiectasia and Rad3 (ATR), ataxia telangiectasia mutated protein (ATM), p53, p73 and MAPK.[367] The p53 tumour suppressor protein is one of the most

important cell cycle regulators in normal and cancer cells.[140] It is responsible for suppressing cell growth under physiological stress, including DNA damage and activates apoptosis pathways when DNA repair is no longer possible or incomplete,[419] which occurs when cisplatin adducts change the DNA structure.[367,379]

Activation of ATR subsequently activates the MAPK pathway, which integrates a number of extracellular signals including phosphorylation of p53 activity, thus regulating cell proliferation, differentiation, cell survival and apoptosis.[420] However; extracellular signal-regulated kinase (ERK) is probably the most important pathway activated for cisplatin-induced apoptosis through phosphorylation of p53 at serine 15.[421] Cisplatin-induced BCL2 associated X (BAX) from the cytosol to the mitochondria results in the release of apoptogenic factors, such as cytochrome *c* and activates caspase 9 and downstream caspases, such as caspase 3, that result in apoptosis.[367,422] Apoptosis is inhibited by activation of the PI3K/Akt pathway, which is a hallmark of cancer and results in a loss of p53 functionality and interference of caspase activation.[423]

Doxorubicin, ((8S-*cis*)-10-[(3-amino-2,3,6-trideoxy-α-L-lyxo-hexopyranosyl)oxy]-7,8,9,10-tetrahydro-6,8,11-trihydroxy-8-(hydroxyacetyl)-1-methoxynaphthacene-5,12-dione HCl) belongs to a class of anti-cancer drugs known as non-selective antitumour antibiotics or anthracyclines.[140] Its primary action is to inhibit topoisomerase I and II and to intercalate into DNA to prevent its uncoiling during replication, which can lead to apoptosis.[410] Topoisomerases are enzymes that regulate the DNA topology through re-joining or breaking of DNA strands.[424] Therefore, doxorubicin intercalates with DNA to induce its cytotoxic effect, mainly through the interruption of DNA replication and RNA transcription.[140,410]

The modes of action of cisplatin and doxorubicin (**Figure 5.35**) shows how cisplatin binds to specific base pairs in DNA to bend the structure such that an active site is exposed to tumour suppressor proteins such as p53.[379] In the doxorubicin mechanism of action, its planar aromatic structure allows it to intercalate between internal base pairs in the DNA structure, thus interrupting the normal replication processes and triggering biochemical pathways that induce apoptosis.

The combined PCA model of FTIR spectra obtained from HepG2 cells treated with vanadate, cisplatin and doxorubicin (Section 5.3.2.4) revealed that the mode of action of vanadate was distinctly different from those of cisplatin and doxorubicin, which were more similar to each other (**Figure 5.15**).

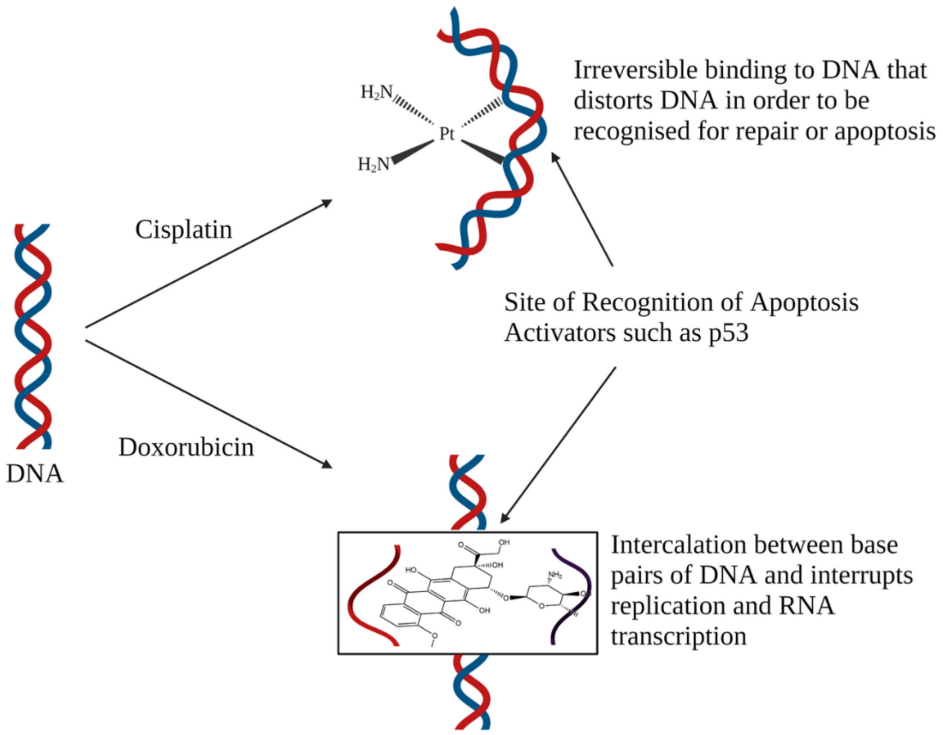

Figure 5.35: Modes of action towards DNA of; a) cisplatin;[379] and b) doxorubicin.[140]

Cisplatin and doxorubicin act mainly through interactions with DNA (**Figure 5.35**), this explains why the two agents clustered closely in multivariate space and were observed to separate from each other in the minor PC3 direction. The PC1 and 2 directions of this model mainly described the biological changes induced by vanadate. In particular, the PC1 direction described the cytotoxic effects associated with the protein aggregation/phenotype stage induced by vanadate, which represented a different mechanism from those induced by cisplatin and doxorubicin.

The chemometric models of changes in FTIR spectra associated with cisplatin cytotoxicity (Section 5.3.2.2) for the t_2 scores vs. [cisplatin] resembled the shape of the MTT assay curve (**Figure 5.10b**), while the t_3 direction showed that a different bioprocess was occurring simultaneously. Surprisingly, the p_2 and p_3 loadings revealed that the main spectral features associated with cisplatin action were changes in protein secondary structures, particularly a shift in α-helix proteins between 1654 to 1648 cm^{-1}, indicative of a dose-dependent conformational change.[425-426] A small change in the DNA base pairing band at 1698 cm^{-1} was observed and associated with induced apoptosis, along with weaker bands at 1121 and 1080 cm^{-1}.[182] Zelig, *et al*. observed that during apoptosis, FTIR bands associated with DNA become less intense and are, therefore, more subtle as a result of opacity and this may explain why DNA bands were not prominent in the cisplatin cytotoxicity study.[205]

In the chemometric model of doxorubicin cytotoxicity (Section 5.3.2.3), the data were very complex and the PCA scores vs. [doxorubicin] plots showed only a slight resemblance to the MTT assay curve. There was, however, an indication that FTIR spectroscopy could assess doxorubicin's cytotoxicity pathways, and the PCA model showed that the major changes occurred in protein secondary structure. Apoptotic pathways are characterised by activation of caspases that result in the generation of protein fragments involved in apoptotic proteolysis signalling.[427] This suggests that while cisplatin and doxorubicin act through targeting DNA, the FTIR spectra are measuring the downstream effects on protein conformational changes. This is consistent with the observations made on DNA opaqueness in FTIR spectra during apoptosis and also shows that FTIR is a method for assessing global change in cellular environments induced by treatments and can provide insights that are then linked to more specific biochemical pathways established by specific antigen testing protocols.[205,410]

Overall, FTIR spectroscopy established that vanadate-induced apoptosis followed more complex biochemical changes compared to cisplatin and doxorubicin, as established by the comparative PLS-DA model in Section 5.3.2.4. Cisplatin and doxorubicin treatments clustered together in scores space, with very little variance within the clusters, and the treatments were separated from each other by the Factor 3 direction, which in the PLS-DA model, contributed nearly as much to the explained **Y**-variance as Factors 1 and 2. Vanadate treatment showed distinct growth, death and fibrosis/phenotype changes in Factors 1-2, where apoptosis was induced through pathways that mediate lipid synthesis and protein aggregation. The final stage of apoptosis induced by vanadate occupied negative Factor 1 scores compared to cisplatin and doxorubicin, which occupied positive Factor 1 scores. Therefore, this information confirmed that vanadate acts in the opposite manner to the other treatments and since vanadate treatments occupied the greatest space in the t_1 vs. t_2 scores plot, its mode of action was diverse over the concentration range as described by the three-phase model proposed in Section 5.4.3.

5.4.5 Fructose Induced Metabolic Changes in HepG2

5.4.5.1 Designed Cytotoxicity Assay Experiment

The factorial design used to decide the conditions to treat HepG2 cells with glucose, fructose and vanadate for FTIR analysis was also amenable to a cytotoxic assay. Using the glucose treated cells as a control, the remaining treatments were compared to assess cell viability. ANOVA,[223] of the response cell viability (%) showed that sugar treated cells uniquely separated from vanadate-sugar treated cells when [V(V)] was set to the

IC_{50} value. This study verified that this concentration induced a cytotoxic effect, however, when the concentration of vanadate was reduced by 50% (i.e., at the centre point of the design), this induced growth in the cells. These data were consistent with the findings of both those in Section 5.3.1 and the literature.[111,150,153,299,390]

The standard two-level factorial design is a linear model, with interaction terms, however, a quadratic (or higher order polynomial) was required to model the response. As such, the results were modelled using a PLSR model, which incorporated quadratic and interaction terms.[223] Even though centre points were not used in the calculation of standard factorial models, they provided three-levels of response that were used to fit a quadratic PLSR model. As a verification, the PLSR predicted results were calculated for the design points of the exact quadratic model (the Box-Behnken model), where the quadratic response surface model showed an excellent fit to the data and confirmed that lower [V(V)] was able to induce growth in HepG2 cells. These results provided a baseline to compare to the FTIR spectroscopic experiments of cytotoxicity.

5.4.5.2 Sugar Metabolism by HepG2 Cells

These studies evaluated the metabolic impact of various dietary sugar loads on HepG2 cells as an *in vitro* model of individuals with diseases, such as T2DM or HCC. The HepG2 cell line has been used as a model for evaluating biochemical changes induced by glucose and fructose metabolism. Although it has been reported that results obtained on HepG2 can be translated to human hepatocyte derived cells,[249] Nakagawa, *et al*. report that hepatocellular carcinoma (HCC) appears to be distinct from other cancers as fructose metabolism is reduced when compared to healthy hepatocytes.[143] The cytotoxicity assay performed on the Block 1 treatments in Section 5.3.3 and the corresponding PLS-DA model of FTIR spectra collected on HepG2 cells confirmed that there were only small differences in the glucose- and fructose-only treatments, consistent with the literature,[143] which resulted in similar cell viabilities.

The PLS-DA model of the Block 1 data showed that the synergistic effect of glucose and fructose separated this class from the other treatments. Hirahatake, *et al*.[249] observed that when HepG2 cells were treated with glucose and fructose (each at 5 mM concentrations), that fructose attenuated glycolytic flux of glucose. This was explained by fructose entering the glycolytic pathway distal to phosphofructokinase (PFK), which provides intermediates that are metabolised to citrate and thus limiting glucose metabolism by PFK. By entering the Kreb's cycle, citrate is converted to acetyl-CoA and then to FFA via FAS.[60,376] Citrate is an activator of acetyl-CoA carboxylase (ACC), which is an

initiator of DNL. The Block 1 model indicated increases in FFA synthesis and DNL.[20] Since this treatment cluster separated uniquely from both fructose and glucose treatments alone, the glycolytic attenuation of glucose mechanism proposed above was supported.[249] These results were in direct opposition to those of Geidl-Flueck, *et al*,[428] who observed that fructose stimulates hepatic glucose uptake through glucokinase activation, however, this observation may be a result of the differences between normal hepatocytes and the HepG2 cell line.[143,362,429]

Fructose metabolism results in the depletion of ATP and the suppression of mitochondrial fatty acid oxidation, increased oxidative and endoplasmic reticulum (ER) stress that leads to DNL.[376] PLS-DA modelling of the Block 1 FTIR data showed a separation of the glucose and fructose only treatments in the factor 2 direction, where the fructose treatment cluster showed increased TAG and FFA synthesis consistent with DNL. This treatment was also associated with an increase in β-sheet proteins at 1625 cm^{-1}, possibly associated with protein aggregation induced by oxidative stress and the onset of fibrosis.[175,376] The separation of these treatment clusters was, however, smaller than the separation of the no-sugar and combined glucose-fructose treatments.

The no-sugar treatments formed a separate cluster from the glucose and fructose treatments along the Factor 3 direction and indicated that these cells had the highest protein content and the lowest lipid and FFA content. Although the no-sugar treatment was associated with increased band intensity at 1382 cm^{-1}, typically associated with fatty acids and lipids,[210-211] this band has also been attributed to amino acid side chains of proteins and this would be the most plausible explanation for the appearance of this band.[210] The glucose and fructose treatments were consistent with increased lipid and fatty acid bands in the Factor 3 direction.

The Block 1 PLS-DA model (**Figure 5.20**) results were consistent with the DoE cell viability assay. In particular, the glucose- and fructose-only treatments were similar to each other in terms of cell viability and they occupied a similar scores space in the PLS-DA model. The separation of the combined glucose-fructose treatments from the glucose and fructose treatments alone were consistent for both the cytotoxicity assay and PLS-DA models and were associated with higher cell viabilities. Therefore, although the lipid and fatty acid band loadings weights were not as intense as those observed in the FTIR spectral cytotoxicity assay (Section 5.3.2.1), these loading weights were associated with pathways that increase cell viability, possibly through fructose bypassing key glucose

regulatory pathways and providing a carbon source for DNL.[376] The no-sugar treatment represented the lowest cell viability of the Block 1 treatments and separated along the Factor 3 direction in the PLS-DA model. This direction described the biochemical differences between the no-sugar and the glucose- and fructose-only treatments and the lowered cell viability was a result of reduced lipids and fatty acid stores essential for maintaining homeostasis in the HepG2 cells.

The effects of dietary sugars on the aggressiveness of cancers have been reviewed by Goncalves, *et al*,[430] where human studies have shown to be inconclusive, however, there is a general consensus that higher dietary sugar intake, resulting in higher circulating glucose stimulates insulin secretion and hyperinsulinemia, which leads to the production of visceral adipose.[31] Although this current study only investigated the effects of sugar intake on HepG2 cells, the synthesis of TAGs and FFA by the liver serve as metabolites for adipose tissue, where they are stored for later use. Adipocyte hypertrophy induced by excess dietary sugar intake leads to the secretion of adipokines and cytokines by adipocytes, which are known mitogens for some cancer types.[31] Therefore, larger deposits of adipose tissue serve as a source of fatty acid reserves that promote tumour growth and aggressiveness.[431]

5.4.5.3 Sugar-Vanadate Metabolism by HepG2 Cells

The Block 2 experimental data treated HepG2 cells using the same sugar combinations as the Block 1 treatments, this time, each treatment contained vanadate at its established IC_{50} concentration (Section 5.3.1). The Block 2 PLS-DA model showed that the fructose-vanadate treatment separated from the rest of the treatments and was the main source of variability described by this model. This condition was described by increased protein and reduced lipid content in these cells compared to the other treatments. Fructose induces pathways that increase protein expression, however, this is typically accompanied with an increase in lipid synthesis.[20,249,376,428,432] In the presence of cytotoxic vanadate concentrations, the combined fructose-vanadate effect increases oxidative stress, which leads to increased fructose-induced protein synthesis and subsequent damage to these proteins by vanadate generated ROS.[20,147,158,433] In particular, Irving and Stoker state that cancer cells are already in a state of sub-lethal oxidative stress and even slight increases in ROS can have detrimental effects on cell viability.[147]

The fructose-vanadate treatment had the highest variability of the treatment conditions (**Figure 5.20**), which indicated the presence of two cell populations. At the IC_{50} value, vanadate would be expected to be lethal to 50% of the cell population, however, as

described in Section 5.4.3.3, the presence of different phenotypes, some of which may be more resistant to vanadate, resulted in higher cell viability due their ability to adapt to changing conditions of oxidative stress.[147] Cancer cells are highly heterogenous and are in a state of dynamic flux in order to adapt under non-ideal conditions (Warburg effect).[31,144] Therefore, the observation that the fructose-vanadate treated cells separated based on their FTIR spectra was most likely due to surviving cells being more resistant to the treatments and could survive under heightened oxidative stress compared to pre-apoptotic cells.[160] For the population of surviving cells treated with fructose-vanadate, the increased cell viability was associated with increased amide I protein band intensity. As was observed in the growth phase model in Section 5.4.3.1, cell proliferation was attributed to increased protein synthesis and a similar mechanism may also be occurring for the fructose-vanadate treated cells where amino acids from cell culture media are also being utilised under conditions of high oxidative stress to generate more GSH to counter the ROS. This would lead to pathways that induce protein synthesis; however, this must be explored in futures studies in order to establish the plausibility of such mechanism on multiple cell cultures.

The net overall effect of vanadate observed in **Figure 5.20** was to significantly reduce cell viability (**Table 5.2**, $p = 0.002$ for the vanadate main effect) and as with the PLS-DA scores in the Block 1 model, the Block 2 model scores also reflected the patterns observed in the cell viability assay results. Further confirmation of the overall cytotoxic effect of vanadate on HepG2 cells was observed in the combined Block1-2 PLS-DA model where a clear separation of the blocks was observed. The loading weights for this model were indicative of events related to apoptosis including overall lipid synthesis induced by vanadate,[311] changes in membrane lipids as a result of loss of membrane integrity and lipid peroxidation[195,202,205] and evidence of fibrosis, related to phenotype changes or cell death.[349]

In the presence of vanadate only, the treated cells separated from the other treatments and this was described by changes in the FTIR spectra associated with increases in the intensities of bands from lipids and α-helix protein secondary structure. A comparison of this treatment with the cell death model of Section 5.4.3.2 indicated that HepG2 cells were converting glycogen stores into lipids in response to a lack of sugar in the growth media and the oxidative stress induced by vanadate.[311] These cells were postulated to be using culture media nutrients, such as glutamine, as a source of carbon for lipid synthesis in a similar manner to that proposed by Brose *et al*. in neuronal cells.[434]

The Block 2 PLS-DA model showed that the glucose-vanadate and glucose-fructose-vanadate clusters overlapped in the Factor 3 direction and separated from the vanadate only treatment. The loading weight patterns were highly complex and indicated that many simultaneous biochemical processes were occurring, however, the data showed that many of these changes were associated with protein secondary changes induced by vanadate and were consistent with mechanism of induced apoptosis.[205]

5.4.5.4 Effect of Sugars and Vanadate at Non-Cytotoxic Concentrations

When the concentrations of all experimental factors were reduced by 50% (i.e., the centre points of the design), the cytotoxicity assay data and the Box-Behnken model (Section 5.3.3) showed that cell viability increased. The vanadate concentration at the centre point was 25 μM and this concentration has been previously reported to increase cell viability in HCC.[153,406] When the centre point treatment FTIR spectra were projected onto the model of Block 1 and Block 2 treatments, the centre points clustered in the expected region between the Block 1 and Block 2 treatments, which served as an external validation of the PLS-DA model.[223]

Therefore, at non-cytotoxic vanadate concentrations, the cytotoxicity assay design confirmed that cell viability increased compared to the sugar treatments alone (Block 1). When the centre points were compared to the results of Block 2 model, the higher vanadate concentration produced results consistent with the cell death model proposed in Section 5.4.3.2. This was evidenced by the increase in lipid content in the Block 2 treatments compared to those in Block 1 and data from the centre point treatments. Correlation of the aggressiveness of some types of cancers and dietary sugar intake was discussed in Section 5.4.5.2 and this was associated with sugars inducing hyperinsulinemia and increased visceral adipose deposits.[31] The action of vanadate at low concentrations has been established to induce insulin-mimetic behaviour[385] and the increased cell viability induced by the centre point treatments may be an indication of the detrimental effect vanadate, as an insulin-mimetic, can have on the treatment of cancer. However, this has to be balanced against the ability of low vanadate concentrations to promote cancer death by oncoviruses and increase the activity of immune system cells,[435] which are likely to override deleterious effects of cancer cell proliferation at low concentrations.

The spectral band contributions at the centre points contained the highest amide I and II band intensities and the lowest contributions from lipid bands and the β-sheet protein

band at 1623 cm^{-1}. These results were consistent with vanadate concentrations below the IC_{50} value, having promoted protein synthesis and minimised lipid synthesis, even in the presence of high fructose concentration and reduced glucose concentration (i.e., 2.5 mM compared to normal physiological concentration of 5.5 mM).[246-247]

The major findings of this study showed that in the presence of fructose and glucose alone, both sugars were metabolised by HepG2 cells resulting in similar cell viability and in the presence of both glucose and fructose, cell viability increased. This was associated with complex biochemical changes to lipids, FFAs and proteins, mainly associated with β-sheet secondary structure. This result is consistent with dietary sugar increases being associated with cancer incidence and increased aggressiveness.[31] The no-sugar treatment was attributed to changes in protein secondary structures and increased amino acid side chain band intensities. Vanadate at the IC_{50} concentration resulted in an overall reduction in cell viability for all sugar combinations, consistent with its cytotoxic effect and the Block 2 treatments were characterised by highest lipid and lowest protein band intensities. This was consistent with the observations made in the vanadate MTT-FTIR model in Section 5.4.3.2 for the cell death phase, no matter which sugar or combination of sugars were used to treat the cells. The centre point data was consistent with the growth phase model in Section 5.4.3.1 where non-cytotoxic [V(V)] promote protein synthesis and reduce DNL. Such results may have positive implications for outcomes from patients who are obese or consume large amounts of dietary sugars, who normally have worse outcomes.[428]

Chapter 6 FPA Imaging of Adipocytes

6.1 Introduction

6.1.1 Laboratory Based FPA Imaging

Chapter 4 described the use of single-cell FTIR microspectroscopy to probe the effects of sugars and vanadate treatments on 3T3-L1 adipocytes using a full factorial designed experiment. This chapter expands on the same experimental design presented in **Figure 4.2**, using single-cell FPA imaging.

FPA imaging was the fastest data acquisition method available at the time. Section 3.8 discussed the advantages of FPA imaging over synchrotron-based chemical mapping in terms of time and spatial resolution. Using chemical mapping, a single 3T3-L1 cell required between 4-8 hr to collect a single chemical map ~15×15 pixels in size, with a high degree of oversampling. Laboratory-based and synchrotron-based FPA systems generated an image of 64×64 pixels, resulting in 4096 spectra, acquired at 512 coadditions, in 24 min, representing a time saving of >90% on average over chemical mapping experiments.

Another advantage of FPA FTIR microspectroscopy is that images can be acquired as montages and each tile of the montage has a field of view (FoV) of approximately 72×72 μm, which resulted in a pixel pitch of 1.1×1.1 μm using a 36× Cassegrain objective.[282] Therefore, larger area maps of FPA images can be constructed, with the size of the montage only limited by the time the cryogenic detector remains at its optimal temperature (~8 hr). This put a practical limit on the collection of large area maps of 4×4 image grids at 512 coadditions or 8×8 at 256 coadditions, which results in an image size of 300×300 μm and 600×600 μm for 512 and 256 coadditions, respectively. Depending on the density of cells fixed to the substrate, between 100-200 cells can be mapped in a typical experiment.

In laboratory-based FPA FTIR microspectrometers, the broad distribution of infrared radiation from the Globar® source over the FPA detector represented an advantage compared to the narrow beam synchrotron systems allowing the widest FoV achievable. A number of synchrotrons around the world have reconfigured their beamlines to combine multiple beams in an attempt to increase the overall beam spot incident on the ROI to take advantage of the brightness of the synchrotron radiation,[255,282] but this current research was confined to experiments performed at the Australian Synchrotron.

6.1.2 Synchrotron Focal Plane Array (FPA) Measurements

In Section 3.8.2, an experimental setup using four beams from the Australian Synchrotron was described.[255] **Figure 3.41** illustrates how the incident expanding beam from the bending magnet is split into four horizontal beams, each refocussed to the same focal point followed by a second refocussing of a 2×2 bundle of beams that are closely matched to the pupil of the spectrometer. Fine adjustment of the mirrors under vacuum was performed to optimise the distribution of the beams over the FPA detector surface.[255]

The Brookhaven National Laboratory had a similar setup and an image (**Figure 6.1**) clearly shows how the four beams were aligned edge-to-edge.[282] In this configuration, it was important to focus the cell at the objective centre to ensure that the majority of the cell imaged was captured by the inner 32×32 pixel array, as the outer pixels were not illuminated to the same intensity. Due to the limited time available at the Australian synchrotron for this experiment, a complete optimisation of the data acquisition parameters was not possible, only the use of three CaF_2 substrate window thicknesses were assessed using data acquisition parameters described in Section 3.8.2.

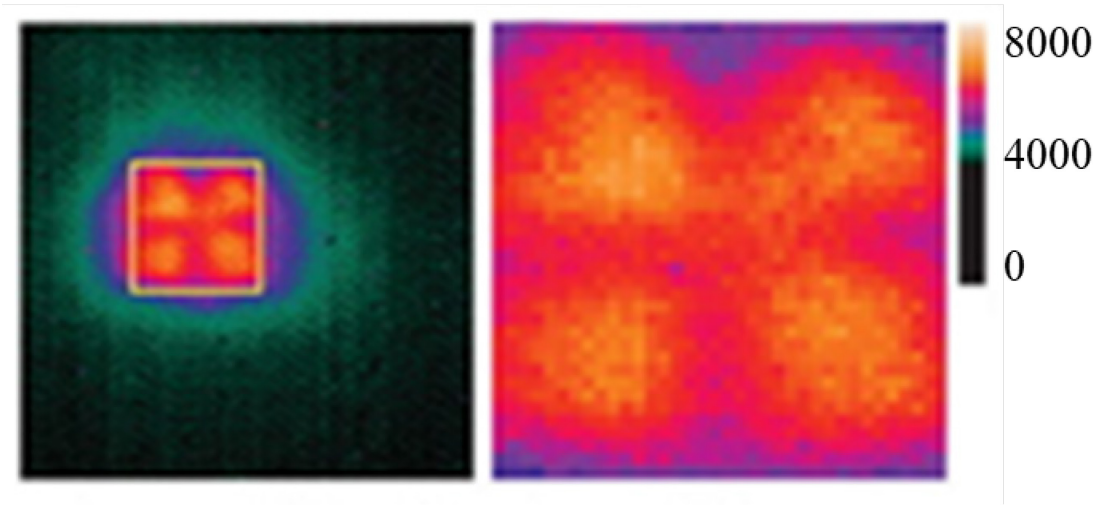

Figure 6.1: Images of four beam spots focussed onto an FPA detector at the Brookhaven National Laboratory. This image was adapted with permission from, Dynamic full field infrared imaging with multiple synchrotron beams, Stavitski, *et al*.[282] Copyright, 2013, American Chemical Society.

FPA imaging, although fast, takes 10-20 times longer to collected data on a single-cell compared to single-point spectrum as discussed in Chapter 4. Therefore, this study was exploratory and while statistical analyses between cells was not possible, three cells were selected per treatment, screened for suitability in terms of image and spectral quality and the best image was used to generate results.

6.1.3 The Diffraction Limit Applied to FPA Imaging

Even though the pixel pitch for the 36× microscope objective is 1.1×1.1 µm, the spatial resolution is still diffraction limited by the wavelength of the incident radiation.[261-262] **Figure 6.2** presents a plot of the calculated spatial resolution Δx (in µm) vs. wavenumber (cm^{-1}). Spatial resolution was calculated based on the numerical aperture (NA) of the 36× objective in Equation 3.1.[217] The red dotted line represents the pixel pitch limit for the FPA detector using the 36× Cassegrain objective.

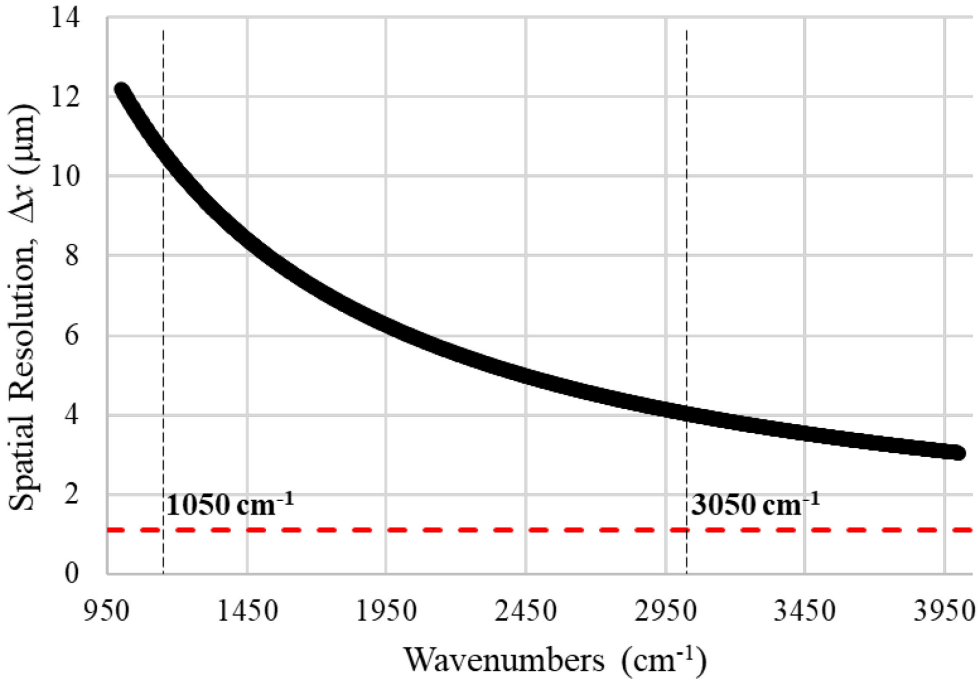

Figure 6.2: Spatial resolution (Δx) vs wavenumbers calculated for a 36× Cassegrain objective with NA = 0.5. The red dotted line is the pixel width for the FoV.

With reference to **Figure 6.2**, at 3000 cm^{-1} (4.1 µm, ν (C-H) region), the wavelength of the radiation covers at least a 4×4 grid of pixels and at 1050 cm^{-1} (11.6 µm, carbohydrate, phosphate bands) a 12×12 grid of pixels is covered. This results in a high degree of oversampling of the pixels at lower wavenumbers and less at higher wavenumbers. Taking this information into consideration, the laboratory-based FPA system produces high quality spectral information and oversampling may be the largest contributor to improved feature resolution in the obtained images.[261]

6.2 Experimental Design and Objectives

It is recognised that individual cells are heterogeneous and could represent different growth cycles, resistance to treatment and other biological variability that could

potentially confound any results obtained. The influence of the substrate material on cell growth and response to treatment has been investigated using Raman spectroscopy where it was found that CaF_2 could influence cell cycle arrest through increased oxidative stress, that can be confounded with cell cycle arrest induced by cell treatments.[436] The purpose of this study was to perform HSI analysis on FPA data collected on single adipocyte cells treated using the DoE protocol defined in Chapter 4. This was a feasibility study to evaluate the validity of this approach for understanding biochemical changes induced in single cells. Results obtained serve to define better approaches in future experiments.

The use of DoE ensured systematic variation in experimental factors and the results obtained were assessed as a closed system, i.e., all experiments were performed on a single culture under similar experimental conditions performed over the same timeframe. In future investigations, the design could be blocked into other factors, including cells propagated from multiple cultures, induction of different cell cycles, different experimenters performing the culturing and 2D vs. 3D cell culturing techniques.[437-438]

FPA images were acquired on 3T3-L1 cells treated under different conditions using laboratory-based and synchrotron FPA imaging. For the images collected using the laboratory-based system, the experimental design in **Figure 4.2** was used to treat the cells. Images collected from single cells were evaluated individually to investigate general trends in treatment induced cell biology and changes in cell morphology.

The synchrotron FPA images in Section 6.3.2 were acquired from cells treated according to the conditions listed in **Table 3.11**. This design is a 2^2 full factorial design run as a single replicate and no centre points. This design was chosen based on the time available at the Australian Synchrotron for the experiment and to determine the feasibility of using this approach in the future. Images were collected on cells cultured on three substrate thicknesses; 0.2 mm; 0.5 mm; and 1.0 mm to evaluate the influence on spectral data induced by substrate thickness, in particular, focussing on the effects of fringing and other spectral aberrations. FPA images were obtained using the methodology described in Sections 2.8.1 and 2.8.2.

6.3 Results

6.3.1 Effects of Sugar and Vanadate on Insulin Sensitive and Resistant 3T3-L1 Cells using Laboratory-Based Focal Plane Array (FPA) FTIR Spectroscopy

FPA FTIR microspectroscopic images were collected on cells treated with sugars and vanadate according to the experimental design of **Figure 4.2**. A 64×64 array was used,

without binning, which resulted in 4096 spectra per image. Spectral data were truncated to the region 3000-1000 cm^{-1}. **Figure 6.3** shows an excellent example of a high-quality image collected on a cell using the Bruker OPUS software package, along with false colour images generated from second derivatised data (13-point smooth) in the fatty acid region (ν (C-H) centred ~2850 cm^{-1}), lipid ester (ν (C=O) centred ~1740 cm^{-1}) and protein amide I, α-helix (ν (C=O) centred ~1650 cm^{-1}). Band assignments as per **Table 1.1**.

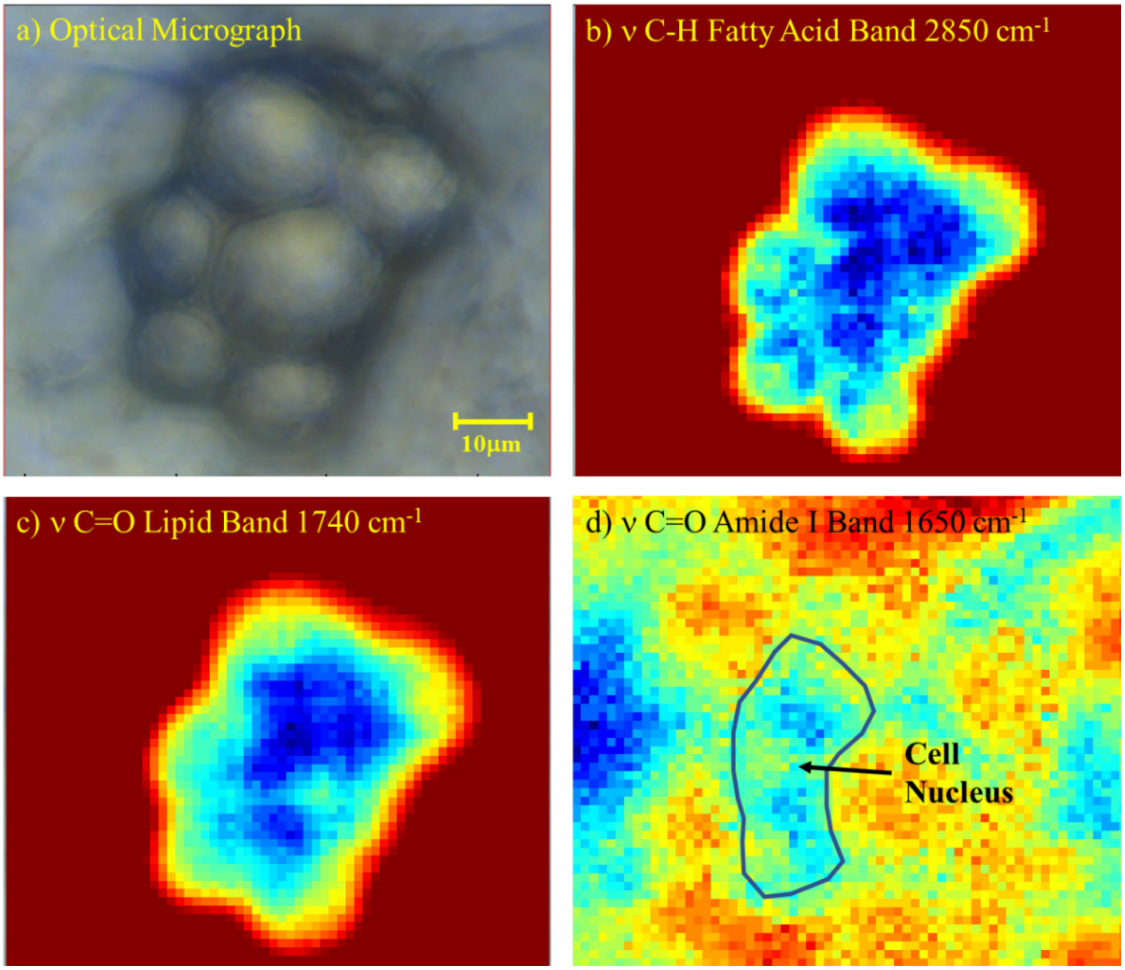

Figure 6.3: FPA images of a single 3T3-L1 adipocyte integrated at a number of wavenumber positions related to the main functionality in the cell; a) optical micrograph captured at 36× magnification; b) integrated for fatty acids (~2850 cm^{-1}); c) integrated for lipid esters (~1740 cm^{-1}); and d) integrated for amide I protein (~1650 cm^{-1}).

FPA imaging revealed the cell morphology as false colour chemical images by integrating the signal using areas based on known functional bands, where the distribution of the biochemical components were visualised. In comparison to the single point spectra assessed in Sections 4.3.1 and 4.3.5, which provided averaged (bulk cell) information, the resolution of the FPA images enabled locations of cellular components, including lipid droplets and the cell nucleus, to be discerned.

The integration method is highly univariate in its approach and while it provides an excellent tool for first pass location of regions with different cellular biochemistry, it cannot provide multivariate information about the relationships between the biochemical compartments within the cell. PCA was applied to the data and after masking the clutter, i.e., non-informative regions in the image,[439] **Figure 6.4** shows the results of a hyperspectral image analysis (HIA) for the first four PCs of the same cell shown in **Figure 6.3**. Since the method of PCA is an unsupervised exploratory method, there was no need to assess full rank models. Hence, the optimal number of PCs selected for interpretation is user defined and validated to explain the main sources of variability within the data set.[440]

The cell depicted in **Figure 6.3** was rendered insulin resistant (Section 2.6.3) and the information revealed in the image provided complex spatially resolved information compared to the single point (bulk) spectral data. The scores image and corresponding loadings for PC1 showed that this PC described an inverse relationship between membrane related lipids and fatty acids compared to lipids and fatty acids internal to the cell.[195,205] The cell outline was identified by the PC1 scores image and was related to a combination of a prominent band at 2850 cm^{-1}, bands over the 1747-1732 cm^{-1} region, 1470 cm^{-1} and 1180 cm^{-1}.[184,196,202,293] The ν (C-H) band ~2850 cm^{-1} measured changes in phospholipids, cholesterol, creatine and fatty acids.[196-197,441] All PC loadings show complex patterns in the ν (C-H) region (3000-2800 cm^{-1}). The region between 1760-1730 cm^{-1}, described the complex environments of ν (C=O) modes of lipids and fatty acid esters, with fatty acids (including oxidised fatty acids) described by absorbance bands at ~1730 cm^{-1}.[160,202]

The PC2 scores and loadings relationships showed the internal morphology of the cell and highlighted two distinct types of biochemicals in the lipid droplets. The data were mean centred before analysis and the highest score heat map intensities (red regions, associated with positive t_1 values) described lipid esters (1747 cm^{-1}),[185,200] particularly in one of the larger lipid droplets and around the inner part of the cell, while the blue regions (negative t_1 scores) were more related to a different lipid ester type or the fatty acid content (1732 cm^{-1}).[200-201] The band at 1180 cm^{-1} was prominent in the p_1 and p_2 directions and was positively weighted in both loadings. This region of the spectrum was related to changes in lipids,[184,197] but is also associated with cellular DNA.[182]

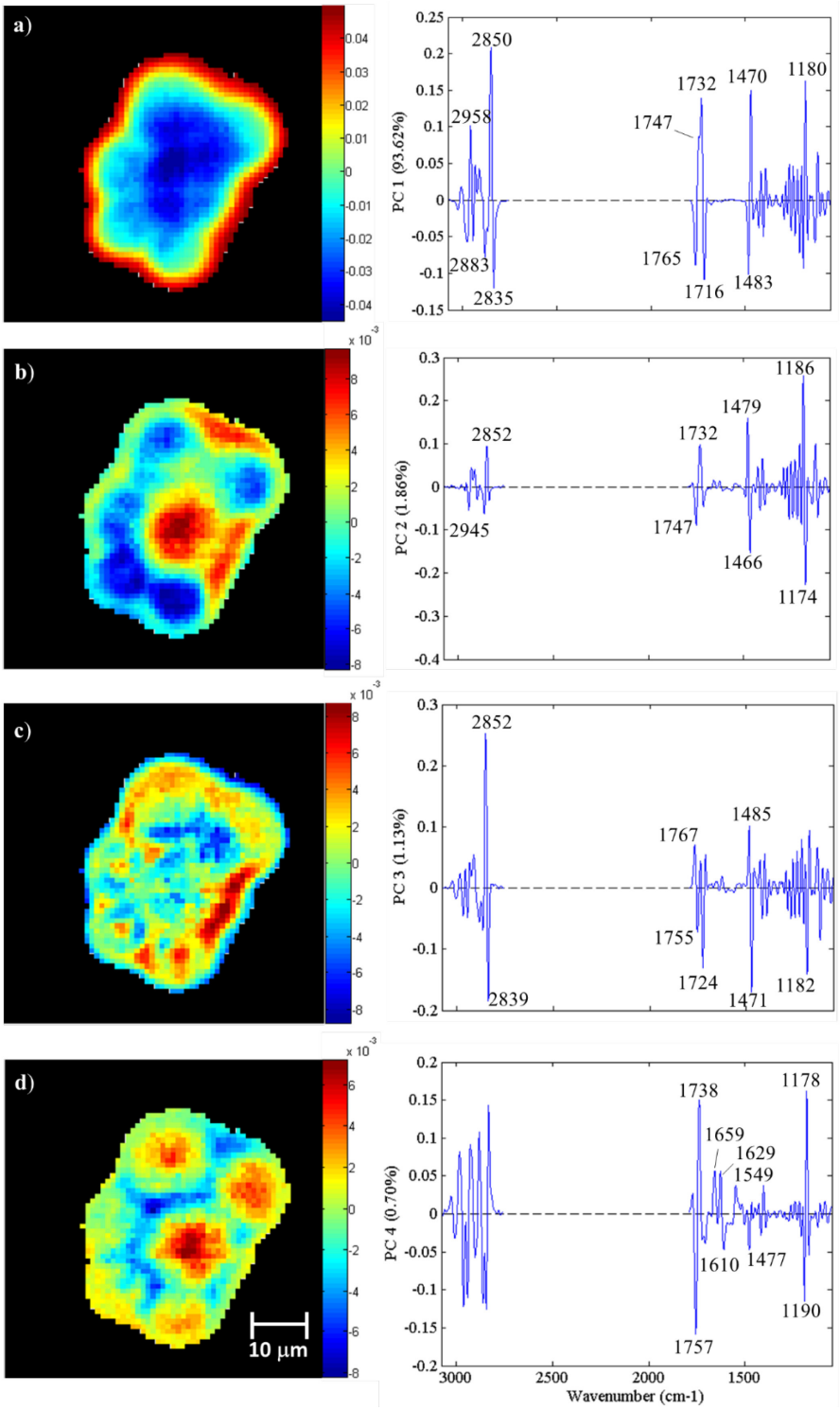

Figure 6.4: HIA assessment of a single 3T3-L1 adipocyte; a) PC1 related to membrane lipids and fatty acids; b) PC2 related the internal lipids and fatty acids; c) PC3 again related to lipids and fatty acids that are different to those of PC2 and; d) PC4 related to complex lipid and protein structures.

The four PCs highlighted the heterogeneous distribution of the various lipid types in the cell and also shows the compartmentalisation of various lipid and fatty acid types, even though the optical micrograph shows that the lipid droplets look visually similar. This approach to data analysis highlighted the complex nature of assessing the biochemical

information in a single cell. The assessment of multiple cells measured in a design of twenty treatments generates large volumes of data for analysis. Therefore, the analyses presented in the following sections provide a summary based on important common observations made when assessing the various treatments. In all of the images acquired, the first three PCs were found to be important for treatment interpretation. The information obtained in the DoE alone represents an entire study by itself and full interpretation has been left to future work as time restrictions and equipment access did not permit a detailed assessment on multiple cultures.

6.3.1.1 HIA Assessment of Block 1 Treatments

In Sections 6.3.1.1 to 6.3.1.4, optical micrographs were presented for selected adipocytes and PCA was performed on masked regions of the image, processed using the Savitzky-Golay second derivative (13-point smooth), then SNV over the wavenumber regions 3000-2800 and 1800-1050 cm^{-1}. Only three PCs were assessed in each case.

Optical micrographs of four selected cell images for the Block 1 treatments; no-sugar (*1*); glucose (*a*); fructose (*b*); and glucose-fructose (*ab*), are shown in **Figure 6.5**. These images highlight one of the challenges of imaging 3T3-L1 cells due to their thickness (height in the *z*-direction) and in some cases, the inability to focus the entire cell. In Section 3.6, a depth profiling study was performed using the confocal data acquisition arrangement at the Australian Synchrotron to investigate how the *z*-direction can impact the quality of spectral data obtained. For a laboratory-based FPA FTIR microspectrometer using a Globar® source, it was anticipated that the broad dispersion of the incident beam over the entire detector area combined with an adequately focussed sample would result in FPA images representative of the cell morphology.

After application of PCA, the clutter was eliminated using a spectral mask drawn around the perimeter of the cell defined by the t_1 scores and the model was recalculated. Higher PCs (> 3), describing increasingly less **X**-variance may be important for identifying subtle differences in biochemistry induced by treatments, however, further investigation into spectral processing methods is required to determine whether the effects of light scattering and other non-chemical phenomena were reducing the amount of information obtainable from these measurements.

Figure 6.6 presents the PC1 scores and loadings for the Block 1 treatments, where this PC described between 80-90% of the variability in the images. The t_1 scores images for each treatment showed that the cell perimeter was clearly defined by scores coloured red-

yellow, represented by positive scores values. The cell interiors were characterised by blue regions due to negative t_1 score values, which showed that the biochemistry in the region of the cell perimeter was different to that of the cell interior. For each treatment, the p_1 loadings direction had a similar profile where the band at 2850 cm^{-1} was the most dominant spectral feature. The next feature of importance was the lipid ester band around 1740 cm^{-1}, which shifted between 1750-1738 cm^{-1}. These spectral features were positively correlated to the bands at 1468 and 1180 cm^{-1} also related to lipids for all loadings.[172,183-184,197] The band ~2837 cm^{-1} was the result of splitting of the band centred at 2850 cm^{-1} and was attributed to the different types of lipids and fatty acids in the cell.[160,195,202,205]

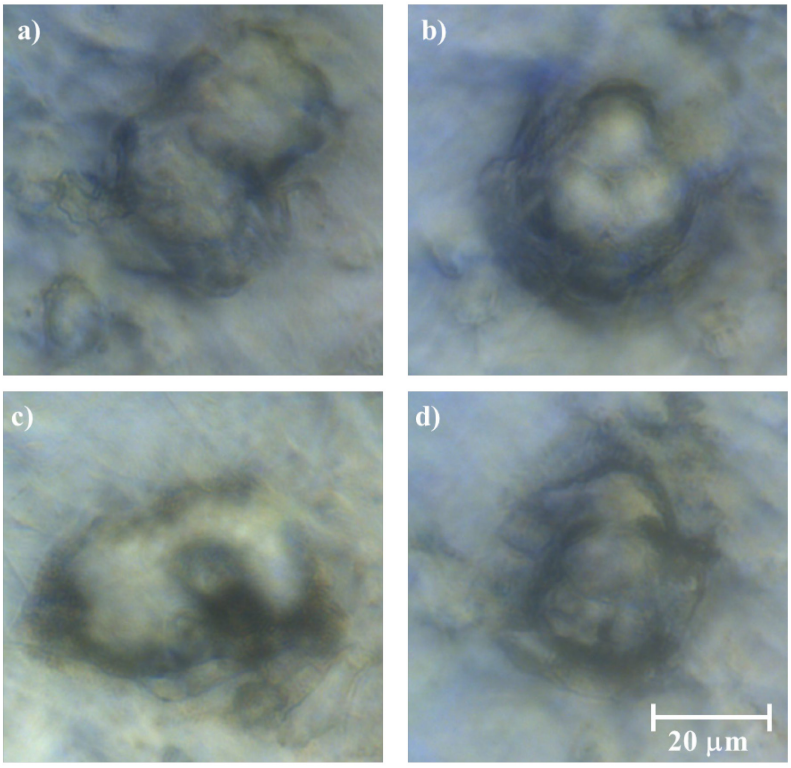

Figure 6.5: Optical micrographs of selected insulin sensitive 3T3-L1 adipocytes; a) treatment *1*, no-sugar; b) treatment *a*, glucose; c) treatment *b*, fructose; and d) treatment *ab*, glucose-fructose. For treatment terminology, refer to **Figure 4.2**. Scale bar for all images is shown in figure d.

The PC1 direction was, therefore a descriptor of the different biochemistries associated with regions close to the cell membrane compared to the biochemistry of the cell interior. In particular, the differences between fatty acid bands close to the cell membrane were characterised by the bands around 2839, 1763 and 1720 cm^{-1},[200,442] and the interior lipids were described by bands at 2852 cm^{-1} and those between 1754-1738 cm^{-1}.[181-182,200] A shift in the lipid ester band for the fructose treatment, (*b*), was observed at 1738 cm^{-1} along with the appearance of the band at 2920 cm^{-1}, which demonstrated a change in biochemistry induced by fructose metabolism.[376,402,428]

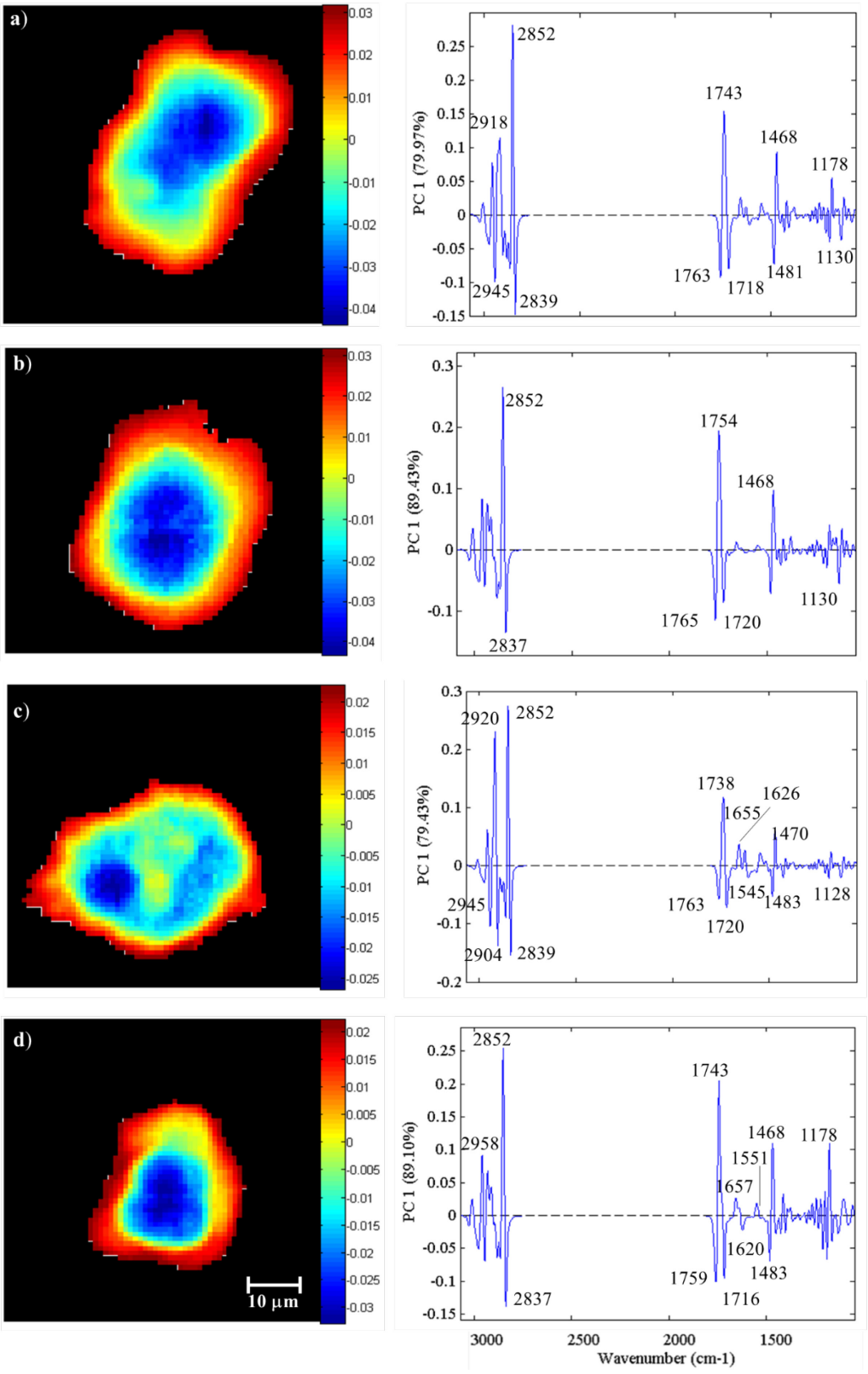

Figure 6.6: PC1 scores and loadings for insulin sensitive 3T3-L1 adipocytes, treated according to **Figure 4.2**, Block 1 treatments; a) treatment *1*, no-sugar; b) treatment *a*, glucose; c) treatment *b*, fructose; and d) treatment *ab*, glucose-fructose. Important loadings are highlighted in this figure.

Bands around 2920 and 2850 cm^{-1} were assigned to membrane lipids and fatty acids,[195] while those at 2960 and 2870 cm^{-1} were assigned to cellular lipids and proteins.[194,306]

These loadings described a fructose induced biochemical change in the distribution of lipids and fatty acids. The increased band intensities of protein associated loadings in the 1650-1550 cm^{-1} region and the 1738 cm^{-1} band was consistent with fructose inducing both protein synthesis and DNL.[20]

The PC2 scores and loadings for the Block 1 treatments are presented in **Figure 6.7** where this PC described between 3-16% of the total **X**-variance in the images. As was observed for the p_1 loadings, the p_2 loadings also have similar profiles to each other. These loadings were characterised by bands at 2920 and 2850 cm^{-1} associated with membrane lipids and fatty acids.[183] In all cases, except for the glucose-fructose (*ab*) treatment (**Figure 6.7d**), these bands were positively correlated to the ν (C=O) lipid ester band between 1750-1730 cm^{-1}. The glucose-fructose treatment (*ab*) showed an inverse relationship of the 2920 and 2850 cm^{-1} bands with the 1749 cm^{-1} band.

In general, the t_2 scores were associated with cellular compartmentalisation of the various lipids and fatty acids. This was observed in the no sugar (*1*) treatment in **Figure 6.7a** where the scores map clearly illustrated a partition of two unique biochemistries in the cell. The positive t_1 scores (red regions) for treatments (*1*) and glucose (*a*) were associated with the lipid ester band (~1740 cm^{-1}) while the blue and green regions were associated with fatty acid bands (~1725 cm^{-1}). The fructose only treatment (*b*) showed that positive t_2 scores (red regions) were related to FFAs at 1732 cm^{-1},[200-201] which were positively correlated to the 2914 and 2945 cm^{-1} bands. These bands were shifted to lower wavenumbers compared to the usual positions at 2920 and 2850 cm^{-1} of the asymmetrical and symmetrical ν (CH_2) bands respectively.[172,183] This was attributed to oxidative stress induced in these cells by fructose,[20] where a similar pattern was observed in the PLS-DA w_2 loading weights in the point scan model for Block 1 in **Figure 4.22b** that was also attributed to oxidative stress induced by the fructose treatment.

As was the case for the p_1 direction for fructose treatment (*b*), the bands associated with protein secondary structure between 1660-1550 cm^{-1} are also weighted more than the no-sugar (*1*) and glucose (*a*) treatments, further supporting the observation that treatments containing fructose induce protein synthesis and oxidative stress.[20] This increase in protein character in the loadings was also observed in the p_2 loadings for treatment (*ab*), which further supporting the observations made above that fructose containing treatments induce protein synthesis in adipocytes.

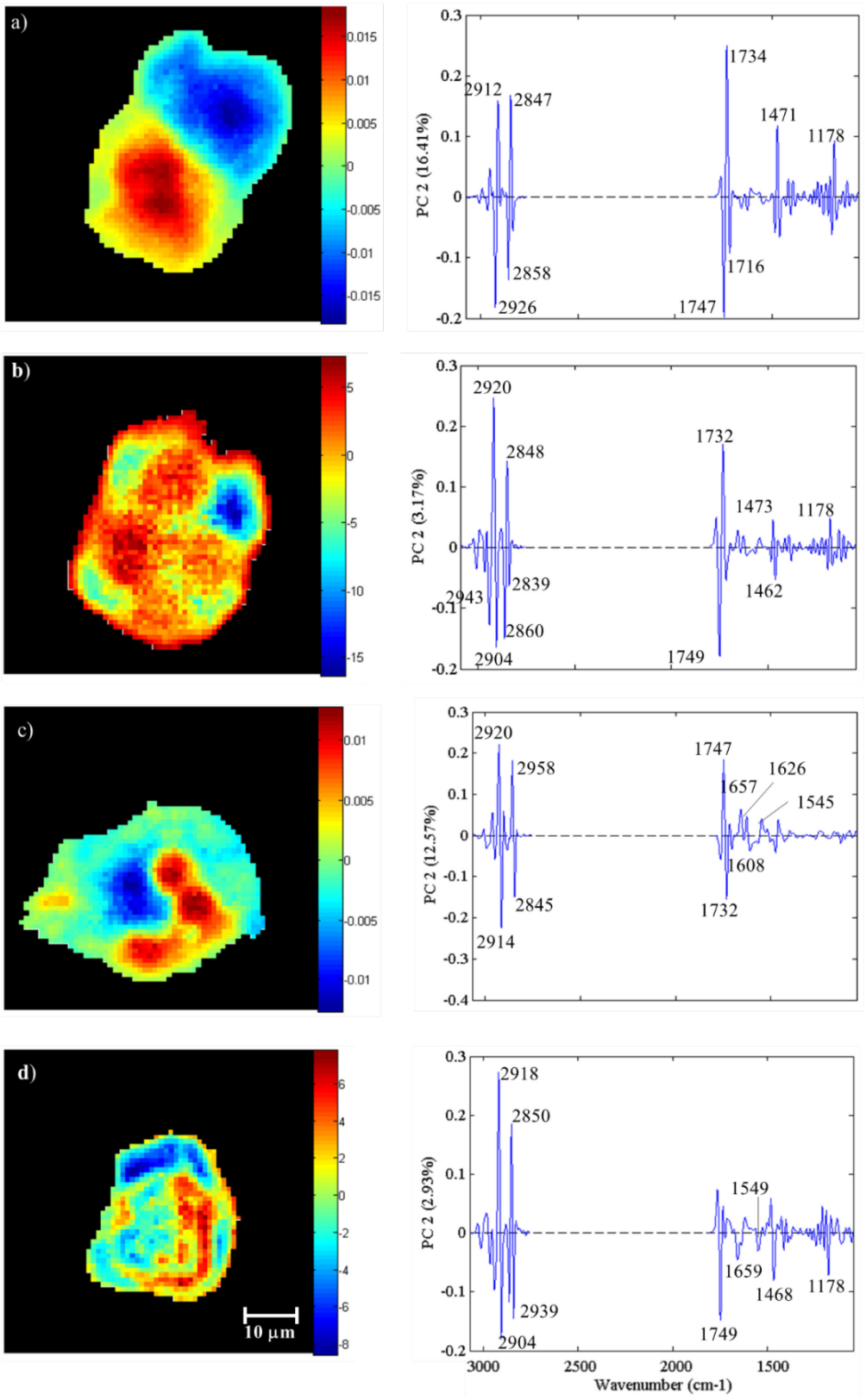

Figure 6.7: PC2 scores and loadings for insulin sensitive 3T3-L1 adipocytes, treated according to **Figure 4.2**. Block 1 treatments; a) treatment *1*, no-sugar; b) treatment *a*, glucose; c) treatment *b*, fructose; and d) treatment *ab*, glucose-fructose. Important loadings are highlighted in this figure.

The PC3 scores and loadings (**Figure 6.8**) accounted for only minor changes in cellular biochemistry (all PCs describe <2.5 % of the data).

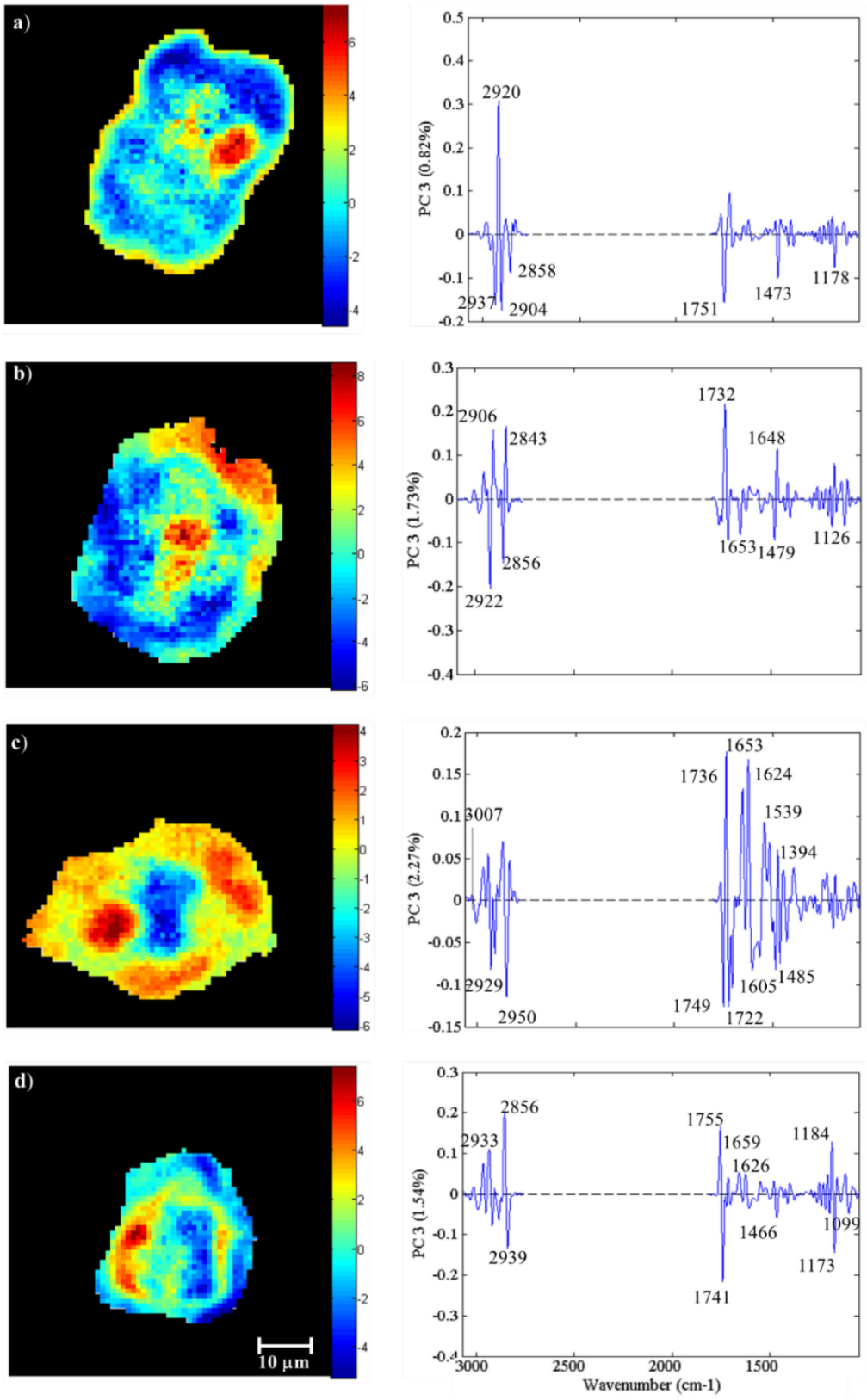

Figure 6.8: PC3 scores and loadings for insulin sensitive 3T3-L1 adipocytes, treated according to **Figure 4.2** Block 1 treatments; a) treatment *1*, no-sugar; b) treatment *a*, glucose; c) treatment *b*, fructose; and d) treatment *ab*, glucose-fructose. Important loadings are highlighted in this figure.

The associated p_3 loadings were very complex for the fructose treatment (*b*), which further indicated that FPA FTIR microspectroscopy identified the different effects of this

treatment compared to the other treatment, which will be elaborated in future work. In general, the PC3 direction was mainly attributed to changes in the lipid in the cells as evidenced by the band loadings ~1743 cm^{-1}, however, as stated above, the fructose only treatment showed a positive correlation between the bands at 1736 cm^{-1} and those at 1653 and 1624 cm^{-1}. This was consistent with fructose inducing protein synthesis and DNL, and in this case, showed that this process was localised to a specific compartment of the cell, identified by the blue region of the t_3 scores image in **Figure 6.8c**. The t_2 scores image (**Figure 6.7c**) also showed a relationship between lipid bands and protein bands in the same spatial region. This may be an indication of the ability of FPA imaging to locate cellular compartments that perform specific biochemical processes.

6.3.1.2 HIA Assessment of Block 2 Treatments

Figure 6.9 presents the optical micrographs of the cells used for the Block 2 treatments; vanadate only *c;* glucose-vanadate *ac*; fructose-vanadate *bc*; and glucose-fructose-vanadate *abc*.

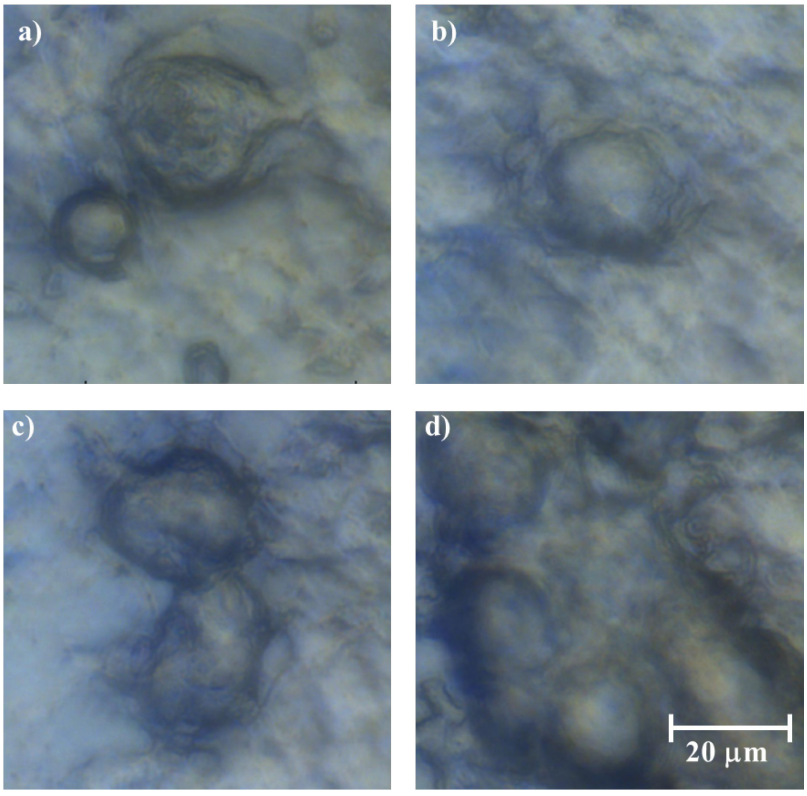

Figure 6.9: Optical micrographs of selected insulin sensitive 3T3-L1 adipocytes; a) treatment *c*, no-sugar and vanadate; b) treatment *ac*, glucose and vanadate; c) treatment *bc*, fructose and vanadate; and d) treatment *abc*, glucose-fructose and vanadate. For treatment terminology, refer to **Figure 4.2**. Scale bar for all images is shown in figure d.

The PC1 scores and loadings are presented in **Figure 6.10** where this PC described between 70-85% of the total variability in the image.

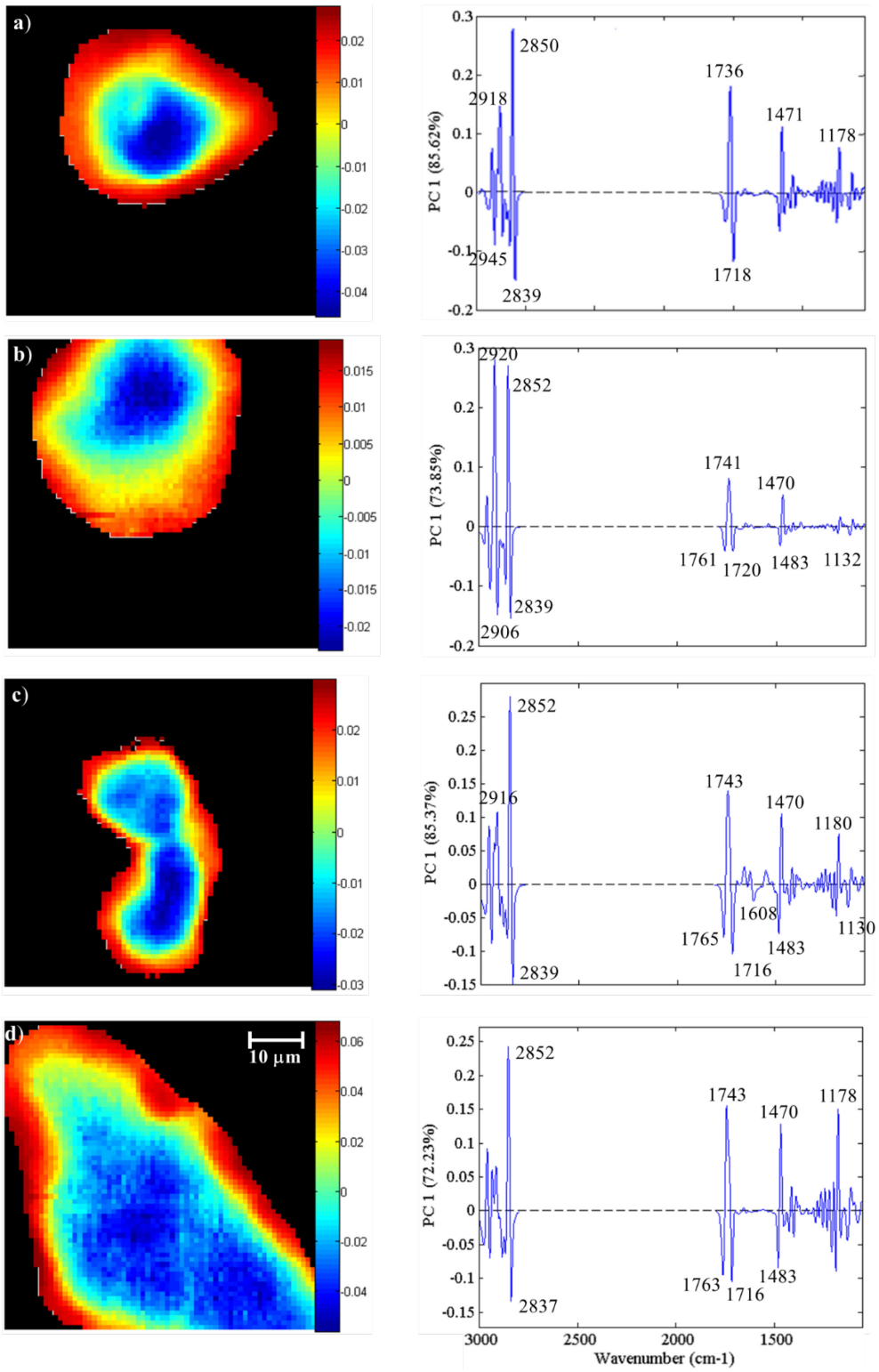

Figure 6.10: PC1 scores and loadings for insulin sensitive 3T3-L1 adipocytes, treated according to **Figure 4.2**. Block 2 treatments; a) treatment *c*, no-sugar-vanadate; b) treatment *ac*, glucose-vanadate; c) treatment *bc*, fructose-vanadate; and d) treatment *abc*, glucose-fructose-vanadate. Important loadings are highlighted in this figure.

As was observed in the PC1 scores and loadings in Section 6.3.1.1, the t_1 scores described the main differences between the regions close to the cell membrane and the internal cellular biochemistry. The p_1 loading associated with all treatments showed very similar profiles with the main observable difference associated with the loadings for the fructose-vanadate treatment (*bc*), which showed the presence of protein associated bands between 1690-1550 cm^{-1}. A similar observation was made in the Block 1 fructose treatment (*b*) loadings (**Figure 6.6c**) and these data were consistent with fructose induced protein synthesis as evidenced by the bands between 1700-1550 cm^{-1} specific to this treatment only.[20,376,428] In **Figure 6.10b** the band at 2920 cm^{-1} was prominent and was assigned to membrane lipid changes as a result of the combined glucose-vanadate action stimulating glucose uptake.

The PC2 scores and loadings for the Block 2 treatments are presented in **Figure 6.11**. As was observed for the corresponding Block 1 data, the Block 2 scores showed cellular compartmentalisation of the lipids and fatty acids. The p_2 loadings for the vanadate only treatment (*c*, **Figure 6.11a**) and the glucose-vanadate treatment (*ac*, **Figure 6.11b**) showed larger loading contributions from the protein secondary structure region between 1660-1500 cm^{-1}. These loadings were attributed to the cell nucleus represented by negative t_2 scores values (blue regions). In adipocytes, the majority of the cell is composed of lipid esters and fatty acids and as a result of the large lipid content, the cell nucleus typically gets pushed to the cell edge and is flattened.[16] In both treatments, the cell showed that the blue region was pushed against the edge of the cell and the treatment (*c*) cell showed this structure was flattened.

The image of the fructose-vanadate treatment (*bc*, **Figure 6.11c**) was most likely two cells in close proximity and showed up to four localised compartments of lipid ester, mainly characterised by the band at 1749 cm^{-1}. The positive t_2 scores (red regions) for the *bc* treatment were associated with the correlated bands at 2916 and 1734 cm^{-1}. These regions of the cell were most likely due to localisation of fatty acids as opposed to lipids. Frühbeck,[16] stated that fatty acid esterification and triglyceride hydrolysis are in constant flux in adipocytes and partitioning of fatty acids into specific organelles (i.e., lipid droplets), which was consistent with the images and showed that the various lipid droplets specifically contained one type of lipid ester/fatty acid preferentially to another.[30]

The glucose-fructose-vanadate treatment (*abc*) was of much larger size compared to the other cells imaged in this study. The optical micrograph (**Figure 6.9c)** showed a number of lipid droplets. The negative t_2 scores (blue regions) in the image were mainly fatty acid

in content as described by the positive correlation of the bands at 2904, 2841 and 1730 cm^{-1}.[200] The positive t_2 scores (red regions of the image) were, therefore, associated with the lipid ester content as verified by the large loading at 1743 cm^{-1}.

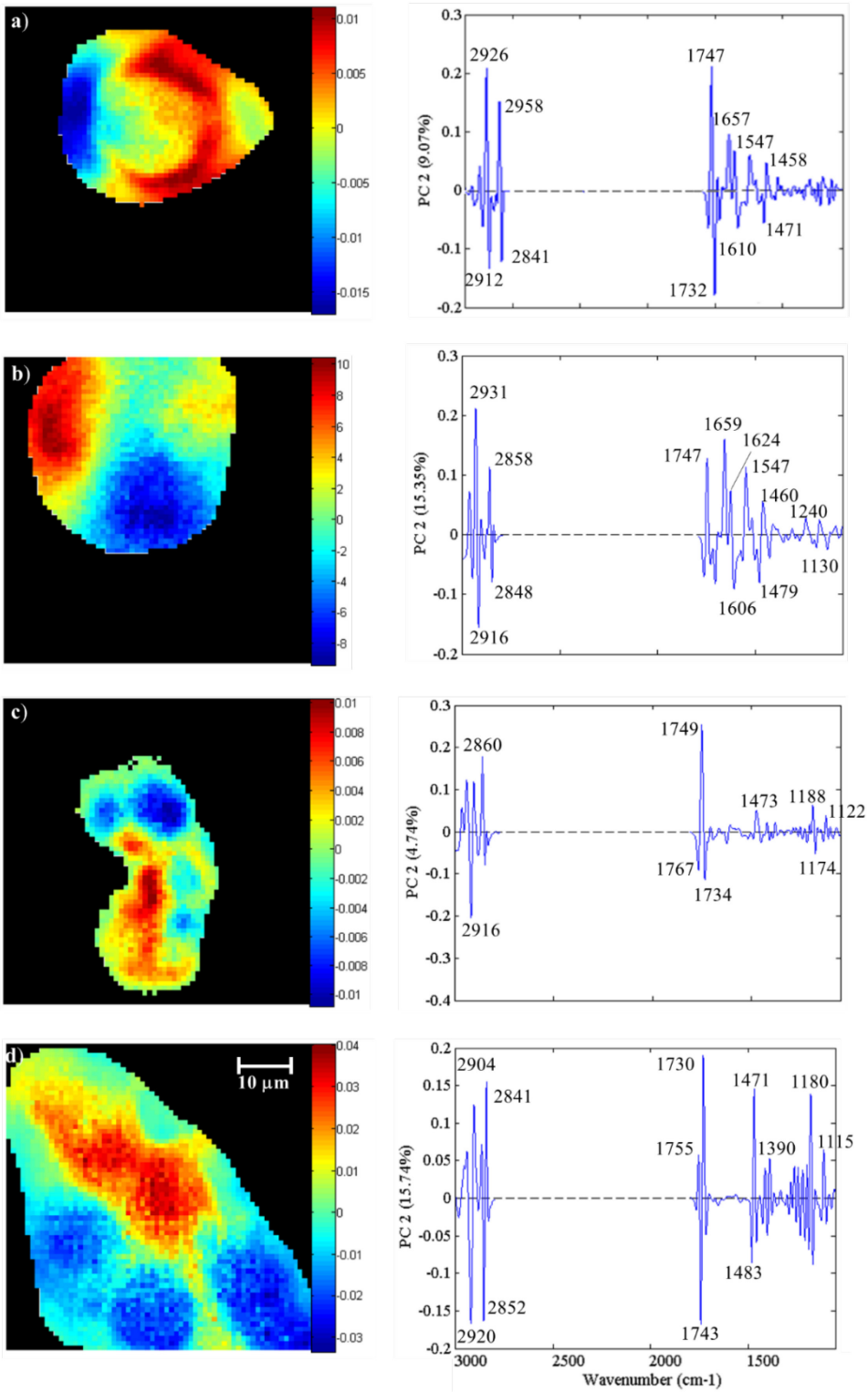

Figure 6.11: PC2 scores and loadings for insulin sensitive 3T3-L1 adipocytes, treated according to **Figure 4.2** Block 2 treatments; a) treatment *c*, no-sugar-vanadate; b) treatment *ac*, glucose-vanadate; c) treatment *bc*, fructose-vanadate; and d) treatment *abc*, glucose-fructose-vanadate. Important loadings are highlighted in this figure.

The PC3 scores and loadings for the Block 2 treatments (**Figure 6.12**) only described minor changes in the cell biochemistry (< 3%) and a similar observation observed was made for the same PC direction in the Block 1 treatments.

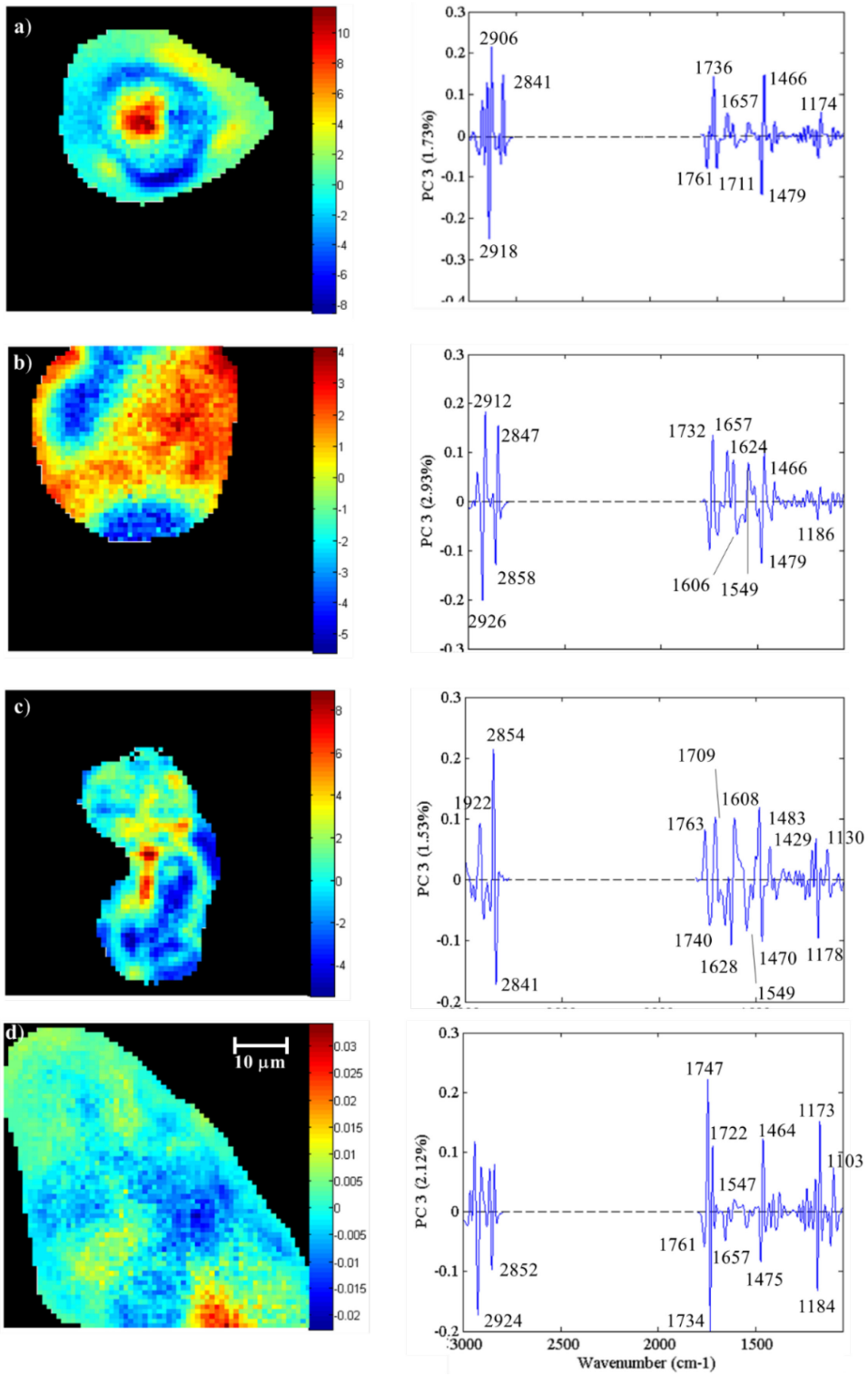

Figure 6.12: PC3 scores and loadings for insulin sensitive 3T3-L1 adipocytes, treated according to **Figure 4.2** Block 2 treatments; a) treatment *c*, no-sugar-vanadate; b) treatment *ac*, glucose-vanadate; c) treatment *bc*, fructose-vanadate; and d) treatment *abc*, glucose-fructose-vanadate. Important loadings are highlighted in this figure.

These loadings showed more secondary protein structural changes possibly related to changes in the cell nucleus, particularly for the glucose-vanadate treatment (*ac*), where the t_2 scores showed a large region attributed to lipids and proteins, however the t_3 image for this treatment showed a smaller and flattened structure at the edge of the cell in the same region of the t_2 image (**Figure 6.11b**). This may be showing a clearer image of the nucleus in this cell. Specific lipid droplets are typically found close to the nucleus and mitochondria due to the greater need of energy stores for these organelles.[443]

The fructose-vanadate treatment (*bc*) scores image (**Figure 6.12c**) showed a small red region associated with positive t_3 scores with a corresponding high loading at 1623 cm^{-1} assigned to changes in β-sheet protein structures. This was expected for a cell in the presence of both fructose and vanadate where increased oxidative stress induced in the cell may lead to fibrosis.[20,147,158]

The glucose-fructose-vanadate treatment (*abc*) also showed a small red hotspot in the image associated with positive t_3 scores; however, this could not be attributed to the cell nucleus due to the small loadings of the protein secondary structures in the region 1660-1550 cm^{-1}. The large loading at 1734 cm^{-1} suggests that this part of the cell contains a different ester lipid type or fatty acids, possibly attributed to DNL induced by the combined fructose-vanadate treatment. This PC only accounts for about 2% of the total **X**-variance and may be too small for interpretation, however, future investigations that also investigate the impact of light scattering phenomena on the spectra may reveal more of the biochemistry and morphology by partitioning the information in the less important PCs towards the more important ones, through further minimisation of physical, light scattering effects not related to biochemistry.[238]

As was observed in the point scans performed on the DoE study in Section 4.3.5, this assessment of the Block 1 and Block 2 treatments showed that there was very little difference between the PCA models and suggested that the differences in the treatments may be subtle and further analysis of the sub-regions may reveal more insights into the small biochemical changes induced by the treatments. This was marked as future work, along with the use of quantum cascade laser (QCL) spectroscopy to capture larger numbers of cells in a faster manner compared to the current FPA technique.[221,444-445]

6.3.1.3 HIA Assessment of Block 3 Treatments

Figure 6.13 presents the optical micrographs of the cells use for the Block 3 treatments, which were rendered insulin-resistant using endothelin-1 (ET-1)[75] and represented by

factor *d*; no-sugar *d*; glucose *ad*; fructose *bd*; and glucose-fructose *abd*. **Figure 6.13a** and **b** show highly detailed images of the cellular morphology of the 3T3-L1 adipocytes, particularly the lipid droplets and the membrane boundaries between them.

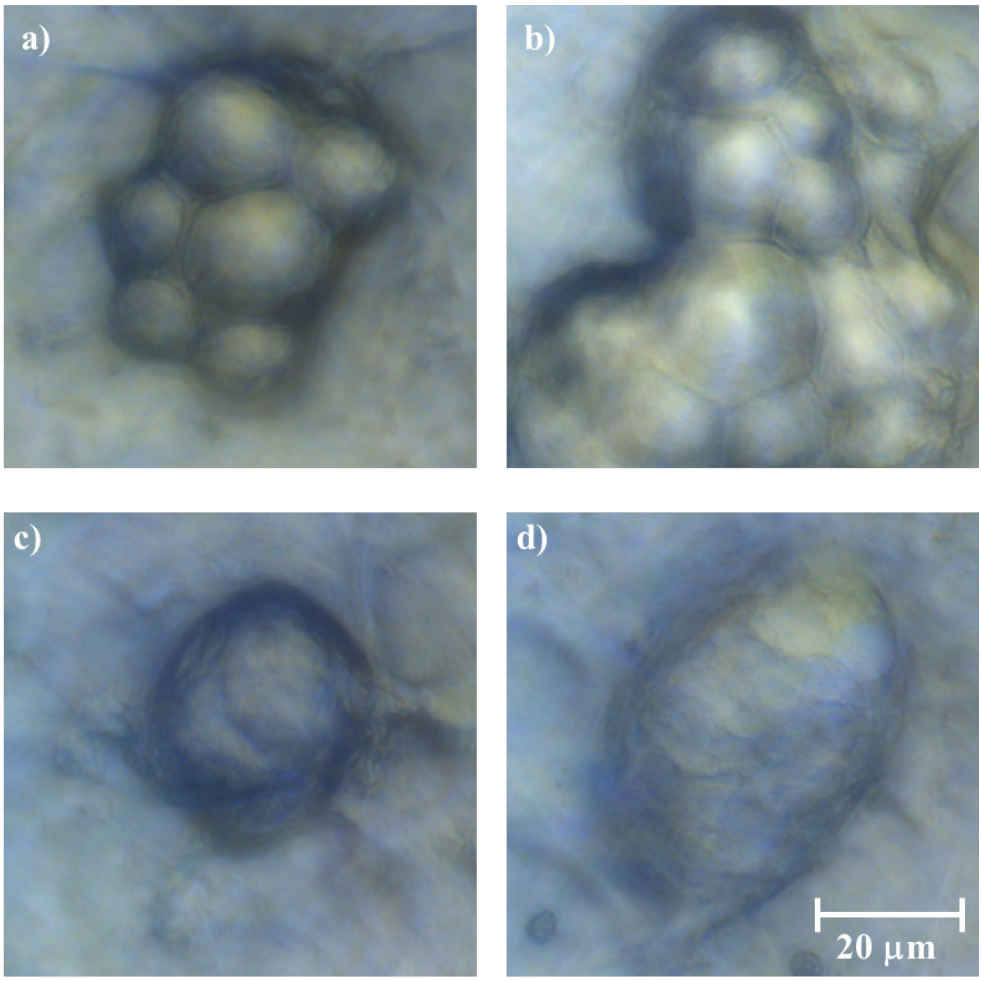

Figure 6.13: Optical micrographs of selected insulin resistant 3T3-L1 adipocytes; a) treatment *d*, no-sugar; b) treatment *ad*, glucose; c) treatment *bd*, fructose; and d) treatment *abd*, glucose-fructose. For treatment terminology, refer to **Figure 4.2**. Scale bar for all images is shown in figure d.

The t_1 scores for all cells in Block 3 (**Figure 6.14**) showed that this PC described between 85-94% of the total **X**-variance in the images. In a similar trend to the previous analyses, the t_1 scores described the main differences between the regions close to the cell membrane and the inner biochemistry and in all cases, the cell boundary was clearly defined. The p_1 loadings associated with all treatments exhibited a very similar profile with the only difference observed in the loadings for the glucose-fructose treatment (*abd*, **Figure 6.14d**). For all Block 3 treatments the ν (C=O) lipid ester bands at 1747 and 1732 cm^{-1} were broad and were different from the observations made in the p_1 loadings for Blocks 1 and 2. This might account for subtle differences observed between insulin-sensitive and -resistant cells as measured by FTIR microspectroscopy (Chapter 4).

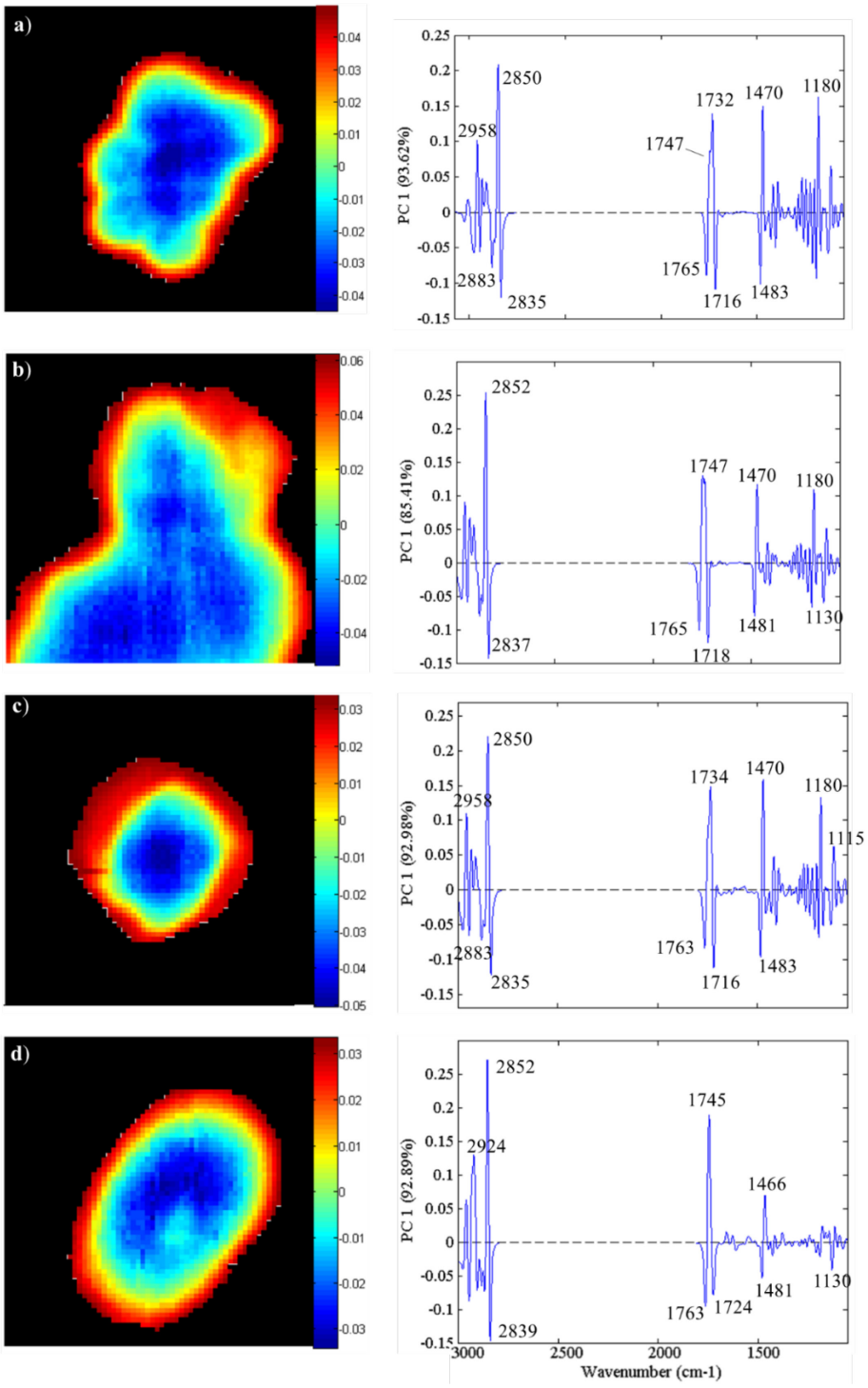

Figure 6.14: PC1 scores and loadings for insulin resistant 3T3-L1 adipocytes, treated according to **Figure 4.2**. Block 3 treatments; a) treatment *d*, no-sugar; b) treatment *ad*, glucose; c) treatment *bd*, fructose; and d) treatment *abd*, glucose-fructose. Important loadings are highlighted in this figure.

The loadings from the no-sugar (*d*, **Figure 6.14a**) and fructose (*bd*, **Figure 6.14c**) treatments have a prominent band at 1734 cm^{-1} associated with lipid esters or fatty acids,[200-201] suggesting that insulin resistant cells utilise a different pathway to metabolise fructose, or when no sugar is present cell culture media components such as glutamine.[399] An alternative hypothesis is that these cells do not utilise any external metabolites and the

internal biochemistry was shifting towards fatty acid synthesis and, therefore, utilising internal energy stores for survival. This may be justified by the observed shift in TAG related bands (~1743 cm^{-1}) to a different lipid ester type or a fatty acid band ~1730 cm^{-1} (although this band was on the higher end for a fatty acid).[200] In **Figure 6.14d** the p_1 loadings for the glucose-fructose treatment (*abd*) was consistent with the glucose treatment (*ad*, **Figure 6.14b**), where the cells may be utilising glucose as evidenced by the increase in the lipid ester band between 1745-1747 cm^{-1}. These data suggested that the insulin resistance induced by ET-1 may not be permanent and the cells were adapting to utilise the glucose present, or the presence of fructose may be enabling glucose uptake as observed by Froesch and Ginsberg,[353] however this observation would not explain the uptake of glucose in the *ad* treatment.

The p_2 loadings (**Figure 6.15**) were also consistent with the observations made for the corresponding loadings for the Block 1 and 2 treatments and described the cellular compartmentalisation of lipids and fatty acids.

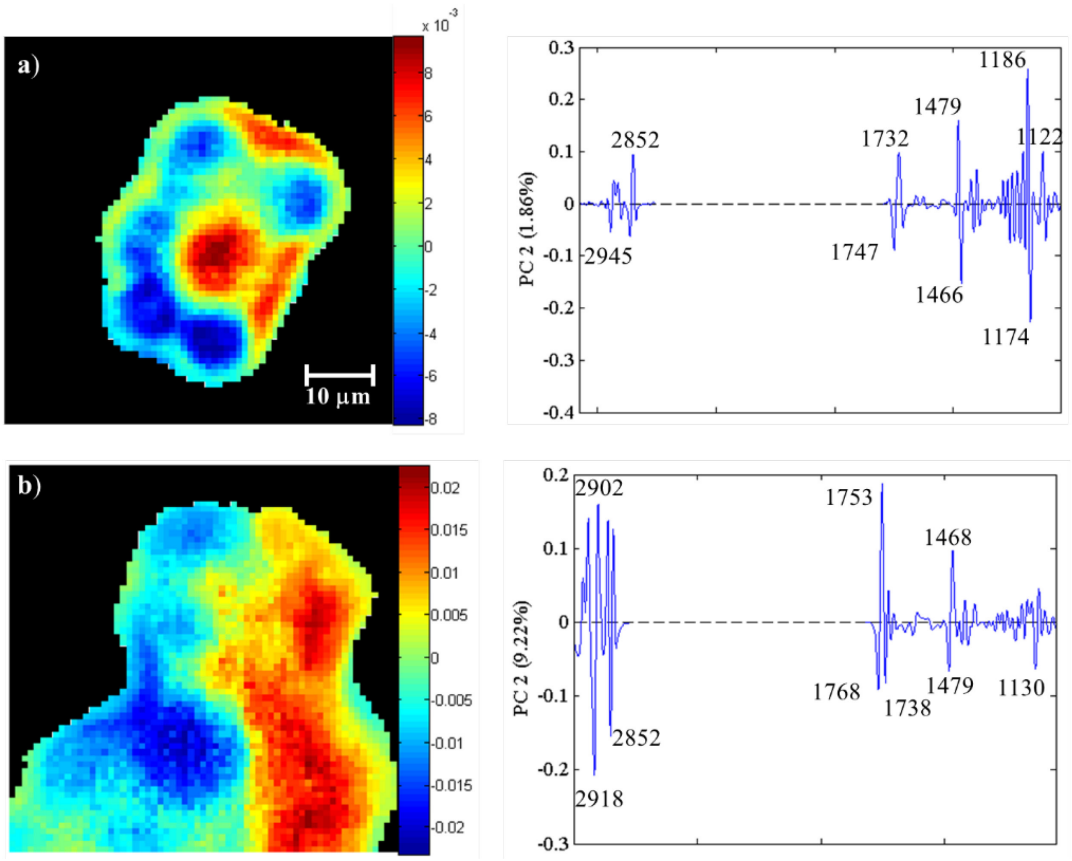

Figure 6.15: PC2 scores and loadings for insulin-resistant 3T3-L1 adipocytes, treated according to **Figure 4.2**. Block 3 treatments; a) treatment *d*, no-sugar; b) treatment *ad*, glucose. Important loadings are highlighted in this figure.

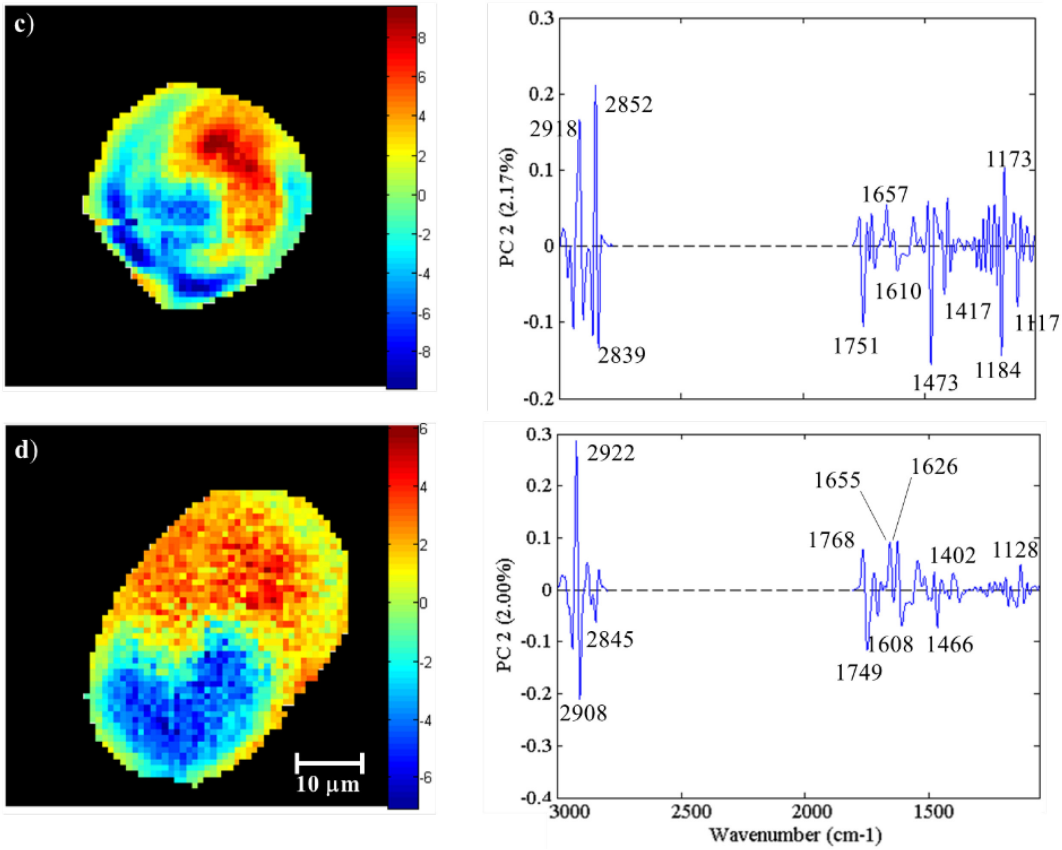

Figure 6.15 (*cont*): PC2 scores and loadings for insulin-resistant 3T3-L1 adipocytes, treated according to **Figure 4.2**. Block 3 treatments; c) treatment *bd*, fructose; and d) treatment *abd*, glucose-fructose. Important loadings are highlighted in this figure.

The fructose-containing treatments (*cd* and *acd*, **Figure 6.15c** and **d**, respectively) showed increased band intensities in the protein secondary structures between 1660-1550 cm^{-1}, consistent with previous findings related to oxidative stress induced protein synthesis by fructose.[20] As was also observed in previous treatments, compartmentalisation into lipid specific and fatty acid specific composition was observed.

The PC3 scores and loadings (**Figure 6.16**) were consistent with the results observed previously for Blocks 1-2 that this was a minor PC contributing < 1.5% to the total **X**-variance. The complex associations between the loadings were indicative of small, localised changes in lipids, lipoproteins and fatty acids.

6.3.1.4 HIA Assessment of Block 4 Treatments

The optical micrographs of the cells used for the Block 4 treatments where insulin resistance was induced by endothelin-1 (ET-1) as factor *d*; vanadate-only *cd,* glucose-vanadate *acd,* fructose-vanadate *bcd* and glucose-fructose-vanadate *abcd*) and revealed the poor health of the cells treated under these conditions (**Figure 6.17**). Notably during

fixation of cells in the glucose-vanadate treatment (*acd*, **Figure 6.17b**), many cells detached and the cell located on this substrate was one of only few that could be investigated.

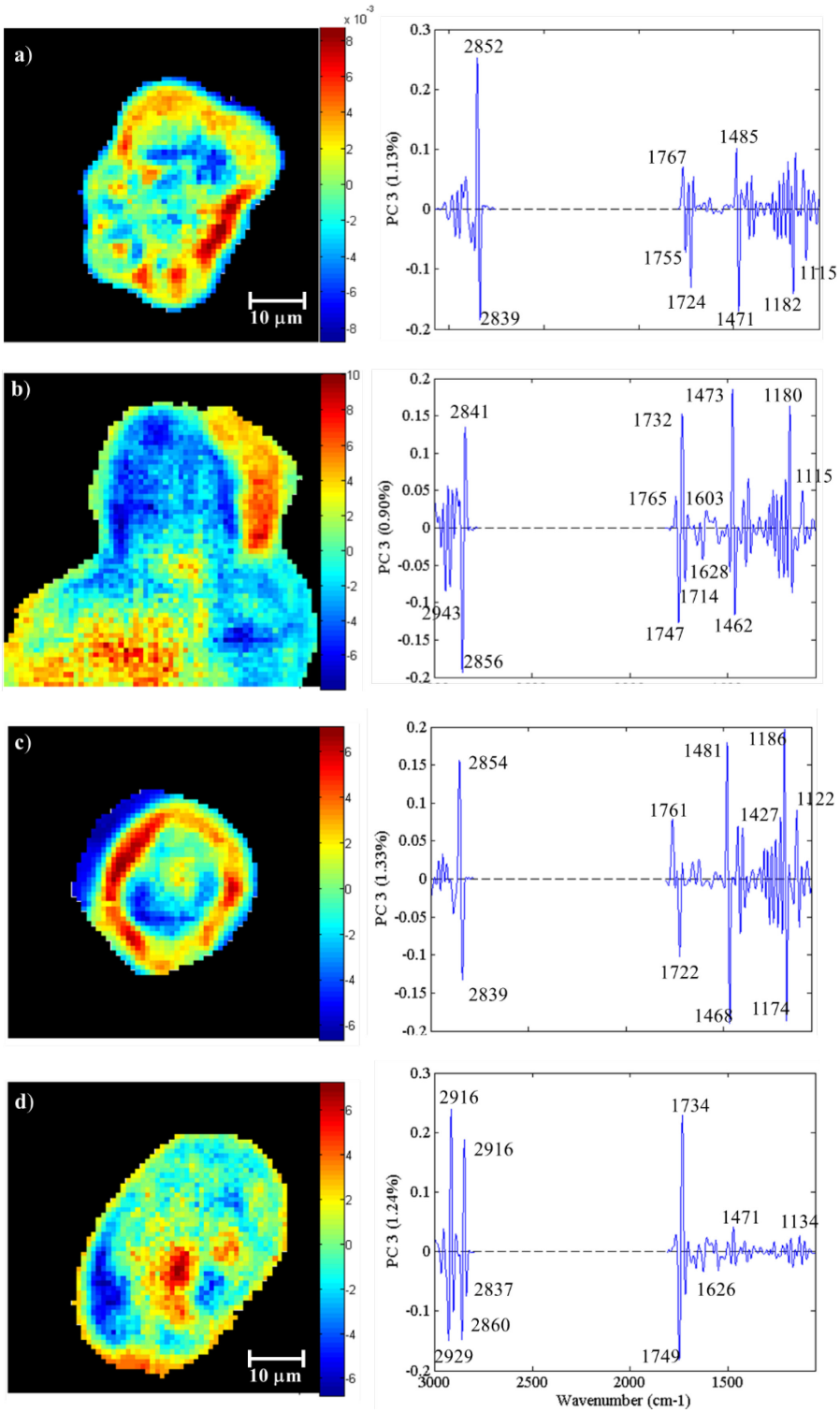

Figure 6.16: PC3 scores and loadings for insulin resistant 3T3-L1 adipocytes, treated according to **Figure 4.2**. Block 3 treatments; a) treatment *d*, no-sugar-vanadate; b) treatment *ad*, glucose-vanadate; c) treatment *bd*, fructose-vanadate; and d) treatment *abd*, glucose-fructose-vanadate. Important loadings are highlighted in this figure.

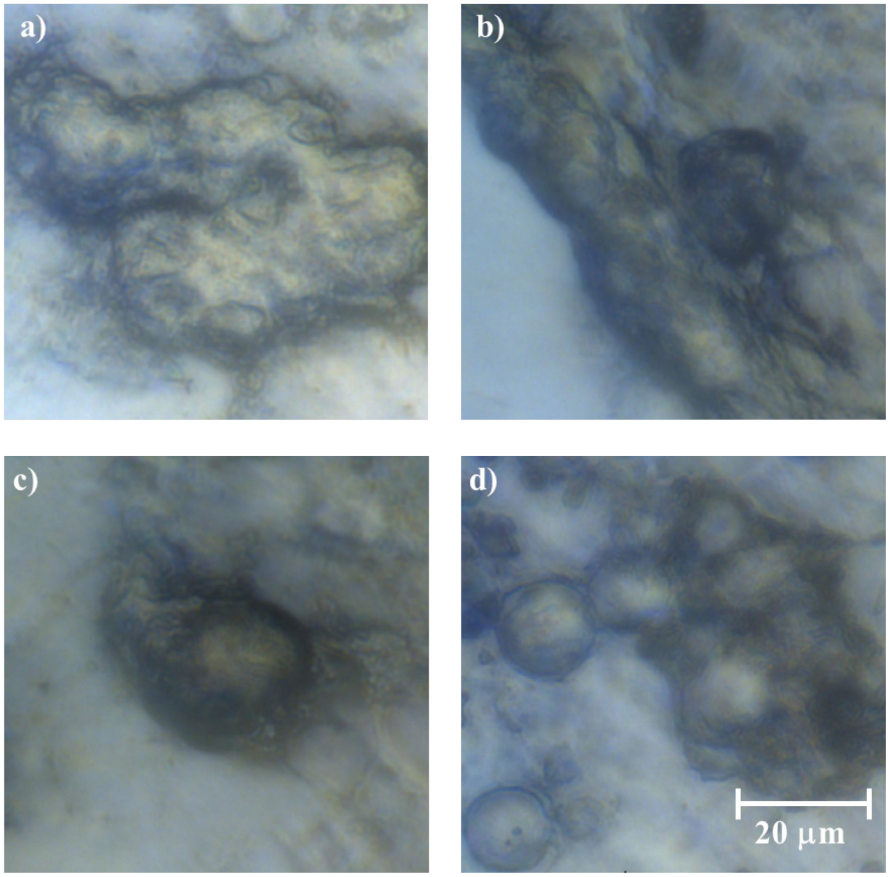

Figure 6.17: Optical micrographs of selected insulin-resistant 3T3-L1 adipocytes; a) treatment c*d*, no-sugar-vanadate; b) treatment *acd*, glucose-vanadate; c) treatment *bcd*, fructose-vanadate; and d) treatment *abcd*, glucose-fructose-vanadate. For treatment terminology, refer to **Figure 4.2**. Scale bar for all images is shown in figure d.

The PC1 scores and loadings (**Figure 6.18**) showed this PC varied highly in explained variance between 36-89.5% of the total variability. The glucose-vanadate treatment (*acd*, **Figure 6.18b**) may not be representative of the other cells in this analysis and was not further interpreted. The t_1 scores described the main differences between the regions close to the cell membrane and the inner biochemistry of the cell as was observed in the Block 1-3 analyses. The cell boundary for the vanadate-only and the fructose-vanadate treatments, *cd* and *bcd* respectively, were well defined (**Figure 6.18a** and **c**), however, the glucose-fructose-vanadate treatment (*abcd*) showed decreased definition of the cell boundary.

The p_1 loading associated with the glucose-fructose treatment (*abd*) was highly weighted in the region where bands due to protein secondary structures were evident (1660-1550 cm^{-1}). This treatment was also associated with large changes in the DNA band at 1705 cm^{-1} and the band at 1606 cm^{-1}, possibly associated with changes in tyrosine and arginine side chains.[206]

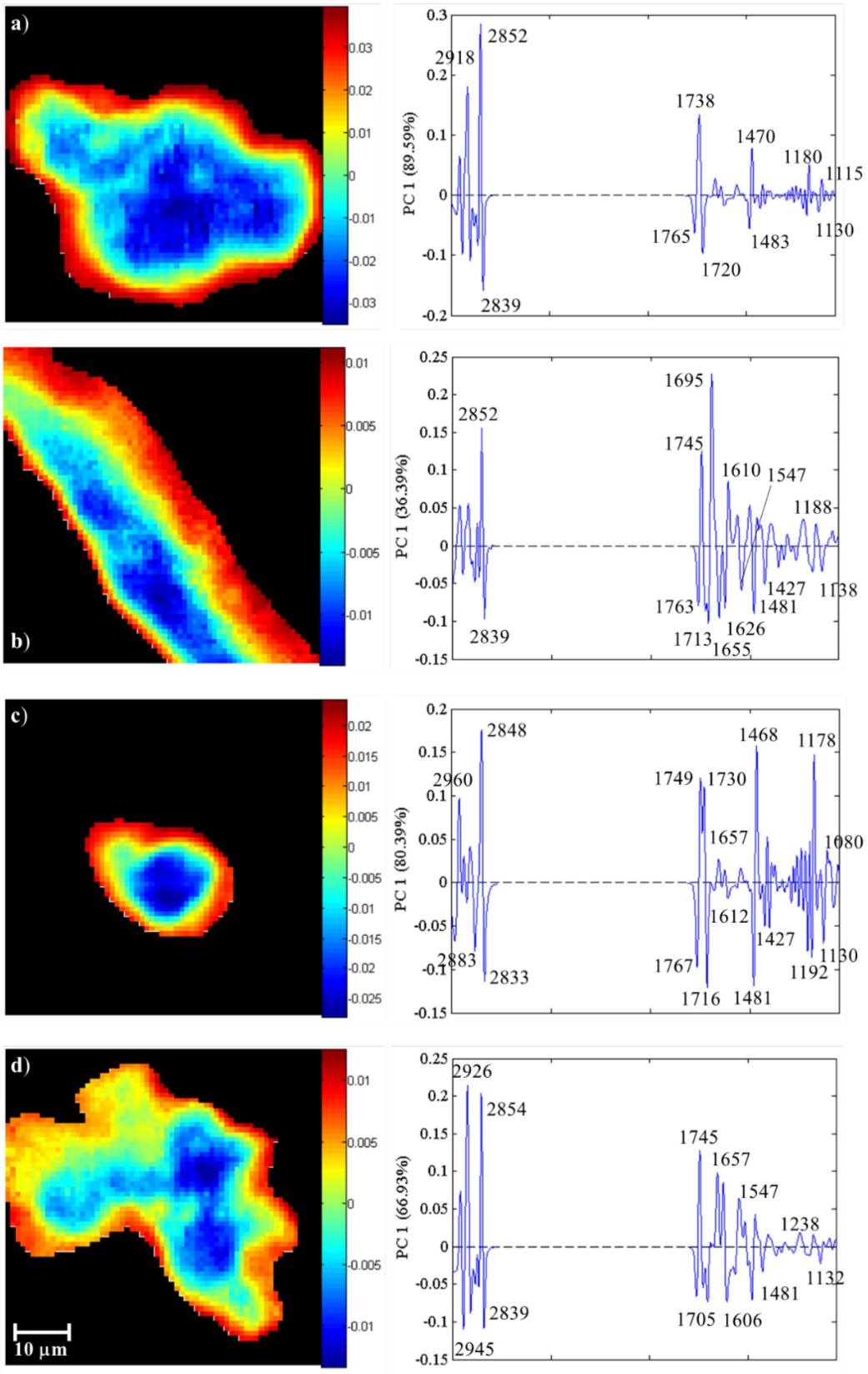

Figure 6.18: PC1 scores and loadings for insulin-resistant 3T3-L1 adipocytes, treated according to **Figure 4.2**. Block 4 treatments; a) treatment *cd*, no-sugar-vanadate; b) treatment *acd*, glucose-vanadate; c) treatment *bcd*, fructose-vanadate; and d) treatment *abcd*, glucose-fructose-vanadate. Important loadings are highlighted in this figure.

One possible explanation for this observation may be the activation of glucose metabolism in the insulin-resistant cell induced by vanadate and characterised by the loading at 1745 cm^{-1} (lipid ester band), while the loadings at 2945, 2839 and 1606 cm^{-1} were indicative of changes in lipid ester/fatty acids and tyrosine phosphorylation in the cell membrane.[309] The increased protein loading intensities at 1657 and 1623 cm^{-1} were consistent with previous observations in Sections 6.3.1.1-6.3.1.3 that fructose was inducing changes in protein secondary structures.

Interestingly, in the fructose-vanadate treatment (*bcd*, **Figure 6.18c**), the bands at 1749 and 1730 cm^{-1} were positively correlated to each other and had equal weighting. This was a hybrid of the results obtained for the fructose treated cells in Blocks 1 and 2 for the insulin-sensitive cells. In the fructose treatment (*b*, **Figure 6.6c**) the 1738 cm^{-1} band was weighted, whereas in the fructose-vanadate treatment (*bc*), the 1743 cm^{-1} band was weighted (**Figure 6.10c**). Along with the loadings at 1716 cm^{-1} (DNA) and protein secondary structural changes (1660-1550 cm^{-1}), these observations were consistent with the ability of fructose to promote protein synthesis.[20] The loading at 1612 cm^{-1} was consistent with changes in tyrosine phosphorylation.[309] In cancer cells, fructose has been reported to enhance protein synthesis through a mechanism that depletes cellular ATP levels and promotes mitochondrial respiration over glycolysis.[20]

The p_2 direction for Block 4 treatments (**Figure 6.19**) showed the same compartmentalisation of lipids and fatty acids as observed in Blocks 1-3. This PC explained between 3.8-10.4 % of the **X**-variance for treatments vanadate (*cd*), fructose-vanadate (*bcd*) and glucose-fructose-vanadate (*abcd*). For the vanadate-only treatment (*cd*), the large loading around 1920 cm^{-1} was the major contributor to the t_2 scores image and the splitting in this band was consistent with diverse cellular lipid ester/fatty acid composition. The lipid ester C=O band around 1740 cm^{-1} was split into a number of discrete loadings, again demonstrating the diverse cellular lipid composition. The combined insulin-resistance and vanadate-only treatment (*cd*) resulted in high levels of oxidative stress and the lack of carbohydrate metabolites (glucose and fructose) was postulated to induce complex bioreactions to adapt to the stress through the partitioning of the fatty acids to specific parts of the cell and in this manner, lipid and fatty acid reserves can provide energy to organelles such as the mitochondria or nucleus. Similar partitioning was observed for the fructose-vanadate treatment (*bcd*), and represented a state of increased oxidative stress.

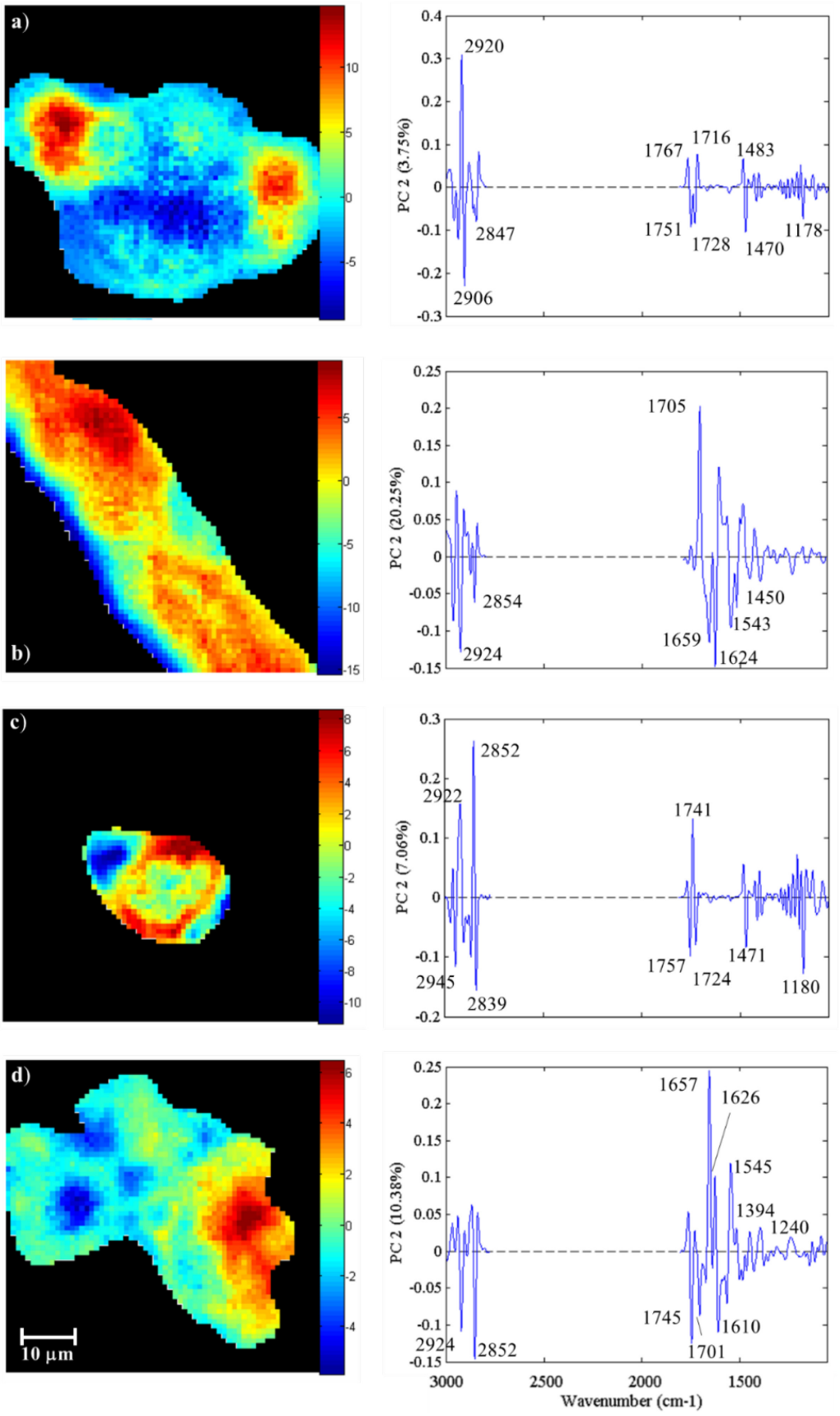

Figure 6.19: PC2 scores and loadings for insulin resistant 3T3-L1 adipocytes, treated according to **Figure 4.2**. Block 4 treatments; a) treatment *cd*, no-sugar-vanadate; b) treatment *acd*, glucose-vanadate; c) treatment *bcd*, fructose-vanadate; and d) treatment *abcd*, glucose-fructose-vanadate. Important loadings are highlighted in this figure.

The largest p_2 loadings in the glucose-fructose-vanadate treatment (*abcd*, **Figure 6.19c**) were associated with the positive correlation of the protein amide I α-helix band (1657 cm^{-1}), the β-sheet band (1626 cm^{-1}) and the amide II band (1545 cm^{-1}). These bands were negatively correlated to the lipid bands at 2924, 2852 and 1745 cm^{-1}, which were also positively correlated to the bands at 1701 cm^{-1} (DNA) and 1610 cm^{-1} (tyrosine and arginine side chains).[182,206] These observations were attributed to increased protein synthesis induced by fructose, represented by the blue regions in **Figure 6.19d** and the red region was most likely representing the nucleus and/or mitochondria, with the mitochondria being the most likely site due to its association with lipid synthesis and changes in DNA/RNA.[446] However, it was most likely that both the nucleus and mitochondria were contributing since they are in close proximity.[16]

The PC3 direction (**Figure 6.20**) described a similar level of treatment variability as observed in the PC2 direction and also described cellular compartmentalisation. The remaining biochemical processes being explained were minor, however, they may also be important and cannot be completely discarded. The p_3 direction for the vanadate-only treatment (*cd*, **Figure 6.20a**), described the partitioning of fatty acids (1732 cm^{-1}) and lipid esters (1749 cm^{-1}). A similar trend was observed in the fructose-vanadate treatment (*bcd*, **Figure 6.20c**), however, the position of the lipid ester band was positively weighted at 1759 cm^{-1} and negatively weighted at 1743 cm^{-1}, which was also positively correlated to the fatty acid (or DNA) band at 1720 cm^{-1}. This observation was consistent with the diverse lipid biochemistry found in adipocytes.[185,293]

The p_3 loadings for the glucose-fructose-vanadate treatment (*abcd*, **Figure 6.20d**) were dominated by changes in secondary protein structure and showed changes in β-turns (1660 cm^{-1}) positively correlated to the amide II band at 1551 cm^{-1}). These loadings were weighted in similar regions as the p_2 loadings, which showed that there were different protein structures in the region of the mitochondria (red region in the t_2 scores image) and the main part of the cell (red region of the t_3 image). With reference to the optical micrograph of **Figure 6.17d**, the protein regions highlighted in the p_3 loading may also be associated with the stromal cells used to support the cell.[201]

This current study has shown the power of the multivariate approach over the univariate approach of peak integration, however, it also generated complex data that required in-depth analysis and comparison of many analyses. This approach is therefore superior in

information extraction, however, more work is required on larger cell numbers and multiple culture to fully understand the mechanism revealed in this short feasibility study.

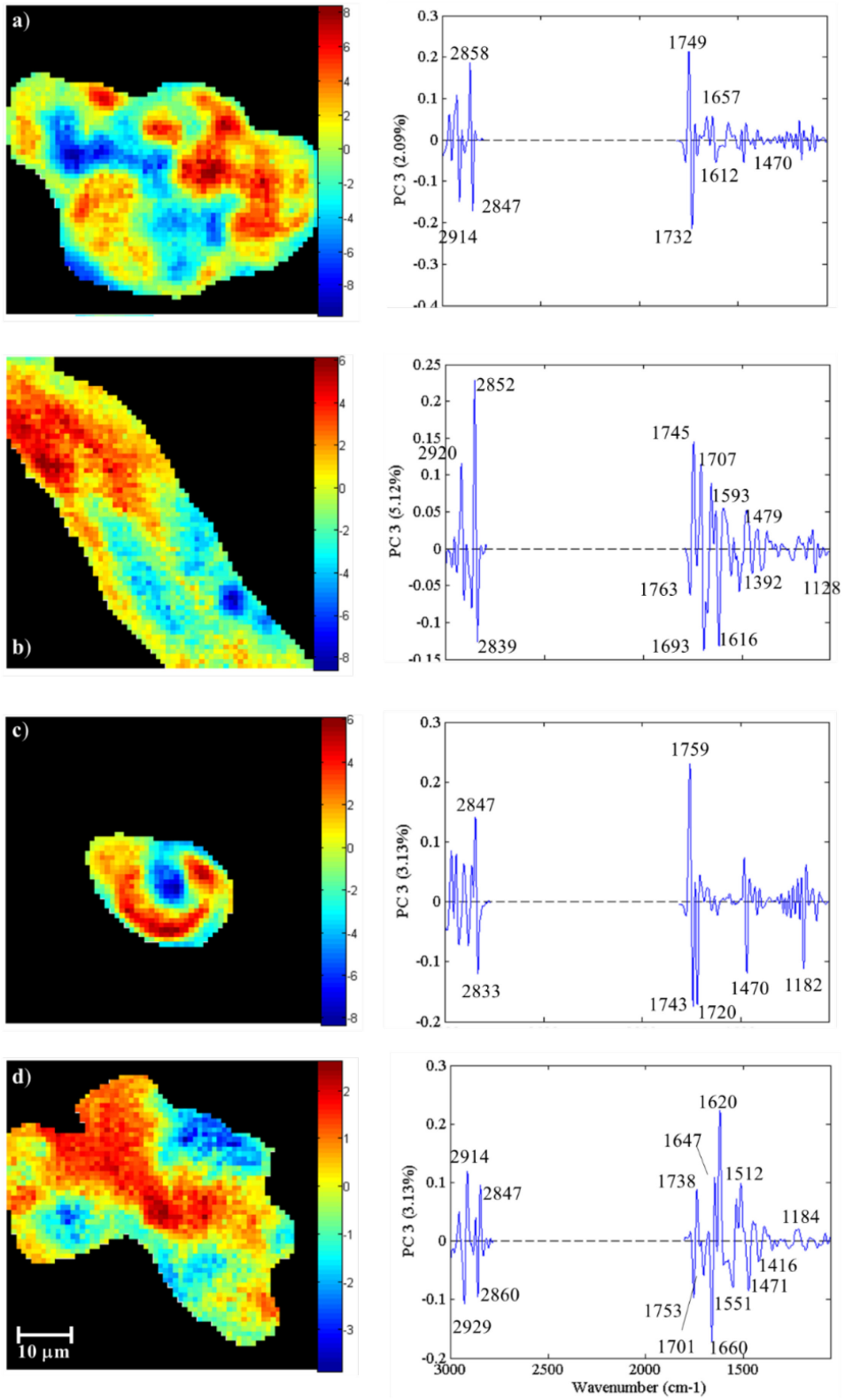

Figure 6.20: PC3 scores and loadings for insulin resistant 3T3-L1 cells, treated according to **Figure 4.2**. Block 4 treatments; a) treatment *cd*, no-sugar-vanadate; b) treatment *acd*, glucose-vanadate; c) treatment *bcd*, fructose-vanadate; and d) treatment *abcd*, glucose-fructose-vanadate. Important loadings are highlighted in this figure.

6.3.2 Effects of Sugar Treatments of 3T3-L1 Adipocytes Using Synchrotron FPA Microspectroscopy

6.3.2.1 FPA Analysis of Glucose Treated Adipocytes on 0.2 mm CaF_2 Substrates

A CaF_2 substrate thickness of 0.2 mm was the thinnest available for these experiments and represented a balance of improved transmission and mechanical resistance to breakage. PCA was applied to the FPA images collected on a selected 3T3-L1 adipocyte chemically fixed to the CaF_2 substrate (**Figure 6.21**). To evaluate the sensitivity for detecting cellular composition, morphology and to investigate PCA's ability to implicitly model unwanted variation into noise components no masking was performed. The PCA loadings for the images in **Figure 6.21** are shown in **Figure 6.22**.

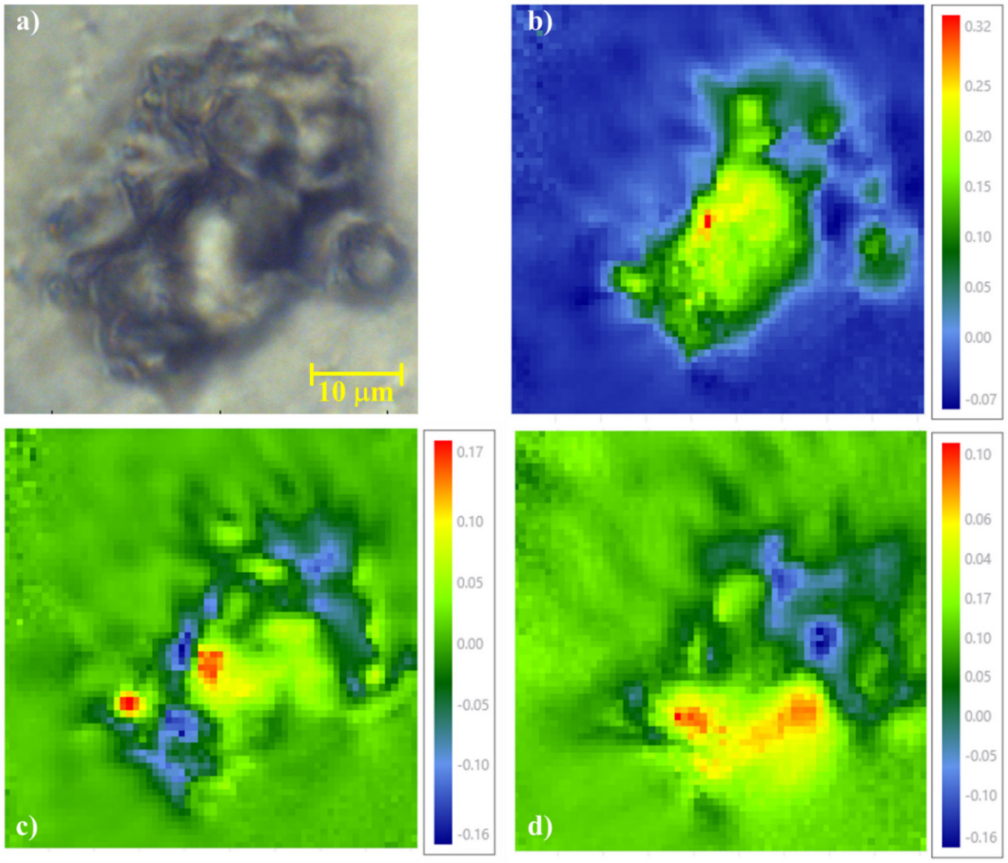

Figure 6.21: Optical micrograph and PCA scores images of a single 3T3-L1 adipocyte chemically fixed to a 0.2 mm CaF_2 substrate; a) optical micrograph; b) t_1 scores image; c) t_2 scores image; and d) t_3 scores image.

The combined scores and loadings showed that a three PC model described 85.6% of the total **X**-variance and the information was dominated by lipid and fatty acid bands between 2920-2800 cm^{-1}, 1750-1720 cm^{-1} 1480-1450 cm^{-1} and bands between 1240-1080 cm^{-1} (**Table 1.1**). The scores images (**Figure 6.21b-d**) displayed minimal aberrations as was observed in Chapter 3. Analysis of higher order PCs only showed small contributions

from proteins and the PC4 scores and loadings (**Figure 6.23**) indicated that there may only be small regions of protein associated with the selected cell.

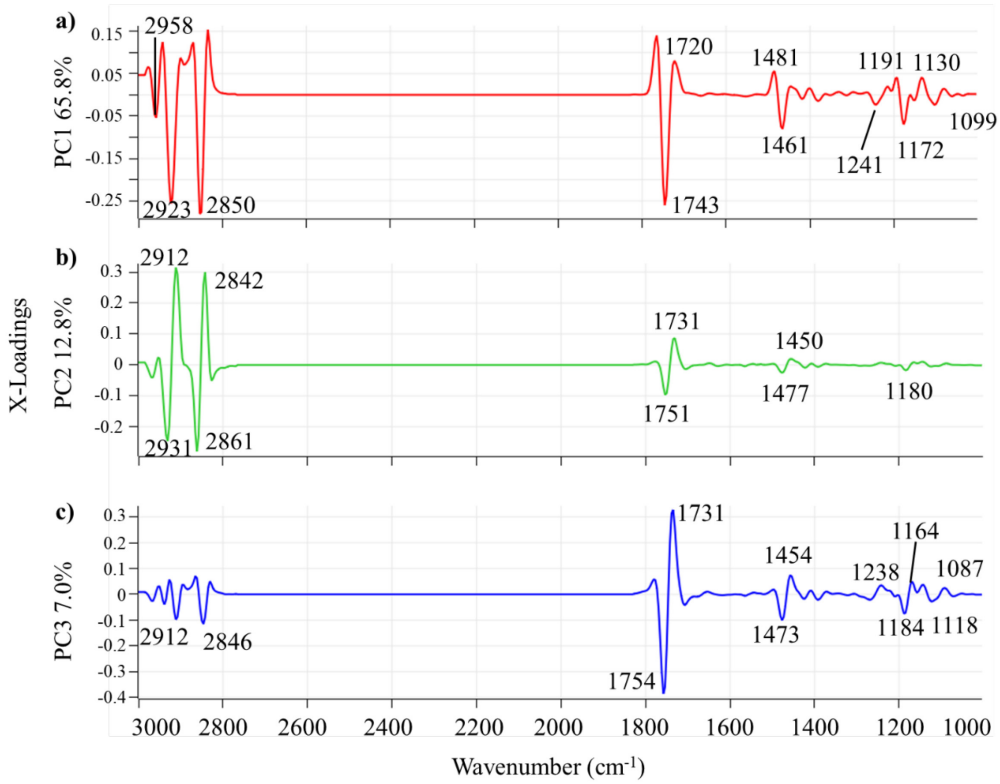

Figure 6.22: PCA loadings for FPA images of a 3T3-L1 adipocyte treated with glucose and chemically fixed to a 0.2 mm CaF_2 substrate; a) p_1 loadings; b) p_2 loadings; and c) p_3 loadings.

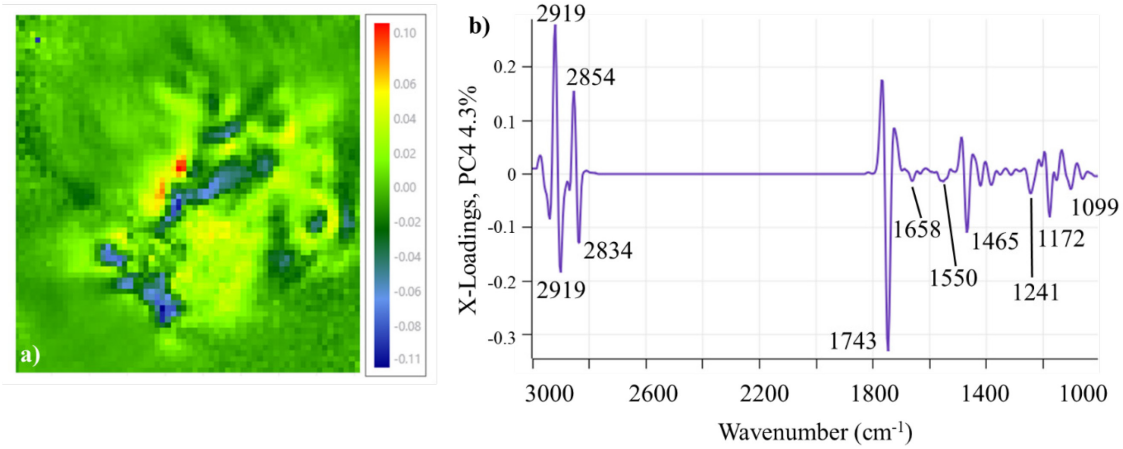

Figure 6.23: a) t_4 scores image; and b) p_4 loadings for a 3T3-L1 adipocyte treated with glucose and chemically fixed to a 0.2 mm CaF_2 substrate.

The images of the selected cell showed the typical high lipid content of an adipocyte treated under conditions that promote growth, as adipocytes are typically >90% lipid in composition.[30] The lack of protein in the selected adipocyte could also be related sampling, i.e., the selected cell for this assessment had a lower protein content, however,

it was more likely that this adipocyte was at an advanced stage of cell development associated with the large lipid bands observed in the p_1 loadings.

6.3.2.2 FPA Analysis of Glucose Treated Adipocytes on 0.5 mm CaF_2 Substrates

PCA was applied to the FPA images collected on a selected 3T3-L1 adipocyte chemically fixed to a 0.5 mm CaF_2 substrate (**Figure 6.24**). The associated PCA loadings for the images in **Figure 6.24** are shown in **Figure 6.25**.

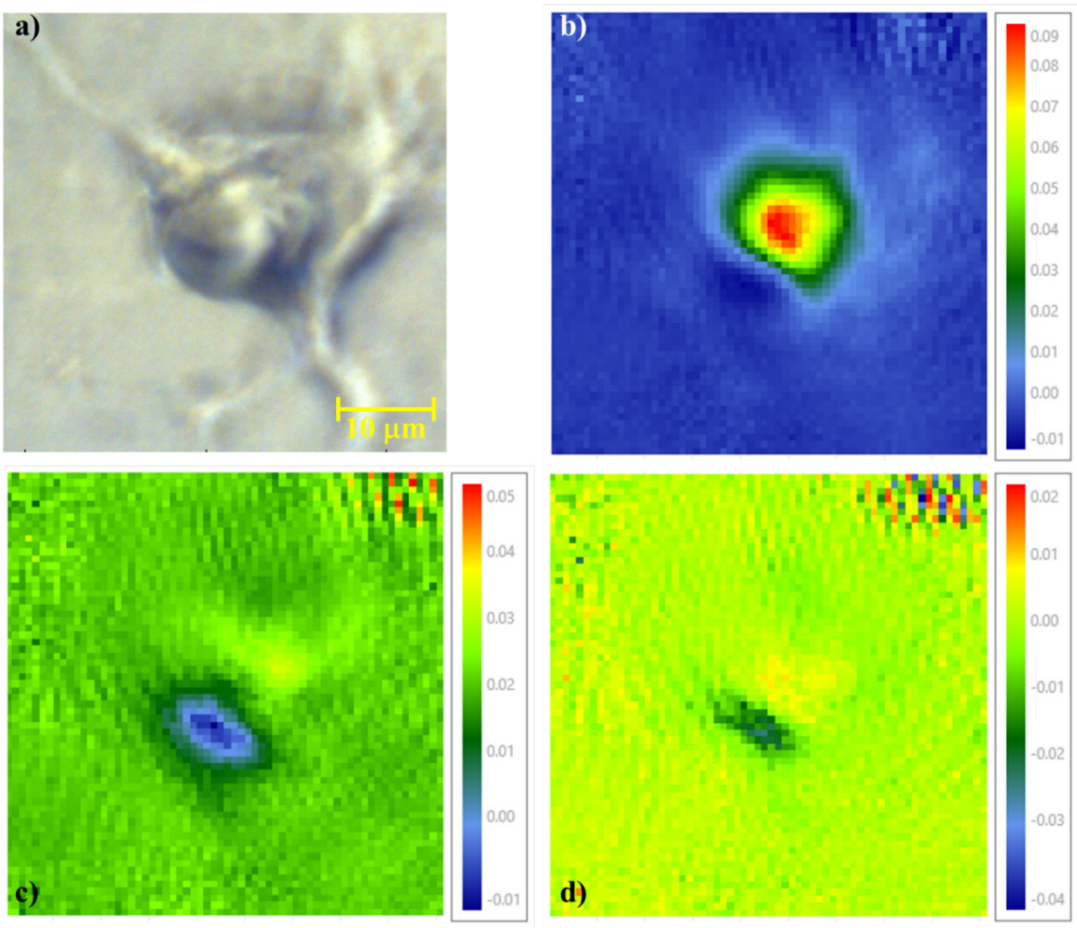

Figure 6.24: Optical micrograph and PCA scores images of a single 3T3-L1 adipocyte chemically fixed to a 0.5 mm CaF_2 substrate; a) optical micrograph; b) t_1 scores image; c) t_2 scores image; and d) t_3 scores image.

The aberrations observed by Tobin, *et al.*[215,255] and Findlay, *et al.*[286] were also observed in the scores images (**Figure 6.24**) from the t_1 image and became progressively more pronounced in the t_3 image. An outline of the cell morphology was observed in the first two scores images, while the third image showed a shadow of the cell dispersed in the Moire-like pattern caused by the aberrations.[286] The t_1 scores image showed that the protein content of this cell was different to the cell imaged in Section 6.3.2.1, where bands at 1654 cm^{-1} and 1546 cm^{-1} were observed, related to amide I and amide II bands, respectively.[172]

The p_3 loadings (**Figure 6.25c**) displayed a highly complex pattern in the 1800-1400 cm^{-1} region. Due to the reduced information of the cell morphology observed in the t_3 image, masking was applied to the background using the cell outline information in the t_1 and t_2 scores image and a PCA model was generated for the cell region only for the first three PCs (**Figure 6.26**). Masking eliminated the main effects of the aberrations and revealed more biochemical information in the loadings.

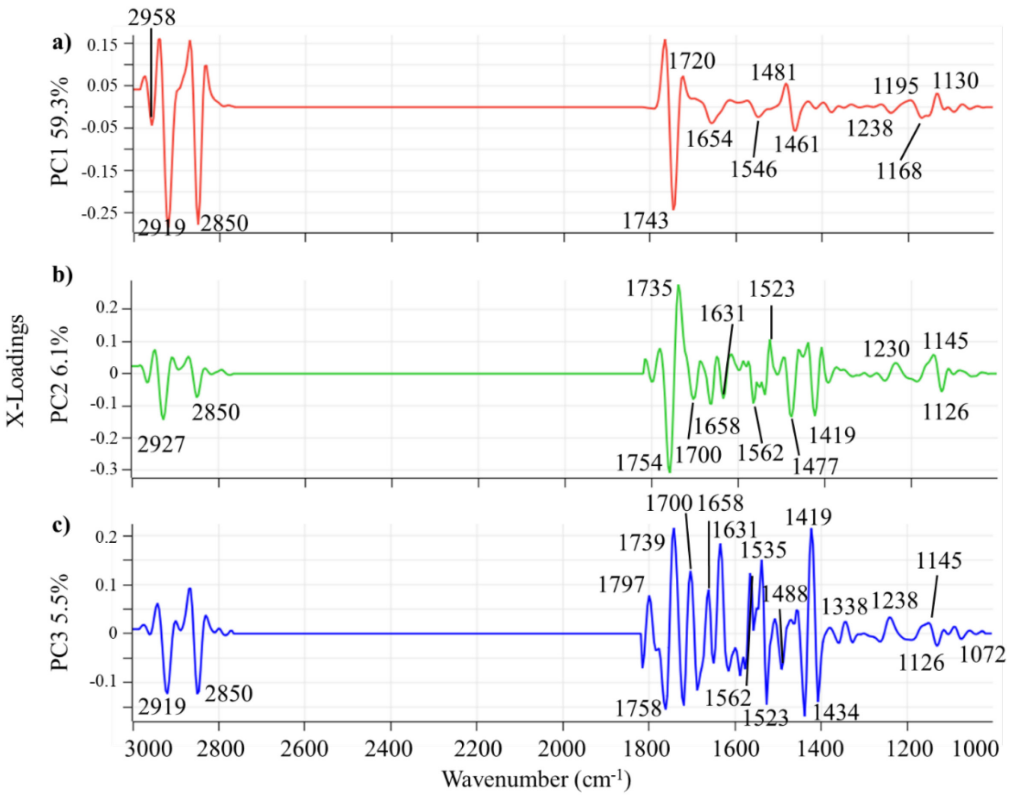

Figure 6.25: PCA loadings for FPA images of a 3T3-L1 adipocyte treated with glucose and chemically fixed to a 0.5 mm CaF_2 substrate; a) p_1 loadings; b) p_2 loadings; and c) p_3 loadings.

Comparison of **Figure 6.25a** and **Figure 6.26a** reveal that the p_1 loadings showed very similar information to the unmasked image, however, assessment of the masked image (**Figure 6.26a**), showed the spectral contributions from proteins were reduced and the PC1 direction (as was the case in Section 6.3.1) was a descriptor of the lipid content in the adipocyte cell. As was also observed in Section 6.3.1, the PC2 direction in **Figure 6.26b** described a partitioning of the lipid droplets into those consisting of lipid esters (positive scores, red regions) and described by loadings at 2927, 1754, 1473 and 1126 cm^{-1} versus those described by negative t_2 scores (blue regions) and loadings at 1735, 1454 and 1145 cm^{-1}. The band at 1735 cm^{-1} was most likely a lipid ester band,[200] therefore, the large spitting of the band around 1743 cm^{-1} was indicative of two different types of lipid in the cell. The PC3 direction described similar information to that in PC2,

however, in PC3, the splitting of the bands at ~2920 and 2850 cm^{-1} further confirmed the presence of two lipid types in different compartments within the cell.

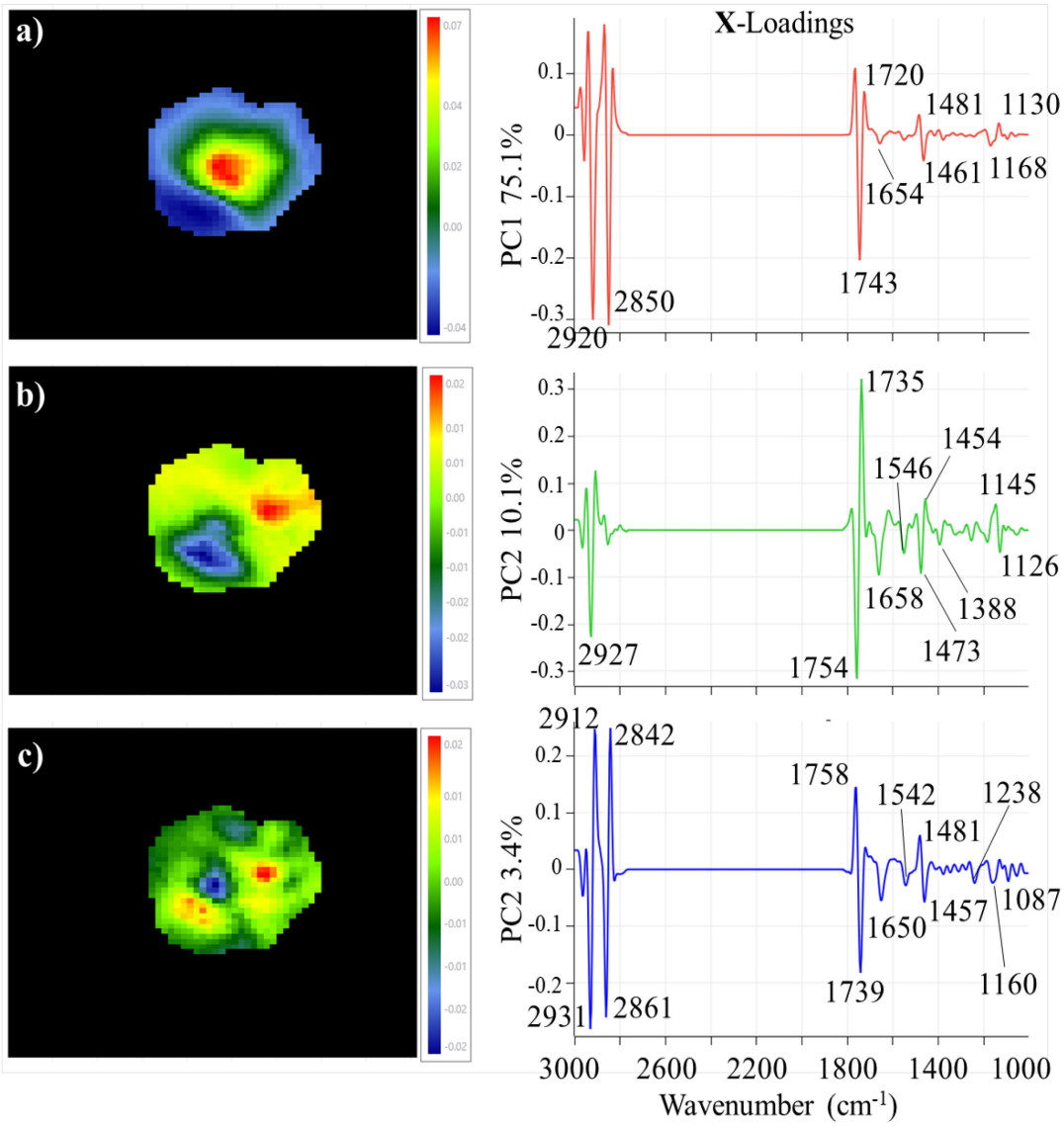

Figure 6.26: Masked PCA scores images and loadings for a single 3T3-L1 adipocyte chemically fixed to a 0.5 mm CaF_2 substrate. Scores image and loadings for; a) PC1; b) PC2; and c) PC3.

The deconvolution of separate bands over the wavenumber region 2920-2850 cm^{-1} correlated with those observed in the band at 1743 cm^{-1}. In particular, the bands at 2931, 2861 and 1739 cm^{-1} in the negative p_3 direction were positively correlated, as were the bands at 2912, 2842 and 1758 cm^{-1} bands in the positive p_3 direction. The 2931 and 2861 cm^{-1} bands were assigned to cholesterol,[441] and due to the lack of a C=O moiety in cholesterol, the band at 1739 cm^{-1} was most likely attributed to cholesterol esters that are known to be present in adipocytes in small amounts,[447] and commensurate with the smaller contribution from the p_3 (and p_2) loadings.

6.3.2.3 FPA Analysis of Glucose Treated Adipocytes on 1.0 mm CaF_2 Substrates

PCA was applied to the FPA images collected on a selected 3T3-L1 adipocyte chemically fixed to a 1.0 mm CaF_2 substrate (**Figure 6.27**). The associated PCA loadings for the images in **Figure 6.27** are shown in **Figure 6.28**. Aberrations were also observed in the scores images (**Figure 6.27**) and were of a similar magnitude to those observed in the adipocyte fixed to a 0.5 mm substrate. The selected cell was the best available for this study and due to its size, it was not possible to focus the entire cell. The t_1 scores image showed the general outline of the focussed portion of the cell, while the t_2 scores image highlighted internal cellular compartments. This observation was consistent with the finding made for t_2 in this entire study.

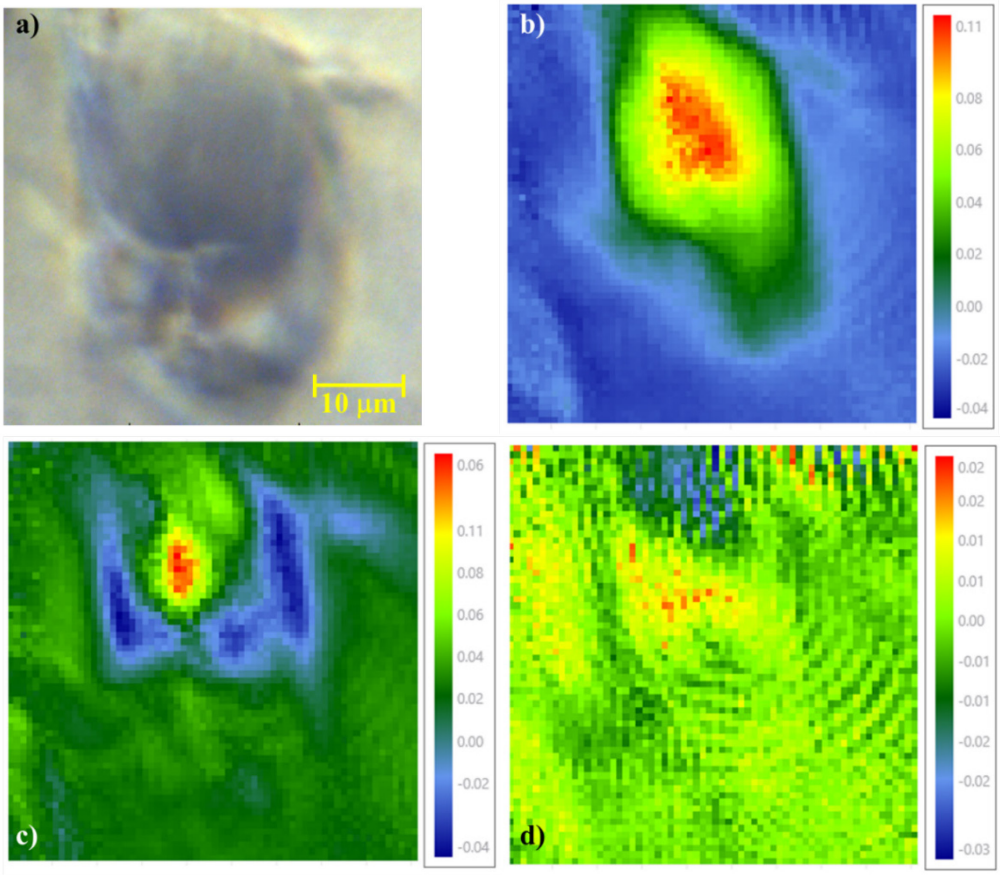

Figure 6.27: Optical micrograph and PCA scores images of a single 3T3-L1 adipocyte chemically fixed to a 1.0 mm CaF_2 substrate; a) optical micrograph; b) t_1 scores image; c) t_2 scores image; and d) t_3 scores image.

The p_3 loadings (**Figure 6.28c**) displayed a similar complexity in the 1800-1400 cm^{-1} region as the cell fixed onto the 0.5 mm substrate (**Figure 6.25c**). The t_3 scores image did not describe the cell morphology, and after masking was applied to the background using information in the t_1 and t_2 scores images, a PCA model was generated for the cell region only for the first three PCs. The first two PCs of this model described the majority of the

information in the data and this time, the PC3 direction isolated the fringing pattern in the loadings (**Figure 6.29**). Similar fringing patterns were observed in Section 3.5. for chemical mapping studies performed at the Australian Synchrotron using the single beam/detector configuration and was attributed to aberrations induced by CaF_2.[215,255]

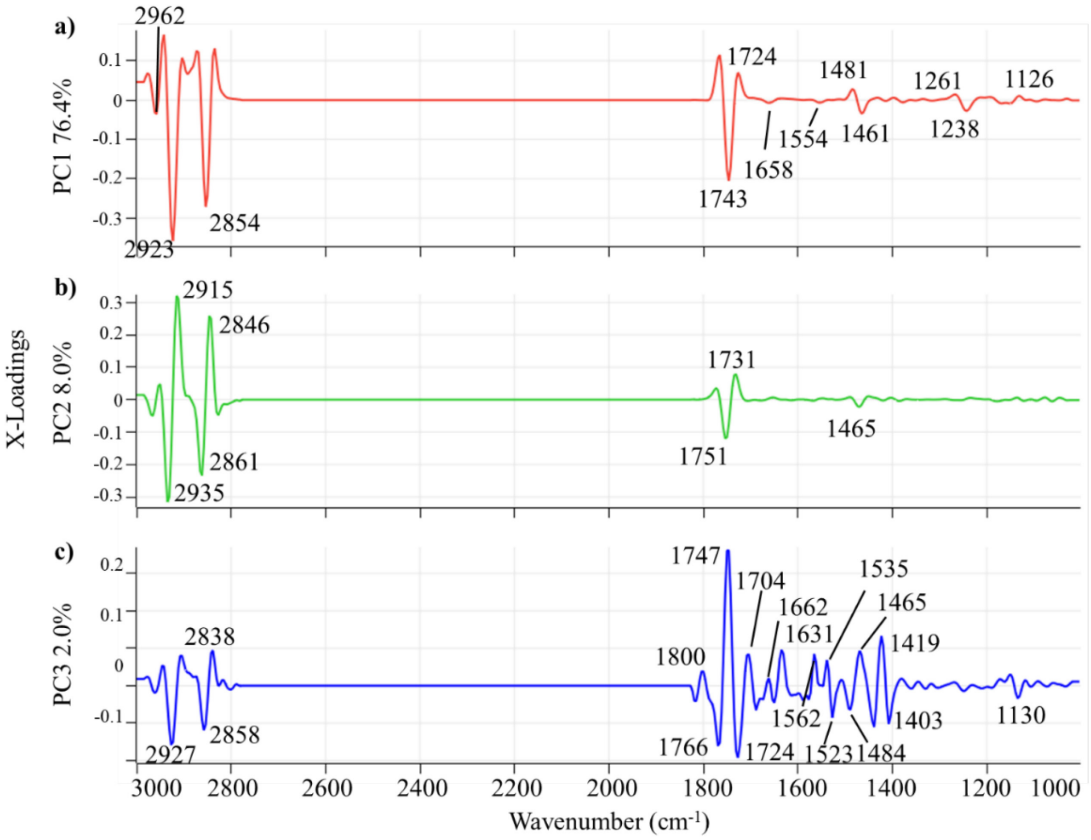

Figure 6.28: PCA loadings for FPA images of a 3T3-L1 adipocyte treated with glucose and chemically fixed to a 1.0 mm CaF_2 substrate; a) p_1 loadings; b) p_2 loadings; and c) p_3 loadings.

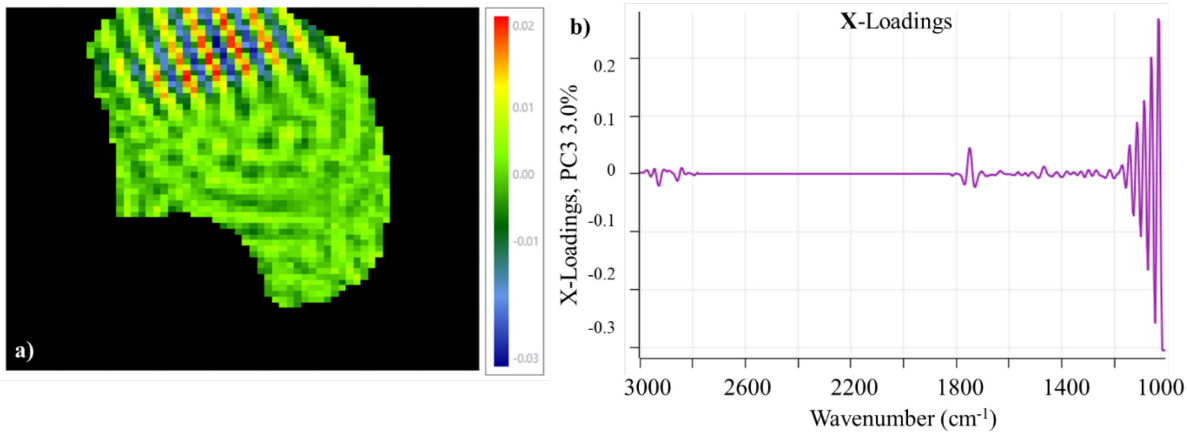

Figure 6.29: a) t_3 scores image; and b) p_3 loadings for a 3T3-L1 adipocyte treated with glucose and showing the fringing pattern induced by the 1.0 mm CaF_2 substrate.

6.4 Discussion

Modern hyperspectral imaging (HSI) software packages combined with FPA FTIR microspectroscopy enabled the acquisition and analysis of highly complex biochemical and morphological data generated from single adipocytes. Post-acquisition, HSI software packages provided masking tools that allow the ROI to be assessed without the influence of clutter, which is defined in the HSI literature as any information not related to the ROI.[232] The advantage of software masking is that it avoids having to use knife edge apertures of the FTIR microscope, that restrict the acquired image to a rectangular area, by allowing the use of free form polygon selection of the ROI.[448] In this manner, only the most relevant biochemical information can be modelled from the images, providing greater insights into complex biological pathways.

This feasibility study was performed to investigate whether useful information could be obtained from FPA images of single isolated adipocytes chemically fixed onto CaF_2 substrates. The cell populations were heterogeneous and were affected by treatment conditions, fixation conditions and cell cycle stage.[201] The CaF_2 substrate, although infrared transparent and versatile for many applications in infrared spectroscopy produced aberrations, restricted transmission below 1000 cm^{-1} and induced cell cycle arrest, that could be a confounding effect with respect to any treatments applied, especially cytotoxic treatments that induced cell cycle arrest prior to inducing apoptosis.[436]

Simple processing methods, such as derivatives and sample-based normalisation, were used to minimise the majority of physical effects induced by sampling and light scatter.[223] This resulted in PCA models that typically described the majority of the cell composition and morphology in the first two PCs. In the case of 3T3-L1 adipocytes, which are ~ 90% lipid in composition,[16] the PC loadings were reflective of the lipid bands and the corresponding scores images provided details into how the various biochemicals distribute in the cell. The most interesting finding was that lipid droplets compartmentalise into specific areas that store neutral lipids and those that store fatty acids. This information can be used to complement the spectral analysis on point spectra in Chapter 4 by isolating localised organelles in the cell that may be responsible for observed biochemical changes induced by treatments.

Compartmentalisation has been associated with lipid droplets performing specific roles with the cell nucleus or mitochondria for the provision of immediate energy and conversion into energy reserves for the cell or for use in peripheral tissues.[443] The location

of specific lipid droplets may also be an indicator of the location of various organelles in the cell. The images acquired in this study showed that in some treatments, associations between lipid and protein synthesis were correlated, particularly for treatments containing fructose and it was postulated that these regions of high correlations defined specific organelles within the cell responsible for DNL.

FPA imaging offered the advantage of faster data acquisition compared to single point mapping and produced high detail images that were obtained in minutes, rather than hours on laboratory-based instruments. Although SR-based light sources offered more focussed and brighter beams compared to Globar® sources, the application of SR-mapping was best suited for investigating localised regions obtained from a larger map where fine detail data acquisition on a smaller ROI was required. For these smaller ROIs, oversampling was applied to obtained finer detailed, high-quality spectral data within the cryogenic cooling time (~8 hrs) of the MCT detector.

FPA imaging provided enhanced spatial detail over larger sample areas. To take advantage of the synchrotron advantage of brilliance, facilities such as IRENI in the United States combined 12-beams and focussed them onto the 64×64 sub-array of a 128×128 FPA detector.[282,286] In the study at the Australian Synchrotron, four-beams were combined and focussed onto the aperture of a Bruker Hyperion 3000 FTIR microspectrometer where the energy was focused onto the inner 32×32 sub-array of the 64×64 FPA detector,[255] where the non-collimated beam dispersion covered 75% of the detector area (**Figure 3.41**).

Therefore, when applied to FPA detection, the small beam spot advantage is lost in favour of the increased brilliance of incident radiation over a larger region of the detector. The combination and focussing of beams can enhance aberrations observed in acquired images and Findlay, *et al*.[286] described this phenomenon as interferences induced by overlap of the beam edges (**Figure 6.1**). In this study, similar aberrations were also observed in FPA imaging and to a lesser extent in the mapping studies performed in Chapter 3, which were also attributed to effects induced by the CaF_2 substrate.[215,270] Overall, the use of laboratory-based Globar® FPA FTIR microspectroscopy provided similar results to the combination of multiple synchrotron beams. Where there may be advantages to using such multiple-beam set ups, this is sample specific, however, for the assessment of 3T3-L1 cells, which are relatively large and heterogenous in composition

and morphology, the laboratory-based system provided images that were interpretable and comparable in information to the four-beam synchrotron setup.

Although the current study was not as detailed as the study presented in Chapter 4, the results obtained were consistent with changes in cellular biochemistry induced by the different treatments. FPA imaging provided important information on the cellular compartmentalisation of lipid droplets within individual adipocytes, which was not possible using single-point spectra. Single-cell imaging identified differences in lipid droplet composition, which indicated that lipid droplets were associated with other organelles, such as the mitochondria or nucleus where they provide lipid ester/fatty acids related to the energy requirements of the specific organelle. The acquisition of more images of a single culture and over multiple cultures will provide more information on the biological variability associated with single-cell images and future work will elaborate on the feasibility study described in this chapter.

Chapter 7 Conclusions and Further Work

7.1 Conclusions

7.1.1 FTIR Microspectroscopy as a Tool for Investigating Pro-drug Induced Biochemical Changes

The FTIR microspectroscopy studies elucidated biochemical and morphological effects of anti-diabetic and anti-cancer pro-drugs in insulin-sensitive cell lines. Three modes of data acquisition were evaluated: single-point spectra of whole cells, raster scanning chemical maps and focal-plane-array (FPA) imaging of single cells. Each method was optimised and assessed in terms of the quality of information obtained using standard spectral processing methods and multivariate data analysis (MVDA). While FTIR microspectroscopy does not measure discrete biological pathways in cells to the same levels of bioassay techniques, it provided measurements of the overall biochemical changes induced by different treatment conditions, *in vitro*. Thus, information about overall metabolic shifts and morphological changes induced by anti-diabetic and anti-cancer treatments were evaluated and interpreted at the microscopic-level, to provide insights into cellular bioprocesses.[410]

7.1.2 Optimisation of Spectral Data Acquisition Parameters and Processing Methods

FTIR spectra were acquired at the Australian Synchrotron where point scanning and chemical mapping data acquisition parameters were optimised using the 3T3-L1 mouse adipocyte *in vitro* model of type 2 diabetes mellitus and metabolic syndrome.[449] FTIR confocal microspectroscopy was performed with mechanical pinholes inserted between the sample and the detector, to result in spatial resolution improvements of up to $\sim\lambda/2$ compared to diffraction-limited spatial resolution of $\sim 2\lambda/3$ for a single objective.[270,450] Although a number of publications describe the best scanning parameters for FTIR microspectroscopic spectral data acquisition,[189,257] a definitive work on the optimisation of spectral coadditions was not evident. The pharmaceutical and related industries use methods that evaluate the repeatability and reproducibility of data acquisition parameters based on empirical studies applied to the sample type under investigation.[225,268] The method of fixed block standard deviation (FBSD)[281] was used to objectively define the optimal number of coadditions to use for spectral data acquisition of the 3T3-L1 cell line. This cell line provided a highly challenging sample type due to its multilocular structure that induced multiple cell boundaries between lipid droplets. This resulted in a number of light scattering effects that must be corrected prior to multivariate analysis.

For the mapping studies, the larger the pinhole used, the smaller the spectral variance when assessed by PCA and FBSD methods on single measurement points taken over four locations of a cell of known biochemical content. Normalisation of the spectra, post derivatisation, is a recommended approach prior to multivariate data assessment,[257,273] and improved the separability of the cell positions, compared to derivatives alone, as assessed by PCA scores. There are a number of normalisation techniques available, some based on training sets (such as multiplicative and extended multiplicative scatter correction, MSC/EMSC),[238,274,451] column-wise scaling, such as vector normalisation,[233,452] hybrid empirical and mechanistic information models (resonant Mie Scatter, RMieS and Mie extinction methods)[265,275,277-278] and SNV,[236] which is a row-wise normalisation technique that corrects each spectrum to the mean and standard deviation of the spectrum itself.

While simple in its application, SNV has the propensity to propagate noise across the entire spectrum, especially if a second derivative was applied as the first processing method. This is because SNV is based on the mean and standard deviation calculated from the spectrum and the wavenumber range selected to perform these calculations. Therefore, the addition of noisy regions into the SNV calculation can amplify noise in a spectrum due to the calculation of small, second differences between adjacent data points.[223] The amount of noise propagated is a function of the spectral resolution and the size of the smoothing filter used by the derivative function. Therefore, it was important to explicitly improve the signal-to-noise ratio (S/N) in raw data acquisition by performing an objective spectral coaddition optimisation study prior to defining an optimised processing strategy.

The Savitzky-Golay filters fit standard polynomials to data points in a defined smoothing window.[234] Moving the filter in a boxcar manner over the entire spectral region results in further reduction in noise, such that when the derivative is applied, the amplification of noise is minimised and the retention of information is maximised.[223] Over-smoothing resulted in a loss of resolution of overlapping spectral bands and under-smoothing propagated noise. The task of defining a spectral filter was a combination of subject matter expertise and a well-designed empirical study to ensure critical spectral bands were not ‘averaged’ out.

Normalisation of the smoothed spectra then required another empirical study to be performed to ensure that low and high frequency artefacts did not propagate across the derivatised data. The optimal removal of noisy spectral regions minimised artefacts that

would otherwise require implicit correction by multivariate modelling.[238] The noise in the spectra was determined to be a function of detector sensitivity and optical characteristics of the CaF_2 substrate. A practical cut off limit of 1000 cm^{-1} was imposed on the use of CaF_2 substrates due to the decreased light transmission below 1000 cm^{-1}.[214-215] CaF_2 also induced coherent aberrations into the spectra as a result of refractive index changes between 1800-1000 cm^{-1}.[215]

Noise considerations were most important when using a small pinhole in FTIR confocal microscopy, as the reduced light flux resulted in a smaller wavenumber range (cut off limit of 1200 cm^{-1}) available to obtain biochemical information. This had practical ramifications when using CaF_2 as a substrate in combination with a small pinhole, as more coadditions were required to acquire spectra of low noise characteristics, therefore reducing the size of the map due to detector cooling time limitations. In future work, these limitations will be addressed using other substrates such as silicon nitride (Si_3N_4).[243] CaF_2 is a more robust substrate than Si_3N_4, which is highly fragile, particularly when cold methanol fixation is used and does not travel well from one laboratory to another, thus adding another practical limitation, however, one that has been managed using caution.[243]

Application of principal component analysis (PCA) is the multivariate visual equivalent to analysis of variance (ANOVA), where the repeatability of a method was assessed by how tightly points within a group cluster together versus the between sample groupings induced by different treatments. Therefore, PCA provided a non-biased means of evaluating complex multivariate data as single points in multivariate space, which enabled an objective and visual evaluation of the data. PCA can be used to determine whether a particular combination of spectral data acquisition parameters, processing and sampling methods provides improvements in overall variability and biochemical information obtainable from the spectra.

When considering overall spectral data quality, there is, however, a trade-off between precision and time. While the large pinhole provided spectra with less noise characteristics, this was at the cost of fine detail, as evidenced in the mapping studies that compared the large and the small pinholes. The pixel size in a raster scan map was diffraction limited, therefore, finer detailed maps are a function of the beam spot size and the amount of oversampling.[263] When the data were displayed as pixel maps, it was difficult to discern morphological information without the use of mathematical rendering, in the form of contour plots. Such plots made the maps appear to be more interpretable than they really are. To map a complete cell to a high degree of precision (i.e., using a

larger number of coadditions), required a small pinhole with a large amount of oversampling. The time taken to collect a map of reasonable resolution would take longer than the time the detector can be effectively cryogenically cooled, as refilling a detector during spectral acquisition requires the system to be restabilised before the measurement can be continued.[221] Therefore, it was concluded that SR-FTIR microspectroscopy was a useful tool for acquiring high quality single cell spectra, or to focus down on a small region of interest (ROI) using a small pinhole to obtain high quality maps of a particular region, however, to produce detailed images, the use of FPA was the preferred method.

Optimisation of a laboratory based Globar® instrument was assessed in a similar manner as the SR-FTIR microspectroscopic setup, this time using mechanical knife edge apertures to exclude extraneous information outside of the cell ROI when performing point scan experiments. Studies performed using aperture sizes ranging from 4×4 to 30×30 μm were investigated using the HepG2 cell line. Assessment of the selected aperture sizes, showed that spectra with low noise were obtained for a 12×12 μm aperture with best results obtained when the aperture was set to 20×20 μm, in agreement with the literature.[257] For this study, aperture sizes were not set to under 16×16 μm and 256 coadditions were used for all spectral acquisitions.

Images acquired using a laboratory Globar® FPA FTIR microspectrometer were recorded using the systems full field of view (FoV) and a 36× Cassegrain objective. An optimisation study showed that spectra of low noise characteristics were acquired on 3T3-L1 adipocytes using 256 coadditions and for detailed work on cells of interest, images were acquired using 512 coadditions. Setting the integration time of the detector was one of the biggest challenges of the FPA method, as it was sample specific and required assessment prior to the collection of each image to avoid detector saturation. Images were collected over a time ranging from 7 min for 256 coadditions to 15 min for 512 coadditions. In all cases, acceptable, high-quality images were obtained.

When a multiple-beam synchrotron light source was used for FPA imaging,[255] many scattering effects and aberrations resulted. To date, advanced processing methods using corrections algorithms for Mie scattering[275-276,278] applied to the spectra in this study did not improve the quality of the spectra, or the information obtained from the processed spectra after multivariate modelling. However, these algorithms will be explored in greater detail in future studies. The best processing method was a Savitzky-Golay second derivative using nine-point smoothing for the synchrotron FPA study. Normalisation

propagated too much noise across the spectral data due to the enhanced aberration effects, however; PCA was able to implicitly model out the aberrations into higher order PCs. In general, for all modes of data acquisition, provided an empirical study was performed prior to data collection that optimised the number of spectral coadditions (i.e., improved the S/N), simple processing methods resulted in multivariate models that were interpretable when modelled using a small number of PCs/Factors, when using PCA or PLS-DA, respectively.

7.1.3 FTIR Microspectroscopic Assessment of 3T3-L1 Adipocytes

The novel use of FTIR microspectroscopy enabled much more insight into biochemical changes than standard cytotoxic cell assays related to the insulin-mimetic and cytotoxic action of vanadate on treated 3T3-L1 adipocytes. FTIR microspectroscopy applied to vanadate treated adipocytes enabled interpretation of biochemical changes induced by increased states of oxidative stress and the results obtained were assigned to a number of established biochemical pathways, including those that induced apoptosis.[195,202,205] Oxidative stress is defined as the imbalance of oxidants and antioxidants in favour of the former.[159]

Over the concentration range 0-15 μM, vanadate treatments induced insulin-mimetic actions, which became increasingly cytotoxic as vanadate concentration was increased. The results obtained showed that insulin-sensitive cells were more tolerant to vanadate than were insulin-resistant cells. Such differences were attributed to the increased oxidative stress environment caused by insulin resistance and amplified when vanadate concentration induced critical levels of ROS.[75] Redox cycling of V(IV)/V(V) induced the production of oxidants, such as H_2O_2 that self-perpetuate increased oxidative stress and finally apoptosis.[129]

FTIR microspectroscopy showed that increasing vanadate concentration correlated with lipid peroxidation and modifications of plasma membrane lipids that were associated with changes expected during apoptosis.[195,202,205] The biochemical responses of insulin-sensitive and -resistant cells towards vanadate resulted in subtle changes in FTIR spectral bands and required multivariate methods of analysis to extract the information. Spectral features of adipocytes were dominated by lipid ester and fatty acid bands. Multivariate analysis revealed that the major changes were associated with lipid composition and corresponding changes in protein secondary structures. Since adipocytes are > 90% lipid

and fatty acid in composition,[16] changes in lipid biochemistry and lipotoxicity were expected to be the main drivers of biological changes induced by vanadate treatments.

The factorial experimental design used to evaluate treatments applied to adipocytes in four factors: glucose, fructose, vanadate and insulin-resistance revealed that glucose and fructose were metabolised differently by adipocytes. This was evidenced in multivariate spectral modelling that revealed fructose induced FFA synthesis and glucose induced TAG synthesis was consistent with the literature.[353] FTIR microspectroscopy showed that equal concentrations of glucose and fructose resulted in a decrease in glucose metabolism and an increase in fructose metabolism. Baena, *et al*.[453] reported that fructose impairs insulin signalling and also reduced GLUT4 levels in plasma membranes. The integrity of the plasma membrane was modelled as FTIR band shifts and intensity changes associated with plasma membrane lipids, fatty acids and lipoproteins.[195,205] Biochemical changes were observed mainly for fructose or vanadate treatments, consistent with induced oxidative stress, lipid peroxidation, membrane fluidity and other structural changes that influence the integrity of the cell membrane.[200]

The largest effects observed in FTIR spectra and the greatest separation between treatment blocks was apparent for insulin-resistant cells. Glucose treatment of insulin-resistant cells resulted in minimal glucose uptake and metabolism, whereas the combined glucose-fructose treatment improved cell growth, however, only small increases in lipid band intensities were observed, which indicated that while adipocytes were using fructose as an energy source, it was not being metabolised to the same extent as glucose in an insulin-sensitive state. When vanadate was added to the treatment regimen of sugar treated insulin-resistant adipocytes, it acted as an insulin-mimetic, to promote the uptake of glucose, as evidenced by TAG synthesis. In the presence of glucose alone, vanadate promoted higher TAG synthesis than the combined glucose-fructose treatment, again consistent with the observations made by Froesch and Ginsberg,[353] that fructose may decrease glucose metabolism in adipocytes.

The use of DoE systematically changed all treatment variables and provided interpretable results that were consistent with known actions of glucose, fructose and vanadate on adipocytes. Although the processing applied minimised spectral noise and improved interpretability, the high heterogeneity of adipocytes and the scattering artefacts generated result in the highest sources of variability being extracted into the first three components/factors of the PCA/PLS-DA model, respectively. It was possible that smaller, but important biochemical changes might be excluded using the simpler

processing methods and that these smaller biochemical changes were confounded with noise. Detailed studies incorporating correction procedures such as RMieS,[276-278] and ME-EMSC[275] will be further explored in future work on focussed data sets consisting of larger sample numbers to determine whether any improvements in regards to interpretability can be made.

The quantum cascade laser (QCL) based methods described in Section 7.2 provide a means of collecting more data in a shorter time frame. This will enable more comprehensive investigations to be performed on multiple cell cultures to better understand the inter and intra culture biochemical variability, particularly for the 3T3-L1 cell line, which showed that differences in FTIR spectra between insulin-sensitive and -resistant cells were only subtle. The results obtained and reported herein showed that FTIR microspectroscopy provided in-depth biochemical information on vanadate action. Future work is expected to provided further insights into variability between cell cultures.

7.1.4 FTIR Microspectroscopic Assessment of HepG2 Cells

Unlike the 3T3-L1 adipocyte cell line, which required differentiation from pre-adipocyte fibroblasts, HepG2 cells were cultured directly onto CaF_2 substrates, where control of the seeding rate and confluence allowed the use of the MTT cytotoxic assay to be performed with vanadate, cisplatin and doxorubicin. In this way, a direct comparison of the FTIR spectra acquired on single cells and the results from MTT assay curves could be made.

Excellent correlations were established between the multivariate models and the cytotoxicity MTT assay curves. However, the FTIR spectra not only modelled cell viability, but also provided deeper insights into simultaneous biochemical changes induced by the treatments that were not obtainable with MTT assays. Consistent with the literature, the combined multivariate model of vanadate, cisplatin and doxorubicin showed that the actions of cisplatin and doxorubicin were closer to each other than vanadate and were related to DNA changes, whereas the action of vanadate was characterised by changes in lipids and lipid peroxidation induced by oxidative stress. Vanadate also induced a wider range of systematic biochemical changes compared to the other treatments, as evidenced by the larger multivariate space these treatments occupied.

The MTT assay and multivariate model of vanadate action was described in three phases: growth, apoptotic changes and death, and fibrosis/phenotype changes in surviving cells. During the growth phase, low concentrations of vanadate promoted protein synthesis, possibly through activation of the mTOR/mTORC1 pathway and using amino acids from

cell media in preference to glucose to promote this growth.[399] As the vanadate concentration was increased, the growth phase transitioned to an apoptotic and cell death phase, consistent with vanadate changing to a cytotoxic agent. This phase was characterised by two dose-dependent biochemical processes: initial lipid accumulation followed by a transition to lipid depletion and lipid peroxidation. These changes were postulated to be the result of vanadate redox-cycling that generated higher levels of ROS to result in mitochondrial dysfunction, lipid peroxidation and apoptosis, as evidenced by changes in the FTIR spectra of membrane lipids and, in particular, the loss of cell membrane integrity.[195,202,205]

The third phase of vanadate action on HepG2 cells was postulated to result from one of two possibilities: the HepG2 cell culture was composed of a number of phenotypes, some more resistant to treatment than others, or surviving cells that underwent an epithelial to mesenchymal transition (EMT) as a response to harsh treatment conditions. It has been reported that cells that remain fixed to the substrate after treatment are the most resistant,[160] and may represent a phenotype that pre-existed in the main population that could only be detected after the harshest of treatments. The pre-existing phenotype postulate requires more investigation on multiple cultures using analysis of larger populations through the use of the new QCL systems, while the EMT transition is contradictory to the reported action of vanadate and its ability to inhibit EMT.[144,153] However, FTIR microspectroscopy showed that during the third phase of vanadate action, bands consistent with fibrosis were observed and biochemical processes similar to those that occur in neurodegenerative diseases may result from the breakdown of actin to produce stress fibrils and eventually lead to EMT.[349,412]

Investigation of optical micrographs acquired from HepG2 cells treated with increasing cytotoxic vanadate concentrations showed that the cell morphology rounded at lower cytotoxic doses, consistent with apoptosis,[327] until a point where those cells remaining displayed the typical stellated, fusiform morphology of mesenchymal cells.[374] Further experiments were performed on HepG2 cells treated with higher vanadate concentrations for 72 hr, where similar results were generated to the initial experiments. The cells that remained on the CaF_2 substrate were then re-proliferated in normal glucose-supplemented media and incubated for 72 hr. Evidence of re-proliferation was observed, even at 1000 μM V(V) where a possible mesenchymal to epithelial transition (MET) occurred that supported the initial EMT postulate, however, future work will investigate whether such EMT/MET transitions were occurring.

Extending the experimental design to include fructose treatments and using vanadate concentrations at the IC_{50} values and 50% of the IC_{50} value showed that non-vanadate treated cells separated from vanadate treated cells. At the IC_{50} value, vanadates cytotoxic effect was the most significant factor influencing cell viability (p = 0.002). An initial ANOVA showed that the linear model was not an appropriate fit to the data as evidenced by the significant curvature effect (p = 0.003). This effect was induced by the centre points of the design where [V(V)] was at 50% of the IC_{50} value. Consistent with the observations made in the initial vanadate growth phase model, vanadate was promoting cell viability in the presence of both glucose and fructose and this was associated with increased protein synthesis.

An important outcome of this observation for both 3T3-L1 and HepG2 cells was the dichotomy of concentration. Low concentrations of vanadate promoted cellular growth in adipocytes and HepG2 cells, therefore, concentrations used in trials to treat insulin-resistance/T2DM can promote cancer growth and *vice versa*, cytotoxic concentrations of vanadate used to treat cancers could also be detrimental to normal glucose uptake in adipocytes. The heterogeneity of the HepG2 cell populations could also confound the concentration situation further as the treatment resistant cells could re-proliferate after treatment is completed. The damage done to other cell types may compromise an individual's immune system, thus making them more susceptible to the detrimental effects of cancer re-proliferation. However, when considered *in vivo*, the positive effects of vanadate on immune system activation to promote cancer cell death must be considered.[102,105]

Multivariate modelling of FTIR spectra obtained from performing the DoE protocol produced results consistent with the ANOVA model of cell viability. A combined model of vanadate-treated vs. non-treated cells showed two clusters in multivariate space. The cluster defined by the vanadate treatments was more variable compared to the non-vanadate treatments consistent with the observation made when vanadate was compared to cisplatin and doxorubicin treatments. This was attributed to the action of vanadate inducing highly diverse biochemical changes related to increased lipid synthesis in HepG2 cells induced by oxidative stress.[454] The non-vanadate treated cells clustered tighter compared to those treated with vanadate and the multivariate model showed that HepG2 cells could equally use fructose or glucose as a source of energy. Combined glucose-fructose treatment led to less utilisation of both sugars; however, this effect was

small compared to the overall effect of vanadate, that induced apoptotic pathways at the IC_{50} value.

The combined fructose-vanadate treatment induced the most variability as evidenced in the ANOVA assessment of cell viability and the multivariate models. As cancer cells are already in a high state of oxidative stress,[147] the effect of vanadate was to induce further stress through the generation of ROS. Fructose is also known to induce higher levels of oxidative stress in cells through the promotion of protein synthesis and DNL[20] and, therefore, can contribute further to lowering cell viability. However, it was observed that in approximately half of the replicate cells, increased cell viability resulted. This was explained by considering that vanadate was at its IC_{50} value and statistically, was expected to result in 50% cell death. Fructose would be expected to further contribute to cell death due to increased oxidative stress. Therefore, the increased viability observed for this treatment was postulated to result from a population of cells displaying higher resistance and may further support EMT occurring. This may also be a result of fructose being metabolised in a different manner to glucose, such that HepG2 cells may be utilising a pathway that induces a change to a mesenchymal phenotype for survival. Alternatively, a highly resistant phenotype already existed in the cell culture, to result in higher observed overall cell viability. In the non-vanadate treated cells, fructose also showed the highest variability in cell viability, which was consistent with its ability to increase cellular oxidative stress and may result in cells inducing other pathways in an attempt to reduce increased stresses. Future work will be performed to investigate these observations further.

A similar cytotoxicity investigation (not reported in the current study) to the one on HepG2 cells was also performed using the MCF-7 epithelial breast cancer cell line.[455] The chemometric models developed on vanadate treated cells showed a dose-dependent relationship with cell viability and results were consistent with standard cytotoxic assays. The DoE used for the HepG2 cell line was also performed on the MCF-7 cell line, where the effects of fructose and vanadate were found to induce apoptotic pathways. These results will be published in a peer reviewed journal in the near future.

Interestingly, the MCF-7 cell line was highly resistant to the cytotoxic effects of vanadate with an IC_{50} value estimated ~500 μM. It was also observed that fructose was cytotoxic towards MCF-7 cells and these finding will be further elaborated on in future work.

7.1.5 FPA Hyperspectral Image Analysis of 3T3-L1 Adipocytes

These experiments were performed using a laboratory-based Globar® FTIR microscope to investigate any trends observed between cells for the entire treatment protocol. Single cells were selected based on visual morphological qualities and the number of multilocular structures in the cell. Image data (64×64 FPA detector, resulting in 4096 spectra per image) were assessed by PCA in hyperspectral image analysis (HIA) mode. The full FoV PCA scores (associated with the pixels in the 64×64 array) were a combination of the region of interest and the clutter not related to the ROI. The use of masking allowed the ROI to be assessed free from clutter.

For the laboratory-based FPA images, Savitzky-Golay second derivatives followed by SNV over the regions of spectral importance resulted in three-PC models that described >90% of the spectral **X**-variance. Interestingly, the individual PCs described specific cell morphologies for all treated cells, such that the first PC always described the difference in biochemical composition of the cell interior compared to the cell perimeter. The cell perimeter was always characterised by fatty acid bands while the cell interior was described by lipid ester bands. Therefore, PC1 was interpreted to be a contrasting PC describing the major differences between interior biochemistry and biochemistry of the cell interface where it interacts with its external environment. Despite the dominance of the first two PCs describing the majority of the biochemical variability, higher PCs also provided biochemical information, although they only explained a small amount of the total **X**-variance. These higher PCs were describing subtle changes that will be investigated in future work, along with the use of model-based processing methods to further minimise the effects of light scattering.

The second PC always described compartments within the adipocytes mainly related to large lipid droplets, observed in the optical images of the cells. In many of the cells, FTIR spectroscopy revealed that the majority of the droplets consisted of lipid esters, however, one of the droplets tended to be fatty acid in content. This was consistent with the lipid droplets being unique organelles in adipocytes where some act in a storage capacity, while others provided energy reserves directly to other organelles.[152,456] It has been reported that lipid droplets in close proximity to the mitochondria may provide a source of fatty acids for β-oxidation, used as an energy supply to the cell,[152] and possibly related to changes observed in the PC3 direction of most cell images analysed. The second PC also described changes in secondary protein structures in some cells, however, the third PC showed contributions that were more protein in character, while still maintaining a high

level of lipid character. In some cases, co-localisation of protein and lipids indicated the location of specific organelles in the cell, such as the nucleus or endoplasmic reticulum (ER). To further verify the findings of the single cell FPA experiments, future work requires imaging of a larger number of cells over multiple cultures to determine whether consistent results can be obtained.

The four-beam synchrotron study was used evaluate its feasibility for single adipocyte imaging and to better understand the effects of substrate thickness on the spectral range, including an investigation of aberrations present in the images. As was the case with the laboratory-based FPA image analyses, the first two PCs in the synchrotron FPA images highlighted the contrasts between the cell perimeter and interior, and the compartmentalisation within the cells, respectively. While some improvements in image quality may have resulted, the four-beam system did not represent a major improvement when compared to the Globar® FPA images and aberrations were introduced into the images as a result of the overlap of multiple beam spots. These aberrations were also enhanced with increasing CaF_2 substrate thickness, but further optimisation may be possible.

7.2 Future Work

The comprehensive optimisation of spectral data acquisition parameters and application of these optimised settings to challenging cell lines using a systematic design of experiments (DoE) approach led to a large amount of information-rich data that required multivariate approaches to interpret. Compared to univariate approaches, the multivariate approach provided greater insights into the data, however, even in such a comprehensive study, the number of single point spectra of individual cells acquired was small. While the DoE approach provides a large number of overall samples, future studies will aim at more focussed assessments of the blocks within a design where larger numbers of replicate spectra per treatment will be collected over multiple cultures.

Time and resources were the limiting factors behind the generation of larger sets and while a more focussed study may have resulted in more information on one aspect of this study, the numerous experiments performed were based on equipment availability and the amount of time that could be spent in a session to collect data. Even with the faster FPA systems used for data acquisition, the collection of larger data sets could add months onto an investigation. New technologies based on quantum cascade lasers (QCLs) represent a major time advantage over standard FPA-based FTIR imaging systems.[221]

QCL microscopes, do not use cryogenically cooled detectors, thus the limitation of time and human intervention is reduced when large sample areas (of the order of cm^2) are measured at pixel sizes of the order of $1.36 \times 1.36\ \mu m^2$.[221] Therefore, samples of the size of standard microscope slides used in histology can be imaged in less than 1 hr to result in the acquisition of spectra over a wide range of spatially different cell colonies and using hyperspectral analysis software, regions of interest can be selected, extracted, averaged and analysed in a much more efficient manner compared to the methods used in the current study.

QCL system also have their disadvantages, including aberrations induced by the laser and the need for multiple laser systems to cover the complete 3000-1000 cm^{-1} region.[221] Even taking these limitations into consideration, the 1800-1000 cm^{-1} region is still capable of extracting relevant biochemical information from such samples,[214] even though information on lipid peroxidation may be lost. Complimentary information from Raman spectroscopy could also be generated and compared with the information obtained from the QCL system and through the use of image registration techniques, multimodal hyperspectral data analysis may reveal even more detail compared to one technology alone. This includes new Raman-based instrumentation designed to rapidly image cell cultures grown in 96-well plates.

The MCF-7 study performed using glucose, fructose and vanadate treatments will be investigated further using the QCL and Raman imaging systems. The results obtained from the cytotoxicity and DoE studies performed on MCF-7 will be compared to the HepG2 results to determine whether there were any similarities between the cell lines with respect to the action of sugars and vanadate.

The principle of parsimony holds in the development of multivariate models,[223] where the simplest processing methods often lead to the simplest multivariate models. In the current study, simple derivative and normalisation techniques resulted in widely interpretable models in three PCs/Factors or less. New and old methods based on QCLs and synchrotron beams, respectively, can introduce Mie scattering effects that occur when the wavelength of the incident radiation is similar to, or substantially less than the size or morphological features on the surface of the object being measured.[276] To minimise the effects of Mie scattering, the resonant Mie scattering (RMieS) and the Mie extinction extended multiplicative scatter correction (ME-EMSC) algorithms are model based correction techniques that incorporate the physics of scattering phenomena to correct for

artefacts not related to biochemistry.[275-277] Future work with experts in the ME-EMSC algorithm may result in corrections that better partition the large variances described by the PC1 direction using simple processing methods into directions that reveal an even more diverse biochemistry in the cells.

With regard to the spectral cut off of CaF_2 substrates, future work will concentrate on 0.2 mm thick CaF_2 or silicon nitride (Si_3N_4) substrates in combination with condenser defocussing to improve the energy throughput in the 1000-750 cm^{-1} region. This region may reveal more information on carbohydrates and DNA structures in the treated cells. Due to the fragility of the 3T3-L1 cell line to chemical fixation protocols,[201,457] a comparison of the cold-methanol vs. paraformaldehyde fixation methods will be investigated in detail to assess the impact cell fixation has on adipocytes. Live cell techniques offer the best approach to investigating cell treatments, however, due to the thickness of adipocytes, the two plate live cell incubators used in conventional FTIR microspectroscopic set ups resulted in transmission pathlengths that were too long for full range spectral data acquisition and the thickness of the substrates used result in chromatic aberrations, which were confounded with the spectra and cannot be modelled out using chemometric techniques.[215] These issues may be resolved using the live cell incubator set ups used with Raman and QCL systems that do not require a top substrate to enclose the chamber and can be used to collect a wider range of cells compared to focussing on a single cell in conventional live cell imaging set ups.

The investigation of biochemical changes induced by treatments on entire cells represents only one aspect of better understanding of disease pathologies. Therefore, as part of the current study, initial work was performed on characterising extracellular vesicles (EVs), in particular microvesicles (MVs), which are produced by all mammalian cells under normal physiological conditions by outward budding from the plasma membrane and carry many of the characteristics of the cell from which they originated.[458] MVs have a typical size range between 100 nm to 1 μm,[459] making them small enough to interact with the membrane of host cells and under conditions of inflammation, infectious diseases, etc., the population of MVs changes where different components of the population can have either protective effects or contribute to disease pathologies.[222]

Recent technological advances have resulted in the combination of high spatial resolution methods such as atomic force microscopy (AFM) and high precision tuneable lasers in both Raman[460] and infrared spectroscopy.[461] Optical diffraction limits the spatial

resolution achievable to $\lambda/2$ where λ is the incident wavelength. In the 3000-1000 cm^{-1} range, this limits the theoretical spatial resolution achievable between 3.3-10 μm, with some reports of 1 μm spatial resolution using a thermal source.[286] In contrast, AFM has a spatial resolution limited by the size of the tip used to measure the sample and can achieve resolutions of 20 nm or less.[222] By itself, AFM measures topology and cannot produce detailed chemical information from the interior of the samples, therefore, by focussing the output of a tuneable QCL onto an AFM tip, the tip acts as the IR detector (through the process of thermal expansion). These expansions are transmitted as oscillations through the cantilever of the AFM tip and when measured as a function of wavelength, can readily generate a MIR absorbance spectrum.[461] These instruments can be configured using a tuneable laser to exact band frequencies, e.g., the 1654 cm^{-1} band where a map of the amide I content over the surface of the sample can be generated, or the QCL can be used to perform spectroscopy over specific wavenumber regions.

The high spatial resolution compared to conventional and SR-FTIR instruments means that higher resolution images of entire cells is possible with spatial resolution 1000 times less than the diffraction limit.[222] This is highly important for assessing MVs as they are typically smaller than the diffraction limit of synchrotron-based systems. To overcome the disadvantage of the AFM-IR method being a topological method, instrument setups for AFM-IR are available that allow it to run in photothermal mode that allows samples to be measured in transmission mode, however, in this mode, spatial resolution is slightly reduced.[462]

Figure 7.1 provides a preliminary AFM image and replicated spectra taken from the surface of a MV extracted from a sugar treated 3T3-L1 adipocyte. The size of the vesicle was ~200 nm and appeared to be spherical in shape. The main spectral band at 1515 cm^{-1} was attributed to surface active tyrosine kinases,[206] which are known to be part of the cargo of MVs,[463] and would be expected to be a surface active kinase associated with cell signalling.[464] The bands at 1578 and 1610 cm^{-1} were assigned to the imidazole rings of DNA and RNA and RNA is also known to be part of the cargo of MVs.[465]

Future work will aim to characterise MVs in 3T3-L1 adipocytes extracted after performing the DoE protocol of glucose, fructose and vanadate treatments on insulin-sensitive and -resistant cells. The extracted MVs will then be co-cultured with adipocytes, and other cell lines, grown in normal glucose supplemented media to investigate whether

they induce any biochemical changes using QCL, Raman and conventional FPA FTIR microspectroscopy.

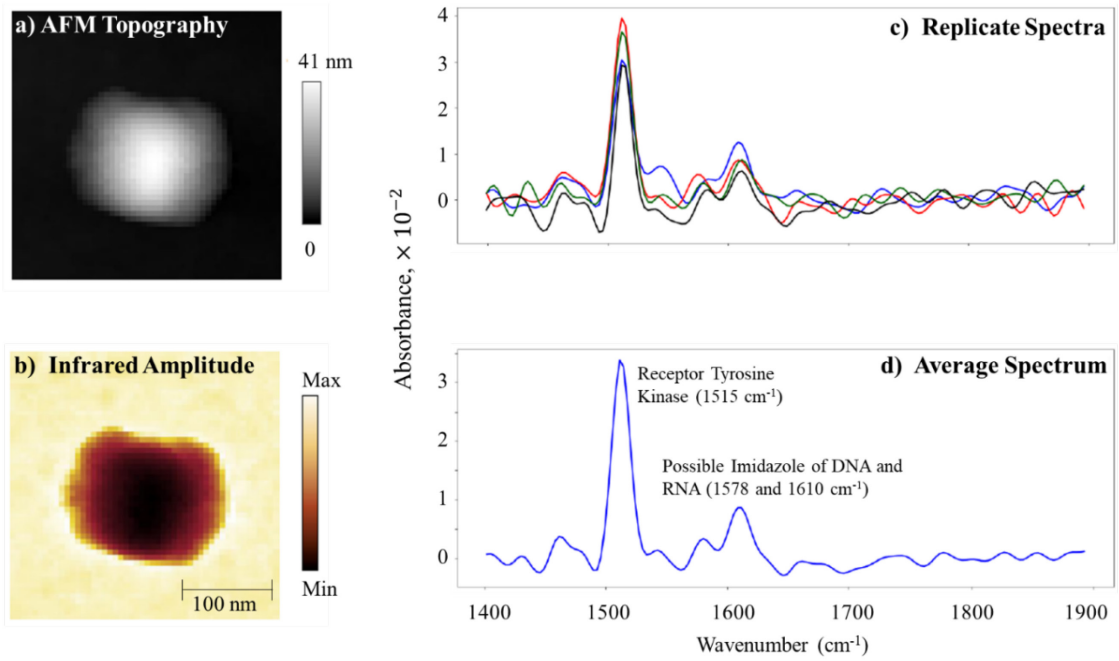

Figure 7.1: Preliminary AFM-IR images and spectra collected from an MV extracted from a sugar treated 3T3-L1 adipocyte; a) AFM topographic image; b) infrared intensity map; c) spectra collected from four locations on the vesicle and; d) the average spectrum of the four positions. Data courtesy of Dr Adrian Cernescu, NeaSpec GmbH.

This current study provided evidence that the combination of optimised FTIR data acquisition parameters and the use of rational designed experiments applied to treated biological cells can reveal deeper insights into the biochemical pathways induced when cells were treated with sugars and vanadate. Biological assays and methods are notorious for generating data of high variability due to the natural variations in cell cultures and their inherent heterogeneity. Although the results generated in this study were based on small sample numbers, they provided data that could be interpreted based on known biochemical pathways, but most importantly, the multivariate analysis of the spectral data revealed that concurrent processes were occurring that cannot be detected using the univariate bioassay methods.

Image analysis also revealed common phenomena were occurring in single cells when treated using the designed experiment approach. Limitations of the instrumentation used to acquire data in this study restricted the samples sizes required for such a comprehensive study and resolution of these limitations will now form the focus of future work using QCL systems.

References

1. Gillespie, D., *Sweet poison : why sugar makes us fat / David Gillespie*. Viking, an imprint of Penguin Books: Camberwell, Vic, 2008.
2. Gross, L. S.; Li, L.; Ford, E. S.; Liu, S., Increased consumption of refined carbohydrates and the epidemic of type 2 diabetes in the United States: an ecologic assessment. *The American Journal of Clinical Nutrition* **2004,** *79* (5), 774-779.
3. Lyssiotis, C. A.; Cantley, L. C., F stands for fructose and fat. *Nature* **2013,** *502* (7470), 181-182.
4. Goran, M.; Ulijaszek, S.; Ventura, E., High fructose corn syrup and diabetes prevalence: A global perspective. *Global Public Health* **2013,** *8*, 55 - 64.
5. Nutrition Australia Fructose. https://paulyeatman.net.au/wp-content/uploads/2013/08/Fructose-_-Nutrition-Australia.pdf.
6. Lanaspa, M. A.; Ishimoto, T.; Li, N.; Cicerchi, C.; Orlicky, D. J.; Ruzycki, P.; Rivard, C.; Inaba, S.; Roncal-Jimenez, C. A.; Bales, E. S.; Diggle, C. P.; Asipu, A.; Petrash, J. M.; Kosugi, T.; Maruyama, S.; Sanchez-Lozada, L. G.; McManaman, J. L.; Bonthron, D. T.; Sautin, Y. Y.; Johnson, R. J., Endogenous fructose production and metabolism in the liver contributes to the development of metabolic syndrome. *Nature Communications* **2013,** *4* (1), 2434.
7. Dolan, L. C.; Potter, S. M.; Burdock, G. A., Evidence-Based Review on the Effect of Normal Dietary Consumption of Fructose on Development of Hyperlipidemia and Obesity in Healthy, Normal Weight Individuals. *Critical Reviews in Food Science and Nutrition* **2009,** *50* (1), 53-84.
8. Douard, V.; Ferraris, R. P., Regulation of the fructose transporter GLUT5 in health and disease. *American Journal of Physiology-Endocrinology and Metabolism* **2008,** *295* (2), E227-E237.
9. Reaven, G., The metabolic syndrome or the insulin resistance syndrome? Different names, different concepts, and different goals. *Endocrinology and Metabolism Clinics of North America* **2004,** *33* (2), 283-303.
10. Tran, L. T.; Yuen, V. G.; McNeill, J. H., The fructose-fed rat: a review on the mechanisms of fructose-induced insulin resistance and hypertension. *Molecular and Cellular Biochemistry* **2009,** *332* (1), 145-159.
11. Mayes, P. A., Intermediary metabolism of fructose. *The American Journal of Clinical Nutrition* **1993,** *58* (5), 754S-765S.
12. Nelson, D. L., *Lehninger principles of biochemistry*. 6 ed.; Sixth edition. New York : W.H. Freeman, 2013.: 2013.

13. Bryant, N. J.; Govers, R.; James, D. E., Regulated transport of the glucose transporter GLUT4. *Nature Reviews Molecular Cell Biology* **2002,** *3* (4), 267-277.
14. Klip, A.; McGraw, T. E.; James, D. E., Thirty sweet years of GLUT4. *Journal of Biological Chemistry* **2019,** *294* (30), 11369-11381.
15. Oh, W.; Abu-Elheiga, L.; Kordari, P.; Gu, Z.; Shaikenov, T.; Chirala, S. S.; Wakil, S. J., Glucose and fat metabolism in adipose tissue of acetyl-CoA carboxylase 2 knockout mice. *Proc Natl Acad Sci U S A* **2005,** *102* (5), 1384.
16. Frühbeck, G., Overview of Adipose Tissue and Its Role in Obesity and Metabolic Disorders. In *Adipose Tissue Protocols*, Yang, K., Ed. Humana Press: Totowa, NJ, 2008; pp 1-22.
17. Pradhan, G.; Samson, S. L.; Sun, Y., Ghrelin: much more than a hunger hormone. *Curr Opin Clin Nutr Metab Care* **2013,** *16* (6), 619-624.
18. Frederich, R. C.; Löllmann, B.; Hamann, A.; Napolitano-Rosen, A.; Kahn, B. B.; Lowell, B. B.; Flier, J. S., Expression of ob mRNA and its encoded protein in rodents. Impact of nutrition and obesity. *J Clin Invest* **1995,** *96* (3), 1658-1663.
19. Kelesidis, T.; Kelesidis, I.; Chou, S.; Mantzoros, C. S., Narrative review: the role of leptin in human physiology: emerging clinical applications. *Ann Intern Med* **2010,** *152* (2), 93-100.
20. Port, A. M.; Ruth, M. R.; Istfan, N. W., Fructose consumption and cancer: is there a connection? *Current opinion in endocrinology, diabetes, and obesity* **2012,** *19* (5), 367-74.
21. Kolaczynski, J. W.; Ohannesian, J. P.; Considine, R. V.; Marco, C. C.; Caro, J. F., Response of leptin to short-term and prolonged overfeeding in humans. *The Journal of Clinical Endocrinology & Metabolism* **1996,** *81* (11), 4162-4165.
22. Wang, J.; Obici, S.; Morgan, K.; Barzilai, N.; Feng, Z.; Rossetti, L., Overfeeding Rapidly Induces Leptin and Insulin Resistance. *Diabetes* **2001,** *50* (12), 2786.
23. Considine, R. V.; Caro, J. F.; Considine, E. L.; Williams, C. J.; Hyde, T. M., Identification of Incidental Sequence Polymorphisms and Absence of the db/db Mouse and fa/fa Rat Mutations. *Diabetes* **1996,** *45* (7), 992.
24. Riby, J. E.; Fujisawa, T.; Kretchmer, N., Fructose absorption. *The American Journal of Clinical Nutrition* **1993,** *58* (5), 748S-753S.
25. Babish, J. G.; Pacioretty, L. M.; Bland, J. S.; Minich, D. M.; Hu, J.; Tripp, M. L., Antidiabetic screening of commercial botanical products in 3T3-L1 adipocytes and db/db mice. *J Med Food* **2010,** *13* (3), 535-547.

26. Muir, L. A.; Neeley, C. K.; Meyer, K. A.; Baker, N. A.; Brosius, A. M.; Washabaugh, A. R.; Varban, O. A.; Finks, J. F.; Zamarron, B. F.; Flesher, C. G.; Chang, J. S.; DelProposto, J. B.; Geletka, L.; Martinez-Santibanez, G.; Kaciroti, N.; Lumeng, C. N.; O'Rourke, R. W., Adipose tissue fibrosis, hypertrophy, and hyperplasia: Correlations with diabetes in human obesity. *Obesity (Silver Spring)* **2016,** *24* (3), 597-605.
27. Hajduch, E.; Darakhshan, F.; Hundal, H. S., Fructose uptake in rat adipocytes: GLUT5 expression and the effects of streptozotocin-induced diabetes. *Diabetologia* **1998,** *41* (7), 821-828.
28. Stuart Wood, I.; Wang, B.; Lorente-Cebrián, S.; Trayhurn, P., Hypoxia increases expression of selective facilitative glucose transporters (GLUT) and 2-deoxy-d-glucose uptake in human adipocytes. *Biochemical and Biophysical Research Communications* **2007,** *361* (2), 468-473.
29. Abdelmalek, M. F.; Lazo, M.; Horska, A.; Bonekamp, S.; Lipkin, E. W.; Balasubramanyam, A.; Bantle, J. P.; Johnson, R. J.; Diehl, A. M.; Clark, J. M., Higher dietary fructose is associated with impaired hepatic adenosine triphosphate homeostasis in obese individuals with type 2 diabetes. *Hepatology* **2012,** *56* (3), 952-960.
30. Frühbeck, G.; Gomez-Ambrosi, J.; Muruzabal, F.; Burrell, M., The adipocyte: A model for integration of endocrine and metabolic signaling in energy metabolism regulation. *American journal of physiology. Endocrinology and metabolism* **2001,** *280*, E827-47.
31. Brand-Miller, J. C.; Holt, S. H.; Pawlak, D. B.; McMillan, J., Glycemic index and obesity. *The American Journal of Clinical Nutrition* **2002,** *76* (1), 281S-285S.
32. Stenkula, K. G.; Erlanson-Albertsson, C., Adipose cell size: importance in health and disease. *American Journal of Physiology-Regulatory, Integrative and Comparative Physiology* **2018,** *315* (2), R284-R295.
33. Hannou, S. A.; Haslam, D. E.; McKeown, N. M.; Herman, M. A., Fructose metabolism and metabolic disease. *J Clin Invest* **2018,** *128* (2), 545-555.
34. Le, M. T.; Frye, R. F.; Rivard, C. J.; Cheng, J.; McFann, K. K.; Segal, M. S.; Johnson, R. J.; Johnson, J. A., Effects of high-fructose corn syrup and sucrose on the pharmacokinetics of fructose and acute metabolic and hemodynamic responses in healthy subjects. *Metabolism: clinical and experimental* **2012,** *61* (5), 641-651.

35. Teff, K. L.; Grudziak, J.; Townsend, R. R.; Dunn, T. N.; Grant, R. W.; Adams, S. H.; Keim, N. L.; Cummings, B. P.; Stanhope, K. L.; Havel, P. J., Endocrine and Metabolic Effects of Consuming Fructose- and Glucose-Sweetened Beverages with Meals in Obese Men and Women: Influence of Insulin Resistance on Plasma Triglyceride Responses. *The Journal of Clinical Endocrinology & Metabolism* **2009,** *94* (5), 1562-1569.
36. Afzali, A.; Weiss, N. S.; Boyko, E. J.; Ioannou, G. N., Association between serum uric acid level and chronic liver disease in the United States. *Hepatology* **2010,** *52* (2), 578-589.
37. Stanhope, K. L.; Schwarz, J. M.; Keim, N. L.; Griffen, S. C.; Bremer, A. A.; Graham, J. L.; Hatcher, B.; Cox, C. L.; Dyachenko, A.; Zhang, W.; McGahan, J. P.; Seibert, A.; Krauss, R. M.; Chiu, S.; Schaefer, E. J.; Ai, M.; Otokozawa, S.; Nakajima, K.; Nakano, T.; Beysen, C.; Hellerstein, M. K.; Berglund, L.; Havel, P. J., Consuming fructose-sweetened, not glucose-sweetened, beverages increases visceral adiposity and lipids and decreases insulin sensitivity in overweight/obese humans. *Journal of Clinical Investigation* **2009,** *119* (5), 1322-34.
38. Islam, A.; Civitarese, A. E.; Hesslink, R. L.; Gallaher, D. D., Viscous Dietary Fiber Reduces Adiposity and Plasma Leptin and Increases Muscle Expression of Fat Oxidation Genes in Rats. *Obesity* **2012,** *20* (2), 349-355.
39. Johnson, R. J.; Perez-Pozo, S. E.; Sautin, Y. Y.; Manitius, J.; Sanchez-Lozada, L. G.; Feig, D. I.; Shafiu, M.; Segal, M.; Glassock, R. J.; Shimada, M.; Roncal, C.; Nakagawa, T., Hypothesis: Could Excessive Fructose Intake and Uric Acid Cause Type 2 Diabetes? *Endocrine Reviews* **2009,** *30* (1), 96-116.
40. World Health Organisation Diabetes. https://www.who.int/health-topics/diabetes#tab=tab_1.
41. International Diabetes Foundation Type-2 Diabetes. https://www.idf.org/aboutdiabetes/type-2-diabetes.html.
42. Walker, R. W.; Dumke, K. A.; Goran, M. I., Fructose content in popular beverages made with and without high-fructose corn syrup. *Nutrition* **2014,** *30* (7), 928-935.
43. Peretti, J., Fat profits: how the food industry cashed in on obesity. *The Guardian* 2013.
44. Dean, S., Children of the Corn Syrup. *The Believer* 2003.
45. Davy, B. M.; Melby, C. L., The effect of fiber-rich carbohydrates on features of Syndrome X. *Journal of the American Dietetic Association* **2003,** *103* (1), 86-96.
46. Wilcox, G., Insulin and insulin resistance. *Clin Biochem Rev* **2005,** *26* (2), 19-39.

47. Taylor, R., Type 2 Diabetes. *Etiology and reversibility* **2013,** *36* (4), 1047-1055.
48. Eiselein, L.; Schwartz, H. J.; Rutledge, J. C., The Challenge of Type 1 Diabetes Mellitus. *ILAR Journal* **2004,** *45* (3), 231-236.
49. Martín-Timón, I.; Sevillano-Collantes, C.; Segura-Galindo, A.; Del Cañizo-Gómez, F. J., Type 2 diabetes and cardiovascular disease: Have all risk factors the same strength? *World J Diabetes* **2014,** *5* (4), 444-470.
50. Singleton, J. R.; Smith, A. G.; Russell, J. W.; Feldman, E. L., Microvascular Complications of Impaired Glucose Tolerance. *Diabetes* **2003,** *52* (12), 2867.
51. Campfield, L. A.; Smith, F. J.; Guisez, Y.; Devos, R.; Burn, P., Recombinant mouse OB protein: evidence for a peripheral signal linking adiposity and central neural networks. *Science* **1995,** *269* (5223), 546.
52. Weinhouse, S.; Warburg, O.; Burk, D.; Schade, A. L., On Respiratory Impairment in Cancer Cells. *Science* **1956,** *124* (3215), 267.
53. Uebelhoer, M.; Iruela-Arispe, L., Cross-talk between signaling and metabolism in the vasculature. *Vascular Pharmacology* **2016,** *83*.
54. Inoue, Y.; Tsukamoto, Y.; Yamanaka, M.; Nakamura, S.; Inoue, A.; Nishino, N.; Kawahara, H., Efficient production of recombinant IgG by metabolic control and co-expression with GLUT5 in a fructose-based medium. *Cytotechnology* **2010,** *62* (4), 301-306.
55. Petch, D.; Butler, M., The effect of alternative carbohydrates on the growth and antibody production of a murine hybridoma. *Applied Biochemistry and Biotechnology* **1996,** *59* (1), 93-104.
56. Stuart, C. A.; Howell, M. E. A.; Yin, D., Overexpression of GLUT5 in Diabetic Muscle Is Reversed by Pioglitazone. *Diabetes Care* **2007,** *30* (4), 925.
57. Takeuchi, M.; Iwaki, M.; Takino, J.-i.; Shirai, H.; Kawakami, M.; Bucala, R.; Yamagishi, S.-i., Immunological detection of fructose-derived advanced glycation end-products. *Laboratory Investigation* **2010,** *90* (7), 1117-1127.
58. Cheng, Z.; Tseng, Y.; White, M. F., Insulin signaling meets mitochondria in metabolism. *Trends Endocrinol Metab* **2010,** *21* (10), 589-598.
59. Bezerra, R. n. M. N.; Ueno, M.; Silva, M. S.; Tavares, D. Q.; Carvalho, C. R. O.; Saad, M. r. J. A., A High Fructose Diet Affects the Early Steps of Insulin Action in Muscle and Liver of Rats. *The Journal of Nutrition* **2000,** *130* (6), 1531-1535.
60. Saltiel, A. R.; Kahn, C. R., Insulin signalling and the regulation of glucose and lipid metabolism. *Nature* **2001,** *414* (6865), 799-806.

61. Higashiura, K.; Ura, N.; Takada, T.; Li, Y.; Torii, T.; Togashi, N.; Takada, M.; Takizawa, H.; Shimamoto, K., The effects of an angiotensin-converting enzyme inhibitor and an angiotensin II receptor antagonist on insulin resistance in fructose-fed rats. *American Journal of Hypertension* **2000,** *13* (3), 290-297.

62. Jiang, G.; Zhang, B. B., Glucagon and regulation of glucose metabolism. *American Journal of Physiology-Endocrinology and Metabolism* **2003,** *284* (4), E671-E678.

63. Saltiel, A. R.; Pessin, J. E., Insulin Signaling in Microdomains of the Plasma Membrane. *Traffic* **2003,** *4* (11), 711-716.

64. Amery, C. M.; Nattrass, M., Fatty acids and insulin secretion. *Diabetes, Obesity and Metabolism* **2000,** *2* (4), 213-221.

65. Wheatcroft, S. B.; Williams, I. L.; Shah, A. M.; Kearney, M. T., Pathophysiological implications of insulin resistance on vascular endothelial function. *Diabetic Medicine* **2003,** *20* (4), 255-268.

66. Teff, K. L.; Elliott, S. S.; Tschöp, M.; Kieffer, T. J.; Rader, D.; Heiman, M.; Townsend, R. R.; Keim, N. L.; D'Alessio, D.; Havel, P. J., Dietary Fructose Reduces Circulating Insulin and Leptin, Attenuates Postprandial Suppression of Ghrelin, and Increases Triglycerides in Women. *The Journal of Clinical Endocrinology & Metabolism* **2004,** *89* (6), 2963-2972.

67. Masharani, U.; German, M. S., Pancreatic Hormones and Diabetes Mellitus. In *Greenspan's Basic & Clinical Endocrinology, 10e*, Gardner, D. G.; Shoback, D., Eds. McGraw-Hill Education: New York, NY, 2017.

68. Smith, U.; Axelsen, M.; Carvalho, E.; Eliasson, B.; Jansson, P. A.; Wesslau, C., Insulin signaling and action in fat cells: associations with insulin resistance and type 2 diabetes. *Ann N Y Acad Sci* **1999,** *892*, 119-126.

69. Dresner, A.; Laurent, D.; Marcucci, M.; Griffin, M. E.; Dufour, S.; Cline, G. W.; Slezak, L. A.; Andersen, D. K.; Hundal, R. S.; Rothman, D. L.; Petersen, K. F.; Shulman, G. I., Effects of free fatty acids on glucose transport and IRS-1-associated phosphatidylinositol 3-kinase activity. *J Clin Invest* **1999,** *103* (2), 253-259.

70. Axelsen, M.; Smith, U.; Eriksson, J. W.; Taskinen, M.-R.; Jansson, P.-A., Postprandial Hypertriglyceridemia and Insulin Resistance in Normoglycemic First-Degree Relatives of Patients with Type 2 Diabetes. *Ann Intern Med* **1999,** *131* (1), 27-31.

71. Zhou, G.; Myers, R.; Li, Y.; Chen, Y.; Shen, X.; Fenyk-Melody, J.; Wu, M.; Ventre, J.; Doebber, T.; Fujii, N.; Musi, N.; Hirshman, M. F.; Goodyear, L. J.; Moller, D. E., Role of AMP-activated protein kinase in mechanism of metformin action. *J Clin Invest* **2001,** *108* (8), 1167-1174.

72. Kahn, C. R.; Chen, L.; Cohen, S. E., Unraveling the mechanism of action of thiazolidinediones. *J Clin Invest* **2000,** *106* (11), 1305-1307.

73. Bhanot, S.; McNeill, J. H.; Bryer-Ash, M., Vanadyl sulfate prevents fructose-induced hyperinsulinemia and hypertension in rats. *Hypertension* **1994,** *23* (3), 308-312.

74. Pinkney, J. H.; Stehouwer, C. D. A.; Coppack, S. W.; Yudkin, J. S., Endothelial dysfunction: Cause of the insulin resistance syndrome. *Diabetes* **1997,** *46*, S9-13.

75. Ishibashi, K.-i.; Imamura, T.; Sharma, P.; Huang, J.; Ugi, S.; Olefsky, J., Chronic endothelin-1 treatment leads to heterologous desensitization of insulin signaling in 3T3-L1 adipocytes. *J Clin Invest* **2001,** *107*, 1193-202.

76. Mérial-Kieny, C.; Lonchampt, M.; Cogé, F.; Verwaerde, P.; Galizzi, J.-P.; Boutin, J. A.; Lafontan, M.; Levens, N.; Galitzky, J.; Félétou, M., Endothelin-1 inhibits TNF alpha-induced iNOS expression in 3T3-F442A adipocytes. *Br J Pharmacol* **2003,** *139* (5), 935-944.

77. Wilkes, J. J.; Hevener, A.; Olefsky, J., Chronic Endothelin-1 Treatment Leads to Insulin Resistance In Vivo. *Diabetes* **2003,** *52* (8), 1904.

78. Iyer, S. N.; Katovich, M. J., Effect of Acute and Chronic Losartan Treatment on Glucose Tolerance and Insulin Sensitivity in Fructose-Fed Rats*. *American Journal of Hypertension* **1996,** *9* (7), 662-668.

79. Rees, D. D.; Palmer, R. M.; Moncada, S., Role of endothelium-derived nitric oxide in the regulation of blood pressure. *Proc Natl Acad Sci U S A* **1989,** *86* (9), 3375-3378.

80. Nakagawa, T.; Tuttle, K. R.; Short, R. A.; Johnson, R. J., Hypothesis: fructose-induced hyperuricemia as a causal mechanism for the epidemic of the metabolic syndrome. *Nature Clinical Practice Nephrology* **2005,** *1* (2), 80-86.

81. Paolisso, G.; D'Amore, A.; Volpe, C.; Balbi, V.; Saccomanno, F.; Galzerano, D.; Giugliano, D.; Varricchio, M.; D'Onofrio, F., Evidence for a relationship between oxidative stress and insulin action in non-insulin-dependent (type II) diabetic patients. *Metabolism* **1994,** *43* (11), 1426-1429.

82. Rudich, A.; Tirosh, A.; Potashnik, R.; Hemi, R.; et al., Prolonged oxidative stress impairs insulin-induced GLUT4 translocation in 3T3-L1 adipocytes. *Diabetes* **1998,** *47* (10), 1562-9.

83. Cai, H.; Harrison, D. G., Endothelial Dysfunction in Cardiovascular Diseases: The Role of Oxidant Stress. *Circulation Research* **2000,** *87* (10), 840-844.

84. Rimm, E. B.; Stampfer, M. J.; Ascherio, A.; Giovannucci, E.; Colditz, G. A.; Willett, W. C., Vitamin E Consumption and the Risk of Coronary Heart Disease in Men. *New England Journal of Medicine* **1993,** *328* (20), 1450-1456.

85. Ting, H. H.; Timimi, F. K.; Boles, K. S.; Creager, S. J.; Ganz, P.; Creager, M. A., Vitamin C improves endothelium-dependent vasodilation in patients with non-insulin-dependent diabetes mellitus. *J Clin Invest* **1996,** *97* (1), 22-28.

86. King, G. L.; Park, K.; Li, Q., Selective Insulin Resistance and the Development of Cardiovascular Diseases in Diabetes: The 2015 Edwin Bierman Award Lecture. *Diabetes* **2016,** *65* (6), 1462.

87. Rask-Madsen, C.; King, G. L., Mechanisms of Disease: endothelial dysfunction in insulin resistance and diabetes. *Nature Clinical Practice Endocrinology & Metabolism* **2007,** *3* (1), 46-56.

88. Gray, S.; Kim, J. K., New insights into insulin resistance in the diabetic heart. *Trends Endocrinol Metab* **2011,** *22* (10), 394-403.

89. Smith, U., Impaired ('diabetic') insulin signaling and action occur in fat cells long before glucose intolerance--is insulin resistance initiated in the adipose tissue? *International journal of obesity and related metabolic disorders : journal of the International Association for the Study of Obesity* **2002,** *26* (7), 897-904.

90. Choi, S. H.; Ginsberg, H. N., Increased very low density lipoprotein (VLDL) secretion, hepatic steatosis, and insulin resistance. *Trends Endocrinol Metab* **2011,** *22* (9), 353-363.

91. Perheentupa, J.; Raivio, K., Fructose Induced Hyperuricaemia. *The Lancet* **1967,** *290* (7515), 528-531.

92. Glushakova, O.; Kosugi, T.; Roncal, C.; Mu, W.; Heinig, M.; Cirillo, P.; Sánchez-Lozada, L. G.; Johnson, R. J.; Nakagawa, T., Fructose Induces the Inflammatory Molecule ICAM-1 in Endothelial Cells. *Journal of the American Society of Nephrology* **2008,** *19* (9), 1712.

93. Roy, D.; Perreault, M.; Marette, A., Insulin stimulation of glucose uptake in skeletal muscles and adipose tissues in vivo is NO dependent. *American Journal of Physiology-Endocrinology and Metabolism* **1998,** *274* (4), E692-E699.

94. Sautin, Y. Y.; Nakagawa, T.; Zharikov, S.; Johnson, R. J., Adverse effects of the classic antioxidant uric acid in adipocytes: NADPH oxidase-mediated oxidative/nitrosative stress. *American Journal of Physiology-Cell Physiology* **2007,** *293* (2), C584-C596.

95. Furukawa, S.; Fujita, T.; Shimabukuro, M.; Iwaki, M.; Yamada, Y.; Nakajima, Y.; Nakayama, O.; Makishima, M.; Matsuda, M.; Shimomura, I., Increased oxidative stress in obesity and its impact on metabolic syndrome. *J Clin Invest* **2004,** *114* (12), 1752-1761.

96. Ames, B. N.; Cathcart, R.; Schwiers, E.; Hochstein, P., Uric acid provides an antioxidant defense in humans against oxidant- and radical-caused aging and cancer: a hypothesis. *Proc Natl Acad Sci U S A* **1981,** *78* (11), 6858-6862.

97. Lee, Y.-C.; Juan, C.-C.; Fang, V. S.; Hsu, Y.-P.; Lin, S.-H.; Kwok, C.-F.; Ho, L.-T., Evidence that endothelin-1 (ET-1) inhibits insulin-stimulated glucose uptake in rat adipocytes mainly through ETa receptors. *Metabolism* **1998,** *47* (12), 1468-1471.

98. Zhong, Q.; Lin, C.-Y.; Clarke, K. J.; Kemppainen, R. J.; Schwartz, D. D.; Judd, R. L., Endothelin-1 inhibits resistin secretion in 3T3-L1 adipocytes. *Biochemical and Biophysical Research Communications* **2002,** *296* (2), 383-387.

99. Hirata, Y.; Takagi, Y.; Fukuda, Y.; Maruno, F., Endothelin is a potent mitogen for rat vascular smooth muscle cells. *Atherosclerosis* **1989,** *78* (2), 225-228.

100. Ishida, F.; Saeki, K.; Saeki, T.; Ishikawa, K.; Ihara, M.; Kamei, T.; Yano, M., Suppressive effects of the endothelin receptor (ETA) antagonist BQ-123 on ET-1-induced reduction of lipoprotein lipase activity in 3T3-L1 adipocytes. *Biochemical Pharmacology* **1992,** *44* (7), 1431-1436.

101. Begum, N.; Leitner, W.; Reusch, J. E.; Sussman, K. E.; Draznin, B., GLUT-4 phosphorylation and its intrinsic activity. Mechanism of Ca(2+)-induced inhibition of insulin-stimulated glucose transport. *Journal of Biological Chemistry* **1993,** *268* (5), 3352-3356.

102. Crans, D. C., Antidiabetic, Chemical, and Physical Properties of Organic Vanadates as Presumed Transition-State Inhibitors for Phosphatases. *The Journal of Organic Chemistry* **2015,** *80* (24), 11899-11915.

103. Insulin Administration. *Diabetes Care* **2002,** *25* (suppl 1), s112.

104. Rehder, D.; Costa Pessoa, J.; Geraldes, C. F.; Castro, M. M.; Kabanos, T.; Kiss, T.; Meier, B.; Micera, G.; Pettersson, L.; Rangel, M.; Salifoglou, A.; Turel, I.; Wang, D., In vitro study of the insulin-mimetic behaviour of vanadium(IV, V)

coordination compounds. *JBIC Journal of Biological Inorganic Chemistry* **2002,** *7* (4), 384-396.

105. Crans, D.; Henry, L.; Cardiff, G.; Posner, B., Developing Vanadium as an Antidiabetic or Anticancer Drug: A Clinical and Historical Perspective. *Metal ions in life sciences* **2019,** *19*.

106. Faneca, H.; Figueiredo, V. A.; Tomaz, I.; Gonçalves, G.; Avecilla, F.; Pedroso de Lima, M. C.; Geraldes, C. F. G. C.; Pessoa, J. C.; Castro, M. M. C. A., Vanadium compounds as therapeutic agents: Some chemical and biochemical studies. *Journal of Inorganic Biochemistry* **2009,** *103* (4), 601-608.

107. Fantus, I. G.; Deragon, G.; Lai, R.; Tang, S., Modulation of insulin action by vanadate: evidence of a role for phosphotyrosine phosphatase activity to alter cellular signaling. *Molecular and Cellular Biochemistry* **1995,** *153* (1), 103-112.

108. Korbecki, J.; Baranowska-Bosiacka, I.; Gutowska, I.; Chlubek, D., Biochemical and medical importance of vanadium compounds. *Acta biochimica Polonica* **2012,** *59*, 195-200.

109. Levina, A.; Lay, P. A., Chemical Properties and Toxicity of Chromium(III) Nutritional Supplements. *Chemical Research in Toxicology* **2008,** *21* (3), 563-571.

110. Levina, A.; Lay, P. A., Metal-based anti-diabetic drugs: advances and challenges. *Dalton Transactions* **2011,** *40* (44), 11675-11686.

111. Levina, A.; Lay, P. A., Stabilities and Biological Activities of Vanadium Drugs: What is the Nature of the Active Species? *Chemistry – An Asian Journal* **2017,** *12* (14), 1692-1699.

112. Levina, A.; McLeod, A. I.; Gasparini, S. J.; Nguyen, A.; De Silva, W. G. M.; Aitken, J. B.; Harris, H. H.; Glover, C.; Johannessen, B.; Lay, P. A., Reactivity and Speciation of Anti-Diabetic Vanadium Complexes in Whole Blood and Its Components: The Important Role of Red Blood Cells. *Inorg Chem* **2015,** *54* (16), 7753-7766.

113. Levina, A.; McLeod, A. I.; Kremer, L. E.; Aitken, J. B.; Glover, C. J.; Johannessen, B.; Lay, P. A., Reactivity–activity relationships of oral anti-diabetic vanadium complexes in gastrointestinal media: an X-ray absorption spectroscopic study. *Metallomics* **2014,** *6* (10), 1880-1888.

114. Levina, A.; McLeod, A. I.; Pulte, A.; Aitken, J. B.; Lay, P. A., Biotransformations of Antidiabetic Vanadium Prodrugs in Mammalian Cells and Cell Culture Media: A XANES Spectroscopic Study. *Inorg Chem* **2015,** *54* (14), 6707-6718.

115. Mehdi, M. Z.; Pandey, S. K.; Théberge, J.-F.; Srivastava, A. K., Insulin signal mimicry as a mechanism for the insulin-like effects of vanadium. *Cell Biochemistry and Biophysics* **2006,** *44* (1), 73-81.

116. Pandey, G.; Jain, G.; Mathur, N., Journal of Molecular Pathophysiology Therapeutic potential of metals in managing diabetes mellitus: a review. *Journal of Molecular Pathophysiology* **2012,** *1*, 63-76.

117. Sakurai, H.; Kojima, Y.; Yoshikawa, Y.; Kawabe, K.; Yasui, H., Antidiabetic vanadium(IV) and zinc(II) complexes. *Coordination Chemistry Reviews* **2002,** *226* (1), 187-198.

118. Sakurai, H.; Yoshikawa, Y.; Yasui, H., Current state for the development of metallopharmaceutics and anti-diabetic metal complexes. *Chemical Society Reviews* **2008,** *37* (11), 2383-2392.

119. Thompson, K. H.; Chiles, J.; Yuen, V. G.; Tse, J.; McNeill, J. H.; Orvig, C., Comparison of anti-hyperglycemic effect amongst vanadium, molybdenum and other metal maltol complexes. *Journal of Inorganic Biochemistry* **2004,** *98* (5), 683-690.

120. Thompson, K. H.; Orvig, C., Vanadium in diabetes: 100 years from Phase 0 to Phase I. *Journal of Inorganic Biochemistry* **2006,** *100* (12), 1925-1935.

121. Willsky, G. R.; Chi, L.-H.; Godzala, M.; Kostyniak, P. J.; Smee, J. J.; Trujillo, A. M.; Alfano, J. A.; Ding, W.; Hu, Z.; Crans, D. C., Anti-diabetic effects of a series of vanadium dipicolinate complexes in rats with streptozotocin-induced diabetes. *Coordination Chemistry Reviews* **2011,** *255* (19), 2258-2269.

122. Fillat, C.; Rodríguez-Gil, J.; Guinovart, J., Molybdate and tungstate act like vanadate on glucose metabolism in isolated hepatocytes. *Biochem J* **1992,** *282 (Pt 3)*, 659-63.

123. Thompson, K. H.; McNeill, J. H.; Orvig, C., Vanadium Compounds as Insulin Mimics. *Chemical Reviews* **1999,** *99* (9), 2561-2572.

124. Thompson, K. H.; Godin, D. V., Micronutrients and antioxidants in the progression of diabetes. *Nutrition Research* **1995,** *15* (9), 1377-1410.

125. Marzban, L.; McNeill, J. H., Insulin-like actions of vanadium: Potential as a therapeutic agent. *The Journal of Trace Elements in Experimental Medicine* **2003,** *16* (4), 253-267.

126. Reaven, G. M., Role of Insulin Resistance in Human Disease (Syndrome X): An Expanded Definition. *Annual review of medicine* **1993,** *44* (1), 121-131.

127. Wu, L. E.; Levina, A.; Harris, H. H.; Cai, Z.; Lai, B.; Vogt, S.; James, D. E.; Lay, P. A., Carcinogenic Chromium(VI) Compounds Formed by Intracellular Oxidation of Chromium(III) Dietary Supplements by Adipocytes. *Angewandte Chemie International Edition* **2016,** *55* (5), 1742-1745.
128. Doucette, K. A.; Hassell, K. N.; Crans, D. C., Selective speciation improves efficacy and lowers toxicity of platinum anticancer and vanadium antidiabetic drugs. *Journal of Inorganic Biochemistry* **2016,** *165*, 56-70.
129. Evangelou, A. M., Vanadium in cancer treatment. *Critical Reviews in Oncology/Hematology* **2002,** *42* (3), 249-265.
130. Gresser, M. J.; Tracey, A. S., Vanadates as Phosphate Analogs in Biochemistry. In *Vanadium in Biological Systems: Physiology and Biochemistry*, Chasteen, N. D., Ed. Springer Netherlands: Dordrecht, 1990; pp 63-79.
131. Crans, D. C.; Zhang, B.; Gaidamauskas, E.; Keramidas, A. D.; Willsky, G. R.; Roberts, C. R., Is Vanadate Reduced by Thiols under Biological Conditions? Changing the Redox Potential of V(V)/V(IV) by Complexation in Aqueous Solution. *Inorg Chem* **2010,** *49* (9), 4245-4256.
132. Crans, D. C.; Smee, J. J.; Gaidamauskas, E.; Yang, L., The Chemistry and Biochemistry of Vanadium and the Biological Activities Exerted by Vanadium Compounds. *Chemical Reviews* **2004,** *104* (2), 849-902.
133. Mathew, M.; Brown, W. E.; Schroeder, L. W.; Dickens, B., Crystal structure of octacalcium bis(hydrogenphosphate) tetrakis(phosphate)pentahydrate, Ca8(HP04)2(PO4)4·5H2O. *Journal of Crystallographic and Spectroscopic Research* **1988,** *18* (3), 235-250.
134. Vlasse, M.; Salmon, R.; Parent, C., Crystal structure of sodium lanthanum orthovanadate, Na3La(VO4)2. *Inorg Chem* **1976,** *15* (6), 1440-1444.
135. Cheatham, B.; Kahn, C. R., Insulin Action and the Insulin Signaling Network*. *Endocrine Reviews* **1995,** *16* (2), 117-142.
136. Rehder, D., Vanadium in health issues. *ChemTexts* **2018,** *4* (4), 20.
137. Poucheret, P.; Verma, S.; Grynpas, M. D.; McNeill, J. H., Vanadium and diabetes. *Molecular and Cellular Biochemistry* **1998,** *188* (1), 73-80.
138. Organisation, W. H. Cancer. https://www.who.int/health-topics/cancer#tab=tab_1.
139. Hanahan, D.; Weinberg, Robert A., Hallmarks of Cancer: The Next Generation. *Cell* **2011,** *144* (5), 646-674.

140. Tacar, O.; Sriamornsak, P.; Dass, C. R., Doxorubicin: an update on anticancer molecular action, toxicity and novel drug delivery systems. *Journal of Pharmacy and Pharmacology* **2013,** *65* (2), 157-170.

141. Williams, G. H.; Stoeber, K., The cell cycle and cancer. *The Journal of Pathology* **2012,** *226* (2), 352-364.

142. Croce, C. M. M. D., Oncogenes and CancerMolecular Origins of Cancer. *The New England Journal of Medicine* **2008,** *358* (5), 502-511.

143. Nakagawa, T.; Lanaspa, M. A.; Millan, I. S.; Fini, M.; Rivard, C. J.; Sanchez-Lozada, L. G.; Andres-Hernando, A.; Tolan, D. R.; Johnson, R. J., Fructose contributes to the Warburg effect for cancer growth. *Cancer & Metabolism* **2020,** *8* (1), 16.

144. Kioseoglou, E.; Petanidis, S.; Gabriel, C.; Salifoglou, A., The chemistry and biology of vanadium compounds in cancer therapeutics. *Coordination Chemistry Reviews* **2015,** *301-302*, 87-105.

145. Kowalski, S.; Wyrzykowski, D.; Inkielewicz-Stępniak, I., Molecular and Cellular Mechanisms of Cytotoxic Activity of Vanadium Compounds against Cancer Cells. *Molecules* **2020,** *25* (7), 1757.

146. Gonçalves, A. P.; Videira, A.; Soares, P.; Máximo, V., Orthovanadate-induced cell death in RET/PTC1-harboring cancer cells involves the activation of caspases and altered signaling through PI3K/Akt/mTOR. *Life Sciences* **2011,** *89* (11), 371-377.

147. Irving, E.; Stoker, A. W., Vanadium Compounds as PTP Inhibitors. *Molecules* **2017,** *22* (12), 2269.

148. Yoshinaga, M.; Ueki, T.; Yamaguchi, N.; Kamino, K.; Michibata, H., Glutathione transferases with vanadium-binding activity isolated from the vanadium-rich ascidian Ascidia sydneiensis samea. *Biochimica et Biophysica Acta (BBA) - General Subjects* **2006,** *1760* (3), 495-503.

149. Sakurai, H.; Tsuchiya, K.; Nukatsuka, M.; Kawada, J.; Ishikawa, S.; Yoshida, H.; Komatsu, M., Insulin-Mimetic Action of Vanadyl Complexes. *Journal of Clinical Biochemistry and Nutrition* **1990,** *8* (3), 193-200.

150. Zhao, Q.; Chen, D.; Liu, P.; Wei, T.; Zhang, F.; Ding, W., Oxidovanadium(IV) sulfate-induced glucose uptake in HepG2 cells through IR/Akt pathway and hydroxyl radicals. *Journal of Inorganic Biochemistry* **2015,** *149*, 39-44.

151. Gudbergsson, J. M.; Johnsen, K. B., Exosomes and autophagy: rekindling the vesicular waste hypothesis. *J Cell Commun Signal* **2019,** *13* (4), 443-450.

152. Wen, Y.-A.; Xing, X.; Harris, J. W.; Zaytseva, Y. Y.; Mitov, M. I.; Napier, D. L.; Weiss, H. L.; Mark Evers, B.; Gao, T., Adipocytes activate mitochondrial fatty acid oxidation and autophagy to promote tumor growth in colon cancer. *Cell Death & Disease* **2017,** *8* (2), e2593-e2593.

153. Wu, Y.; Ma, Y.; Xu, Z.; Wang, D.; Zhao, B.; Pan, H.; Wang, J.; Xu, D.; Zhao, X.; Pan, S.; Liu, L.; Dai, W.; Jiang, H., Sodium orthovanadate inhibits growth of human hepatocellular carcinoma cells in vitro and in an orthotopic model in vivo. *Cancer Letters* **2014,** *351* (1), 108-116.

154. Kalniņa, D.; Levina, A.; Pei, A.; Gross, K. A.; Lay, P. A., Synthesis, characterization and in vitro anti-cancer activity of vanadium-doped nanocrystalline hydroxyapatite. *New Journal of Chemistry* **2019,** *43* (45), 17891-17901.

155. Le, M.; Rathje, O.; Levina, A.; Lay, P. A., High cytotoxicity of vanadium(IV) complexes with 1,10-phenanthroline and related ligands is due to decomposition in cell culture medium. *JBIC Journal of Biological Inorganic Chemistry* **2017,** *22* (5), 663-672.

156. Zhang, Y.-L.; Wang, X.-S.; Fang, W.; Cai, X.-Y.; Li, H.-Z.; Mao, J.-W.; Jin, X.-B.; Bai, Y.-L.; Lu, J.-Z., In vitro study of the cytotoxicities of two mixed-ligand oxovanadium complexes on human hepatoma cells. *Die Pharmazie - An International Journal of Pharmaceutical Sciences* **2013,** *68* (10), 827-834.

157. Tiwari, N.; Gheldof, A.; Tatari, M.; Christofori, G., EMT as the ultimate survival mechanism of cancer cells. *Seminars in Cancer Biology* **2012,** *22* (3), 194-207.

158. Reichmann, D.; Voth, W.; Jakob, U., Maintaining a Healthy Proteome during Oxidative Stress. *Molecular Cell* **2018,** *69* (2), 203-213.

159. Sies, H., Oxidative stress: impact in redox biology and medicine. *Archives of Medical and Biomedical Research* **2016,** *2*, 146.

160. Vileno, B.; Jeney, S.; Sienkiewicz, A.; Marcoux, P. R.; Miller, L. M.; Forró, L., Evidence of lipid peroxidation and protein phosphorylation in cells upon oxidative stress photo-generated by fullerols. *Biophysical Chemistry* **2010,** *152* (1), 164-169.

161. Brehme, M.; Voisine, C.; Rolland, T.; Wachi, S.; Soper, James H.; Zhu, Y.; Orton, K.; Villella, A.; Garza, D.; Vidal, M.; Ge, H.; Morimoto, Richard I., A Chaperome Subnetwork Safeguards Proteostasis in Aging and Neurodegenerative Disease. *Cell Reports* **2014,** *9* (3), 1135-1150.

162. Lodhi, I. J.; Semenkovich, C. F., Peroxisomes: a nexus for lipid metabolism and cellular signaling. *Cell Metab* **2014,** *19* (3), 380-392.

163. Forman, H. J.; Fukuto, J. M.; Miller, T.; Zhang, H.; Rinna, A.; Levy, S., The chemistry of cell signaling by reactive oxygen and nitrogen species and 4-hydroxynonenal. *Archives of Biochemistry and Biophysics* **2008,** *477* (2), 183-195.

164. Levina, A.; Crans, D. C.; Lay, P. A., Speciation of metal drugs, supplements and toxins in media and bodily fluids controls in vitro activities. *Coordination Chemistry Reviews* **2017,** *352*, 473-498.

165. Byczkowski, J. Z.; Kulkarni, A. P., Vanadium redox cycling, lipid peroxidation and co-oxygenation of benzo(a)pyrene-7,8-dihydrodiol. *Biochimica et Biophysica Acta (BBA) - Lipids and Lipid Metabolism* **1992,** *1125* (2), 134-141.

166. Birben, E.; Sahiner, U. M.; Sackesen, C.; Erzurum, S.; Kalayci, O., Oxidative Stress and Antioxidant Defense. *World Allergy Organization Journal* **2012,** *5* (1), 9-19.

167. Hildebrandt, T.; Knuesting, J.; Berndt, C.; Morgan, B.; Scheibe, R., Cytosolic thiol switches regulating basic cellular functions: GAPDH as an information hub? *Biological Chemistry* **2015,** *396* (5), 523-537.

168. Halliwell, B.; Gutteridge, J. M. C., Reactive species can pose special problems needing special solutions: some examples. In *Free Radicals in Biology and Medicine*, 5 ed.; Oxford University Press: Oxford, 2015.

169. Marengo, B.; Nitti, M.; Furfaro, A. L.; Colla, R.; Ciucis, C. D.; Marinari, U. M.; Pronzato, M. A.; Traverso, N.; Domenicotti, C., Redox homeostasis and cellular antioxidant systems: Crucial players in cancer growth and therapy. *Oxidative Medicine and Cellular Longevity* **2016,** *2016*.

170. Winterbourn, C. C.; Kettle, A. J.; Hampton, M. B., Reactive Oxygen Species and Neutrophil Function. *Annual Review of Biochemistry* **2016,** *85* (1), 765-792.

171. Winter, J.; Ilbert, M.; Graf, P. C. F.; Özcelik, D.; Jakob, U., Bleach Activates a Redox-Regulated Chaperone by Oxidative Protein Unfolding. *Cell* **2008,** *135* (4), 691-701.

172. Naumann, D., FT-infrared and FT-Raman spectroscopy in biomedical research. *Applied spectroscopy reviews* **2001,** *36* (2-3), 239-298.

173. Dobson, C. M., Protein folding and misfolding. *Nature* **2003,** *426* (6968), 884-890.

174. Thomas, P. J.; Qu, B.-H.; Pedersen, P. L., Defective protein folding as a basis of human disease. *Trends in Biochemical Sciences* **1995,** *20* (11), 456-459.

175. Shivu, B.; Seshadri, S.; Li, J.; Oberg, K. A.; Uversky, V. N.; Fink, A. L., Distinct β-Sheet Structure in Protein Aggregates Determined by ATR–FTIR Spectroscopy. *Biochemistry* **2013,** *52* (31), 5176-5183.

176. Litvinov, Rustem I.; Faizullin, Dzhigangir A.; Zuev, Yuriy F.; Weisel, John W., The Alpha Helix to Beta-Sheet Transition in Stretched and Compressed Hydrated Fibrin Clots. *Biophysical Journal* **2012,** *103* (5), 1020-1027.

177. Pan, K. M.; Baldwin, M.; Nguyen, J.; Gasset, M.; Serban, A.; Groth, D.; Mehlhorn, I.; Huang, Z.; Fletterick, R. J.; Cohen, F. E.; et al., Conversion of alpha-helices into beta-sheets features in the formation of the scrapie prion proteins. *Proc Natl Acad Sci U S A* **1993,** *90* (23), 10962-10966.

178. Nilsson, M. R.; Driscoll, M.; Raleigh, D. P., Low levels of asparagine deamidation can have a dramatic effect on aggregation of amyloidogenic peptides: implications for the study of amyloid formation. *Protein Sci* **2002,** *11* (2), 342-349.

179. Chalmers, J. M., Chapter 2 Mid-infrared Spectroscopy: The Basics. In *Biomedical Applications of Synchrotron Infrared Microspectroscopy: A Practical Approach*, The Royal Society of Chemistry: 2011; pp 29-66.

180. Barth, A., Infrared spectroscopy of proteins. *Biochimica et Biophysica Acta (BBA) - Bioenergetics* **2007,** *1767* (9), 1073-1101.

181. Movasaghi, Z.; Rehman, S.; ur Rehman, D. I., Fourier Transform Infrared (FTIR) Spectroscopy of Biological Tissues. *Applied Spectroscopy Reviews* **2008,** *43* (2), 134-179.

182. Wood, B. R., The importance of hydration and DNA conformation in interpreting infrared spectra of cells and tissues. *Chemical Society Reviews* **2016,** *45* (7), 1980-1998.

183. Naumann, D., Infrared Spectroscopy of Cells, Tissues, and Biofluids. In *Encyclopedia of Biophysics*, Roberts, G. C. K., Ed. Springer Berlin Heidelberg: Berlin, Heidelberg, 2013; pp 1057-1065.

184. Dovbeshko, G. I.; Gridina, N. Y.; Kruglova, E. B.; Pashchuk, O. P., FTIR spectroscopy studies of nucleic acid damage. *Talanta* **2000,** *53* (1), 233-246.

185. Bader, C. A.; Carter, E. A.; Safitri, A.; Simpson, P. V.; Wright, P.; Stagni, S.; Massi, M.; Lay, P. A.; Brooks, D. A.; Plush, S. E., Unprecedented staining of polar lipids by a luminescent rhenium complex revealed by FTIR microspectroscopy in adipocytes. *Molecular BioSystems* **2016,** *12* (7), 2064-2068.

186. Vibrational spectroscopy for medical diagnosis. *Scitech Book News* **2008,** *32* (3).
187. Vibrational Spectroscopic Imaging of Soft Tissue. In *Infrared and Raman Spectroscopic Imaging*, 2014; pp 111-152.
188. Lasch, P.; Haensch, W.; Naumann, D.; Diem, M., Imaging of colorectal adenocarcinoma using FT-IR microspectroscopy and cluster analysis. *Biochimica et biophysica acta. Molecular basis of disease* **2004,** *1688* (2), 176-186.
189. Lasch, P.; Petrich, W., Chapter 6 Data Acquisition and Analysis in Biomedical Vibrational Spectroscopy. In *Biomedical Applications of Synchrotron Infrared Microspectroscopy: A Practical Approach*, The Royal Society of Chemistry: 2011; pp 192-225.
190. Romeo, M.; Boydston-White, S.; Matthäus, C.; Miljković, M.; Bird, B.; Chernenko, T.; Lasch, P.; Diem, M., Infrared and Raman Microspectroscopic Studies of Individual Human Cells. 2008.
191. Griffiths, P. R., Infrared and Raman Instrumentation for Mapping and Imaging. In *Infrared and Raman Spectroscopic Imaging*, 2009; pp 1-64.
192. Pilling, M. J.; Bassan, P.; Gardner, P., Comparison of transmission and transflectance mode FTIR imaging of biological tissue. *Analyst (London)* **2015,** *14* (7), 2383-2392.
193. Guillén, M. D.; Cabo, N., Infrared spectroscopy in the study of edible oils and fats. *Journal of the Science of Food and Agriculture* **1997,** *75* (1), 1-11.
194. Junhom, C.; Weerapreeyakul, N.; Tanthanuch, W.; Thumanu, K., FTIR microspectroscopy defines early drug resistant human hepatocellular carcinoma (HepG2) cells. *Experimental Cell Research* **2016,** *340* (1), 71-80.
195. Ricciardi, V.; Portaccio, M.; Piccolella, S.; Manti, L.; Pacifico, S.; Lepore, M., Study of SH-SY5Y Cancer Cell Response to Treatment with Polyphenol Extracts Using FT-IR Spectroscopy. *Biosensors (Basel)* **2017,** *7* (4), 57.
196. Ami, D.; Mereghetti, P.; Leri, M.; Giorgetti, S.; Natalello, A.; Doglia, S. M.; Stefani, M.; Bucciantini, M., A FTIR microspectroscopy study of the structural and biochemical perturbations induced by natively folded and aggregated transthyretin in HL-1 cardiomyocytes. *Scientific Reports* **2018,** *8* (1), 12508.
197. Dreissig, I.; Machill, S.; Salzer, R.; Krafft, C., Quantification of brain lipids by FTIR spectroscopy and partial least squares regression. *Spectrochimica Acta Part A: Molecular and Biomolecular Spectroscopy* **2009,** *71* (5), 2069-2075.

198. Davis, R.; Mauer, L. J., Fourier Transform Infrared (FT-IR) Spectroscopy: A Rapid Tool for Detection and Analysis of Foodborne Pathogenic Bacteria. 2010; Vol. 2, pp 1582-1594.

199. Sukprasert, J.; Thumanu, K.; Phung-on, I.; Jirarungsatean, C.; Erickson, L. E.; Tuitemwong, P.; Tuitemwong, K., Synchrotron FTIR Light Reveals Signal Changes of Biofunctionalized Magnetic Nanoparticle Attachment on Salmonella sp. *Journal of Nanomaterials* **2020,** *2020*, 6149713.

200. Gómez-Fernández, J. C.; Villalaín, J., The use of FT-IR for quantitative studies of the apparent pKa of lipid carboxyl groups and the dehydration degree of the phosphate group of phospholipids. *Chemistry and Physics of Lipids* **1998,** *96* (1), 41-52.

201. Gazi, E.; Gardner, P.; Lockyer, N. P.; Hart, C. A.; Brown, M. D.; Clarke, N. W., Direct evidence of lipid translocation between adipocytes and prostate cancer cells with imaging FTIR microspectroscopy. *Journal of Lipid Research* **2007,** *48* (8), 1846-1856.

202. Oleszko, A.; Olsztyńska-Janus, S.; Walski, T.; Grzeszczuk-Kuć, K.; Bujok, J.; Gałecka, K.; Czerski, A.; Witkiewicz, W.; Komorowska, M., Application of FTIR-ATR Spectroscopy to Determine the Extent of Lipid Peroxidation in Plasma during Haemodialysis. *Biomed Res Int* **2015,** *2015*, 245607-245607.

203. Buijs, J.; Norde, W.; Lichtenbelt, J. W. T., Changes in the Secondary Structure of Adsorbed IgG and F(ab‘)2 Studied by FTIR Spectroscopy. *Langmuir* **1996,** *12* (6), 1605-1613.

204. Nevskaya, N. A.; Chirgadze, Y. N., Infrared spectra and resonance interactions of amide-I and II vibrations of α-helix. *Biopolymers* **1976,** *15* (4), 637-648.

205. Zelig, U.; Kapelushnik, J.; Moreh, R.; Mordechai, S.; Nathan, I., Diagnosis of cell death by means of infrared spectroscopy. *Biophysical journal* **2009,** *97* (7), 2107-2114.

206. Chirgadze, Y. N.; Fedorov, O. V.; Trushina, N. P., Estimation of amino acid residue side-chain absorption in the infrared spectra of protein solutions in heavy water. *Biopolymers* **1975,** *14* (4), 679-694.

207. Fukuyama, Y.; Yoshida, S.; Yanagisawa, S.; Shimizu, M., A study on the differences between oral squamous cell carcinomas and normal oral mucosas measured by Fourier transform infrared spectroscopy. *Biospectroscopy* **1999,** *5* (2), 117-126.

208. Fringeli, U. P.; Günthard, H. H., Infrared Membrane Spectroscopy. In *Membrane Spectroscopy*, Grell, E., Ed. Springer Berlin Heidelberg: Berlin, Heidelberg, 1981; pp 270-332.
209. Koca, N.; Rodriguez-Saona, L. E.; Harper, W. J.; Alvarez, V. B., Application of Fourier Transform Infrared Spectroscopy for Monitoring Short-Chain Free Fatty Acids in Swiss Cheese. *Journal of Dairy Science* **2007,** *90* (8), 3596-3603.
210. Lozano, M.; Rodriguez-Ulibarri, P.; Echeverría, J.; Beruete, M.; Sorolla Ayza, M.; Beriain, M. J., Mid-Infrared Spectroscopy (MIR) for Simultaneous Determination of Fat and Protein Content in Meat of Several Animal Species. *Food Analytical Methods* **2017,** *10*, 3462-3469.
211. Arrondo, J. L. R.; Goñi, F. M., Infrared studies of protein-induced perturbation of lipids in lipoproteins and membranes. *Chemistry and Physics of Lipids* **1998,** *96* (1), 53-68.
212. Petibois, C.; Melin, A.-M.; Perromat, A.; Cazorla, G.; Déléris, G., Glucose and lactate concentration determination on single microsamples by Fourier-transform infrared spectroscopy. *Journal of Laboratory and Clinical Medicine* **2000,** *135* (2), 210-215.
213. Griffiths, P. R.; Miseo, E. V., Infrared and Raman Instrumentation for Mapping and Imaging. In *Infrared and Raman Spectroscopic Imaging*, 2014; pp 1-56.
214. Fabian, H.; Jackson, M.; Murphy, L.; Watson, P. H.; Fichtner, I.; Mantsch, H. H., A comparative infrared spectroscopic study of human breast tumors and breast tumor cell xenografts. *Biospectroscopy* **1995,** *1* (1), 37-45.
215. Tobin, M. J.; Puskar, L.; Barber, R. L.; Harvey, E. C.; Heraud, P.; Wood, B. R.; Bambery, K. R.; Dillon, C. T.; Munro, K. L., FTIR spectroscopy of single live cells in aqueous media by synchrotron IR microscopy using microfabricated sample holders. *Vibrational Spectroscopy* **2010,** *53* (1), 34-38.
216. Marcelli, A.; Cinque, G., Chapter 3 Infrared Synchrotron Radiation Beamlines: High Brilliance Tools for IR Spectromicroscopy. In *Biomedical Applications of Synchrotron Infrared Microspectroscopy: A Practical Approach*, The Royal Society of Chemistry: 2011; pp 67-104.
217. Lasch, P.; Naumann, D., Spatial resolution in infrared microspectroscopic imaging of tissues. *Biochim Biophys Acta* **2006,** *1758* (7), 814-29.
218. Diem, M.; Matthäus, C.; Chernenko, T.; Romeo, M. J.; Miljković, M.; Bird, B.; Schubert, J.; Papamarkakis, K.; Laver, N., Infrared and Raman Spectroscopy and

Spectral Imaging of Individual Cells. In *Infrared and Raman Spectroscopic Imaging*, 2009; pp 173-201.

219. Papamarkakis, K.; Bird, B.; Schubert, J.; Miljković, M.; Wein, R.; Bedrossian, K.; Laver, N.; Diem, M., Cytopathology by Optical Methods: Spectral Cytopathology of the Oral Mucosa. *Laboratory investigation; a journal of technical methods and pathology* **2010,** *90*, 589-98.
220. Diem, M.; Romeo, M.; Matthäus, C.; Miljkovic, M.; Miller, L.; Lasch, P., Comparison of Fourier transform infrared (FTIR) spectra of individual cells acquired using synchrotron and conventional sources. *Infrared physics & technology* **2004,** *45* (5), 331-338.
221. Bassan, P.; Weida, M.; Rowlette, J., Large scale infrared imaging of tissue micro arrays (TMAs) using a tunable Quantum Cascade Laser (QCL) based microscope. *The Analyst* **2014,** *139*.
222. Kim, S. Y.; Khanal, D.; Tharkar, P.; Kalionis, B.; Chrzanowski, W., None of us is the same as all of us: resolving the heterogeneity of extracellular vesicles using single-vesicle, nanoscale characterization with resonance enhanced atomic force microscope infrared spectroscopy (AFM-IR). *Nanoscale Horizons* **2018,** *3* (4), 430-438.
223. Esbensen, K.; Swarbrick, B.; Westad, F.; Whitcomb, P. J.; Anderson, M. J.; Esbensen, K., *Multivariate data analysis : an introduction to multivariate analysis, process analytical technology and quality by design*. IM Publishing: Chichester, UK, 2018.
224. Box, G. E. P.; Hunter, W. G.; Hunter, J. S., *Statistics for experimenters : an introduction to design, data analysis, and model building*. Wiley: New York, 1978.
225. Swarbrick, B., Chapter 6 - Quality by Design in Practice. In *Multivariate Analysis in the Pharmaceutical Industry*, Ferreira, A. P.; Menezes, J. C.; Tobyn, M., Eds. Academic Press: 2018; pp 125-171.
226. Montgomery, D. C., *Design and analysis of experiments*. 6th ed. ed.; John Wiley & Sons: Hoboken, NJ, 2005.
227. Esbensen, K. H.; Julius, L. P.; Minkkinen, P., *Representative Sampling in Science, Technology and Industry: Theory, Practice, Case Histories, Exercises*. Wiley: 2021.
228. Esbensen, K. H.; Romañach, R. J.; Román-Ospino, A. D., Chapter 4 - Theory of Sampling (TOS): A Necessary and Sufficient Guarantee for Reliable Multivariate

Data Analysis in Pharmaceutical Manufacturing. In *Multivariate Analysis in the Pharmaceutical Industry*, Ferreira, A. P.; Menezes, J. C.; Tobyn, M., Eds. Academic Press: 2018; pp 53-91.

229. Esbensen, K. H.; Paasch-Mortensen, P., Process Sampling: Theory of Sampling – the Missing Link in Process Analytical Technologies (PAT). In *Process Analytical Technology*, 2010; pp 37-80.
230. Wold, S., Chemometrics; what do we mean with it, and what do we want from it? *Chemometrics and Intelligent Laboratory Systems* **1995,** *30* (1), 109-115.
231. Otto, M., What is Chemometrics? In *Chemometrics*, 2016; pp 1-13.
232. Grahn, H.; Geladi, P., *Techniques and Applications of Hyperspectral Image Analysis*. John Wiley & Sons, Incorporated: Hoboken, UNITED KINGDOM, 2007.
233. Swarbrick, B.; Westad, F., An Overview of Chemometrics for the Engineering And Measurement Sciences. In *Handbook of Measurement in Science and Engineering*, 2016; pp 2307-2407.
234. Savitzky, A.; Golay, M. J. E., Smoothing and Differentiation of Data by Simplified Least Squares Procedures. *Analytical Chemistry* **1964,** *36* (8), 1627-1639.
235. Steinier, J.; Termonia, Y.; Deltour, J., Smoothing and differentiation of data by simplified least square procedure. *Analytical Chemistry* **1972,** *44* (11), 1906-1909.
236. Barnes, R. J.; Dhanoa, M. S.; Lister, S. J., Standard Normal Variate Transformation and De-Trending of Near-Infrared Diffuse Reflectance Spectra. *Applied Spectroscopy* **1989,** *43* (5), 772-777.
237. Wold, H., 11 - Path Models with Latent Variables: The NIPALS Approach**NIPALS = Nonlinear Iterative PArtial Least Squares. In *Quantitative Sociology*, Blalock, H. M.; Aganbegian, A.; Borodkin, F. M.; Boudon, R.; Capecchi, V., Eds. Academic Press: 1975; pp 307-357.
238. Martens, H.; Nielsen, J. P.; Engelsen, S. B., Light Scattering and Light Absorbance Separated by Extended Multiplicative Signal Correction. Application to Near-Infrared Transmission Analysis of Powder Mixtures. *Analytical Chemistry* **2003,** *75* (3), 394-404.
239. Jackson, J. E., *A user's guide to principal components*. Wiley: New York, 1991.
240. Hotelling, H., Simplified calculation of principal components. *Psychometrika* **1936,** *1* (1), 27-35.

241. Kiers, H. A. L., Towards a standardized notation and terminology in multiway analysis. *Journal of Chemometrics* **2000,** *14* (3), 105-122.

242. Rasmus Bro, A. S., Paul Geladi, Array Definitions and Properties. In *Multi-Way Analysis with Applications in the Chemical Sciences*, 2004; pp 13-34.

243. Carter, E. A.; Rayner, B. S.; McLeod, A. I.; Wu, L. E.; Marshall, C. P.; Levina, A.; Aitken, J. B.; Witting, P. K.; Lai, B.; Cai, Z.; Vogt, S.; Lee, Y.-C.; Chen, C.-I.; Tobin, M. J.; Harris, H. H.; Lay, P. A., Silicon nitride as a versatile growth substrate for microspectroscopic imaging and mapping of individual cells. *Molecular BioSystems* **2010,** *6* (7), 1316-1322.

244. Donato, M. T.; Tolosa, L.; Gómez-Lechón, M. J., Culture and Functional Characterization of Human Hepatoma HepG2 Cells. In *Protocols in In Vitro Hepatocyte Research*, Vinken, M.; Rogiers, V., Eds. Springer New York: New York, NY, 2015; pp 77-93.

245. Govers, R.; Coster, A. C. F.; James, D. E., Insulin Increases Cell Surface GLUT4 Levels by Dose Dependently Discharging GLUT4 into a Cell Surface Recycling Pathway. *Mol Cell Biol* **2004,** *24* (14), 6456-6466.

246. Liakat, S.; Bors, K. A.; Huang, T.-Y.; Michel, A. P. M.; Zanghi, E.; Gmachl, C. F., In vitro measurements of physiological glucose concentrations in biological fluids using mid-infrared light. *Biomed Opt Express* **2013,** *4* (7), 1083-1090.

247. Nielsen, M. F.; Caumo, A.; Aagaard, N. K.; Chandramouli, V.; Schumann, W. C.; Landau, B. R.; Schmitz, O.; Vilstrup, H., Contribution of defects in glucose uptake to carbohydrate intolerance in liver cirrhosis: assessment during physiological glucose and insulin concentrations. *American Journal of Physiology-Gastrointestinal and Liver Physiology* **2005,** *288* (6), G1135-G1143.

248. Nseir, W.; Nassar, F.; Assy, N., Soft drinks consumption and nonalcoholic fatty liver disease. *World J Gastroenterol* **2010,** *16* (21), 2579-2588.

249. Hirahatake, K. M.; Meissen, J. K.; Fiehn, O.; Adams, S. H., Comparative effects of fructose and glucose on lipogenic gene expression and intermediary metabolism in HepG2 liver cells. *PloS one* **2011,** *6* (11), e26583-e26583.

250. Capella, M. A. M.; Capella, L. S.; Valente, R. C.; Gefé, M.; Lopes, A. G., Vanadate-induced cell death is dissociated from H2O2 generation. *Cell Biology and Toxicology* **2007,** *23* (6), 413-420.

251. Gordon, J. A., [41] Use of vanadate as protein-phosphotyrosine phosphatase inhibitor. In *Methods in Enzymology*, Academic Press: 1991; Vol. 201, pp 477-482.

252. McLeod, A. I. Elucidating the Metabolism of Vanadium in the Treatment of Diabetes. Honours, University of Sydney, 2007.
253. Mosmann, T., Rapid colorimetric assay for cellular growth and survival: Application to proliferation and cytotoxicity assays. *Journal of Immunological Methods* **1983,** *65* (1), 55-63.
254. Stockert, J. C.; Horobin, R. W.; Colombo, L. L.; Blázquez-Castro, A., Tetrazolium salts and formazan products in Cell Biology: Viability assessment, fluorescence imaging, and labeling perspectives. *Acta Histochemica* **2018,** *120* (3), 159-167.
255. Tobin, M. J.; Vongsvivut, J.; Martin, D. E.; Sizeland, K. H.; Hackett, M. J.; Takechi, R.; Fimorgnari, N.; Lam, V.; Mamo, J. C.; Carter, E. A.; Swarbrick, B.; Lay, P. A.; Christensen, D. A.; Perez-Guaita, D.; Lowery, E.; Heraud, P.; Wood, B. R.; Puskar, L.; Bambery, K. R., Focal plane array IR imaging at the Australian Synchrotron. *Infrared Physics & Technology* **2018,** *94*, 85-90.
256. Rehder, D.; Polenova, T.; Bühl, M., Vanadium-51 NMR. In *Annual Reports on NMR Spectroscopy*, Webb, G. A., Ed. Academic Press: 2007; Vol. 62, pp 49-114.
257. Baker, M. J.; Trevisan, J.; Bassan, P.; Bhargava, R.; Butler, H. J.; Dorling, K. M.; Fielden, P. R.; Fogarty, S. W.; Fullwood, N. J.; Heys, K. A.; Hughes, C.; Lasch, P.; Martin-Hirsch, P. L.; Obinaju, B.; Sockalingum, G. D.; Sule-Suso, J.; Strong, R. J.; Walsh, M. J.; Wood, B. R.; Gardner, P.; Martin, F. L., Using Fourier transform IR spectroscopy to analyze biological materials. *Nat Protoc* **2014,** *9* (8), 1771-91.
258. Carter, E. A.; Tam, K. K.; Armstrong, R. S.; Lay, P. A., Vibrational spectroscopic mapping and imaging of tissues and cells. *Biophysical Reviews* **2009,** *1* (2), 95-103.
259. Esbensen, K.; Geladi, P., Strategy of multivariate image analysis (MIA). *Chemometrics and Intelligent Laboratory Systems* **1989,** *7* (1), 67-86.
260. Diem, M., *Modern Vibrational Spectroscopy and Micro-Spectroscopy : Theory, Instrumentation and Biomedical Applications*. John Wiley & Sons, Incorporated: Chicester, UK, 2015.
261. Bhargava, R., Infrared Spectroscopic Imaging: The Next Generation. *Applied Spectroscopy* **2012,** *66* (10), 1091-1120.
262. Bhargava, R.; Levin, I. W., Fourier Transform Mid-infrared Spectroscopic Imaging. In *Spectrochemical Analysis Using Infrared Multichannel Detectors*, 2005; pp 1-24.

263. Stelzer, E. H. K., Contrast, resolution, pixelation, dynamic range and signal-to-noise ratio: fundamental limits to resolution in fluorescence light microscopy. *Journal of Microscopy* **1998,** *189* (1), 15-24.

264. Optics, B. Application Note AN M161, Detector characterization using FTIR spectrometer 2019. https://www.bruker.com/en/products-and-solutions/infrared-and-raman/ft-ir-routine-spectrometer/what-is-ft-ir-spectroscopy.html.

265. Bassan, P.; Kohler, A.; Martens, H.; Lee, J.; Jackson, E.; Lockyer, N.; Dumas, P.; Brown, M.; Clarke, N.; Gardner, P., RMieS-EMSC correction for infrared spectra of biological cells: Extension using full Mie theory and GPU computing. *Journal of Biophotonics* **2010,** *3* (8-9), 609-620.

266. Q2(R1) Validation of Analytical Procedures. In *ICH Quality Guidelines*, pp 127-166.

267. Agency, E. M. Guideline on the use of near infrared spectroscopy by the pharmaceutical industry and the data requirements for new submissions and variations. https://www.ema.europa.eu/en/documents/scientific-guideline/guideline-use-near-infrared-spectroscopy-pharmaceutical-industry-data-requirements-new-submissions_en.pdf.

268. Gouveia, F. F.; Felizardo, P. M.; Menezes, J. C., Chapter 14 - Lifecycle Management of PAT Procedures: Applications to Batch and Continuous Processes. In *Multivariate Analysis in the Pharmaceutical Industry*, Ferreira, A. P.; Menezes, J. C.; Tobyn, M., Eds. Academic Press: 2018; pp 323-345.

269. Miller, L. M.; Dumas, P., Chemical imaging of biological tissue with synchrotron infrared light. *Biochimica et Biophysica Acta (BBA) - Biomembranes* **2006,** *1758* (7), 846-857.

270. Carr, G. L., Resolution limits for infrared microspectroscopy explored with synchrotron radiation. *Review of Scientific Instruments* **2001,** *72* (3), 1613-1619.

271. Rees, O. J., *Fourier Transform Infrared Spectroscopy : Developments, Techniques and Applications*. Nova Science Publishers, Incorporated: New York, United States, 2010.

272. Kimura, S.-i.; Okamura, H., Infrared and Terahertz Spectroscopy of Strongly Correlated Electron Systems under Extreme Conditions. *Journal of the Physical Society of Japan* **2012,** *82* (2), 021004.

273. Beebe, K. R.; Pell, R. J.; Seasholtz, M. B., *Chemometrics : a practical guide*. Wiley: New York, 1998.

274. Geladi, P.; MacDougall, D.; Martens, H., Linearization and Scatter-Correction for Near-Infrared Reflectance Spectra of Meat. *Applied Spectroscopy* **1985,** *39* (3), 491-500.

275. Solheim, J. H.; Gunko, E.; Petersen, D.; Großerüschkamp, F.; Gerwert, K.; Kohler, A., An open-source code for Mie extinction extended multiplicative signal correction for infrared microscopy spectra of cells and tissues. *Journal of Biophotonics* **2019,** *12* (8), e201800415.

276. Bassan, P.; Byrne, H. J.; Bonnier, F.; Lee, J.; Dumas, P.; Gardner, P., Resonant Mie scattering in infrared spectroscopy of biological materials – understanding the 'dispersion artefact'. *Analyst* **2009,** *134* (8), 1586-1593.

277. Bassan, P.; Kohler, A.; Martens, H.; Lee, J.; Byrne, H. J.; Dumas, P.; Gazi, E.; Brown, M.; Clarke, N.; Gardner, P., Resonant Mie Scattering (RMieS) correction of infrared spectra from highly scattering biological samples. *Analyst* **2010,** *135* (2), 268-277.

278. Kohler, A.; Sulé-Suso, J.; Sockalingum, G. D.; Tobin, M.; Bahrami, F.; Yang, Y.; Pijanka, J.; Dumas, P.; Cotte, M.; van Pittius, D. G.; Parkes, G.; Martens, H., Estimating and Correcting Mie Scattering in Synchrotron-Based Microscopic Fourier Transform Infrared Spectra by Extended Multiplicative Signal Correction. *Applied Spectroscopy* **2008,** *62* (3), 259-266.

279. Lasch, P., Spectral pre-processing for biomedical vibrational spectroscopy and microspectroscopic imaging. *Chemometrics and Intelligent Laboratory Systems* **2012,** *117*, 100-114.

280. Rinnan, Å.; Berg, F. v. d.; Engelsen, S. B., Review of the most common pre-processing techniques for near-infrared spectra. *TrAC Trends in Analytical Chemistry* **2009,** *28* (10), 1201-1222.

281. Besseling, R.; Damen, M.; Tran, T.; Nguyen, T.; van den Dries, K.; Oostra, W.; Gerich, A., An efficient, maintenance free and approved method for spectroscopic control and monitoring of blend uniformity: The moving F-test. *Journal of Pharmaceutical and Biomedical Analysis* **2015,** *114*, 471-481.

282. Stavitski, E.; Smith, R. J.; Bourassa, M. W.; Acerbo, A. S.; Carr, G. L.; Miller, L. M., Dynamic Full-Field Infrared Imaging with Multiple Synchrotron Beams. *Analytical Chemistry* **2013,** *85* (7), 3599-3605.

283. Tobin, M., Australian Synchrotron, 2021.

284. Tobin, M. J., Personal Communication. Australian Synchrotron, ANSTO: 2021.

285. Kimber, J. A.; Foreman, L.; Turner, B.; Rich, P.; Kazarian, S. G., FTIR spectroscopic imaging and mapping with correcting lenses for studies of biological cells and tissues. *Faraday Discussions* **2016,** *187* (0), 69-85.

286. Findlay, C. R.; Wiens, R.; Rak, M.; Sedlmair, J.; Hirschmugl, C. J.; Morrison, J.; Mundy, C. J.; Kansiz, M.; Gough, K. M., Rapid biodiagnostic ex vivo imaging at 1 μm pixel resolution with thermal source FTIR FPA. *Analyst* **2015,** *140* (7), 2493-2503.

287. Nasse, M. J.; Bellehumeur, B.; Ratti, S.; Olivieri, C.; Buschke, D.; Squirrell, J.; Eliceiri, K.; Ogle, B.; Patterson, C. S.; Giordano, M.; Hirschmugl, C. J., Opportunities for multiple-beam synchrotron-based mid-infrared imaging at IRENI. *Vibrational Spectroscopy* **2012,** *60*, 10-15.

288. Hastie, T.; Tibshirani, R.; Friedman, J., Kernel Smoothing Methods. In *The Elements of Statistical Learning: Data Mining, Inference, and Prediction*, Springer New York: New York, NY, 2009; pp 191-218.

289. Altschuler, S. J.; Wu, L. F., Cellular Heterogeneity: Do Differences Make a Difference? *Cell* **2010,** *141* (4), 559-563.

290. Desruisseaux, M. S.; Nagajyothi; Trujillo, M. E.; Tanowitz, H. B.; Scherer, P. E., Adipocyte, Adipose Tissue, and Infectious Disease. *Infection and Immunity* **2007,** *75* (3), 1066.

291. Kiess, W.; Petzold, S.; Töpfer, M.; Garten, A.; Blüher, S.; Kapellen, T.; Körner, A.; Kratzsch, J., Adipocytes and adipose tissue. *Best Practice & Research Clinical Endocrinology & Metabolism* **2008,** *22* (1), 135-153.

292. Green, H.; Kehinde, O., An established preadipose cell line and its differentiation in culture II. Factors affecting the adipose conversion. *Cell* **1975,** *5* (1), 19-27.

293. Bader, C.; Shandala, T.; Carter, E.; Ivask, A.; Guinan, T.; Hickey, S.; Werrett, M.; Wright, P.; Simpson, P.; Stagni, S.; Voelcker, N.; Lay, P.; Massi, M.; Plush, S.; Brooks, D., A Molecular Probe for the Detection of Polar Lipids in Live Cells. *PloS one* **2016,** *11*, e0161557.

294. Rutkowski, J. M.; Stern, J. H.; Scherer, P. E., The cell biology of fat expansion. *Journal of Cell Biology* **2015,** *208* (5), 501-512.

295. Lagathu, C.; Bastard, J.-P.; Auclair, M.; Maachi, M.; Capeau, J.; Caron, M., Chronic interleukin-6 (IL-6) treatment increased IL-6 secretion and induced insulin resistance in adipocyte: prevention by rosiglitazone. *Biochemical and Biophysical Research Communications* **2003,** *311* (2), 372-379.

296. Hannich, J. T.; Umebayashi, K.; Riezman, H., Distribution and Functions of Sterols and Sphingolipids. *Cold Spring Harbor Perspectives in Biology* **2011,** *3* (5).

297. Mazur, A. I.; Marcsisin, E. J.; Bird, B.; Miljković, M.; Diem, M., Evaluating different fixation protocols for spectral cytopathology, part 1. *Analytical chemistry* **2012,** *84* (3), 1259-1266.

298. Rehder, D., *Bioinorganic vanadium chemistry*. John Wiley & Sons: Chichester, England ;, 2008.

299. Lu, B.; Ennis, D.; Lai, R.; Bogdanovic, E.; Nikolov, R.; Salamon, L.; Fantus, C.; Le-Tien, H.; Fantus, I. G., Enhanced Sensitivity of Insulin-resistant Adipocytes to Vanadate Is Associated with Oxidative Stress and Decreased Reduction of Vanadate (+5) to Vanadyl (+4)*. *Journal of Biological Chemistry* **2001,** *276* (38), 35589-35598.

300. Dunkhunthod, B.; Thumanu, K.; Eumkeb, G., Application of FTIR microspectroscopy for monitoring and discrimination of the anti-adipogenesis activity of baicalein in 3T3-L1 adipocytes. *Vibrational Spectroscopy* **2017,** *89*, 92-101.

301. Mookerjee, S. A.; Goncalves, R. L. S.; Gerencser, A. A.; Nicholls, D. G.; Brand, M. D., The contributions of respiration and glycolysis to extracellular acid production. *Biochimica et Biophysica Acta (BBA) - Bioenergetics* **2015,** *1847* (2), 171-181.

302. Wang, Q.; Kretlow, A.; Beekes, M.; Naumann, D.; Miller, L., In situ characterization of prion protein structure and metal accumulation in scrapie-infected cells by synchrotron infrared and X-ray imaging. *Vibrational Spectroscopy* **2005,** *38* (1), 61-69.

303. Gaschler, M. M.; Stockwell, B. R., Lipid peroxidation in cell death. *Biochemical and Biophysical Research Communications* **2017,** *482* (3), 419-425.

304. Shibata, T.; Iio, K.; Kawai, Y.; Shibata, N.; Kawaguchi, M.; Toi, S.; Kobayashi, M.; Kobayashi, M.; Yamamoto, K.; Uchida, K., Identification of a Lipid Peroxidation Product as a Potential Trigger of the p53 Pathway. *Journal of Biological Chemistry* **2006,** *281* (2), 1196-1204.

305. Monteiro, H. P.; Winterbourn, C. C.; Stern, A., Tetravalent Vanadium Releases Ferritin Iron which Stimulates Vanadium-Dependent Lipid Peroxidation. *Free Radical Research Communications* **1991,** *12* (1), 125-129.

306. Guillén, M. D.; Cabo, N., Characterization of edible oils and lard by fourier transform infrared spectroscopy. Relationships between composition and frequency of concrete bands in the fingerprint region. *Journal of the American Oil Chemists' Society* **1997,** *74* (10), 1281-1286.

307. Shirazi, F.; Wong, P.; Goel, R., Interaction of Cisplatin with Cellular Macromolecules: A Fourier Transform Infrared Spectroscopy Study. *Iranian Journal of Pharmaceutical Research* **2003**, 11-15.

308. Scherer, P. E., Adipose Tissue. *Diabetes* **2006,** *55* (6), 1537.

309. Xie, Y.; Zhang, D.; Jarori, G. K.; Davisson, V. J.; Ben-Amotz, D., The Raman detection of peptide tyrosine phosphorylation. *Analytical Biochemistry* **2004,** *332* (1), 116-121.

310. Chiang, S.-H.; Baumann, C. A.; Kanzaki, M.; Thurmond, D. C.; Watson, R. T.; Neudauer, C. L.; Macara, I. G.; Pessin, J. E.; Saltiel, A. R., Insulin-stimulated GLUT4 translocation requires the CAP-dependent activation of TC10. *Nature* **2001,** *410* (6831), 944-948.

311. Boren, J.; Brindle, K. M., Apoptosis-induced mitochondrial dysfunction causes cytoplasmic lipid droplet formation. *Cell Death Differ* **2012,** *19* (9), 1561-1570.

312. Fontaine, J.; Tavernier, G.; Morin, N.; Carpéné, C., Vanadium-dependent activation of glucose transport in adipocytes by catecholamines is not mediated via adrenoceptor stimulation or monoamine oxidase activity. *World J Diabetes* **2020,** *11* (12), 622-643.

313. Petrus, P.; Rosqvist, F.; Edholm, D.; Mejhert, N.; Arner, P.; Dahlman, I.; Rydén, M.; Sundbom, M.; Risérus, U., Saturated fatty acids in human visceral adipose tissue are associated with increased 11- β-hydroxysteroid-dehydrogenase type 1 expression. *Lipids Health Dis* **2015,** *14*, 42-42.

314. Azain, M. J., Role of fatty acids in adipocyte growth and development1,2. *Journal of Animal Science* **2004,** *82* (3), 916-924.

315. Lee, J.; Wen, B.; Carter, E. A.; Combes, V.; Grau, G. E. R.; Lay, P. A., Infrared spectroscopic characterization of monocytic microvesicles (microparticles) released upon lipopolysaccharide stimulation. *The FASEB Journal* **2017,** *31* (7), 2817-2827.

316. Shapaval, V.; Brandenburg, J.; Blomqvist, J.; Tafintseva, V.; Passoth, V.; Sandgren, M.; Kohler, A., Biochemical profiling, prediction of total lipid content and fatty acid profile in oleaginous yeasts by FTIR spectroscopy. *Biotechnology for Biofuels* **2019,** *12* (1), 140.

317. Levina, A.; Pires Vieira, A.; Wijetunga, A.; Kaur, R.; Koehn, J. T.; Crans, D. C.; Lay, P. A., A Short-Lived but Highly Cytotoxic Vanadium(V) Complex as a Potential Drug Lead for Brain Cancer Treatment by Intratumoral Injections. *Angewandte Chemie International Edition* **2020,** *59* (37), 15834-15838.
318. Thompson, K. H.; Lichter, J.; LeBel, C.; Scaife, M. C.; McNeill, J. H.; Orvig, C., Vanadium treatment of type 2 diabetes: A view to the future. *Journal of Inorganic Biochemistry* **2009,** *103* (4), 554-558.
319. Silva, J. C. P.; Marques, C.; Martins, F. O.; Viegas, I.; Tavares, L.; Macedo, M. P.; Jones, J. G., Determining contributions of exogenous glucose and fructose to de novo fatty acid and glycerol synthesis in liver and adipose tissue. *Metabolic Engineering* **2019,** *56*, 69-76.
320. Kim, J.; Song, G.; Wu, G.; Bazer, F. W., Functional roles of fructose. *Proceedings of the National Academy of Sciences* **2012,** *109* (25), 9680.
321. Szalontai, B.; Nishiyama, Y.; Gombos, Z.; Murata, N., Membrane dynamics as seen by Fourier transform infrared spectroscopy in a cyanobacterium, Synechocystis PCC 6803: The effects of lipid unsaturation and the protein-to-lipid ratio. *Biochimica et Biophysica Acta (BBA) - Biomembranes* **2000,** *1509* (1), 409-419.
322. Portner, H. O., Contributions of anaerobic metabolism to pH regulation in animal tissues: theory. *Journal of Experimental Biology* **1987,** *131* (1), 69-87.
323. Erdmann, E.; Werdan, K.; Krawietz, W.; Schmitz, W.; Scholz, H., Vanadate and its significance in biochemistry and pharmacology. *Biochemical Pharmacology* **1984,** *33* (7), 945-950.
324. Koprowski, J. A.; Allen Tucker, H., Bovine Serum Growth Hormone, Corticoids and Insulin During Lactation. *Endocrinology* **1973,** *93* (3), 645-651.
325. Tsiani, E.; Bogdanovic, E.; Sorisky, A.; Nagy, L.; Fantus, I. G., Tyrosine phosphatase inhibitors, vanadate and pervanadate, stimulate glucose transport and GLUT translocation in muscle cells by a mechanism independent of phosphatidylinositol 3-kinase and protein kinase C. *Diabetes* 1998/11//, 1998, p 1676+.
326. Willsky, G. R.; White, D. A.; McCabe, B. C., Metabolism of added orthovanadate to vanadyl and high-molecular-weight vanadates by Saccharomyces cerevisiae. *The Journal of biological chemistry* **1984,** *259* (21), 13273-13281.
327. Nakamura, M.; Yamada, M.; Ohsawa, T.; Morisawa, H.; Nishine, T.; Nishimura, O.; Toda, T., Phosphoproteomic profiling of human SH-SY5Y neuroblastoma

cells during response to 6-hydroxydopamine-induced oxidative stress. *Biochimica et Biophysica Acta (BBA) - Molecular Cell Research* **2006,** *1763* (9), 977-989.

328. Hurrle, S.; Hsu, W. H., The etiology of oxidative stress in insulin resistance. *Biomed J* **2017,** *40* (5), 257-262.
329. Kowalczyk, A.; Kleniewska, P.; Kolodziejczyk, M.; Skibska, B.; Goraca, A., The role of endothelin-1 and endothelin receptor antagonists in inflammatory response and sepsis. *Arch Immunol Ther Exp (Warsz)* **2015,** *63* (1), 41-52.
330. Scalera, F.; Dittrich, R.; Beckmann, M. W.; Beinder, E., Effect of endothelin-1 on intracellular glutathione and lipid peroxide availability and on the secretion of vasoactive substances by human umbilical vein endothelial cells. *European Journal of Clinical Investigation* **2002,** *32* (8), 556-562.
331. Sabbioni, E.; Pozzi, G.; Devos, S.; Pintar, A.; Casella, L.; Fischbach, M., The intensity of vanadium(V)-induced cytotoxicity and morphological transformation in BALB/3T3 cells is dependent on glutathione-mediated bioreduction to vanadium(IV). *Carcinogenesis* **1993,** *14* (12), 2565-2568.
332. Shaver, A.; Ng, J. B.; Hall, D. A.; Posner, B. I., The chemistry of peroxovanadium compounds relevant to insulin mimesis. *Molecular and Cellular Biochemistry* **1995,** *153* (1), 5-15.
333. Huyer, G.; Liu, S.; Kelly, J.; Moffat, J.; Payette, P.; Kennedy, B.; Tsaprailis, G.; Gresser, M. J.; Ramachandran, C., Mechanism of Inhibition of Protein-tyrosine Phosphatases by Vanadate and Pervanadate*. *Journal of Biological Chemistry* **1997,** *272* (2), 843-851.
334. Dinsmore, C. J.; Soriano, P., MAPK and PI3K signaling: At the crossroads of neural crest development. *Developmental Biology* **2018,** *444*, S79-S97.
335. Germinario, R. J.; Colby-Germinario, S. P.; Posner, B. I.; Nahm, K., Different Forms of Vanadate on Sugar Transport in Insulin Target and Nontarget Cells. *J Biomed Biotechnol* **2002,** *2* (1), 22-30.
336. Dong, F.; Zhang, X.; Wold, L. E.; Ren, Q.; Zhang, Z.; Ren, J., Endothelin-1 enhances oxidative stress, cell proliferation and reduces apoptosis in human umbilical vein endothelial cells: role of ETB receptor, NADPH oxidase and caveolin-1. *Br J Pharmacol* **2005,** *145* (3), 323-333.
337. Ma, M.; Quan, Y.; Li, Y.; He, X.; Xiao, J.; Zhan, M.; Zhao, W.; Xin, Y.; Lu, L.; Luo, L., Bidirectional modulation of insulin action by reactive oxygen species in 3T3-L1 adipocytes. *Mol Med Rep* **2018,** *18* (1), 807-814.

338. Keller, R. J.; Sharma, R. P.; Grover, T. A.; Piette, L. H., Vanadium and lipid peroxidation: Evidence for involvement of vanadyl and hydroxyl radical. *Archives of Biochemistry and Biophysics* **1988,** *265* (2), 524-533.

339. Ding, M.; Li, J.-J.; Leonard, S. S.; Ye, J.-P.; Shi, X.; Colburn, N. H.; Castranova, V.; Vallyathan, V., Vanadate-induced activation of activator protein-1: role of reactive oxygen species. *Carcinogenesis* **1999,** *20* (4), 663-668.

340. Huang, C.; Zhang, Z.; Ding, M.; Li, J.; Ye, J.; Leonard, S. S.; Shen, H.-M.; Butterworth, L.; Lu, Y.; Costa, M.; Rojanasakul, Y.; Castranova, V.; Vallyathan, V.; Shi, X., Vanadate Induces p53 Transactivation through Hydrogen Peroxide and Causes Apoptosis*. *Journal of Biological Chemistry* **2000,** *275* (42), 32516-32522.

341. Pandey, S. K.; Chiasson, J.-L.; Srivastava, A. K., Vanadium salts stimulate mitogen-activated protein (MAP) kinases and ribosomal S6 kinases. *Molecular and Cellular Biochemistry* **1995,** *153* (1), 69-78.

342. Cenini, G.; Sultana, R.; Memo, M.; Butterfield, D. A., Elevated levels of pro-apoptotic p53 and its oxidative modification by the lipid peroxidation product, HNE, in brain from subjects with amnestic mild cognitive impairment and Alzheimer's disease. *J Cell Mol Med* **2008,** *12* (3), 987-994.

343. Anderson, E. J.; Katunga, L. A.; Willis, M. S., Mitochondria as a source and target of lipid peroxidation products in healthy and diseased heart. *Clin Exp Pharmacol Physiol* **2012,** *39* (2), 179-193.

344. Duchen, M. R., Roles of Mitochondria in Health and Disease. *Diabetes* **2004,** *53*, S96-102.

345. Aon, M. A.; Bhatt, N.; Cortassa, S. C., Mitochondrial and cellular mechanisms for managing lipid excess. *Frontiers in Physiology* **2014,** *5* (282).

346. Douglas, D. N.; Pu, C. H.; Lewis, J. T.; Bhat, R.; Anwar-Mohamed, A.; Logan, M.; Lund, G.; Addison, W. R.; Lehner, R.; Kneteman, N. M., Oxidative Stress Attenuates Lipid Synthesis and Increases Mitochondrial Fatty Acid Oxidation in Hepatoma Cells Infected with Hepatitis C Virus. *The Journal of biological chemistry* **2016,** *291* (4), 1974-1990.

347. Mikalayeva, V.; Ceslevičienė, I.; Sarapinienė, I.; Žvikas, V.; Skeberdis, V. A.; Jakštas, V.; Bordel, S., Fatty Acid Synthesis and Degradation Interplay to Regulate the Oxidative Stress in Cancer Cells. *Int J Mol Sci* **2019,** *20* (6), 1348.

348. Nowinski, S. M.; Solmonson, A.; Rusin, S. F.; Maschek, J. A.; Bensard, C. L.; Fogarty, S.; Jeong, M.-Y.; Lettlova, S.; Berg, J. A.; Morgan, J. T.; Ouyang, Y.;

Naylor, B. C.; Paulo, J. A.; Funai, K.; Cox, J. E.; Gygi, S. P.; Winge, D. R.; DeBerardinis, R. J.; Rutter, J., Mitochondrial fatty acid synthesis coordinates oxidative metabolism in mammalian mitochondria. *eLife* **2020,** *9*, e58041.

349. Haynes, J.; Srivastava, J.; Madson, N.; Wittmann, T.; Barber, D. L., Dynamic actin remodeling during epithelial-mesenchymal transition depends on increased moesin expression. *Mol Biol Cell* **2011,** *22* (24), 4750-4764.

350. Patel, I. I.; Shearer, D. A.; Fogarty, S. W.; Fullwood, N. J.; Quaroni, L.; Martin, F. L.; Weisz, J., Infrared microspectroscopy identifies biomolecular changes associated with chronic oxidative stress in mammary epithelium and stroma of breast tissues from healthy young women. *Cancer Biology & Therapy* **2014,** *15* (2), 225-235.

351. Mirghani, M. E. S.; Man, Y. B. C.; Jinap, S.; Baharin, B. S.; Bakar, J., Rapid method for determining malondialdehyde as secondary oxidation product in palm olein system by Fourier transform infrared spectroscopy. *Phytochemical Analysis* **2002,** *13* (4), 195-201.

352. Romero, M. d. M.; Sabater, D.; Fernández-López, J. A.; Remesar, X.; Alemany, M., Glycerol Production from Glucose and Fructose by 3T3-L1 Cells: A Mechanism of Adipocyte Defense from Excess Substrate. *PLOS ONE* **2015,** *10* (10), e0139502.

353. Froesch, E. R.; Ginsberg, J. L., Fructose Metabolism of Adipose Tissue: I. Comparison of fructose and glucose matabolism in epidydimal apidpose tissue of normal rats. *Journal of Biological Chemistry* **1962,** *237* (11), 3317-3324.

354. Werman, M. J.; Bhathena, S. J., Fructose metabolizing enzymes in the rat liver and metabolic parameters: Interactions between dietary copper, type of carbohydrates, and gender. *The Journal of Nutritional Biochemistry* **1995,** *6* (7), 373-379.

355. Zielke, H. R.; Sumbilla, C. M.; Zielke, C. L.; Tildon, J. T.; Ozand, P. T. In *Glutamine Metabolism by Cultured Mammalian Cells*, Glutamine Metabolism in Mammalian Tissues, Berlin, Heidelberg, 1984//; Häussinger, D.; Sies, H., Eds. Springer Berlin Heidelberg: Berlin, Heidelberg, 1984; pp 247-254.

356. Lecoutre, S.; Maqdasy, S.; Petrus, P.; Ludzki, A.; Couchet, M.; Mejhert, N.; Rydén, M., Glutamine metabolism in adipocytes: a bona fide epigenetic modulator of inflammation. *Adipocyte* **2020,** *9* (1), 620-625.

357. Masschelin, P. M.; Cox, A. R.; Chernis, N.; Hartig, S. M., The Impact of Oxidative Stress on Adipose Tissue Energy Balance. *Frontiers in Physiology* **2020,** *10* (1638).

358. Hudgins, L. C.; Parker, T. S.; Levine, D. M.; Hellerstein, M. K., A dual sugar challenge test for lipogenic sensitivity to dietary fructose. *J Clin Endocrinol Metab* **2011,** *96* (3), 861-868.

359. Stanhope, K. L.; Bremer, A. A.; Medici, V.; Nakajima, K.; Ito, Y.; Nakano, T.; Chen, G.; Fong, T. H.; Lee, V.; Menorca, R. I.; Keim, N. L.; Havel, P. J., Consumption of fructose and high fructose corn syrup increase postprandial triglycerides, LDL-cholesterol, and apolipoprotein-B in young men and women. *J Clin Endocrinol Metab* **2011,** *96* (10), E1596-E1605.

360. Goldstein, B. J.; Mahadev, K.; Wu, X.; Zhu, L.; Motoshima, H., Role of insulin-induced reactive oxygen species in the insulin signaling pathway. *Antioxid Redox Signal* **2005,** *7* (7-8), 1021-1031.

361. Ly, L. D.; Xu, S.; Choi, S.-K.; Ha, C.-M.; Thoudam, T.; Cha, S.-K.; Wiederkehr, A.; Wollheim, C. B.; Lee, I.-K.; Park, K.-S., Oxidative stress and calcium dysregulation by palmitate in type 2 diabetes. *Experimental & Molecular Medicine* **2017,** *49* (2), e291-e291.

362. Wiśniewski, J. R.; Vildhede, A.; Norén, A.; Artursson, P., In-depth quantitative analysis and comparison of the human hepatocyte and hepatoma cell line HepG2 proteomes. *Journal of Proteomics* **2016,** *136*, 234-247.

363. Leclercq, I. A.; Da Silva Morais, A.; Schroyen, B.; Van Hul, N.; Geerts, A., Insulin resistance in hepatocytes and sinusoidal liver cells: Mechanisms and consequences. *Journal of Hepatology* **2007,** *47* (1), 142-156.

364. Bianchini, F.; Kaaks, R.; Vainio, H., Overweight, obesity, and cancer risk. *The Lancet Oncology* **2002,** *3* (9), 565-574.

365. Jang, C.; Hui, S.; Lu, W.; Cowan, A. J.; Morscher, R. J.; Lee, G.; Liu, W.; Tesz, G. J.; Birnbaum, M. J.; Rabinowitz, J. D., The Small Intestine Converts Dietary Fructose into Glucose and Organic Acids. *Cell Metab* **2018,** *27* (2), 351-361.e3.

366. Chakraborty, A.; Selvaraj, S., Differential modulation of xenobiotic metabolizing enzymes by vanadium during diethylnitrosamine-induced hepatocarcinogenesis in Sprague-Dawley rats. *Neoplasma* **2000,** *47* (2), 81-89.

367. Siddik, Z. H., Cisplatin: mode of cytotoxic action and molecular basis of resistance. *Oncogene* **2003,** *22* (47), 7265-7279.

368. Jamali, B.; Nakhjavani, M.; Hosseinzadeh, L.; Amidi, S.; Nikounezhad, N.; Shirazi, F., Intracellular GSH Alterations and Its Relationship to Level of Resistance following Exposure to Cisplatin in Cancer Cells. *Iranian journal of pharmaceutical research : IJPR* **2015,** *14*, 513-9.

369. Mi, L.; Kuang, H., Melatonin Regulates Cisplatin Resistance and Glucose Metabolism Through Hippo Signaling in Hepatocellular Carcinoma Cells. *Cancer Management and Research* **2020,** *Volume 12*, 1863-1874.

370. Pascale, F.; Bedouet, L.; Baylatry, M.; Namur, J.; Laurent, A., Comparative Chemosensitivity of VX2 and HCC Cell Lines to Drugs Used in TACE. *Anticancer Research* **2015,** *35* (12), 6497.

371. van Tonder, A.; Joubert, A. M.; Cromarty, A. D., Limitations of the 3-(4,5-dimethylthiazol-2-yl)-2,5-diphenyl-2H-tetrazolium bromide (MTT) assay when compared to three commonly used cell enumeration assays. *BMC Res Notes* **2015,** *8*, 47-47.

372. Bruun, S. W.; Kohler, A.; Adt, I.; Sockalingum, G. D.; Manfait, M.; Martens, H., Correcting Attenuated Total Reflection—Fourier Transform Infrared Spectra for Water Vapor and Carbon Dioxide. *Applied Spectroscopy* **2006,** *60* (9), 1029-1039.

373. Liu, X.-N.; Wang, S.; Yang, Q.; Wang, Y.-J.; Chen, D.-X.; Zhu, X.-X., ESC reverses epithelial mesenchymal transition induced by transforming growth factor-β via inhibition of Smad signal pathway in HepG2 liver cancer cells. *Cancer Cell International* **2015,** *15* (1), 114.

374. Ma, Y.; Li, M.; Liu, J.; Pang, C.; Zhang, J.; Li, Y.; Fu, X., Location, Isolation, and Identification of Mesenchymal Stem Cells from Adult Human Sweat Glands. *Stem Cells International* **2018,** *2018*, 2090276.

375. Westad, F.; Gidskehaug, L.; Swarbrick, B.; Flåten, G. R., Assumption free modeling and monitoring of batch processes. *Chemometrics and Intelligent Laboratory Systems* **2015,** *149*, 66-72.

376. Softic, S.; Cohen, D. E.; Kahn, C. R., Role of Dietary Fructose and Hepatic De Novo Lipogenesis in Fatty Liver Disease. *Dig Dis Sci* **2016,** *61* (5), 1282-1293.

377. Crans, D. C.; Gambino, D.; Etcheverry, S. B., Vanadium science: chemistry, catalysis, materials, biological and medicinal studies. *New Journal of Chemistry* **2019,** *43* (45), 17535-17537.

378. Crans, D. C.; Keramidas, A. D.; Hoover-Litty, H.; Anderson, O. P.; Miller, M. M.; Lemoine, L. M.; Pleasic-Williams, S.; Vandenberg, M.; Rossomando, A. J.; Sweet, L. J., Synthesis, Structure, and Biological Activity of a New

Insulinomimetic Peroxovanadium Compound: Bisperoxovanadium Imidazole Monoanion. *Journal of the American Chemical Society* **1997,** *119* (23), 5447-5448.

379. Hambley, T. W., Platinum binding to DNA: structural controls and consequences. *Journal of the Chemical Society, Dalton Transactions* **2001,** (19), 2711-2718.

380. Agudelo, D.; Bourassa, P.; Bérubé, G.; Tajmir-Riahi, H.-A., Intercalation of antitumor drug doxorubicin and its analogue by DNA duplex: Structural features and biological implications. *International Journal of Biological Macromolecules* **2014,** *66*, 144-150.

381. Sies, H., What is Oxidative Stress? In *Oxidative Stress and Vascular Disease*, Keaney, J. F., Ed. Springer US: Boston, MA, 2000; pp 1-8.

382. Chandra, J.; Samali, A.; Orrenius, S., Triggering and modulation of apoptosis by oxidative stress. *Free Radical Biology and Medicine* **2000,** *29* (3), 323-333.

383. Cunha - de Padua, M. M.; Suter Correia Cadena, S. M.; de Oliveira Petkowicz, C. L.; Martinez, G. R.; Merlin Rocha, M. E.; Mercê, A. L. R.; Noleto, G. R., Toxicity of native and oxovanadium (IV/V) galactomannan complexes on HepG2 cells is related to impairment of mitochondrial functions. *Carbohydrate Polymers* **2017,** *173*, 665-675.

384. Liu, T.-T.; Liu, Y.-J.; Wang, Q.; Yang, X.-G.; Wang, K., Reactive-oxygen-species-mediated Cdc25C degradation results in differential antiproliferative activities of vanadate, tungstate, and molybdate in the PC-3 human prostate cancer cell line. *JBIC Journal of Biological Inorganic Chemistry* **2012,** *17* (2), 311-320.

385. Wu, J.-X.; Hong, Y.-H.; Yang, X.-G., Bis(acetylacetonato)-oxidovanadium(IV) and sodium metavanadate inhibit cell proliferation via ROS-induced sustained MAPK/ERK activation but with elevated AKT activity in human pancreatic cancer AsPC-1 cells. *JBIC Journal of Biological Inorganic Chemistry* **2016,** *21* (8), 919-929.

386. Roy, S.; Banerjee, S.; Chakraborty, T., Vanadium quercetin complex attenuates mammary cancer by regulating the P53, Akt/mTOR pathway and downregulates cellular proliferation correlated with increased apoptotic events. *Biometals* **2018,** *31* (4), 647-671.

387. Pannala, R.; Basu, A.; Petersen, G. M.; Chari, S. T., New-onset diabetes: a potential clue to the early diagnosis of pancreatic cancer. *The Lancet Oncology* **2009,** *10* (1), 88-95.

388. Yap, T. A.; Garrett, M. D.; Walton, M. I.; Raynaud, F.; de Bono, J. S.; Workman, P., Targeting the PI3K–AKT–mTOR pathway: progress, pitfalls, and promises. *Current Opinion in Pharmacology* **2008,** *8* (4), 393-412.

389. Molinuevo, M. S.; Barrio, D. A.; Cortizo, A. M.; Etcheverry, S. B., Antitumoral properties of two new vanadyl(IV) complexes in osteoblasts in culture: role of apoptosis and oxidative stress. *Cancer Chemotherapy and Pharmacology* **2004,** *53* (2), 163-172.

390. Fu, Y.; Wang, Q.; Yang, X.-G.; Yang, X.-D.; Wang, K., Vanadyl bisacetylacetonate induced G1/S cell cycle arrest via high-intensity ERK phosphorylation in HepG2 cells. *JBIC Journal of Biological Inorganic Chemistry* **2008,** *13* (6), 1001.

391. +Hayes, J. D.; Dinkova-Kostova, A. T.; Tew, K. D., Oxidative Stress in Cancer. *Cancer Cell* **2020,** *38* (2), 167-197.

392. Kuehne, A.; Emmert, H.; Soehle, J.; Winnefeld, M.; Fischer, F.; Wenck, H.; Gallinat, S.; Terstegen, L.; Lucius, R.; Hildebrand, J.; Zamboni, N., Acute Activation of Oxidative Pentose Phosphate Pathway as First-Line Response to Oxidative Stress in Human Skin Cells. *Molecular Cell* **2015,** *59* (3), 359-371.

393. Thorens, B., GLUT2, glucose sensing and glucose homeostasis. *Diabetologia* **2015,** *58* (2), 221-232.

394. Macheda, M. L.; Rogers, S.; Best, J. D., Molecular and cellular regulation of glucose transporter (GLUT) proteins in cancer. *Journal of Cellular Physiology* **2005,** *202* (3), 654-662.

395. Zimmerman, R. L.; Fogt, F.; Burke, M.; Murakata, L. A., Assessment of Glut-1 expression in cholangiocarcinoma, benign biliary lesions and hepatocellular carcinoma. *Oncol Rep* **2002,** *9* (4), 689-692.

396. Cooper, R.; Sarioğlu, S.; Sökmen, S.; Füzün, M.; Küpelioğlu, A.; Valentine, H.; Görken, I. B.; Airley, R.; West, C., Glucose transporter-1 (GLUT-1): a potential marker of prognosis in rectal carcinoma? *Br J Cancer* **2003,** *89* (5), 870-876.

397. Oliver, R. J.; Woodwards, R. T. M.; Sloan, P.; Thakker, N. S.; Stratford, I. J.; Airley, R. E., Prognostic value of facilitative glucose transporter Glut-1 in oral squamous cell carcinomas treated by surgical resection: results of EORTC Translational Research Fund studies. *European Journal of Cancer* **2004,** *40* (4), 503-507.

398. Amann, T.; Maegdefrau, U.; Hartmann, A.; Agaimy, A.; Marienhagen, J.; Weiss, T. S.; Stoeltzing, O.; Warnecke, C.; Schölmerich, J.; Oefner, P. J.; Kreutz, M.;

Bosserhoff, A. K.; Hellerbrand, C., GLUT1 expression is increased in hepatocellular carcinoma and promotes tumorigenesis. *Am J Pathol* **2009,** *174* (4), 1544-1552.

399. Kandasamy, P.; Gyimesi, G.; Kanai, Y.; Hediger, M. A., Amino acid transporters revisited: New views in health and disease. *Trends in Biochemical Sciences* **2018,** *43* (10), 752-789.

400. Eagle, H., Amino Acid Metabolism in Mammalian Cell Cultures. *Science* **1959,** *130* (3373), 432.

401. Bracken, W. M.; Sharma, R. P.; Elsner, Y. Y., Vanadium accumulation and subcellular distribution in relation to vanadate induced cytotoxicity in vitro. *Cell Biology and Toxicology* **1985,** *1* (4), 259-268.

402. Chadt, A.; Al-Hasani, H., Glucose transporters in adipose tissue, liver, and skeletal muscle in metabolic health and disease. *Pflugers Arch* **2020,** *472* (9), 1273-1298.

403. Kristin, A.; Janine, K.-M., Interrelation Between Protein Synthesis, Proteostasis and Life Span. *Current Genomics* **2014,** *15* (1), 66-75.

404. Dibble, Christian C.; Elis, W.; Menon, S.; Qin, W.; Klekota, J.; Asara, John M.; Finan, Peter M.; Kwiatkowski, David J.; Murphy, Leon O.; Manning, Brendan D., TBC1D7 Is a Third Subunit of the TSC1-TSC2 Complex Upstream of mTORC1. *Molecular Cell* **2012,** *47* (4), 535-546.

405. Hackett, M. J.; Sylvain, N. J.; Hou, H.; Caine, S.; Alaverdashvili, M.; Pushie, M. J.; Kelly, M. E., Concurrent Glycogen and Lactate Imaging with FTIR Spectroscopy To Spatially Localize Metabolic Parameters of the Glial Response Following Brain Ischemia. *Analytical Chemistry* **2016,** *88* (22), 10949-10956.

406. Sugiyama, H.; Matsugo, S.; Misu, H.; Takamura, T.; Kaneko, S.; Kanatani, Y.; Kaido, M.; Mihara, C.; Abeywardana, N.; Sakai, A.; Sato, K.; Miyashita, Y.; Kanamori, K., Regulation of the physiological effects of peroxidovanadium(V) complexes by the electronic nature of ligands. *Journal of Inorganic Biochemistry* **2013,** *121*, 66-76.

407. Sheikh, M. Y.; Choi, J.; Qadri, I.; Friedman, J. E.; Sanyal, A. J., Hepatitis C virus infection: Molecular pathways to metabolic syndrome. *Hepatology* **2008,** *47* (6), 2127-2133.

408. Bensaad, K.; Tsuruta, A.; Selak, M. A.; Vidal, M. N. C.; Nakano, K.; Bartrons, R.; Gottlieb, E.; Vousden, K. H., TIGAR, a p53-Inducible Regulator of Glycolysis and Apoptosis. *Cell* **2006,** *126* (1), 107-120.

409. Fu, X.; Wan, S.; Lyu, Y. L.; Liu, L. F.; Qi, H., Etoposide Induces ATM-Dependent Mitochondrial Biogenesis through AMPK Activation. *PLOS ONE* **2008,** *3* (4), e2009.

410. Mignolet, A.; Derenne, A.; Smolina, M.; Wood, B. R.; Goormaghtigh, E., FTIR spectral signature of anticancer drugs. Can drug mode of action be identified? *Biochim Biophys Acta* **2016,** *1864* (1), 85-101.

411. Munker, S.; Wu, Y.-L.; Ding, H.-G.; Liebe, R.; Weng, H.-L., Can a fibrotic liver afford epithelial-mesenchymal transition? *World J Gastroenterol* **2017,** *23* (26), 4661-4668.

412. Naumanen, P.; Lappalainen, P.; Hotulainen, P., Mechanisms of actin stress fibre assembly. *Journal of Microscopy* **2008,** *231* (3), 446-454.

413. Wang, X.-H.; Chen, Z.-G.; Xu, R.-L.; Lv, C.-Q.; Liu, J.; Du, B., TGF-β1 signaling pathway serves a role in HepG2 cell regulation by affecting the protein expression of PCNA, gankyrin, p115, XIAP and survivin. *Oncol Lett* **2017,** *13* (5), 3239-3246.

414. Lee, D.; Chung, Y. H.; Kim, J. A.; Lee, Y. S.; Lee, D.; Jang, M. K.; Kim, K. M.; Lim, Y. S.; Lee, H. C.; Lee, Y. S., Transforming Growth Factor Beta 1 Overexpression Is Closely Related to Invasiveness of Hepatocellular Carcinoma. *Oncology* **2012,** *82* (1), 11-18.

415. Rousseau, S.; Houle, F.; Landry, J.; Huot, J., p38 MAP kinase activation by vascular endothelial growth factor mediates actin reorganization and cell migration in human endothelial cells. *Oncogene* **1997,** *15* (18), 2169-2177.

416. Song, C.; Perides, G.; Wang, D.; Liu, Y. F., β-Amyloid peptide induces formation of actin stress fibers through p38 mitogen-activated protein kinase. *Journal of Neurochemistry* **2002,** *83* (4), 828-836.

417. Koudinova, N. V.; Berezov, T. T.; Koudinov, A. R., Multiple inhibitory effects of Alzheimer's peptide Aβ1–40 on lipid biosynthesis in cultured human HepG2 cells. *FEBS Letters* **1996,** *395* (2-3), 204-206.

418. Rocha, C. R. R.; Silva, M. M.; Quinet, A.; Cabral-Neto, J. B.; Menck, C. F. M., DNA repair pathways and cisplatin resistance: an intimate relationship. *Clinics (São Paulo, Brazil)* **2018,** *73* (suppl 1), e478s-e478s.

419. Harris, S. L.; Levine, A. J., The p53 pathway: positive and negative feedback loops. *Oncogene* **2005,** *24* (17), 2899-2908.

420. Dent, P.; Grant, S., Pharmacologic Interruption of the Mitogen-activated Extracellular-regulated Kinase/Mitogen-activated Protein Kinase Signal Transduction Pathway. *Clinical Cancer Research* **2001,** *7* (4), 775.
421. Persons, D. L.; Yazlovitskaya, E. M.; Pelling, J. C., Effect of Extracellular Signal-regulated Kinase on p53 Accumulation in Response to Cisplatin *. *Journal of Biological Chemistry* **2000,** *275* (46), 35778-35785.
422. Wang, X.; Martindale, J. L.; Holbrook, N. J., Requirement for ERK Activation in Cisplatin-induced Apoptosis *. *Journal of Biological Chemistry* **2000,** *275* (50), 39435-39443.
423. Fruman, D. A.; Chiu, H.; Hopkins, B. D.; Bagrodia, S.; Cantley, L. C.; Abraham, R. T., The PI3K Pathway in Human Disease. *Cell* **2017,** *170* (4), 605-635.
424. Champoux, J. J., DNA topoisomerases: Structure, function, and mechanism. *Annual Review of Biochemistry* **2001,** *70*, 369-413.
425. Alhazmi, H. A., FT-IR Spectroscopy for the Identification of Binding Sites and Measurements of the Binding Interactions of Important Metal Ions with Bovine Serum Albumin. *Scientia Pharmaceutica* **2019,** *87* (1), 5.
426. Lorenz-Fonfria, V. A., Infrared Difference Spectroscopy of Proteins: From Bands to Bonds. *Chemical Reviews* **2020,** *120* (7), 3466-3576.
427. Eldeeb, M. A.; Fahlman, R. P.; Esmaili, M.; Ragheb, M. A., Regulating Apoptosis by Degradation: The N-End Rule-Mediated Regulation of Apoptotic Proteolytic Fragments in Mammalian Cells. *Int J Mol Sci* **2018,** *19* (11), 3414.
428. Geidl-Flueck, B.; Hochuli, M.; Németh, Á.; Eberl, A.; Derron, N.; Köfeler, H. C.; Tappy, L.; Berneis, K.; Spinas, G. A.; Gerber, P. A., Fructose- and sucrose- but not glucose-sweetened beverages promote hepatic de novo lipogenesis: A randomized controlled trial. *Journal of Hepatology* **2021,** *75* (1), 46-54.
429. Wilkening, S.; Stahl, F.; Bader, A., Comparison Of Primary Human Hepatocytes and Hepatoma Cell Line HepG2 With Regard To Their Biotransformation Properties. *Drug Metabolism and Disposition* **2003,** *31* (8), 1035.
430. Goncalves, M. D.; Hopkins, B. D.; Cantley, L. C., Dietary Fat and Sugar in Promoting Cancer Development and Progression. *Annual Review of Cancer Biology* **2019,** *3* (1), 255-273.
431. Balaban, S.; Shearer, R. F.; Lee, L. S.; van Geldermalsen, M.; Schreuder, M.; Shtein, H. C.; Cairns, R.; Thomas, K. C.; Fazakerley, D. J.; Grewal, T.; Holst, J.; Saunders, D. N.; Hoy, A. J., Adipocyte lipolysis links obesity to breast cancer

growth: adipocyte-derived fatty acids drive breast cancer cell proliferation and migration. *Cancer & Metabolism* **2017,** *5* (1), 1.

432. Liang, R. J.; Taylor, S.; Nahiyaan, N.; Song, J.; Murphy, C. J.; Dantas, E.; Cheng, S.; Hsu, T.-W.; Ramsamooj, S.; Grover, R.; Hwang, S.-K.; Ngo, B.; Cantley, L. C.; Rhee, K. Y.; Goncalves, M. D., GLUT5 (SLC2A5) enables fructose-mediated proliferation independent of ketohexokinase. *Cancer & Metabolism* **2021,** *9* (1), 12.

433. Pizzino, G.; Irrera, N.; Cucinotta, M.; Pallio, G.; Mannino, F.; Arcoraci, V.; Squadrito, F.; Altavilla, D.; Bitto, A., Oxidative Stress: Harms and Benefits for Human Health. *Oxidative medicine and cellular longevity* **2017,** *2017*, 8416763-8416763.

434. Brose, S. A.; Marquardt, A. L.; Golovko, M. Y., Fatty acid biosynthesis from glutamate and glutamine is specifically induced in neuronal cells under hypoxia. *Journal of Neurochemistry* **2014,** *129* (3), 400-412.

435. Crans, D. C.; Yang, L.; Haase, A.; Yang, X., Metallo-Drugs: Development and Action of Anticancer Agents. In *9. HEALTH BENEFITS OF VANADIUM AND ITS POTENTIAL AS AN ANTICANCER AGENT*, Astrid, S.; Helmut, S.; Eva, F.; Roland, K. O. S., Eds. De Gruyter: 2018; pp 251-280.

436. Gargotti, M.; Efeoglu, E.; Byrne, H. J.; Casey, A., Raman spectroscopy detects biochemical changes due to different cell culture environments in live cells in vitro. *Analytical and bioanalytical chemistry* **2018,** *410* (28), 7537-7550.

437. Breslin, S.; O'Driscoll, L., Three-dimensional cell culture: the missing link in drug discovery. *Drug Discovery Today* **2013,** *18* (5), 240-249.

438. Kim, J. B., Three-dimensional tissue culture models in cancer biology. *Seminars in Cancer Biology* **2005,** *15* (5), 365-377.

439. Gallagher, N. B., Detection, Classification, and Quantification in Hyperspectral Images Using Classical Least Squares Models. In *Techniques and Applications of Hyperspectral Image Analysis*, 2007; pp 181-202.

440. Marini, F.; Amigo, J. M., Chapter 2.4 - Unsupervised exploration of hyperspectral and multispectral images. In *Data Handling in Science and Technology*, Amigo, J. M., Ed. Elsevier: 2020; Vol. 32, pp 93-114.

441. Gupta, U.; Singh, V.; Kumar, V.; Khajuria, Y., Spectroscopic Studies of Cholesterol: Fourier Transform Infra-Red and Vibrational Frequency Analysis. *Material Focus* **2014,** *3*, 1-7.

442. Rothschild, K. J., The early development and application of FTIR difference spectroscopy to membrane proteins: A personal perspective. *Biomedical Spectroscopy and Imaging* **2016,** *5*, 231-267.

443. Gao, Q.; Goodman, J., The lipid droplet—a well-connected organelle. *Frontiers in Cell and Developmental Biology* **2015,** *3* (49).

444. Faist, J.; Capasso, F.; Sivco, D. L.; Sirtori, C.; Hutchinson, A. L.; Cho, A. Y., Quantum Cascade Laser. *Science* **1994,** *264* (5158), 553-556.

445. Kuepper, C.; Kallenbach-Thieltges, A.; Juette, H.; Tannapfel, A.; Großerueschkamp, F.; Gerwert, K., Quantum Cascade Laser-Based Infrared Microscopy for Label-Free and Automated Cancer Classification in Tissue Sections. *Scientific Reports* **2018,** *8* (1), 7717.

446. Horvath, S. E.; Daum, G., Lipids of mitochondria. *Progress in Lipid Research* **2013,** *52* (4), 590-614.

447. Aguilar, D.; Fernandez, M. L., Hypercholesterolemia Induces Adipose Dysfunction in Conditions of Obesity and Nonobesity. *Advances in Nutrition* **2014,** *5* (5), 497-502.

448. Amigo, J. M.; Santos, C., Chapter 2.1 - Preprocessing of hyperspectral and multispectral images. In *Data Handling in Science and Technology*, Amigo, J. M., Ed. Elsevier: 2020; Vol. 32, pp 37-53.

449. Guilherme, A.; Virbasius, J. V.; Puri, V.; Czech, M. P., Adipocyte dysfunctions linking obesity to insulin resistance and type 2 diabetes. *Nature Reviews Molecular Cell Biology* **2008,** *9* (5), 367-377.

450. Miller, L. M.; Dumas, P., Chemical imaging of biological tissue with synchrotron infrared light. *Biochim Biophys Acta* **2006,** *1758* (7), 846-57.

451. Martens, H.; Stark, E., Extended multiplicative signal correction and spectral interference subtraction: New preprocessing methods for near infrared spectroscopy. *Journal of Pharmaceutical and Biomedical Analysis* **1991,** *9* (8), 625-635.

452. Esbensen, K. H.; Swarbrick, B.; Westad, F.; Whitcombe, P.; Anderson, M. J., *Multivariate Data Analysis: An Introduction to Multivariate Analysis, Process Analytical Technology and Quality by Design*. CAMO: 2018.

453. Baena, M.; Sangüesa, G.; Dávalos, A.; Latasa, M.-J.; Sala-Vila, A.; Sánchez, R. M.; Roglans, N.; Laguna, J. C.; Alegret, M., Fructose, but not glucose, impairs insulin signaling in the three major insulin-sensitive tissues. *Scientific Reports* **2016,** *6* (1), 26149.

454. Seo, E.; Kang, H.; Choi, H.; Choi, W.; Jun, H.-S., Reactive oxygen species-induced changes in glucose and lipid metabolism contribute to the accumulation of cholesterol in the liver during aging. *Aging Cell* **2019,** *18* (2), e12895.

455. Soule, H. D.; Vazquez, J.; Long, A.; Albert, S.; Brennan, M., A Human Cell Line From a Pleural Effusion Derived From a Breast Carcinoma2. *JNCI: Journal of the National Cancer Institute* **1973,** *51* (5), 1409-1416.

456. Cohen, S., Lipid Droplets as Organelles. *Int Rev Cell Mol Biol* **2018,** *337*, 83-110.

457. Gazi, E.; Dwyer, J.; Lockyer, N. P.; Miyan, J.; Gardner, P.; Hart, C.; Brown, M.; Clarke, N. W., Fixation protocols for subcellular imaging by synchrotron-based Fourier transform infrared microspectroscopy. *Biopolymers* **2005,** *77* (1), 18-30.

458. Piccin, A.; Murphy, W.; Smith, O., Circulating microparticles: pathophysiology and clinical implications. *Blood Reviews* **2007,** *21* (3), 157-171.

459. Ling, Z.; Combes, V.; Grau, G.; King, N., Microparticles as Immune Regulators in Infectious Disease – An Opinion. *Frontiers in Immunology* **2011,** *2* (67).

460. Kumar, N.; Weckhuysen, B. M.; Wain, A. J.; Pollard, A. J., Nanoscale chemical imaging using tip-enhanced Raman spectroscopy. *Nature Protocols* **2019,** *14* (4), 1169-1193.

461. Dazzi, A.; Prater, C. B., AFM-IR: Technology and Applications in Nanoscale Infrared Spectroscopy and Chemical Imaging. *Chemical Reviews* **2017,** *117* (7), 5146-5173.

462. Morsch, S.; Lyon, S.; Edmondson, S.; Gibbon, S., Reflectance in AFM-IR: Implications for Interpretation and Remote Analysis of the Buried Interface. *Analytical Chemistry* **2020,** *92* (12), 8117-8124.

463. Schwager, S. C.; Reinhart-King, C. A., Chapter Seven - Mechanobiology of microvesicle release, uptake, and microvesicle-mediated activation. In *Current Topics in Membranes*, Levitan, I.; Trache, A., Eds. Academic Press: 2020; Vol. 86, pp 255-278.

464. Lemmon, M. A.; Schlessinger, J., Cell signaling by receptor tyrosine kinases. *Cell* **2010,** *141* (7), 1117-1134.

465. O'Brien, K.; Breyne, K.; Ughetto, S.; Laurent, L. C.; Breakefield, X. O., RNA delivery by extracellular vesicles in mammalian cells and its applications. *Nature Reviews Molecular Cell Biology* **2020,** *21* (10), 585-606.

Appendices

Appendix 1

Section 3.6: Depth Profiling Spectra

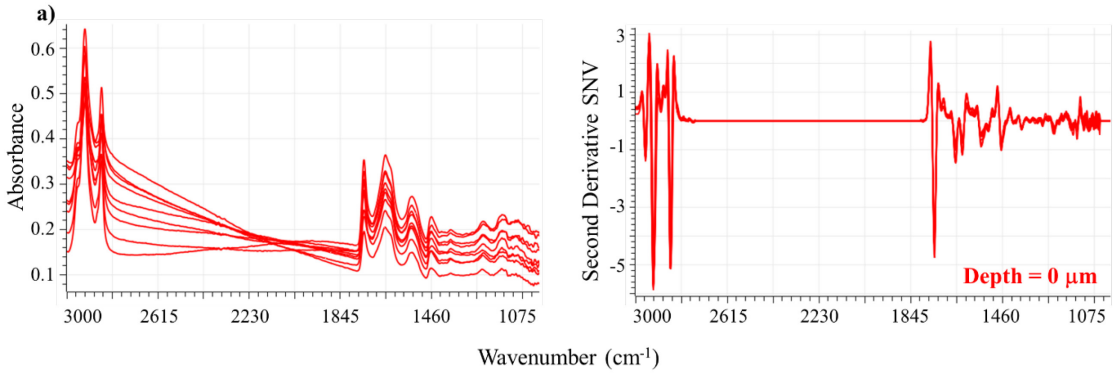

Figure A1 1: Depth profile spectra acquired from a 3T3-L1 cell with the objective set to complete focus (0 µm): a) raw spectra; and b) second derivative, SNV processed spectra.

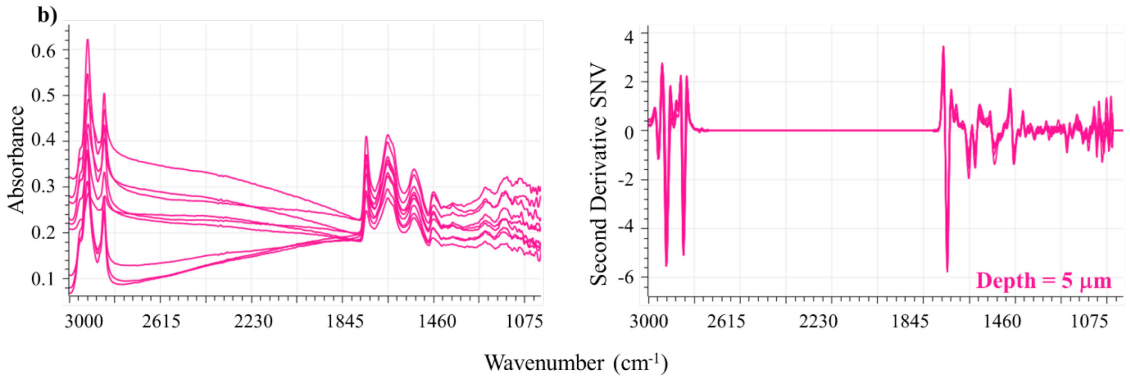

Figure A1 2: Depth profile spectra acquired from a 3T3-L1 cell with the objective set to 5 µm from complete focus: a) raw spectra; and b) second derivative, SNV processed spectra.

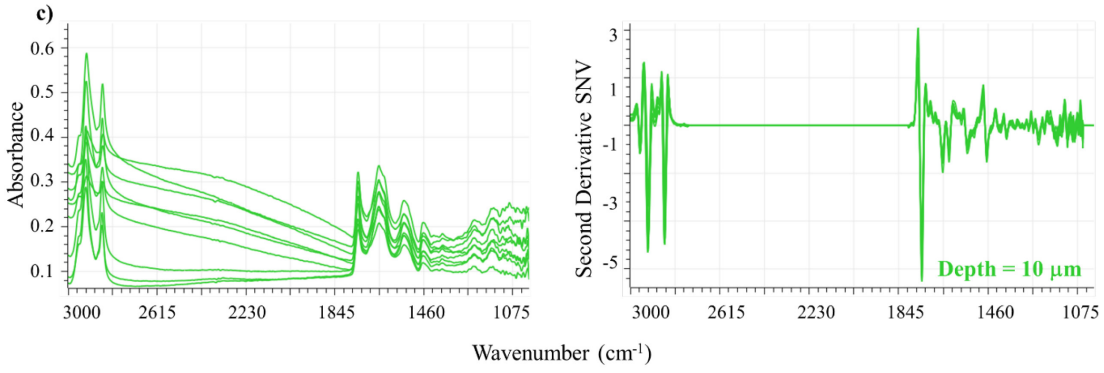

Figure A1 3: Depth profile spectra acquired from a 3T3-L1 cell with the objective set to 10 µm from complete focus: a) raw spectra; and b) second derivative, SNV processed spectra.

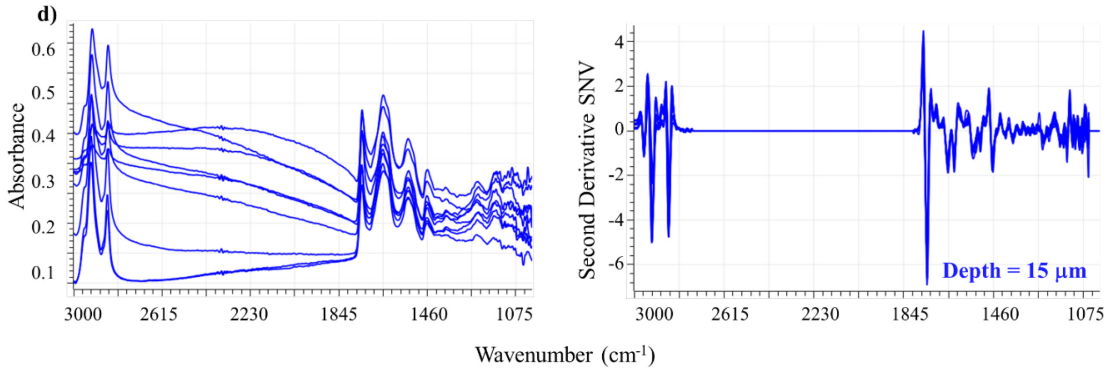

Figure A1 4: Depth profile spectra acquired from a 3T3-L1 cell with the objective set to 15 µm from complete focus: a) raw spectra; and b) second derivative, SNV processed spectra.

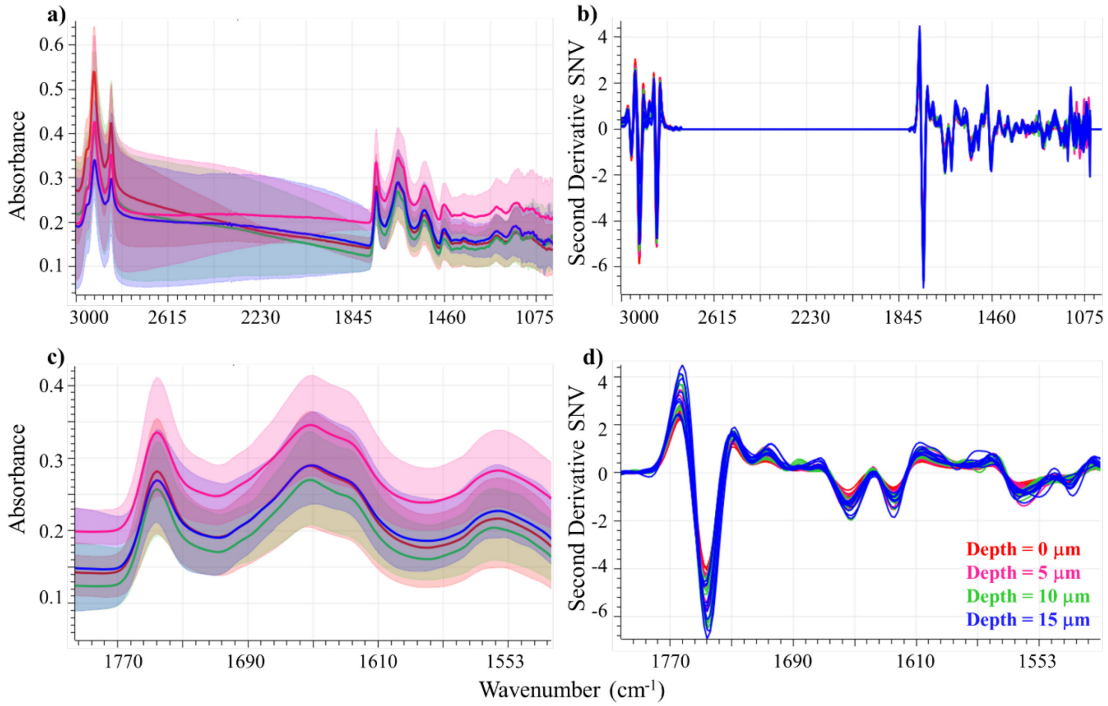

Figure A1 5: Averaged depth profile spectra for all objective offsets: a) raw spectra over the 3000-1050 cm^{-1} region; b) second derivative, SNV processed spectra over the 3000-1050 cm^{-1} region; c) raw spectra over the 1800-1500 cm^{-1} region; and d) second derivative, SNV processed spectra over the 1800-1500 cm^{-1} region

Appendix 2

Section 6.3.2: Four-beam FPA SR-FTIR Microspectroscopic Assessment of 3T3-L1 Adipocytes.

A2-1 No-sugar treated 3T3-L1 adipocyte fixed to a 0.2 mm CaF_2 Substrate.

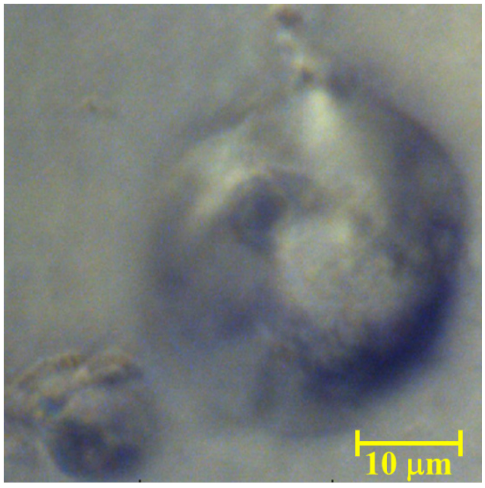

Figure A2 1: Optical micrograph of a 3T3-L1 adipocyte treated with no sugar.

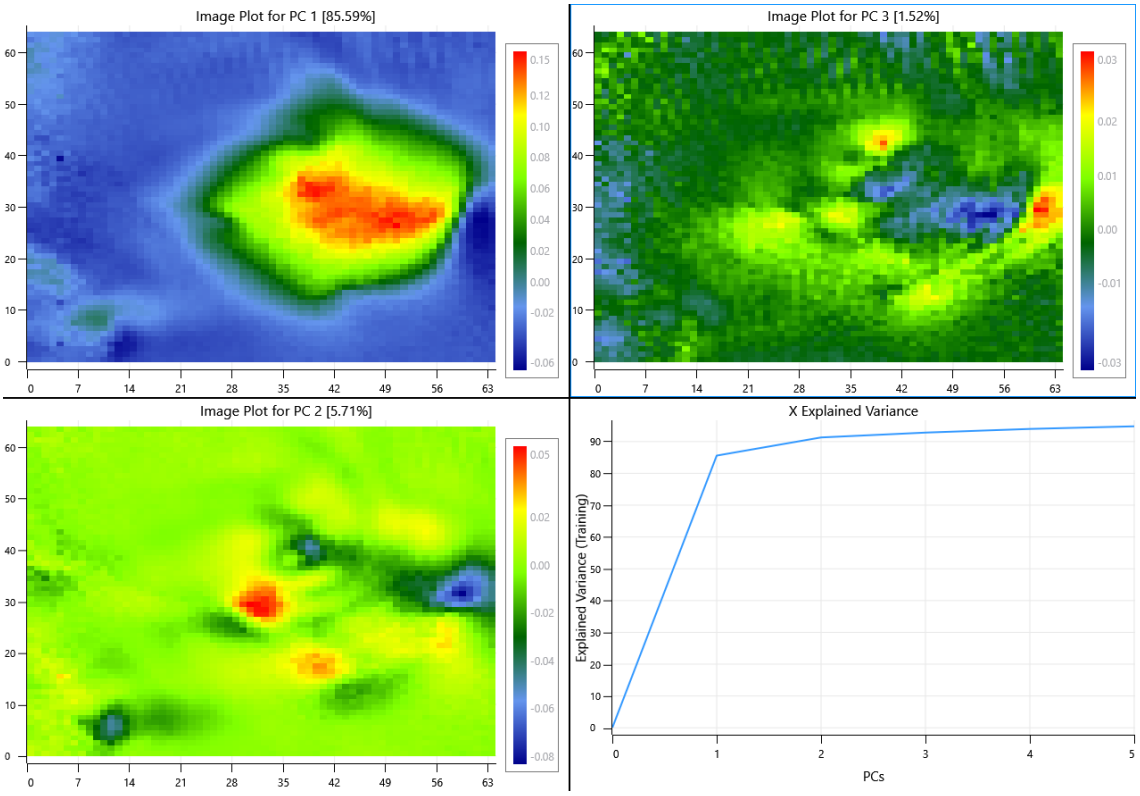

Figure A2 2: Umasked scores images of 3T3-L1 adipocyte treated with no-sugar and chemically fixed to a 0.2 mm CaF_2 substrate; a) PC1 scores image; b) PC2 scores image; c) PC3 scores image; and d) X-explained variance plot.

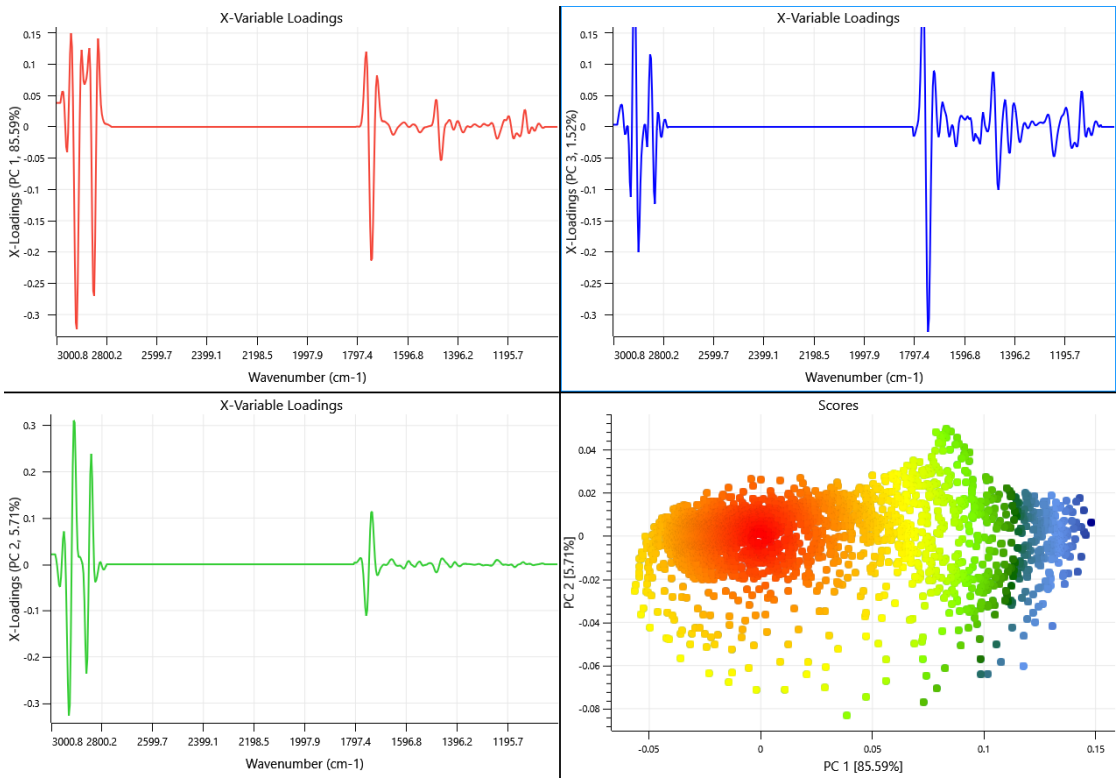

Figure A2 3: Unmasked image loadings: a) PC1 loadings; b) PC2 loadings; c) PC2 loadings; and d) scores density map of 3T3-L1 cell treated with no-sugar and chemically fixed to a CaF_2 substrate.

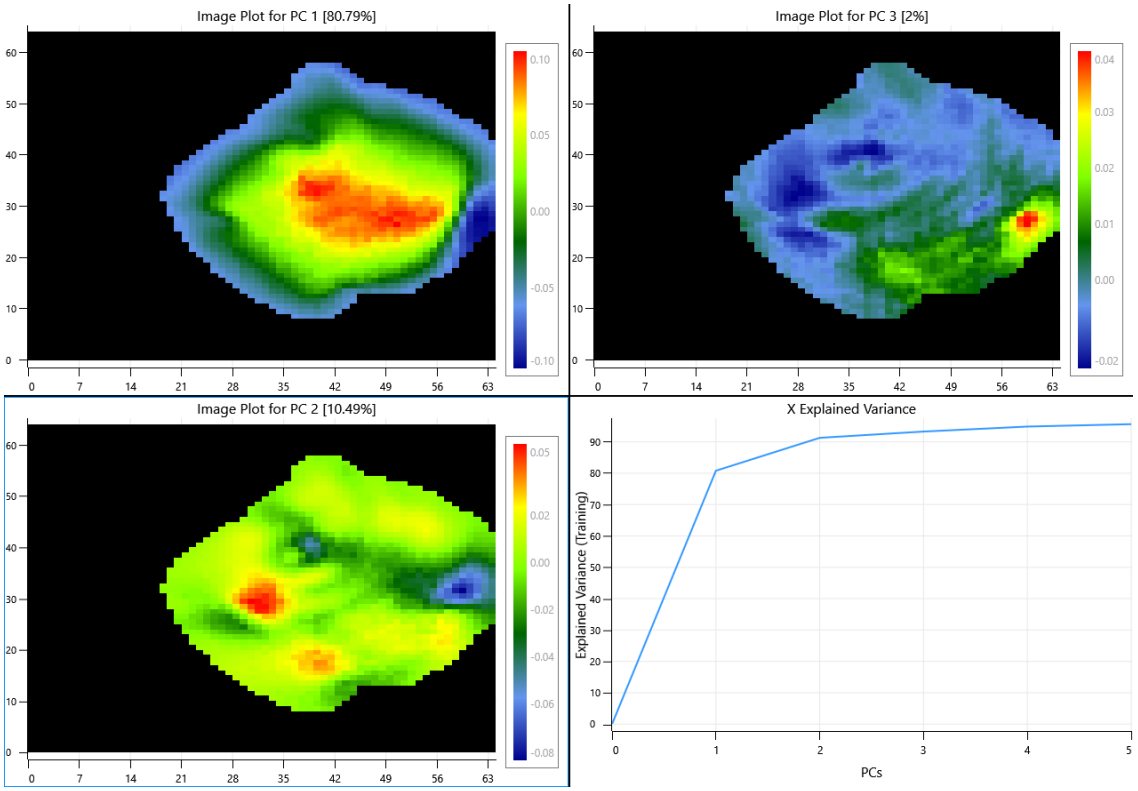

Figure A2 4: Masked scores images of 3T3-L1 adipocyte treated with no-sugar and chemically fixed to a 0.2 mm CaF_2 substrate; a) PC1 scores image; b) PC2 scores image; c) PC3 scores image; and d) X-explained variance plot.

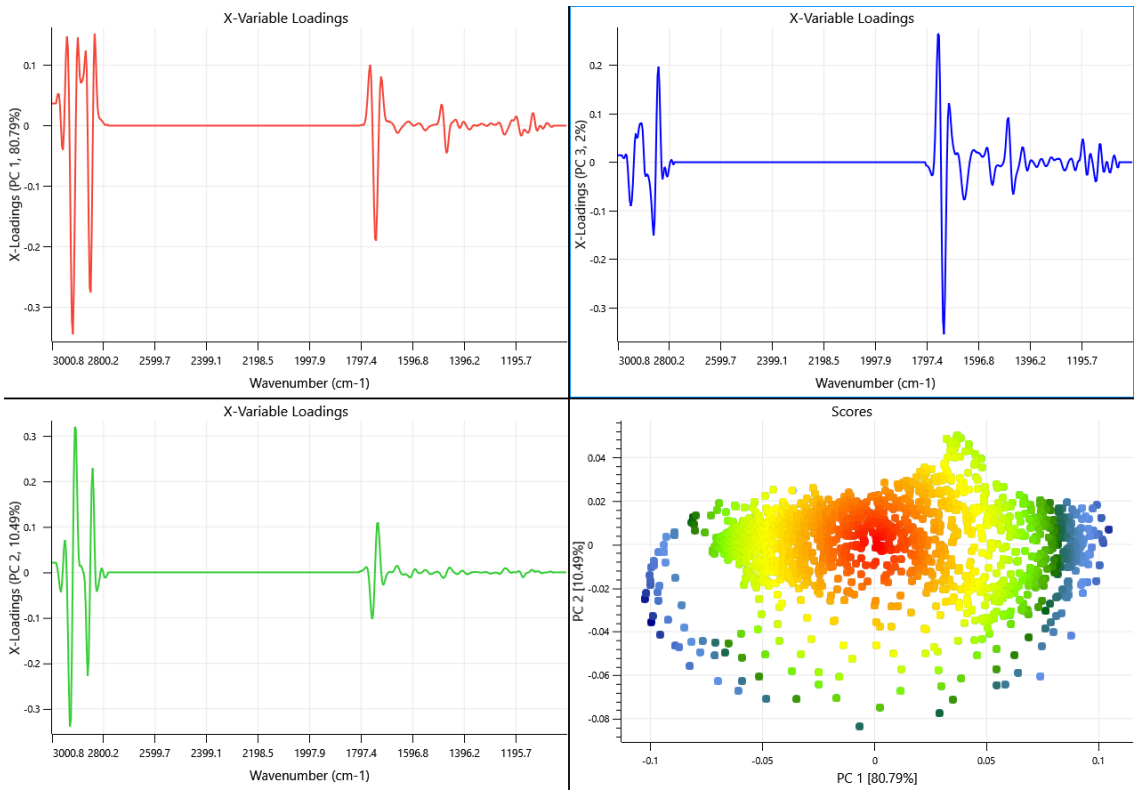

Figure A2 5: Masked image loadings: a) PC1 loadings; b) PC2 loadings; c) PC2 loadings; and d) scores density map of 3T3-L1 cell treated with no-sugar and chemically fixed to a CaF_2 substrate.

A2-2 Glucose treated 3T3-L1 adipocyte fixed to a 0.2 mm CaF_2 Substrate.

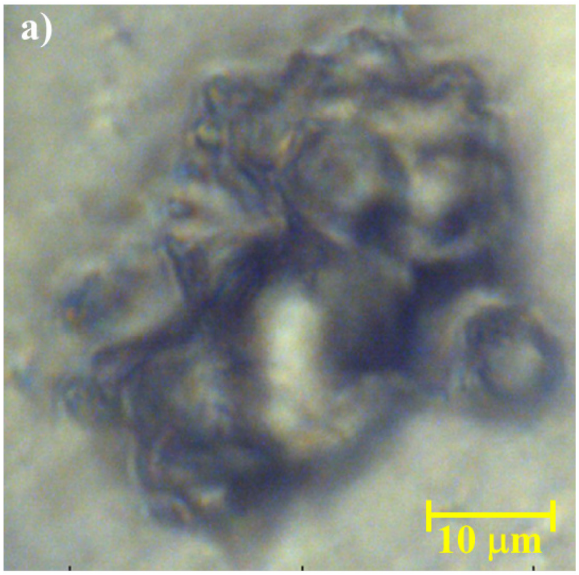

Figure A2 6: Optical micrograph of a 3T3-L1 adipocyte treated with glucose.

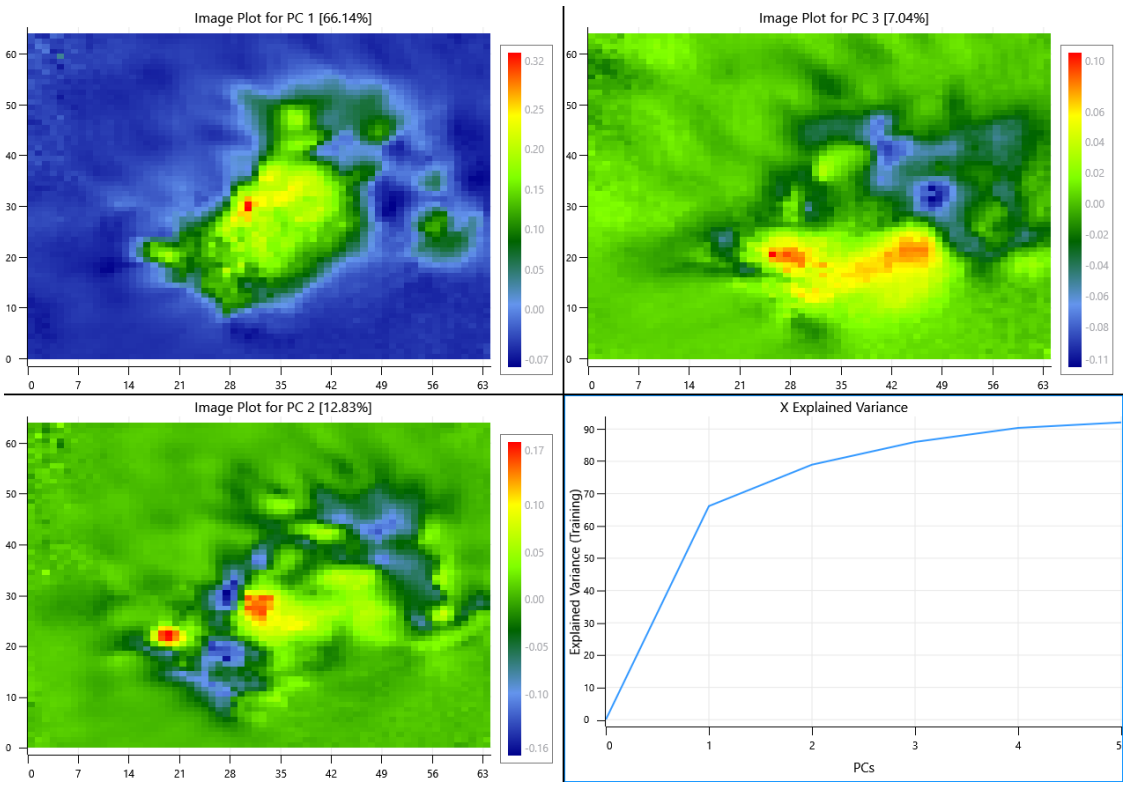

Figure A2 7: Umasked scores images of 3T3-L1 adipocyte treated with glucose and chemically fixed to a 0.2 mm CaF_2 substrate; a) PC1 scores image; b) PC2 scores image; c) PC3 scores image; and d) X-explained variance plot.

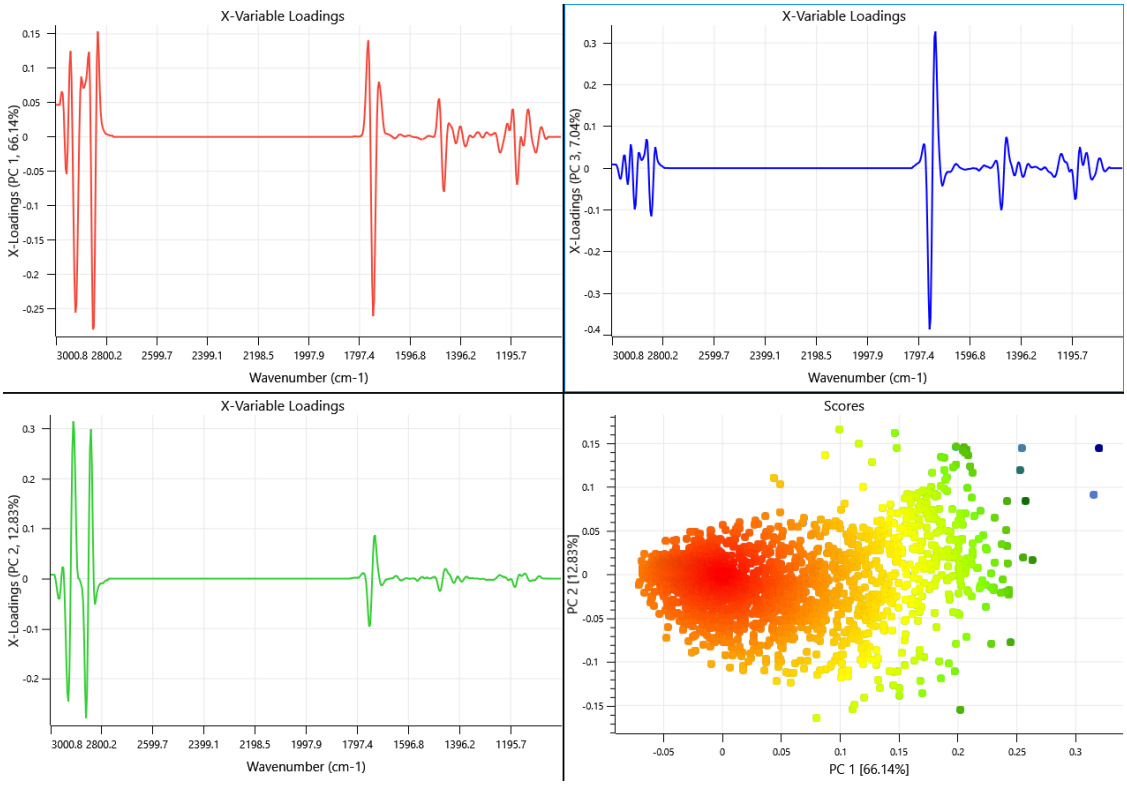

Figure A2 8: Unmasked image loadings: a) PC1 loadings; b) PC2 loadings; c) PC2 loadings; and d) scores density map of 3T3-L1 cell treated with glucose and chemically fixed to a CaF_2 substrate.

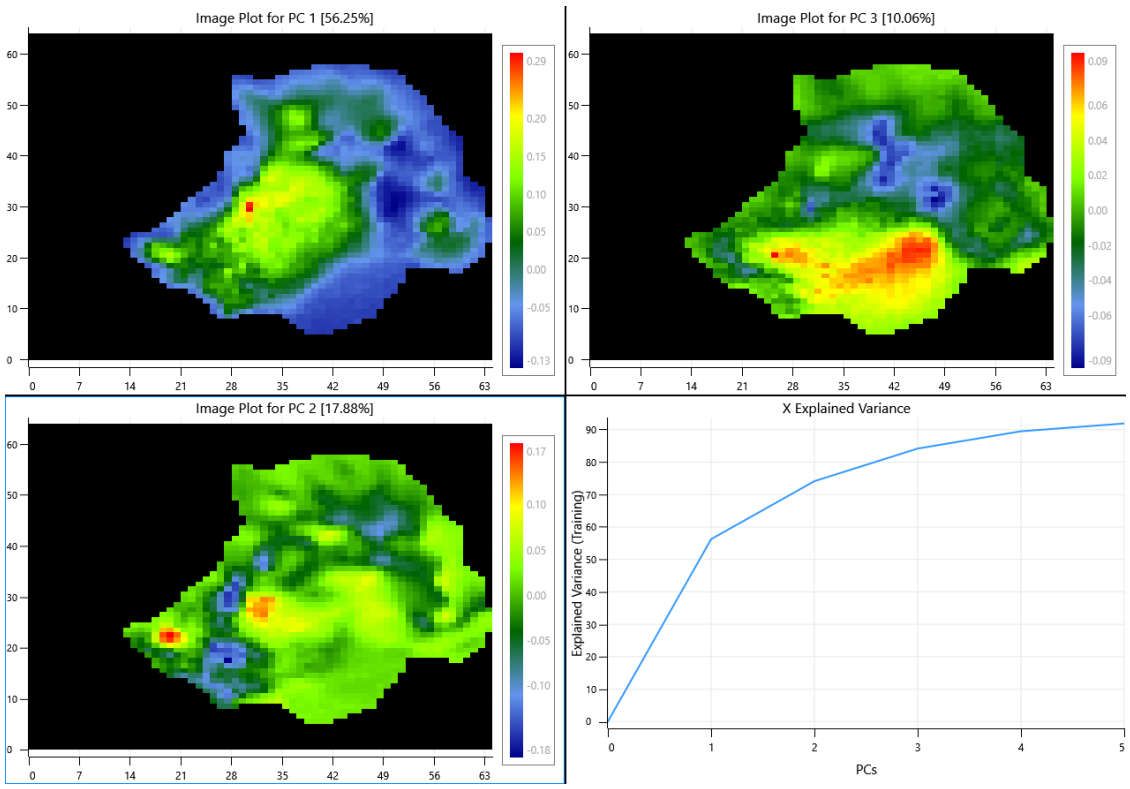

Figure A2 9: Masked scores images of 3T3-L1 adipocyte treated with glucose and chemically fixed to a 0.2 mm CaF_2 substrate; a) PC1 scores image; b) PC2 scores image; c) PC3 scores image; and d) X-explained variance plot.

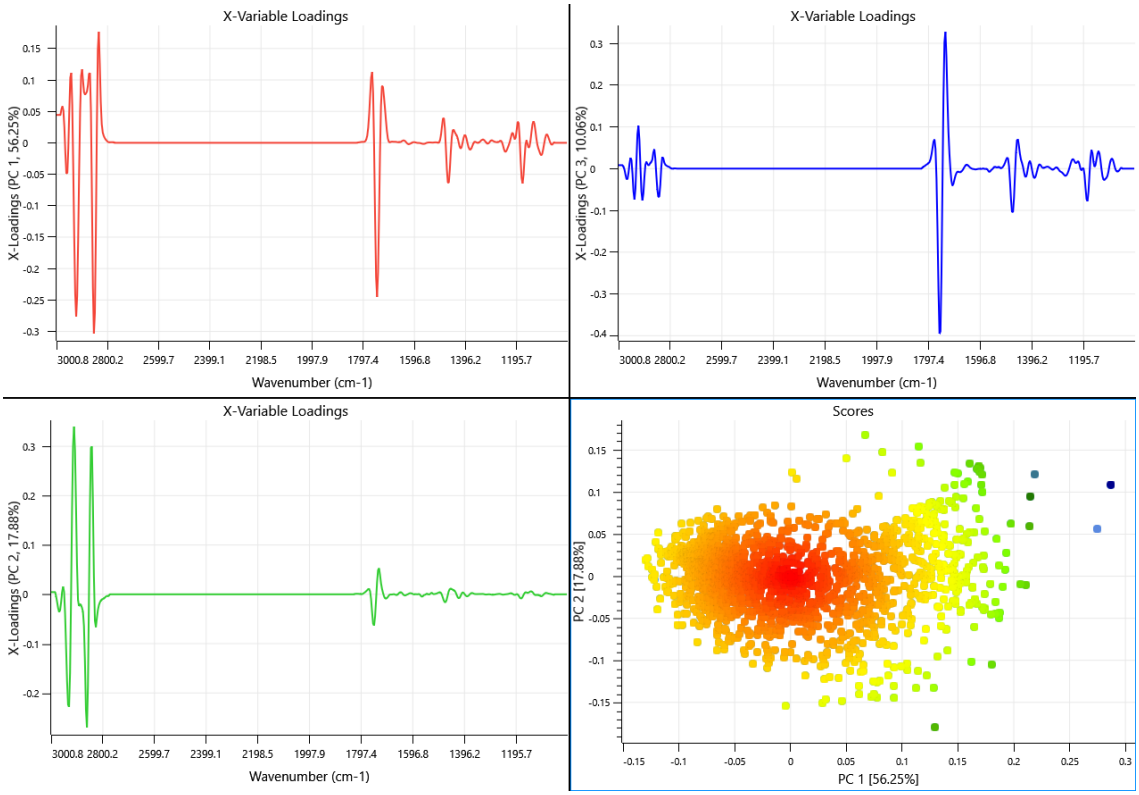

Figure A2 10: Masked image loadings: a) PC1 loadings; b) PC2 loadings; c) PC2 loadings; and d) scores density map of 3T3-L1 cell treated with glucose and chemically fixed to a CaF_2 substrate.

A2-3 Fructose treated 3T3-L1 adipocyte fixed to a 0.2 mm CaF_2 Substrate.

Figure A2 11: Optical micrograph of a 3T3-L1 adipocyte treated with fructose.

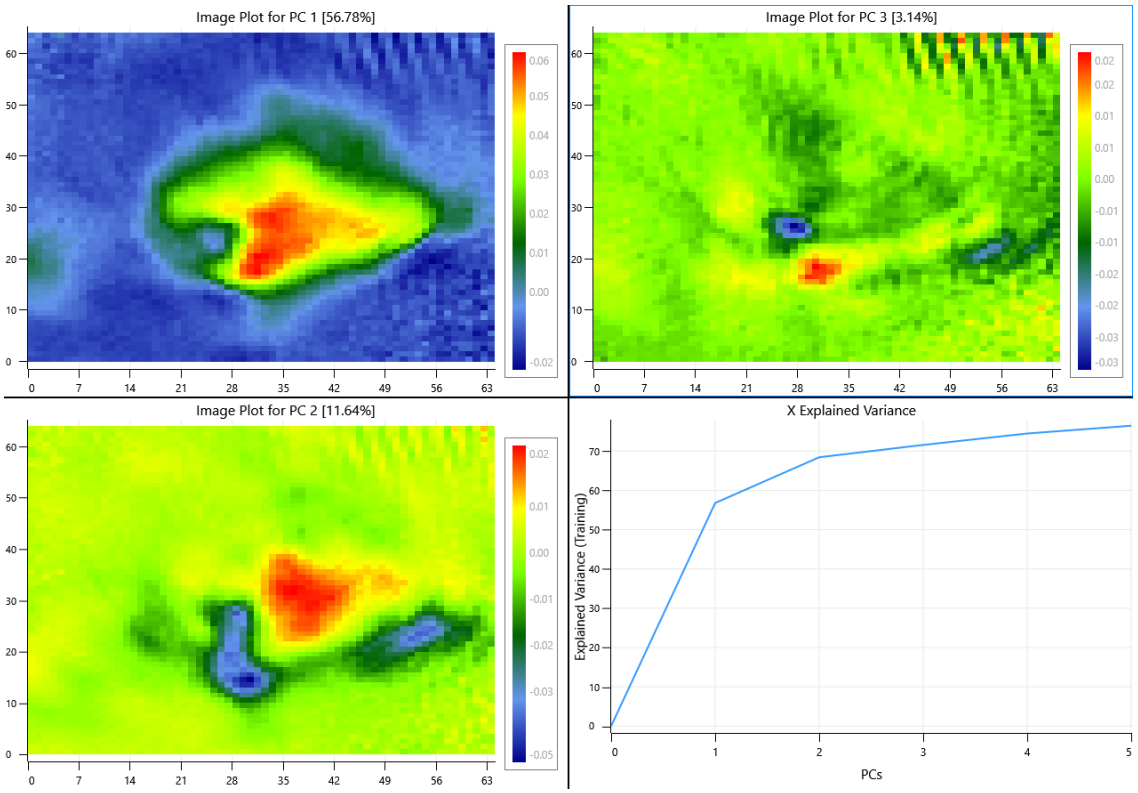

Figure A2 12: Umasked scores images of 3T3-L1 adipocyte treated with fructose and chemically fixed to a 0.2 mm CaF_2 substrate; a) PC1 scores image; b) PC2 scores image; c) PC3 scores image; and d) X-explained variance plot.

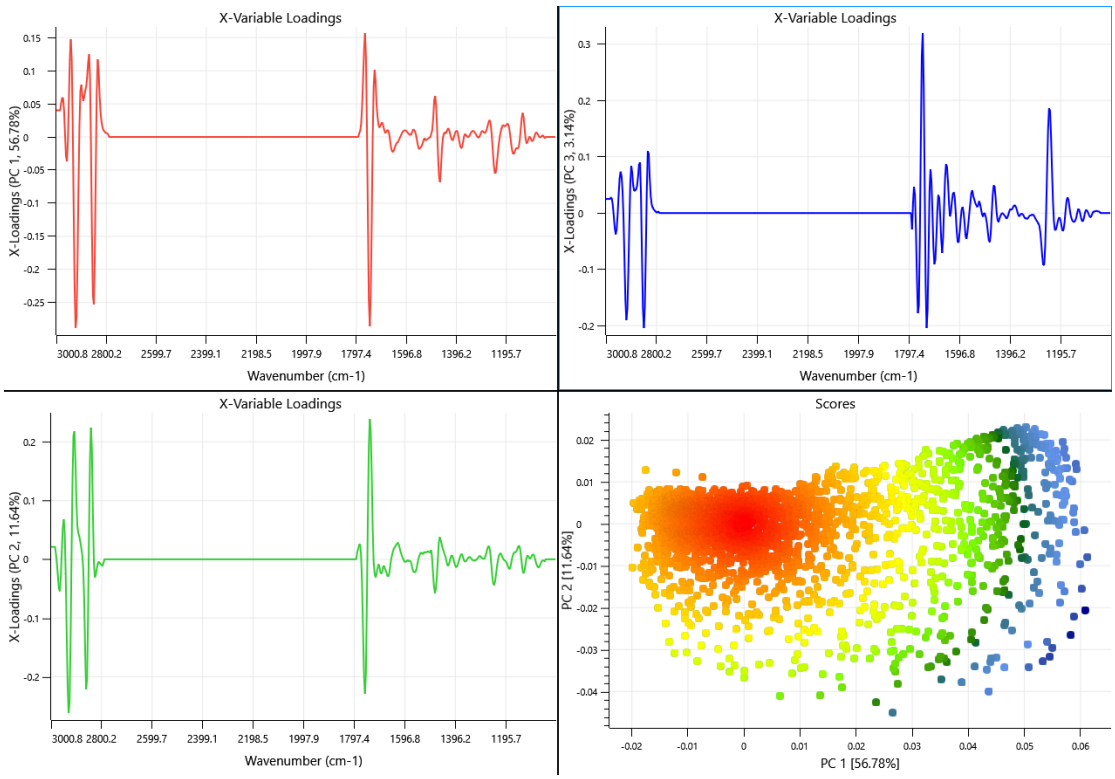

Figure A2 13: Unmasked image loadings: a) PC1 loadings; b) PC2 loadings; c) PC2 loadings; and d) scores density map of 3T3-L1 cell treated with fructose and chemically fixed to a CaF_2 substrate.

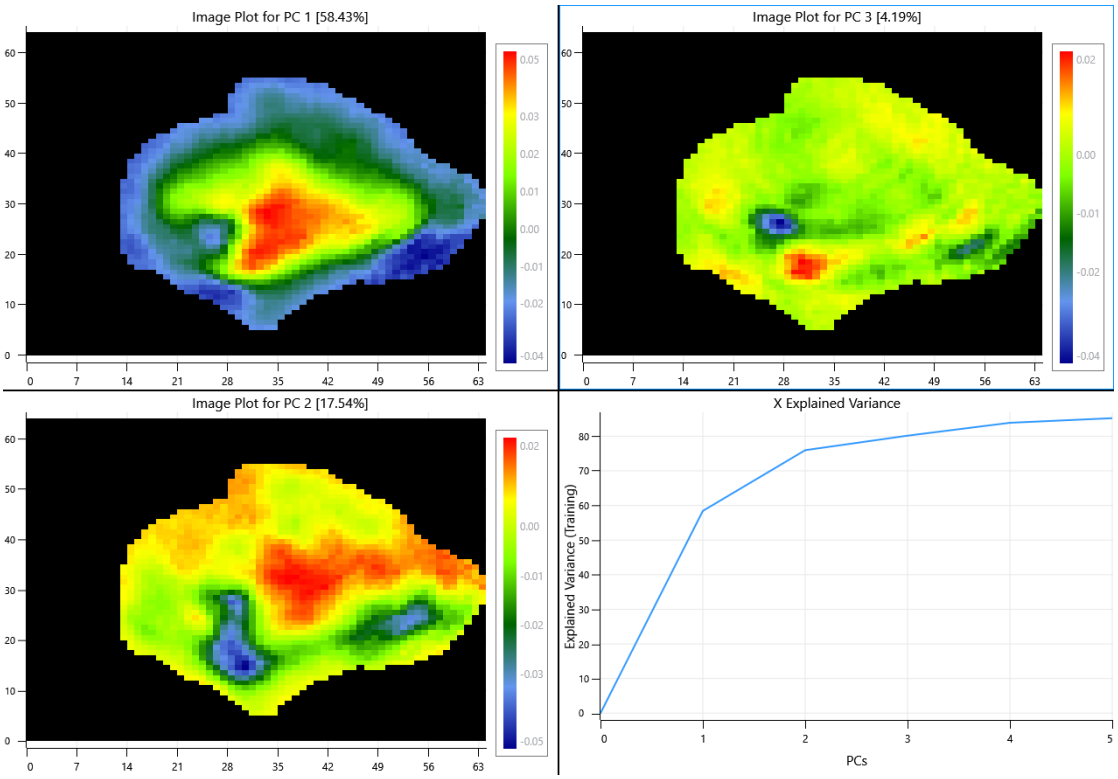

Figure A2 14: Masked scores images of 3T3-L1 adipocyte treated with fructose and chemically fixed to a 0.2 mm CaF_2 substrate; a) PC1 scores image; b) PC2 scores image; c) PC3 scores image; and d) X-explained variance plot.

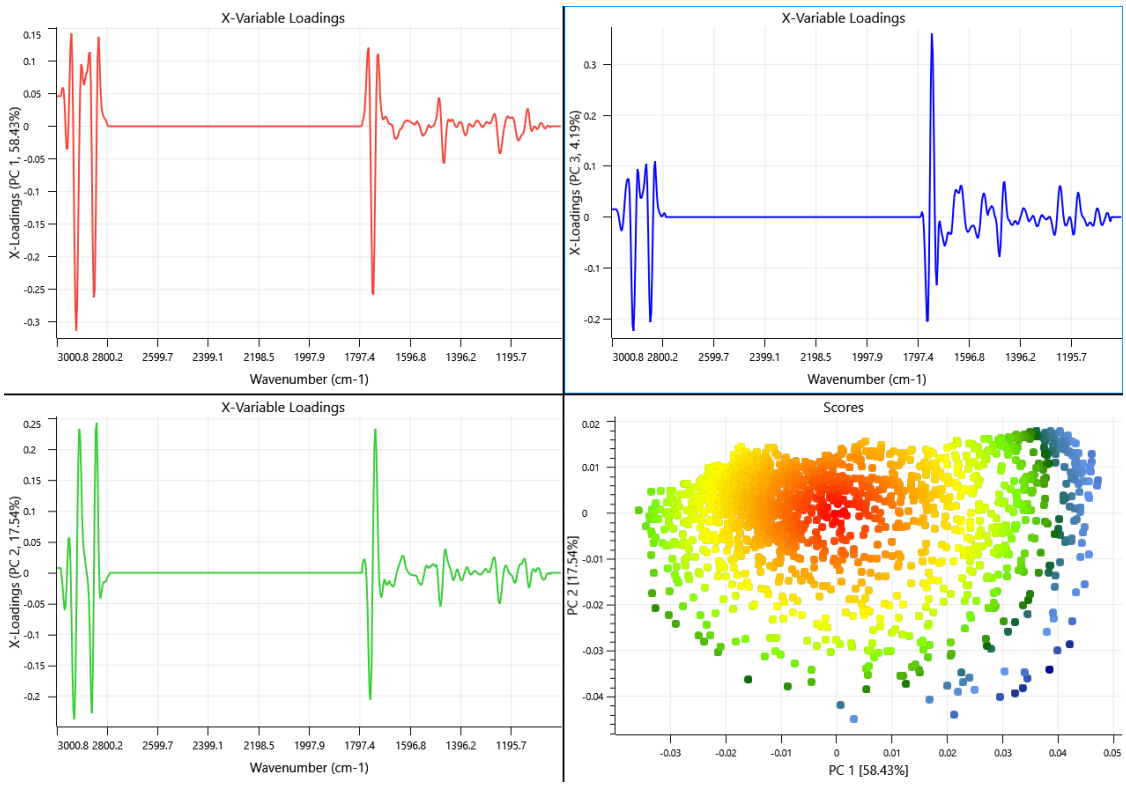

Figure A2 15: Masked image loadings: a) PC1 loadings; b) PC2 loadings; c) PC2 loadings; and d) scores density map of 3T3-L1 cell treated with fructose and chemically fixed to a CaF_2 substrate.

A2-4 Glucose-fructose treated 3T3-L1 adipocyte fixed to a 0.2 mm CaF_2 Substrate.

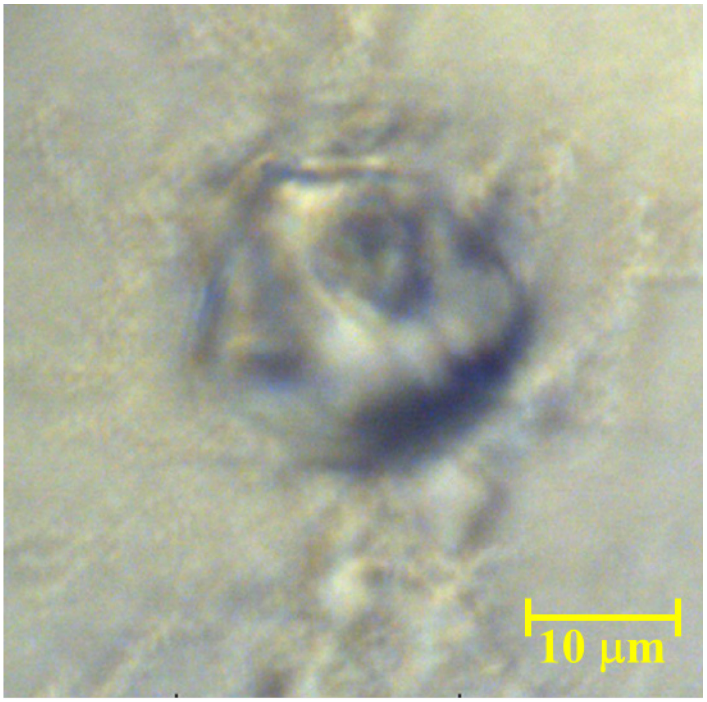

Figure A2 16: Optical micrograph of a 3T3-L1 adipocyte treated with glucose and fructose.

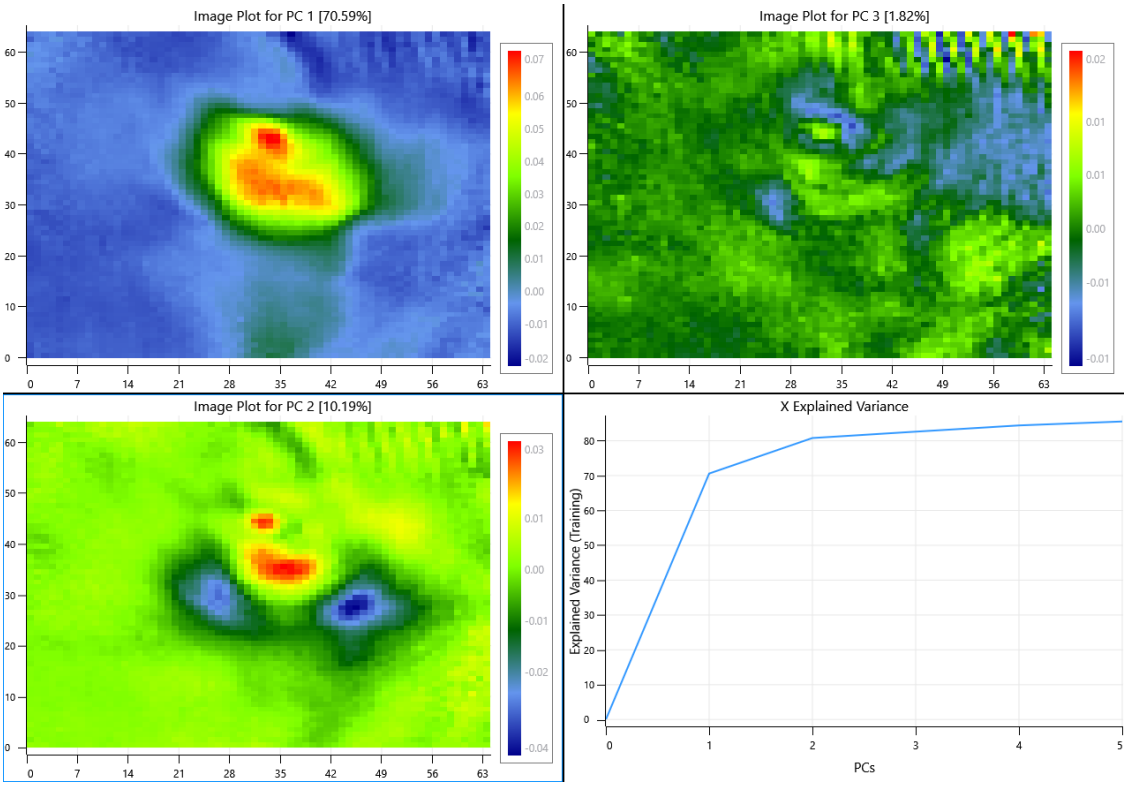

Figure A2 17: Umasked scores images of 3T3-L1 adipocyte treated with glucose and fructose and chemically fixed to a 0.2 mm CaF_2 substrate; a) PC1 scores image; b) PC2 scores image; c) PC3 scores image; and d) X-explained variance plot.

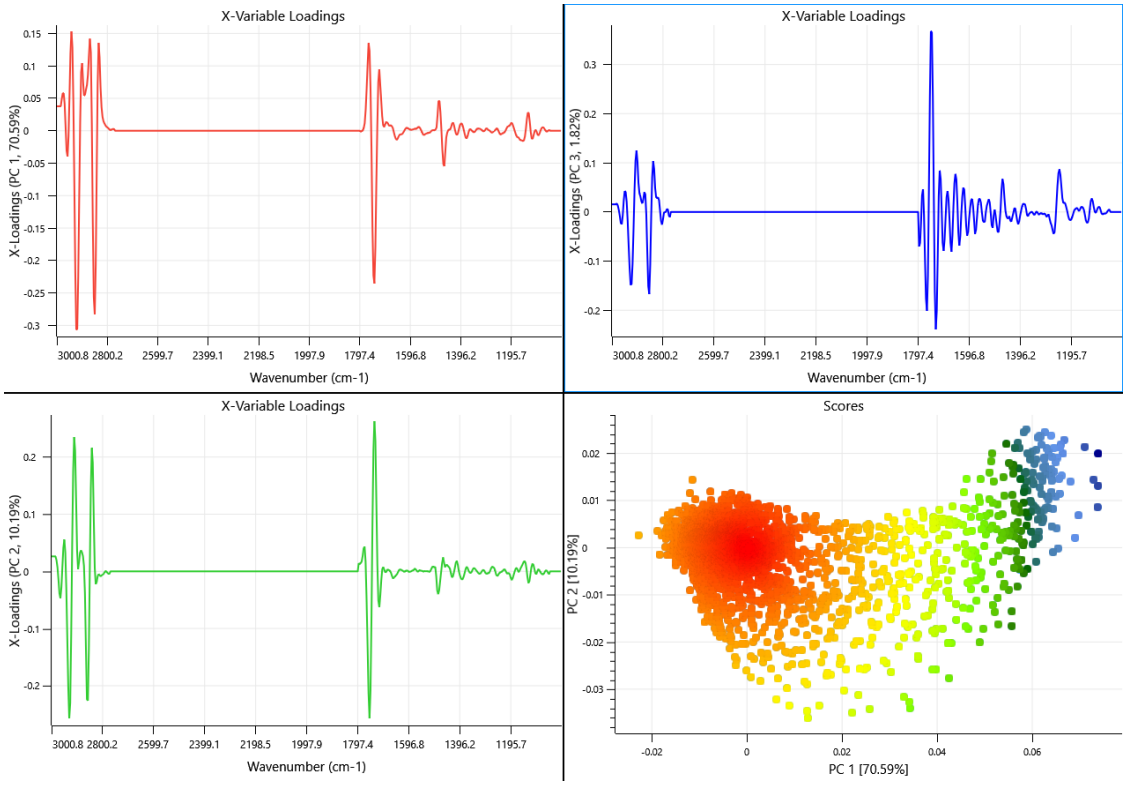

Figure A2 18: Unmasked image loadings: a) PC1 loadings; b) PC2 loadings; c) PC2 loadings; and d) scores density map of 3T3-L1 cell treated with glucose and fructose and chemically fixed to a CaF_2 substrate.

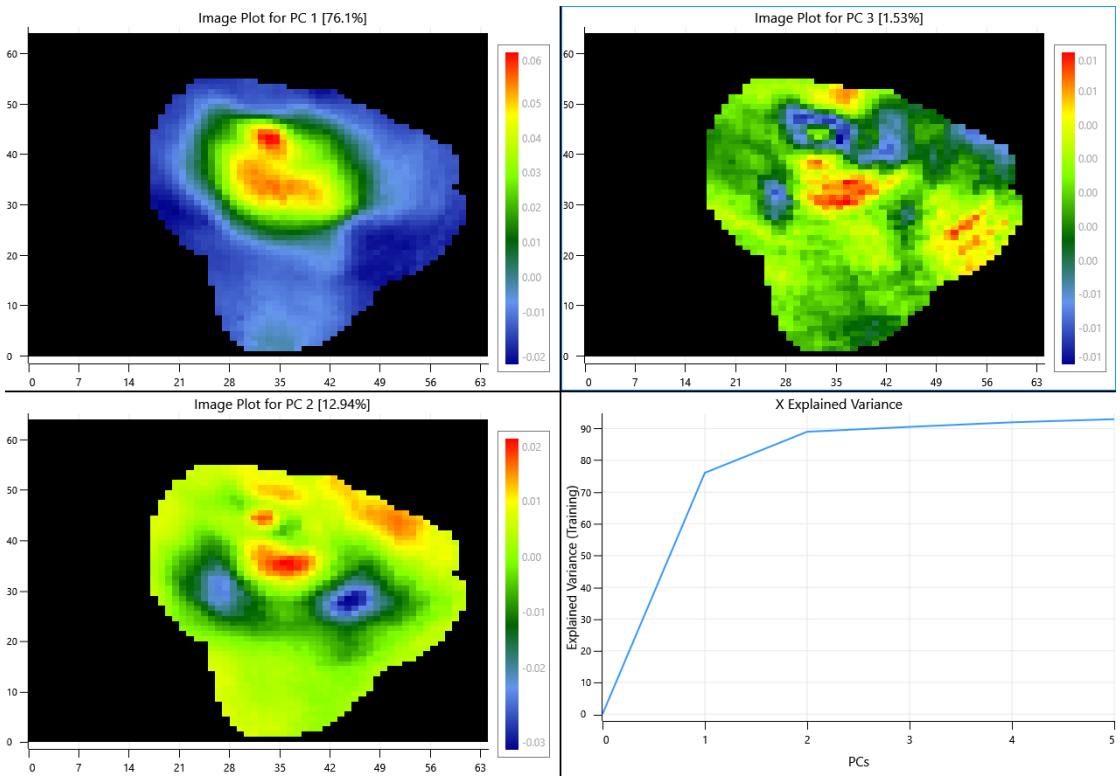

Figure A2 19: Masked scores images of 3T3-L1 adipocyte treated with glucose and fructose and chemically fixed to a 0.2 mm CaF_2 substrate; a) PC1 scores image; b) PC2 scores image; c) PC3 scores image; and d) X-explained variance plot.

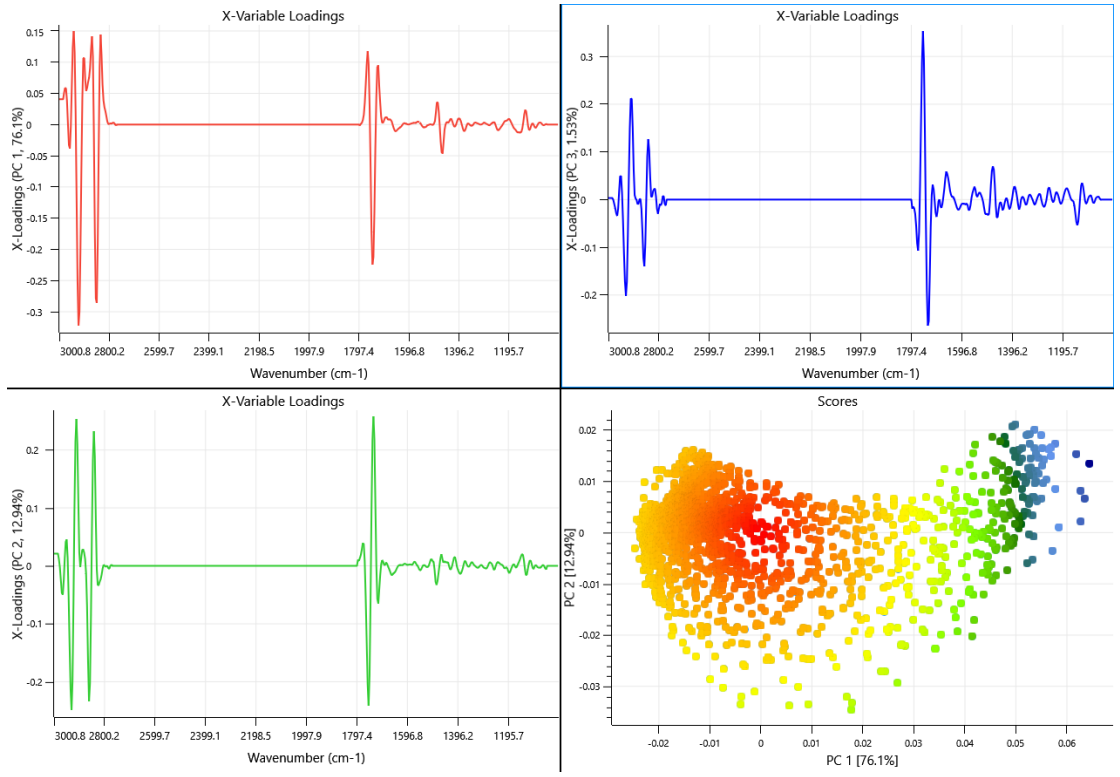

Figure A2 20: Masked image loadings: a) PC1 loadings; b) PC2 loadings; c) PC2 loadings; and d) scores density map of 3T3-L1 cell treated with glucose and fructose and chemically fixed to a CaF_2 substrate.

A2-5 No-sugar treated 3T3-L1 adipocyte fixed to a 0.5 mm CaF_2 Substrate.

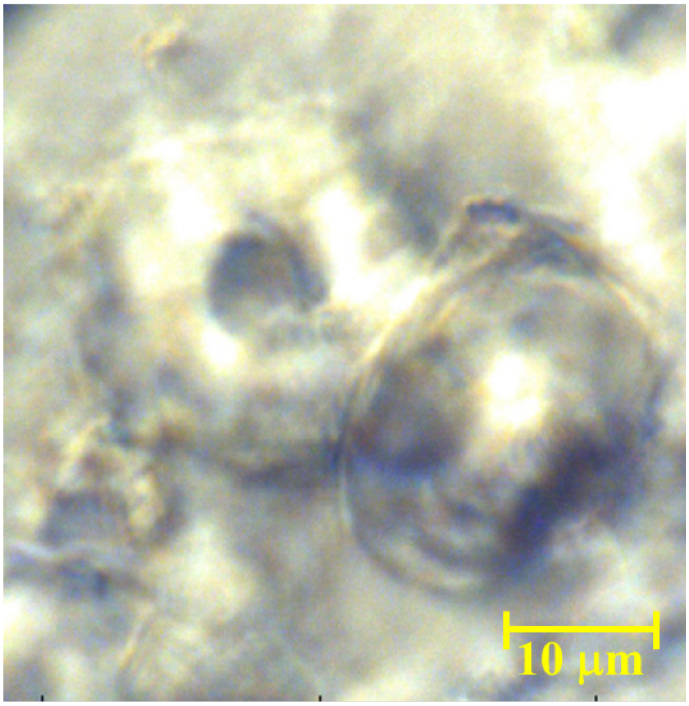

Figure A2 21: Optical micrograph of a 3T3-L1 adipocyte treated with no sugar.

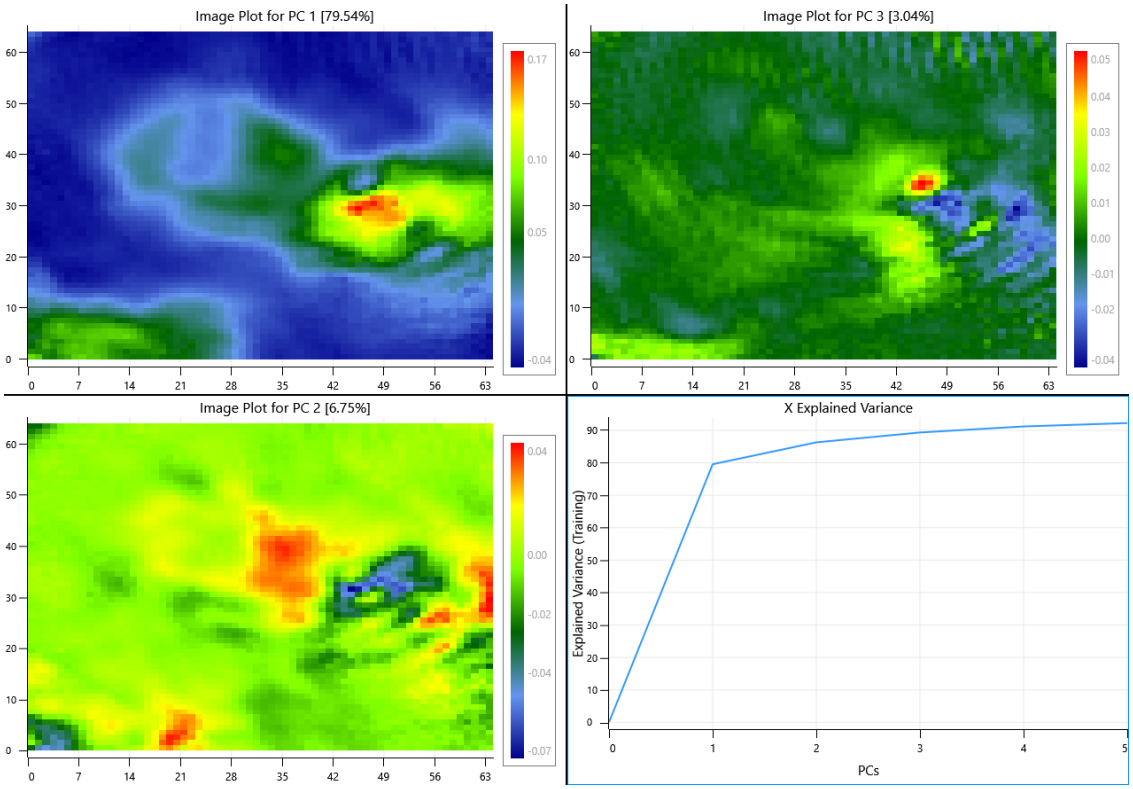

Figure A2 22: Umasked scores images of 3T3-L1 adipocyte treated with no sugar and chemically fixed to a 0.5 mm CaF_2 substrate; a) PC1 scores image; b) PC2 scores image; c) PC3 scores image; and d) X-explained variance plot.

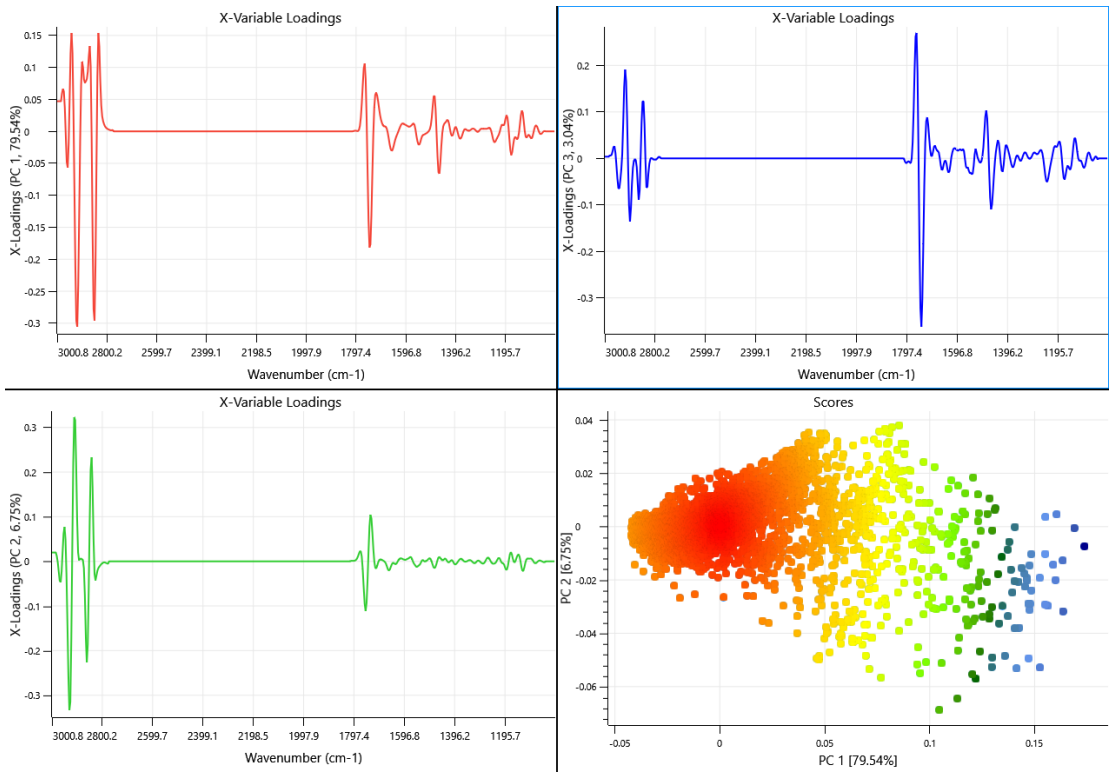

Figure A2 23: Unmasked image loadings: a) PC1 loadings; b) PC2 loadings; c) PC2 loadings; and d) scores density map of 3T3-L1 cell treated with no sugar and chemically fixed to a CaF_2 substrate.

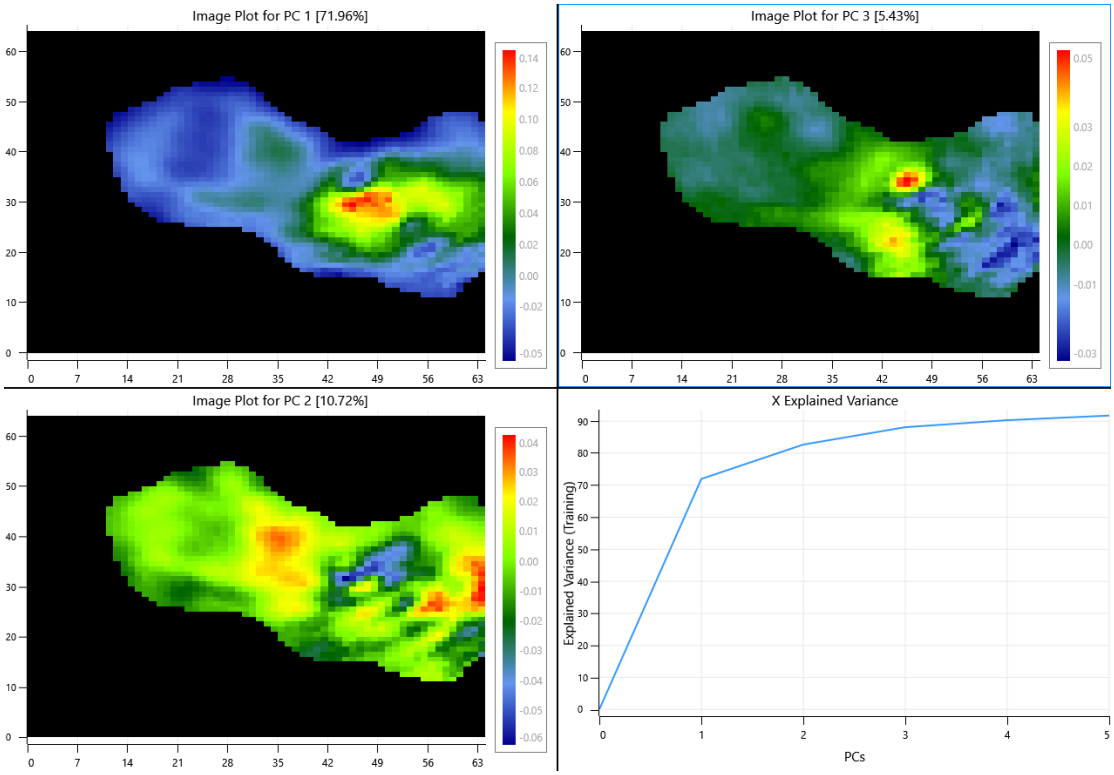

Figure A2 24: Masked scores images of 3T3-L1 adipocyte treated with no sugar and chemically fixed to a 0.5 mm CaF_2 substrate; a) PC1 scores image; b) PC2 scores image; c) PC3 scores image; and d) X-explained variance plot.

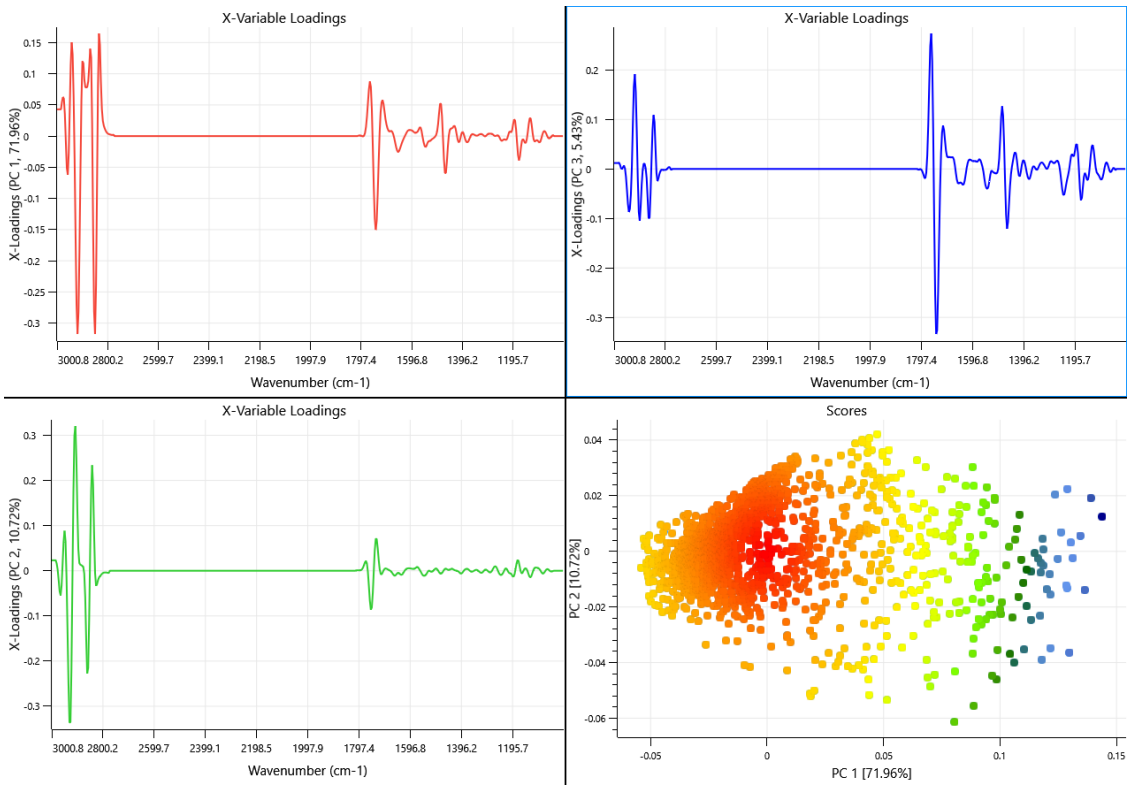

Figure A2 25: Masked image loadings: a) PC1 loadings; b) PC2 loadings; c) PC2 loadings; and d) scores density map of 3T3-L1 cell treated with no sugar and chemically fixed to a CaF_2 substrate.

A2-6 Glucose treated 3T3-L1 adipocyte fixed to a 0.5 mm CaF_2 Substrate.

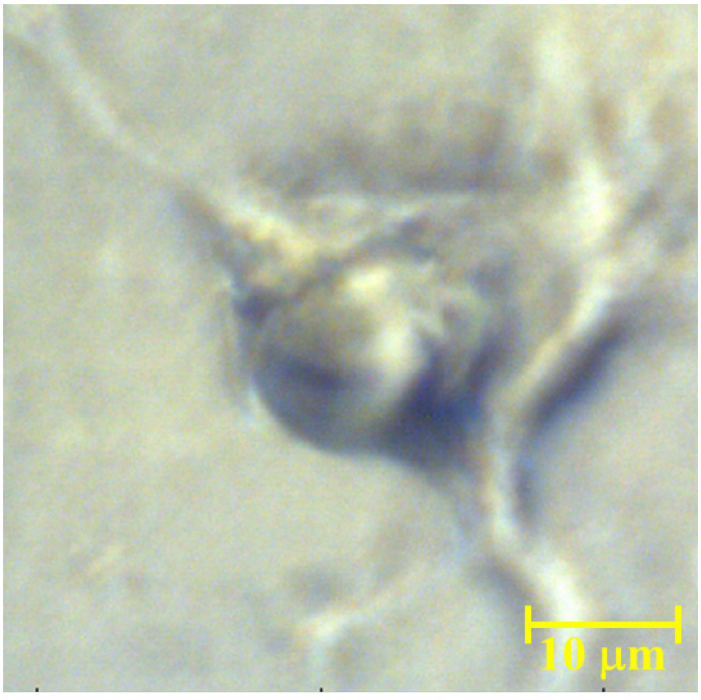

Figure A2 26: Optical micrograph of a 3T3-L1 adipocyte treated with glucose.

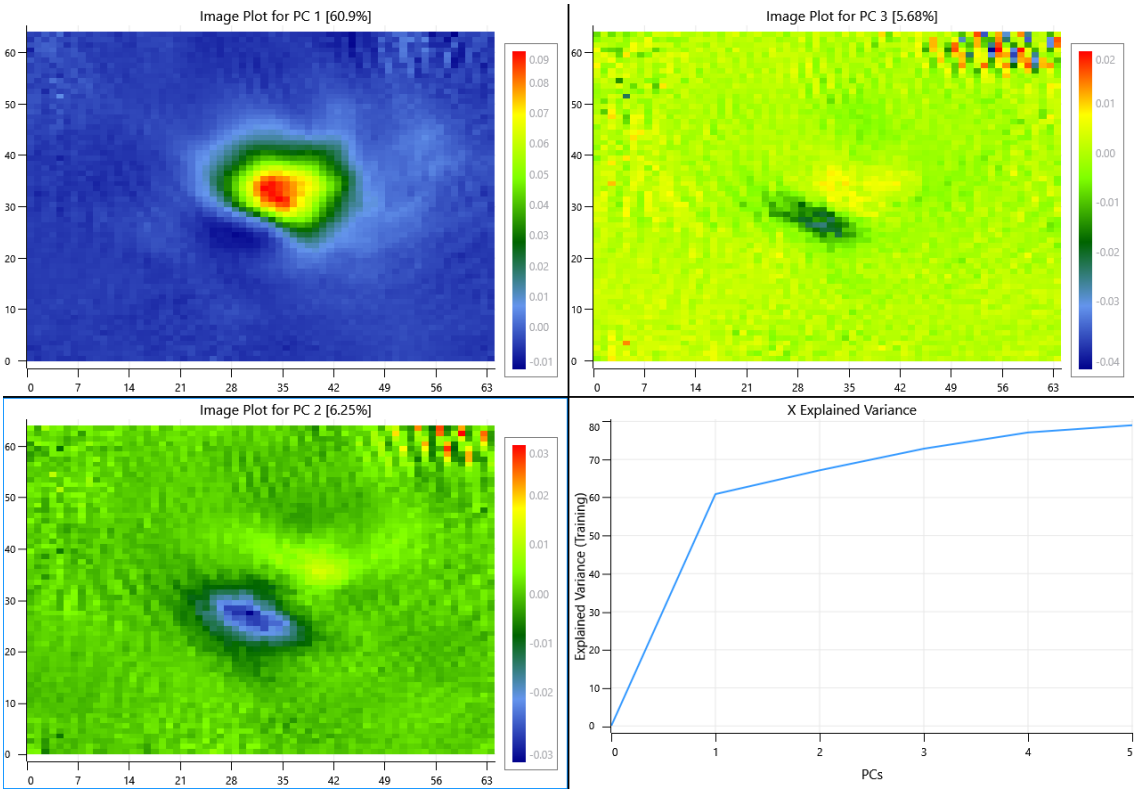

Figure A2 27: Umasked scores images of 3T3-L1 adipocyte treated with glucose and chemically fixed to a 0.5 mm CaF_2 substrate; a) PC1 scores image; b) PC2 scores image; c) PC3 scores image; and d) X-explained variance plot.

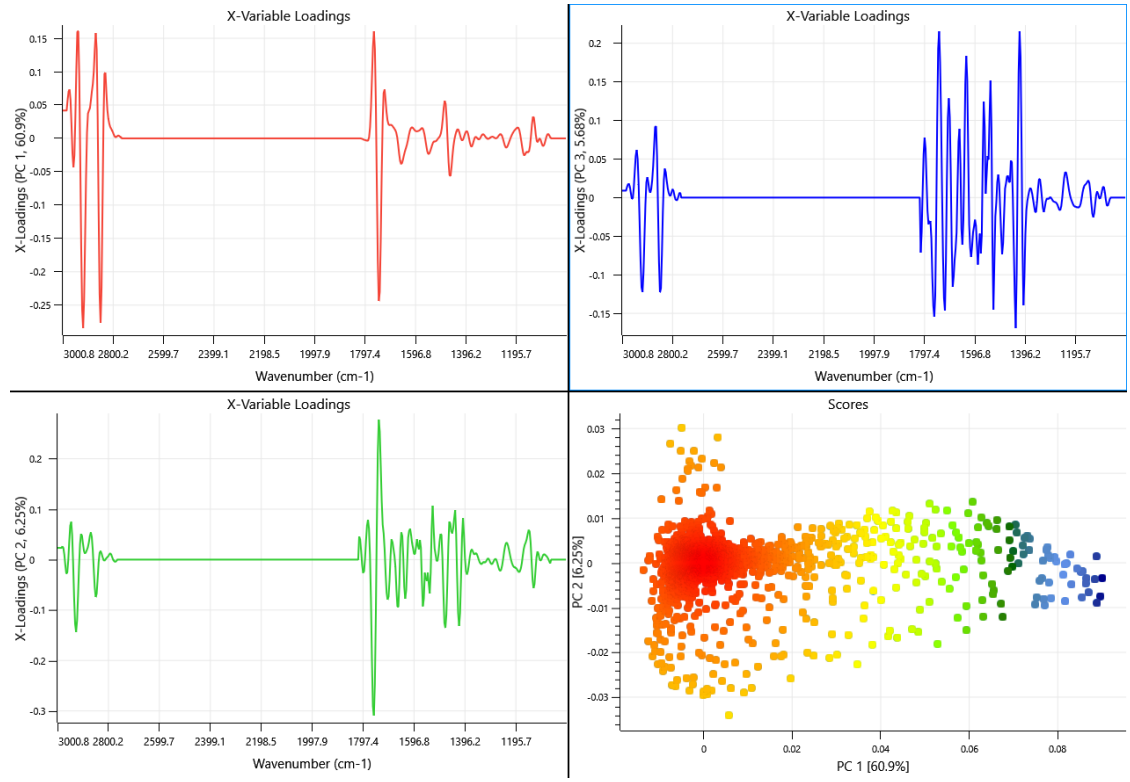

Figure A2 28: Unmasked image loadings: a) PC1 loadings; b) PC2 loadings; c) PC2 loadings; and d) scores density map of 3T3-L1 cell treated with glucose and chemically fixed to a CaF_2 substrate.

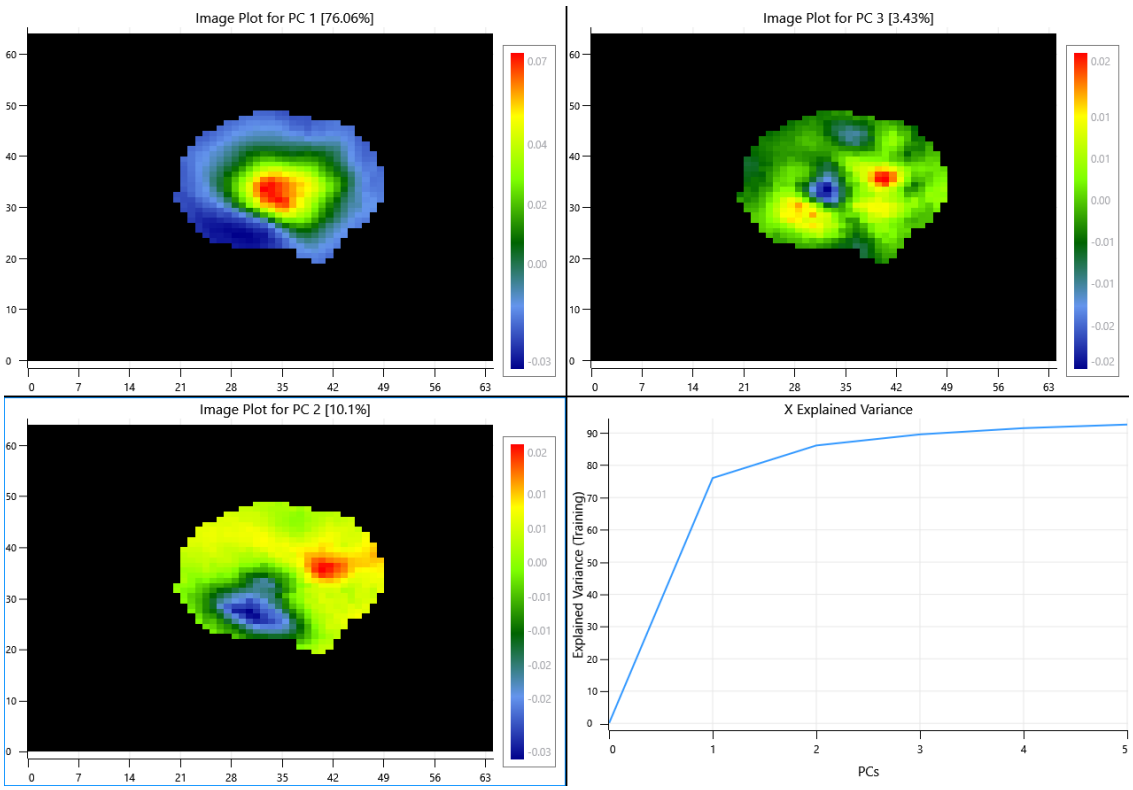

Figure A2 29: Masked scores images of 3T3-L1 adipocyte treated with glucose and chemically fixed to a 0.5 mm CaF_2 substrate; a) PC1 scores image; b) PC2 scores image; c) PC3 scores image; and d) X-explained variance plot.

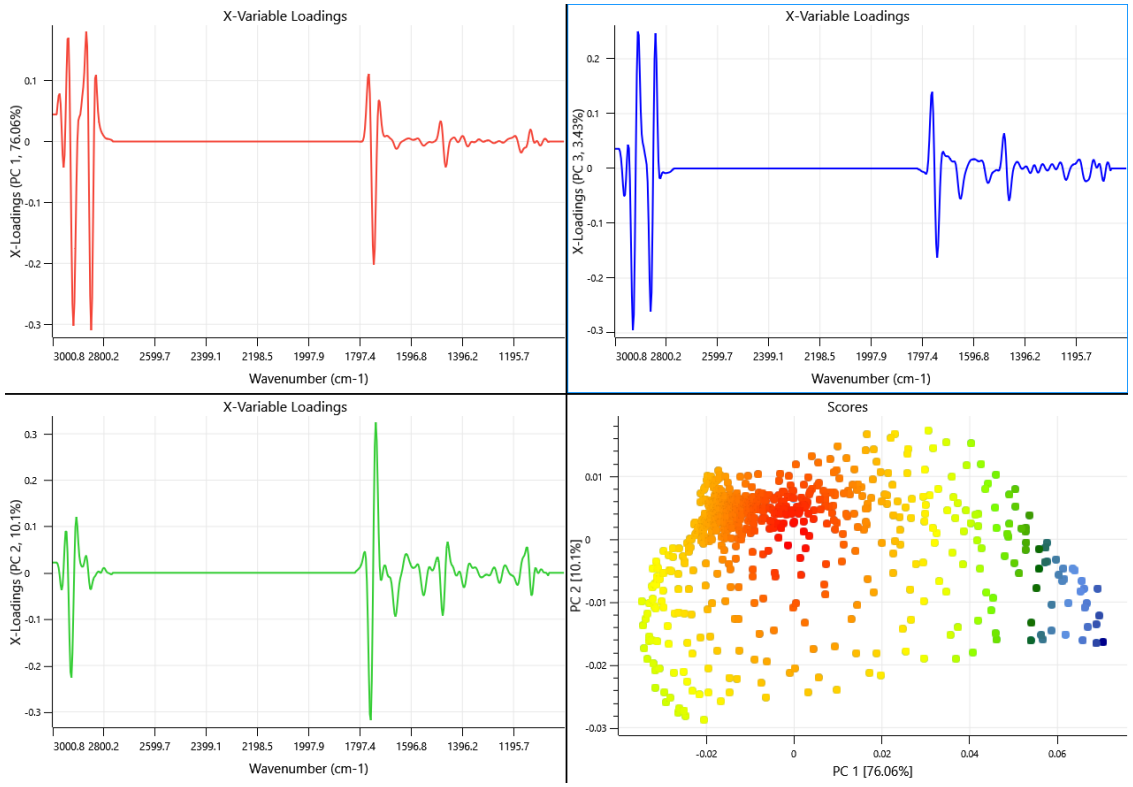

Figure A2 30: Masked image loadings: a) PC1 loadings; b) PC2 loadings; c) PC2 loadings; and d) scores density map of 3T3-L1 cell treated with glucose and chemically fixed to a CaF_2 substrate.

A2-7 Fructose treated 3T3-L1 adipocyte fixed to a 0.5 mm CaF_2 Substrate.

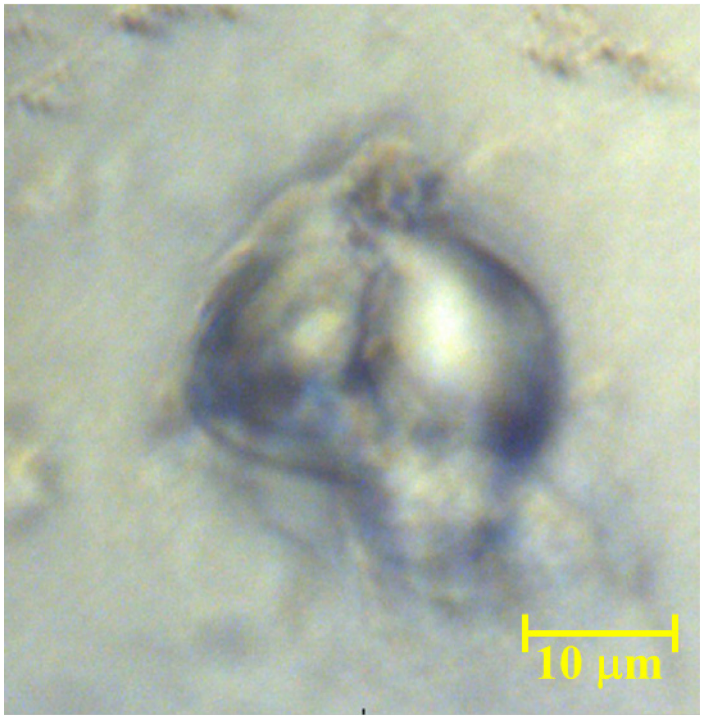

Figure A2 31: Optical micrograph of a 3T3-L1 adipocyte treated with fructose.

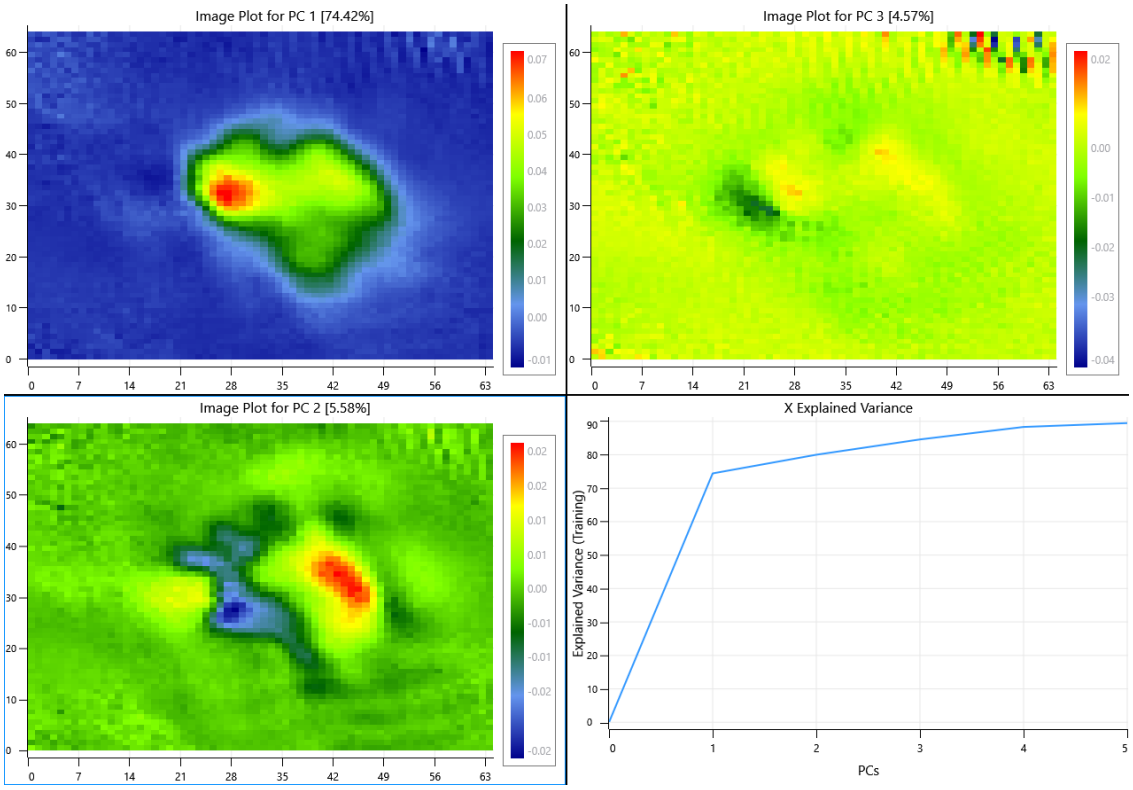

Figure A2 32: Umasked scores images of 3T3-L1 adipocyte treated with fructose and chemically fixed to a 0.5 mm CaF_2 substrate; a) PC1 scores image; b) PC2 scores image; c) PC3 scores image; and d) X-explained variance plot.

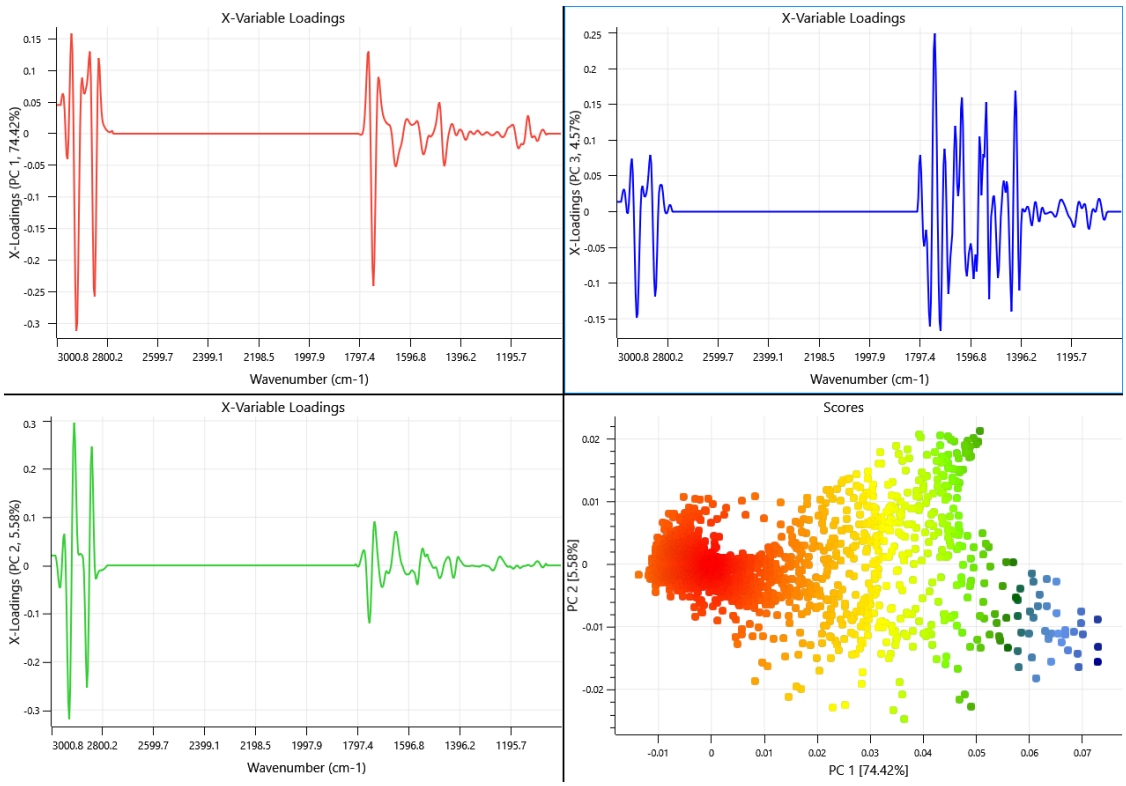

Figure A2 33: Unmasked image loadings: a) PC1 loadings; b) PC2 loadings; c) PC2 loadings; and d) scores density map of 3T3-L1 cell treated with fructose and chemically fixed to a CaF_2 substrate.

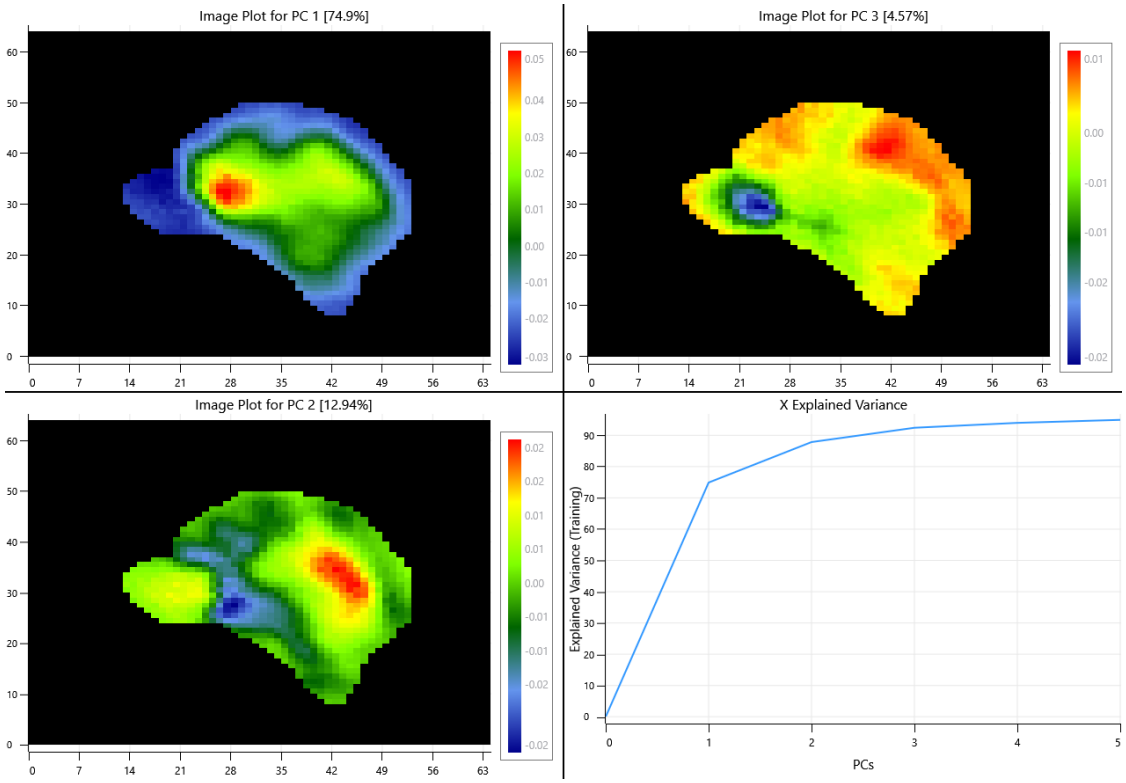

Figure A2 34: Masked scores images of 3T3-L1 adipocyte treated with fructose and chemically fixed to a 0.5 mm CaF_2 substrate; a) PC1 scores image; b) PC2 scores image; c) PC3 scores image; and d) X-explained variance plot.

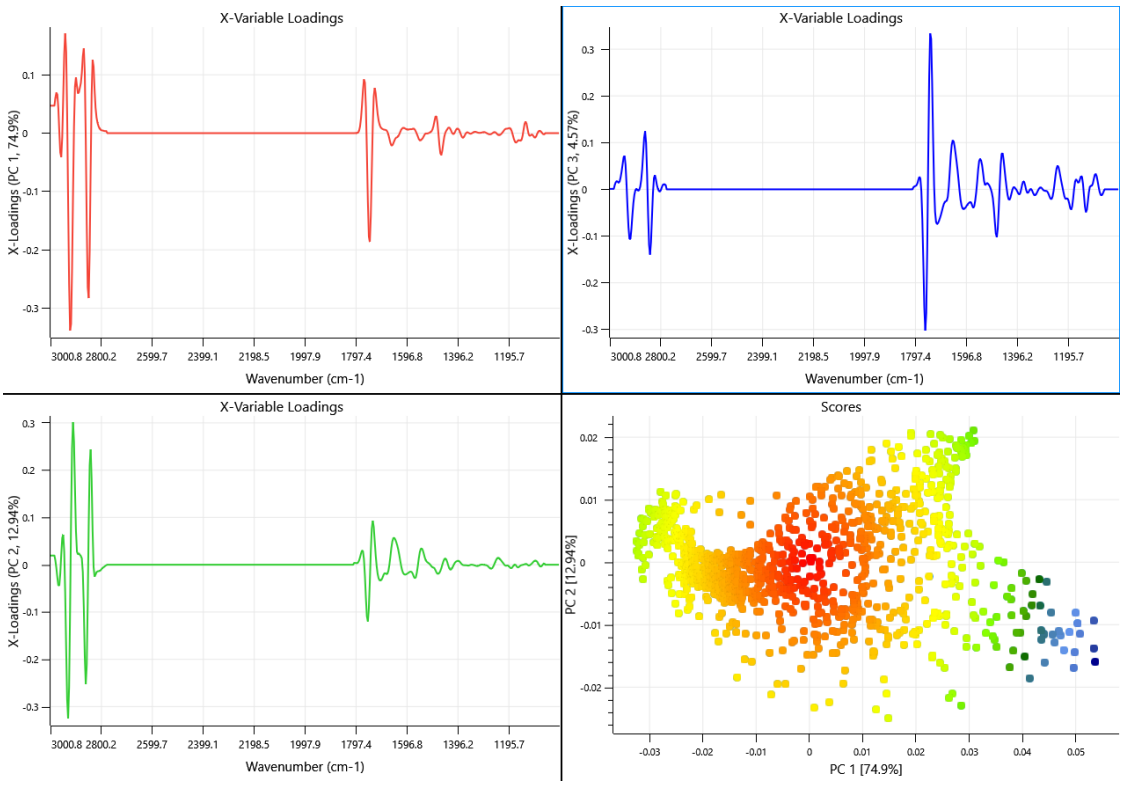

Figure A2 35: Masked image loadings: a) PC1 loadings; b) PC2 loadings; c) PC2 loadings; and d) scores density map of 3T3-L1 cell treated with fructose and chemically fixed to a CaF_2 substrate.

A2-8 Glucose-Fructose treated 3T3-L1 adipocyte fixed to a 0.5 mm CaF_2 Substrate.

Figure A2 36: Optical micrograph of a 3T3-L1 adipocyte treated with glucose and fructose.

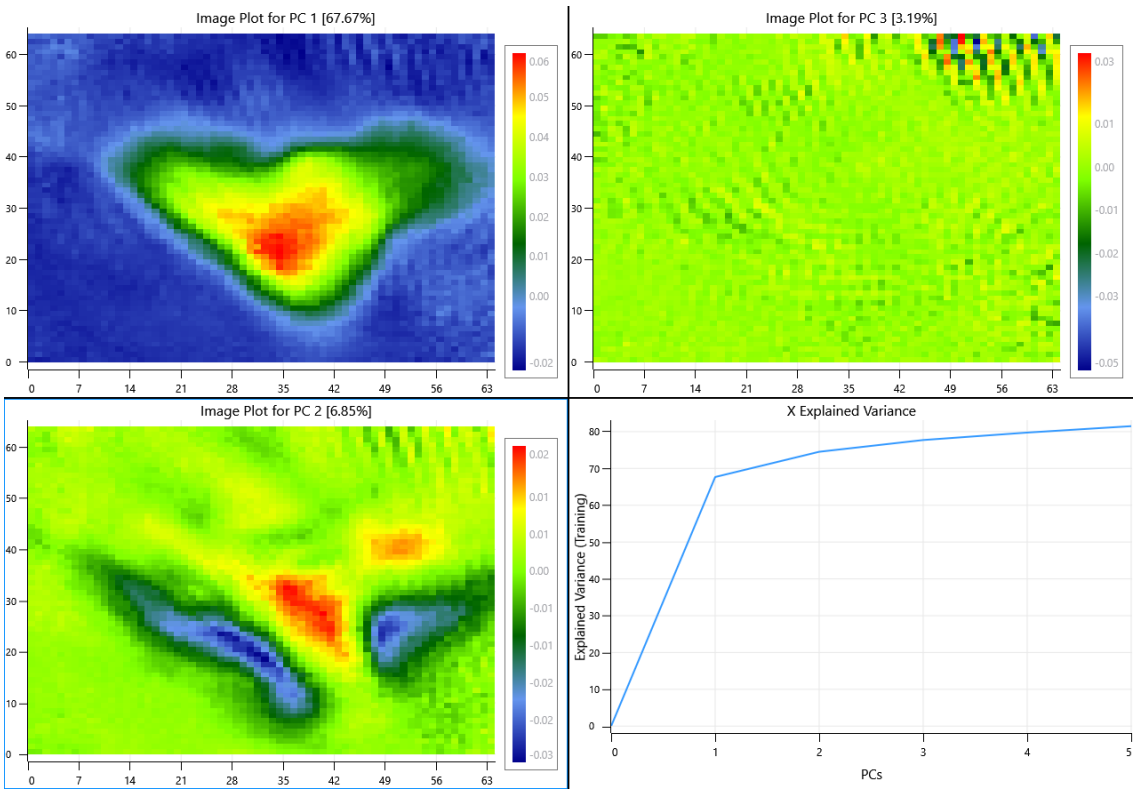

Figure A2 37: Umasked scores images of 3T3-L1 adipocyte treated with glucose and fructose and chemically fixed to a 0.5 mm CaF_2 substrate; a) PC1 scores image; b) PC2 scores image; c) PC3 scores image; and d) X-explained variance plot.

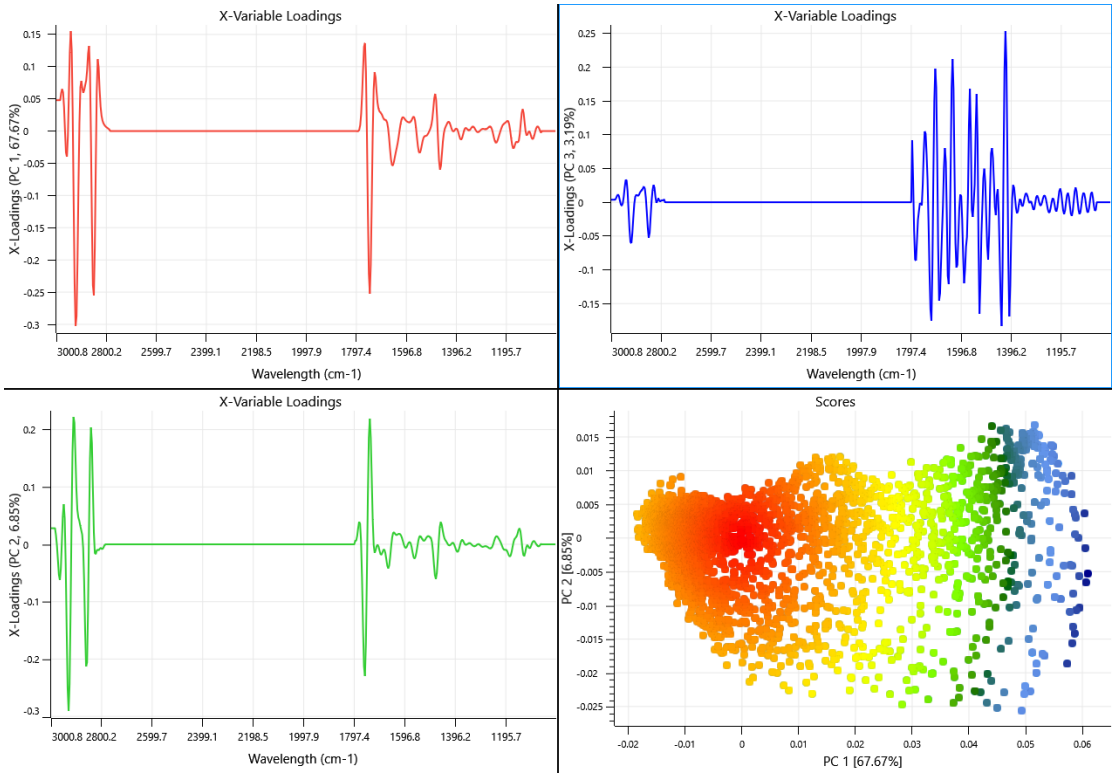

Figure A2 38: Unmasked image loadings: a) PC1 loadings; b) PC2 loadings; c) PC2 loadings; and d) scores density map of 3T3-L1 cell treated with glucose and fructose and chemically fixed to a CaF_2 substrate.

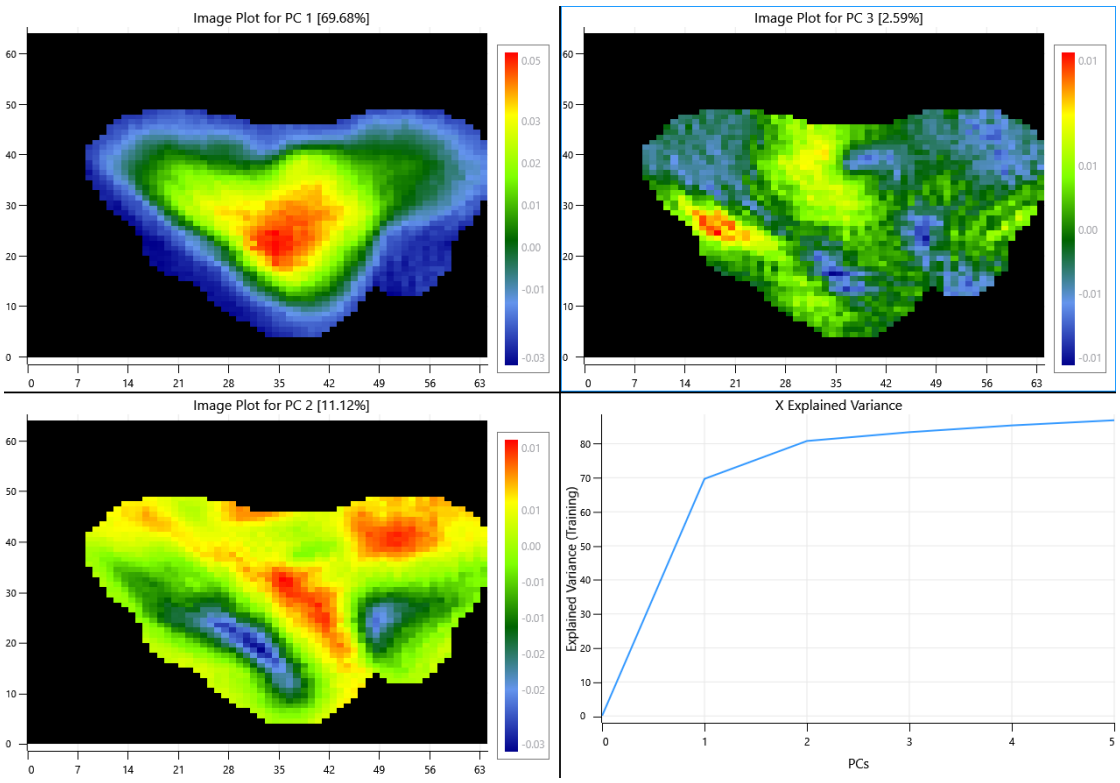

Figure A2 39: Masked scores images of 3T3-L1 adipocyte treated with glucose and fructose and chemically fixed to a 0.5 mm CaF_2 substrate; a) PC1 scores image; b) PC2 scores image; c) PC3 scores image; and d) X-explained variance plot.

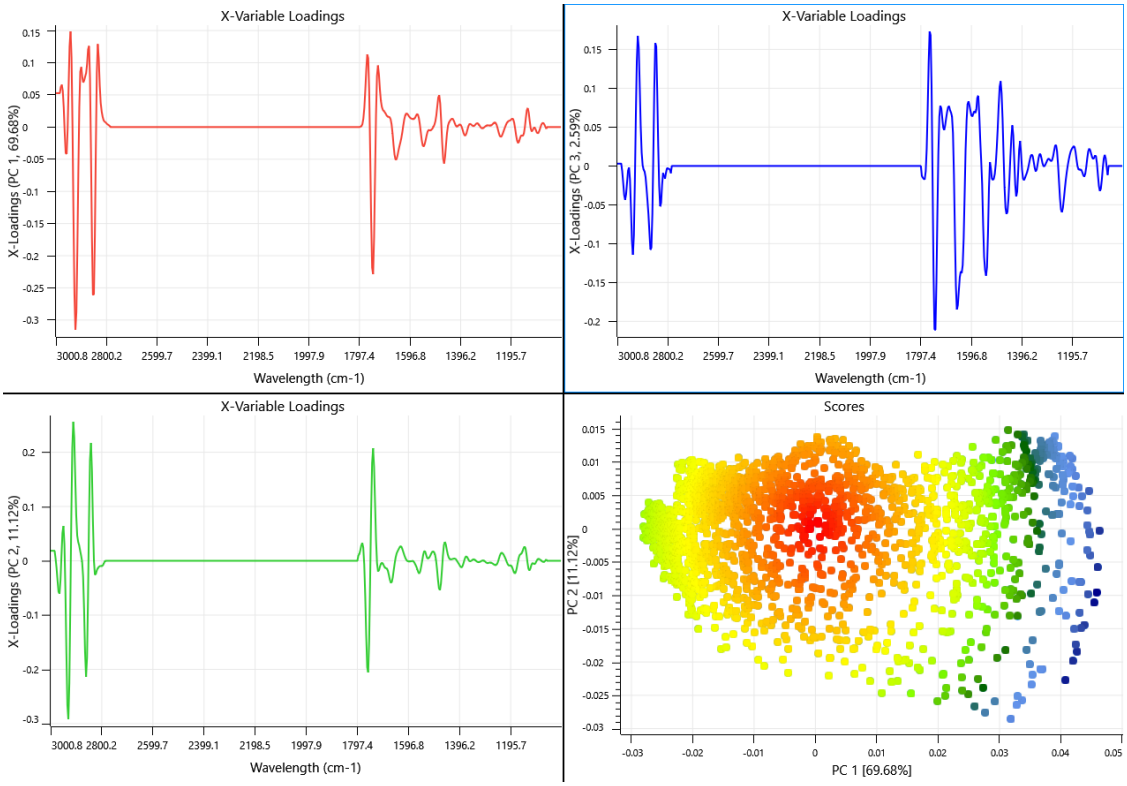

Figure A2 40: Masked image loadings: a) PC1 loadings; b) PC2 loadings; c) PC2 loadings; and d) scores density map of 3T3-L1 cell treated with glucose and fructose and chemically fixed to a CaF_2 substrate.

A2-9 No sugar treated 3T3-L1 adipocyte fixed to a 1.0 mm CaF_2 Substrate.

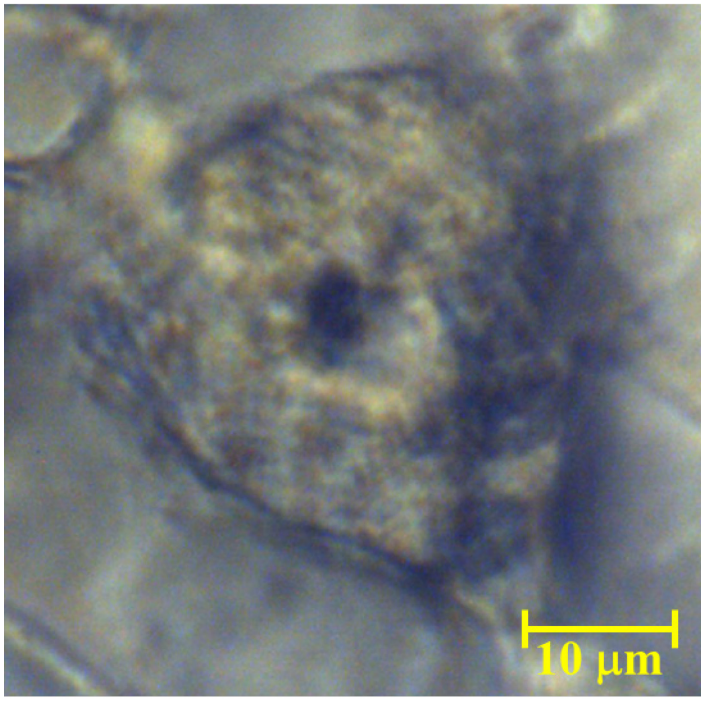

Figure A2 41: Optical micrograph of a 3T3-L1 adipocyte treated with no sugar.

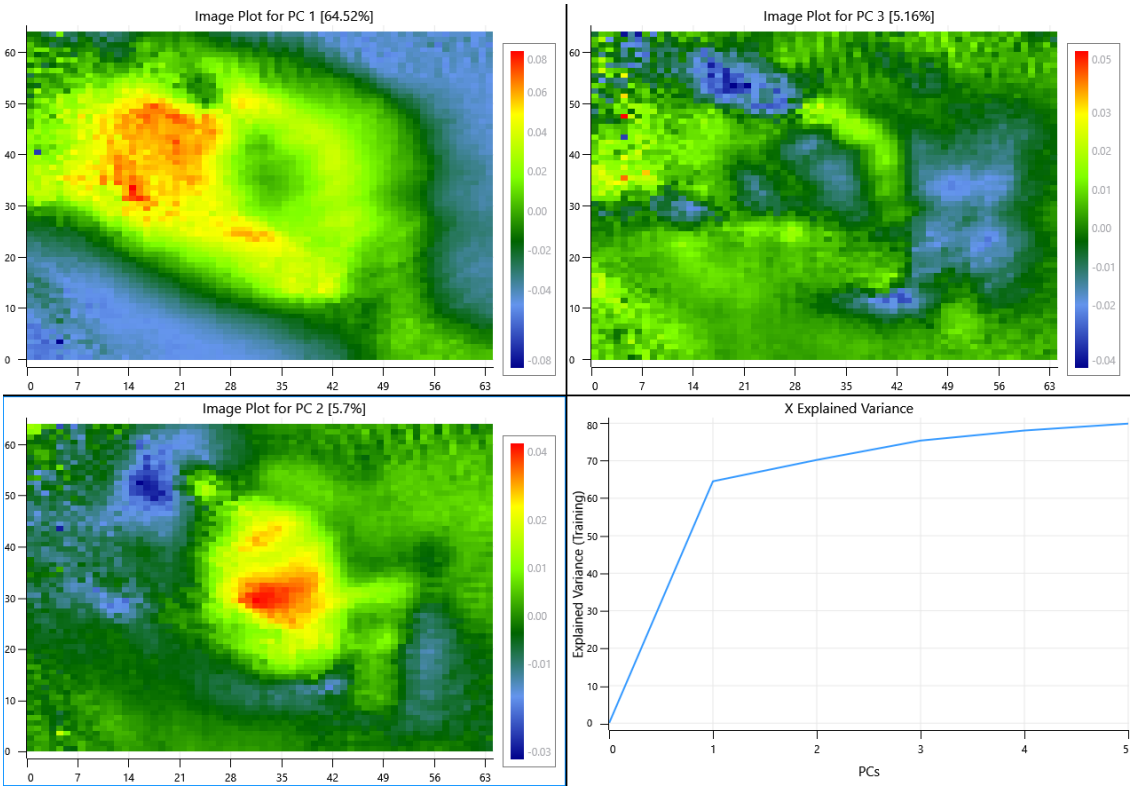

Figure A2 42: Umasked scores images of 3T3-L1 adipocyte treated with no sugar and chemically fixed to a 1.0 mm CaF_2 substrate; a) PC1 scores image; b) PC2 scores image; c) PC3 scores image; and d) X-explained variance plot.

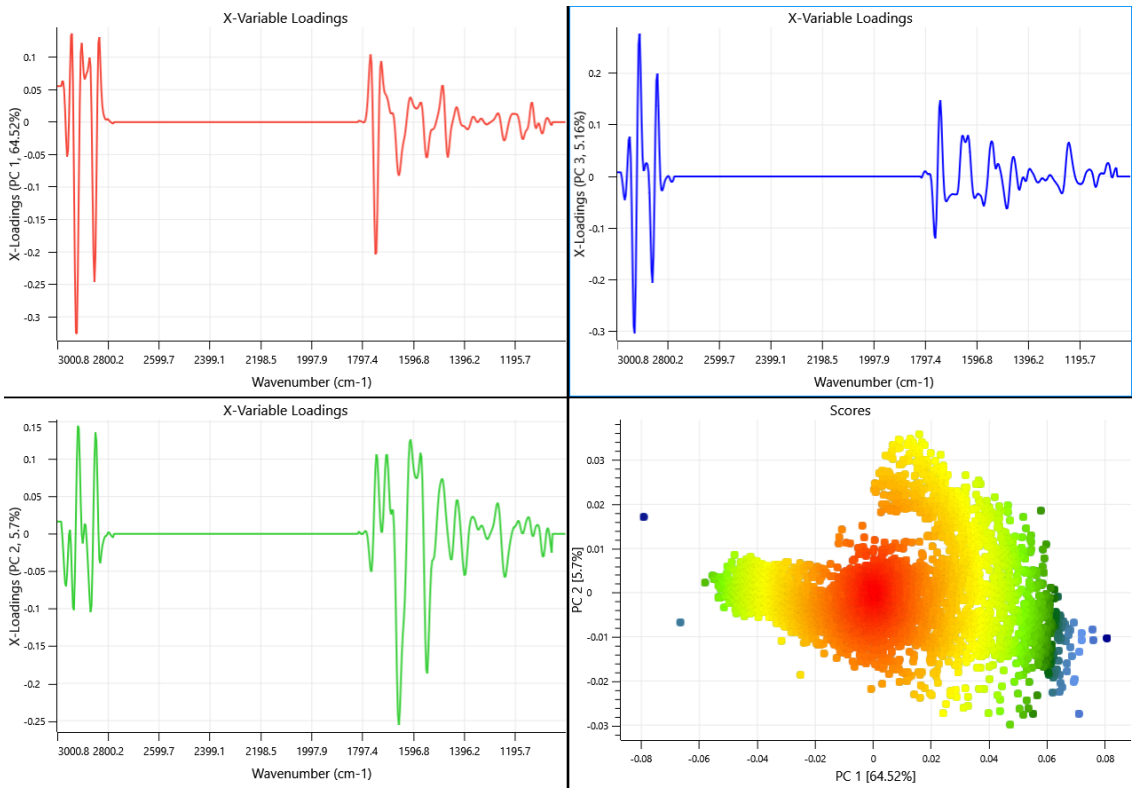

Figure A2 43: Unmasked image loadings: a) PC1 loadings; b) PC2 loadings; c) PC2 loadings; and d) scores density map of 3T3-L1 cell treated with no sugar and chemically fixed to a CaF_2 substrate.

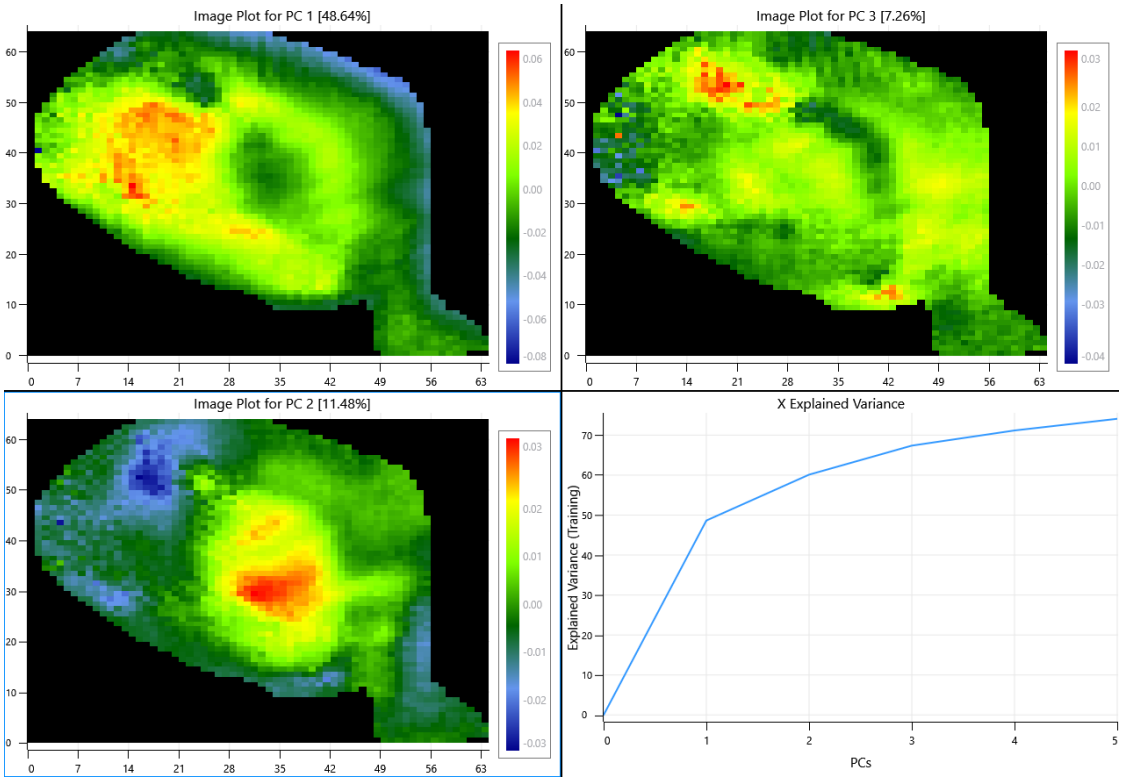

Figure A2 44: Masked scores images of 3T3-L1 adipocyte treated with no sugar and chemically fixed to a 1.0 mm CaF_2 substrate; a) PC1 scores image; b) PC2 scores image; c) PC3 scores image; and d) X-explained variance plot.

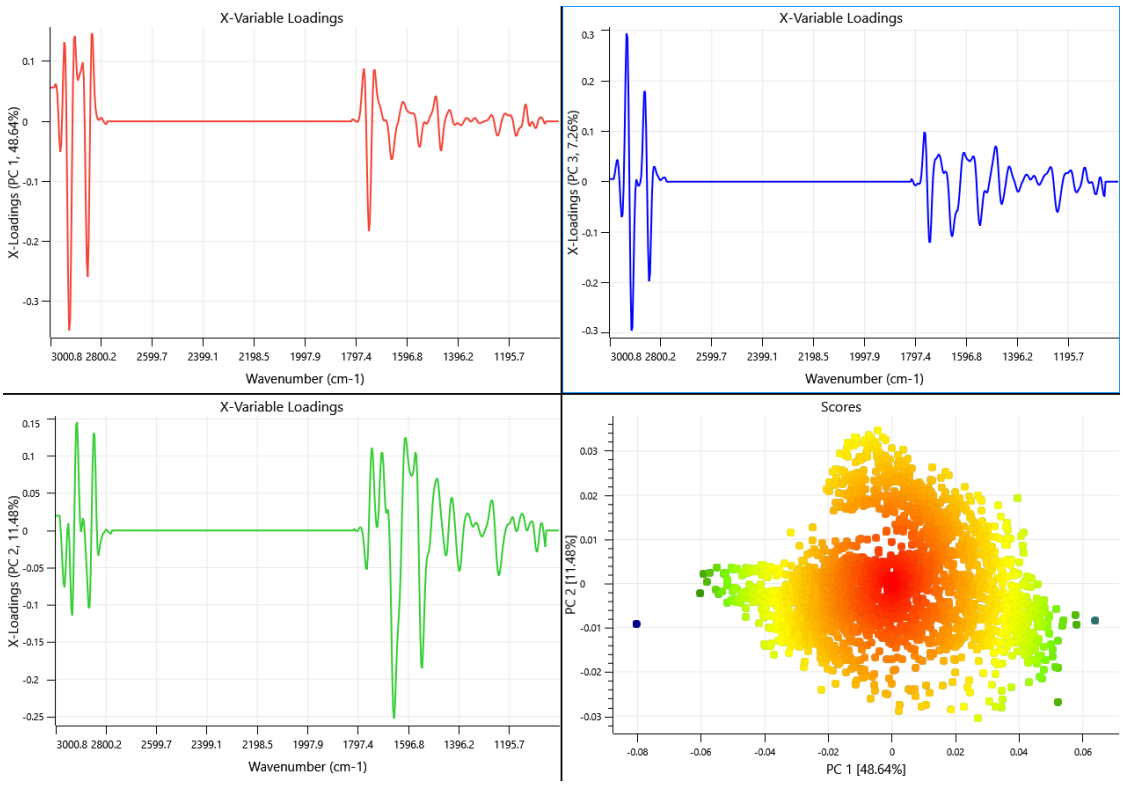

Figure A2 45: Masked image loadings: a) PC1 loadings; b) PC2 loadings; c) PC2 loadings; and d) scores density map of 3T3-L1 cell treated with no sugar and chemically fixed to a CaF_2 substrate.

A2-10 Glucose treated 3T3-L1 adipocyte fixed to a 1.0 mm CaF_2 Substrate.

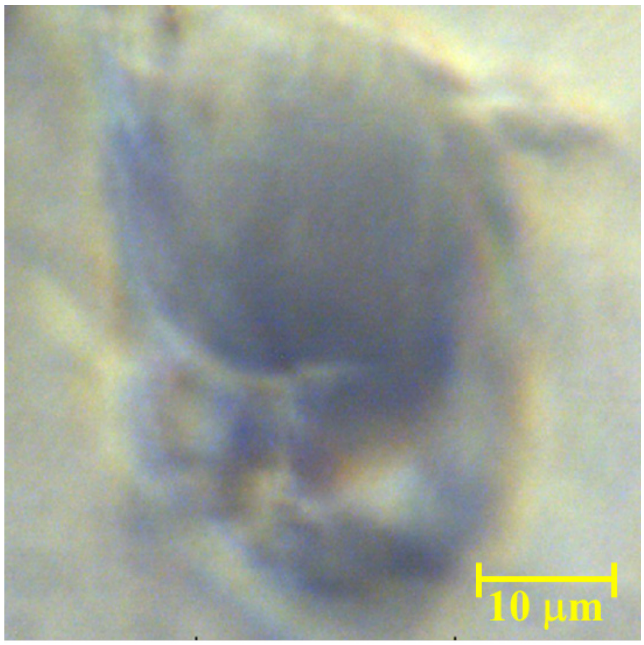

Figure A2 46: Optical micrograph of a 3T3-L1 adipocyte treated with glucose.

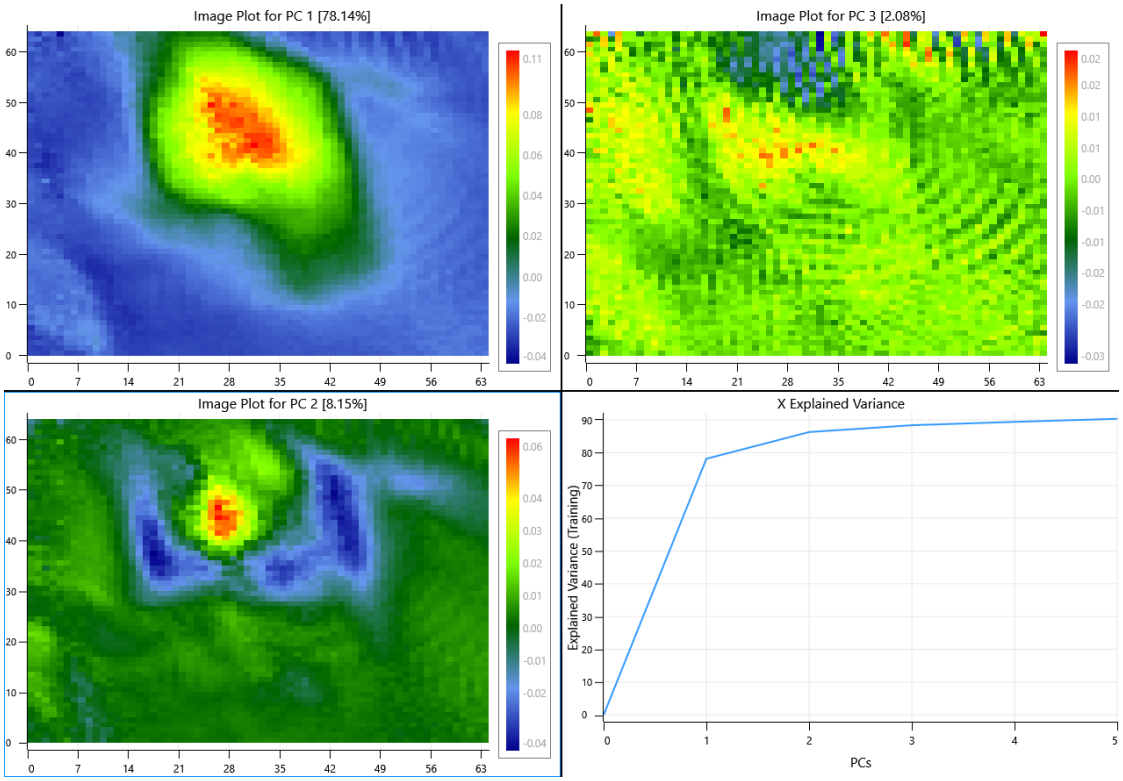

Figure A2 47: Umasked scores images of 3T3-L1 adipocyte treated with glucose and chemically fixed to a 1.0 mm CaF_2 substrate; a) PC1 scores image; b) PC2 scores image; c) PC3 scores image; and d) X-explained variance plot.

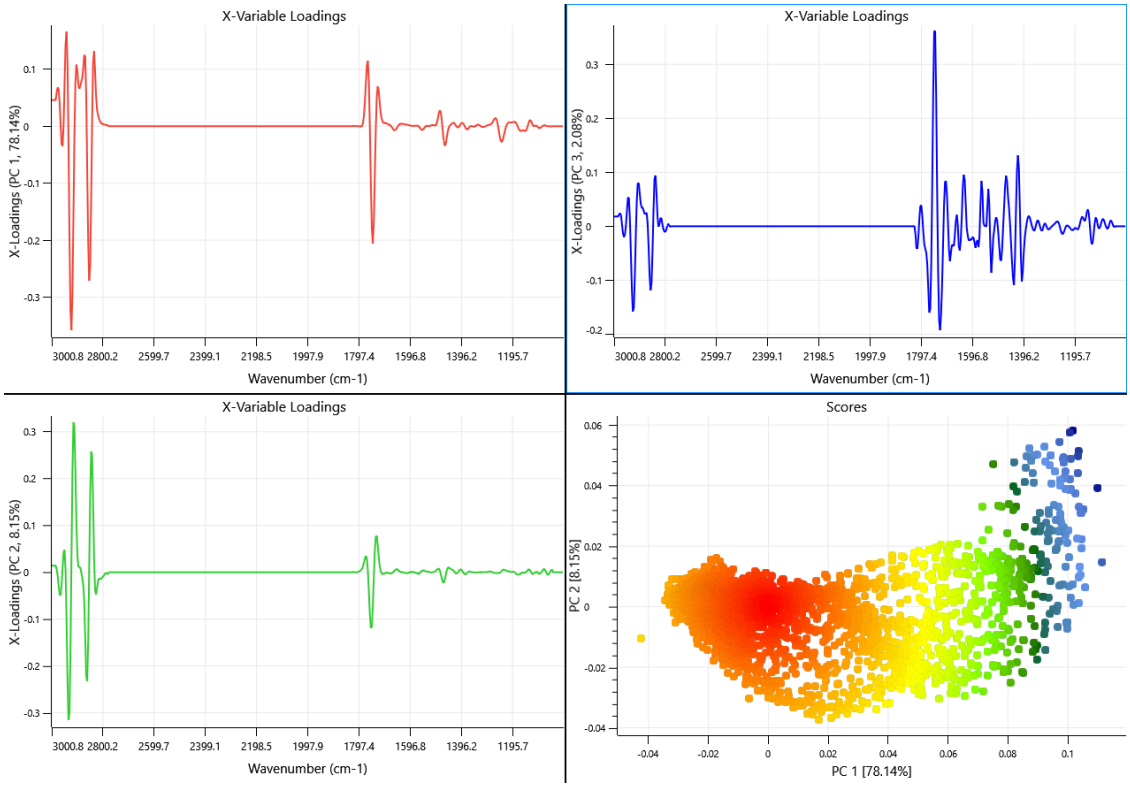

Figure A2 48: Unmasked image loadings: a) PC1 loadings; b) PC2 loadings; c) PC2 loadings; and d) scores density map of 3T3-L1 cell treated with glucose and chemically fixed to a CaF_2 substrate.

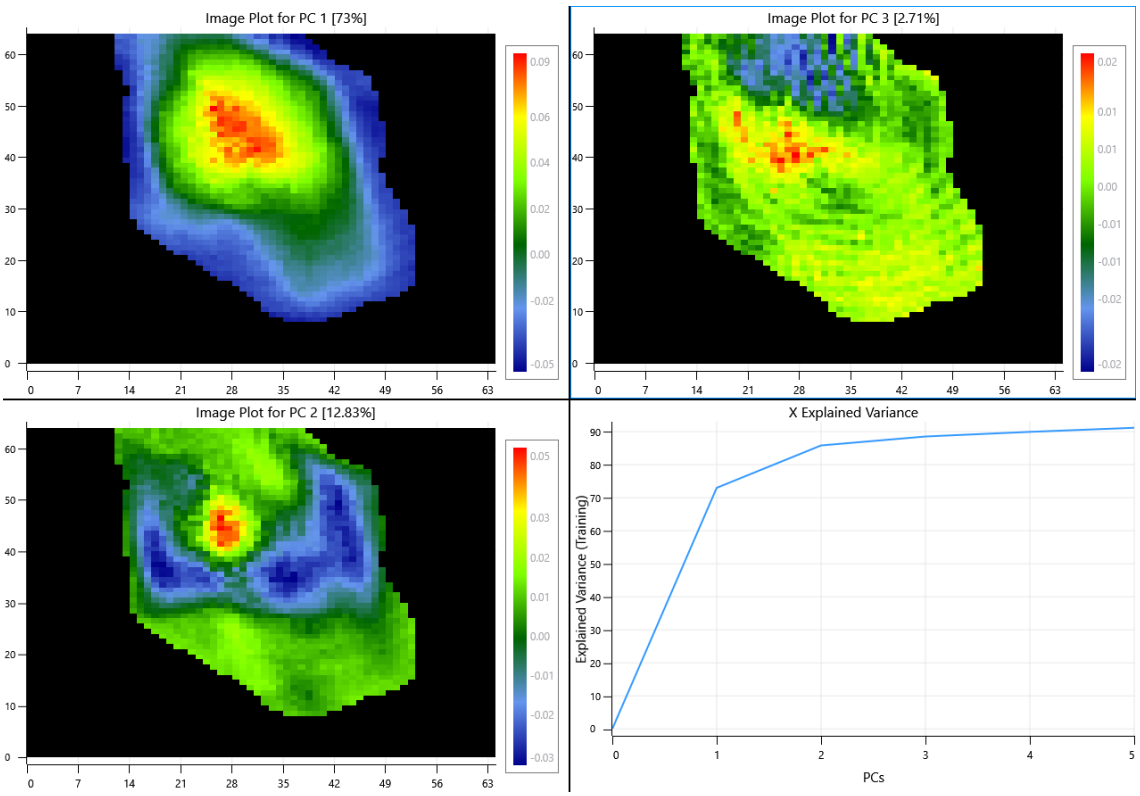

Figure A2 49: Masked scores images of 3T3-L1 adipocyte treated with glucose and chemically fixed to a 1.0 mm CaF_2 substrate; a) PC1 scores image; b) PC2 scores image; c) PC3 scores image; and d) X-explained variance plot.

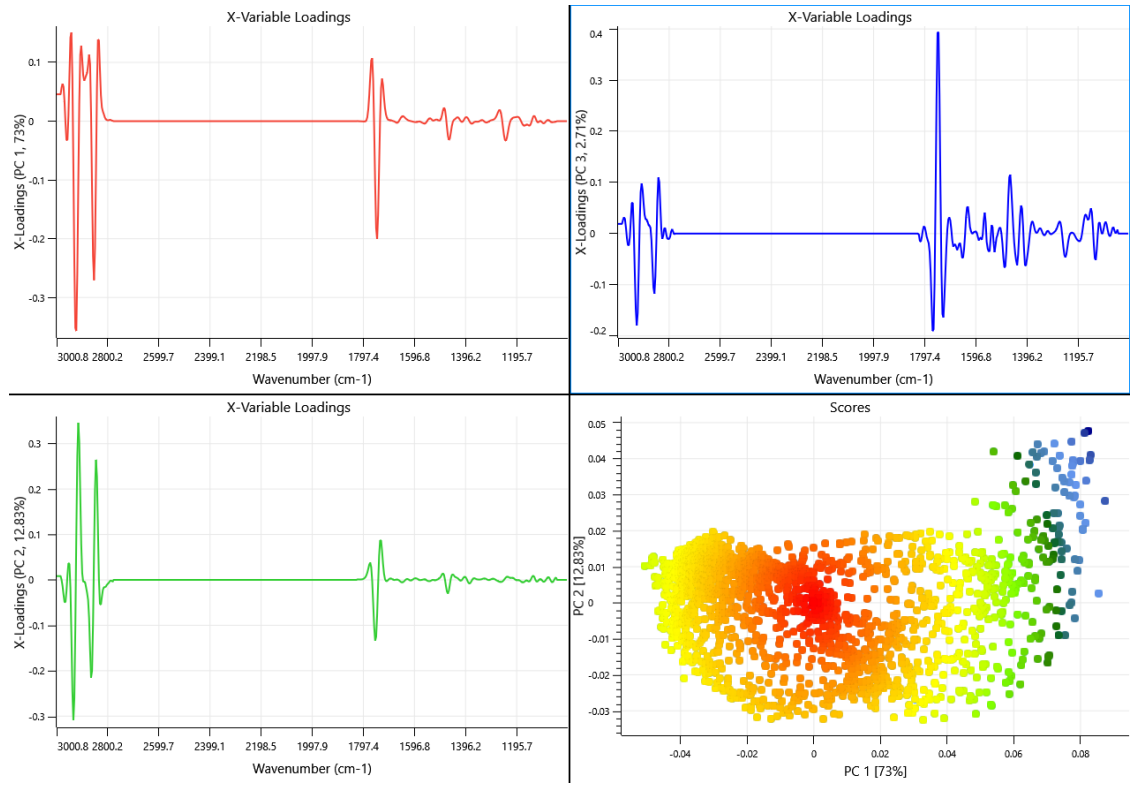

Figure A2 50: Masked image loadings: a) PC1 loadings; b) PC2 loadings; c) PC2 loadings; and d) scores density map of 3T3-L1 cell treated with glucose and chemically fixed to a CaF_2 substrate.

A2-11 Fructose treated 3T3-L1 adipocyte fixed to a 1.0 mm CaF_2 Substrate.

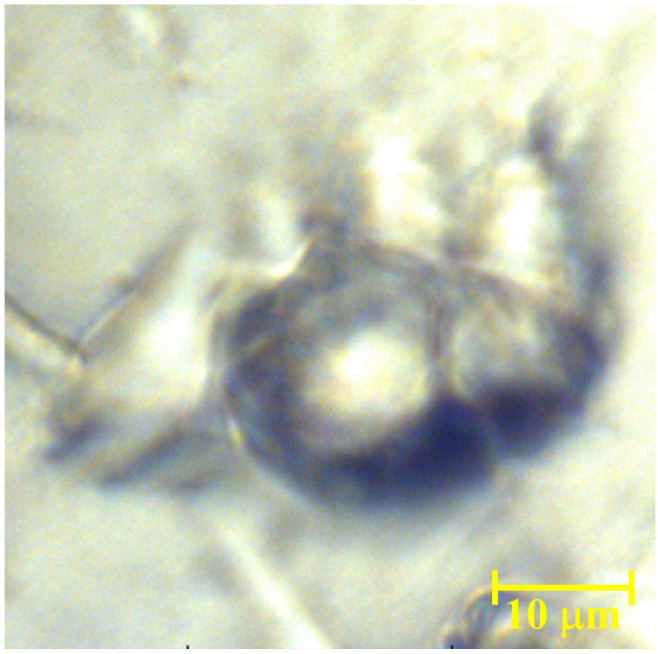

Figure A2 51: Optical micrograph of a 3T3-L1 adipocyte treated with fructose.

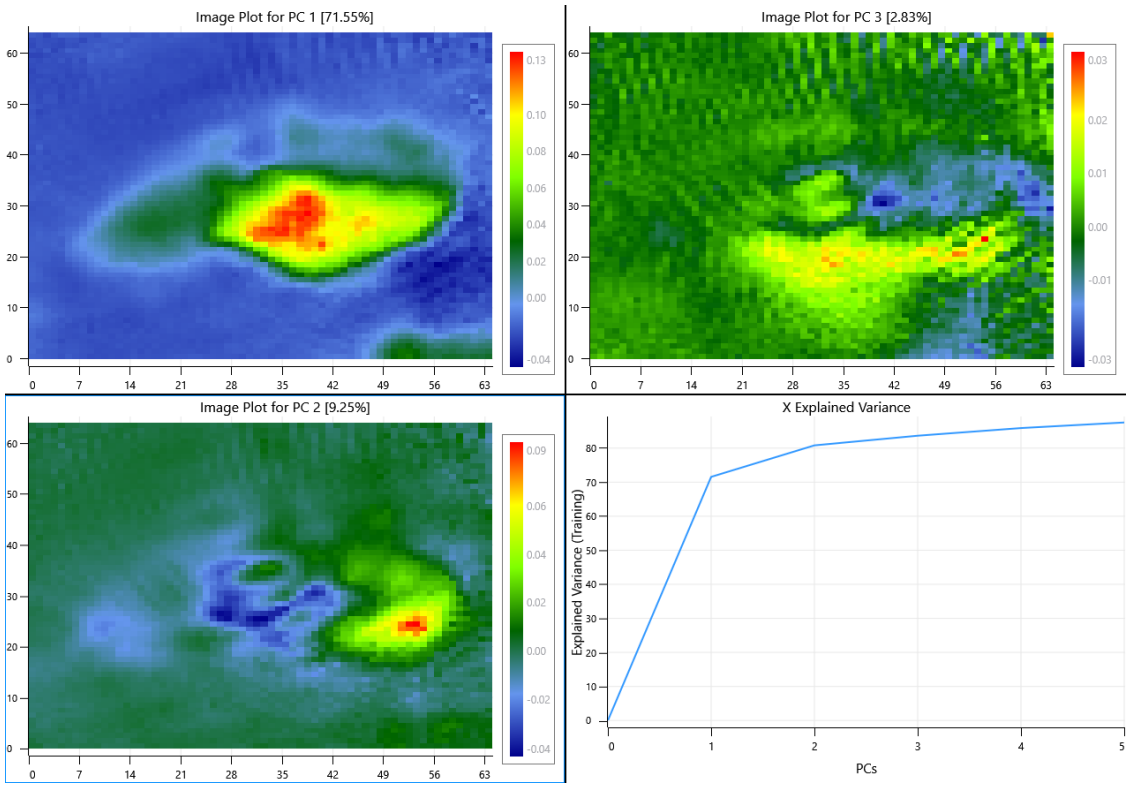

Figure A2 52: Umasked scores images of 3T3-L1 adipocyte treated with fructose and chemically fixed to a 1.0 mm CaF_2 substrate; a) PC1 scores image; b) PC2 scores image; c) PC3 scores image; and d) X-explained variance plot.

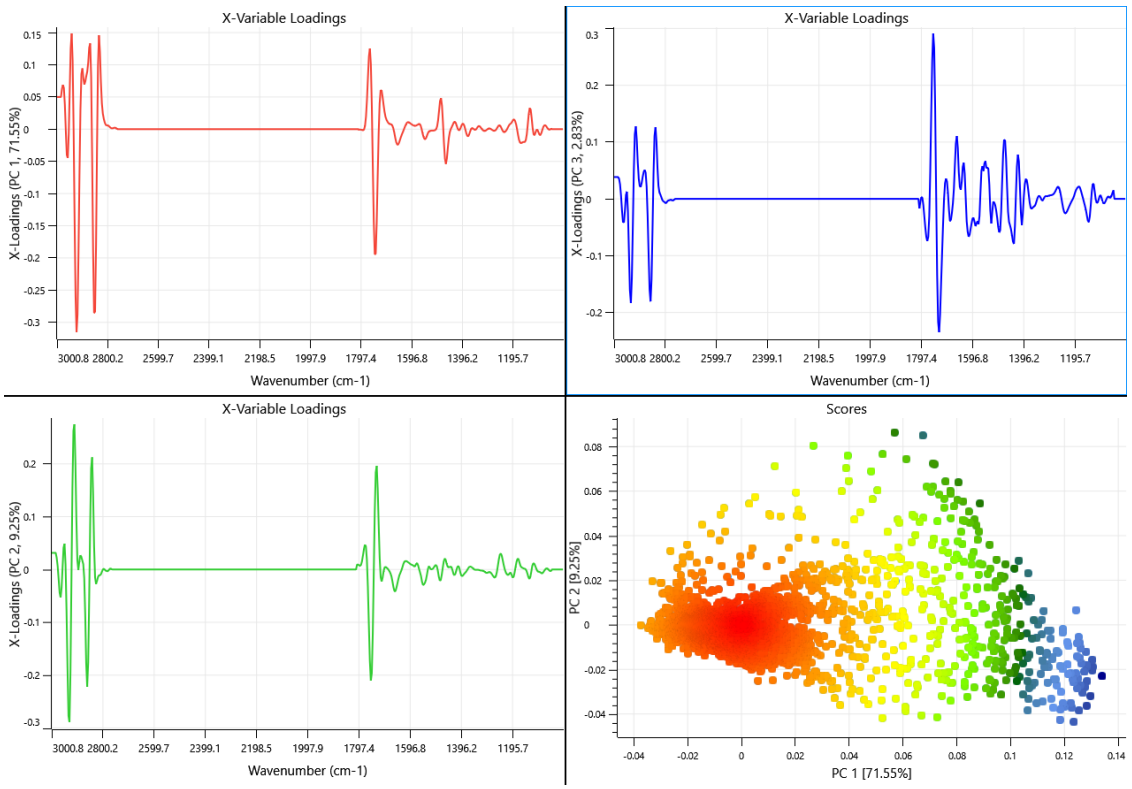

Figure A2 53: Unmasked image loadings: a) PC1 loadings; b) PC2 loadings; c) PC2 loadings; and d) scores density map of 3T3-L1 cell treated with fructose and chemically fixed to a CaF_2 substrate.

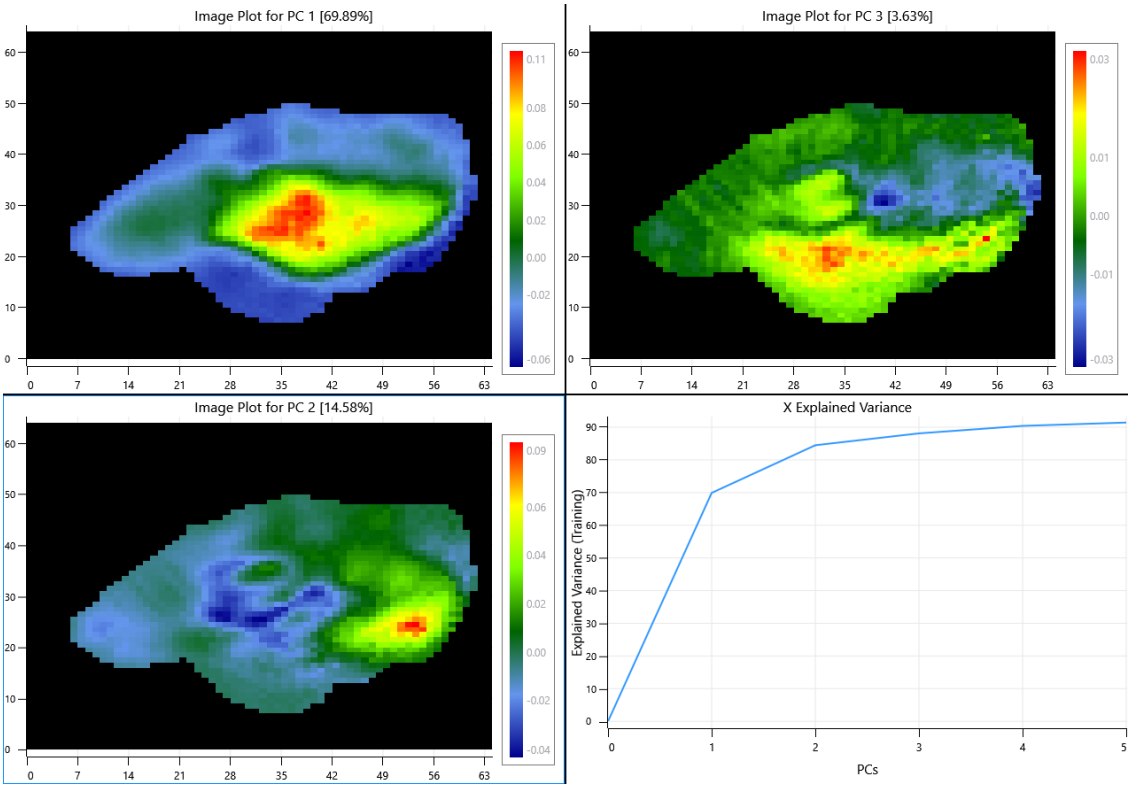

Figure A2 54: Masked scores images of 3T3-L1 adipocyte treated with fructose and chemically fixed to a 1.0 mm CaF_2 substrate; a) PC1 scores image; b) PC2 scores image; c) PC3 scores image; and d) X-explained variance plot.

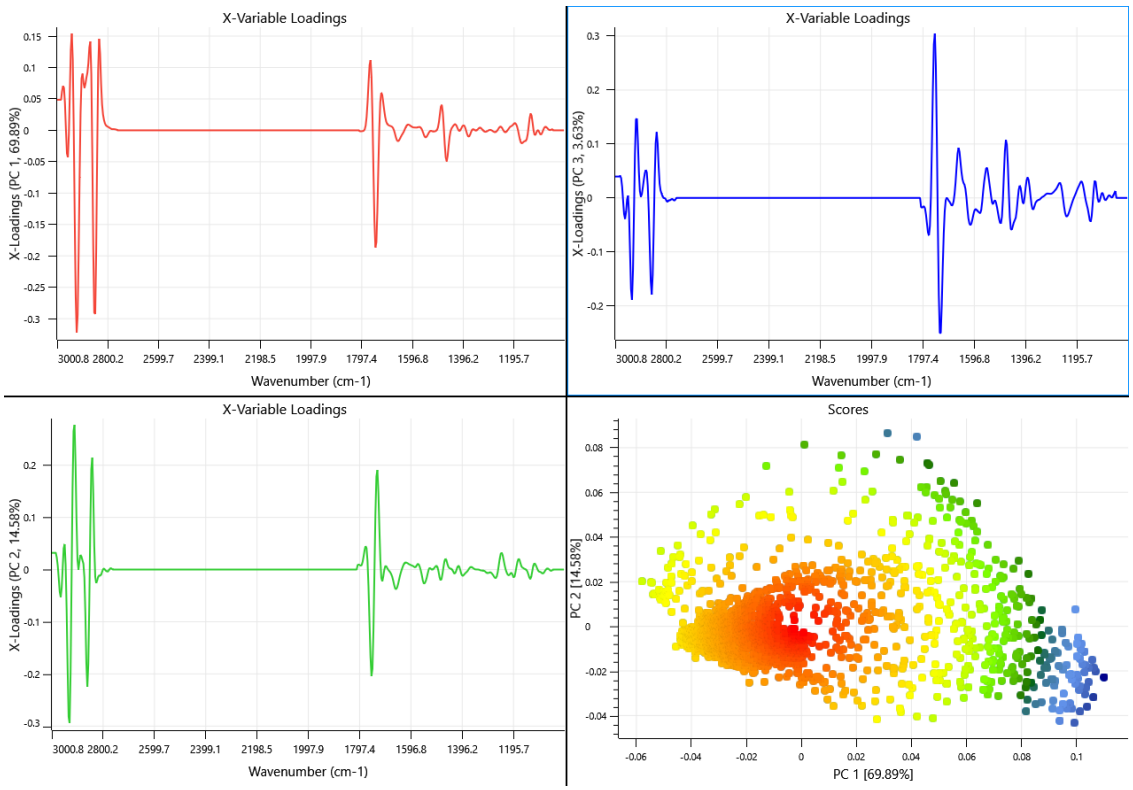

Figure A2 55: Masked image loadings: a) PC1 loadings; b) PC2 loadings; c) PC2 loadings; and d) scores density map of 3T3-L1 cell treated with fructose and chemically fixed to a CaF_2 substrate.

A2-12 Glucose-fructose treated 3T3-L1 adipocyte fixed to a 1.0 mm CaF_2 Substrate.

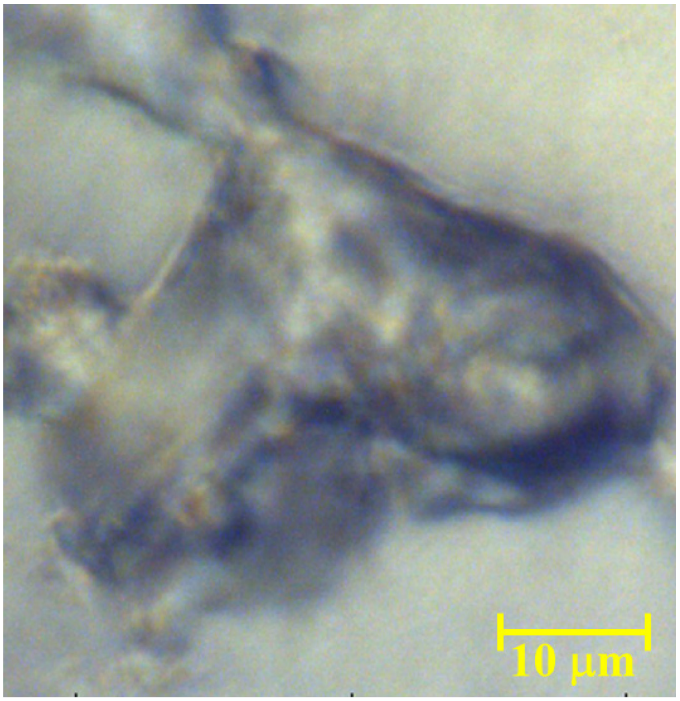

Figure A2 56: Optical micrograph of a 3T3-L1 adipocyte treated with glucose and fructose.

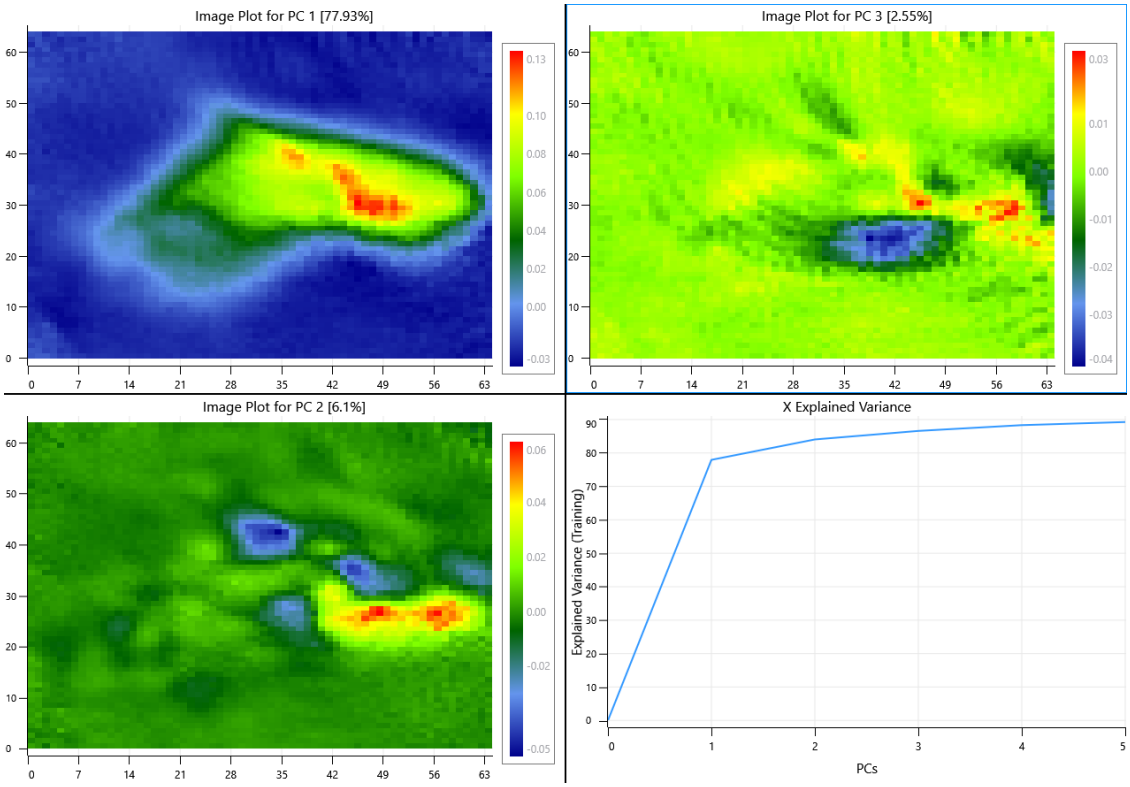

Figure A2 57: Umasked scores images of 3T3-L1 adipocyte treated with glucose and fructose and chemically fixed to a 1.0 mm CaF_2 substrate; a) PC1 scores image; b) PC2 scores image; c) PC3 scores image; and d) X-explained variance plot.

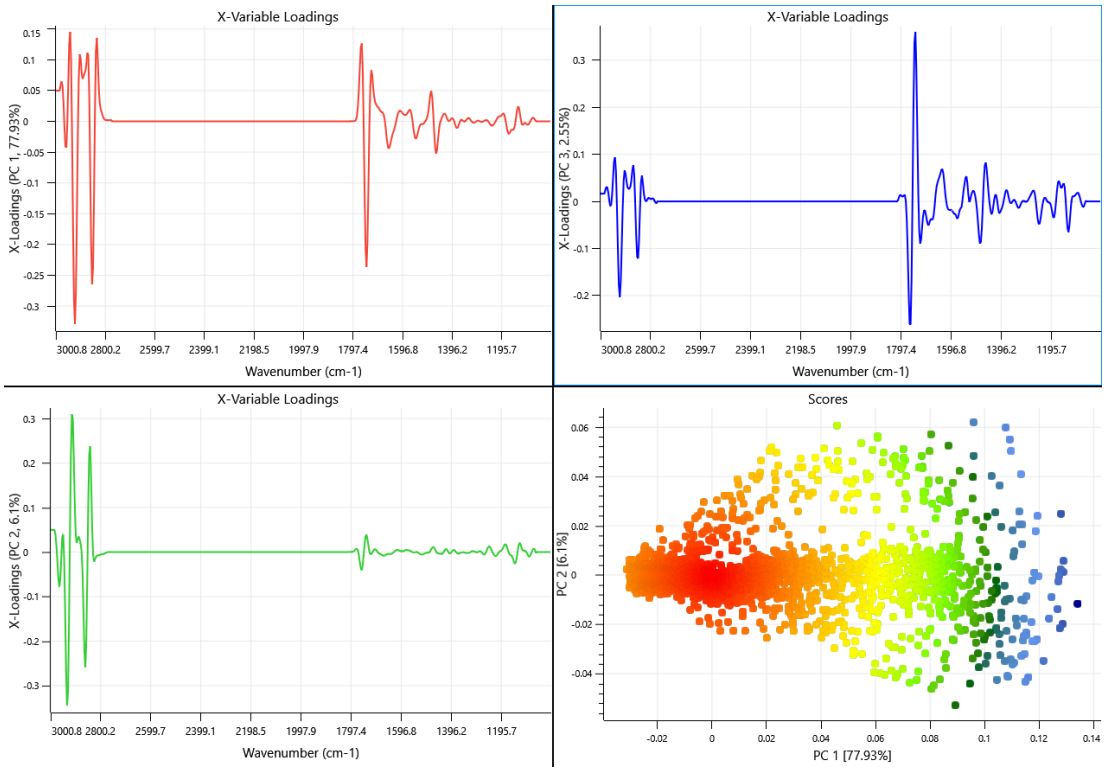

Figure A2 58: Unmasked image loadings: a) PC1 loadings; b) PC2 loadings; c) PC2 loadings; and d) scores density map of 3T3-L1 cell treated with glucose and fructose and chemically fixed to a CaF_2 substrate.

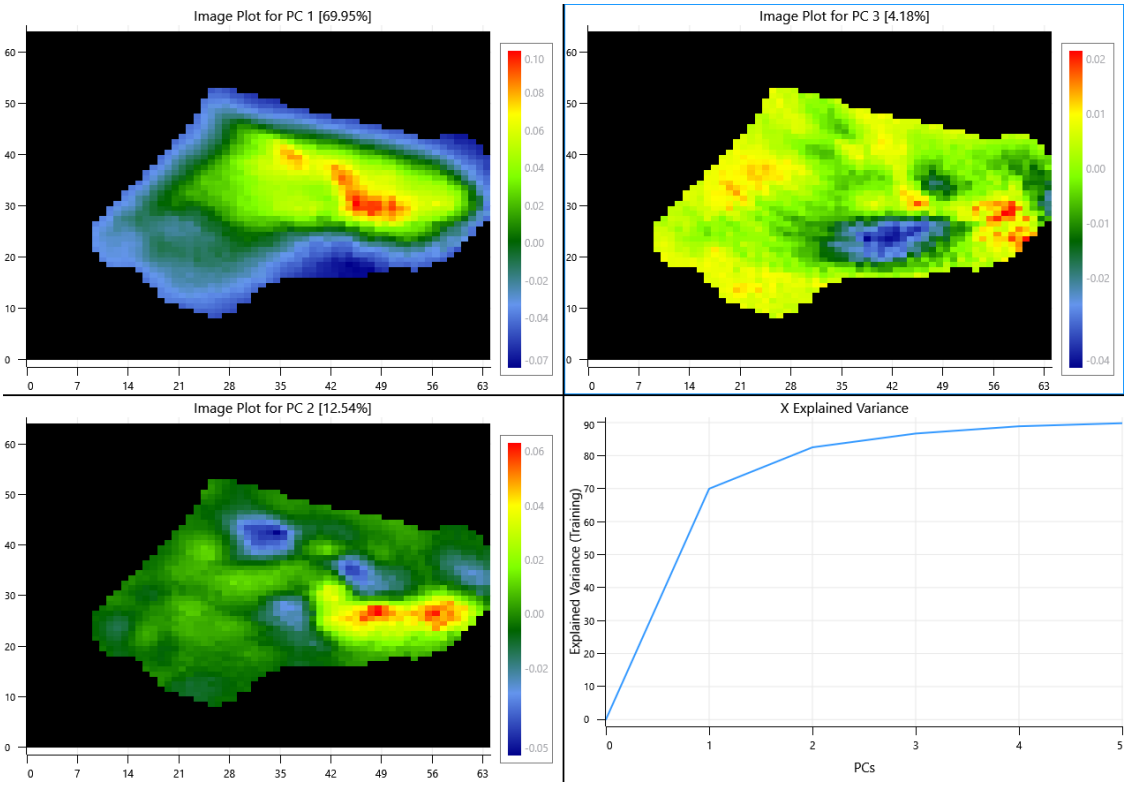

Figure A2 59: Masked scores images of 3T3-L1 adipocyte treated with glucose and fructose and chemically fixed to a 1.0 mm CaF_2 substrate; a) PC1 scores image; b) PC2 scores image; c) PC3 scores image; and d) X-explained variance plot.

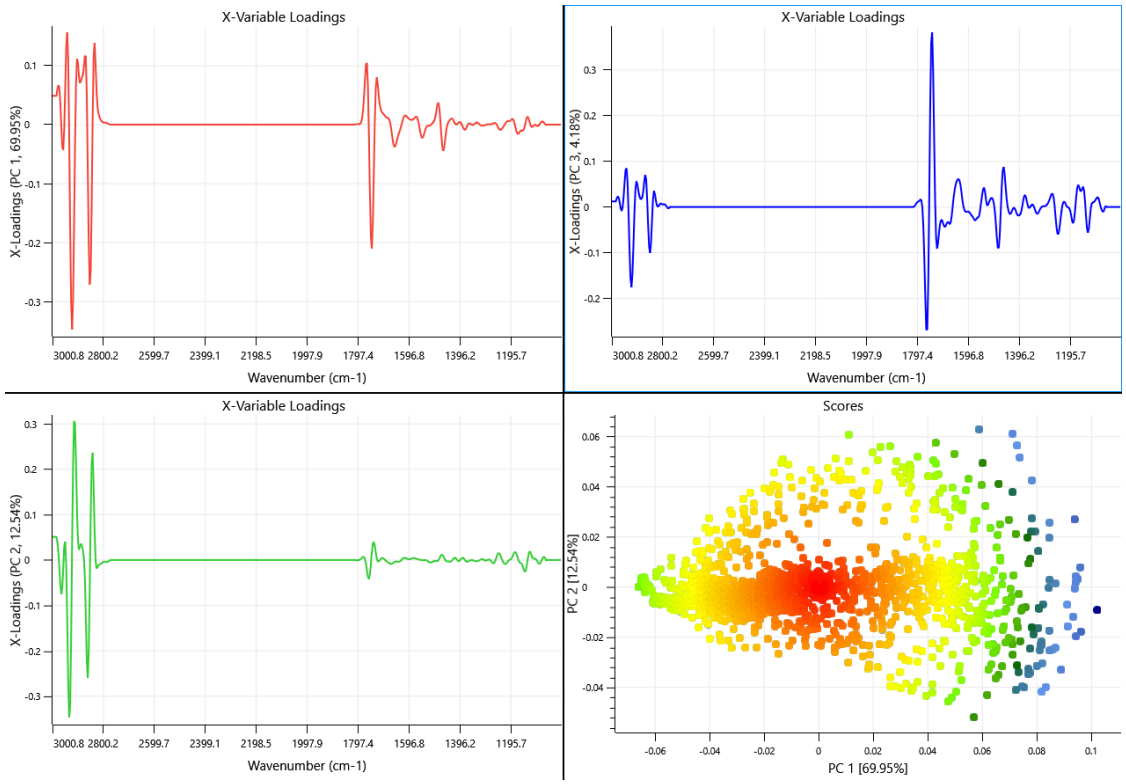

Figure A2 60: Masked image loadings: a) PC1 loadings; b) PC2 loadings; c) PC2 loadings; and d) scores density map of 3T3-L1 cell treated with glucose and fructose and chemically fixed to a CaF_2 substrate.